Ferdowsi University of Mashhad

Journal of Agricultural Machinery

Iranian Society of Mechanical Engineers (ISME)

Vol. 16 No. 3

2026

ISSN: 2228-6829

Contents

Research Articles

An Assessment of the Potential of Multispectral Sentinel-2 Satellite Imagery for Detecting Dubas Bug Infestations in Date Palm Cultivation Regions 365
H. Karimi, M. J. Assari, H. Zohdi, F. Ranjbar-Varandi

Optimization of Energy Use in Pinto Bean Planting Systems: A Multi-Objective Genetic Algorithm Approach 383
R. Raeisi, M. Gholami Parashkoohi, H. Afshari, A. Mohammadi

Modification and Analysis of Integrated Enset (*Ensete ventricosum*) Processing Machine Components 399
B. Adugna, K. Purushottam Kolhe, M. Gutu

Assessing Viscosity and Contaminant Levels in Diesel Lubricant through Dielectric Spectroscopy Utilizing Soft Computing Approaches 427
M. R. Pourramezan, A. Rohani, M. H. Abbaspour-Fard

Investigating the Rates, Severity and Affecting Factors of Accidents Related to Agricultural Tractors and Grain Combine Harvesters in Ilam Province of Iran 449
J. Allahnouri, A. Marzban, M. Ghasemi-Nejad-Raeini, M. Rahnama, M. Savari

Predicting Vitamin C and Color Change of Orange Powder in Four Dryers Using an Electronic Nose 469
M. Roshan Moghadam, R. Amiri Chayjan, N. Aghilinategh

A Weighted Group Learning Model for Classification of Grape Leaf Disease Using Image Processing and Machine Learning 487
M. Najafabadiha, D. Mohammad Zamani, M. Gholami Par-Shokohi

Assessing the Influence of Copper Oxide Nanoparticles Combined with Distilled Water on PVT System Performance 507
M. Ghaderi, P. Salami, H. Samimi-Akhijahani, S. Zareei, M. Safvati

Optimization of the Canola Harvester Blade Based on Energy Reduction Approach and Life Cycle Assessment 525
Gh. Ahmadzade, M. R. Maleki, P. Salami, K. Mollazade

Physical Property Characterization of Ethiopian Maize Varieties for Adaptive Multi-Crop Planter Design 549
D. Girma Gadisa, K. Purushottam Kolhe, S. Kedir Busse, M. Mohammed Issa, T. Aseffa Abeye, D. Alemu Anawte

Feasibility of Detecting Different Genotypes of *Mentha* plant by E-nose Technique 563
H. Zaki Dizaji, M. Mahmoodi Surestani, N. Aghilinategh, A. Boveiri Dehsheikh

Comparative Modeling of Drying Kinetics for Potato Slices: AI-Based vs. Empirical and Semi-Empirical Approaches 579
R. Raeesi, M. Moradi, A. Dehghani

Review Article

A Review on the Physicomechanical Properties of Polysaccharide-Based Edible Films Incorporating Essential Oil-Loaded Pickering Emulsions 599
H. Mirzaee Moghaddam, A. Nahalkar, A. Rajaei

Journal of Agricultural Machinery

Vol. 16 **No. 3** **2026**

Published by: Ferdowsi University of Mashhad, (College of Agriculture), Iran

Director-in-Charge: Prof. M. R. Modarres Razavi, Dept. of Mechanical Eng. Ferdowsi University of Mashhad

Editor-in-Chief: Prof. M. H. Abbaspour-Fard, Dept. of Biosystems Eng. Ferdowsi University of Mashhad

Editorial Board:

Abbaspour-Fard, M. H.	Department of Biosystems Engineering, Ferdowsi University of Mashhad, Iran
Aboonajmi, M.	Department of Agrotechnology, College of Abouraihan, University of Tehran, Tehran, Iran
Aghbashlo, M.	Department of Agricultural Machinery Engineering, Faculty of Agricultural Engineering and Technology, University of Tehran, Karaj, Iran
Aghkhani, M. H.	Department of Biosystems Engineering, Ferdowsi University of Mashhad, Iran
Alimardani, R.	Department of Agricultural Machinery Engineering, Faculty of Agricultural Engineering and Technology, University of Tehran, Karaj, Iran
Emadi, B.	Department of Chemical and Biological Engineering, University of Saskatchewan, Saskatoon, Canada
Ghazanfari Moghaddam, A.	Department of Mechanical Engineering of Biosystems, Shahid Bahonar University of Kerman, Iran
Kadkhodayan, M.	Department of Mechanical Engineering, Ferdowsi University of Mashhad, Iran
Khoshtaghaza, M. H.	Department of Biosystems Engineering, Tarbiat Modares University, Tehran. Iran
Loghavi, M.	Department of Biosystems Engineering, Shiraz University, Iran
Modarres Razavi, M.	Department of Mechanical Engineering, Ferdowsi University of Mashhad, Iran
Mohtasebi, S. S.	Department of Agricultural Machinery Engineering, Faculty of Agricultural Engineering and Technology, University of Tehran, Karaj, Iran
Nasirahmadi, A.	Department of Agricultural Engineering University of Kassel, Nordbahnhofstrasse, Witzenhausen, Germany
Raji, A.	Department of Agricultural and Environmental Engineering, Faculty of Technology, University of Ibadan, Nigeria
Rohani, A.	Department of Biosystems Engineering, Ferdowsi University of Mashhad, Iran
Saiedirad, M. H.	Agricultural Engineering Research Institute, Mashhad, Iran
Sayasoonthorn, S	Department of Farm Mechanics, Faculty of Agriculture, Kasetsart University, Thailand

Publisher: Ferdowsi University of Mashhad

Address: College of Agriculture, Ferdowsi University of Mashhad, Iran

P.O. BOX: 91775-1163

Fax: +98-05138787430

E-Mail: jame@um.ac.ir

Web Site: https://jame.um.ac.ir

Contents

Research Articles

An Assessment of the Potential of Multispectral Sentinel-2 Satellite Imagery for Detecting Dubas Bug Infestations in Date Palm Cultivation Regions 365
H. Karimi, M. J. Assari, H. Zohdi, F. Ranjbar-Varandi

Optimization of Energy Use in Pinto Bean Planting Systems: A Multi-Objective Genetic Algorithm Approach 383
R. Raeisi, M. Gholami Parashkoohi, H. Afshari, A. Mohammadi

Modification and Analysis of Integrated Enset (*Ensete ventricosum*) Processing Machine Components 399
B. Adugna, K. Purushottam Kolhe, M. Gutu

Assessing Viscosity and Contaminant Levels in Diesel Lubricant through Dielectric Spectroscopy Utilizing Soft Computing Approaches 427
M. R. Pourramezan, A. Rohani, M. H. Abbaspour-Fard

Investigating the Rates, Severity and Affecting Factors of Accidents Related to Agricultural Tractors and Grain Combine Harvesters in Ilam Province of Iran 449
J. Allahnouri, A. Marzban, M. Ghasemi-Nejad-Raeini, M. Rahnama, M. Savari

Predicting Vitamin C and Color Change of Orange Powder in Four Dryers Using an Electronic Nose 469
M. Roshan Moghadam, R. Amiri Chayjan, N. Aghilinategh

A Weighted Group Learning Model for Classification of Grape Leaf Disease Using Image Processing and Machine Learning 487
M. Najafabadiha, D. Mohammad Zamani, M. Gholami Par-Shokohi

Assessing the Influence of Copper Oxide Nanoparticles Combined with Distilled Water on PVT System Performance 507
M. Ghaderi, P. Salami, H. Samimi-Akhijahani, S. Zareei, M. Safvati

Optimization of the Canola Harvester Blade Based on Energy Reduction Approach and Life Cycle Assessment 525
Gh. Ahmadzade, M. R. Maleki, P. Salami, K. Mollazade

Physical Property Characterization of Ethiopian Maize Varieties for Adaptive Multi-Crop Planter Design 549
D. Girma Gadisa, K. Purushottam Kolhe, S. Kedir Busse, M. Mohammed Issa, T. Aseffa Abeye, D. Alemu Anawte

Feasibility of Detecting Different Genotypes of *Mentha* plant by E-nose Technique 563
H. Zaki Dizaji, M. Mahmoodi Surestani, N. Aghilinategh, A. Boveiri Dehsheikh

Comparative Modeling of Drying Kinetics for Potato Slices: AI-Based vs. Empirical and Semi-Empirical Approaches 579
R. Raeesi, M. Moradi, A. Dehghani

Review Articles

A Review on the Physicomechanical Properties of Polysaccharide-Based Edible Films Incorporating Essential Oil-Loaded Pickering Emulsions 599
H. Mirzaee Moghaddam, A. Nahalkar, A. Rajaei

Journal of Agricultural Machinery

Homepage: https://jame.um.ac.ir

Research Article
Vol. 16, No. 3, 2026, p. 365-381

An Assessment of the Potential of Multispectral Sentinel-2 Satellite Imagery for Detecting Dubas Bug Infestations in Date Palm Cultivation Regions

H. Karimi[1*], M. J. Assari[2], H. Zohdi[2], F. Ranjbar-Varandi[3]

1- Agricultural Engineering Research Department, Kerman Agricultural and Resource Research and Education Center, AREEO, Kerman, Iran
2- Plant Protection Research Department, Kerman Agricultural and Natural Resources Research and Education Center, AREEO, Kerman, Iran
3- Department of Plant Protection, Faculty of Agriculture, University of Tabriz, Tabriz, Iran
(*- Corresponding Author Email: h_karimi@areeo.ac.ir)

Received: 16 October 2024
Revised: 09 March 2025
Accepted: 29 April 2025
Available Online: 07 July 2025

How to cite this article:
Karimi, H., Assari, M. J., Zohdi, H., & Ranjbar-Varandi, F. (2026). An Assessment of the Potential of Multispectral Sentinel-2 Satellite Imagery for Detecting Dubas Bug Infestations in Date Palm Cultivation Regions. *Journal of Agricultural Machinery*, *16*(3), 365-381. https://doi.org/10.22067/jam.2025.90276.1297

Abstract

The Dubas bug (*Ommatissus lybicus*) poses a significant threat to agriculture in the Middle East by weakening palm trees and reducing fruit production. Effective pest control depends on accurate and timely localization of the infestation. However, regular field inspections are difficult and time-consuming, especially for large areas. This research investigates the potential of Sentinel-2 satellite imagery for detecting Dubas bug infestations. The aim is to improve monitoring capabilities, accelerate intervention strategies, and mitigate the associated economic impact. The field trial to assess the infestation occurred in May 2023, coinciding with the peak of the pest outbreak. The severity of the infestation was assessed through pest counts conducted in date palm groves within the urban area of Bam, Iran. Sentinel-2 multispectral images of a specific area were acquired and processed for correction, raw data preparation, and information extraction. The Fast Line-of-sight Atmospheric Analysis of Spectral Hypercubes (FLAASH) method was used for the atmospheric correction of the acquired images. The Nearest Neighbor Interpolation method was used to resample satellite images, standardizing all bands to a uniform 10-meter resolution. Following the pre-processing phase, the KD-tree-based K-Nearest Neighbor classifier model was selected to develop a model specifically designed for identifying areas infested by the Dubas bug. For training, 70% of the measured field data were used, including uninfested areas and areas with three levels of infestation from light to heavy, as well as other land features such as buildings, roads, etc. The remaining 30% of the data was utilized to evaluate the trained model, using the correct prediction rate as the assessment criterion. The trained classifier, validated against the ground truth data, achieved an accuracy of approximately 83% on the test dataset. This accuracy highlights the ability of Sentinel-2 multispectral imagery and machine learning to detect Dubas bug infestations in date palm groves and can facilitate targeted and sustainable pest management strategies.

Keywords: Classification model, Date fruit, Field inspections, Remote sensing

Introduction

Ommatissus lybicus de Bergevin (Hemiptera: Tropiduchidae), commonly known as the date palm dubas bug, is a major pest that has a detrimental effect on date fruit production in many countries (Al-Kindi, Kwan, Andrew, & Welch, 2017; Khan *et al.*, 2020). The decline in date fruit yields caused by infestations of the date palm Dubas bug is a significant concern for farmers in the Middle East and North Africa (Al Shidi, Kumar, Al-Khatri, Albahri, & Alaufi, 2018). Pests like the

Authors retain the copyright. This is an open access article distributed under Creative Commons Attribution 4.0 International License (CC BY 4.0).

https://doi.org/10.22067/jam.2025.90276.1297

Dubas bug can cause an economic loss of up to 28% in date fruit production. The insect feeds on the nutrient-rich sap of palm trees, damaging palm trees (Shah *et al.*, 2016). The consumption of palm sap by nymphs and adult insects results in the formation of honeydew on the leaf surface (Al-Khatri, 2004; Howard, 2001). Over time, dust accumulates on the honeydew, fostering the growth of black sooty mold on the leaves, which can impede the photosynthesis process of the date palm (Neteler, Roiz, Rocchini, Castellani, & Rizzoli, 2011; Shah *et al.*, 2012). This pest disrupts the plant's vital functions, weakens the tree, and leads to poor fruit quality and considerable financial losses. Prolonged and severe infestations can also result in the deterioration and eventual destruction of the palm tree (Carpenter & Elmer, 1978). This damage can be minimized if the Dubas bug is controlled.

Before addressing this pest issue, it is of utmost importance to accurately identify and pinpoint the location of the pest. Once this step is completed, farmers can implement various control measures and pest management techniques. A prevalent approach within this field involves the use of chemical insecticides, which can be applied through ground-based or aerial spraying methods (Al-Khatri, 2011). Identifying and localizing infestations through visual field inspection by farmers can be quite a challenge. This is mainly because the symptoms of the infestation can vary greatly depending on the tree species and the initial location of the infestation. Existing detection methods often prove ineffective when applied to large areas, as each tree must be examined individually (Wakil, Faleiro, & Miller, 2015). Human eye-based field inspections of extensive agricultural areas are limited by their high cost, complexity, time, and lack of precision (Pontius, Schaberg, & Hanavan, 2020; Samuel Adelabu, Mutanga, & Cho, 2012). Remote sensing has emerged as a critical tool for monitoring the health and condition of date palm plantations, offering a cost-effective and scalable alternative to traditional field inspections. Advances in this field have made this technology a promising option for detecting and mapping pests. Pests can cause considerable damage to plants, which manifests itself in a number of visible signs and symptoms. These signs can include a reduction in leaf size, loss of color, and changes in the overall layout of the plant canopy. These changes to the health and appearance of the plant can be attributed to the effects of the pests on the wavelengths of light reflected in the visible and near-infrared ranges (Silva, Olthoff, de la Mata, & Alonso, 2013).

The ability of remote sensing to detect changes in soil and vegetation provides valuable information for the implementation of site-specific management practices (Hicke & Logan, 2009; Weiss, Jacob, & Duveiller, 2020). Hicke and Logan (2009) have shown that by using multispectral Quickbird satellite imagery with a spatial resolution of 2.4 m in conjunction with the maximum likelihood classification method, a map can be created depicting the mortality in whitebark pine caused by the mountain pine beetle outbreak. Oumar and Mutanga (2013) developed a model using Worldview-2 satellite data to assess its ability to predict the impact of the bronze beetle (*Thaumastocoris peregrinus*) on plantation forests. The monitoring model successfully predicted the extent of damage caused by the bronze beetle. It achieved a coefficient of determination of 65% and a root mean square error of 3.62 when tested with independent experimental data sets. In this investigation, the WorldView-2 sensor's red-edge and near-infrared bands, along with specific pigment indices and red-edge indices, were found to play a critical role in accurately predicting damage. The characteristic leaf symptoms of Blumeria graminis, also known as surface powdery mildew, can be identified through the use of remote sensing technology. Zhang *et al.* (2014) attempted to create a distribution map of powdery mildew of winter wheat at the regional level using medium-resolution satellite images (CCD sensor on the Huanjing satellite) using time series. The result of this study was an overall accuracy of

78%. Yuan, Pu, Zhang, Wang, and Yang (2016) also investigated the use of high-resolution (6 m) multispectral SPOT-6 satellite imagery to monitor the powdery mildew of winter wheat in an area of high disease incidence. They identified five key spectral features sensitive to the problem and developed a system to identify powdery mildew using the spectral angle mapping method. Validation with field data showed that the system achieved an accuracy of 78% and a kappa coefficient of 0.55.

Using hyperspectral data, S. Adelabu, Mutanga, Adam, and Sebego (2014) conducted a study on the degree of forest canopy cover change due to insect defoliation. The classification accuracy of the model created using the random forest algorithm was found to be 82.42%. The leaf loss in plants caused by the eucalyptus weevil (*Gonipterus scutellatus*) showed a strong relationship with the vegetation indices (VIs) calculated from the red edge bands of the WorldView-2 satellite images (Lottering & Mutanga, 2016). A study Haghighian, Yousefi, and Keesstra (2022) investigated the performance of Sentinel-2 imagery in detecting oaks infested by *T. viridana* in the Zagros forest habitat. VIs were derived from *T. viridana* infested and non-infested areas. The results of this study revealed significant differences in VIs between infested and non-infested zones within the study site, with a confidence level of 99%. Al Shidi, Kumar, and Al-Khatri (2019) conducted a study on the detection of date palm Dubas bug infestation by analyzing the changes in reflectance at different degrees of infestation. They used high-resolution multispectral images from the WorldView-3 satellite to capture images of infested areas. The researchers identified 32 vegetation indicators and found that reflectance in the red and near-infrared edge bands decreased with higher infestation levels. They also observed significant differences in the red edge, NIR1, and NIR2 spectral bands in high-infested areas compared to uninfested, low-infested, and medium-infested areas.

While accessibility and affordability have been challenges, the Sentinel-2 A + B satellites from the European Space Agency have addressed these issues by offering free enhanced resolution and frequent revisits to monitor fields effectively. The spectral resolution of the data captures a wide range of bands crucial for assessing vegetation health, making it a valuable tool in various agricultural applications (Segarra, Buchaillot, Araus, & Kefauver, 2020). The timely identification of date palm infestation with the Dubas bug can be greatly supported by analyzing multispectral satellite images. This method offers a significant advantage in controlling the spread of the infestation. However, there is a notable absence of documented cases where researchers have used the readily available and free multispectral data from the Sentinel-2 satellite to detect date palm infestations. Every year, more than 200,000 tonnes of dates are harvested from groves in the eastern province of Kerman, Iran, and Dubas bugs infest between 2,000 and 3,000 hectares of these groves in the northern part of this province. The findings of Rostami, Assari, Pejman, and Shaker (2019) indicate that the majority of palm groves surveyed for Dubas bug pest density in Bam, Kerman Province, Iran, showed moderate to high levels of damage. In particular, over 69% of the orchards had moderate, high, or very high infestation densities. Consequently, more than 69% of the groves in the region require urgent intervention. Due to the significant presence of the Dubas bug in the area, the current study focuses on determining the possibility of detecting date Dubas bug infestation in the urban area of Bam by analyzing changes in reflectance at different levels of infestation using multispectral images from the Sentinel-2 satellite.

Materials and Methods

Research site

The palm groves in the urban area in the Iranian province of Kerman were selected as the study area (Fig. 1). The study area is located at approximately 29.00° north latitude

and 58.30° east longitude and is characterized by its pronounced desert climate, which falls under the Köppen climate classification. This climate is characterized by very hot summers, during which temperatures can rise considerably, and mild winters, starkly contrasting to the summer months' heat. In addition, the region has low annual rainfall, which further determines the region's environmental conditions and affects the growth and survival of palm trees in urban groves. The first generation of Dubas bug in urban groves typically first appears in April. The pest infestation peak occurs during the most nourishing period of the insect's life cycle, precisely in May, when the nymph is in its third and fourth stages of growth (Mahmoudi, Gheybi, & Khoshnoud, 2020). Therefore, field and satellite measurements from the research site were conducted in May. The date palms in the urban area of Bam were divided into grids. Within each grid, a focal point was designated for collecting information, conducting training, and evaluating the classification model.

Fig. 1. An aerial photo captured with a UAV of date fruit plantations in the urban area of Bam

Field inspection

A grid-based survey covering the 480.22 km^2 urban area of Bam (divided into 48 individual 1 km^2 grids) was conducted to map the spatial distribution and intensity of Dubas bug infestations following a seasonal regular pest outbreak. Tree density varied across grids due to the heterogeneous urban landscape of Bam, including houses, roads, and open spaces, with trees spaced approximately 8×8 meters apart. Within each grid, the degree of infestation was determined using the average measurements of three randomly selected trees with a minimum distance of 20 meters to ensure an adjustment to the resolution of the Sentinel-2 images. This methodology enabled a comprehensive assessment of infestation patterns across the urban environment. As recommended by (Hussain, 1963), pest density was documented during the field measurements by categorizing the infestation at each point into three levels: low (with an average of 0-5 eggs per leaflet), medium (5-10 eggs per leaflet), and high (more than 10 eggs per leaflet). Fig. 2 showcases an inspected

example of date palm leaflets infested with the Dubas bug pest.

Fig. 2. An instance of the inspected leaflets from a date palm tree infested with the Dubas bug

The GPS device (GARMIN eTrex Summit) was used to record the geographical coordinates of the sampling points with an accuracy of three meters. In May 2023, the research site underwent field visits, sampling, and the acquisition of satellite images concurrently. The time of sampling was chosen as close as possible to the time at which the satellite flew over the study area. The provided Fig. 3 displays the specific locations where inspections were conducted to gather data on infestation in the urban area of Bam.

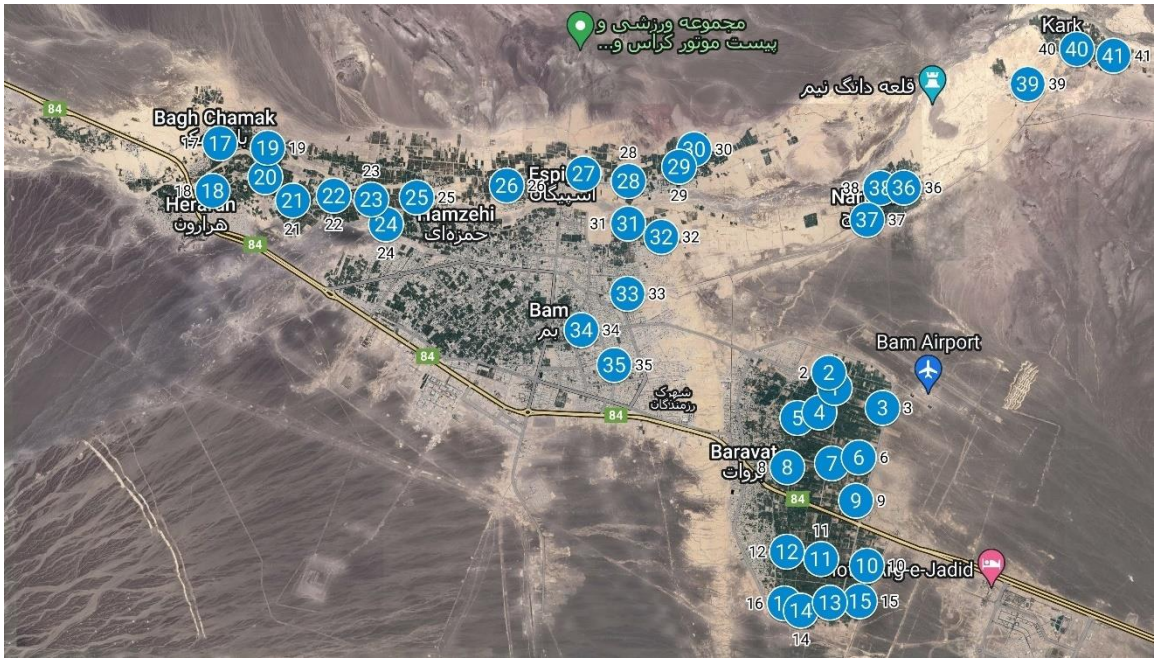

Fig. 3. The locations in the Bam urban area were inspected for information on infestation

Sensing information and selected bands

The Sentinel-2 satellite captures multispectral imagery across 13 bands in the visible and infrared ranges, providing high-resolution data for vegetation analysis (Table 1). The benefits of this satellite include free public information, resolutions of 10, 20, and 60 meters, a wide field of view of 290 km, and global coverage. The spatial resolution for the RGB and infrared bands is 10 meters (EOS, 2018). For this particular study, eleven bands were selected for modeling, with bands 1 and 10 excluded due to their sensitivity to aerosols and clouds as well as their lower spatial resolution. These bands are not suitable for mapping vegetation (Kumbula, Mafongoya, Peerbhay, Lottering, & Ismail, 2019).

Table 1- Specifications of Sentinel-2 satellite bands (EOS, 2018)

Band number	Spatial resolution (meters)	Bandwidth (nm)	Characteristic
1	60	453-433	Coastal aerosol
2	10	523-458	Blue
3	10	578-543	Green
4	10	680-650	Red
5	20	713-698	Red Edge
6	20	748-734	Red Edge
7	20	785-765	Red Edge
8	10	900-785	Near Infrared (NIR)
8A	20	875-855	Narrow NIR
9	60	950-930	Water vapour
10	60	1385-1365	Short Wave Infrared (SWIR) – Cirrus
11	20	1655-1565	SWIR
12	20	2280-2100	SWIR

Downloading satellite data

With a review period of 5 days, the Sentinel-2 satellite is suitable for detecting pest infestations in a timely manner. The sensor's image covers a large area with a width of 290 km (Segarra *et al.*, 2020). The large size of the image poses a challenge in capturing and pre-processing the image. In this study, using the USGS website (https://earthexplorer.usgs.gov), the images of the Sentinel-2 satellite were divided into smaller sections prior to processing. Among the images reviewed in the specified time period, the image received from the region on May 8, 2023, with the Sentinel-2 sensor, had the lowest cloud cover (0.056). Therefore, this image was selected for further processing (Fig. 4).

Data preprocessing and modeling a classifier

The SNAP software platform, developed by the European Space Agency (ESA) for Sentinel mission support, was utilized for image processing, modeling, and data visualization. With the application of the SNAP software, the Fast Line-of-sight Atmospheric Analysis of Spectral Hypercubes (FLAASH) method was employed for atmospheric correction of the acquired images. The ground references were validated by including specific points such as buildings, roads, and other relevant elements. The Nearest Neighbor interpolation method was used when resampling satellite images to standardize all bands to a uniform 10-meter resolution. This technique assigns values to each "corrected" pixel based on the proximity of the nearest "uncorrected" pixel. The Nearest Neighbor method is recognized for its ease of implementation and its ability to maintain the original values within the unaltered scene. In particular, it transfers the digital number (DN) of the nearest input pixel to the corresponding output pixel determined by its spatial coordinates.

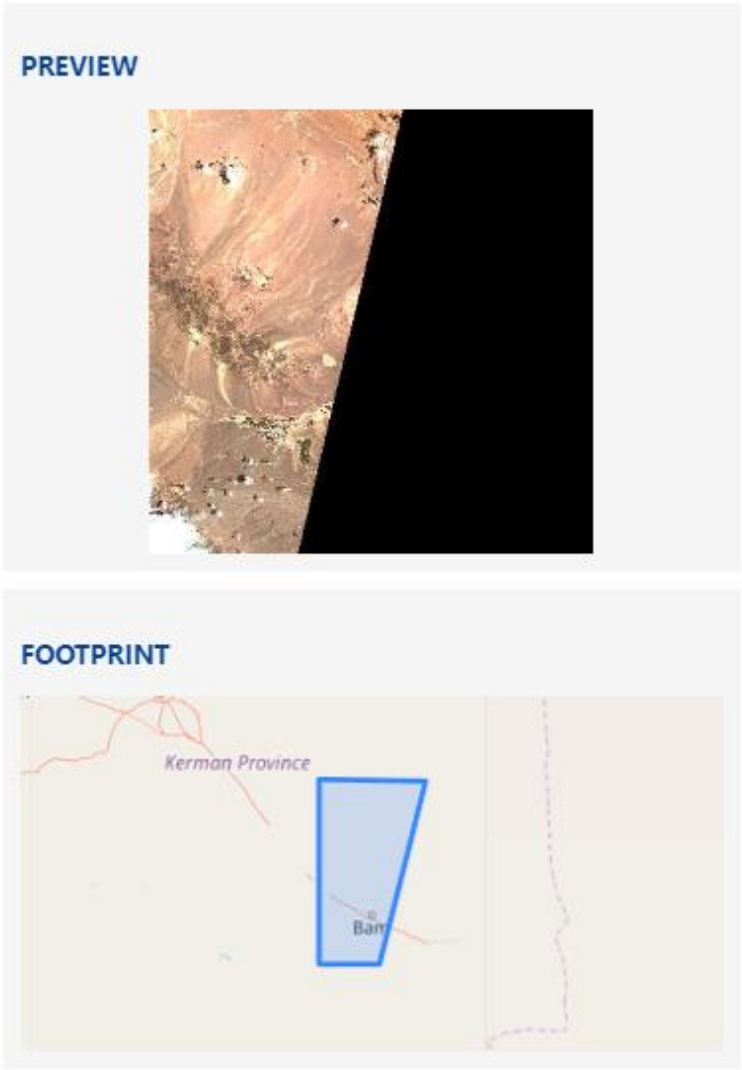

Fig. 4. Sentinel-2 image, May 8, 2023

Plant stress is evident through the presence of honeydew and dust deposits on the leaves, which cause the green color of the leaf to turn yellow over time. Vegetation indices (VIs) are used to analyze and explore vegetation in spectral satellite imagery, which requires mathematical conversions of specific wavelength bands. Previous studies have highlighted vegetation indicators associated with this color change (Mirik, Michels, Kassymzhanova-Mirik, & Elliott, 2007; Reisig & Godfrey, 2006; Saadikhani, Maharlooei, Rostami, & Edalat, 2023). In this study, the Normalized Difference Vegetation Index (NDVI) and Normalized Difference Moisture Index (NDMI) indicators were first analyzed to evaluate the effectiveness of the Sentinel-2 satellite spectral bands in detecting vegetation and stress caused by Dobas insect infestations (Table 2).

Table 2- List of spectral VIs derived from satellite imagery

Index	Equation	Reference
NDVI	(NIR- Red)/(NIR+ Red)	(Rouse, Haas, Schell, & Deering, 1974)
NDMI	(NIR1- NIR2)/(NIR1+ NIR2)	(Bernstein, Jin, Gregor, & Adler-Golden, 2012)

In addition to NDVI and NDMI, a number of remote sensing indices are available for analyzing Sentinel-2 satellite images (IDB, 2024). To overcome the challenge of selecting an appropriate vegetation index for detecting vegetation stress due to Dubas bug infestation, one can use principal component analysis (PCA) to leverage the full spectral data of a satellite image. PCA, a statistical technique, simplifies the dimensions of the dataset to create an index for each specific location. By incorporating all spectral information from the satellite image, PCA can effectively highlight vegetation stress and pest infestations. This method enables comprehensive data analysis by taking into account all the captured bands. Reducing the data set through PCA helps identify hidden patterns and relationships that may not be apparent with a single vegetation index. After acquiring the multispectral images and performing a principal component analysis, a classification model based on the K-nearest neighbor using the KD-tree is created. The model takes into account data obtained from field measurements of date palm groves. Seventy percent of the field survey data from each degree of infestation (uninfested, low-infested, medium-infested, and high-infested areas) and other land features such as buildings, roads, etc., were used to train the model, while the remaining thirty percent was used for evaluation. Once the model is trained, its accuracy is assessed by comparing its predictions with the data obtained from field measurements. In this way, it is possible to assess how well the model can identify and classify the different infestation levels.

Evaluation metrics of the classification model

The confusion matrix provides a detailed evaluation of how well the model's predictions align with the actual class labels. It allows for the evaluation of a classification model's accuracy by comparing its results to a predetermined set of test data with known true values (Kulkarni, Chong, & Batarseh, 2020). It provides valuable insights, including True Positive (TP), for accurate predictions of positive cases, such as the correct diagnosis of a pest infestation. False Positive (FP) occurs when negative cases are mistakenly predicted as positive, for example, when a pest infestation is inaccurately diagnosed (Type I error). False Negative (FN) points out instances where positive cases are inaccurately predicted as negative, such as when a pest infestation is overlooked even though it is present (Type II error). Finally, True Negative (TN) signifies correct predictions of negative cases, e.g., when the absence of an infestation is correctly detected (Tiwari, 2022). These results could contribute significantly to understanding the performance of the model in scenarios related to infestation diagnosis.

The metrics of accuracy (Eq. 1) and precision (Eq. 2) were also considered to assess the validity of the classification. Accuracy refers to the overall correctness of the classification results, indicating how well the model identified and categorized different data points. Although accuracy is important for evaluating the results, it may not be reliable in cases of significant class imbalance, as it can be misleading. In such situations, alternative metrics such as precision should be considered. Due to the partial imbalance in the spatial infestation data, the precision metric was also considered. Precision measures the proportion of correctly predicted positive instances out of all instances predicted as positive, helping to assess the model's ability to identify true positive instances and avoid false positive instances. Analyzing these metrics together with the elements of the confusion matrix enables a more detailed evaluation of the performance of the classification model. This comprehensive approach provides a clearer understanding of the model's strengths and weaknesses.

$$\text{Accuracy} = \frac{TP}{TP + TN + FP + FN} \quad (1)$$

$$\text{Precision} = \frac{TP}{TP + FP} \quad (2)$$

Results and Discussion

Data analysis

Fig. 5 shows the map of the NDVI for the urban area of Bam, a simple and efficient method for quantifying vegetation. This index serves as an indicator of vegetation health and is determined by the reflection of light from plants at specific wavelengths ranging from -1 to 1. Negative NDVI values (close to -1) indicate the presence of water, while values close to zero (-0.1 to 0.1) typically indicate barren areas such as rocks or sand. Low to moderately positive values (around 0.2 to 0.4) are associated with shrubs and grasslands, while high values are associated with trees and, in the context of Bam, with palm groves.

The NDMI is used to assess the water content of plants and to monitor drought conditions, with a scale ranging from -1 to 1. Negative NDMI values (close to -1) usually indicate poor soils, while values close to zero (-0.2 to 0.4) are generally associated with water stress. On the other hand, high positive values indicate lush vegetation cover without water stress (around 0.4 to 1). This normalized index of moisture difference can also serve as an indicator of vegetation stress in the studied area. The normalized index map illustrating the estimated moisture difference for the urban area of Bam is shown in Fig. 6. It shows the effective differentiation of vegetation from other land features such as buildings, roads, and open land.

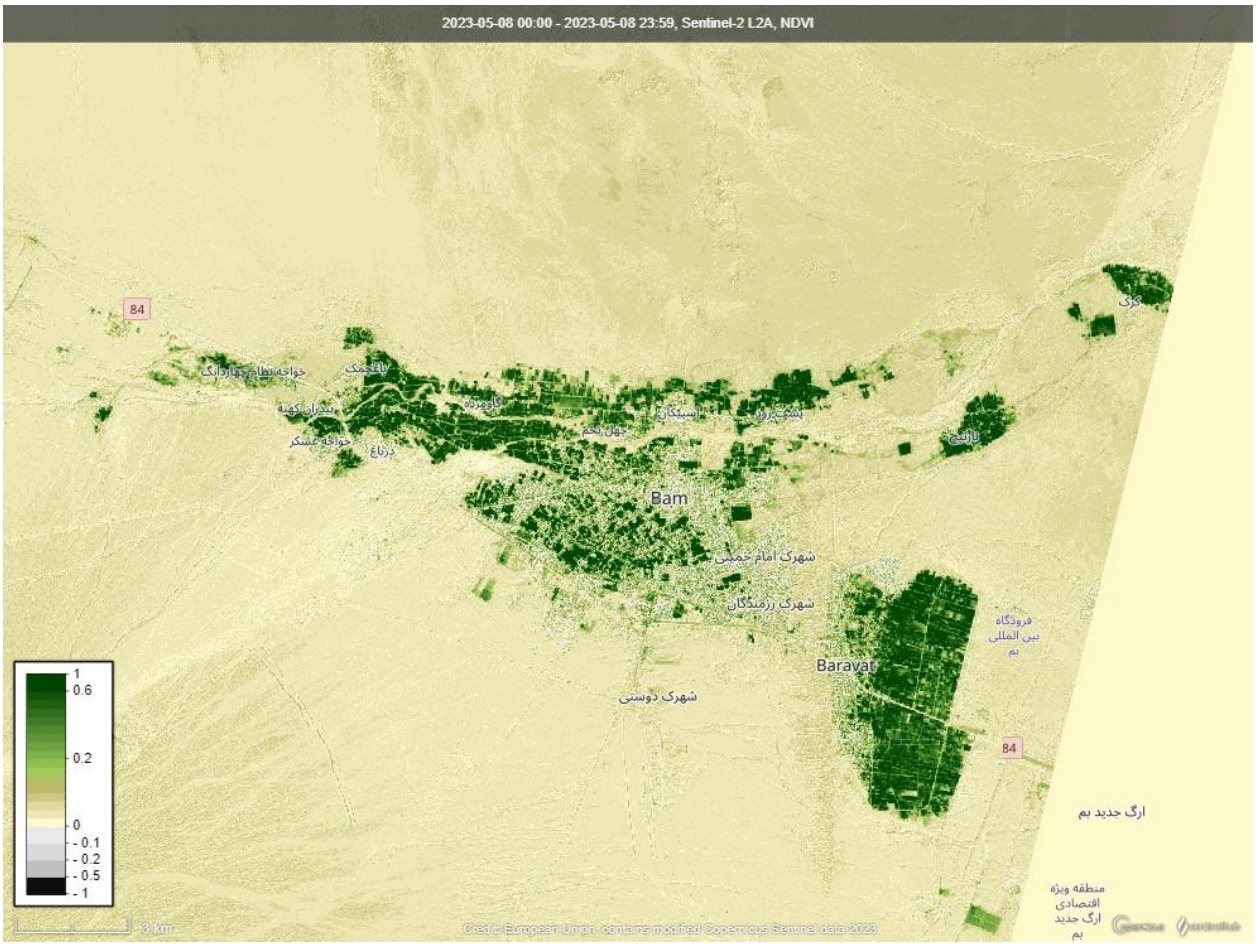

Fig. 5. Map of the Normalized Difference Vegetation Index estimated in the urban area of Bam

Fig. 5 and Fig. 6 show the suitability of NDVI and NDMI for date palm detection and the likely ability to diagnose the dubas bus. However, in the field of vegetation analysis,

other indices such as Green Chlorophyll Index-Green (CI-G), Green Difference Vegetation Index (GDVI), Green Normalized Difference Vegetation Index (GNDVI), Green Ratio Vegetation Index (GRVI), Normalized Red (NR), and Simple Ratio (SR) have also attracted interest. Atmospheric conditions, background noise, and sensor variations limit the indices. A study in Oman focused on the detection of palm Dubas bug invasions using WorldView-3 satellite imagery, which led to alternative indices being considered (Al Shidi *et al.*, 2019).

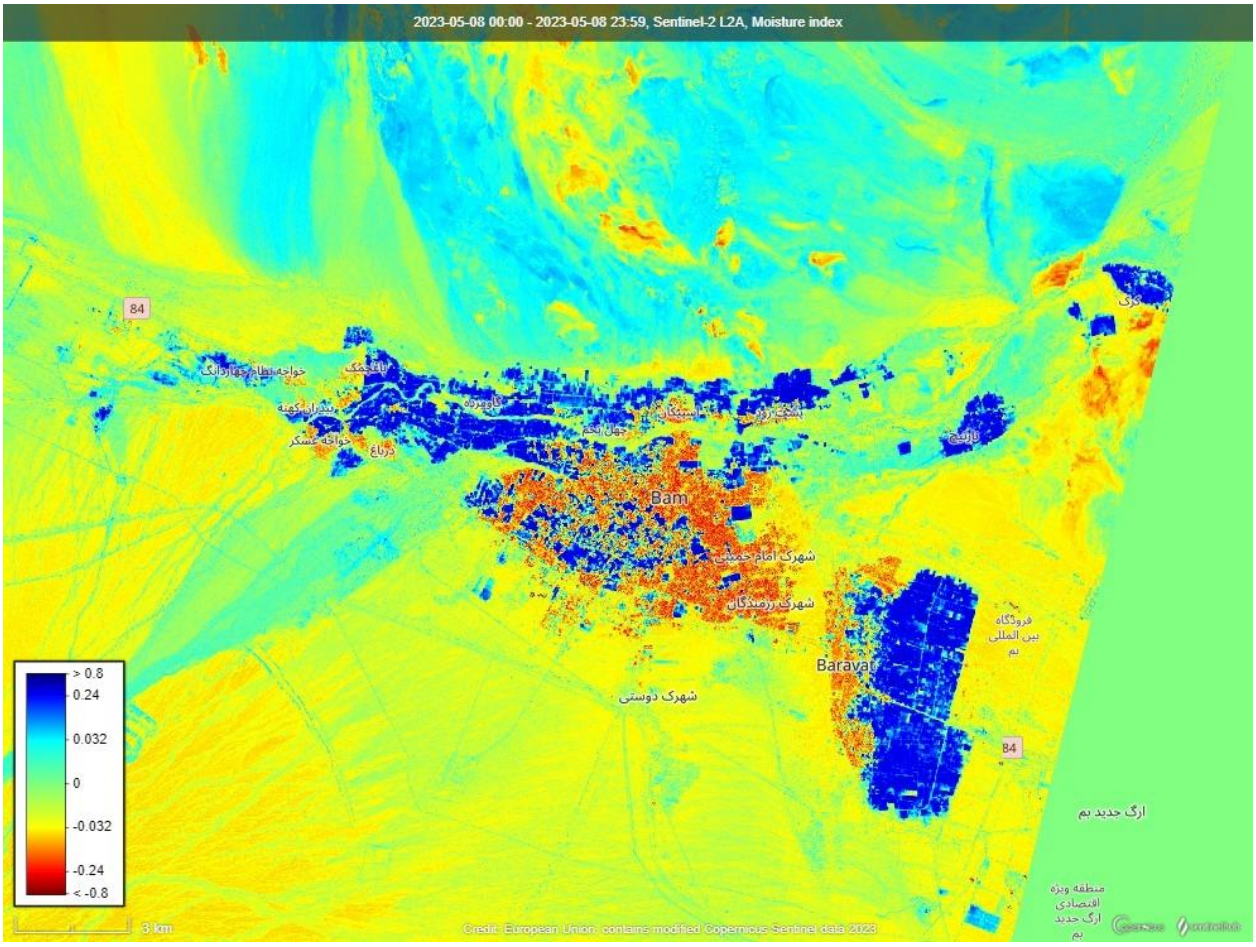

Fig. 6. The Normalized Difference Moisture Index map of the estimated humidity difference for the urban area of Bam

One technique is to use tasseled cap indices to assess changes in green, yellow, and lightness by merging data from different bands (Baig, Lifu, Tong, & Tong, 2014). The tasseled cap transformation converts the original image bands into a new set of bands with specific meanings that are useful for vegetation mapping. This process involves the formation of "linear combinations" of the original image bands, a concept similar to PCA (Kauth & Thomas, 1976; Peerbhay, Ilaria, Romano, & Naicker, 2022). Rather than calculating numerous vegetation indices, this study utilizes PCA analysis of all spectral bands of satellite imagery to identify key variables associated with Dubas bug pest infestation, soil composition, water bodies, and various land cover attributes. By using PCA, we can effectively reduce the dimensionality of the data while retaining essential information about plant health. This approach allows us to identify patterns and relationships in the data that may not be as obvious when analyzing vegetation indices separately. In addition, PCA analysis provides a comprehensive overview of all available

spectral information, enabling a more holistic assessment of plant health. This method can help identify subtle variations and correlations between different spectral bands, leading to a more accurate and nuanced understanding of plant conditions.

Classification results

The K-nearest neighbor classification model was first trained and developed to distinguish date trees from other land features such as buildings, roads, and soil. They were then used to identify areas of pest infestation and categorize the degree of infestation into three levels: low, medium, and high. As mentioned above, 70% of the labeled samples were assigned for training, while the remaining 30% were used for evaluation.

In the first step of building the model, field measurements were collected and categorized into two classes: 0 and 1. Class 0 represents features that are not date palms, such as buildings, roads, and land, while class 1 represents date palms. The results show that the K-nearest neighbor classification model using the KD-tree was able to effectively identify the unique features of date palms and distinguish them from other land features (Table 3). The calculated Root Mean Squared Error (RMSE) of 0.1311 indicates the average variance between the values predicted by the model and the actual values and shows the ability of the model to accurately predict the target value. In addition, the KD Tree KNN Classifier showed 98.28 percent correct predictions when evaluating the test dataset, demonstrating its effectiveness in discriminating date palms.

Table 3- A summary of the results of classifying date palms from other land feature pixels

Classification metrics	Class 1: date tree	Class 0: other
Accuracy	0.9828	0.9828
Precision	0.9801	0.9855
Correlation	0.9662	0.9662
Error Rate	0.0172	0.0172
True Positives	2464	2450
False Positives	50	36
True Negatives	2450	2464
False Negatives	36	50

In addition, classification models were developed to identify infestation by categorizing the field measurement data into four classes based on the degree of tree infestation: uninfested, light-infested, moderate-infested, and heavy-infested. Other land factors were assigned to a separate category. After training and evaluation of the classification algorithms, the KD-tree-based K-nearest neighbor classifier again showed the best performance in detecting the presence and severity of infestation at the date palm sites. The classifier uses a KD-tree, a data structure that organizes the training data for an efficient nearest neighbor search. To evaluate the accuracy of the classification, the classification value for each measurement point was extracted, and corresponding evaluation metrics were created. These metrics are calculated by conducting a pixel-by-pixel comparison between the training samples in the ground truth and the corresponding pixels in the classification results.

Table 4 provides an overview of the classification assessment for different levels of infestation of the date palm Dubas bug. The precision metric, which indicates the accuracy of the classification model, was calculated for each category. A precision value of 0.98 for the detection of other land features shows that the model is very accurate in identifying these pixels. For date palm locations without infestation, the precision score is 0.67, which means that the model correctly identifies 67% of these pixels. This suggests that uninfested areas may be misclassified as Dubas bug

infestations. Also, for low, medium, and high infestations, the precision values are 0.74, 0.77, and 0.66, respectively, indicating varying degrees of accuracy in identifying the severity of Dubas bug infestation. These metrics suggest that the model performs relatively well in identifying low and medium infestations but is less accurate in identifying severe infestations.

Table 4- An overview of the classification results for multiple infestation levels of the date palm Dubas bug

Classification metrices	Class 0: other	Class 1: level_0	Class 2: level_1	Class 3: level_2	Class 4: level_3
Accuracy	0.9951	0.9586	0.9140	0.9093	0.8920
Precision	0.9970	0.6667	0.7450	0.7709	0.6649
Correlation	0.9899	0.4131	0.7583	0.7146	0.6771
Error Rate	0.0049	0.0414	0.0860	0.0907	0.1080
True Positives	1982	60	789	636	629
False Positives	6	30	270	189	317
True Negatives	2902	4645	3697	3827	3749
False Negatives	18	173	152	256	213

The KD classifier achieved an accuracy of 83%, correctly predicting the infestation category for 83% of the test dataset. Furthermore, the root mean square error (RMSE) for the classifier's predictions is 0.7693. The RMSE is a measure of the average difference between the predicted and actual values, with lower values indicating better accuracy. In this case, the RMSE indicates that the classifier's predictions are relatively close to the actual values. Overall, the scoring metric performs well in accurately categorizing Dubas bug infestations, with some room for improvement in distinguishing between infested and non-infested areas.

Fig. 7 illustrates the predicted distribution of Dubas bug infestations in the urban area of Bam, as derived from multispectral satellite imagery. On Monday, May 8, 2023, the areas with high infestation are highlighted in red. Through the utilization of multispectral satellite data and machine learning-based classification, a method for detecting Dubas bug infestation in date palms using remote sensing was successfully developed and evaluated with high validity and accuracy.

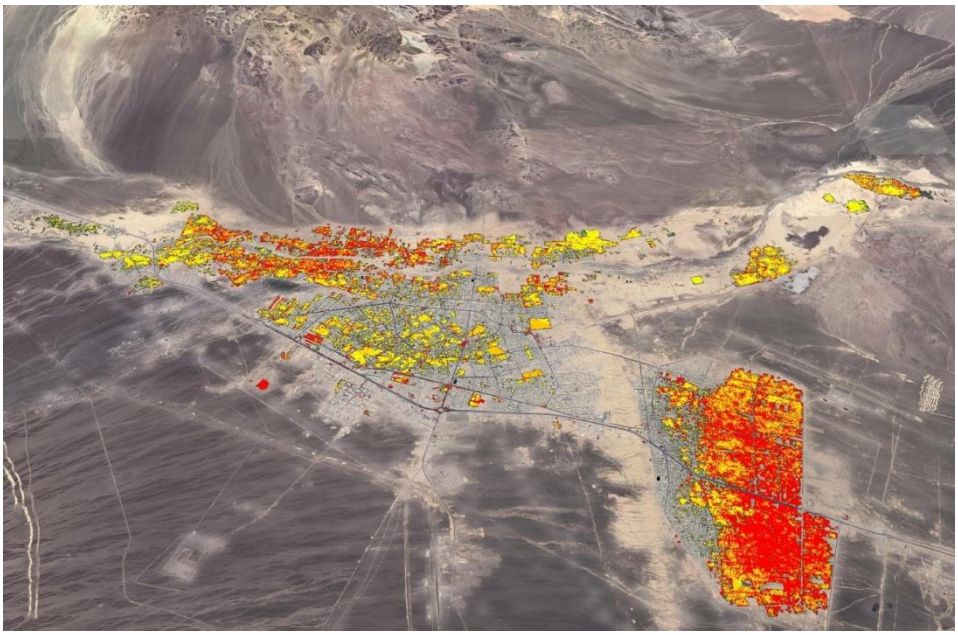

Fig. 7. Prediction of the pixels infected with the palm weevil pest in Bam city

Conclusion

This research signifies a substantial advancement in the management of palm dubas within the Bam urban region through the integration of Sentinel-2 multispectral data with conventional pest management techniques. This combination of technological innovation and established practices has the capacity to improve the safeguarding of date palms against this harmful pest. The suggested remote sensing methodology presents a cost-efficient and accessible approach, functioning as a practical resource for farmers and agricultural managers. A key benefit of this strategy lies in its capacity for the early identification of Dubas bug infestations, in addition to the continuous observation of pest populations and their distribution throughout date palm groves. Early identification and continuous monitoring are essential as they empower stakeholders to enact timely responses to potential outbreaks. By averting extensive infestations, this proposed method could significantly diminish fruit damage, leading to increased yields and enhanced date quality. As a result, the livelihoods of farmers and communities reliant on date palm agriculture could be bolstered. Subsequent research initiatives should emphasize leveraging the capabilities of convolutional neural networks (CNNs) to enhance the precision of Dubas bug detection. Greater detection accuracy will facilitate more effective and focused interventions, ultimately optimizing pest management strategies. However, the expansion of this innovative approach to broader geographic regions or varying environmental conditions necessitates a meticulous and comprehensive evaluation of numerous factors. These factors encompass discrepancies in climate, topography, and the distinctive attributes of date palm cultivation across different areas.

Conflict of Interest: The authors declare no competing interests.

Author Contributions

H. Karimi: Conceptualization, Data pre and post processing, Writing- Original draft, Statistical analysis and Software services

M. J. Assari: Technical advice, Methodology and Data acquisition

H. Zohdi: Conceptualization and Supervision

F. Ranjbar-Varandi: Technical advice, Review and editing services

References

1. Adelabu, S., Mutanga, O., Adam, E., & Sebego, R. (2014). Spectral Discrimination of Insect Defoliation Levels in Mopane Woodland Using Hyperspectral Data. *IEEE Journal of Selected Topics in Applied Earth Observations and Remote Sensing, 7*(1), 177-186. https://doi.org/10.1109/JSTARS.2013.2258329
2. Adelabu, S., Mutanga, O., & Cho, M. A. (2012). A review of remote sensing of insect defoliation and its implications for the detection and mapping of *Imbrasia belina* defoliation of Mopane Woodland. *The African Journal of Plant Science and Biotechnology, 6*.
3. Al-Khatri, S. (2004). Date palm pests and their control. *In Proceedings of the Date Palm Regional Workshop on Ecosystem-Based IPM for Date Palm in Gulf Countries* (pp. 84-88). Al Ain, UAE.
4. Al-Khatri, S. A. H. (2011). *Biological, ecological and phylogenic studies of Pseudoligosita babylonica Viggiani, a native egg parasitoid of Dubas bug Ommatissus lybicus de Bergevin, the major pest of date palm in the Sultanate of Oman* (Ph.D. thesis). University of Reading, Reading, UK.
5. Al-Kindi, K. M., Kwan, P., Andrew, N., & Welch, M. (2017). Impact of environmental variables on Dubas bug infestation rate: A case study from the Sultanate of Oman. *PloS one,*

12(5), e0178109. https://doi.org/10.1371/journal.pone.0178109
6. Al Shidi, R. H., Kumar, L., & Al-Khatri, S. A. (2019). Detecting Dubas bug infestations using high resolution multispectral satellite data in Oman. *Computers and Electronics in Agriculture, 157*, 1-11. https://doi.org/10.1016/j.compag.2018.12.037
7. Al Shidi, R. H., Kumar, L., Al-Khatri, S. A., Albahri, M. M., & Alaufi, M. S. (2018). Relationship of date palm tree density to Dubas bug Ommatissus lybicus infestation in Omani orchards. *Agriculture, 8*(5), 64. https://doi.org/10.3390/agriculture8050064
8. Baig, M. H. A., Lifu, Z., Tong, S., & Tong, Q. (2014). Derivation of a tasselled cap transformation based on Landsat 8 at-satellite reflectance. *Remote Sensing Letters, 5*(5), 423-431. https://doi.org/10.1080/2150704X.2014.915434
9. Bernstein, L. S., Jin, X., Gregor, B., & Adler-Golden, S. M. (2012). Quick atmospheric correction code: algorithm description and recent upgrades. *Optical engineering, 51*(11), 111719. https://doi.org/10.1117/1.OE.51.11.111719
10. Carpenter, J. B., & Elmer, H. S. (1978). *Pests and diseases of the date palm* (USDA Agriculture Handbook No. 527). Washington, DC: U.S. Department of Agriculture. Retrieved from https://www.govinfo.gov/content/pkg/GOVPUB-A-PURL-gpo29615/pdf/GOVPUB-A-PURL-gpo29615.pdf
11. EOS. (2018). Sentinel-2 imagery. Earth Observing System. Retrieved from https://eos.com/sentinel-2/
12. Haghighian, F., Yousefi, S., & Keesstra, S. (2022). Identifying tree health using sentinel-2 images: a case study on Tortrix viridana L. infected oak trees in Western Iran. *Geocarto International, 37*(1), 304-314. https://doi.org/10.1080/10106049.2020.1716397
13. Hicke, J. A., & Logan, J. (2009). Mapping whitebark pine mortality caused by a mountain pine beetle outbreak with high spatial resolution satellite imagery. *International Journal of Remote Sensing, 30*(17), 4427-4441. https://doi.org/10.1080/01431160802566439
14. Howard, F. (2001). Insect pests of palms and their control. *Pesticide outlook, 12*(6), 240-243. https://doi.org/10.1039/B110547G
15. Hussain, A. A. (1963). Biology and control of the dubas bug, Ommatissus binotatus lybicus de Berg. (Homoptera, Tropiduchidae), infesting date palms in Iraq. *Bulletin of Entomological Research, 53*(4), 737-745. https://doi.org/10.1017/S0007485300048458
16. IDB. (2024). Sentinel-2 RS indices. Retrieved from https://custom-scripts.sentinel-hub.com/custom-scripts/sentinel-2/indexdb/
17. Kauth, R. J., & Thomas, G. (1976). The tasselled cap — A graphic description of the spectral-temporal development of agricultural crops as seen by Landsat. In *Proceedings of the LARS Symposium on Machine Processing of Remotely Sensed Data* (pp. 41–51). West Lafayette, IN: Purdue University.
18. Khan, A. L., Asaf, S., Khan, A., Khan, A., Imran, M., Al-Harrasi, A., ..., & Al-Rawahi, A. (2020). Transcriptomic analysis of Dubas bug (*Ommatissus lybicus Bergevin*) infestation to Date Palm. *Scientific Reports, 10*(1), 1-15. https://doi.org/10.1038/s41598-020-67438-z
19. Kulkarni, A., Chong, D., & Batarseh, F. A. (2020). 5 - Foundations of data imbalance and solutions for a data democracy. In F. A. Batarseh & R. Yang (Eds.), *Data Democracy* (pp. 83-106): Academic Press. https://doi.org/10.1016/b978-0-12-818366-3.00005-8
20. Kumbula, S. T., Mafongoya, P., Peerbhay, K. Y., Lottering, R. T., & Ismail, R. (2019). Using Sentinel-2 Multispectral Images to Map the Occurrence of the Cossid Moth (Coryphodema tristis) in Eucalyptus Nitens Plantations of Mpumalanga, South Africa. *Remote Sensing, 11*(3), 278. https://doi.org/10.3390/rs11030278
21. Lottering, R., & Mutanga, O. (2016). Optimising the spatial resolution of WorldView-2 pan-sharpened imagery for predicting levels of Gonipterus scutellatus defoliation in KwaZulu-Natal, South Africa. *ISPRS Journal of Photogrammetry and Remote Sensing, 112*, 13-22.

https://doi.org/10.1016/j.isprsjprs.2015.11.010
22. Mahmoudi, M., Gheybi, M., & Khoshnoud, M. (2020). A study on different sampling techniques for dubas bug, Ommatissus lybicus (Hem.: Tropiduchidae). *Plant Pest Research, 10*(3). https://doi.org/10.22124/IPRJ.2020.4425
23. Mirik, M., Michels, G. J., Kassymzhanova-Mirik, S., & Elliott, N. C. (2007). Reflectance characteristics of Russian wheat aphid (*Hemiptera: Aphididae*) stress and abundance in winter wheat. *Computers and Electronics in Agriculture, 57*(2), 123-134. https://doi.org/10.1016/j.compag.2007.03.002
24. Neteler, M., Roiz, D., Rocchini, D., Castellani, C., & Rizzoli, A. (2011). Terra and Aqua satellites track tiger mosquito invasion: modelling the potential distribution of Aedes albopictus in north-eastern Italy. *International Journal of Health Geographics, 10*(1), 1-14. https://doi.org/10.1186/1476-072X-10-49
25. Oumar, Z., & Mutanga, O. (2013). Using WorldView-2 bands and indices to predict bronze bug (*Thaumastocoris peregrinus*) damage in plantation forests. *International Journal of Remote Sensing, 34*(6), 2236-2249. https://doi.org/10.1080/01431161.2012.743694
26. Peerbhay, K., Ilaria, G., Romano, L., & Naicker, R. (2022). Remote sensing wattle rust induced defoliation across black wattle timber plantations in Southern Africa. *International Journal of Remote Sensing, 43*(6), 2212-2226. https://doi.org/10.1080/01431161.2022.2058891
27. Pontius, J., Schaberg, P., & Hanavan, R. (2020). Remote Sensing for Early, Detailed, and Accurate Detection of Forest Disturbance and Decline for Protection of Biodiversity. In J. Cavender-Bares, J. A. Gamon, & P. A. Townsend (Eds.), *Remote Sensing of Plant Biodiversity* (pp. 121-154). Cham: Springer International Publishing. https://doi.org/10.1007/978-3-030-33157-3_6
28. Reisig, D., & Godfrey, L. (2006). Remote Sensing for Detection of Cotton Aphid– (Homoptera: Aphididae) and Spider Mite– (Acari: Tetranychidae) Infested Cotton in the San Joaquin Valley. *Environmental Entomology, 35*(6), 1635-1646. https://doi.org/10.1093/ee/35.6.1635
29. Rostami, M. A., Assari, M. J., Pejman, A., & Shaker, M. (2019). Preparation of distribution and severity map for Dubas bug (*Ommatissus lybicus*) in Bam region by Geographic Information System. *Plant Pests Research, 9*(1), 63-73. https://doi.org/10.22124/iprj.1970.3432
30. Rouse, J., Haas, J., Schell, J., & Deering, D. (1974). Monitoring vegetation systems in the Great Plains with ERTS. In *Proceedings of the Third ERTS-1 Symposium* (NASA SP-351, Vol. 1, pp. 309–317). Washington, DC: NASA. Retrieved from https://ntrs.nasa.gov/archive/nasa/casi.ntrs.nasa.gov/19740022614.pdf
31. Saadikhani, M., Maharlooei, M., Rostami, M. A., & Edalat, M. (2023). Fusion of Multispectral and Radar Images to Enhance Classification Accuracy and Estimate the Area under Various Crops Cultivation. *Journal of Agricultural Machinery, 13*(4), 493-508. https://doi.org/10.22067/jam.2022.78446.1123
32. Segarra, J., Buchaillot, M. L., Araus, J. L., & Kefauver, S. C. (2020). Remote Sensing for Precision Agriculture: Sentinel-2 Improved Features and Applications. *Agronomy, 10*(5). https://doi.org/10.3390/agronomy10050641
33. Shah, Ata-ul-Mohsin, M., Naeem, M., Nasir, M. F., Irfan-ul-Haq, M., & Hafeez, Z. (2012). Biology of Dubas Bug, *Ommatissus lybicus* (Homoptera: Tropiduchidae), a pest on date palm during spring and summer seasons in Panjgur, Pakistan. *Pakistan Journal of Zoology, 44*(6), 1603-1611.
34. Shah, A., Zia, A., Rafi, M. A., Mehmood, S. A., Aslam, S., & Chaudhry, M. T. (2016). Quantification of honeydew production caused by dubas bug on three date palm cultivars. *Journal of Entomology and Zoology Studies, 4*(4), 478-484.
35. Silva, C. R., Olthoff, A., de la Mata, J. A. D., & Alonso, A. P. (2013). Remote monitoring of

forest insect defoliation. A review. *Forest Systems*, *22*(3), 377-391. https://doi.org/10.5424/fs/2013223-04417

36. Tiwari, A. (2022). Chapter 2- Supervised learning: From theory to applications. In R. Pandey, S. K. Khatri, N. k. Singh, & P. Verma (Eds.), *Artificial Intelligence and Machine Learning for EDGE Computing* (pp. 23-32): Academic Press. https://doi.org/10.1016/b978-0-12-824054-0.00026-5
37. Wakil, W., Faleiro, J. R., & Miller, T. A. (2015). *Sustainable pest management in date palm: current status and emerging challenges*: Springer. https://doi.org/10.1007/978-3-319-24397-9
38. Weiss, M., Jacob, F., & Duveiller, G. (2020). Remote sensing for agricultural applications: A meta-review. *Remote Sensing of Environment*, *236*, 111402. https://doi.org/10.1016/j.rse.2019.111402
39. Yuan, L., Pu, R., Zhang, J., Wang, J., & Yang, H. (2016). Using high spatial resolution satellite imagery for mapping powdery mildew at a regional scale. *Precision Agriculture*, *17*(3), 332-348. https://doi.org/10.1007/s11119-015-9421-x
40. Zhang, J., Pu, R., Yuan, L., Wang, J., Huang, W., & Yang, G. (2014). Monitoring powdery mildew of winter wheat by using moderate resolution multi-temporal satellite imagery. *PloS one*, *9*(4), e93107. https://doi.org/10.1371/journal.pone.0093107

نشریه ماشین‌های کشاورزی
https://jame.um.ac.ir

مقاله پژوهشی

جلد ۱۶، شماره ۳، پاییز ۱۴۰۵، ص ۳۸۱-۳۶۵

ارزیابی پتانسیل تصاویر ماهواره‌ای چندطیفی سنتینل-۲ برای شناسایی هجوم آفت زنجرک در مناطق کشت نخل خرما

هادی کریمی[1*]، محمدجواد عصاری[2]، هادی زهدی[2]، فروغ رنجبر ورندی[3]

تاریخ دریافت: ۱۴۰۳/۰۷/۲۵
تاریخ پذیرش: ۱۴۰۴/۰۲/۰۹

چکیده

زنجرک خرما با تضعیف درختان خرما و کاهش تولید میوه، کشاورزی در خاورمیانه را تهدید می‌کند. شناسایی محل آلودگی برای کنترل موثر آفات بسیار مهم است. با این حال، بازرسی منظم میدانی می‌تواند پرهزینه، دشوار و زمان‌بر باشد، به‌خصوص در مناطق وسیع. این مطالعه توانایی تصاویر ماهواره‌ای چندطیفی سنتینل-۲ را برای شناسایی مکان‌های هجوم زنجرک خرما برای بهبود نظارت و فعال کردن کنترل فوری آفات، در نتیجه کاهش خسارات مالی، ارزیابی می‌کند. آزمایش صحرایی برای ارزیابی آلودگی در اردیبهشت ۱۴۰۲ همزمان با اوج شیوع آفت انجام شد. شدت آلودگی از طریق شمارش آفات در نخلستان‌های منطقه شهری بم تعیین شد. تصاویر چندطیفی سنتینل-۲ از یک منطقه خاص به‌دست آمد، برای تصحیح، آماده‌سازی داده‌های خام و استخراج اطلاعات پردازش شد. پس از مرحله پیش‌پردازش، مدل طبقه‌بندی‌کننده K-Nearest Neighbor مبتنی بر درخت KD برای توسعه مدلی با تمرکز بر شناسایی مکان‌های آلوده انتخاب شد. برای آموزش، ۷۰ درصد از داده‌های میدانی اندازه‌گیری‌شده، شامل مناطق غیرآلوده و مناطق با سه سطح آلودگی از سبک تا شدید و همچنین سایر ویژگی‌های زمین مانند ساختمان‌ها، جاده‌ها و غیره استفاده شد. ۳۰ درصد باقی‌مانده داده‌ها برای ارزیابی مدل آموزش‌دیده استفاده شد. مدل طبقه‌بند آموزش‌دیده در مقایسه با داده‌های حقیقت پایه، در حدود ۸۳ درصد پیش‌بینی‌های درست را با مجموعه داده آزمایشی به‌دست آورد. این دقت، توانایی تصاویر چندطیفی سنتینل-۲ و یادگیری ماشینی را برای شناسایی هجوم حشرات به زنجرک خرما در نخلستان‌ها برجسته می‌کند و می‌تواند مدیریت هدفمند و پایدار آفات را تسهیل کند.

واژه‌های کلیدی: بازرسی‌های میدانی، سنجش از دور، مدل طبقه‌بندی، میوه خرما

۱- بخش تحقیقات فنی و مهندسی کشاورزی، مرکز تحقیقات و آموزش کشاورزی و منابع طبیعی استان کرمان، سازمان تحقیقات، آموزش و ترویج کشاورزی، کرمان، ایران
۲- بخش تحقیقات گیاهپزشکی، مرکز تحقیقات و آموزش کشاورزی و منابع طبیعی استان کرمان، سازمان تحقیقات، آموزش و ترویج کشاورزی، کرمان، ایران
۳- گروه گیاه‌پزشکی، دانشکده کشاورزی، دانشگاه تبریز، تبریز، ایران
(*- نویسنده مسئول: Email: h_karimi@areeo.ac.ir)

https://doi.org/10.22067/jam.2025.90276.1297

Journal of Agricultural Machinery

Homepage: https://jame.um.ac.ir

Research Article
Vol. 16, No. 3, 2026, p. 383-397

Optimization of Energy Use in Pinto Bean Planting Systems: A Multi-Objective Genetic Algorithm Approach

R. Raeisi[1], M. Gholami Parashkoohi[2*], H. Afshari[3], A. Mohammadi[2]

1- Department of Biosystem Engineering, Tak.C., Islamic Azad University, Takestan, Iran
2- Department of Mechanical Engineering, ShQ.C., Islamic Azad University, Shahr-e Qods, Iran
3- Department of Food Science and Engineering, CT.C., Islamic Azad University, Tehran, Iran
(*- Corresponding Author Email: Mohammad.gholami@iau.ac.ir)

Received: 07 January 2025
Revised: 21 February 2025
Accepted: 08 March 2025
Available Online: 26 August 2025

How to cite this article:
Raeisi, R., Gholami Parashkoohi, M., Afshari, H., & Mohammadi, A. (2026). Optimization of Energy Use in Pinto Bean Planting Systems: A Multi-Objective Genetic Algorithm Approach. *Journal of Agricultural Machinery*, *16*(3), 383-397. https://doi.org/10.22067/jam.2025.91535.1331

Abstract

Bean planting systems are essential to global agriculture, serving as a vital food source for many populations. Optimizing these planting methods is crucial for enhancing efficiency and reducing environmental impacts. This study evaluates the energy inputs and outputs associated with two pinto bean cultivation techniques: flat and strip systems. Conducted in Fars province, southern Iran, the research involved 90 farms, 60 employing flat systems and 30 utilizing strip systems. Energy consumption was assessed in MJ ha^{-1} for various inputs, including labor, machinery, diesel, chemical fertilizers, biocides, electricity, and seeds. The flat system exhibited energy consumption of 20,067.12 MJ ha^{-1}, while the strip system utilized 18,171.76 MJ ha^{-1}. In terms of yield, the flat system produced 3000 kg ha^{-1}, in comparison to 3500 kg ha^{-1} from the strip system. Energy efficiency metrics indicated that the strip system outperformed the flat system with a higher energy use efficiency ratio (3.85 against 2.99) and better energy productivity (0.19 kg MJ^{-1} vs. 0.15 kg MJ^{-1}). Additionally, the strip system demonstrated lower specific energy consumption at 5.19 MJ kg^{-1}, compared to 6.69 MJ kg^{-1} for the flat system. The net energy gain was also greater for the strip system, recording 51,828.24 MJ ha^{-1} versus 39,932.88 MJ ha^{-1} for the flat system. Overall, the results highlight the favorable energy requirements and efficiency of the strip planting method over the traditional flat system, underscoring its potential for optimized resource allocation in pinto bean cultivation. The MOGA results indicated that strip systems achieve substantial energy savings of 3749.11 MJ ha^{-1} (25.99%), compared to flat systems, which save 3707.62 MJ ha^{-1} (22.66%). This further highlights the efficiency benefits of strip planting.

Keywords: Bean planting systems, Energy consumption, Energy use efficiency, Multi-objective genetic algorithm

Introduction

Energy efficiency is increasingly acknowledged as a vital element of sustainable agricultural practices, particularly within crop production systems (Noorani *et al.*, 2023). This concept focuses on reducing energy consumption while either maintaining or enhancing productivity (Jamali *et al.*, 2021). Strategies to achieve this include the adoption of energy-efficient technologies, optimization of resource utilization, and improvement of operational methods (Amoozad-Khalili *et al.*, 2021). Energy efficiency's importance transcends mere cost savings; it is essential in mitigating greenhouse gas emissions and tackling challenges posed by climate change in agriculture. Given that agriculture significantly contributes to energy consumption and

Authors retain the copyright. This is an open access article distributed under Creative Commons Attribution 4.0 International License (CC BY 4.0).

https://doi.org/10.22067/jam.2025.91535.1331

environmental degradation, optimizing energy use within these systems is crucial for promoting sustainability and minimizing the ecological footprint of the sector (Kaab *et al.*, 2023).

Pinto beans, scientifically known as *Phaseolus vulgaris*, are a widely cultivated variety of bean found in many regions around the globe (Fonseca Hernández *et al.*, 2023). Cultivating pinto beans involves several essential steps. First, soil preparation is critical, as these beans flourish in well-drained soil with a pH level ranging from 6.0 to 7.0. The soil should be rich in organic matter and nutrients, so it is important to till the soil and remove any weeds or debris prior to planting (Abad-González *et al.*, 2024). Next, planting typically occurs in the spring, following the last frost. Seeds can either be sown directly into the soil or started indoors and transplanted later. When planting, the seeds should be placed about 1-2 inches deep and spaced 2-4 inches apart in rows that are 18-24 inches apart (Bordonal *et al.*, 2018). Watering is another crucial aspect, as pinto beans require consistent moisture, particularly during dry spells. Care must be taken to avoid overwatering, which can cause root rot. It is best to water at the base of the plants to keep the foliage dry, as wet leaves can encourage disease. Fertilizing also plays a role in the successful growth of pinto beans. These plants are nitrogen-fixing, meaning they can utilize nitrogen from the air, but they may still benefit from an application of balanced fertilizer during the growing season (Heusala *et al.*, 2020). Weeding the area around pinto bean plants is important to prevent competition for nutrients and water. Regularly removing weeds by hand or using a hoe can help maintain a healthy growing environment without harming the plants. Harvesting usually occurs 90-120 days after planting, depending on the specific variety and environmental conditions (Mawof *et al.*, 2022). The beans are ready for harvest when the pods are plump and filled out, though not yet dried. To harvest, pull up the entire plant and remove the pods. Finally, once harvested, pinto beans must be dried thoroughly before storage. It's recommended to spread the beans in a single layer in a warm, dry area for 1-2 weeks until they are completely dry. For optimal preservation, store the dried beans in a cool, dark place in airtight containers (Altieri *et al.*, 2012).

Pinto beans, a staple food source for numerous communities globally, exemplify the challenges associated with conventional agricultural practices (Fonseca Hernández *et al.*, 2023). Traditional planting and harvesting methods for pinto beans typically incur high energy consumption and considerable environmental consequences. To combat these issues, researchers are increasingly employing advanced optimization techniques, such as multi-objective genetic algorithms (MOGA), to enhance the efficiency and sustainability of pinto bean production systems (Aghili Nategh *et al.*, 2021; Kaab *et al.*, 2019; Pourreza Movahed *et al.*, 2020). MOGA facilitates the simultaneous assessment of multiple objectives, including maximizing energy efficiency, minimizing greenhouse gas emissions, and optimizing economic returns, ultimately guiding the discovery of the most effective agricultural practices (Fathollahi-Fard *et al.*, 2023). In recent years, multi-objective optimization techniques have emerged as valuable tools for navigating the complex trade-offs inherent in agricultural systems. Genetic algorithms (GAs), modeled on the principles of natural selection, have proven effective for addressing optimization problems by exploring multiple solutions concurrently (Rahman & Szabó, 2021). By utilizing a MOGA framework to assess energy use in pinto bean planting systems, researchers can evaluate various factors, including yield enhancement, cost-effectiveness, and environmental impact reduction. This study delves into the use of MOGA in optimizing pinto bean planting systems, emphasizing the delicate balance between competing objectives intrinsic to agricultural production (Nategh *et al.*, 2021). By generating and iteratively refining a diverse array of potential solutions inspired by natural selection, MOGA aims to

pinpoint optimal strategies that enhance energy use while diminishing environmental impact. This methodology not only underscores the trade-offs among various objectives but also provides a framework for developing sustainable farming practices that can adapt to the evolving challenges of climate change and resource scarcity (Pourreza Movahed *et al.*, 2020). One paper addresses low agricultural production efficiency by studying multi-objective optimization of sustainable agricultural structures using genetic algorithms. It reviews agricultural development, the status of optimization algorithms, and establishes a model for optimal industrial allocation. The improved genetic algorithm enhances both the economic value and sustainability of the agricultural structure (Zhou & Fan, 2018). The quest for energy optimization in pinto bean planting systems through a multi-objective genetic algorithm presents a promising pathway toward bolstering agricultural sustainability. By integrating advanced optimization techniques into farming practices, this research aspires to offer insightful contributions to sustainable agriculture and practical recommendations for improving energy efficiency in bean production systems. Growing concerns regarding sustainable agricultural practices have underscored the need to optimize energy use across various cropping systems (Rahman & Szabó, 2021). As a vital legume in numerous diets and a key crop in diverse agricultural settings, pinto beans serve as a crucial case study for investigating energy efficiency in planting systems. Traditional farming practices often result in significant energy consumption, driven by machinery usage, fertilizer applications, and irrigation techniques, which can exacerbate environmental challenges and diminish overall sustainability (Boix-Cots *et al.*, 2022). Energy consumption and its environmental impacts have become significant concerns in recent centuries. Agriculture, as both an energy user and bioenergy supplier, is crucial for global economics and food security. Research in developing countries shows inefficiencies in energy flow in crop production. To address this, MOGAs were used to optimize agricultural inputs, minimizing greenhouse gas (GHG) emissions while maximizing energy output and benefit-cost ratios. Results indicated a potential 28% reduction in energy use and a 33% decrease in GHG emissions in watermelon production, with a significant increase in the benefit-cost ratio (Shamshirband *et al.*, 2015).

Optimizing energy use in pinto bean planting systems is a key advancement in sustainable agriculture, balancing productivity and environmental impact. A MOGA addresses trade-offs between yield, energy consumption, and costs by simulating natural selection. Solutions are refined through selection, crossover, and mutation, identifying strategies that harmonize energy efficiency with economic viability. This adaptable approach integrates with precision farming and eco-friendly practices, enhancing sustainability and resource management. Ultimately, applying this algorithm can transform farming, promoting economic and environmental sustainability, contributing to food security, and addressing challenges like climate change.

This study seeks to harness MOGA to develop optimized planting strategies that lower energy consumption while maximizing agricultural outputs. By pinpointing best practices customized for the specific conditions of pinto bean cultivation, this research not only aims to enhance productivity but also supports the broader movement toward sustainable agriculture. The findings from this work are expected to extend beyond pinto beans, offering valuable insights applicable to other crops and farming systems facing similar sustainability challenges.

Materials and Methods

Background information about the studied region

The research was conducted in Fars province, located in southern Iran, spanning latitudes from 27° 2′ to 31° 42′ and longitudes from 50° 42′ to 55° 36′ , with an area of 133,299 km^2 characterized by an

arid and semi-arid climate (Ministry of Jihad-e-Agriculture of Iran, 2024). The location of the case study is illustrated in Figure 1.

Fig. 1. The area of study in Fars province, Iran

The study involved 90 farms, comprising 60 that utilized flat cultivating systems and 30 that employed strip cultivating systems. A random survey was conducted with pinto bean producers to collect data on various agricultural input parameters, including seed quantities, fertilizer use, biocide application, energy sources, equipment and machinery, cultivated land areas, and Pinto bean yields. The sample size was determined using the method outlined in Eq. (1) (Cochran, 1977), and data collection was performed through in-person interviews.

$$\boldsymbol{n} = \frac{\frac{z^2 pq}{d^2}}{1 + \frac{1}{N}\left(\frac{z^2 pq}{d^2} - 1\right)} \quad (1)$$

The sample size (n) needed is calculated using the number of farms in the target population (N), a reliability coefficient (z) of 1.96 for a 95% confidence level, an estimated population attribute proportion (p) of 0.5, the complement of the estimated proportion (q) also at 0.5, and an allowable error deviation from the average population (d) of 0.05.

Energy use analysis

Energy analysis involves evaluating and assessing the energy consumption and efficiency of systems, buildings, or processes (Ghasemi-Mobtaker, Kaab, & Rafiee, 2020). This process includes gathering data on energy usage, pinpointing areas of waste, and formulating strategies to reduce consumption and enhance efficiency. Energy analysis can be applied across various sectors, such as residential, commercial, industrial, and transportation (Kaab *et al.*, 2019). It enables organizations and individuals to comprehend their energy usage patterns, identify potential savings, and make informed choices regarding energy conservation. Common methodologies in energy analysis include energy audits and energy modeling (Ghasemi-Mobtaker, Kaab, Rafiee, & Nabavi-Pelesaraei, 2022). These tools facilitate the quantification of energy consumption and identification of energy-saving opportunities. Ultimately, energy analysis is vital for promoting energy efficiency, decreasing greenhouse gas emissions, and meeting sustainability targets. It supports informed decision-making, propels energy conservation initiatives, and contributes to a more sustainable and resilient energy future. The energy equivalent of each input is outlined in Table 1.

Table 1- Conversion factors of energy inputs and outputs in the production of pinto bean

Item	Unit	Energy equivalent (MJ unit^{-1})	Reference
A. Input			
1. Human labor	h	1.96	(Mohammadi & Omid, 2010)
2. Machinery	kg yr^{-1a}	62.70	(Kaab, Khanali, Shadamanfar, & Jalalvand, 2024)
3. Diesel fuel	L	56.31	(Ghasemi-Mobtaker, Akram, & Keyhani, 2012)
4. Chemical fertilizers	kg		
(a) Nitrogen		78.10	(Hosseinzadeh-Bandbafha, Safarzadeh, Ahmadi, Nabavi-Pelesaraei, & Hosseinzadeh-Bandbafha, 2017)
(b) Phosphate		17.40	(Zangina, Suleiman, & Ahmed, 2023)
(c) Potassium		13.70	(Ramedani *et al.*, 2019)
5. Biocides	kg	250.00	(Khosruzzaman, Asgar, Karim, & Akbar, 2010)
7. Electricity	kWh	12.00	(Mandal *et al.*, 2015)
8. Seed	kg	20.00	(Boydston *et al.*, 2018)
B. Output			
1. Pinto bean	kg	20.00	(Boydston *et al.*, 2018)

[a] the economic life of machine (year)

Energy indicators refer to the metrics used to evaluate and monitor energy consumption, efficiency, and performance. These indicators offer meaningful insights into energy usage trends, highlight opportunities for improvement, and guide decisions aimed at optimizing energy use and minimizing costs (Hassan Ghasemi-Mobtaker *et al.*, 2024). Common energy indicators encompass energy intensity, energy efficiency ratios, energy consumption per production unit, and energy cost per output unit. Some of these indicators are outlined in equations (2) to (5). Businesses, industries, and governments can leverage these indicators to oversee and enhance their energy usage and sustainability initiatives.

$$\text{Energy use efficiency} = \frac{\text{Output energy (MJ)}}{\text{Input energy (MJ)}} \quad (2)$$

$$\text{Energy productivity} = \frac{\text{Production (kg)}}{\text{Input energy (MJ)}} \quad (3)$$

$$\text{Specific energy} = \frac{\text{Input energy (MJ)}}{\text{Production (kg)}} \quad (4)$$

$$\text{Net energy} = \text{Output energy (MJ)} - \text{Input energy (MJ)} \quad (5)$$

MOGA analysis

MOGA comprises multi criteria decision-making units (DMUs) that are associated with mathematical optimization problems when more than one objective function is to be quickly optimized. Multi-objective optimization (MOO) has been used in many fields, including preparation, economics, and engineering, where optimal decisions are entailed to be derived in the presence of compensation among multiple inconsistent objectives. Typical examples of MOO problems include maximizing tranquility while minimizing costs in purchasing a car, and minimizing emission of pollutants and fuel use while simultaneously maximizing vehicle performance, etc. There can be three or even more objectives in actual problems (Abidi *et al.*, 2018).

For a typical MOO problem, there cannot exist a solitary resolution that is able to optimize every objective. Instead, there exist unlimited numbers of Pareto optimal solutions, which are all considered good solutions. As such, the objectives are to determine a set of Pareto optimal solutions, or quantify trade-offs in fulfilling various aims, or assign a solitary resolution that can fulfil largely intrinsic priorities of a decision maker (DM) (Hu *et al.*, 2017).

An MOO problem is an optimization problem involving multi-objective functions. A typical MOO problem is expressed mathematically as Eq. (6):

$$\min(f_1(x), f_2(x),..., f_k(x)) \quad s.t. x \in X \tag{6}$$

where the set X signifies the possible set of determination directions and the integer $k \geq 2$ denotes the number of aims. The possible set usually comprises some constraint functions. Furthermore, the objective function vector is expressed as Eq. (7):

$$f: X \to \Re^k, f(x) = (f_1(x),..., f_k(x))^T \tag{7}$$

where x signifies a possible solution and $f(x) \in \Re$ denotes the compatibility of the possible solution. Pareto optimal solutions provide a way to solve this limitation. In real-world cases, the dissolutions that are not overmatched by other dissolutions across the entire search area constitute the collection of Pareto optimal solutions. The underlying significance is that these dissolutions cannot be altered for each purpose without inevitably compromising at least one of the other objectives (Konak *et al.*, 2006).

This study presents a technique used in MOGA to address these contradictory objectives simultaneously when solving MOO problems. GA usually functions by a set of chromosomes, which is named the population. The population is usually initialized randomly. As the calculation progresses, the population includes fitter and fitter solutions, and eventually it converges towards a solitary dissolution. GA employs two factors to produce new dissolutions from existing ones, crossover and mutation. During crossover operation, the chromosomes are re-composed to generate new chromosomes, resulting in viable offspring. In selecting chromosomes from the population, parents prioritize those that exhibit a higher compatibility function. Using a repetitious crossover operator, a good chromosome gene is expected to be more visible in the population and eventually converge to a single solution. The mutation operator furnishes a random transformation to the characteristics of the chromosome. In a generic GA, the mutation ratio is usually low. Whilst the crossover operation attempts to guide towards a convergent population with similar chromosomes in the population, the mutation operation again enters the genetic diversity of the population and helps to escape from local optimum. The proliferation comprises selection of chromosomes for the subsequent generation. Different fitness functions in GA include proportionate choices, grading, and competition, etc. (Deb *et al.*, 2003). GA is considered one of the best customary artificial intelligence (AI) methods owing to its robustness (Taghdisian *et al.*, 2015). Older systems of AI usually reverse, even if the outputs are only altered to a slight extent (Habibi-Yangjeh *et al.*, 2009). Moreover, when it comes to operating an exceptional conditional space, multimodal conditional space GA offers considerable advantages compared to other popular optimization techniques (Arthur *et al.*, 2016).

Given its population-based methodology, GA is well suited to solve MOO problems. A single-objective GA can be configured to deliver a set of multiple solutions in a single step. The capability of GA to probe different regions of a dissolution space presents it feasible to determine various sets of dissolutions for hard difficulties by multimodal, interchangeable, and non-convex dissolutions spaces. The crossover manager of GA is able to extract accurate solutions to various objectives, identifying new solutions in unexplored sectors of the Pareto front. As such, GA has been one of the most popular heuristic method to solve MOO problems (Mousavi-Avval *et al.*, 2017).

In this study, MOGA is employed for MOO in pinto bean production with two objectives comprising: (1) Minimizing energy consumption, (2) Maximizing the performance of pinto bean farms. The aim function is demonstrated as follows:

$$F_{\max/\min} = \sum_{i=1}^{j} C_i X_i + e_i \tag{8}$$

where C_i denotes model coefficient, X_i denotes variable inputs, and $F_{max/min}$ signifies the objective function to be minimized or maximized. When tackling an optimization problem, the MATLAB workbox solely permits the minimization of the target goal function. Therefore, for a maximized objective

function, it must be multiplied by (-1).

Results and Discussion

Energy use analysis

Table 2 illustrates the energy inputs and outputs associated with two different planting systems used in pinto bean production: Flat and Strip. It outlines various energy inputs for each system, including human labor, machinery, diesel fuel, chemical fertilizers (nitrogen, phosphate, and potassium), biocides, electricity, and seeds. The energy consumption for these inputs is expressed in MJ ha^{-1} for both systems. For the flat planting system, the total energy usage amounts to 20,067.12 MJ ha^{-1}, whereas the strip system records a total of 18,171.76 MJ ha^{-1}. Additionally, the table presents the production yields in kilograms for each system: the Flat system yields 3000 kg (equivalent to 60,000 kg ha^{-1}), while the strip system yields 3500 kg (or 70,000 kg ha^{-1}). This information sheds light on the energy efficiency and productivity of the two planting approaches, enabling stakeholders to make informed decisions regarding resource allocation and productivity in pinto bean farming. Figure 2 illustrates the distribution of energy sources used in different planting systems for pinto bean production. This depiction likely highlights the various energy inputs involved in cultivating pinto beans across multiple agricultural methods. These inputs may encompass human labor, machinery, fertilizers, pesticides, water, electricity, and other necessary resources for bean cultivation. By examining this distribution, researchers and farmers can evaluate the energy efficiency and sustainability of the various planting systems employed in pinto bean production. Efficient energy use in crop production can reduce greenhouse gas emissions (GHG) and promote sustainable agriculture. The study utilizes a MOGA to optimize energy inputs and reduce GHG emissions in wetland rice production in Malaysia. The findings indicated that farmers are using 37.8% more energy than needed for transplanting and 40% more for broadcast seeding. By implementing MOGA, GHG emissions could be decreased by 95.89 kg CO_2eq ha^{-1} for transplanting and by 236.13 kg CO_2eq ha^{-1} for broadcast seeding. Notably, even with reduced energy inputs, crop yields remained robust at 9.4 tonnes ha^{-1} and 9.2 tonnes ha^{-1}, respectively (Elsoragaby *et al.*, 2020).

Table 2- Energy inputs and outputs of different planting systems production of pinto bean

Item	Planting system			
	Flat land		Strip	
	Unit per ha	Energy use (MJ ha^{-1})	Unit per ha	Energy use (MJ ha^{-1})
1. Human labor (h)	350.00	686.00	300.00	588.00
2. Machinery (kg)	26.00	1630.20	35.00	2194.50
3. Diesel fuel (L)	32.00	1801.92	46.00	2590.26
4. Chemical fertilizers (kg)				
(a) Nitrogen	150.00	11715.00	150.00	9372.00
(b) Phosphate (P_2O_5)	50.00	870.00	40.00	696.00
(c) Potassium	20.00	274.00	20.00	274.00
5. Biocides (kg)	3.00	750.00	2.50	625.00
6. Electricity (kwh)	45.00	540.00	36.00	432.00
8. Seed (kg)	90.00	1800.00	70.00	1400.00
Total energy use (MJ)	**-**	**20067.12**		**18171.76**
B. Output (kg)				
1. Flat	3000.00	60000.00	-	-
1. Strip	-	-	3500.00	70000.00

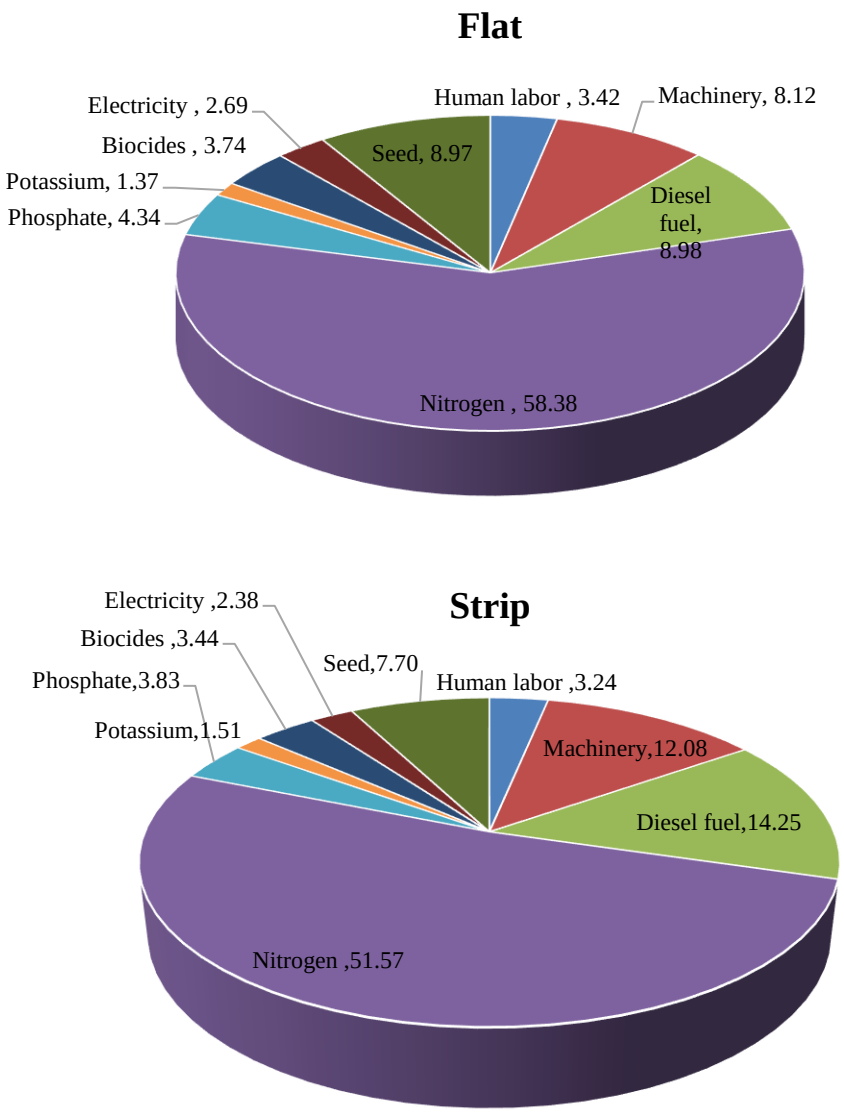

Fig. 2. Distribution of energy sources for the production of pinto beans in flat and strip planting systems

The information presented in Table 3 offers a comparative analysis of energy-related metrics for pinto bean production under two different planting systems: flat and strip. Firstly, the strip system exhibits a significantly higher energy use efficiency of 3.85, in contrast to the flat system's 2.99. This ratio reflects how effectively energy inputs are utilized during production. Secondly, when examining energy productivity, the strip system again outperforms the flat system with values of 0.19 kg MJ^{-1} versus 0.15 kg MJ^{-1}. This indicates greater output relative to energy consumption in the strip system. In terms of specific energy, the strip system shows an advantage with a lower value of 5.19 MJ kg^{-1} compared to 6.69 MJ kg^{-1} for the flat system, revealing that it requires less energy for production. Furthermore, the net energy gain is significantly higher in the strip system, reaching 51,828.24 MJ ha^{-1}, compared to 39,932.88 MJ ha^{-1} in the flat system. This metric illustrates the overall energy balance and productivity per unit area. In summary, the

data indicates that the strip planting system demonstrates superior performance regarding energy efficiency, productivity, and net energy gain when compared to the flat planting system for pinto bean production. One study compared energy consumption in sugarcane production at Salman Farsi Sugarcane Agro-Industrial Company, Iran, highlighting that plant cane requires more energy than ratoon cycles but is less efficient. Recommendations included optimizing machinery use and irrigation. The research also assessed health impacts, species loss, and cost differences, advocating for improved sustainability practices (Behnia *et al.*, 2025).

Table 3- Different energy indices for the different planting systems of pinto bean production

Energy indices (unit)	Planting system	
	Flat	Strip
Energy use efficiency (ratio)	2.99	3.85
Energy productivity (kg MJ^{-1})	0.15	0.19
Specific energy (MJ kg^{-1})	6.69	5.19
Net energy gain (MJ ha^{-1})	39932.88	51828.24

Optimization results

MOGA is a sophisticated method for addressing multi-criteria decision-making units (DMUs) within mathematical optimization frameworks, particularly when involving the simultaneous optimization of multiple objective functions. In many real-world scenarios, such as in engineering and economics, MOO is crucial for making optimal decisions when faced with conflicting objectives. For instance, in purchasing a vehicle, one may aim to maximize comfort while minimizing costs. Typical MOO problems often yield a multitude of Pareto optimal solutions, which represent trade-offs between the different objectives, rather than a sole optimal solution. A fundamental characteristic of MOO problems is that no single solution can achieve perfection for every objective. Instead, one seeks to identify a set of Pareto optimal solutions or to quantify trade-offs that fulfill various objectives. Mathematically, an MOO problem is represented as an optimization problem involving multiple objective functions, typically expressed through specific equations where the solution set is subject to various constraints.

In this context, MOGA is employed to handle conflicting objectives effectively. The algorithm operates on a population of potential solutions, represented as chromosomes. This population is initially generated randomly, and through successive iterations, the algorithm refines the solutions, guiding them towards more optimal states. Essential to this process are two genetic operators: crossover and mutation. Crossover allows for the recombination of existing chromosomes to produce offspring solutions, while mutation introduces random alterations, promoting diversity and assisting in escaping local optima. GA's selection mechanisms, including proportionate selection and tournament selection, drive the reproductive process, allowing fitter chromosomes to propagate through generations. This adaptability makes GA a robust method for solving complex optimization problems, especially in multi-modal landscapes typical of MOO. This study utilizes MOGA to optimize pinto bean production with the dual objectives of minimizing energy input and maximizing farm performance. The objective functions incorporated in the analysis consider various inputs and their associated energy requirements. The results in Table 4 indicate that the strip planting method outperforms the flat planting method in terms of energy efficiency across several input categories. For instance, in human labor energy requirements, strip systems require 470.23 MJ ha^{-1}, leading to a 25.05% energy saving compared to 547.15 MJ ha^{-1} for flat systems. Similarly, for

machinery, strip systems demand more overall energy but achieve significant savings in other input categories, such as nitrogen and phosphate, where they show lower energy requirements and higher percentage savings. The total energy inputs and savings reinforce the finding that strip planting consistently offers lower energy demands and better energy-saving benefits than flat systems, highlighting its efficacy in pinto bean production.

One study utilized a MOGA to optimize mixing energy, economic, and environmental indices in canola production. Data were gathered from oilseed farms in Mazandaran, Iran. A life cycle assessment evaluated environmental emissions, while econometric modeling identified relationships among energy inputs and three outputs: emissions, energy output, and productivity. The MOGA model aimed to maximize output energy and benefit-cost ratio, while minimizing emissions. Results showed a 32.1% reduction in emissions, with increases of 24.1% in output energy and 14.2% in benefit-cost ratio. Reductions in chemical use further benefited environmental, energy, and economic aspects (Mousavi-Avval *et al.*, 2017). Energy consumption and environmental damage from agriculture have increased in recent centuries. A study used life cycle assessment to evaluate the impacts of chickpea production, employing data envelopment analysis and MOGA techniques. Data from 110 enterprises during the 2014-2015 season revealed that MOGA significantly reduced energy requirements to 27,570.61 MJ ha^{-1}, a 17% decrease compared to DEA's 31,511.72 MJ ha^{-1}. MOGA also lowered environmental impacts, reducing acidification potential by 29% and global warming potential by 10%. Overall, MOGA outperformed DEA in optimizing energy use and minimizing environmental impacts (Elhami *et al.*, 2016).

Another study investigated biodiesel production from waste cooking palm oil containing 6% free fatty acids. The process involves both esterification and trans-esterification, which were simulated and optimized using Aspen Plus and Excel-based multi-objective optimization techniques. The findings indicate that this method is more efficient, reducing organic waste by 32% and decreasing heat duty requirements by 39%. Additionally, it is 1.6% more profitable (Patle *et al.*, 2014).

Table 4- Optimum energy requirement and saving energy of different planting systems of pinto bean production

Input	Optimum energy requirement (MJ ha^{-1})		Saving energy (MJ ha^{-1})		Saving energy (%)	
	Flat	Strip	Flat	Strip	Flat	Strip
1. Human labor	547.15	470.23	138.85	117.77	25.38	25.05
2. Machinery	1356.14	1872.65	274.06	321.85	20.21	17.19
3. Diesel fuel	1426.42	2145.35	375.5	444.91	26.32	20.74
4.Nitrogen	9546.23	7125.49	2168.77	2246.51	22.72	31.53
5.Phosphate	640.00	487.00	230.00	209.00	35.94	42.92
6.Potassium	210.56	210.56	63.44	63.44	30.13	30.13
7. Biocides	650.00	510.25	100.00	114.75	15.38	22.49
8. Electricity	410.00	326.54	130.00	105.46	31.71	32.30
9. Seed	1546.00	1274.58	254.00	125.42	16.43	9.84
Total energy input	**16359.50**	**14422.65**	**3707.62**	**3749.11**	**22.66**	**25.99**

Conclusion

The evaluation of pinto bean cultivation methods in Fars province, southern Iran, underscores the significant advantages of adopting the strip planting system over the traditional flat system. The comprehensive analysis of energy inputs and outputs demonstrates that the strip system not only consumes less energy—18,171.76 MJ ha^{-1} compared to the 20,067.12 MJ ha^{-1} required by the flat system—but also produces higher yields, with 3,500 kg ha^{-1} against the 3,000 kg

ha^{-1} from the flat method. This translates into a more favorable energy efficiency ratio (3.85 versus 2.99) and enhanced energy productivity (0.19 kg MJ^{-1} compared to 0.15 kg MJ^{-1}), reflecting the efficacy of the strip system in optimizing resource allocation and reducing environmental impacts. Moreover, the net energy gain of the strip system, at 51,828.24 MJ ha^{-1}, surpasses that of the flat system, which records 39,932.88 MJ ha^{-1}. This substantial difference in energy performance illustrates the pressing need for transformation in agricultural practices, advocating for a shift that aligns with global sustainability goals in food production. The findings from this study not only highlight the economic viability of the strip planting method but also suggest profound implications for future agricultural practices as the sector faces mounting pressures to enhance efficiency and reduce carbon footprints. To realize the benefits of strip planting, it is essential to promote educational initiatives aimed at training farmers and agricultural workers in its principles. Enhanced understanding of the technique's advantages—including energy savings and improved yields—will empower farmers to adopt this innovative approach. Furthermore, supportive policy measures, such as grants and subsidies for sustainable agricultural practices, should be prioritized to encourage the transition towards more energy-efficient methodologies. Overall, the current research advocates for a critical reassessment of traditional farming techniques. By encouraging the adoption of modern, efficient alternatives like the strip planting system, stakeholders can pave the way for a more sustainable future in pinto bean cultivation—one that promotes both environmental stewardship and economic prosperity. The urgency of such a transformation is paramount as agriculture evolves to meet global challenges, ensuring food security while safeguarding our planet's resources.

Conflict of Interest: The authors declare no competing interests.

Author Contributions

R. Raisi: Data acquisition, Text mining, technical advice, Methodology

M. Gholami Parashkoohi: Supervision, Validation, Software cervices

H. Afshari: Technical advice, Visualization, Review and editing services

A. Mohammadi: Numerical/computer simulation, Validation

References

1. Abad-González, J., Nadi, F., & Pérez-Neira, D. (2024). Energy-water-food security nexus in mung bean production in Iran: An LCA approach. *Ecological Indicators, 158*, 111442. https://doi.org/10.1016/J.ECOLIND.2023.111442
2. Abidi, M. H., Al-Ahmari, A. M., Umer, U., & Rasheed, M. S. (2018). Multi-objective optimization of micro-electrical discharge machining of nickel-titanium-based shape memory alloy using MOGA-II. *Measurement, 125*, 336-349. https://doi.org/10.1016/J.MEASUREMENT.2018.04.096
3. Aghili Nategh, N., Banaeian, N., Gholamshahi, A., & Nosrati, M. (2021). Optimization of energy, economic, and environmental indices in sunflower cultivation: A comparative analysis. *Environmental Progress & Sustainable Energy, 40*(2), e13505. https://doi.org/10.1002/EP.13505
4. Altieri, M. A., Funes-Monzote, F. R., & Petersen, P. (2012). Agroecologically efficient agricultural systems for smallholder farmers: Contributions to food sovereignty. *Agronomy for Sustainable Development, 32*(1), 1-13. https://doi.org/10.1007/s13593-011-0065-6
5. Amoozad-Khalili, M., Feizabadi, Y., & Norouzi, G. (2021). Application of artificial neural network for prediction of energy flow in wheat production based on mechanization development approach. *Energy Equipment and Systems, 9*(2), 191-207.

https://doi.org/10.22059/EES.2021.244667
6. Arthur, D. E., Uzairu, A., Mamza, P., Stephen, A. E., & Shallangwa, G. (2016). Quantum modelling of the Structure-Activity and toxicity relationship studies of some potent compounds on SR leukemia cell line. *Chemical Data Collections, 5-6*, 46-61. https://doi.org/10.1016/J.CDC.2016.10.004
7. Behnia, M., Ghahderijani, M., Kaab, A., & Behnia, M. (2025). Evaluation of sustainable energy use in sugarcane production: A holistic model from planting to harvest and life cycle assessment. *Environmental and Sustainability Indicators, 26*, 100617. https://doi.org/10.1016/J.INDIC.2025.100617
8. Boix-Cots, D., Pardo-Bosch, F., Blanco, A., Aguado, A., & Pujadas, P. (2022). A systematic review on MIVES: A sustainability-oriented multi-criteria decision-making method. *Building and Environment, 223*, 109515. https://doi.org/10.1016/J.BUILDENV.2022.109515
9. Bordonal, R. de O., Carvalho, J. L. N., Lal, R., de Figueiredo, E. B., de Oliveira, B. G., & La Scala, N. (2018). Sustainability of sugarcane production in Brazil. A review. *Agronomy for Sustainable Development, 38*(2), 1-23. https://doi.org/10.1007/S13593-018-0490-X
10. Boydston, R. A., Porter, L. D., Chaves-Cordoba, B., Khot, L. R., & Miklas, P. N. (2018). The impact of tillage on pinto bean cultivar response to drought induced by deficit irrigation. *Soil and Tillage Research, 180*, 63-72. https://doi.org/10.1016/J.STILL.2018.02.011
11. Cochran, W. G. (1977). The estimation of sample size. *Sampling Techniques, 3*, 72-90. John Wiley & Sons, New York.
12. Deb, K., Zope, P., & Jain, A. (2003). Distributed computing of pareto-optimal solutions with evolutionary algorithms. *International Conference on Evolutionary Multi-Criterion Optimization*, 534-549. https://doi.org/10.1007/3-540-36970-8_38
13. Elhami, B., Akram, A., & Khanali, M. (2016). Optimization of energy consumption and environmental impacts of chickpea production using data envelopment analysis (DEA) and multi objective genetic algorithm (MOGA) approaches. *Information Processing in Agriculture, 3*(3), 190-205. https://doi.org/10.1016/j.inpa.2016.07.002
14. Elsoragaby, S., Yahya, A., Mahadi, M. R., Nawi, N. M., Mairghany, M., M Elhassan, S. M., & Kheiralla, A. F. (2020). Applying multi-objective genetic algorithm (MOGA) to optimize the energy inputs and greenhouse gas emissions (GHG) in wetland rice production. *Energy Reports, 6*, 2988-2998. https://doi.org/10.1016/J.EGYR.2020.10.010
15. Fathollahi-Fard, A. M., Tian, G., Ke, H., Fu, Y., & Wong, K. Y. (2023). Efficient multi-objective metaheuristic algorithm for sustainable harvest planning problem. *Computers & Operations Research, 158*, 106304. https://doi.org/10.1016/J.COR.2023.106304
16. Fonseca Hernández, D., Mojica, L., Berhow, M. A., Brownstein, K., Lugo Cervantes, E., & Gonzalez de Mejia, E. (2023). Black and pinto beans (*Phaseolus vulgaris* L.) unique mexican varieties exhibit antioxidant and anti-inflammatory potential. *Food Research International, 169*, 112816. https://doi.org/10.1016/J.FOODRES.2023.112816
17. Ghasemi-Mobtaker, H., Kaab, A., & Rafiee, S. (2020). Application of life cycle analysis to assess environmental sustainability of wheat cultivation in the west of Iran. *Energy, 193*. https://doi.org/10.1016/j.energy.2019.116768
18. Ghasemi-Mobtaker, Hassan, Akram, A., & Keyhani, A. (2012). Energy use and sensitivity analysis of energy inputs for alfalfa production in Iran. E*nergy for Sustainable Development, 16*(1), 84-89. https://doi.org/10.1016/j.esd.2011.10.009
19. Ghasemi-Mobtaker, Hassan, Ataiee, F. S., Akram, A., & Kaab, A. (2024). Feasibility study of using photovoltaic cells for a commercial hydroponic greenhouse: Energy analysis and life cycle assessment. *E-Prime - Advances in Electrical Engineering, Electronics and Energy, 8*, 100597. https://doi.org/10.1016/J.PRIME.2024.100597
20. Ghasemi-Mobtaker, Hassan, Kaab, A., Rafiee, S., & Nabavi-Pelesaraei, A. (2022). A

comparative of modeling techniques and life cycle assessment for prediction of output energy, economic profit, and global warming potential for wheat farms. *Energy Reports, 8*, 4922-4934. https://doi.org/10.1016/J.EGYR.2022.03.184

21. Habibi-Yangjeh, A., Pourbasheer, E., & Danandeh-Jenagharad, M. (2009). Application of principal component-genetic algorithm-artificial neural network for prediction acidity constant of various nitrogen-containing compounds in water. *Monatshefte Für Chemie- Chemical Monthly, 140*(1), 15-27. https://doi.org/10.1007/s00706-008-0049-7
22. Heusala, H., Sinkko, T., Sözer, N., Hytönen, E., Mogensen, L., & Knudsen, M. T. (2020). Carbon footprint and land use of oat and faba bean protein concentrates using a life cycle assessment approach. *Journal of Cleaner Production, 242*, 118376. https://doi.org/10.1016/J.JCLEPRO.2019.118376
23. Hosseinzadeh-Bandbafha, H., Safarzadeh, D., Ahmadi, E., Nabavi-Pelesaraei, A., & Hosseinzadeh-Bandbafha, E. (2017). Applying data envelopment analysis to evaluation of energy efficiency and decreasing of greenhouse gas emissions of fattening farms. *Energy, 120*, 652-662. https://doi.org/10.1016/j.energy.2016.11.117
24. Hu, N., Zhou, P., & Yang, J. (2017). Comparison and combination of NLPQL and MOGA algorithms for a marine medium-speed diesel engine optimisation. *Energy Conversion and Management, 133*, 138-152. https://doi.org/10.1016/J.ENCONMAN.2016.11.066
25. Jamali, M., Soufizadeh, S., Yeganeh, B., & Emam, Y. (2021). A comparative study of irrigation techniques for energy flow and greenhouse gas (GHG) emissions in wheat agroecosystems under contrasting environments in south of Iran. *Renewable and Sustainable Energy Reviews, 139*, 110704. https://doi.org/10.1016/J.RSER.2021.110704
26. Kaab, A., Ghasemi-Mobtaker, H., & Sharifi, M. (2023). A study of changes in energy consumption trend and environmental indicators in the production of agricultural crops using a life cycle assessment approach in the years 2018-2022. *Iranian Journal of Biosystem Engineering, 54*(3), 1-18. https://doi.org/10.22059/ijbse.2023.364738.665522
27. Kaab, A., Khanali, M., Shadamanfar, S., & Jalalvand, M. (2024). Assessment of energy audit and environmental impacts throughout the life cycle of barley production under different irrigation systems. *Environmental and Sustainability Indicators, 22*, 100357. https://doi.org/10.1016/J.INDIC.2024.100357
28. Kaab, A., Sharifi, M., Mobli, H., Nabavi-Pelesaraei, A., & Chau, K. (2019). Use of optimization techniques for energy use efficiency and environmental life cycle assessment modification in sugarcane production. *Energy, 181*, 1298-1320. https://doi.org/10.1016/J.ENERGY.2019.06.002
29. Khosruzzaman, S., Asgar, M. A., Karim N., & Akbar S. (2010). Energy intensity and productivity in relation to agriculture-Bangladesh perspective. *Journal of Agricultural Technology, 6*(4), 615-630. http://www.ijat-aatsea.com/pdf/October_v6_n4_10/1-104-IJAT2009_84R.pdf
30. Konak, A., Coit, D. W., & Smith, A. E. (2006). Multi-objective optimization using genetic algorithms: A tutorial. *Reliability Engineering & System Safety, 91*(9), 992-1007. https://doi.org/10.1016/j.ress.2005.11.018
31. Mandal, S., Roy, S., Das, A., Ramkrushna, G. I., Lal, R., Verma, B. C., Kumar, A., Singh, R. K., & Layek, J. (2015). Energy efficiency and economics of rice cultivation systems under subtropical Eastern Himalaya. *Energy for Sustainable Development, 28*, 115-121. https://doi.org/10.1016/j.esd.2015.08.002
32. Mawof, A., Prasher, S. O., Bayen, S., Anderson, E. C., Nzediegwu, C., & Patel, R. (2022). Barley Straw Biochar and Compost Affect Heavy Metal Transport in Soil and Uptake by Potatoes Grown under Wastewater Irrigation. *Sustainability, 14*(9), 5665. https://doi.org/10.3390/SU14095665

33. Ministry of Jihad-e-Agriculture of Iran. (2024). Annual Agricultural Statistics. (in Persian). Retrieved from: https://www.maj.ir/
34. Mohammadi, A., & Omid, M. (2010). Economical analysis and relation between energy inputs and yield of greenhouse cucumber production in Iran. *Applied Energy*, *87*(1), 191-196. https://doi.org/10.1016/J.APENERGY.2009.07.021
35. Mousavi-Avval, S. H., Rafiee, S., Sharifi, M., Hosseinpour, S., Notarnicola, B., Tassielli, G., & Renzulli, P. A. (2017). Application of multi-objective genetic algorithms for optimization of energy, economics and environmental life cycle assessment in oilseed production. *Journal of Cleaner Production*, *140*, 804-815. https://doi.org/10.1016/j.jclepro.2016.03.075
36. Nategh, N. A., Banaeian, N., Gholamshahi, A., & Nosrati, M. (2021). Optimization of energy, economic, and environmental indices in sunflower cultivation: A comparative analysis. *Environmental Progress & Sustainable Energy*, *40*(2), e13505. https://doi.org/10.1002/EP.13505
37. Noorani, M. H., Asakereh, A., & Siahpoosh, M. R. (2023). Investigating cumulative energy and exergy consumption and environmental impact of sesame production systems, a case study. *International Journal of Exergy*, *42*(1), 96-114. https://doi.org/10.1504/IJEX.2023.134289
38. Patle, D. S., Sharma, S., Ahmad, Z., & Rangaiah, G. P. (2014). Multi-objective optimization of two alkali catalyzed processes for biodiesel from waste cooking oil. *Energy Conversion and Management*, *85*, 361-372. https://doi.org/10.1016/J.ENCONMAN.2014.05.034
39. Pourreza Movahed, Z., Kabiri, M., Ranjbar, S., & Joda, F. (2020). Multi-objective optimization of life cycle assessment of integrated waste management based on genetic algorithms: A case study of Tehran. *Journal of Cleaner Production*, *247*, 119153. https://doi.org/10.1016/J.JCLEPRO.2019.119153
40. Rahman, M. M., & Szabó, G. (2021). Multi-objective urban land use optimization using spatial data: A systematic review. *Sustainable Cities and Society*, *74*, 103214. https://doi.org/10.1016/J.SCS.2021.103214
41. Ramedani, Z., Alimohammadian, L., Kheialipour, K., Delpisheh, P., & Abbasi, Z. (2019). Comparing energy state and environmental impacts in ostrich and chicken production systems. *Environmental Science and Pollution Research*, *26*(27), 28284-28293. https://doi.org/10.1007/s11356-019-05972-8
42. Shamshirband, S., Khoshnevisan, B., Yousefi, M., Bolandnazar, E., Anuar, N. B., Wahab, A. W. A., & Khan, S. U. R. (2015). A multi-objective evolutionary algorithm for energy management of agricultural systems-a case study in Iran. *Renewable and Sustainable Energy Reviews*, *44*, 457-465. https://doi.org/10.1016/j.rser.2014.12.038
43. Taghdisian, H., Pishvaie, M. R., & Farhadi, F. (2015). Multi-objective optimization approach for green design of methanol plant based on CO_2-efficeincy indicator. *Journal of Cleaner Production*, *103*, 640-650. https://doi.org/10.1016/J.JCLEPRO.2014.05.032
44. Zangina, J. S., Suleiman, M. A., & Ahmed, A. (2023). Energy analysis and optimization of heat integrated air separation column based on non-equilibrium stage model. *Results in Engineering*, *19*, 101211. https://doi.org/10.1016/J.RINENG.2023.101211
45. Zhou, Y., & Fan, H. (2018). Research on multi objective optimization model of sustainable agriculture industrial structure based on genetic algorithm. *Journal of Intelligent & Fuzzy Systems*, *35*(3), 2901-2907. https://doi.org/10.3233/JIFS-169645

نشریه ماشین‌های کشاورزی
https://jame.um.ac.ir

مقاله پژوهشی

جلد ۱۶، شماره ۳، پاییز ۱۴۰۵، ص ۳۹۷-۳۸۳

بهینه‌سازی مصرف انرژی در سامانه‌های کاشت لوبیا چیتی: با رویکرد الگوریتم ژنتیک چندهدفه

رضا رئیسی[۱]، محمد غلامی پرشکوهی[۲*]، حامد افشاری[۳]، احمد محمدی[۲]

تاریخ دریافت: ۱۴۰۳/۱۰/۱۸
تاریخ پذیرش: ۱۴۰۳/۱۲/۱۸

چکیده

سامانه‌های کاشت لوبیا برای کشاورزی جهانی ضروری است و به‌عنوان یک منبع غذایی حیاتی برای بسیاری از جمعیت‌ها عمل می‌کند. بهینه‌سازی این روش‌های کاشت برای افزایش کارایی و کاهش اثرات زیست‌محیطی بسیار مهم است. این مطالعه ورودی‌ها و خروجی‌های انرژی مرتبط با دو تکنیک کشت لوبیا چیتی را ارزیابی می‌کند: سیستم‌های تخت و نواری. این تحقیق که در استان فارس، جنوب ایران انجام شد، شامل ۹۰ مزرعه، ۶۰ مزرعه با استفاده از سیستم‌های تخت و ۳۰ با استفاده از سیستم نواری بود. این ارزیابی مصرف انرژی بر حسب مگاژول در هکتار برای نهاده‌های مختلف از جمله نیروی کار، ماشین‌ها، گازوئیل، کودهای شیمیایی، سموم شیمیایی، برق و بذر را پوشش می‌دهد. سامانه تخت مصرف ۲۰۰۶۷/۱۲ مگاژول در هکتار را نشان می‌دهد، در حالی‌که سیستم نواری از ۱۸۱۷۱/۷۶ مگاژول در هکتار استفاده می‌کند. از نظر عملکرد، سامانه تخت ۳۰۰۰ کیلوگرم در هکتار در مقایسه با ۳۵۰۰ کیلوگرم در هکتار برای سامانه نواری تولید می‌کند. این مطالعه بیشتر معیارهای بهره‌وری انرژی را بررسی می‌کند و عملکرد برتر سامانه نوار را با نسبت کارایی مصرف انرژی بالاتر (۳/۸۵ در مقابل ۲/۹۹) و بهره‌وری انرژی بیشتر ۰/۱۹ کیلوگرم بر مگاژول در مقایسه با ۰/۱۵کیلوگرم بر مگاژول برجسته می‌کند. معیارهای انرژی خاص نشان می‌دهد که سامانه نواری انرژی کمتری به‌ازای هر کیلوگرم لوبیا تولیدشده مصرف می‌کند ۵/۱۹ در مقابل ۶/۶۹ مگاژول بر کیلوگرم علاوه بر این، سود خالص انرژی برای سامانه نواری با ۵۱۸۲۸/۲۴ مگاژول در هکتار بالاتر است، در مقابل ۳۹۹۳۲/۸۸ مگاژول در هکتار برای سامانه تخت یافته‌ها بر نیازهای بهینه انرژی برای هر دو سامانه تأکید می‌کنند، به‌طور کلی، نتایج، نیازمندی‌های انرژی مطلوب و کارایی روش کاشت نواری را نسبت به سیستم مسطح سنتی نشان می‌دهد و بر پتانسیل آن برای تخصیص بهینه منابع در کشت لوبیا چیتی تاکید می‌کند. نتایج الگوریتم ژنتیک چندهدفه نشان داد که سامانه‌های نواری در مقایسه با سامانه‌های مسطح که ۳۷۰۷/۶۲ مگا ژول در هکتار (۲۲/۶۶ درصد) صرفه‌جویی می‌کنند، به میزان قابل‌توجهی ۳۷۴۹/۱۱ مگاژول در هکتار (۲۵/۹۹ درصد) صرفه‌جویی انرژی می‌کنند. این بیشتر مزایای کارایی کاشت نواری را برجسته می‌کند.

واژه‌های کلیدی: الگوریتم ژنتیک چندهدفه، سامانه‌های کاشت لوبیا، کارایی مصرف انرژی، مصرف انرژی

۱- گروه مهندسی بیوسیستم، دانشگاه آزاد اسلامی، تاکستان، ایران
۲- گروه مهندسی مکانیک، دانشگاه آزاد اسلامی، شهر قدس، ایران
۳- گروه علوم و مهندسی صنایع غذایی، دانشگاه آزاد اسلامی، تهران، ایران
(*- نویسنده مسئول: Email: Mohammad.gholami@iau.ac.ir)

https://doi.org/10.22067/jam.2025.91535.1331

Journal of Agricultural Machinery

Homepage: https://jame.um.ac.ir

Research Article
Vol. 16, No. 3, 2026, p. 399-425

Modification and Analysis of Integrated Enset (*Ensete ventricosum*) Processing Machine Components

B. Adugna[1], K. Purushottam Kolhe[2*], M. Gutu[1]

1- Department of Mechanical Engineering, School of Mechanical, Chemical and Materials Engineering at Adama Science and Technology University, Adama, Ethiopia
Department of Mechanical Engineering, Sinhgad College of Engineering, Vadgaon (BK.), 411041, SPPU Pune University, India
(*- Corresponding Author Email: kishorkolhe05@gmail.com)

Received: 22 January 2025
Revised: 09 March 2025
Accepted: 16 March 2025
Available Online: 21 June 2025

How to cite this article:
Adugna, B., Purushottam Kolhe, K., & Gutu, M. (2026). Modification and Analysis of Integrated Enset (*Ensete ventricosum*) Processing Machine Components. *Journal of Agricultural Machinery, 16*(3), 399-425. https://doi.org/10.22067/jam.2025.91751.1334

Abstract

This research aimed to enhance the design and functionality of an integrated enset processing machine by focusing on key components such as the shaft, cylinder drum, breastplate, and drum blade. Existing enset processing machines suffer from inefficiencies due to component wear, mechanical breakdowns, and suboptimal design, leading to operational challenges. To address these issues, targeted design modifications were planned for the machine's components. The materials for these components were selected according to ASTM standards. The modified components were rigorously analyzed using the Finite Element Method in the Workbench module of ANSYS 2023 R1 software at Adama Science and Technology University, Adama, Ethiopia. The study reported maximum stresses of 120 MPa, 250 MPa, 400 MPa, and 260 MPa, and minimum stresses of 30 MPa, 70 MPa, 120 MPa, and 80 MPa for the shaft, cylinder drum, blade, and breastplate, respectively. Maximum deformations were found to be 0.15 mm, 0.3 mm, 0.55 mm, and 0.35 mm for these components, with a maximum safety factor of 15 for all. These results indicate that the modifications provide safe working conditions. The design ensures that the drum, drum blade, and breastplate possess sufficient rigidity to withstand operational forces, with minimal deformation (2.39×10^{-6} mm for the drum blade), remaining within a safety factor limit of 1.25. Additionally, the machine demonstrated excellent energy dissipation and vibrational response, indicating structural robustness.

Keywords: Breastplate, Cylinder drum, Deformation, Drum blade, Enset, Stress

Introduction

Processing *Ensete ventricosum*, commonly known as Enset, is essential to local economies and food production, serving as a major crop in Ethiopia and other parts of East Africa (Borrell *et al*., 2020). It has diverse uses in food processing, including its fibrous stalks and tubers, and plays a significant role in subsistence farming (Nabeshima, Moro, Campelo, Sant'Ana, & Clerici, 2020). The need for efficient processing equipment has driven the development of integrated machines aimed at increasing output and reducing labor intensity (Duflou *et al*., 2012; Jima, Kolhe, & Jiru, 2025). Components of enset processing machines, such as the shaft, cylinder drum, breastplate, and drum blade, are designed with standard mechanical properties and supported by relevant research literature (David Müzel, Bonhin, Guimarães, & Guidi, 2020).

Despite its significance, enset processing faces challenges due to the lack of advanced technology for efficient processing. Traditional manual methods are time-consuming and often yield inconsistent results. Mechanical devices intended to assist

Authors retain the copyright. This is an open access article distributed under Creative Commons Attribution 4.0 International License (CC BY 4.0).

https://doi.org/10.22067/jam.2025.91751.1334

processing have not been widely adopted, mainly due to issues related to their efficiency, design, and integration into local agricultural practices. Attempts to mechanize corm grating have converted old manual methods into mechanical systems that reduce labor, time, and drudgery, helping communities address these challenges. However, integrated processing machines still suffer from inefficiencies, particularly in power consumption, component wear, and inconsistent quality of kocho and bulla products, which are limited by machine quality (Kudama, Tolera, & Gebeyehu, 2022). Literature reports that the shaft and power transmitters of decorticator and corm grater machines operate from a single power source (Workesa, Gebresenbet, Fanta, & Chaka, 2021). To ensure quality in decorticated pulpy tissue and minimize fiber damage, parameters including the breastplate's concave clearance, beater drum speed, and sheath feeding rate must be precisely adjusted, avoiding harm to fibers or residual pulpy sheath tissue (Deressa, Derese, & Dula, 2023). These challenges hinder the widespread adoption of such machines in rural communities where enset processing is a common practice.

To predict the mechanical behavior of enset processing machine components and refine the designs before physical prototyping, Finite Element Analysis (FEA) is employed (Jemghili, Ait Taleb, & Mansouri, 2023; Jima *et al*., 2025). This study focuses on technical aspects of modifying and analyzing integrated enset processing machines. FEA is a computational technique used to predict the behavior of materials and structures under various conditions such as stress, deformation, and movement (David Müzel *et al*., 2020). It divides complex structures into smaller elements and evaluates their performance, providing insights into real-world behavior. Key concepts in this analysis include stress analysis, which examines the internal forces acting on components, and fatigue analysis, which assesses material degradation from repeated stress. Additionally, understanding the material properties of the components is crucial for improving strength, flexibility, and durability (Hollaway, 2010). As noted, precise adjustment of parameters like breastplate concave clearance, drum speed, and sheath feeding rate is critical to maintain product quality without damaging fibers (Deressa *et al*., 2023).

Fabrication and assembly of enset machine components are facilitated by using materials without prior engineering property prediction, which can be improved by applying finite element analysis through computer-aided design (CAD) software (Digvijay & Kiran, 2015). Numerous numerical methods exist to solve complex physical problems with acceptable accuracy (Hamming, 2012). Among these, the finite element method is the most widely used in engineering. Its fundamental principle involves determining unknown node values using variational principal, as described by Xing, Qin, and Guo (2017), with the governing equation expressed in matrix form:

$$[C] \times [L] = [S] \quad (1)$$

where vector $[C]$ represents the unknown value of the quantity area at nodes, $[L]$ is the known load vector, and $[S]$ is the known constant matrix in the stress analysis.

The components of the integrated enset processing machine, such as shaft, beater drum, drum blade, breastplate, and power transmission elements are constructed from various engineering materials, designed to perform their functions without failure or damage to the fibers (Bekele, Lemu, & Jiru, 2022). Specific agricultural machinery parameters, such as operational load, force, torque, weight, torsion, dimension, and the shape of functional components were determined and used as input data in ANSYS software to optimize efficiency through the application of engineering principles (Chen *et al*., 2023).

Motion analysis and stress distribution were conducted using the finite element approach, confirming that all machine components operate without sustaining damage (Tezuka, 2006). For validation, finite element simulation of the model was employed (Szabó,

Actis, & Rusk, 2021). The model was validated by comparing theoretical and simulation results for shear stress and angle of twist, both of which fell within acceptable limits. Key design considerations include the weight of the decorticator and grater cylinder, power requirements, pulley and belt design, shaft diameter, threshing torque, torsional moment, bearing design, and critical speed. It is important to note that even the most refined model remains an approximation of the real physical system (Szabó *et al*., 2021).

To ensure safe working conditions, the machine components will be manufactured with careful attention to design quality, feeding rate, operating speed, and the clearance between the beater and concave breastplate curve of the machines, all while maintaining cost effectiveness (Wang, Huang, & Yin, 2021). Additionally, any major issues that could compromise the machine's high safety factor, which may result in costly failures, will be addressed (Colledani *et al*., 2014).

The objective of this study is to modify the design and functionality of an integrated enset processing machine by enhancing key components, including the shaft, cylinder drum, breastplate, and cylinder drum blade. These modifications aim to address common inefficiencies in existing machines, which are often affected by component wear, mechanical breakdowns, and poor design. These factors contribute to reduced operational efficiency. The proposed modifications focus on improving the machine's overall performance, durability, and safety.

This research specifically focuses on the redesign of the critical components of the integrated enset processing machine. The study entails the selection of materials according to ASTM standards for the components. It also involved simulating modified parts (Mahmood & Mohammed, 2022) using the Finite Element Method (FEM) in ANSYS Workbench 2023 R1. Furthermore, it includes a thorough analysis of the resulting mechanical behavior under operational conditions. The scope encompasses the evaluation of stresses, deformations, and the safety factor for each component, ensuring the machine's ability to withstand operating forces while minimizing operational risks.

The novelty of this study lies in the integration of advanced simulation techniques (FEM using ANSYS) to optimize the design of enset processing machine components. Unlike previous machines that suffer from frequent mechanical breakdowns and inefficiencies due to poor design and material choices, this research offers a solution by focusing on component-level modifications with a rigorous analytical approach. Another aspect of this study is the use of high safety factor values of 15 for all components and concentrates on minimizing deformation and maximizing energy dissipation and vibrational response. Additionally, the choice of materials based on ASTM standards and the thorough computational analysis represent an innovative approach to improving the overall functionality and durability of enset processing machines.

Materials and Methods

Materials

The design analysis focuses on the integration of mechanisms that enhance enset processing techniques, ensuring collaboration among the machine's components such as the shaft, beater drum, cylinder drum blade, and breastplate (Jima *et al.*, 2025). This involves coordinating the operating parts essential for the machine's functionality. The analysis emphasizes the importance of making critical design decisions that ensure the machine's structural stability, as highlighted by (Digvijay & Kiran, 2015). Key components such as the shaft, beater drum, drum blade, and breastplate are designed according to analytical formulas and standards to achieve this stability to guarantee efficiency in agricultural settings and lower economic losses for users (Zewdie, 2012).

Following the design phase, a computer-aided model using ANSYS 2023 R1 software was created. This model represents the computed and derived dimensions of the

critical components, including the frame, shaft, cylinder drum, cylinder drum blade, and breastplate assembly. The design process integrates analytical tools, basic scientific principles, mathematics, and engineering software predictions to create an accurate product model. These methodologies are grounded in established engineering practices, as outlined by Silveira Velloso, Luis Gonçalves Costa, Rodrigues Magalhães, Lúcio Santos, and Tavares de Andrade (2018). The study conducted a detailed analysis of the integrated enset processing machine components to ensure a precise and reliable assessment of the system's performance.

Structure of sheath and corm enset

The enset is a perennial plant that grows between 4 and 11 meters tall and matures after 3-5 years for harvesting. It has corms and leaf sheaths overlapping to form the pseudo stem or trunk, which is important for food security in Ethiopia (Olango, Tesfaye, Catellani, & Pè, 2014). The corms are formed by extravagant tuber portions, including leaf sheaths, that are underneath and basal. When the enset plant reaches full maturity, its corms turn a vibrant orange color. To better understand the structure of the fibers in the corms, a study was conducted to examine the surface morphology of these fibers. A scanning electron microscope (SEM) (Philips XL-30 SEM, from the Netherlands) was used to observe the fine details of the surface. The SEM analysis revealed that fibers of the fully ripe, orange-colored corms have a somewhat fibrous texture, which is crucial for understanding the material properties of enset. This type of analysis helps researchers gain insight into the characteristics of the fibers, which may be important for applications such as processing and utilizing enset for various purposes, as noted by Huertas, Schmelzer, Hoehenwarter, Heyroth, and Heinz (2016).

In this case, the whole sheath was determined, where the overlapping leaf sheaths form the pseudo-stem containing broken, pulpy tissue and deformable fiber (Chen *et al*., 2023). Also, to determine the weight of the samples of corm, an electronic balance with a sensitivity of 0.01 g was used (Bekele *et al*., 2022). Three linear dimensions length (L), width (W), and thickness (T) were measured with a digital caliper (DC-515; Taiwan) with an accuracy of 0.01 mm to establish the average size of the cut corms (Ahangarnezhad, Najafi, & Jahanbakhshi, 2019).

To avoid polymer charging in electron beams, which can cause astigmatism (issues with focus and blurred images), fiber specimens were sputter-coated with a thin layer of gold-palladium before SEM examination. Next, the specimens were placed using carbon tabs on the SEM tube, which had a diameter of 12 mm by 12 mm with an accelerating voltage of 10.0 kV, fiber surfaces were scanned, and electron micrographs were captured. According to Bekele *et al.* (2022), in the exploration of the mechanical properties of enset fiber, the tensile strength of enset fiber is 513 ± 57.7 MPa and the tensile modulus is 26.7 ± 3 GPa with 1.92% elongation. These values highlight the fiber's strength, stiffness, and its ability to stretch under stress. Additionally, Yemataw *et al.* (2017) analyzed the morphological properties of enset by examining the recorded scans, providing insights into the structural characteristics of the fiber.

Design of components for an integrated enset processing machine

Physical and mechanical properties of the utilized materials

The input materials used for the fabrication of integrated enset processing machine components include stainless steel, mild steel, aluminum metals, and rubber. The physical and mechanical properties of the used material are presented in Table 1.

Design of the integrated enset processing machine

The disassembled overall components of the designed and developed Integrated Enset Processing (IEP) machine are schematically shown in Figure 1.A, and modified specifications of the functional processing parts and assembled diagram is illustrated in Figure 1.B.

Table 1- Physical and mechanical properties of the materials based on the items provided

Type of material	Input materials component	Physical properties	Mechanical properties
Stainless steel	Cylinder drum	Dia. 25 cm (r = 12.5 cm), thickness = 2 mm, length = 45 cm for each, density (ρ) = 8000 kg m^{-3}	Durability, Poisson's Ratio (ν) = 0.3, Young's Modulus (E) = Yield Strength (σ_y) = 250 MPa
	Breastplate	Curvature = 17 cm, height = 45 cm, clearance 1-3 mm, length = 98 cm, density (ρ) = 8000 kg m^{-3}	Poisson's Ratio (ν) = 0.3, Young's Modulus (E) = Yield Strength (σ_y) = 250 MPa
	Blade	Length = 35 cm, thickness = 3 mm, density (ρ) = 8000 kg m^{-3}	Modulus (E) = Yield Strength (σ_y) = 250 MPa
Mild steel	Shafts	Dia. = 20 mm, length = 130 cm, density (ρ) = 7850 kg m^{-3}	Young's Modulus (E) = 210 GPa, Yield Strength (σy) = 250 MPa
	Angle	Width = 5 cm, length = thickness = 3 mm, density (ρ) = 7850 kg m^{-3}	Young's Modulus (E) = 210 GPa, Yield Strength (σy) = 250 MPa
Aluminum	Hopper and feeder	Thickness = 2 mm, lightweight, density (ρ) = 2700 kg m^{-3}	Poisson's Ratio (ν) = 0.33, Young's Modulus (E) = 70 GPa, Yield Strength (σy) = 120 MPa
	Conveyor	Thickness = 2 mm, lightweight, density (ρ) = 2700 kg m^{-3}	Poisson's Ratio (ν) = 0.33, Young's Modulus (E) = 70 GPa, Yield Strength (σy) = 120 MPa
	Cover	Thickness = 2 mm, lightweight, density (ρ) = 2700 kg m^{-3}	Poisson's Ratio (ν) = 0.33, Young's Modulus (E) = 70 GPa, Yield Strength (σy) = 120 MPa
	Pulley	Thickness = 4 mm, dia. = 20 cm, 12 cm, and 8 cm, lightweight, density (ρ) = 2700 kg m^{-3}	Poisson's Ratio (ν) = 0.33, Young's Modulus (E) = 70 GPa, Yield Strength (σy) = 120 MPa
Rubber	Belts	Length = 180.5 cm, 140.65 cm, and 107.7 cm, top width of the belt = 13 mm, bottom width of the belt = 8 mm, thickness of the belt (t) = 8 mm, density = 1100-1200 kg m^{-3}	Elasticity, Durability, Flexibility, Poisson's Ratio (ν) = 0.49, Young's Modulus (E) = 0.01-0.1 GPa Yield Strength (σy) = 10-20 MPa

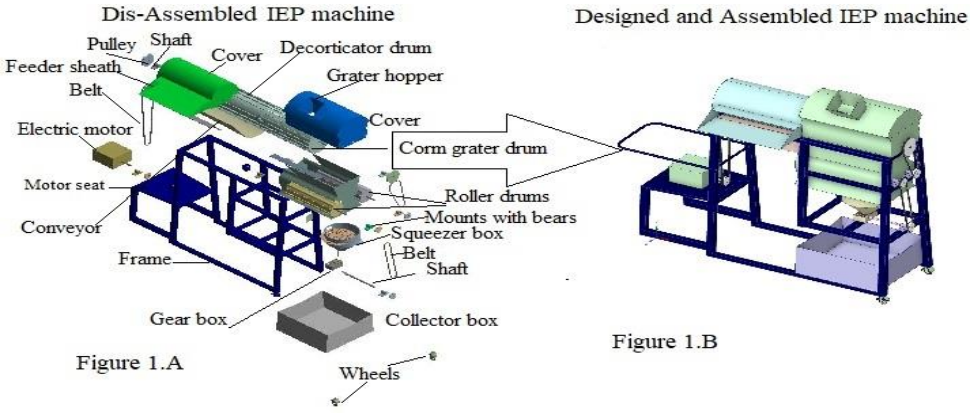

Fig. 1. Schematic illustration of the modified IEP machine components (A) disassembled, and (B) assembled

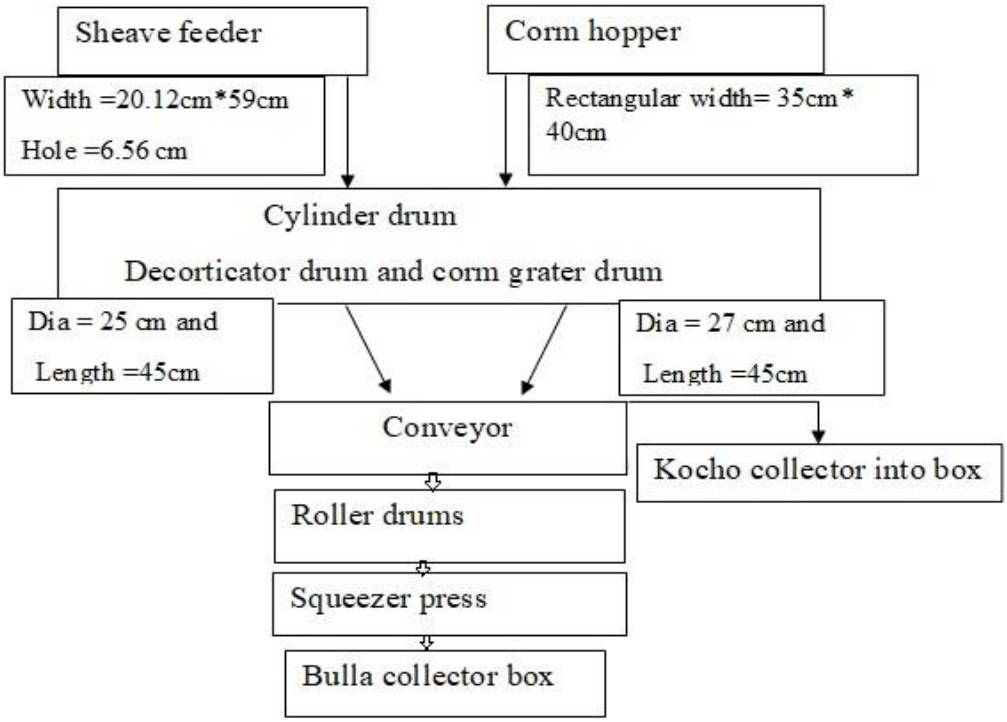

Fig. 2. Diagrammatic presentation of the device showing parts and dimensions of the integrated enset processing machine

Design calculations of the enset processing machine components

The machine requires an electric motor to operate the enset processing machine's parts, which involve two primary operations: decorticating the sheave (removing the outer layers of the enset plant) and grating the corm (grinding the inner part of the plant). Based on the data provided in Table 2, its power was determined as follows (Bello, Lamidi, & Oshinlaja, 2020):

$$Pd = \frac{2\pi N\tau}{60}\left(1-\frac{S}{100}\right) = \frac{2\pi \times N \times r \times (T1-T2)}{60}\left(1-\frac{S}{100}\right) = 1.166 \text{ kW} \quad (2)$$

where Pd is the output power required for both decorticate the sheave and corm grating in kW, τ is the twisting moment developed on the drum shaft (N m), N is the angular speed of the drum shaft (864 rpm), S is slippage (21.2%), $T1$ is tight side belt tension (221.57 N), $T2$ = slack side belt tension (90.07 N), $r = \frac{D2}{2}$, and $D2$ is the diameter of the pulley on the rotating shaft at the point of applying torque (0.20 m). τ = 0.10 m × (221.57 N − 90.07 N), V = 8.86 m s^{-1}, and slip on the smaller pulley at the first instance was considered as 2%.

The power source from the electric motor to operate the machine decorticating sheave and corm grating as of Figure (2) is well determined (Table 2). Therefore, the total sum of the power required to drive the decorticating unit (beater drum), and rollers to rotate the shaft of the squeeze press with its blade is determined. The output power recorded for grating the sheave and corn is 0.8875 kW, as determined by Equation (2). The total power (Pt) required for processing and overcoming friction can be determined as:

$$Pt = Pd + 0.3Pd = 1.52 \text{ kW} \quad (3)$$

$$Pd = (T1 - T2)V = 1.166 \text{ kW} \quad (4)$$

where, Pt = total power required to drive the machine (1.52 kW), Pd = power required to drive the decorticating and grating unit and rollers unit (1.166 kW), and V = 8.86 m s^{-1}.

$$\tau = (T_1 - T_2)\frac{D_2}{2} = 13.15 \text{ N m} \quad (5)$$

$$T_1 = T_{max} - T_c \quad (6)$$

$$\frac{T1}{T2} = e^{\frac{\mu\alpha 1}{\sin\beta}} = T2 = \frac{T1}{e^{\mu\theta}} = 90.7 \text{ N} \quad (7)$$

where, $T1$ = tight side belt tension (221.57N),

$T2$ = slack side belt tension (90.07N), and V = speed of belt (8.867m s^{-1}). μ = friction coefficient between contacting surfaces, $\alpha 1$, β, and θ = angles that affect the torque transmission efficiency in the system, e = the exponential constant used to model torque reductions due to friction and angular displacement, approximately (2.718), T_{max} = maximum torque applied in the system, T_c = torque loss or energy loss due to friction or inefficiencies, and $\frac{T1}{T2}$ is the ratio of the torques at two points in the system, indicating how torque changes through friction and other factors. The term $e^{\mu\Theta}$ shows how friction and angular displacement interact to reduce the torque at the second point.

According to Khurmi and Gupta (2019), the transmitted tension force T_1 is 221.57 N for shaft 1 with belt 1 system at 8.867 m s^{-1}; for shaft 2 opposite the rolling shaft 3, T_1 is 225.01 N at the belt speed of V = 8.69 m s^{-1}; and also shaft 4 with belt 3, T_1 is 228.145 N at speed of belt V = 8.52 m s^{-1}, derived from Equation (7). The torques on shaft 1, shaft 2, shaft 3, and shaft 4 would be determined by substituting these values in Equation (5), which were 10.42 N.m, 6.5 N.m, 6.5 N.m, and 6.17 N.m, respectively (refer to Table 2).

Rubber belts with a density of 1140 kg m^{-3} were utilized in this design because they are a common power transmission method in agricultural machines as recommended by ASME. This leads to an estimate of 0.096 kg m^{-1} for the rubber belt's mass per meter. T belt velocity as it passes over each pulley is calculated as:

$$V = \frac{\pi DN}{60}\left(1 - \frac{s}{100}\right) \quad (8)$$

Since the active arc of contact is unknown, when inserting the value in Equation (8) the belt slip on the smaller pulley at the first instance was considered 2%. The velocity was estimated as 8.867 m s^{-1} over belt 1, 8.69 m s^{-1} over belt 2, and 8.52 m s^{-1} over belt 3.

The belt centrifugal tension (T_c) is determined as:

$$T_c = mv^2 \quad (9)$$

Accordingly, the centrifugal force at belt 1, belt 2, and belt 3 were 13. 63 N, 10.19 N, and 7.505 N, respectively.

Each belt's mass, cross-sectional area, maximum tension, and coefficient of friction between the belt and pulley are calculated using the following Equations (Bechtel, Vohra, Jacob, & Carlson, 2000):

$$T_{max} = \sigma A \quad (10)$$

$$m = \rho A \quad (11)$$

$$A = \left(\frac{b-x}{2}\right)t + x \times t \quad (12)$$

$$\mu = 0.54 - \frac{0.7}{2.4+v} \quad (13)$$

where: V = velocity of belt (m s^{-1}), T_c and T_{max} = the centrifugal and maximum tension of the belt (N); A = cross-sectional area of belt (mm^2); m = mass per unit length (0.096 kg m^{-1}) of belt; v = speed of belt (m s^{-1}); b = top width of the belt (mm); χ = bottom width of the belt (mm); d_1 = diameter of driving pulley (mm), N_1 = speed of the driving pulley (rpm); S = slip (%); σ = Maximum allowable stress of belt (28337.35pa) for coefficient of friction 0.35; t = thickness of the belt (mm); ρ = density of belt material (Rubber) (kg m^{-3}); T_2 = belt tension in slank side (N); μ = coefficient of friction between belt and pulley.

The power transmitted by the belt from the middle shaft pulley to the roller drum does not require a high load due to mixing only the soft materials of the pulpy tissue and grated corm is determined as (Khurmi & Gupta, 2019):

$$P = \tau \times \omega = 1.17 \text{ kW} \quad (14)$$

The rolling force in the mixer drum is as follows:

$$F_C = M_f \times S_f = 55.32 \text{ N} \quad (15)$$

where F_c is the rolling force of the design 55.32 N, M_f is the mass of roller, which is 36.88 N, and S_f is the factor of safety, which is 1.5, the diameter of the driver roller D is 19.5 cm with bar mild steel coated, r = 11.75 cm.

The torque transmitted to the roller mixer drum is calculated by (Yang, Zeng, Zhu, & An, 2017):

$$\tau = F \times r = 6.55 \text{ N m} \quad (16)$$

where τ = torque = 6.5 N m, F = force, and r = the radius of roller which is 11.75 cm.

Table 2- Parameters, equations, and results of modifications for the integrated enset processing machine

Parameter	Formula	Belt 1	Belt 2	Belt 3
Torque on a shaft (T)	$\tau = (T_1 - T_2)\frac{D_2}{2}$	13.15 Nm	12.98 Nm	7.92 Nm
Tension on the right side	$T_1 = T_{max} - T_c$	221.57 N	225.01 N	228.145 N
Tension on the slack side	$T2 = \frac{T1}{e^{\mu\Theta}}$	90.07 N	95.23 N	96.55 N
Diameter of the driven pulley (D_2)	20cm	20 cm	12 cm	12 cm
Center of distance (c)		65	45	35
Diameter of the drive pulley (D_2)		12 cm	20 cm	12 cm
Belt length	$l = 2C + 1.57(D1 + D2) + \frac{(D_2 - D_1)^2}{4C}$	180.5 cm	140.65 cm	107.7 cm
The maximum tension (T_{max})	$T_{max} = \sigma A$	235.20 N	235.20 N	235.20 N
The centrifugal tension (T_C)	$T_C = mv^2$	13.63 N	10.19 N	7.505 N
The mass of the belt (M)	$m = \rho A$	0.1733 + 18 kg	0.135 + 18 kg	0.10339 + 12 kg
Cross sectional area of a belt (A)	$A = (\frac{b-x}{2})t + xt$	0.0084m^2	0.0084m^2	0.0084m^2
Top width of the belt (b)		13	13	13
Bottom width of the belt (x)		8	8	8
Thickness of the belt (t)		8	8	8
The velocity of belt passing (V)	V= $\frac{\pi dN}{60}(1 - \frac{S}{100})$	8.867 m s^{-1}	$v = v\left(1 - \frac{S2}{100}\right)$ = 8.69 m s^{-1}	$v = v\,(1 - \frac{S3}{100})$ = 8.52 m s^{-1}
Maximum allowable stress of belt (σ)	$\frac{MY}{I}$ = σ	28337.35 Pa	28337.35 Pa	28337.35 Pa
Density of belt material (rubber) (ρ)		1140 kg m^{-3}	1140 kg m^{-3}	1140 kg m^{-3}
Slip (S)		2%	1.8%	1.2%
Speed of the driving pulley (N)		864 rpm	1080 rpm	1080 rpm
angle of wrap on smaller pulley (α_1)	$\alpha1 = 180° - 2\sin^{-1}(\frac{D2 - D1}{2C})$	172.94°	180°	180°
Angle of wrap on larger pulley (α_2)	$\alpha2 = 180° + 2\sin^{-1}(\frac{D2 - D1}{2C})$	172.94°	180°	180°
Belt wedge angle (β)	40°	40°	40°	40°
Angle of contact at drive (θ_1)	$\theta1 = 180° + 2\alpha1 = 2\cos^{-1}(\frac{c}{2r})$	525.88°	540°	540°
Angle of contact driven (θ_2)	$\theta2 = 180° + 2\alpha2$	3.2648 rad	2.9638 rad	3.1426 rad
Coefficient of friction between pulleys and belt (μ)	$\mu = 0.54 - \frac{0.7}{2.4 + v}$	0.3	0.27	0.27
Groove angle	Standard (φ)	34°	34°	34°

Torsion and polar moment of inertia of shafts

The relationship between the torque (τ), shear stress (σ), and angle of twist (θ) in a circular shaft is determined from the general torsion equation as (De Felice & Sorrentino, 2019):

$$(\mathrm{T}) = \frac{J \times G \times \theta}{L} \quad (17)$$

where: T = torque or twisting moment (N m), J = polar moment of inertia about the shaft axis (m^4), G = modulus of rigidity or shear modulus (Pa), θ = angle of twist (rad), and L = length of

the shaft (m).

The polar moment of inertia, *J*, represents the resistance of the shaft to twisting deformation. For a solid circular shaft, *J* is given by:

$$J = \frac{\pi D^4}{32} \quad (18)$$

where *d* is the diameter of the shaft.

The diameter of a solid shaft made of mild steel with little to no axial loading should be determined using the following formula, which comes from the American Society of Mechanical Engineering as:

$$\tau = \frac{\text{HP}\times 4500}{2\times\pi\times\text{N}} \quad (19)$$

where the shaft is subjected to a twisting moment (or torque) only, the diameter of the shaft may be obtained by using the torsion equation:

$$\frac{\sigma}{J} = \frac{\tau}{r} \quad (20)$$

where: τ = twisting moment (or torque) acting upon the shaft, *J* = polar moment of inertia of the shaft about the axis of rotation, σ = torsional shear stress, and *r* = radius of the pulley.

According to Hosseini and Khadem (2009), the twisting moment acting on the shaft can be written as below:

$$\tau = \frac{\pi}{16} \times \text{d}^3 \times \text{fs} \quad (21)$$

The machine weight applied at two places, W_1 and W_2, supported on two bearings "A" and "B". Then it is apparent from the shear force diagram and bending moment well determined the correct shaft diameter to ensure satisfactory strength and rigidity that shaft is transmitting 2 hp power operating and loading conditions for 2 cm diameter. It reveals that 19.65 kg of both pully and belt weight supported by the shaft and the applied tension load weight on both sides, substituting the value in Equation (22):

$$\text{Wn} = \frac{Mn\times l}{2} \quad (22)$$

where; *Mn* = applied weight of machine, *Wn* = applied load weight, *l* = length of shafts in cm.

Hence, the equivalent twisting moment, τ_{eq} is given by Equation (23) (Yakoob Pasha, Devi, & Maheswari, 2024):

$$\tau\text{eq} = \sqrt{\text{W}^2 + \tau^2} \quad (23)$$
$$= \sqrt{1277.38^{\,2} + 11946.13^2}$$
$$= 12014.229 \text{ kg. cm}$$

The equivalent twisting moment, when acting alone, produces the same shear stress as an actual twisting moment. Then both Equations (22) and (23) (Sinha & Turner, 2011) can be written as:

$$\tau\text{eq} = \sqrt{\text{W}^2 + \tau^2} = \frac{\pi}{16} \times \text{d}^3 \times \text{fs} \quad (24)$$

Assuming permissible shear stress as 760 kg cm^{-2} steel shaft, the diameter of the shaft can be calculated as follows (Khurmi & Gupta, 2019):

$$d = \sqrt[3]{\frac{16(W^2+\text{T}^2)}{\pi\times fs}}^{0.5} = \quad (25)$$
$$\sqrt[3]{\frac{16(1{,}277.38^2+11{,}946.13^2)}{3.14\times 760kg}}^{0.5} = 20 \text{ mm}$$

The linear velocity of leaf sheath for decorticating is:

$$v = \frac{\rho\omega n}{2\pi} = \frac{0.0079m\times 13.119m\,s^{-1}\times 18}{2\times\pi} = \frac{0.364m}{s} \quad (26)$$

Whereas, the pitch of the pulpy tissue extracted from the leaf sheath is:

$$p = \frac{2\pi v}{\omega n} \quad (27)$$

where: *P* = pitch of the tissue extracted from the leaf sheath (0.0079 m by assumption),

v = linear feeding speed of the leaf sheath to the decorticator (0.364 m s^{-1}), ω = angular velocity of the drum beater (864 rpm), *n* = number of blades on the cylinder (18), and θ = angle between two consecutive blades (20°), the power required for squeezing is:

$$\text{p} = \frac{\text{FR}\times\text{t}\times\text{b}\times\omega}{75} \times \eta \quad (28)$$

where: *P* is power requirement (1.2 hp), *FR* is fiber resistance (0.5 kgf cm^{-2}), *t* is blade thickness (3 mm), *b* is the effective width of the blade (13.5 cm), ω is the operational speed (2.7 m s^{-1}), and η is transmission efficiency (92%).

Accordingly, the corresponding torque generated by the squeezing press blade is calculated as (Lu, Li, Zhang, Fang, & Bin, 2023):

$$\text{Torque } (\tau) = \frac{Power}{Angular\ velocity} \quad (29)$$

$= \frac{1{,}2\ hp}{\frac{2\pi \times 12 \times 540}{60}} = 1.313$ N.cm

Power and load at worm and gear assembly

The worm gears are assembled on a 20 mm diameter shaft used for transmitting power at high-velocity ratios between non-intersecting shafts as shown in Figure 3. The load is applied at the end of the driving teeth when contact first forms and to be at the end of the driving teeth when contact ends (Mao, 2007).

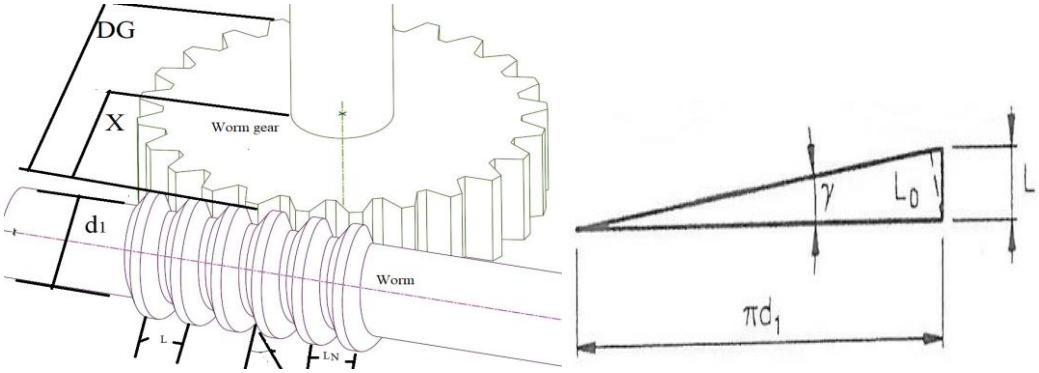

Fig. 3. Worm and gear when meshing

$$X = \frac{D_W + D_G}{2} \quad (30)$$

The pitch circle diameter of the worm (d_1) in terms of the center distance between the shafts can be written as (Radzevich, 2012):

$$d_1 = \frac{(x)^{0.875}}{1.416} \quad (31)$$

$$= \frac{(4.9)^{0.875}}{1.416} = 20\text{mm}$$

The lead "L" is the product of axial pitch and the number of starts and is determined mathematically as:

$$L = P_a \times n \quad (32)$$

where, P_a = axial pitch (9.3 mm); and n = number of starts.

The lead angle between the tangent to the thread helix on the pitch cylinder and the plane normal to the axis of the worm is determined as (Vullo & Vullo, 2020):

$$\tan\lambda = \frac{\text{Lead of the worm}}{\text{Pitch circumference of the worm}} = \left(\frac{N_G}{N_W}\right)^{\frac{1}{3}} = \frac{L}{\pi d_1} = \frac{P_a \times n}{\pi D_W} = \frac{P_c \times n}{\pi d_1} = \frac{\pi m \times n}{\pi d_1} = \frac{m \times n}{d_1} \quad (33)$$

where, N_G is the speed of the worm gear and N_W is the speed of the worm, axial pitch (P_a) = circular pitch (P_c), $P_c = \pi$m, m = module, and d_1 = pitch circle diameter of worm. The lead angle (λ) may vary from 9° to 45°. It has been shown that a lead angle less than 9° results in rapid wear, and the safe value for λ is 12.5° (Ambrus, Skadsem, & Mihai, 2018). For a compact design, the lead angle may be determined by equation (33).

The distance measured perpendicular to the threads between two corresponding points on two adjacent threads of the worm normal pitch is defined as Wu and Hsu (2014):

$$P_n = P_a \times \cos\lambda \quad (34)$$

The angle between the tangent to the thread helix on the pitch cylinder and the axis of the worm helix angle is determined as:

$$\text{Helix angle } (\alpha_w) \times \lambda = 90^{\circ} \quad (35)$$

Where, 90° is the shaft angle.

The ratio of the speed of the worm (N_w) in rpm to the speed of the worm gear (N_G) in rpm is the velocity ratio, determined as:

$$V_R = \frac{N_W}{N_G} = \frac{P_c T_G}{L} = \frac{P_a T_G}{P_a L} = \frac{T_G}{n} \quad (36)$$

The linear velocity of the worm is:

$$V_W = \frac{L \times N_W}{60} = \frac{\pi \times D_G N_G}{60} \quad (37)$$

The pitch circle diameter of the worm gear is expressed as:

$$DG = m \times TG \quad (38)$$

where, m = module, D_G = pitch circle diameter of the worm gear, T_G = the number of teeth on the worm gear (twice of transmission ratio),

and n = number of starts of the worm.

$$V_R = \frac{N_G}{N_W} = \frac{\pi D_G}{L} = \frac{\pi m T_G}{L} \quad (39)$$

According to Lewis equation, the strength of worm gear teeth size that is safe to assume is:

$$W_T = (\sigma o \,.Cv)\, b.\pi\, m\,.y \quad (40)$$

= (84 × 0.93) 28 × π × 3 × 0.107 N = 2825 N

where, W_T = permissible tangential tooth load or beam strength of gear tooth, σo = allowable static stress, value may be taken as 84 MPa for cast iron, Cv = velocity factor (0.64), b = face width (28mm), m = module (3 mm), y = tooth form factor or Lewis's factor.

The velocity factor is given by:

$$C_V = \frac{6}{6+V} \quad (41)$$

where; v is the peripheral velocity of the worm gear in m s^{-1}.

The tooth form factor or Lewis's factor (y) may be obtained in Equation (42). Therefore, the peripheral velocity was calculated at 0.38 m s^{-1} by substituting the value in Equation (41):

$$Y = 0.124 - \frac{0.684}{T_G} \quad (42)$$

The dynamic tooth load on the worm gear is determined (Mohanraj *et al.*, 2021) as:

$$W_D = \frac{W_T}{C_V} = W_T\left(\frac{6+V}{6}\right) \quad (43)$$

where, W_T = actual tangential load on the tooth.

The static tooth load or endurance strength of the tooth (WS) may also be obtained (Al-Omiri, Mahmoud, Rayyan, & Abu-Hammad, 2010) as:

$$WS = \sigma e.b\,\pi\, m.y \quad (44)$$

= 168 × 28 × π × 3 × 0.107 = 6075 N, where, σe is the flexural endurance limit.

Its value may be taken as 84 MPa for cast iron and 168 MPa for phosphor bronze gears.

$$W_W = D_G.b.K \quad (45)$$

where, D_G = pitch circle diameter of the worm gear, 162 mm, b = face width of the worm gear, and K = load stress factor (also known as material combination factor).

The forces acting on worm gears that transmit power to the worm are determined as (Yeh & Wu, 2009):

Tangential force on the worm:

$$W_T = \frac{2\times \text{Torque on worm}}{\text{Pitch circle diameter of worm } D_W} \quad (46)$$

Axial force or thrust on the worm gear:

$$W_A = \frac{2\times \text{Torque on worm}}{\text{Pitch circle diameter of worm } D_G} = \frac{W_T}{\tan\lambda} \quad (47)$$

The tangential force (W_T) on the worm produces a twisting moment of magnitude $\left(W_T \times \frac{D_W}{2}\right)$ and bends the worm in the horizontal plane (Murugan, 2020).

The axial force on the worm tends to move the worm axially, induces an axial load on the bearings, and bends the worm in a vertical plane with a bending moment of magnitude $\left(W_A \times \frac{D_W}{2}\right)$.

Radial or separating force on the worm is (Mei *et al.*, 2022):

$$W_R = W_A \times \tan\lambda \quad (48)$$

where, tan λ = radial or separating force on the worm gear known as permissible input power:

$$p = \frac{3650\times x^{(1.7)}}{VR+5} \quad (49)$$

$= \frac{3650\times 0.02^{1.7}}{4+5}$ = 0.524 kW, where VR = Transmission ratio.

Since this power is more than the given power to be transmitted (1.1 kW), therefore the design is safe from heat dissipation point of view. The radial or separating force tends to force the worm and worm gear out of the mesh. This force also bends the worm in the vertical plane. The gearbox encompasses the transmission units' worm and worm gear shaft at one end, achieving a reduction of 4:1 at the gearbox. This results in a rotation speed of 270 rpm at the shaft of the rotary blade. Suitable nuts and bolts are used for fastening the gearbox to the main frame, which can be removed when repair and maintenance is required.

Design analysis of major modified components of IEPM

This section describes the flow chart diagram modification (Figure 4) of the Integrated Enset Processing Machine (IEPM), which operates by electric motors derived from the integrated enset processing method and their functional parts.

The principle feeding unit and mechanical operation system, through which the enset sheath is fed into the machine's inclined plate for scraping, has been improved (Jima *et al.*, 2025). Enhancements were made with a focus on economic efficiency by considering factors such as size, power, production capacity, material loss, and overall operational efficiency, while maintaining product quality. Subsequently, the functional IEPM was modified and optimized, with certain parts being approved for testing. Its performance was evaluated through experimental analysis. Following the analysis, field experiments were conducted and validated against standard benchmarks, and the results were documented and analyzed.

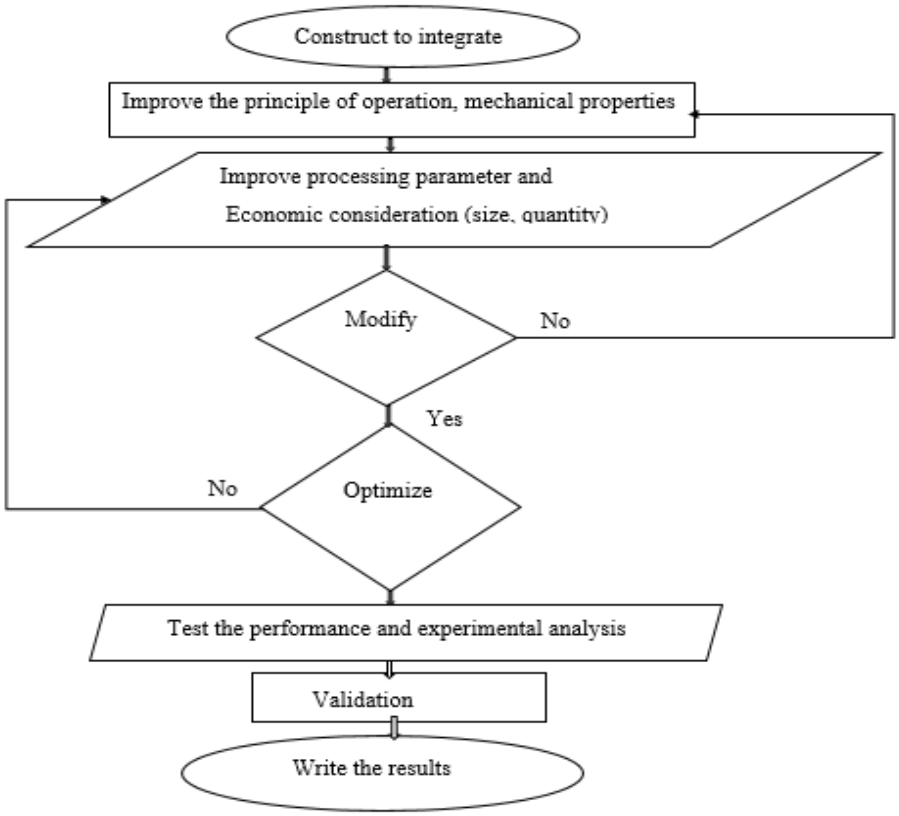

Fig.4. Flow chart diagram of the integrated enset processing machine (IEPM)

Finite element analysis of the IEPM components

A detailed computer-aided design (CAD) model of the integrated processing machine, illustrated in Figure 5, must be created to include components such as the shaft, beater drum, breastplate, and blade, with precision values calculated based on prior equations. The finite element method is utilized to analyze the distribution of shear stress, maximum deformation, and the safety factor of static structures. To ensure proper performance and assembly of the modified integrated enset processing machine, the weight of the machine components, and maximum allowable stress of belts with operational speed are considered.

The majority of the integrated enset processing machine's components have a modulus of rigidity of about 77.2 GPa, constructed from stainless steel and Mild Steel. The mesh sizes used in the FEM analysis of each component vary as shown in Table 3. For a more thorough examination of their structural behavior, the mesh size for drum shaft, cylinder drum, drum blade, and breastplate as small as possible in contrast, a bigger mesh size for the main shaft. The

grid convergence index values used in Equation (50) as shown in Table 3, the summary of materials' properties of components used for finite element simulations including discretization value, grid convergence ratio to determine real mesh size values as:

$$GCI = FS\frac{\varepsilon}{r^{p}-1}, \quad p = \frac{\ln|(f_{coarse}-f_{medium})/(f_{medium}-f_{fine})|}{\ln r} \quad (50)$$

where, ε = error, r = refine ratio, p = ordinary polynomial, and f = simulation results.

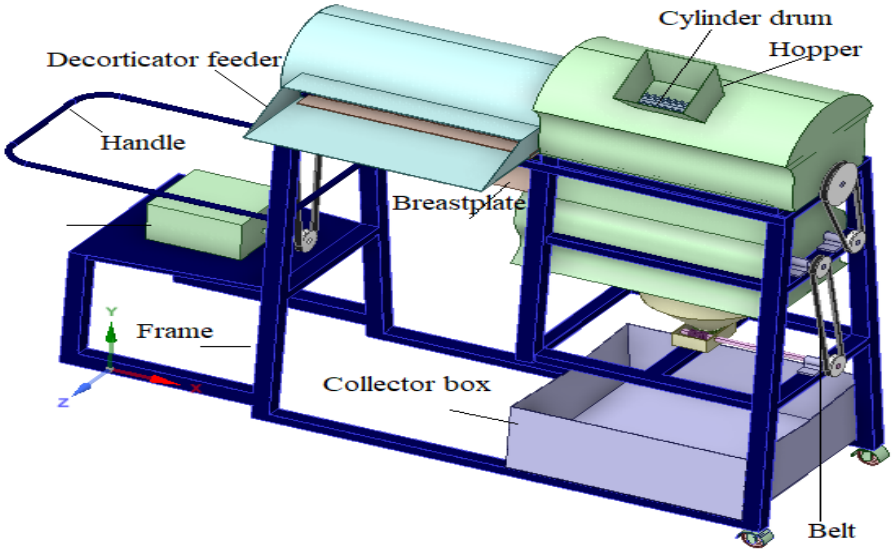

Fig. 5. The modified integrated enset processing machine

The simulation shows a low grid convergence index (GCI 0.66% at 21% refinement), indicating good accuracy in the results. The safety factor (S.F.) is 1.25, ensuring the shaft and other components operate within safe limits. The mesh refinement influences the accuracy of the simulation, with GCI values helping assess the need for further refinement in the model.

Static structural analysis (SSA)

The goal of static structural analysis (SSA) is to evaluate stress, strain, and deformation to ensure the machine could handle operational loads without failure on the integrated enset processing machine (Khodabakhshian & Emadi, 2015). The process involves assessing the machine's components (including the shaft, cylinder drum, breastplate, drum blade) under the application of forces or loads (Aygören & Türkdoğdu, 2024). The validation of the model is analyzed with the theoretical and simulation results of shear stress and angle of twist, are observed within the limits. The weight of the decorticator and grater cylinder, power, pulley design, belt design, shaft diameter, threshing torque, torsional moment, bearing design, and critical speed are considered. This analysis of the utilized materials, which may sustain higher stress values, highlights their significance. Interestingly, the drum shaft has an even greater modulus of 80 GPa, indicating increased rigidity in this crucial part. Commonly, for metallic materials with strong ductility, the Poisson ratios for the drum components and the breastplate are consistently 0.3 (Murugan, 2020). The belt, on the other hand (as shown in Table 2), has a noticeably greater Poisson ratio, indicating distinct material properties that would be more suited for flexibility.

A. Shafts

Under the analysis of static structure, the drum shaft has a modulus of even greater than 80 GPa (as depicted in Figure 6), indicating increased rigidity in this crucial part (Yang,

Ma, Qin, Guan, & Xiong, 2022). This is common for metallic materials and is a sign of strong ductility. The Poisson ratios for the drum components are consistently 0.3 with a mesh size of 10 mm. The analysis of static structure results of the shafts shows a consistent stress distribution, indicating a well-balanced design with a diameter of 2 cm and a length of 130 cm. The belt tensions on either side of pulleys are *T1* = 221.5 N, *T2* = 90.07 N, *T3* = 225.01 N, and *T4* = 95.2 N, subject to a torque of 13.15 N m and a system's maximum tension of 235.20 N. The shaft is fixed in the middle (boundary condition). With the torque and belt forces operating within the system's design parameters and stability provided by the fixed midway, this configuration proposes a balanced tension distribution.

According to the analysis, the current shaft design is capable of withstanding operational loads without deforming (Bruyère, 1965; Jima *et al.*, 2025). The findings from the static structural analysis reveal a maximum stress of 120 MPa, a minimum stress of 30 MPa, a maximum deformation of 0.15 mm, and a minimum deformation of 0.03 mm.

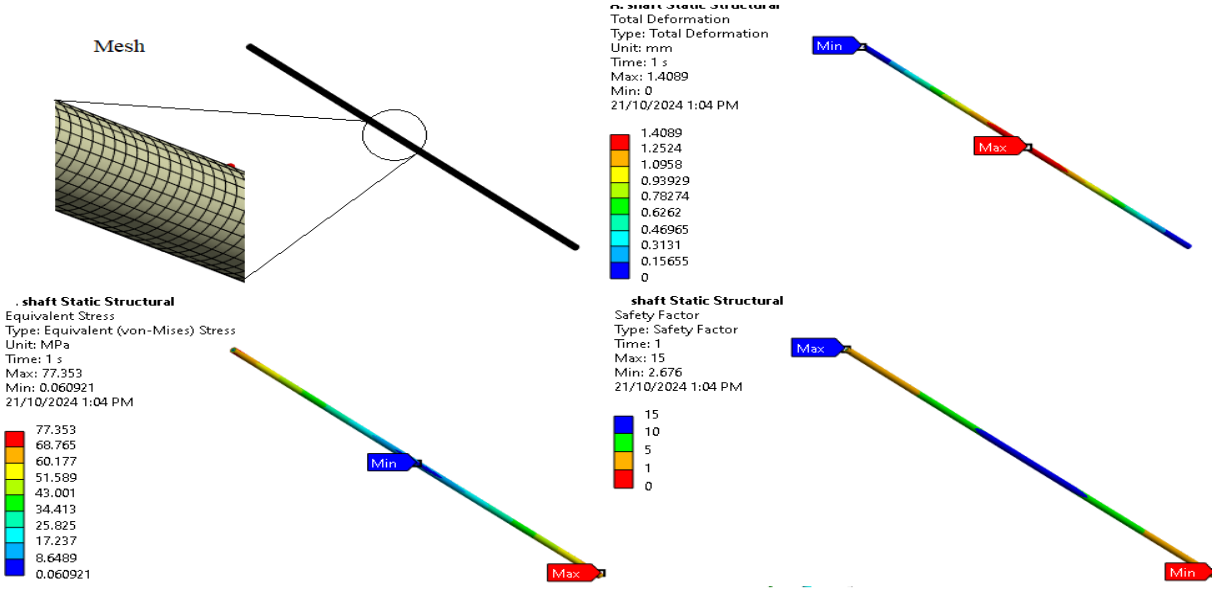

Fig. 6. Static structural analysis of shafts

B. Cylinder drum

The analysis of the static structure of the cylinder decorticator drum and grater drum with the properties of the same material is shown in Figure 7. The drum is mounted on the shaft, resulting in the following belt tensions on either side of the pulley: *T1* = 221.5 N, *T2* = 90.07 N, *T3* = 225.01 N, and *T4* = 95.2 N. With a consistent torque of 13.15 N m, the system reaches a maximum tension of 235.20 N. Additionally, the cylinder drum is fixed internally to the shaft (boundary condition). With the torque and belt forces operating within the system's design parameters and stability provided by the fixed, this configuration proposes a balanced tension distribution. The results of static drum cylinder structure reveal a minimum stress of 70 MPa, a maximum stress of 250 MPa, a maximum deformation of 0.3 mm, and a minimum deformation of 0.08 mm (Ambekar & Shinde, 2019). The analysis demonstrates that, under static load circumstances, the cylinder drum retains its structural integrity with little to no deformation. The results confirm the effectiveness of the drum's design (Carlson & McKean, 1955). Its performance could be further enhanced by reinforcement in high-stress areas, making it appropriate for heavy-duty applications (Sidhu & El-Sayegh, 2024). Discretizing a cylindrical drum into finite elements with a linear model allows for the

analysis of optimal stiffness and damping properties for each element, as shown in Table 3.

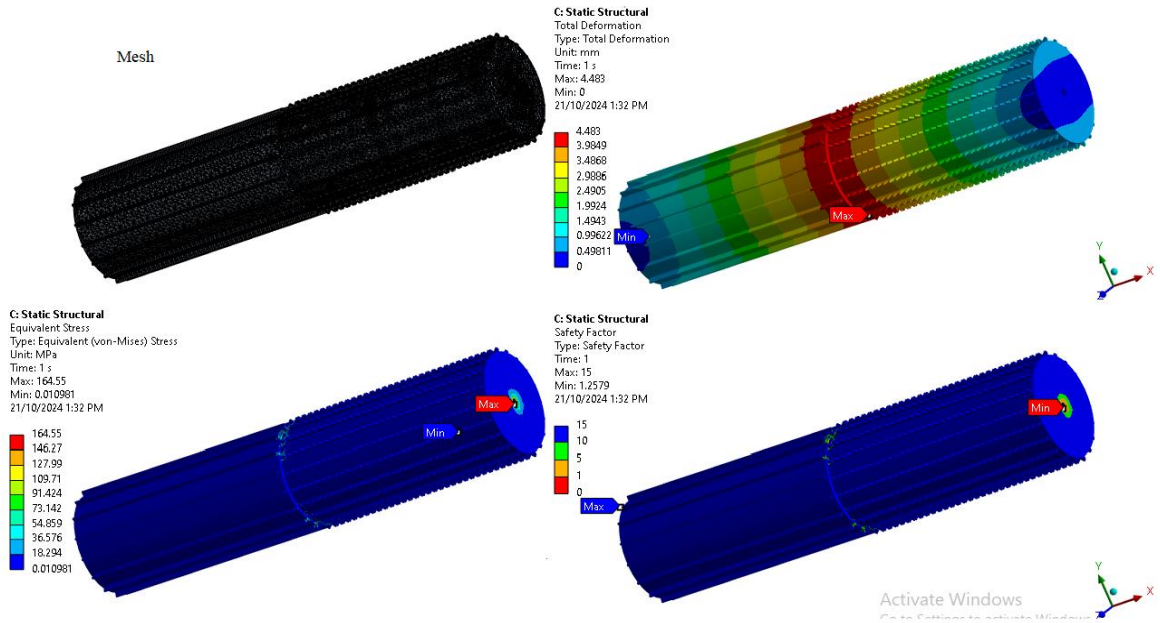

Fig. 7. Static structural analysis of the cylindrical drum

C. Cylindrical drum blade

The geometry of the cylindrical drum's blade is discretized into a finite element mesh using the data in Table 3. The element types were selected based on the nature of the generated boundary conditions, and certain nodes were fixed to represent supports or constraints (Upadhyay, Sonigra, & Daxini, 2021). The design should ensure that the mesh is fine enough in critical areas to capture stress gradients and deformation accurately. A total load of 235 N, the equal torque of both the shaft and the cylinder drum, is applied as a distributed load of 19.56 kg m^{-1} to the blade. This configuration influences the performance of the blade model and reflects its rotary dynamic design and intended cutting efficiency (Li *et al*., 2021). The cylinder drum blade static structural stability results are shown in Figure 7, with a minimum stress of 80 MPa, a maximum stress of 260 MPa, and 0.35 mm maximum deformation and 0.1 mm minimum deformation. The cylinder drum blade can withstand anticipated operating loads without experiencing appreciable deformation, according to the static structural study (Kordestani, Saif, Orchard, Razavi-Far, & Khorasani, 2019; O'Brien, Draper, & An, 2023). These results imply the robustness of the current drum design. However, to improve performance and lower manufacturing costs, lightweight composite materials should be investigated.

D. Breastplate

Design of the breastplate model faithfully captures its ergonomic shape and protective coverage, with a frame beam supported from below (Jäger, 2023). The model indicates that the design successfully strikes a balance between mobility and protection. Curvature changes could improve comfort and use less material without sacrificing safety (Mansfield, Naddeo, Frohriep, & Vink, 2020). Discretizing the mesh into finite elements with linear elements reveals that each element possesses adequate stiffness and effectively resists the analyzed damping drums (Adamiec-Wójcik, Brzozowska, & Drąg, 2015; Lemos, 2007). The static structural analysis results of the breastplate, shown in Figure 9, identify possible failure locations through regions of significant stress concentration under the distributed static load of 235 N. The analysis

reveals a maximum stress of 400 MPa and a minimum stress of 120 MPa, with corresponding maximum and minimum deformations of 0.55 mm and 0.15 mm, respectively, and a safety factor of 15 (Feng & Young, 2013). To improve the breastplate's durability and protective qualities, it is recommended to utilize advanced materials and reinforce areas expressing high stress, thereby ensuring improved performance in practical situations.

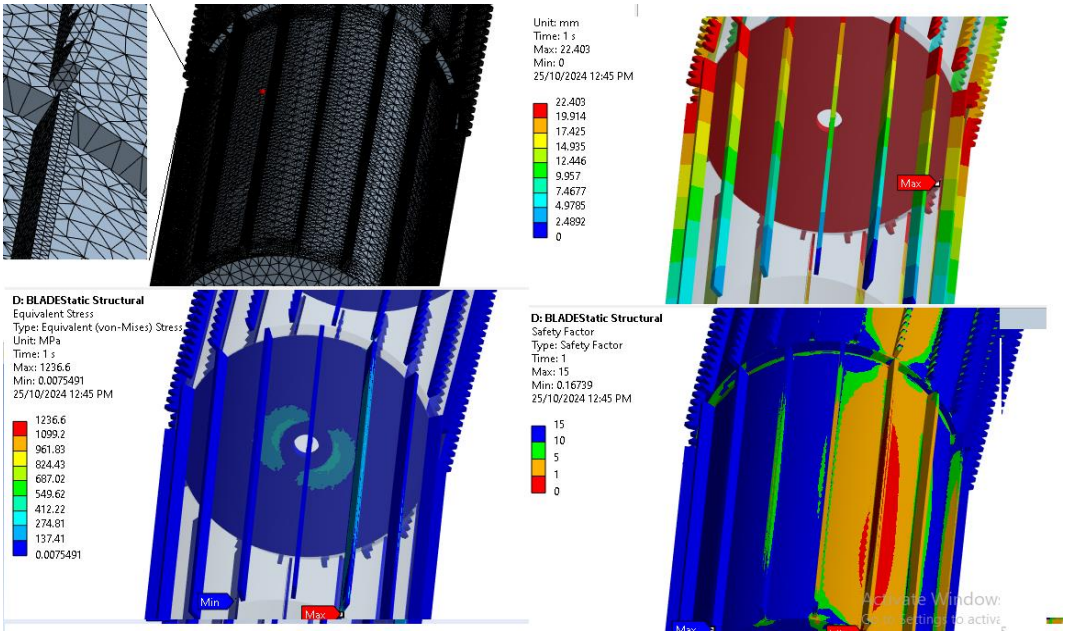

Fig. 8. Static structural analysis of the cylindrical drum's blade

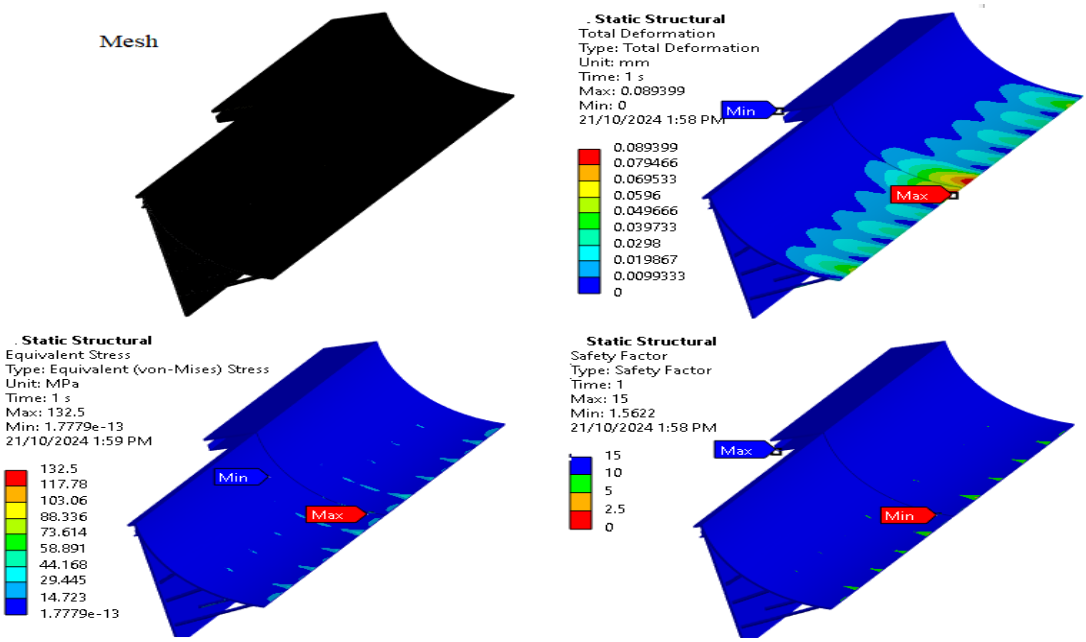

Fig. 9. Static structural analysis of the breastplate

Explicit dynamics structural analysis (EDSA) cylinder drum with breastplate

A computational method for analyzing the dynamic load condition of 942.78 N, using Explicit Dynamics Structural Analysis, determined the structural responses under time-dependent loads (Chopra, 2021). The analysis focuses on two main components: the cylinder drum, a rotating device used for processing materials, and the breastplate, a protective shell enhancing structural integrity through added support as shown in Fig. 10. Critical material parameters, including density, Poisson's ratio, and modulus of rigidity, sourced from Table 3, were incorporated to model mechanical behavior. Equation (51), derived from the analysis, proves valuable for machinery components involved in scraping the pulp from fiber cylinder drums interacting with breastplates, where rapid load fluctuations occur (Ham & Bathe, 2012). The study revealed diverse loading situations, such as beginning scenarios, such as initial conditions, tangential forces, and operating loads, to simulate realistic operational scenarios as:

$$F = m\frac{d^2S}{dt^2} + D\frac{dS}{dt} + RS \quad (51)$$

where: F = external force vector, m = mass matrix (N), D = damping matrix, R = stiffness matrix, and S = displacement vector, d^2S/dt^2 = the acceleration vector, and ds/dt = the velocity vector. The maximum displacement calculated during dynamic loading of the drum under operational conditions is 1.196 mm. The stiffness of the drum is 1.86×10^8 N m^{-1}, and the stiffness of the breastplate is 1.07×10^8 N m^{-1}. The damping coefficient for the drum is 186,000.65 Ns m^{-1}, which dissipates energy over time. The external force vector value was 234.51 N. For each component of the cylinder drum and breastplate, the mass matrix can be calculated based on the density (ρ), volume (v), and mesh size.

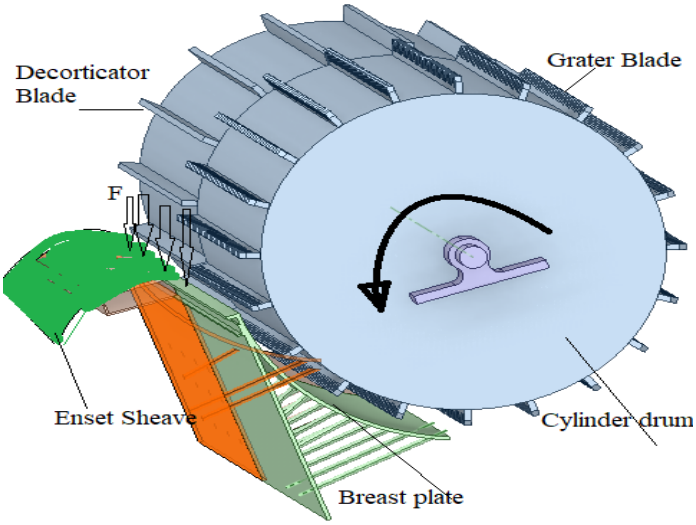

Fig. 10. Cylinder drum with breastplate

The cylinder drum and breastplate are structurally sound under the applied dynamic loads according to the study. Operational truthfulness is maintained by ensuring that the calculated maximum displacement remains within practical limits. Both components can sustain large loads without experiencing excessive deformation, according to the stiffness values. The damping properties imply efficient energy dissipation, reducing vibrations, and improving stability while in use.

Analyzing the stiff dynamics of a cylinder drum under applied load reveals a complex

oscillatory behavior that is essential to evaluating the mechanical performance of the drum. The drum shows no displacement at the beginning (t = 0 seconds), suggesting a stable starting position. Severe displacement variations are seen in the data throughout time, concluding at about 2.39×10^{-6} mm at t = 0.82 seconds, indicating severe deformation under load.

Results and Discussion

The mass of the belt, its cross-sectional area, and the maximum tension of each belt are shown in Table 3. The mass of belts per unit length was 0.096 kg m^{-1}, the cross-sectional area of the belts was determined as 0.0084 m^2, and the coefficient of friction between pulleys and the belts was estimated to be 0.3. The analysis of the mechanical properties of integrated machine components reveals that the drum shaft, with a rigidity modulus of 80 GPa, along with the drums and other components at 77.2 GPa, exhibits strong resistance to deformation. The modulus of rigidity and the drums' modulus of stiffness is nevertheless quite high.

Table 3- Mechanical properties of the machine materials used for simulations

Model	Modulus of rigidity (GPa)	Poisson ratio	Mesh size (mm)	No.E/t 1	No.E/t 2	No.E/t 3	V1	V2	V3	S.F.	GCI 21% (%)	GCI 32% (%)
Drum shaft	80	0.27-0.3	10	70992	7344	612	77353019.79	76950604.06	101584956.4	1.25	0.66	30.82
Drums	77.2	0.3	3	279933	138011	76320	379958408.5	168617655.8	159769668	1.25	3.04	6.94
Decorticator blade	77.2	0.3	3.5	898820	499928	175817	20986878.4	19685794.1	15706624.73	1.25	3.76	8.57
Breastplate	77.2	0.3	3.5	187123	58438	12712	33610046.27	31808901.7	25821077.33	1.25	2.88	7.104
Belt	0.0003	0.45-0.5	2	7832	537	158	0.007174795	0.007147995	0.006294032	1.25	0.02	2.344
Frame	80	0.27-0.3	10	699523	240970	67420	597707.6887	597005.3962	518674.0509	1.25	0	3

Note: "No. E/t" values represent the number of elements per thickness for different parts, while V1, V2, and V3 represent the number of elements for different parts.

The correctness of the mesh and simulation results are indicated by the grid convergence index (GCI) values; higher percentages indicate more reliability, as shown in Table 3. The simulation records intricate reactions with a mesh size of 10, and the high No.E/t value of 70992 indicates significant stiffness. The design can safely bear expected loads, according to the safety factor (S.F.) of 1.25. The GCI values, which indicate good stability and performance, especially under complex geometrical configurations, are 0.66% for 21% and 30.82% for 32%.

For example, the decorticator blade drum displays a GCI of 3.76% at 21%, suggesting moderate reliability in its analysis and performance predictions. The No.E/t value of 279933 indicates strong stiffness in the major loading direction, while the mesh size of 3 offers sufficient information for simulations. Reliability during operation is indicated by the S.F. of 1.25. With performance improving as geometrical complexity grows, the GCI values of 3.04% (21%) and 6.94% (32%) show good design integrity. A Poisson ratio of 0.27 to 0.3 indicates moderate lateral expansion upon compression, making it suitable for various loads.

Consistency between components is ensured by the decorticator blade drum's 77.2 GPa stiffness modulus. A somewhat more in-depth investigation is possible with a mesh size of 3.5. The No.E/t numbers indicate different stiffness properties for different orientations, especially the first one at 898820. A significant reactivity to geometrical changes is implied by the GCI values of 3.76% and 8.57%, suggesting possible areas for structural modification. The safety factor stays at 1.25, showing constant reliability.

Additionally, the breastplate exhibits a homogeneous material selection with a modulus of stiffness of 77.2 GPa. It has enough information for simulations with a

mesh size of 3.5, but its No.E/t value of 187123 suggests that it is slightly less rigid than the drums. Under operational settings, reliability is reinforced by the consistent safety factor of 1.25. GCI ratings of 7.104% and 2.88% demonstrate the breastplate's resilience to changing geometrical conditions without compromising structural integrity. The four shafts' mechanical characteristics and applicability for different applications are emphasized by the study results shown in Table 4.

Table 4- The shafts' mechanical properties based on the given parameters

Parameter	Shaft 1	Shaft 2	Shaft 3	Shaft 4
Weight (W)	19.65 kg	4 kg	4 kg	2 kg
Load (L)	235 N	221.5 N	225 N	228.2 N
Tangential Force($\boldsymbol{F_t}$)	131.5 N	234 N	-234 N	2825 N
Length (l)	130 cm	65 cm	65 cm	45 cm
Diameter (d)	20 cm	12 cm	12 cm	12 cm
Speed (RPM)	864	1080	1080	1080
Polar Moment of Inertia (J)	1.57×10^{-3} m⁴	1.77×10^{-4} m⁴	1.77×10^{-4} m⁴	1.77×10^{-4} m⁴
Modulus of Rigidity (G)	80 GPa	80 GPa	80 GPa	80 GPa
Power (P)	1.5 kW	1.17 kW	1.17 kW	1.117 kW
Torque ($\boldsymbol{\tau}$)	13.15 Nm	6.50 Nm	6.50 Nm	6.17 Nm
Torsion	1000 Nm	1000 Nm	1000 Nm	1000 Nm
Shear Force (F)	131.5 N	234 N	234 N	2825 N
Maximum Stress (σ_max)	16.73 MPa	55.67 MPa	55.67 MPa	49.27 MPa
Allowable Stress (σ_allow)	84 MPa	84 MPa	84 MPa	84 MPa
Safety Factor (SF)	5.02	1.51	1.51	1.71
Twist moment (θ)	1.67 degrees	1.13 degrees	1.13 degrees	1.01 degrees

Excellent resistance to torsional deformation is provided by shaft 1, which is the heaviest at 19.65 kg, bears a maximum load of 235 N, and has a polar moment of inertia of 1.57×10^{-3} m⁴. However, the structural integrity of shafts 2 and 3, which weigh only 4 kg apiece and support loads of roughly 225 N, is called into question due to their higher maximum stress levels (55.67 MPa), which are close to their permitted limit of 84 MPa. Shaft 4 shows an abnormally high tangential force of 2825 N, suggesting possible design issues, even though it weighs only 2 kg. According to torque measurements, shaft 1 can withstand higher twisting forces (10.42 N m), but the others range. Also, this shaft can withstand twisting forces of up to 10.42 N m, whereas the others can withstand twisting forces between 6.17 and 6.50 N m. While shafts 2 and 3 have lower safety factors of about 1.51, shaft 1 likewise has a high safety factor of 5.02, demonstrating resilience under unforeseen pressures. Subsequently, the strength and longevity of shaft 1 make it perfect for high-load applications, but lighter shafts can be preferable in situations where weight is a concern but need close supervision to avoid failing under pressure. This analysis highlights how crucial it is to choose shaft designs according to particular operational requirements and safety considerations.

Several important interpretations that are ne cessary for analyzing the cylinder drum and br eastplate's performance in an enset processing machine were obtained from the explicit dyna mic structural analysis. Critical information systems performed in various operational cylinder drums can be obtained by analyzing dynamic and operational load conditions. With a torque of 10.42 N m at 864 rpm, the computed dynamic load of 942.78 N is obtained, demonstrating the strong rotating forces at work. On the other hand, the highest tension and centrifugal tension acting on the belt system are considered when determining the operational loads, which vary between 207.94 N and 220.64 N across three scenarios.

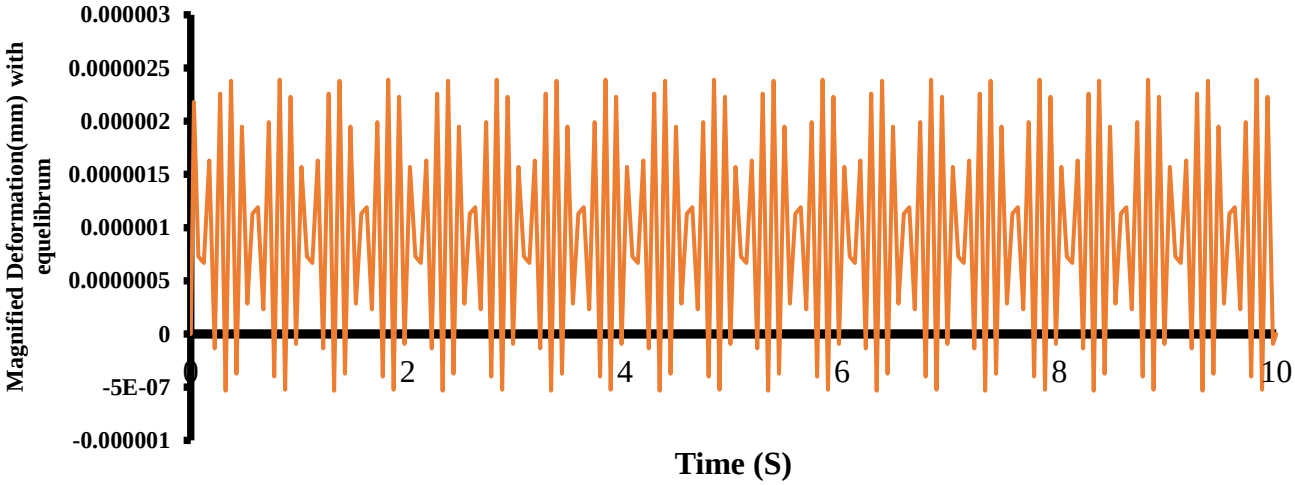

Fig. 11. Magnified directional deformation of the cylinder drum under applied dynamic load

The relationship between time and the magnified deformation of the cylindrical drum under a dynamic load of 942.78 N is depicted in Figure (11). The results of the CAD model analysis were recorded using ANSYS 2023 R1 software. The y-axis displays the magnified deformation value in millimeters, with values ranging from 0 mm to around 0.000003 mm. The x-axis depicts time in seconds, ranging from 0 to 10 seconds. The material's instantaneous reaction to dynamic stress is demonstrated by the initial, fast rise in deformation that occurs when the load is first applied on the blade, getting 2.39×10^{-6} mm. A stabilization period ensues, during which the deformation achieves equilibrium under the applied load. The cylindrical drum's greatest recorded deformation indicates how much it has distorted as a result of this dynamic load. Critical information on the material's mechanical characteristics, such as its elasticity and yield strength, which are crucial for engineering applications, can be gained by analyzing these results. Design concerns are informed by knowledge of how materials respond to dynamic loads, ensuring that structures can sustain anticipated stress without suffering from excessive deformation or failure.

The drum's maximum displacement under operating load was estimated to be around 1.196 mm, demonstrating that the structure stays within allowable deformation bounds and maintains its integrity while in use. The stiffness values were determined to be 1.86×10^{8} N m^{-1} for the drum and 1.07×10^{8} N m^{-1} for the decorticator blade, showing that both parts are sufficiently rigid to bear applied forces without buckling or deforming too much.

The drum's damping coefficient of 186,000.65 Ns m^{-1} and the blade's damping coefficient of 107,000.2 Ns m^{-1} indicate excellent energy dissipation, reducing vibrational response while in use and extending the machinery's lifespan. Furthermore, the design's safety factor of 1.25 confirms its dependability under normal operating settings by reflecting a reasonable margin against potential failures. According to these findings, the breastplate and cylinder drum are both suitable for the dynamic stresses that are encountered during processing and are hence well suited for their intended uses. It is advised that these components be periodically inspected and monitored in order to handle any unexpected problems that might occur during extended operation. Overall, this research demonstrates the design's structural soundness and practicality of operation.

Table 5- The performance of the modified integrated machine compared to the existing machine

Machine	Operation speed (rpm)	Clearance (mm)	Power consumption (L h^{-1})	Efficiency (%)	Output quality	Loss	Damage to fiber (%)	Capacity (kg h^{-1})
Combined decorticating & corm grating machine	880	1-4	1.4	94.6	Very high	5.4%	3.4	1543.5
Engine driven Warqe EnseteVentricosum	1050	1-6	1.2	92	High	8%	6	315-615
Design improvement and analysis of kocho, bulla, and fiber production machine	650-1050	< 2 and > 2	1.3	86.5-93.12	Medium	0.83kg	10.16-1.92	57.63
Fiber decorticator	860	1-3	1.1	94	High	0.54 kg	3.5	978
Fuel-powered decorticator	950	1-6	1.1	93-96	High	0.6 kg	6	565
Corn granting machine	2,200	5×5 sieve	1.3	98	Very high	2%	No	1048.3
Stainless steel decorticating machine	950 - 1050	1-2	1.2	97	Very high	3%	4-2.5	581
Modified and an integrated enset processing machine	864	1- 4	1.4	96	Very high	4 %	2.3	1643.5

The modified and integrated enset processing machine stands out for its excellent performance across several key factors. With an operation speed of 864 rpm, it provides a high efficiency of 96%, making it an ideal choice for large-scale operations where both speed and energy efficiency are critical. The machine maintains low fiber damage at 2.3% and losses at 4%, which makes it one of the better options when it comes to preserving the quality of the processed material. Additionally, it has a capacity of 1643.5 kg h^{-1}, which is comparable to the Combined Decorticating & Corm Grating Machine (also at 1543.5 kg h^{-1}) and positions it as a high-output machine in this comparison.

When compared with other machines, the Modified and Integrated Enset Processing Machine offers significant advantages (Table 5). It has a similar capacity and efficiency to the Combined Decorticating & Corm Grating Machine but achieves a slightly higher fiber preservation rate (2.3% compared to 3.4% in the Combined Decorticating & Corm Grating Machine), making it more favorable in terms of product quality. When compared with the Engine Driven Warqe, which operates at a higher rpm (1050) but has a lower capacity (315-615 kg h^{-1}) and higher fiber damage (6%), the Modified and Integrated Enset Processing Machine is far superior in terms of throughput, efficiency, and fiber quality. Furthermore, the Design Improvement and Analysis of Kocho, Bulla, and Fiber Production Machine, despite a similar efficiency range (86.5%-93.12%), falls short in terms of both capacity (57.63 kg h^{-1}) and fiber damage (up to 10.16%), making it less competitive for large-scale processing.

Conclusion

Crucial conclusions include the maximum tension in the belt system, which was calculated to be 235.2 N, and the importance of component stiffness and safety factors in ensuring the machine's operational reliability. The analysis of the shafts shows that shaft 1, with its superior resistance to torsional deformation and high safety factor, is optimal for high-load applications, while the lighter shafts (2, 3, and 4) are more suited to lower-load scenarios but require careful monitoring to avoid failure. The cylinder drum and breastplate dynamic study highlights the significance of stiffness and energy dissipation. The drum's low deformation under load, coupled with its rigidity and damping qualities, validates its capacity to sustain dynamic loads without failing.

Both the drum and the breastplate function well under operating conditions, and the design's safety factor (S.F.) for all components is 1.25, ensuring that the components operate within safe limits. A safety factor above 1

indicates a margin of safety between the material's strength and the stress it experiences during operation. Important information about the performance of the cylinder drum is revealed by the examination and analysis of its rigid dynamics under applied load. The figure representing the deformation behavior demonstrates that when the load is first applied, the drum experiences a quick initial distortion. This is followed by a stabilized period during which the deformation achieves equilibrium. The cylinder drum exhibits very little deformation when in use, as seen by the magnified deformation values, which range from 0 mm to roughly 0.000003 mm, and the deformation of the blade was 2.39×10^{-6} mm. This indicates that both the material and design of the drum are highly effective in withstanding dynamic loads. The analysis demonstrates the drum's elasticity, yield strength, and structural integrity, demonstrating its capacity to remain stable under the pressures present in normal operating circumstances. The drum's long-term dependability is indicated by this little deformation. The Modified and Integrated Enset Processing Machine offers a balanced combination of high capacity, excellent efficiency, low fiber damage, and optimal performance, making it a more reliable and effective option when compared to many of the other machines listed in Table 4. Its performance in terms of both speed and quality preservation positions it as a top contender for large-scale enset processing operations.

Conflict of Interest: The authors declare no competing interests.

Author Contributions

Beka Adugna: Conceptualization, Experiment design and execution, Data analysis, Resource provision, Draft, Reviewing and Editing, and Proofreading.

Kishor Purushottam: Supervision, Conceptualization, Providing technical advice, Conducting research analysis, Resource allocation, Draft, Reviewing and Editing, and Visualization.

Moera Gutu: Resource allocation, Draft, Reviewing and Editing.

References

1. Adamiec-Wójcik, I., Brzozowska, L., & Drąg, Ł. (2015). An analysis of dynamics of risers during vessel motion by means of the rigid finite element method. *Ocean Engineering*, *106*, 102-114. https://doi.org/10.1016/j.oceaneng.2015.06.053
2. Ahangarnezhad, N., Najafi, G., & Jahanbakhshi, A. (2019). Determination of the physical and mechanical properties of a potato (the Agria variety) in order to mechanise the harvesting and post-harvesting operations. *Research in Agricultural Engineering*, *65*(2), 33-39. https://doi.org/10.17221/122/2017-RAE
3. Al-Omiri, M. K., Mahmoud, A. A., Rayyan, M. R., & Abu-Hammad, O. (2010). Fracture resistance of teeth restored with post-retained restorations: an overview. *Journal of Endodontics*, *36*(9), 1439-1449. https://doi.org/10.1016/j.joen.2010.06.005
4. Ambekar, M. S., & Shinde, S. S. (2019). Structural Analysis and Optimization of 'C'Frame of Mechanical Press. *International Research Journal of Engineering and Technology (IRJET)*, *6*(6), 843-849.
5. Ambrus, A., Skadsem, H. J., & Mihai, R. G. (2018). Similarity analysis for downscaling a full size drill string to a laboratory scale test drilling rig. *International Conference on Offshore Mechanics and Arctic Engineering*, *51296*, V008T11A005. https://doi.org/10.1115/OMAE2018-77202
6. Aygören, S. M., & Türkdoğdu, H. (2024). Forces, Structures, and the Evolution of Natural and Artificial Forms. *SETSCI-Conference Proceedings*, *18*, 50-59. https://doi.org/10.36287/setsci.18.1.0050

7. Bechtel, S. E., Vohra, S., Jacob, K. I., & Carlson, C. D. (2000). The stretching and slipping of belts and fibers on pulleys. *Journal of Applied Mechanics*, *67*(1), 197-206. https://doi.org/10.1115/1.321164
8. Bekele, A. E., Lemu, H. G., & Jiru, M. G. (2022). Exploration of Mechanical Properties of Enset–Sisal Hybrid Polymer Composite. *Fibers*, *10*(2). https://doi.org/10.3390/fib10020014
9. Bello, S. K., Lamidi, S. B., & Oshinlaja, S. A. (2020). Design and fabrication of cassava grating machine. *International Journal of Advances in Scientific Research and Engineering (IJASRE)*, *6*(1), 162-167. https://doi.org/10.31695/IJASRE.2020.33915
10. Borrell, J. S., Goodwin, M., Blomme, G., Jacobsen, K., Wendawek, A. M., Gashu, D., Lulekal, E., Asfaw, Z., Demissew, S., & Wilkin, P. (2020). Enset-based agricultural systems in Ethiopia: A systematic review of production trends, agronomy, processing and the wider food security applications of a neglected banana relative. *Plants, People, Planet*, *2*(3), 212-228. https://doi.org/10.1002/ppp3.10084
11. Bruyère, M. (1965). Modern Solutions to Coupling and Transmission Problems of Aircraft Engines. *The Aeronautical Journal*, *69*(654), 365-379. https://doi.org/10.1017/S0001924000059248
12. Carlson, W. B., & McKean, J. D. (1955). Cylindrical pressure vessels: stress systems in plain cylindrical shells and in plain and pierced drumheads. *Proceedings of the Institution of Mechanical Engineers*, *169*(1), 269-293. https://doi.org/10.1243/PIME_PROC_1955_169_039_02
13. Chen, W., Cao, G., Yuan, D., Ding, Y., Zhu, J., & Chen, X. (2023). Study on Agricultural Machinery-Load-Testing Technology and Equipment Based on Six-Dimensional Force Sensor. In *Agriculture*, *13*(9). https://doi.org/10.3390/agriculture13091649
14. Chopra, A. K. (2021). Modal combination rules in response spectrum analysis: Early history. *Earthquake Engineering & Structural Dynamics*, *50*(2), 260-269. https://doi.org/10.1002/eqe.3333
15. Colledani, M., Tolio, T., Fischer, A., Iung, B., Lanza, G., Schmitt, R., & Váncza, J. (2014). Design and management of manufacturing systems for production quality. *Cirp Annals*, *63*(2), 773-796. https://doi.org/10.1016/j.cirp.2014.05.002
16. David Müzel, S., Bonhin, E. P., Guimarães, N. M., & Guidi, E. S. (2020). Application of the finite element method in the analysis of composite materials: A review. *Polymers*, *12*(4), 818. https://doi.org/10.3390/polym12040818
17. De Felice, A., & Sorrentino, S. (2019). On the dynamic behaviour of rotating shafts under combined axial and torsional loads. *Meccanica*, *54*(7), 1029-1055. https://doi.org/10.1007/s11012-019-00987-4
18. Deressa, A. A., Derese, G. K., & Dula, M. W. (2023). Pre-extension demonstration and evaluation of enset processing technologies in selected districts of west Shewa and southwest Shewa zones, Oromia, Ethiopia. *Journal of Science & Development (JSD)*, *11*(1), 62-67.
19. Digvijay, D. P., & Kiran, M. N. (2015). Design and finite element analysis of rope drum and drum shaft for lifted material loading condition. *International Engineering Research Journal (IERJ), Special Issue 2*, 2034-2040.
20. Duflou, J. R., Sutherland, J. W., Dornfeld, D., Herrmann, C., Jeswiet, J., Kara, S., Hauschild, M., & Kellens, K. (2012). Towards energy and resource efficient manufacturing: A processes and systems approach. *CIRP Annals*, *61*(2), 587-609. https://doi.org/10.1016/j.cirp.2012.05.002
21. Feng, R., & Young, B. (2013). Stress concentration factors of cold-formed stainless steel tubular X-joints. *Journal of Constructional Steel Research*, *91*, 26-41. https://doi.org/10.1016/j.jcsr.2013.08.012
22. Ham, S., & Bathe, K.-J. (2012). A finite element method enriched for wave propagation problems. *Computers & Structures*, *94*, 1-12. https://doi.org/10.1016/j.compstruc.2012.01.001

23. Hamming, R. (2012). *Numerical methods for scientists and engineers*. Courier Corporation.
24. Hollaway, L. C. (2010). A review of the present and future utilisation of FRP composites in the civil infrastructure with reference to their important in-service properties. *Construction and Building Materials*, *24*(12), 2419-2445. https://doi.org/10.1016/j.conbuildmat.2010.04.062
25. Hosseini, S. A. A., & Khadem, S. E. (2009). Free vibrations analysis of a rotating shaft with nonlinearities in curvature and inertia. *Mechanism and Machine Theory*, *44*(1), 272-288. https://doi.org/10.1016/j.mechmachtheory.2008.01.007
26. Huertas, A. C. M., Schmelzer, C. E. H., Hoehenwarter, W., Heyroth, F., & Heinz, A. (2016). Molecular-level insights into aging processes of skin elastin. *Biochimie*, *128*, 163-173. https://doi.org/10.1016/j.biochi.2016.08.010
27. Jäger, F. (2023). The Prince's Prosthetic Body: Orthopedic Armor and Material Self-Fashioning in Sixteenth-Century Europe. *The Art Bulletin*, *105*(3), 61-89. https://doi.org/10.1080/00043079.2023.2176666
28. Jemghili, R., Ait Taleb, A., & Mansouri, K. (2023). A collaborative multidisciplinary design methodology for additive manufacturing with a left-handed mouse as a case study. *The International Journal of Advanced Manufacturing Technology*, *125*(11), 4925-4951. https://doi.org/10.1007/s00170-023-11051-7
29. Jima, B. A., Kolhe, K. P., & Jiru, M. G. (2025). Design and development of an integrated enset processing machine suitable for central highland farmers of west shewa zone Ethiopia. *Discover Agriculture*, *3*(1), 1. https://doi.org/10.1007/s44279-024-00114-2
30. Khodabakhshian, R., & Emadi, B. (2015). Development of a finite element method model to determine mechanical behavior of pumpkin seed. *International Journal of Food Properties*, *18*(2), 231-240. https://doi.org/10.1080/10942912.2013.822883
31. Khurmi, R. S., & Gupta, J. K. (2019). *A Textbook of Machine Design (LPSPE)*. S. Chand publishing.
32. Kordestani, M., Saif, M., Orchard, M. E., Razavi-Far, R., & Khorasani, K. (2019). Failure prognosis and applications—A survey of recent literature. *IEEE Transactions on Reliability*, *70*(2), 728-748. https://doi.org/10.1109/TR.2019.2930195
33. Kudama, G., Tolera, T., & Gebeyehu, L. (2022). Good farm practices and improved processing technology of enset for sustainable hunger solution in Ethiopia. *Journal of Innovation and Entrepreneurship*, *11*(1), 17. https://doi.org/10.1186/s13731-022-00210-x
34. Lemos, J. V. (2007). Discrete element modeling of masonry structures. *International Journal of Architectural Heritage*, *1*(2), 190-213. https://doi.org/10.1080/15583050601176868
35. Li, A., Pirrung, G. R., Gaunaa, M., Madsen, H. A., & Horcas, S. G. (2021). A computationally efficient engineering aerodynamic model for swept wind turbine blades. *Wind Energy Science Discussions*, *2021*, 1-49. https://doi.org/10.5194/wes-7-129-2022
36. Lu, Q., Li, C., Zhang, Y., Fang, H., & Bin, G. (2023). Study on the vibration control method of a turboshaft engine rotor based on piezoelectric squeeze film damper oil film clearance. *Mechanical Sciences*, *14*(1), 237-246. https://doi.org/10.5194/ms-14-237-2023
37. Mahmood, W., & Mohammed, A. (2022). Performance of ANN and M5P-tree to forecast the compressive strength of hand-mix cement-grouted sands modified with polymer using ASTM and BS standards and evaluate the outcomes using SI with OBJ assessments. *Neural Computing and Applications*, *34*(17), 15031-15051. https://doi.org/10.1007/s00521-022-07349-4
38. Mansfield, N., Naddeo, A., Frohriep, S., & Vink, P. (2020). Integrating and applying models of comfort. *Applied Ergonomics*, *82*, 102917. https://doi.org/10.1016/j.apergo.2019.102917
39. Mao, K. (2007). Gear tooth contact analysis and its application in the reduction of fatigue wear. *Wear*, *262*(11-12), 1281-1288. https://doi.org/10.1016/j.wear.2006.06.019
40. Mei, D., Zhao, X., Tang, G., Wang, J., Zhao, C., Li, C., & Wang, Y. (2022). A single-joint

worm-like robot inspired by geomagnetic navigation. *Machines*, *10*(11), 1040. https://doi.org/10.3390/machines10111040
41. Mohanraj, R., Elangovan, S., Chandran, V. K., Sulaiman, M. F. M., Pradhaa, R. H., Poojasri, S., & Ramakrishna, J. R. (2021). Numerical analysis on bending and contact stress of single and double start worm drive. *Materials Today: Proceedings*, *46*, 8038-8044. https://doi.org/10.1016/j.matpr.2021.02.788
42. Murugan, S. S. (2020). Mechanical Properties of Materials: Definition, Testing and Application. *International Journal of Modern Studies in Mechanical Engineering (IJMSME)*, *6*(2), 28-38. https://doi.org/10.20431/2454-9711.0602003
43. Nabeshima, E. H., Moro, T. M. A., Campelo, P. H., Sant'Ana, A. S., & Clerici, M. T. P. S. (2020). Tubers and roots as a source of prebiotic fibers. In *Advances in food and nutrition research* (Vol. 94, pp. 267-293). Elsevier. https://doi.org/10.1016/bs.afnr.2020.06.005
44. O'Brien, D., Draper, S., & An, H. (2023). Stability of Concrete Mattresses. *International Conference on Offshore Mechanics and Arctic Engineering*, *86854*, V003T04A022. https://doi.org/10.1115/OMAE2023-106777
45. Olango, T. M., Tesfaye, B., Catellani, M., & Pè, M. E. (2014). Indigenous knowledge, use and on-farm management of enset (Ensete ventricosum (Welw.) Cheesman) diversity in Wolaita, Southern Ethiopia. *Journal of Ethnobiology and Ethnomedicine*, *10*, 1-18. https://doi.org/10.1186/1746-4269-10-41
46. Radzevich, S. P. (2012). *Practical Gear Design and Manufacture*. Second Edi. Boca Raton London New York: CRC Press Taylor & Francis Group, 307-368.
47. Sidhu, C., & El-Sayegh, Z. (2024). Comparative Analysis of Non-Pneumatic Tire Spoke Designs for On-Road Applications: A Traction Force Perspective. *International Design Engineering Technical Conferences and Computers and Information in Engineering Conference*, *88339*, V001T01A002. https://doi.org/10.1115/DETC2024-145579
48. Silveira Velloso, N., Luis Gonçalves Costa, A., Rodrigues Magalhães, R., Lúcio Santos, F., & Tavares de Andrade, E. (2018). The Finite Element Method Applied to Agricultural Engineering: A Review. *Current Agriculture Research Journal*, *6*(3), 286-299. https://doi.org/10.12944/carj.6.3.08
49. Sinha, S. K., & Turner, K. E. (2011). Natural frequencies of a pre-twisted blade in a centrifugal force field. *Journal of Sound and Vibration*, *330*(11), 2655-2681. https://doi.org/10.1016/j.jsv.2010.12.017
50. Szabó, B., Actis, R., & Rusk, D. (2021). Validation test of a predictor of fatigue failure under biaxial out-of-phase loading conditions. *Computer Methods in Applied Mechanics and Engineering*, *378*, 113718. https://doi.org/10.1016/j.cma.2021.113718
51. Tezuka, A. (2006). *Finite Element and Finite Difference Methods BT - Springer Handbook of Materials Measurement Methods* (H. Czichos, T. Saito, & L. Smith (eds.); pp. 973–1000). Springer Berlin Heidelberg. https://doi.org/10.1007/978-3-540-30300-8_19
52. Upadhyay, B. D., Sonigra, S. S., & Daxini, S. D. (2021). Numerical analysis perspective in structural shape optimization: A review post 2000. *Advances in Engineering Software*, *155*, 102992. https://doi.org/10.1016/j.advengsoft.2021.102992
53. Vullo, V., & Vullo, V. (2020). Worm gears. *Gears: Volume 1: Geometric and Kinematic Design*, 465-568. https://doi.org/10.1007/978-3-030-36502-8_11
54. Wang, Q., Huang, P., & Yin, Y. (2021). Design and optimization of rolling mills pass based on parameterization and orthogonal test. *The International Journal of Advanced Manufacturing Technology*, *112*, 803-818. https://doi.org/10.1007/s00170-020-06353-z
55. Workesa, M., Gebresenbet, G., Fanta, A., & Chaka, A. (2021). Design and Development of Engine Driven Warqe (Ensete Ventricosum) Decorticating Machine. *American Journal of Mechanical and Industrial Engineering*, *6*(2), 17-27.

https://doi.org/10.11648/j.ajmie.20210602.11
56. Wu, Y.-R., & Hsu, W.-H. (2014). A general mathematical model for continuous generating machining of screw rotors with worm-shaped tools. *Applied Mathematical Modelling*, *38*(1), 28-37. https://doi.org/10.1016/j.apm.2013.05.056
57. Xing, Y., Qin, M., & Guo, J. (2017). A Time Finite Element Method Based on the Differential Quadrature Rule and Hamilton's Variational Principle. In *Applied Sciences* (Vol. 7, Issue 2). https://doi.org/10.3390/app7020138
58. Yakoob Pasha, M., Devi, M. T., & Maheswari, T. S. U. (2024). Reliability Analysis of the Shaft Subjected to Twisting Moment and Bending Moment for The Exponential and Weibull Distributed Strength and Stress. *Indian Journal of Science and Technology*, *17*(6), 494-502. https://doi.org/10.17485/IJST/v17i6.1806
59. Yang, J., Zeng, H., Zhu, T., & An, Q. (2017). Study on the dynamic performance of concrete mixer's mixing drum. *Mechanical Sciences*, *8*(1), 165-178. https://doi.org/10.5194/ms-8-165-2017
60. Yang, T., Ma, H., Qin, Z., Guan, H., & Xiong, Q. (2022). Coupling vibration characteristics of the shaft-disk-drum rotor system with bolted joints. *Mechanical Systems and Signal Processing*, *169*, 108747. https://doi.org/10.1016/j.ymssp.2021.108747
61. Yeh, T.-J., & Wu, F.-K. (2009). Modeling and robust control of worm-gear driven systems. *Simulation Modelling Practice and Theory*, *17*(5), 767-777. https://doi.org/10.1016/j.simpat.2009.01.002
62. Yemataw, Z., Chala, A., Ambachew, D., Studholme, D. J., Grant, M. R., & Tesfaye, K. (2017). Morphological variation and inter-relationships of quantitative traits in enset (Ensete ventricosum (welw.) cheesman) germplasm from south and south-western Ethiopia. *Plants*, *6*(4), 1-16. https://doi.org/10.3390/plants6040056
63. Zewdie, A. (2012). *Assessment of performance and adoption of improved enset processing technologies*. University of Applied science Va Hal Larensten.

نشریه ماشین‌های کشاورزی
https://jame.um.ac.ir

مقاله پژوهشی

جلد ۱۶، شماره ۳، پاییز ۱۴۰۵، ص ۴۲۵-۳۹۹

بهبود و تحلیل اجزای دستگاه یکپارچه فرآوری محصول Enset با نام علمی *Ensete ventricosum*

بِکا آدوگنا[۱]، کیشور پوروشوتام کوله[۲*]، موئرا گوتو[۱]

تاریخ دریافت: ۱۴۰۳/۱۱/۰۳
تاریخ پذیرش: ۱۴۰۳/۱۲/۲۶

چکیده

این پژوهش با هدف بهبود طراحی و عملکرد دستگاه یکپارچه فرآوری Enset انجام شد و تمرکز آن بر روی اجزای کلیدی مانند شفت، درام استوانه‌ای، صفحه محافظ (بِرِست‌پلیت) و تیغه درام بود. دستگاه‌های موجود فرآوری Enset به دلیل فرسودگی قطعات، خرابی‌های مکانیکی و طراحی نامناسب با ناکارآمدی‌هایی مواجه هستند که منجر به چالش‌های عملیاتی می‌شود. برای رفع این مشکلات، اصلاحات هدفمند در طراحی قطعات دستگاه برنامه‌ریزی شد. مواد مورد استفاده برای این قطعات بر اساس استانداردهای ASTM انتخاب گردید. قطعات اصلاح‌شده با استفاده از روش اجزای محدود در ماژول ورک‌بنچ نرم‌افزار ANSYS 2023 R1 در دانشگاه علوم و فناوری آداما، اتیوپی، به‌طور دقیق تحلیل شدند. نتایج مطالعه نشان داد که حداکثر تنش‌ها برای شفت، درام استوانه‌ای، تیغه و صفحه محافظ به‌ترتیب برابر با ۱۲۰، ۲۵۰، ۴۰۰ و ۲۶۰ مگاپاسکال و حداقل تنش‌ها به‌ترتیب ۳۰، ۷۰، ۱۲۰ و ۸۰ مگاپاسکال بودند. بیشترین تغییر شکل‌ها نیز به‌ترتیب ۰/۱۵، ۰/۳، ۰/۵۵ و ۰/۳۵ میلی‌متر گزارش شد و ضریب ایمنی بیشینه برای همه قطعات برابر با ۱۵ بود. این نتایج نشان می‌دهد که اصلاحات انجام شده شرایط کاری ایمن را فراهم می‌کند. طراحی به گونه‌ای است که درام، تیغه درام و صفحه محافظ سختی کافی برای تحمل نیروهای عملیاتی را دارند و تغییر شکل حداقلی (۶- ۱۰ * ۲/۳۹ میلی‌متر برای تیغه درام) در محدوده ضریب ایمنی ۱/۲۵ باقی می‌ماند. علاوه بر این، دستگاه عملکرد بسیار خوبی در جذب انرژی و پاسخ ارتعاشی از خود نشان داد که بیانگر استحکام ساختاری آن است.

واژه‌های کلیدی: تغییر شکل، تیغه درام، تنش، درام استوانه‌ای، صفحه محافظ، Enset

۱- گروه مهندسی مکانیک، دانشکده مهندسی مکانیک، شیمی و مواد، دانشگاه علوم و فناوری آداما، آداما، اتیوپی
۲- بخش مهندسی مکانیک، دانشکده مهندسی سینگهد، وادگاون (BK)، ۴۱۱۰۴۱، دانشگاه ساویتری‌بای‌فوله پونه، هند
(*- نویسنده مسئول: Email: kishorkolhe05@gmail.com)

https://doi.org/10.22067/jam.2025.91751.1334

Journal of Agricultural Machinery

Homepage: https://jame.um.ac.ir

Research Article
Vol. 16, No. 3, 2026, p. 427-447

Assessing Viscosity and Contaminant Levels in Diesel Lubricant through Dielectric Spectroscopy Utilizing Soft Computing Approaches

M. R. Pourramezan[1], A. Rohani[1*], M. H. Abbaspour-Fard[1]

1- Department of Biosystems Engineering, Faculty of Agriculture, Ferdowsi University of Mashhad, Mashhad, Iran
(*- Corresponding Author Email: arohani@um.ac.ir)

Received: 29 September 2024
Revised: 19 November 2024
Accepted: 03 December 2024
Available Online: 07 July 2025

How to cite this article:
Pourramezan, M. R., Rohani, A., & Abbaspour-Fard, M. H. (2026). Assessing Viscosity and Contaminant Levels in Diesel Lubricant through Dielectric Spectroscopy Utilizing Soft Computing Approaches. *Journal of Agricultural Machinery*, *16*(3), 427-447. https://doi.org/10.22067/jam.2025.91756.1335

Abstract

Monitoring the status of machinery is a crucial aspect of production and service units to uphold operational efficiency. Timely changes in engine lubricant significantly contribute to enhanced performance and extended engine lifespan. However, determining the precise replacement time remains a challenge. Oil spectral analysis, while effective, is both expensive and time-intensive. This study aims to introduce an alternative method to engine lubricant spectral analysis. The investigation involves analyzing the results of spectral analysis and dielectric coefficients of 17 engine lubricant samples through statistical methods. The primary objective is to develop models for predicting oil contaminants based on dielectric properties, offering a substitute for spectral analysis. To achieve this, several intermediate goals are pursued. Multilayer perceptron artificial neural networks (MLP-ANN) and support vector machine (SVM) methods are employed for modeling. The performance of the two models is assessed using indicators such as Root Mean Square Error (RMSE), model efficiency, and R-squared (R^2). The results indicate that the SVM model consistently demonstrates an efficiency exceeding 0.95 for all predicted indices (Fe, Pb, Cu, Al, Mo, Na, Si, and Vis@100). Consequently, dielectric spectroscopy of lubricant emerges as a viable alternative to traditional oil spectral analysis.

Keywords: Dielectric constant, Engine lubricant condition monitoring, Metrology, Soft computing methods

Abbreviations

ASTM	American Society for Testing and Materials	DS	Dielectric spectroscopy
E	Efficiency	FTIR	Fourier transform infrared
GA	Genetic algorithm	ISM	Industrial, Scientific and Medical
MLP	Multilayer Perceptron	MAPE	Mean absolute percentage error
NN	Neural network	R^2	Coefficient of determination
RBF	Radial basis function	RFE	Recursive feature elimination
RMSE	Root means square error	SA	Spectral Analysis
SC	Soft computing	SVM	Support vector machine
TAN	Total acid number	VNA	Vector network analyzer

Introduction

Condition monitoring, a cornerstone of predictive maintenance, plays a pivotal role in anticipating equipment failures, safeguarding safety, and adhering to regulatory requirements (Mosher, 2007). This is particularly crucial for complex systems, where a comprehensive assessment of operational parameters and human inspection findings is essential for evaluating equipment performance and identifying anomalous conditions (Pourramezan, Rohani, Keramat

Authors retain the copyright. This is an open access article distributed under Creative Commons Attribution 4.0 International License (CC BY 4.0).

https://doi.org/10.22067/jam.2025.91756.1335

Siavash, & Zarein, 2022). As illustrated in Figure 1, the evolution of maintenance strategies has transitioned from reactive approaches to proactive methods, including preventive and condition-based maintenance. This transformation has yielded substantial advancements in safety, reliability, and cost-effectiveness across diverse industries such as manufacturing, transportation, agriculture, and energy production (Lazakis, Raptodimos, & Varelas, 2018; Pourramezan, Rohani, & Abbaspour-Fard, 2023b).

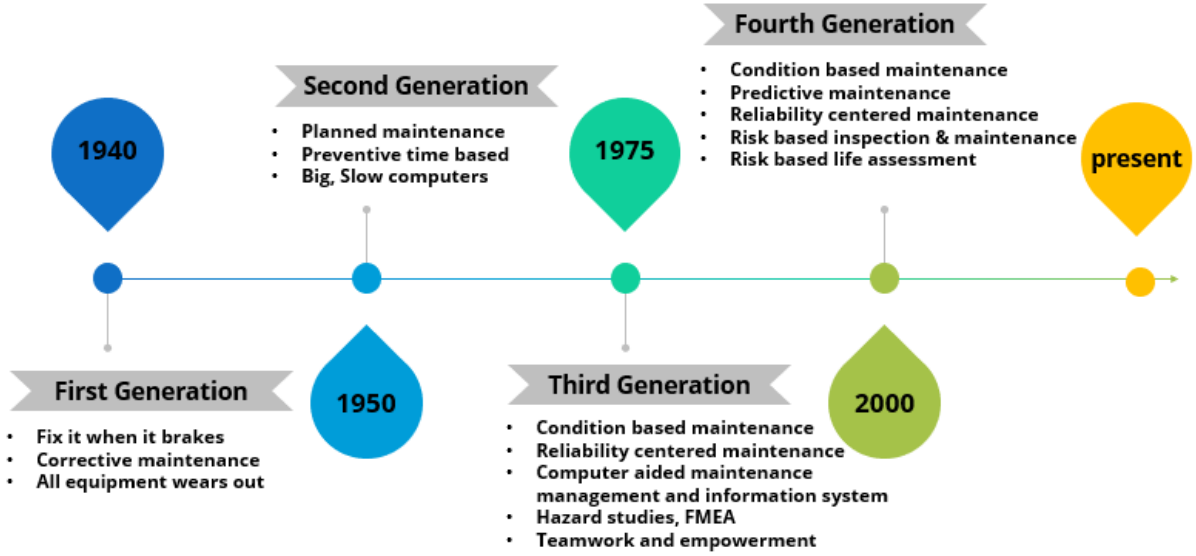

Fig. 1. Evolution of maintenance strategies: a shift from reactive to proactive approaches (Pourramezan *et al.*, 2023b)

Engine lubricants play a multitude of crucial roles in optimizing engine performance (Zhu, Zhong, & Zhe, 2017). These lubricants effectively reduce friction and wear between moving components, facilitate heat transfer and energy distribution, prevent corrosion, and cleanse the internal engine compartments (Kim, Seo, Kang, & Kim, 2016; Mondelin, Claudin, Rech, & Dumont, 2011; Zhu, Wang, Luo, Zhang, & Liu, 2022). However, engine lubricants degrade over time, particularly at elevated temperatures, significantly impacting their tribological performance. This degradation manifests as a reduction in lubricant viscosity, base number (BN), and flash point, accompanied by the formation of detrimental substances such as heavy metals and polycyclic aromatic hydrocarbons (PAHs) (Heredia-Cancino, Ramezani, & Álvarez-Ramos, 2018; Zzeyani, Mikou, & Naja, 2018). traditional machinery maintenance practices often involve monitoring lubricant levels and replacing lubricants based on mileage schedules. However, this "quantity-based" approach is no longer sufficient to ensure optimal lubrication performance and minimize power losses and maintenance costs. The development of advanced engine oil monitoring systems is essential for assessing lubricant degradation and maintaining lubrication effectiveness (Pourramezan, Rohani, & Abbaspour-Fard, 2025). Numerous sensors and systems have been developed by scientists and specialists for monitoring one or more of an engine's performance parameters (Hong & Jeon, 2022). These systems employ a diverse range of techniques, including electrical (magnetic), physical, chemical, and optical methods (Zhu *et al.*, 2017). However, monitoring chemical changes in hydraulic oils and lubricants remains challenging due to the limitations of laboratory-based techniques for real-time industrial applications (Duchowski & Mannebach, 2006). The adoption of low-cost

condition monitoring techniques offers significant practical benefits and economic advantages (Woodley, 1978; You, Liu, & Meng, 2011). Additionally, continuous monitoring of error patterns and parameter variations is crucial for fault diagnosis and condition-based maintenance (Bhattacharya & Dan, 2014).

Presence of contaminants, both solid and liquid particles, can lead to premature bearing wear and performance degradation (Pourramezan *et al.*, 2022). Studies have demonstrated that contamination and physical changes significantly impact lubricant performance, invariably altering the lubricant's dielectric constant (Pourramezan *et al.*, 2023b; Raadnui & Kleesuwan, 2005). The dielectric constant, a crucial indicator of oil aging, is also influenced by factors such as base oil type, additives, temperature, and electric field frequency (Chun, 2006; Gomółka & Augustynowicz, 2019). Published research has established a strong correlation between increased lubricant operating hours, oil sample degradation, and an increase in dielectric constant. In essence, determining the dielectric constant of an oil sample can provide insights into the lubricant's degradation rate. Studies have confirmed that extended oil operating hours lead to further degradation and an elevated dielectric constant (Altıntaş, Aksoy, Ünal, Akgöl, & Karaaslan, 2019). Researchers have employed dielectric spectroscopy to investigate engine lubricant oxidation and determine total acid number (TAN). Their findings, compared to Fourier transform infrared (FTIR) results, demonstrate the effectiveness of both methods in monitoring lubricant condition (Guan, Feng, Xiong, & Xie, 2011). One study has proposed a methodology for locomotive system maintenance. This research investigated the relationship between dielectric properties and metallic and non-metallic particles, including iron (Fe), aluminum (Al), chromium (Cr), lead (Pb), copper (Cu), zinc (Zn), and silicon (Si). Artificial neural networks were employed to explore the correlation between dielectric constant, dielectric loss factor, and oil impurities. The highest regression values (R) were obtained for the dielectric constant and dielectric loss factor at 7.4 GHz, with values of 0.8513 and 0.8015, respectively (Altıntaş *et al.*, 2019). Dielectric or impedance spectroscopy, a non-destructive technique, offers numerous advantages for researchers and engineers. Not only is it a cost-effective method, but it also provides valuable insights into the electrical behavior of materials (Gerhardt, 2022; Sapotta, Schwotzer, Wöll, & Franzreb, 2022).

Fuzzy logic techniques and artificial neural networks (ANNs) have emerged as valuable tools for data analysis in the context of position analysis and equipment troubleshooting within autonomous monitoring systems for industrial equipment (Li, Fei, & Zhang, 2022). Recognizing the importance of reliability, safety, optimal machinery utilization, and the intricate nature of maintenance challenges, researchers have turned to soft computing methodologies for lubrication status monitoring (Król, Gocman, & Giemza, 2015; Li, Chang, Zhou, & Xiao, 2017). Researchers have developed a support vector machine (SVM)-based model to identify and forecast external wear failures based on oil condition monitoring data. This study employed recursive feature elimination (RFE) to reduce independent variables within the model. The highest achieved accuracy in this work was 94.20%. The findings revealed that iron, aluminum, and lead are crucial factors in determining diesel engine erosion status (Li *et al.*, 2017). Yu *et al.* proposed a method for diagnosing oil pump failures using radial basis function (RBF) neural networks (NNs) in conjunction with a genetic algorithm (GA). Their results demonstrated that the proposed model achieved an accuracy exceeding 96% (Yu, Zhao, Chen, & Hou, 2016). Sanga *et al.* employed an RBF neural network to classify breakdowns based on information obtained from the car engine's airway. Their findings indicated that the RBF model could classify failures with an error rate of 2% (Sangha, Gomm, & Yu, 2008).

A soft computing-based method (KNN and

RBF-ANN) was developed to evaluate engine health using a reduced set of lubricant parameters, reducing testing costs. Analyzing 681 engine lubricant reports identified seven key indicators—iron, chromium, lead, copper, aluminum, nickel, and time depending on the particle quantifier (TDPQ)—that significantly impacted distinguishing between normal, caution, and critical wear stages. Both models exhibited high accuracy and sensitivity, with the RBF-ANN achieving an accuracy of approximately 99.85% across all three training set sizes (40%, 60%, and 80%). Overall, the findings suggest that soft computing methods can accurately diagnose engine health using a minimized set of indicators (Pourramezan *et al.*, 2022). The impact of metal and non-metal contaminants on diesel engine conditions was investigated using Support Vector Machines (SVM) and Radial Basis Function (RBF) models. Among the models tested, RBF demonstrated the best generalization performance across varying dataset sizes (10% to 90%). The study also identified key metal contaminants, such as Cr, Si, and Fe, that significantly influenced engine identification in normal and critical states. The confusion matrix approach of RBF-NN achieved an accuracy of 99.38% in diagnosing the critical state of the engine (Rahimi, Pourramezan, & Rohani, 2022). The feasibility of using soft computing models to predict elemental spectroscopy of engine lubricants based on their electrical properties was explored. A dataset of 49 lubricant samples, including elemental spectroscopy and dielectric properties, was utilized to train and test models such as RBF, ANFIS, SVM, MLP, and GPR. The RBF model consistently provided the most accurate predictions for silicon at 7.4 GHz, with root mean squared error (RMSE) and mean absolute percentage error (MAPE) values of 0.4 and 0.7, respectively (Pourramezan *et al.*, 2023b). The potential of soft computing models for predicting the viscosity of used engine lubricant based on oil analysis results was evaluated. A dataset of 555 engine oil analysis reports related to two types of oils (15W40 and 20W50) was employed. Six models, including SVM, ANFIS, GPR, MLR, MLP, and RBF, were developed and assessed for viscosity prediction. The RBF model demonstrated superior accuracy, consistency, and generalizability compared to the other models, achieving RMSE values of 0.20 during training and 0.11 during testing, and efficiency (EF) values of 0.99 during training and 1 during testing (Pourramezan, Rohani, & Abbaspour-Fard, 2023a).

In this work, we propose a novel approach to evaluating engine oil condition by employing dielectric spectroscopy (DS) as a non-invasive and cost-effective alternative to conventional spectral analysis (SA). DS measures the dielectric properties of oil over a wide range of frequencies, providing a wealth of data for developing robust soft computing (SC) models that accurately predict oil indices. Our research utilizes lubricant samples extracted directly from engines, ensuring the relevance of our findings to real-world conditions and enhancing their applicability. Despite the limited sample size, we believe our work serves as a promising proof-of-concept and paves the way for future validation on an industrial scale. The wide frequency range employed (300 MHz to 9 GHz) further enriches the data available for modeling, enabling deeper insights into oil degradation and performance. Additionally, our method holds the potential to significantly reduce the cost and time associated with engine oil spectral analysis, overcoming the limitations inherent in current monitoring practices.

Materials and Methods

The study was carried out in three distinct phases, as depicted in Figure 2.

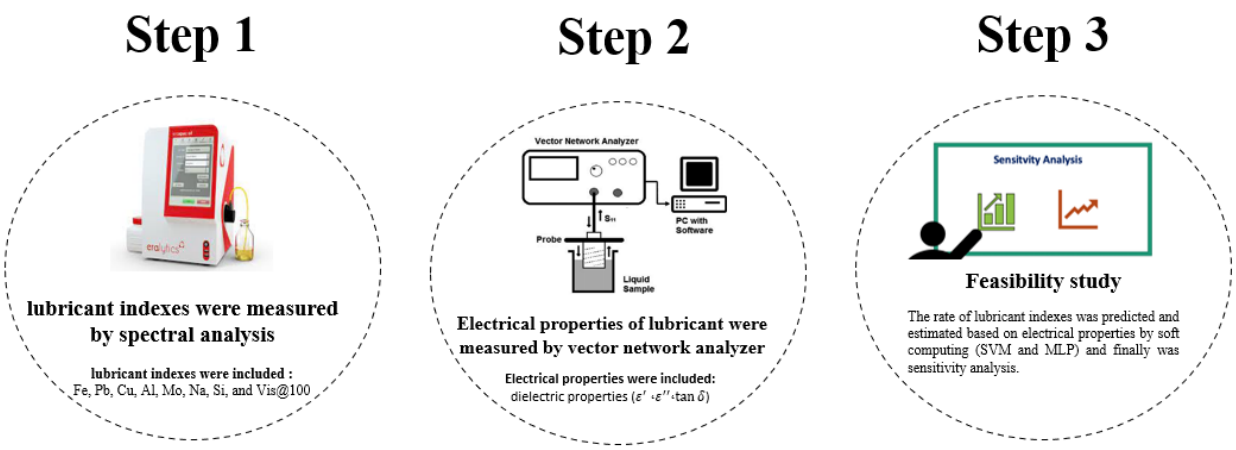

Fig. 2. Research general process flow chart

Spectral analysis method

The study initially employed spectral analysis (SA) to characterize the diesel engine lubricants. Oil analysis involves measuring viscosity, acidity, wear, and metal contamination through spectroscopy (Macián, Tormos, Olmeda, & Montoro, 2003; Newell, 1999). Sixteen diesel engine lubricant samples were obtained from various machines (road construction machines, mainly dump trucks). The oil grade (20W50) and engine type (TYM T2300T3) were identical for all samples. All the machines were property of the Tirage Company in Iran. The concentrations of Fe, Pb, Cu, Al, Mo, Na, and Si were determined according to ASTM D6595. Additionally, the viscosity at 100°C (Vis@100) was determined according to ASTM D445. One sample of fresh 20W50 lubricant was prepared for a more comprehensive study. Measurements were conducted at the commercial laboratory of Tavan Kav Net in Iran. All results are presented in Table 1.

Table 1- The results of spectral analysis on lubricant samples

Sample NO.	Oil Hours	Fe	Pb	Cu	Al	Mo	Na	Si	Vis@100
		Unit: PPM							Unit: Cst
1	100	11.05	0.98	2.83	3.62	48.68	3.46	8.79	16.23
2	150	9.94	0.97	0	1.61	46.11	2.56	17.77	15.3
3	50	30.25	1.64	0	10.18	50.36	8.99	9.23	20.03
4	80	81.17	2.59	0	34.59	52.23	9.32	36.21	15.94
5	100	13.19	0.59	1.8	1.09	36.24	2.33	7.14	15.99
6	160	24.65	1.25	0	5.05	48.78	3.81	9.89	16.35
7	130	9.24	0.92	0	1	45.75	2.86	6.11	15.33
8	160	15.46	1.75	0	0.38	45.81	2.31	4.01	15.02
9	100	39	7.78	4.42	10.93	28.84	9.99	16.29	17.5
10	100	39.76	1.4	3.2	3.77	77.64	13.67	15.44	17.83
11	70	34.69	1.23	0.18	13.45	37.75	4.15	16.55	17.81
12	150	39.67	2.31	3.91	12.45	46.98	5.32	16.33	17.59
13	50	86.06	2.76	1.17	10.95	52.53	3.46	40.05	18.64
14	74	21.73	7.23	3.22	5.31	40.78	3.89	7.27	15.33
15	100	8.17	3.23	1.79	0	26.86	1.2	7.22	7.85
16	100	49.75	4.11	3.51	5.07	12.16	9.57	13.65	13.67
17 (Fresh oil)	0	0	0	0	0	0	0	0	22

Measurement of dielectric properties

The second step involved measuring the dielectric properties of all 17 lubricant samples (16 used and one fresh) at various frequency

points. Every material in nature possesses fundamental electrical parameters, including permittivity, permeability, and conductivity. Permittivity exhibits both real and imaginary components, and their relationship with the dielectric constant is defined by Equation (1) (Altıntaş *et al.*, 2019):

$$k = \varepsilon^* = \varepsilon' - j\varepsilon'' \quad (1)$$

where k is the dielectric constant, also known as relative permittivity (ε^*). ε' represents the real part of the dielectric constant, while ε'' denotes the imaginary part. The symbol j represents the imaginary unit $\sqrt{-1}$.

The dielectric constant of a material quantifies its ability to store electrical energy relative to free space. However, it can vary under different conditions, such as frequency, temperature, composition, and pressure (Mumby, 1989;

Zeng, Zhang, Zhang, & Hu, 2010). The real part of the dielectric constant, ε', reflects a material's ability to store electrical energy when subjected to an electromagnetic field. The imaginary part, ε", indicates the dissipation of electromagnetic energy in the material. The loss coefficient, $\tan\delta$, quantifies the conversion of electromagnetic energy into heat and is calculated using Equation (2) (Pourramezan, Rohani, & Abbaspour-Fard, 2024):

$$\tan\delta = \frac{\varepsilon''}{\varepsilon'} \quad (2)$$

In this study, a wide frequency band was employed to measure the dielectric properties. Furthermore, the probe reflectance method was employed to monitor the environmental state (Pourramezan *et al.*, 2023b). This method involves determining the dielectric properties of lubricant samples by comparing the amplitude and phase values of the reflected wave with the radiated wave (Zarein, Khoshtaghaza, & Ameri Mahabadi, 2019). The dielectric properties (ε', ε", $\tan\delta$) of the lubricant samples were measured using an R&S ZVL 13 vector network analyzer (VNA) manufactured in the USA. This VNA can accurately analyze microwave absorbing properties in the 9 kHz to 13.6 GHz frequency range with ±0.2 dB accuracy (see Fig.3).

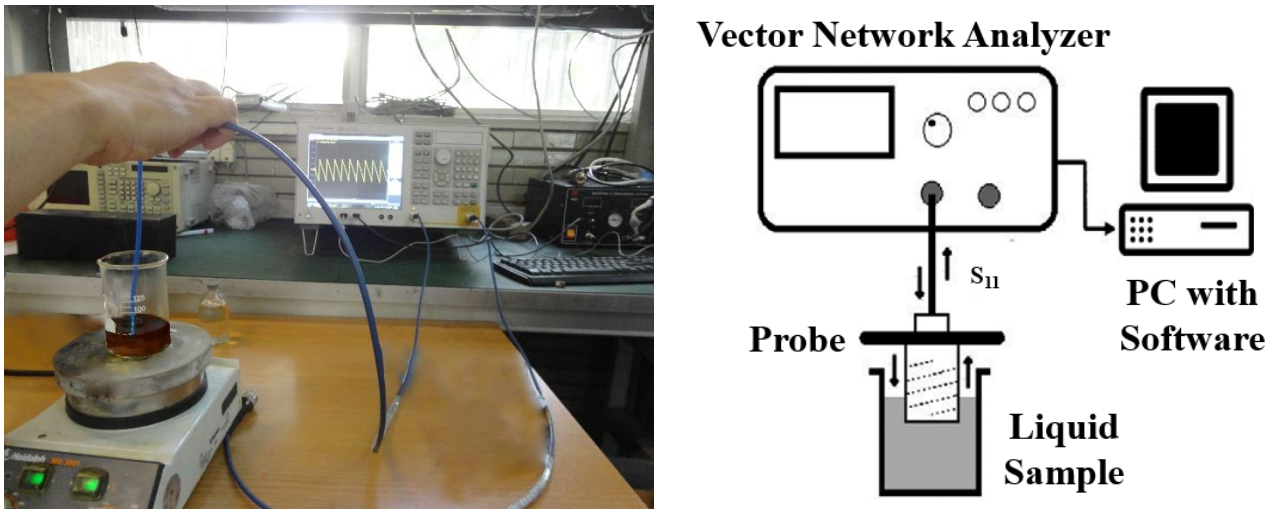

Fig. 3. Experimental and schematic setup for dielectric properties measurement

As shown in Figure 3, 50 ml of each lubricant sample was poured into a beaker, and a coaxial dielectric probe was inserted into the oil sample. Initially, the frequencies of 434, 915, 2450, and 5800 MHz were considered, corresponding to industrial, scientific, and medical (ISM) frequencies (Nüchter, Ondruschka, Bonrath, & Gum, 2004). Subsequently, appropriate frequency points were determined within each frequency range. Finally, the measurements were conducted at 40 frequency points distributed across the 300 MHz to 9 GHz frequency range (Table 2). The measurements for each sample were repeated

three times under identical conditions to ensure consistency and accuracy.

Table 2- Frequency points used in the 300 MHz to 9 GHz frequency range

Symbol	Frequency (GHz)	Symbol	Frequency (GHz)	Symbol	Frequency (GHz)	Symbol	Frequency (GHz)
f1	0.3	f11	2.45	f21	4.6895	f31	6.9495
f2	0.434	f12	2.6	f22	4.9155	f32	7.1755
f3	0.675	f13	2.84	f23	5.1415	f33	7.4015
f4	0.915	f14	3.085	f24	5.3675	f34	7.6275
f5	1.16	f15	3.325	f25	5.5935	f35	7.8535
f6	1.4	f16	3.565	f26	5.8195	f36	8.0795
f7	1.64	f17	3.8	f27	6.0455	f37	8.3055
f8	1.88	f18	4	f28	6.2715	f38	8.5315
f9	2.12	f19	4.2375	f29	6.4975	f39	8.7575
f10	2.36	f20	4.4635	f30	6.7235	f40	9

Design of soft computing models

This section explores the application of soft computing models to predict the values of oil analysis indices (Section 2.1) from their dielectric properties (Section 2.2). Soft computing systems directly utilize data to learn, eliminating the need for predefined equations to identify patterns and trends (Cardoso & Ferreira, 2020; Pourramezan *et al.*, 2024). The backpropagation algorithm (Lillicrap, Cownden, Tweed, & Akerman, 2016) serves as a learning mechanism, providing efficient weight adjustments and achieving low error rates. To enhance the performance of soft computing methods, the dielectric characteristic data are normalized using Equation (3) (Heidari, Rezaei, & Rohani, 2020; Rohani, Abbaspour-Fard, & Abdolahpour, 2011). This normalization technique transforms the data into a range between -1 and 1, ensuring consistency and facilitating the model's training process. Two soft computing models, multilayer perceptron (MLP) and support vector machine (SVM), were employed for this study. Their specific implementation details are described in the subsequent sections.

$$C_N = \frac{(C_i - C_{min})}{(C_{max} - C_{min})} \times (r_{max} - r_{min}) + r_{min} \quad (3)$$

The normalized value (C_N) of each dielectric property is calculated using Equation (3), where C_i represents the original value of the dielectric property, C_{max} and C_{min} represent the maximum and minimum values of the property across all samples, and r_{max} and r_{min} represent the maximum and minimum values considered for the normalized data.

Multilayer perceptron neural network (MLP-NN)

The multilayer perceptron neural network (MLP-NN) comprises an input layer, an output layer, and one hidden layer. In this study, MLP-NN is employed to predict the spectral analysis indices (Fe, Pb, Cu, Al, Mo, Na, Si, and Vis@100) of engine lubricant using the dielectric properties of the oil (ε', ε", tan δ), as illustrated in Figure 4. The input layer is defined based on the correlation analysis of dielectric properties at different frequencies, as shown in Table 2. The output layer represents the desired spectral analysis index of the engine lubricant that we aim to predict. In modeling, the training set constitutes 80% of the dataset, while the testing set accounts for the remaining 20%. The hidden layer incorporates the sigmoid conversion function (Equation 4) (Ashtiani, Rohani, & Aghkhani, 2020; Shi, Song, & Song, 2021).

$$I = \frac{1}{1 + e^{-\sum C_i w_{ij} + b}} \quad (4)$$

where C_i represents the i^{th} input, b denotes the bias factor, and w_{ij} shows the weight of the j^{th} neuron.

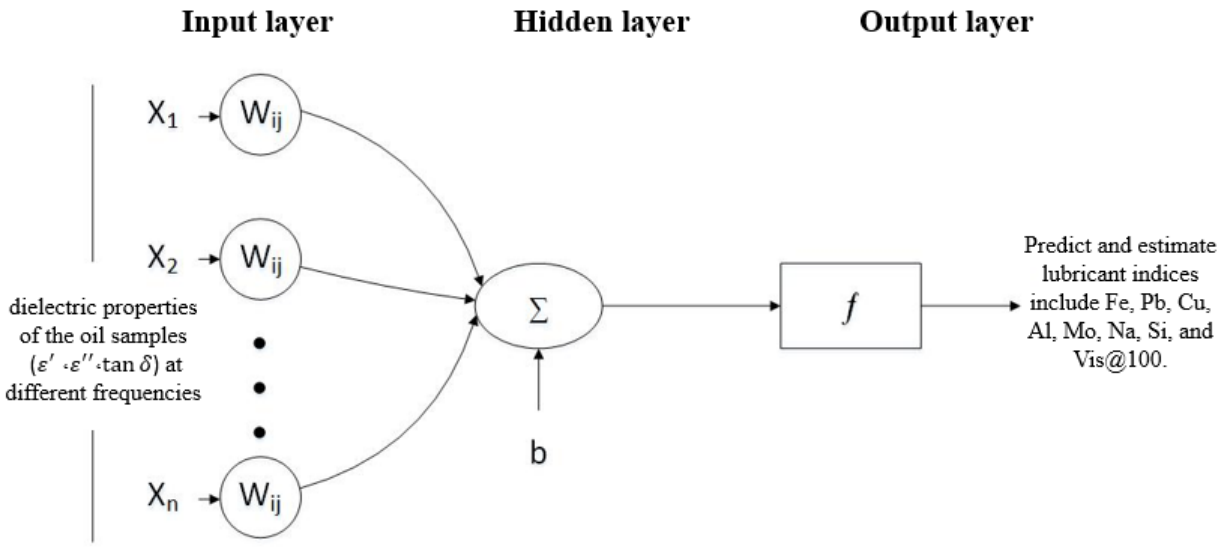

Fig. 4. MLP structure used to predict lubricant indices

Support vector machine (SVM)

Support vector machines (SVMs) were first introduced by Vapnik in the 1990s (Fayazi, Arabloo, Shokrollahi, Zargari, & Ghazanfari, 2014). In this study, SVMs are utilized to predict the spectral analysis indices (Fe, Pb, Cu, Al, Mo, Na, Si, and Vis@100) of engine lubricants based on their dielectric properties (ε', ε", $\tan\delta$) at various frequencies (see Fig.5).

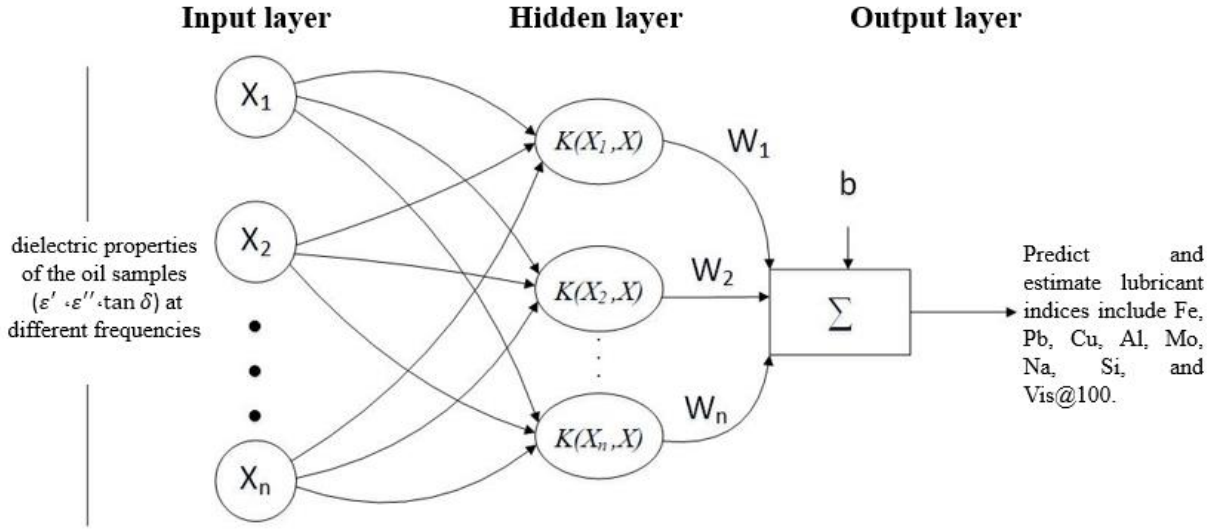

Fig. 5. SVM structure used to predict lubricant indices

Support vector machines (SVMs) are based on statistical learning principles, governed by the following relationships (Chamkalani, Mohammadi, Eslamimanesh, Gharagheizi, & Richon, 2012; Eslamimanesh *et al.*, 2012). The nonlinear function employed in the SVM approach to approximate data sets $\{(X_1, Y_1), (X_2, Y_2), \ldots, (X_n, Y_n)\}$ is given by Equation (5):

$$f(x) = w\varphi(x) + b \quad (5)$$

where $\varphi(x)$ represents a nonlinear mapping function, w represents the weight vector of the

input layer, and *b* represents the bias factor.

SVM optimization is achieved by minimizing Equation (6) using the Lagrange function (Equation (7)):

$$min_{w,b,e} J(w,e) = \frac{1}{2}\|w\|^2 + \frac{1}{2}\gamma\sum_{i=1}^{n}\xi_i^2 \quad (6)$$

$$s.t.\, y_i = w.\varphi(x_i) + b + \xi_i, i = 1,2,\dots,n$$

$$L(w,b,\xi,\alpha) = \frac{1}{2}\|w\|^2 + \frac{\gamma}{2}\sum_{i=1}^{n}\xi_i^2 - \sum_{i=1}^{n}\alpha_i\,(w\varphi(x_i) + b + \xi_i - y_i) \quad (7)$$

where ξ_i represents the regression error for n training items, γ is the regularization parameter, α_i is the Lagrange coefficient, and Equation (7) is obtained by considering partial derivatives of *w*, *b*, *ξ*, and *α*.

Performance evaluation of soft computing models

This study aims to predict spectral analysis indices for engine lubricants based on dielectric properties measured at different frequencies. The performance of the soft computing models, namely MLP and SVM, is assessed using four metrics: root mean square error (RMSE), mean absolute percentage error (MAPE), model efficiency (E), and R-squared (R^2) (Pourramezan, Omidvar, Motavalizadehkakhky, Zhiani, & Darzi, 2024; Pourramezan & Rohani, 2024; Siavash *et al.*, 2021; Soltanali, Rohani, Abbaspour-Fard, & Farinha, 2021):

$$RMSE = \sqrt{\frac{\sum_{i=1}^{n}(y_{pi} - y_{ei})^2}{n}} \quad (8)$$

$$MAPE = \frac{1}{n}\sum_{i=1}^{n}\frac{|y_{pi} - y_{ei}|}{y_{pi}} \quad (9)$$

$$E = \frac{1}{n}\sum_{i=1}^{n}(y_{pi} - y_{ei})^2 \quad (10)$$

$$R^2 = \frac{(\sum_{i=1}^{n}(y_{ei} - \overline{y_{ei}})(y_{pi} - \overline{y_{pi}}))^2}{\sum_{i=0}^{n}(y_{ei} - \overline{y_{ei}})^2 \sum_{i=0}^{n}(y_{pi} - \overline{y_{pi}})^2} \quad (11)$$

where y_{pi} and y_{ei} represent the predicting and the measuring indices of engine lubricant spectral analysis, respectively. Here, n represents the number of oil samples.

To assess the performance of the soft computing models, we evaluated the mean, variance, and normal distribution of the predicted values. After comparing the MLP and SVM models, the regression diagram of the predicted and actual values for the superior model was plotted.

Results and Discussion

The optimal frequency for the study was initially identified based on the highest value of the determination coefficient (R^2) (see Fig.6). Subsequently, the ability of dielectric indices (ε', ε", $\tan\delta$) to predict the spectral analysis indices of engine lubricants was examined using soft computing techniques.

As depicted in Figure 6, the ε' index exhibited superior performance in the pollution assessment at f40 frequency (R^2 = 75.16) and the viscosity assessment at f40 frequency (R^2= 4.95). However, R^2 = 4.95 is insufficient for reliable prediction. The ε' index also demonstrated exceptional performance in the wear and total assessments at f24 frequency (R^2= 99.29). Additionally, Figure 6 reveals that the ε" index achieved the highest R^2 value of 88.21 in the pollution assessment at f26 frequency. Furthermore, the ε" index exhibited the best results in the wear (R^2= 99.41), viscosity (R^2= 26.14), and total assessments at frequency f1, respectively. However, R^2= 26.14 is not sufficiently robust for viscosity prediction. As shown in Figure 6, the $\tan\delta$ index demonstrated exceptional performance in the pollution assessment at f26 frequency (R^2= 88.81) and the viscosity assessment at f1 frequency (R^2= 24.93). While R^2 = 24.93 is insufficient for accurate

prediction, the $\tan\delta$ index also achieved the highest R^2 value of 99.35 in the wear and total assessments at f40 frequency.

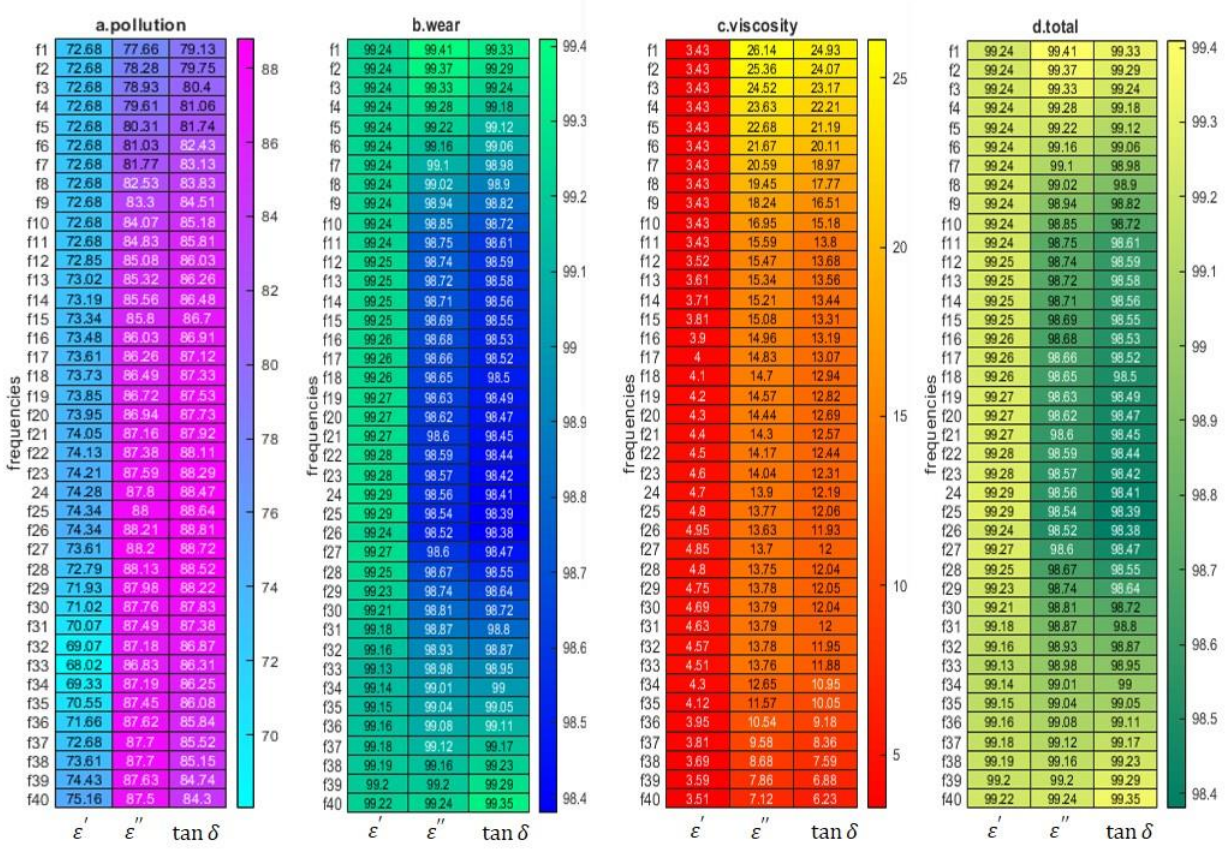

Fig. 6. R^2 of dielectric properties (ε', ε'', $\tan\delta$) at different frequencies (Table 2) by attention to various evaluated lubricant conditions

Setting input parameters for MLP and SVM

As described in the Materials and Methods section, MLP and SVM models were employed to predict the spectral analysis indices of engine lubricants from the measured values of dielectric properties (ε', ε'', $\tan\delta$) at different frequencies. The neural network inputs were determined based on the correlation analysis and expert judgment presented in Table 3.

Table 3- Neural network input parameters for MLP and SVM

Predicted index	Inputs model*
Vis@100	p1, p12, p23, p27, p34, z 1, z2, z27, z34
Si	p12, p27, z1, z2, z12, z34, d 1, d2, d12
Na	p1, p12, p23, p27, p34, z1, z12, z27, z34
Fe	p1, p12, p27, z1, z2, z12, z27, z34, d1, d2, d12, d27
Pb	p1, p12, p15, p16, p23, p27, p28, p34, z1, z2, z12, z27, z30, z34, d1, d2, d3, d12, d24, d25, d26, d27, d35, d39
Cu	z31, z32, z33, z34, z35, z36, z37, z38, z39, d30, d31, d32, d33, d34, d35, d36, d37, d38, d39
Al	p1, p2, p12, p22, p26, p27, p38, z1, z2, z3, z12, z17, z27, z29, z34, d1, d2, d3, d12, d27
Mo	p1, p2, p12, p22, p26, p27, p38, z1, z2, z3, z12, z17, z27, z29, z34, d1, d2, d3, d12, d27

*The p, z, and d are ε', ε'', and $\tan\delta$, respectively. The numeral of each symbol represents the measured frequency point (attention to Table 2).

Comparing the performance of MLP and SVM

In this section, the MLP and SVM models developed in Section 3.1 are evaluated and compared using the performance metrics RMSE, MAPE, and E (Table 4). Generally, smaller values of RMSE and MAPE indicate better model performance, while E values closer to 1 indicate improved model accuracy.

Table 4- Comparative performance of the SVM and MLP models

Predicted index	Phase	SVM			MLP		
		RMSE	MAPE	E	RMSE	MAPE	E
Vis@100	Train	0.23	1.2	0.99	0.38	1.91	0.98
	Test	0.49	2.74	0.96	0.49	1.99	0.96
	Total	0.3	1.5	0.99	0.41	1.93	0.97
Si	Train	0.74	-	0.99	0.5	-	0.99
	Test	1	-	0.99	1.5	-	0.97
	Total	0.8	-	0.99	0.8	-	0.99
Na	Train	0.43	-	0.98	0.69	-	0.96
	Test	0.52	-	0.98	0.93	-	0.92
	Total	0.45	-	0.98	0.75	-	0.95
Fe	Train	1.88	-	0.99	5.83	-	0.92
	Test	4.44	-	0.95	5	-	0.93
	Total	2.59	-	0.98	5.67	-	0.93
Pb	Train	0.21	-	0.98	0.99	-	0.61
	Test	0.46	-	0.91	0.82	-	0.71
	Total	0.28	-	0.97	0.96	-	0.62
Cu	Train	0.34	-	0.96	0.57	-	0.88
	Test	0.46	-	0.96	0.97	-	0.81
	Total	0.37	-	0.96	0.67	-	0.86
Al	Train	0.65	-	0.99	2.38	-	0.86
	Test	1.16	-	0.98	2.09	-	0.94
	Total	0.78	-	0.99	2.32	-	0.89
Mo	Train	1.05	-	0.99	7.25	-	0.82
	Test	1.84	-	0.98	5.47	-	0.82
	Total	1.24	-	0.99	6.94	-	0.82

Table 4 presents the performance of the MLP and SVM models in predicting the spectral analysis indices of engine lubricants. The results indicate that the SVM model consistently exhibits superior performance across all indices, as evidenced by its higher E values and lower RMSE scores. For instance, in the prediction of iron content, the SVM model achieved an E value of 0.98 and an RMSE of 2.59, compared to the MLP model's 0.93 and 5.67, respectively. Similarly, Table 5 compares the MLP and SVM models based on the mean, variance, and normal distribution of the predicted values, confirming the SVM model's superior modeling capabilities. Figure 7 depicts the coefficient of determination (R^2) between the actual and predicted values of the spectral analysis indices. The R^2 values for both training and testing stages demonstrate that the SVM model closely aligns the actual and predicted values. This is further evident from the slopes of the regression lines, which approach unity and zero in the SVM model. Consequently, the SVM model successfully predicts the values of most spectral analysis indices with a high degree of accuracy, achieving an R^2 value of approximately 0.99.

Table 5- Evaluating MLP and SVM models by mean, variance, and normal distribution

Predicted index	Phase	SVM			MLP		
		Mean	Variance	Distribution	Mean	Variance	Distribution
Vis@100	Train	0.95	0.83	0.99	0.83	0.98	0.9
	Test	0.82	0.92	0.11	0.81	0.99	0.11
	Total	0.96	0.86	0.69	0.76	0.99	0.69
Si	Train	0.98	0.85	0.55	0.99	0.99	0.99
	Test	0.92	0.86	0.97	0.99	0.99	0.97
	Total	0.95	0.91	0.37	0.99	0.98	0.96
Na	Train	0.93	0.72	0.55	0.99	0.85	0.9
	Test	0.9	0.89	0.97	0.77	0.99	0.68
	Total	0.89	0.7	0.52	0.89	0.86	0.52
Fe	Train	0.94	0.79	0.9	0.98	0.74	0.99
	Test	0.99	0.71	0.97	0.97	0.94	0.97
	Total	0.94	0.69	0.85	0.99	0.74	0.96
Pb	Train	0.94	0.53	0	0.49	0	0.01
	Test	0.72	0.47	0.31	0.54	0.52	0.68
	Total	0.83	0.39	0	0.36	0	0
Cu	Train	0.94	0.67	0.55	0.71	0.51	0.74
	Test	0.99	0.88	0.97	0.94	0.95	0.97
	Total	0.96	0.65	0.52	0.72	0.65	0.69
Al	Train	0.97	0.85	0.94	0.46	0.08	0.09
	Test	0.74	0.99	0.77	0.8	0.97	0.97
	Total	0.55	0.97	0.52	0.46	0.22	0.06
Mo	Train	0.95	0.81	0.74	0.86	0.15	0.55
	Test	0.95	0.89	0.31	0.85	0.2	0.97
	Total	0.94	0.78	0.37	0.82	0.08	0.52

Sensitivity analysis

The SVM model demonstrated superior performance in predicting the spectral analysis indices of engine lubricants, as evidenced by its higher E values, lower RMSE scores, and closer alignment of actual and predicted values (Tables 4 and 5). Further analysis revealed that the SVM model's regression line closely approximates unity and zero, indicating a high degree of accuracy. Sensitivity analysis plays a crucial role in model development and application by identifying the most influential parameters and simplifying the model (Glagolev, 2012). It enables the assessment of how changes in input parameters affect the model's output (Iooss & Lemaître, 2015). In this study, sensitivity analysis was employed to evaluate the importance of each dielectric index value in predicting the spectral analysis indices of engine lubricants. RMSE was used as the criterion for assessing sensitivity. Therefore, if removing an input increases RMSE, it indicates its significance (RMSE should approach zero). Conversely, if removing an input reduces RMSE, it suggests its lower importance (Chaudhry, Buchwald, & Nagel, 2021; Rezaei, Rohani, Heidari, & Lawson, 2021). Figure 8 illustrates the results of sensitivity analysis conducted by the SVM model to predict the spectral analysis parameters of engine lubricants.

The sensitivity analysis results for predicting viscosity revealed that removing inputs z27, p23, p27, and z34 resulted in increased RMSE, indicating their higher significance. Conversely, removing inputs p34, z1, and z27 did not significantly impact RMSE. Removing inputs p1 and p12 led to reduced RMSE, implying their lower significance. Three models with reduced inputs were subsequently proposed; however, none improved RMSE. The sensitivity analysis for predicting silicon indicated that removing inputs p12, p27, d12, and z34 increased RMSE, while eliminating inputs d1, d2, z1, z2, and z12 reduced RMSE.

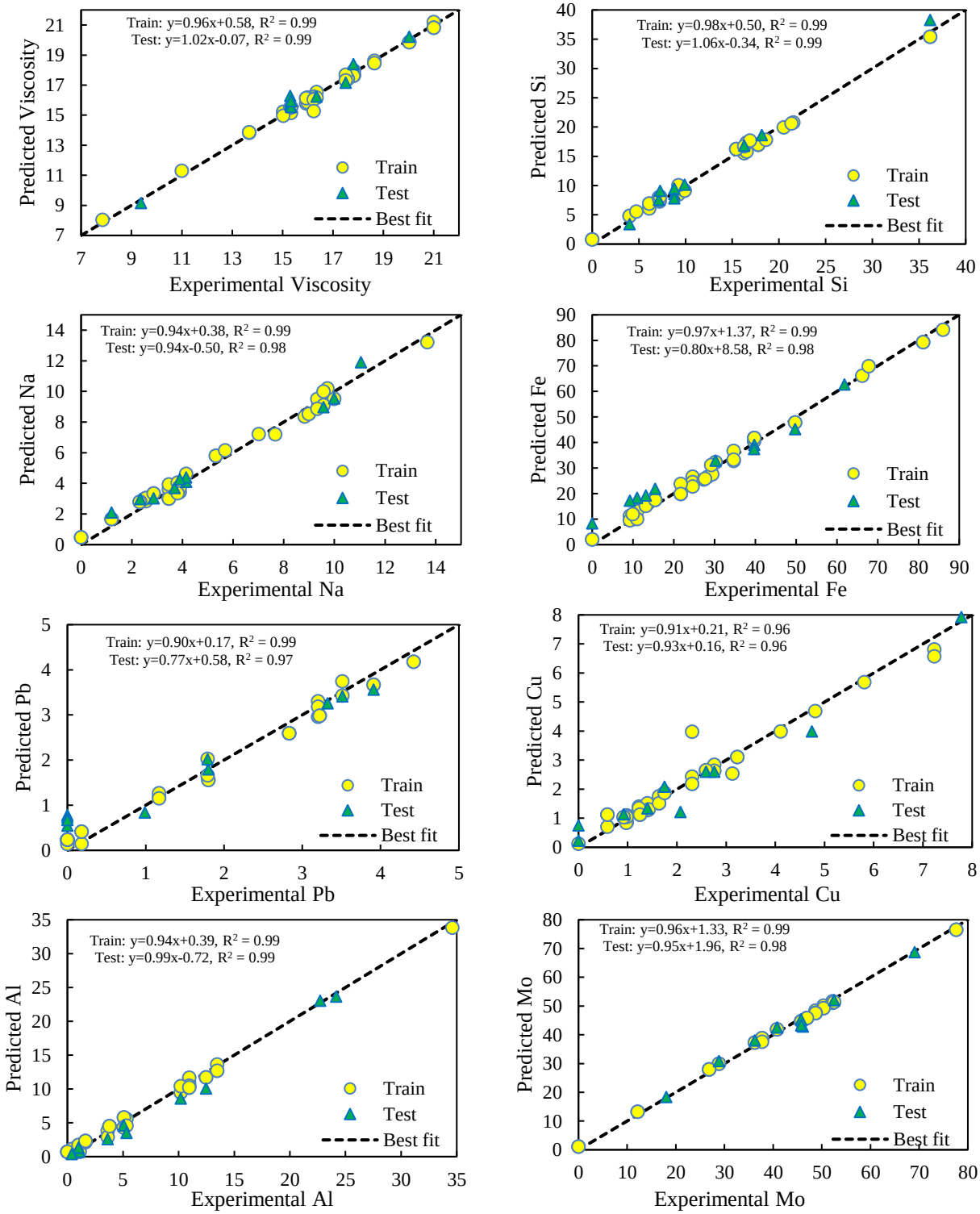

Fig. 7. Comparison of experimental and predicted lubricant spectral analysis (SA) indexes using the SVM model

Two models with limited inputs were proposed, and one (p12, p27, z34, d1, and d12) achieved improved RMSE. Sensitivity analysis for predicting sodium showed that removing inputs z27 and p34 increased RMSE, while removing inputs p1, p12, p27, and z12 had no significant impact. Removing inputs p23, z1, and z34 decreased RMSE, suggesting their

lower significance. One model (p1, p12, p27, p34, z12, and z27) was proposed and successfully improved RMSE. Iron prediction sensitivity analysis revealed that removing inputs p27, d27, and d1 resulted in increased RMSE, while removing inputs z12, z27, z34, p1, p12, z1, d2, d12, and z2 reduced RMSE. One model (z12, z27, z34, p1, p12, p27, d1, and d27) was suggested and improved RMSE. Lead prediction sensitivity analysis indicated that removing inputs d25, z1, d27, d39, d15, z12, d12, z27, p1, d2, d3, z2, p12, p16, p27, p34, d1, p28, d26, z34, d24, d35, and p23 led to increased RMSE, while removing input z30 reduced RMSE. No model with limited inputs improved RMSE. The sensitivity analysis for predicting copper revealed that removing inputs d39, z35, d31, z36, z39, and d33 increased RMSE, while removing input d38 did not affect RMSE and removing inputs d32, d35, z32, z33, z37, z38, d30, d36, d37, z31, z34, and z35 decreased RMSE. One model (d39, z35, d31, z36, z39, d33, d38, d32, and d35) was proposed and successfully improved RMSE.

The sensitivity analysis for predicting aluminum revealed that removing inputs d12, d3, z3, z27, z17, d2, z29, z34, and d27 led to increased RMSE, indicating their higher significance. Conversely, removing inputs p1, p2, p12, p22, p26, p27, z1, z2, z12, and d1 had no significant impact on RMSE. Removing input p38 resulted in reduced RMSE, suggesting its lower significance. A model with the reduced inputs (d12, d3, z3, z27, z17, d2, z29, z34, d27, and p1) was proposed and successfully improved RMSE. Molybdenum prediction sensitivity analysis indicated that removing inputs z27, z12, z34, z17, d3, z2, p38, z1, p2, d12, p12, p1, z29, d27, d2, z3, and d1 led to increased RMSE, while removing inputs p27, p22, and p26 resulted in reduced RMSE. No model with limited inputs improved RMSE.

Building upon the insights gained from sensitivity analysis, the final models for predicting the viscosity, Si, Na, Fe, Pb, Cu, Mo, and Al values of engine lubricant using SVM were proposed. While models with fewer inputs were considered for viscosity prediction, none of them could significantly enhance the RMSE. For Si prediction, a model with reduced inputs was proposed, and it successfully improved RMSE. Similarly, models with less significant inputs were identified for Na and Fe predictions, leading to improved RMSE values. In contrast, a model with more significant inputs was developed for Pb prediction, but it failed to improve RMSE. For Cu and Al prediction, models with less significant inputs were found, and they effectively reduced RMSE. Overall, the final models exhibit promising accuracy, as RMSE improvements were achieved by eliminating less influential inputs.

Conclusion

This study investigated the dielectric properties (ε', ε'', tan δ) of 17 lubricant samples, including 16 used oil samples and one fresh oil sample. Dielectric measurements were performed at 40 frequencies ranging from 300 MHz to 9 GHz. Initially, the correlation between dielectric properties and lubricant conditions was analyzed in four evaluation categories: pollution, erosion, viscosity, and general. The dielectric constant (ε') index exhibited the highest coefficient of determination (R2) for pollution at frequencies f40, f24, and f26, and for erosion, viscosity, and general at frequencies f26, f40, f1, and f40, respectively. The dielectric loss tangent (tan δ) index displayed the strongest correlation with pollution at frequency f27 and with erosion, viscosity, and general at frequencies f1, f26, and f40, respectively. Subsequently, multilayer perceptron (MLP) and support vector machine (SVM) models were designed to predict the spectral analysis indices of engine lubricants based on dielectric properties. The inputs for these models were determined using correlation and speculation analyses. The performance of the models was evaluated and compared using three metrics: root mean squared error (RMSE), mean absolute percentage error (MAPE), and efficiency (E).

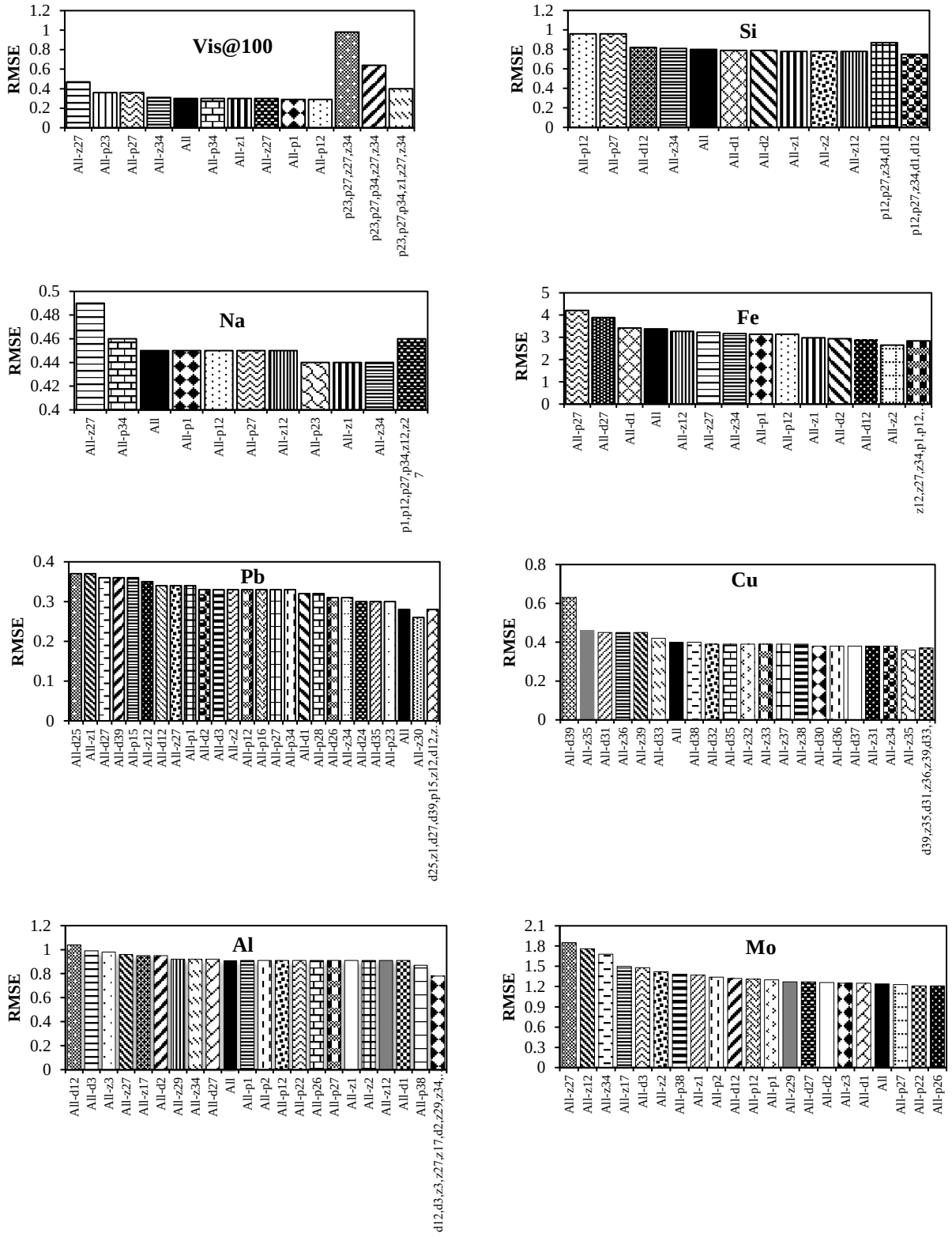

Fig. 8. Result of sensitivity analysis (attention to Table 3)

The SVM model outperformed the MLP model and was selected as the preferred model for predicting lubricant condition indices. Sensitivity analysis was employed to assess the importance of each model input. The findings of this study demonstrate that soft computing techniques can effectively estimate the spectral analysis indices of engine lubricants (Fe, Pb, Cu, Al, Mo, Na, Si, and Vis@100) using their dielectric properties (ε', ε'', tan δ). This approach offers a promising and practical method for monitoring the condition of diesel engine lubricants, particularly for off-road machinery operating in remote areas with limited access to oil analysis laboratories. The SVM model achieved an efficiency score exceeding 0.95 for all predicted indices, highlighting its potential for real-world applications. While the limited sample size somewhat restricts the scope of this research, the results provide a strong proof-of-concept and pave the way for further validation on an industrial scale. Despite the potential for online and portable equipment implementation, the study's laboratory setting under controlled conditions raises concerns about the accuracy and consistency of input data in real-world scenarios. Therefore, further research involving a larger statistical population and a broader range of lubricant types is necessary to fully assess the comprehensiveness and commercialization potential of this method. The accuracy of predictions based on electrical properties may depend on the quality and consistency of the input data, emphasizing the need for rigorous validation in field conditions.

Acknowledgment

We gratefully acknowledge the financial support provided by Ferdowsi University of Mashhad in Iran for this research project. We also appreciate the valuable contribution of Tirage Company for granting us access to their maintenance database.

Conflict of Interest: The authors declare no competing interests.

Compliance with Ethical Standards

This work does not contain any studies with human participants or animals performed by any of the authors.

Funding

This research was supported by Ferdowsi University of Mashhad in Iran (Grant number 59252).

Author Contributions

M. R. Pourramezan: Conceptualization, Investigation, Software, Formal analysis, Writing-original draft.

A. Rohan: Funding acquisition, Software, Formal analysis, Project administration, Supervision, and Validation.

M. H. Abbaspour-Fard: Advisor, Supervision, Validation, Writing-review & editing

Data Availability

The datasets analyzed during the current study are not publicly available but are available from the corresponding author on reasonable request.

References

1. Altıntaş, O., Aksoy, M., Ünal, E., Akgöl, O., & Karaaslan, M. (2019). Artificial neural network approach for locomotive maintenance by monitoring dielectric properties of engine lubricant. *Measurement, 145*, 678-686. https://doi.org/10.1016/j.measurement.2019.05.087
2. Ashtiani, S.-H. M., Rohani, A., & Aghkhani, M. H. (2020). Soft computing-based method for estimation of almond kernel mass from its shell features. *Scientia Horticulturae, 262*, 109071. https://doi.org/10.1016/j.scienta.2019.109071
3. Bhattacharya, A., & Dan, P. K. (2014). Recent trend in condition monitoring for equipment

fault diagnosis. *International Journal of System Assurance Engineering and Management, 5*, 230-244. https://doi.org/10.1007/s13198-013-0151-z

4. Cardoso, D., & Ferreira, L. (2020). Application of predictive maintenance concepts using artificial intelligence tools. *Applied Sciences, 11*(1), 18. https://doi.org/10.3390/app11010018
5. Chamkalani, A., Mohammadi, A. H., Eslamimanesh, A., Gharagheizi, F., & Richon, D. (2012). Diagnosis of asphaltene stability in crude oil through "two parameters" SVM model. *Chemical Engineering Science, 81*, 202-208. https://doi.org/10.1016/j.ces.2012.06.060
6. Chaudhry, A. A., Buchwald, J., & Nagel, T. (2021). Local and global spatio-temporal sensitivity analysis of thermal consolidation around a point heat source. *International Journal of Rock Mechanics and Mining Sciences, 139*, 104662. https://doi.org/10.1016/j.ijrmms.2021.104662
7. Chun, S.-M. (2006). Study on Mutual Relation between the Level of Deterioration Influenced by the Changes of Chemical and Physical Properties and the Change of Dielectric Constant for Engine Oil-Diesel Engine Oil. *Tribology and Lubricants, 22*(5), 290-300. https://doi.org/10.9725/kstle.2006.22.5.290
8. Duchowski, J. K., & Mannebach, H. (2006). A novel approach to predictive maintenance: a portable, multi-component MEMS sensor for on-line monitoring of fluid condition in hydraulic and lubricating systems. *Tribology Transactions, 49*(4), 545-553. https://doi.org/10.1080/10402000600885183
9. Eslamimanesh, A., Gharagheizi, F., Illbeigi, M., Mohammadi, A. H., Fazlali, A., & Richon, D. (2012). Phase equilibrium modeling of clathrate hydrates of methane, carbon dioxide, nitrogen, and hydrogen+ water soluble organic promoters using Support Vector Machine algorithm. *Fluid Phase Equilibria, 316*, 34-45. https://doi.org/10.1016/j.fluid.2011.11.029
10. Fayazi, A., Arabloo, M., Shokrollahi, A., Zargari, M. H., & Ghazanfari, M. H. (2014). State-of-the-art least square support vector machine application for accurate determination of natural gas viscosity. *Industrial & Engineering Chemistry Research, 53*(2), 945-958. https://doi.org/10.1021/ie402829p
11. Gerhardt, R. A. (2022). What is Impedance and Dielectric Spectroscopy? *IEEE Instrumentation & Measurement Magazine, 25*(4), 14-20. https://doi.org/10.1109/MIM.2022.9777776
12. Glagolev, M. (2012). Sensitivity analysis of the model. *Environmental Dynamics and Global Climate Change, 3*(3), 31-53. https://doi.org/10.17816/edgcc3331-53
13. Gomółka, L., & Augustynowicz, A. (2019). Evaluation of applicability of dielectric constant in monitoring aging processes in engine oils. *Eksploatacja i Niezawodność, 21*(2), 177-185. https://doi.org/10.17531/ein.2019.2.1
14. Guan, L., Feng, X., Xiong, G., & Xie, J. (2011). Application of dielectric spectroscopy for engine lubricating oil degradation monitoring. *Sensors and Actuators A: Physical, 168*(1), 22-29. https://doi.org/10.1016/j.sna.2011.03.033
15. Heidari, P., Rezaei, M., & Rohani, A. (2020). Soft computing-based approach on prediction promising pistachio seedling base on leaf characteristics. *Scientia Horticulturae, 274*, 109647. https://doi.org/10.1016/j.scienta.2020.109647
16. Heredia-Cancino, J., Ramezani, M., & Álvarez-Ramos, M. (2018). Effect of degradation on tribological performance of engine lubricants at elevated temperatures. *Tribology International, 124*, 230-237. https://doi.org/10.1016/j.triboint.2018.04.015
17. Hong, S.-H., & Jeon, H.-G. (2022). Monitoring the conditions of hydraulic oil with integrated oil sensors in construction equipment. *Lubricants, 10*(11), 278. https://doi.org/10.3390/lubricants10110278
18. Iooss, B., & Lemaître, P. (2015). A review on global sensitivity analysis methods. *Uncertainty management in simulation-optimization of complex systems: algorithms and applications*, 101-122. https://doi.org/10.1007/978-1-4899-7547-8_5

19. Kim, H.-J., Seo, K.-J., Kang, K. H., & Kim, D.-E. (2016). Nano-lubrication: A review. *International Journal of Precision Engineering and Manufacturing, 17*, 829-841. https://doi.org/10.1007/s12541-016-0102-0
20. Król, A., Gocman, K., & Giemza, B. (2015). Neural networks as a tool to characterise oil state after porous bearings prolonged tests. *Materials Science, 21*(3), 466-472. https://doi.org/10.5755/j01.ms.21.3.7506
21. Lazakis, I., Raptodimos, Y., & Varelas, T. (2018). Predicting ship machinery system condition through analytical reliability tools and artificial neural networks. *Ocean Engineering, 152*, 404-415. https://doi.org/10.1016/j.oceaneng.2017.11.017
22. Li, L., Chang, W., Zhou, S., & Xiao, Y. (2017). *An identification and prediction model of wear-out fault based on oil monitoring data using PSO-SVM method.* Paper presented at the 2017 Annual Reliability and Maintainability Symposium (RAMS). https://doi.org/10.1109/RAM.2017.7889670
23. Li, Z., Fei, F., & Zhang, G. (2022). Edge-to-Cloud IIoT for Condition Monitoring in Manufacturing Systems with Ubiquitous Smart Sensors. *Sensors, 22*(15), 5901. https://doi.org/10.3390/s22155901
24. Lillicrap, T. P., Cownden, D., Tweed, D. B., & Akerman, C. J. (2016). Random synaptic feedback weights support error backpropagation for deep learning. *Nature communications, 7*(1), 13276. https://doi.org/10.1038/ncomms13276
25. Macián, V., Tormos, B., Olmeda, P., & Montoro, L. (2003). Analytical approach to wear rate determination for internal combustion engine condition monitoring based on oil analysis. *Tribology International, 36*(10), 771-776. https://doi.org/10.1016/S0301-679X(03)00060-4
26. Mondelin, A., Claudin, C., Rech, J., & Dumont, F. (2011). Effects of lubrication mode on friction and heat partition coefficients at the tool–work material interface in machining. *Tribology Transactions, 54*(2), 247-255. https://doi.org/10.1080/10402004.2010.538489
27. Mosher, P. (2007). Predicting failure–condition monitoring in action. *World Pumps, 2007*(484), 24-28. https://doi.org/10.1016/S0262-1762(06)71208-1
28. Mumby, S. J. (1989). An overview of laminate materials with enhanced dielectric properties. *Journal of Electronic Materials, 18*(2), 241-250. https://doi.org/10.1007/BF02657415
29. Newell, G. E. (1999). Oil analysis cost-effective machine condition monitoring technique. *Industrial Lubrication and tribology, 51*(3), 119-124. https://doi.org/10.1108/00368799910268066
30. Nüchter, M., Ondruschka, B., Bonrath, W., & Gum, A. (2004). Microwave assisted synthesis–a critical technology overview. *Green Chemistry, 6*(3), 128-141. https://doi.org/10.1039/B310502D
31. Pourramezan, E., Omidvar, M., Motavalizadehkakhky, A., Zhiani, R., & Darzi, H. H. (2024). Enhanced adsorptive removal of methylene blue using ternary nanometal oxides in an aqueous solution. *Biomass Conversion and Biorefinery*, 1-13. https://doi.org/10.1007/s13399-023-05225-2
32. Pourramezan, M.-R., & Rohani, A. (2024). Improved Monitoring and Classification of Engine Oil Condition through Two Machine Learning Techniques. *SAE International Journal of Fuels and Lubricants, 18*(04-18-01-0005). https://doi.org/10.4271/04-18-01-0005
33. Pourramezan, M.-R., Rohani, A., & Abbaspour-Fard, M. H. (2023a). Comparative Analysis of Soft Computing Models for Predicting Viscosity in Diesel Engine Lubricants: An Alternative Approach to Condition Monitoring. *ACS omega*. https://doi.org/10.1021/acsomega.3c07780
34. Pourramezan, M.-R., Rohani, A., & Abbaspour-Fard, M. H. (2023b). Unlocking the Potential of Soft Computing for Predicting Lubricant Elemental Spectroscopy. *Lubricants, 11*(9), 382. https://doi.org/10.3390/lubricants11090382
35. Pourramezan, M.-R., Rohani, A., & Abbaspour-Fard, M. H. (2024). Machine Learning-Based

Predictions of Metal and Non-Metal Elements in Engine Oil Using Electrical Properties. *Lubricants*, *12*(12), 411. https://doi.org/10.3390/lubricants12120411

36. Pourramezan, M.-R., Rohani, A., & Abbaspour-Fard, M. H. (2025). Comprehensive Review of Dielectric, Impedance, and Soft Computing Techniques for Lubricant Condition Monitoring and Predictive Maintenance in Diesel Engines. *Lubricants*, *13*(8), 328. https://doi.org/10.3390/lubricants13080328
37. Pourramezan, M.-R., Rohani, A., Keramat Siavash, N., & Zarein, M. (2022). Evaluation of lubricant condition and engine health based on soft computing methods. *Neural Computing and Applications*, 1-13. https://doi.org/10.1007/s00521-021-06688-y
38. Raadnui, S., & Kleesuwan, S. (2005). Low-cost condition monitoring sensor for used oil analysis. *Wear*, *259*(7-12), 1502-1506. https://doi.org/10.1016/j.wear.2004.11.009
39. Rahimi, M., Pourramezan, M.-R., & Rohani, A. (2022). Modeling and classifying the in-operando effects of wear and metal contaminations of lubricating oil on diesel engine: A machine learning approach. *Expert Systems with Applications*, *203*, 117494. https://doi.org/10.1016/j.eswa.2022.117494
40. Rezaei, M., Rohani, A., Heidari, P., & Lawson, S. (2021). Using soft computing and leaf dimensions to determine sex in immature Pistacia vera genotypes. *Measurement*, *174*, 108988. https://doi.org/10.1016/j.measurement.2021.108988
41. Rohani, A., Abbaspour-Fard, M. H., & Abdolahpour, S. (2011). Prediction of tractor repair and maintenance costs using Artificial Neural Network. *Expert Systems with Applications*, *38*(7), 8999-9007. https://doi.org/10.1016/j.eswa.2011.01.118
42. Sangha, M. S., Gomm, J. B., & Yu, D. (2008). Neural network fault classification of transient data in an automotive engine air path. *International Journal of Modelling, Identification and Control*, *3*(2), 148-155. https://doi.org/10.1504/IJMIC.2008.019352
43. Sapotta, B., Schwotzer, M., Wöll, C., & Franzreb, M. (2022). On the Integration of Dielectrometry into Electrochemical Impedance Spectroscopy to Obtain Characteristic Properties of a Dielectric Thin Film. *Electroanalysis*, *34*(3), 512-522. https://doi.org/10.1002/elan.202100484
44. Shi, Y., Song, X., & Song, G. (2021). Productivity prediction of a multilateral-well geothermal system based on a long short-term memory and multi-layer perceptron combinational neural network. *Applied Energy*, *282*, 116046. https://doi.org/10.1016/j.apenergy.2020.116046
45. Siavash, N. K., Ghobadian, B., Najafi, G., Rohani, A., Tavakoli, T., Mahmoodi, E., & Mamat, R. (2021). Prediction of power generation and rotor angular speed of a small wind turbine equipped to a controllable duct using artificial neural network and multiple linear regression. *Environmental Research*, *196*, 110434. https://doi.org/10.1016/j.envres.2020.110434
46. Soltanali, H., Rohani, A., Abbaspour-Fard, M. H., & Farinha, J. T. (2021). A comparative study of statistical and soft computing techniques for reliability prediction of automotive manufacturing. *Applied Soft Computing*, *98*, 106738. https://doi.org/10.1016/j.asoc.2020.106738
47. Woodley, B. (1978). Failure prediction by condition monitoring (part 1). *International Journal of Materials in Engineering Applications*, *1*(1), 19-26. https://doi.org/10.1016/0141-5530(78)90004-3
48. You, M., Liu, F., & Meng, G. (2011). Benefits from condition monitoring techniques: a case study on maintenance scheduling of ball grid array solder joints. *Proceedings of the Institution of Mechanical Engineers, Part E: Journal of Process Mechanical Engineering*, *225*(3), 205-215. https://doi.org/10.1177/2041300910393426
49. Yu, S., Zhao, D., Chen, W., & Hou, H. (2016). Oil-immersed power transformer internal fault diagnosis research based on probabilistic neural network. *Procedia Computer Science*, *83*, 1327-1331. https://doi.org/10.1016/j.procs.2016.04.276

50. Zarein, M., Khoshtaghaza, M. H., & Ameri Mahabadi, H. (2019). Dielectric Properties of Castor-based Biodiesel Using Microwave. *Fuel and Combustion, 12*(1), 1-12. https://doi.org/10.22034/jfnc.2019.87991
51. Zeng, Y., Zhang, H., Zhang, H., & Hu, Z. (2010). Effective permittivity calculation of composites with interpenetrating phases. *Journal of Electronic Materials, 39*, 1351-1357. https://doi.org/10.1007/s11664-010-1229-x
52. Zhu, B., Wang, X., Luo, L., Zhang, N., & Liu, X. (2022). Influence of lubricant supply on thermal and efficient performances of a gear reducer for electric vehicles. *Journal of Tribology, 144*(1), 011202. https://doi.org/10.1115/1.4052681
53. Zhu, X., Zhong, C., & Zhe, J. (2017). Lubricating oil conditioning sensors for online machine health monitoring–A review. *Tribology International, 109*, 473-484. https://doi.org/10.1016/j.triboint.2017.01.015
54. Zzeyani, S., Mikou, M., & Naja, J. (2018). Physicochemical Characterization of the Synthetic Lubricating Oils Degradation under the Effect of Vehicle Engine Operation. *Eurasian Journal of Analytical Chemistry, 13*(4). https://doi.org/10.29333/ejac/90761

نشریه ماشین‌های کشاورزی
https://jame.um.ac.ir

مقاله پژوهشی

جلد ۱۶، شماره ۳، پاییز ۱۴۰۵، ص ۴۴۷-۴۲۷

ارزیابی ویسکوزیته و سطوح آلاینده در روان‌کننده دیزل از طریق طیف‌سنجی دی‌الکتریک با استفاده از روش‌های محاسباتی نرم

محمدرضا پوررمضان[۱]، عباس روحانی[۱*]، محمدحسین عباسپورفرد[۱]

تاریخ دریافت: ۱۴۰۳/۱۱/۰۵
تاریخ پذیرش: ۱۴۰۴/۰۱/۱۷

چکیده

نظارت بر وضعیت ماشین‌آلات یکی از جنبه‌های حیاتی واحدهای تولیدی و خدماتی برای حفظ کارایی عملیاتی است. از این رو، تعویض به‌موقع روغن موتور به‌طور قابل‌توجهی به افزایش عملکرد و افزایش طول عمر موتور کمک می‌کند. با این حال، تعیین زمان دقیق تعویض همچنان یک چالش است. آنالیز طیفی روغن، در عین این‌که موثر است، هم گران و هم زمان‌بر است. هدف این مطالعه معرفی یک روش جایگزین برای تحلیل طیفی روانکار موتور است. این تحقیق شامل تجزیه و تحلیل نتایج تجزیه و تحلیل طیفی و ضرایب دی‌الکتریک ۱۷ نمونه روغن موتور از طریق روش‌های آماری است. هدف اصلی توسعه مدل‌هایی برای پیش‌بینی آلاینده‌های موجود در روغن بر اساس خواص دی‌الکتریک است که جایگزینی برای تجزیه و تحلیل طیفی ارائه می‌دهد. برای رسیدن به این هدف چند هدف میانی دنبال می‌شود. شبکه عصبی مصنوعی پرسپترون چندلایه (MLP-ANN) و روش ماشین بردار پشتیبان (SVM) برای مدل‌سازی استفاده می‌شوند. عملکرد دو مدل با استفاده از شاخص‌هایی مانند ریشه میانگین مربعات خطا (RMSE)، کارایی مدل و ضریب تبیین (R^2) ارزیابی می‌شود. نتایج نشان می‌دهد که مدل SVM به‌طور مداوم کارایی بیش از ۰/۹۵ را برای همه شاخص‌های پیش‌بینی‌شده (Fe، Pb، Cu، Al، Mo، Na، Si و Vis@100) نشان می‌دهد. در نتیجه، طیف‌سنجی دی‌الکتریک روان‌کننده به‌عنوان یک جایگزین مناسب برای آنالیز مرسوم طیفی روغن متصور می‌باشد.

واژه های کلیدی: ثابت دی‌الکتریک، روش‌های محاسبات نرم، مترولوژی، نظارت بر وضعیت روغن موتور

۱- گروه مهندسی بیوسیستم، دانشکده کشاورزی، دانشگاه فردوسی مشهد، مشهد، ایران
(*- نویسنده مسئول: Email: arohani@um.ac.ir)

https://doi.org/10.22067/jam.2025.91756.1335

Journal of Agricultural Machinery

Homepage: https://jame.um.ac.ir

Research Article
Vol. 16, No. 3, 2026, p. 449-467

Investigating the Rates, Severity and Affecting Factors of Accidents Related to Agricultural Tractors and Grain Combine Harvesters in Ilam Province of Iran

J. Allahnouri[1], A. Marzban[1*], M. Ghasemi-Nejad-Raeini[1], M. Rahnama[1], M. Savari[2]

1- Department of Agricultural Machinery and Mechanization Engineering, Faculty of Agricultural Engineering and Rural Development, Agricultural Sciences and Natural Resources University of Khuzestan, Molla Sani, Iran
2- Department of Agricultural Extension and Education, Faculty of Agricultural Engineering and Rural Development, Agricultural Sciences and Natural Resources University of Khuzestan, Molla Sani, Iran
(*- Corresponding Author Email: afshinmarzban@asnrukh.ac.ir)

Received: 25 January 2025
Revised: 22 February 2025
Accepted: 03 March 2025
Available Online: 21 June 2025

How to cite this article:
Allahnouri, J., Marzban, A., Ghasemi-Nejad-Raeini, M., Rahnama, M., & Savari, M. (2026). Investigating the Rates, Severity and Affecting Factors of Accidents Related to Agricultural Tractors and Grain Combine Harvesters in Ilam Province of Iran. *Journal of Agricultural Machinery*, *16*(3), 449-467. https://doi.org/10.22067/jam.2025.91786.1336

Abstract

Agriculture is the most prominent industry in developing countries and also ranks as one of the most dangerous professions. Tractors and grain combine harvesters are two of the main self-propelled agricultural machines. Agricultural machines, despite their irreplaceable role in increasing productivity, contribute significantly to agricultural accidents. This study was conducted to investigate the current rates and severity of accidents and human casualties related to agricultural tractors and grain combine harvesters in Ilam province, Iran. Evaluations were conducted using data from the years 2019-2023.Over these five years, the accident frequency for agricultural combines and tractors was 61 and 43, respectively, indicating a statistically significant difference. Among the tractor drivers in this research, the most frequent accidents occurred due to the power take-off shaft (P.T.O.), helices, and feeding rollers. Among combine drivers, accidents were most common at the shear points of the machine (cutter bars, gears, etc.). This research evaluated the factors affecting field accidents related to tractors and combines and estimated the accident rates. Accident rates, including AFR (Accident Frequency Rate), ASR (Accident Severity Rate), FIR (Fatal Incident Rate), and FSI (Frequent Severity Index), were calculated. The rates of AFR, ASR, FIR, and FSI were 25.84, 45.82, 1.66, and 1.066% for combine harvesters, and 5.60, 12.63, 4.44, and 0.262% for tractor accidents, respectively. The nonfatal rate for combine harvesters was 6445 per 100,000, and for agricultural tractors, it was 4334 per 100,000. Tractor accidents had a higher fatality rate than combine harvesters, with 445 fatalities per 100,000 for tractors compared to 333 per 100,000 for combine harvesters.

Keywords: Accident survey, Accident indices, Accident factors, Combine, Operator safety, Tractor

Introduction

The occurrence of incidents in agricultural occupations is inevitable. Identifying the factors affecting the incidence of accidents can help reduce accidents among farmers (Moradhaseli, Farhadian, Abbasi & Ghofranipour, 2017). Work-related stress is one of the most important variables affecting productivity, resulting from the interaction of environmental factors, work capacity, and excessive work, and it affects health and performance (Karimi *et al.*, 2024). According to global reports, harmful accidents resulting from work activities cause 150,000 work injuries and 1,400 deaths annually in Iran (Abbasi Balochkhaneh, Ghotbi Ravandi, Golkhani, Baes's mat & Hasan pour Sodre Jani, 2016). An accident is an unforeseen and unexpected event that causes injury (International Labour Organization, 2011). In

Authors retain the copyright. This is an open access article distributed under Creative Commons Attribution 4.0 International License (CC BY 4.0).

https://doi.org/10.22067/jam.2025.91786.1336

order to prevent injuries to tractor operators during agricultural operations, and for them to be able to maintain adequate reaction time, the tractor users should drive less than 8 hours during the work-day (Mohammadi, Kheiralipour, Ghamary, Jahan Bakhshi & Shahidi, 2023). One of the most important debates in agricultural mechanization is the issue of human safety when working with machines, which has become a prominent topic in ergonomics science today (Gholami, Kalantari & Rajabi Vandechli, 2017).

Occupational diseases related to workplaces are typically explained as disorders or illnesses that negatively affect work productivity (Hamalainen, Takala & Kiat, 2017). Despite the use of unsafe implements in tractors compared to other machines, tractors are still used for agricultural activities and transportation on farms (Kasar, Comer pay, Ilhan, Eroğlu, & Deniz, 2023). Recently, attention to health, efficiency, and safety in the workplace has increased. Agriculture is one of the human work activities with the highest risk indices (Cecchini, Bedini, Musetti, Marino, & Stasi, 2018). Mechanization has increased agricultural productivity and made work easier. However, it has also increased accidents and injuries when operators and farmers work with agricultural machinery (Shikha & Chaudhari, 2016). The importance of safety in agricultural activities is promoted by the development of standard rules related to professional work and equipment safety (Fargnoli, Lombardi, Haber, & Puri, 2018). Tractors are a main source of agricultural injuries, particularly those caused by overturning. To prevent accidents due to overturning, rollover protective structures are provided with tractors (Singh, Tewari, & Hota, 2023). Approximately 337 million job accidents occur annually, with occupational injuries and accidents in agriculture occurring for various reasons (Sarkar, Vinay, Raj, Maiti, & Mitra, 2018).

Accidents usually occur as a result of a combination of accumulated problems, such as machine breakdowns, operator interventions, and human error. Studies have identified agriculture as one of the most dangerous jobs in the world (Pawlak, Nowakowicz-Debek, Wlazlo, Maksym, & Sasakova, 2017). The main causes of agricultural machinery accidents are slipping, falling, crush points, and pinch points. Crushing of operators (35%), improper control of the machine during agricultural activities (28.7%), and breakdowns, injuries, or overturning (19.5%) are the most common accident causal factors (Gite, Tiwari, & Khadatkar,2010). Operators are exposed to erosion factors and work injuries while driving. Due to a lack of proper maintenance and service, insufficient management, and non-standard driving, farmers are at risk of injuries (Quendler *et al.*, 2014). Agricultural activities cannot be performed without the use of modern agricultural machinery. The performance of grain combine harvesters depends on factors such as operator skill, distractions, and errors (Du, Dorneich, Steward & Mackenzie, 2016). Moments of error while driving are common and can sometimes have significant consequences. In fact, accidents involving agricultural tractors are the leading cause of work-related deaths in the agricultural industry in many countries (Jun, 2014). Agriculture is one of the most dangerous job sectors for farmers, operators, and workers. Therefore, decisions aimed at improving safety in agricultural workplaces need to take into account the behavior of farmers, operators, workers, and related factors (Damalas, Koutroubas, & Abdollahzadeh, 2019). Accidents in agriculture occur due to neglecting safety factors, lack of knowledge and education, and poor design of agricultural machinery and equipment. Approximately half of the world's population is employed in the agricultural sector, which fulfills the basic needs of their lives through agricultural activities (Maisyaroh, Widianto, & Fibriansari, 2022). Physiological factors during work activities are one of the challenges of occupational health. The force of gravity affects human health at work. Therefore, the mechanization of work can prevent work hazards (Hayati, Marzban, & Asoodar, 2022).

The most significant cause of death in this sector is injuries caused by accidents. The available information on the use of protective equipment in tractors is scarce, and when operators do have access to this equipment, they frequently employ it in an unsafe manner. (Antunes, Cordeiro, & Teixeira, 2018). Studies show that tractors are involved in 14% of agricultural accidents, and fatal accidents related to agricultural machines are 8 times more common than those involving other types of machines (Murphy *et al.*, 2010). Tractors are known to be the leading cause of occupational accidents in agricultural operations. Tractor overturns are the primary cause of fatal accidents, especially when tractors are used without protective structures (Arnal, López-Maestre Salas, Arazuri, Mangado, & Jaren, 2017). Many factors contribute to the increase in fatal tractor accidents, including operator error, tractor technical issues, and environmental conditions related to agricultural activities. To reduce accidents, these factors must be addressed (Ehlers & Field, 2017). Based on incidents in some countries, despite the relatively low number of agricultural machine accidents, the rate of severe injuries and fatalities is higher than the global average (Mayrhofer, Quendler, & Boxberger, 2013).

There are few studies about combine accidents in the world. In one study, 60 accidents were evaluated, and according to research reports, 10 people were killed and 40 people were trapped and injured due to falling from combine harvester (Health & Safety Executive, 2012). Another study examined road and farm accidents related to combine harvesters, investigating 194 accidents with 228 victims (61 dead and 167 injured). Of these, 116 accidents (59.8%) happened on farms, while 78 (40.2%) occurred in road traffic. Two very important types of accidents were farm fires and drivers' bodies getting stuck in the pinch points of the combine machine, accounting for 41.4% and 25.9% of the accidents, respectively (Keskin & Şekerli, 2018). Research on agricultural accidents is crucial for minimizing these incidents, as numerous tragic and fatal accidents related to farming activities take place each year. (Cividino, Pergher, Zucchi Atti, & Gubiani, 2018). Agricultural tractors, being integral to agricultural activities, pose serious risks related to injuries, especially due to side overturns or rear overturns (Abubakar, Ahmad, & Akande, 2010). Agricultural activity in Iranian farms is characterized by a high level of mechanization, where farm tractors are used extensively. Farm machinery is often large and slow-moving. Although the number of tractor-related injuries is increasing, the safety of Iranian farm tractors had not been documented before (Houshyar & Houshyar, 2018). There is no comprehensive concept of the health status of Iranian farmers and the work-related injuries affecting them (Ghafari, Cheraghi, & Dusti Irani, 2017). A study showed that participation in occupational health and safety training courses had the greatest effect (80%) on reducing agricultural occupational injuries among farmers in Ilam province. Other influential factors included education level (69%), farmers' income (68%), safety knowledge (67%), history of farming activity (64%), farm area (60%), and farmers' age (59%) (Parak, Pour Saeed, Eshraghi Samani, & Chaharsoghi Amin, 2021).

Materials and Methods

To carry out this study, the first stage involved investigating the issues related to accidents and safety during working with agricultural machines. The effective factors in the occurrence of tractor and combine accidents (mechanical, human, environmental factors, etc.) were identified in Ilam province, located in the west of Iran. Data were collected through field studies over a period of 5 years, focusing on incidents involving the owners and operators of combines and tractors. Using questionnaires and interviews, insight were gathered from tractor and combine operators, organized based on an analytical framework focusing on human, environmental, and mechanical factors for each incident, The questionnaires encompassed a range of topics., including personal traits (three questions),

professional characteristics (three questions), accidents details (five questions), attitude towards safety (twenty questions), attitude towards health (sixteen questions), level of access to safety information (seven questions), risk tolerance (sixteen questions) and knowledge about safety practices (twenty questions). Additionally, questions related to factors affecting the accident (twenty-two questions) and questions related to measures to prevent accidents (fifteen questions) were included. Statistical data analysis was done using SPSS software, Friedman's test was used to rank accidents related to tractors and combine harvesters, and T-test mean comparison method was used to compare accidents in two groups of combine and tractor operators.

Related statistics, information from questionnaires, and the accident experiences of grain combine harvester and tractor operators were examined. The number of fatal and non-fatal accidents in Ilam province was also collected. The accident frequency and severity of agricultural accidents and injuries were assessed through direct surveys of agricultural operators of tractors and combines. The effective factors influencing accidents involving agricultural combines and tractors were analyzed using SPSS software.

Ilam province is located in the west of the Zagros Mountain range and borders Khuzestan province to the south, Lorestan province to the east, and Kermanshah province to the north. It also shares a 425-kilometer border with Iraq to the west. The province comprises 12 cities, 29 districts, 27 towns, 54 villages, and 750 inhabited villages (Sadat Haeri *et al.*, 2019). Covering an area of 20,164 square kilometers, it represents approximately 1.2 percent of the country's total area and includes 336,000 hectares of agricultural land. The total number of tractors and combines in Ilam province is 6,130 and 163, respectively (Anonymous, 2023). Fig. 1 shows the area under study.

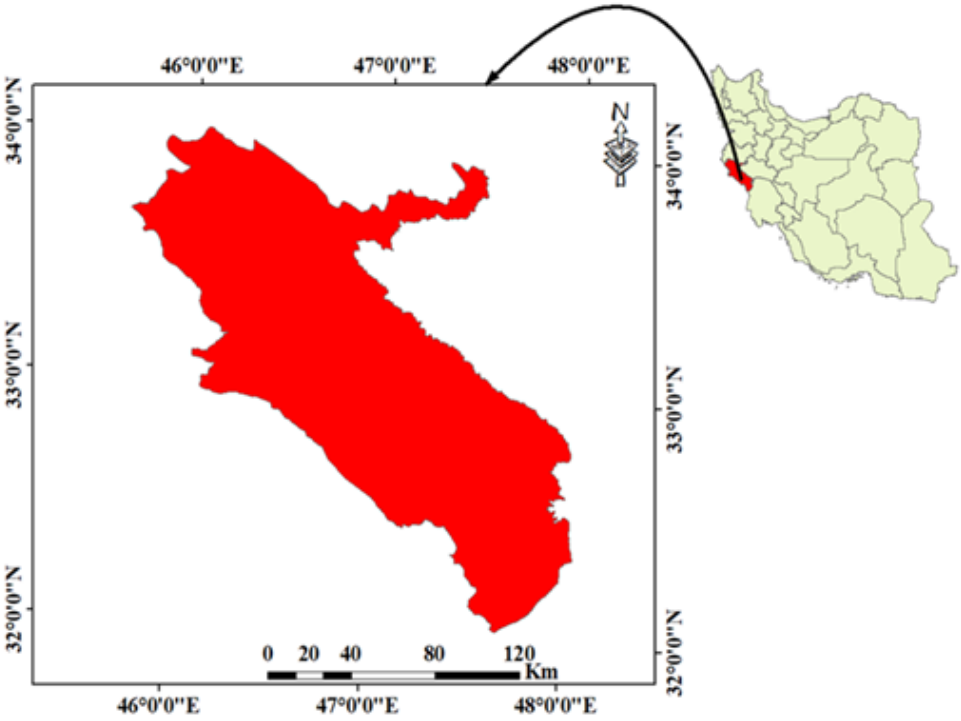

Fig. 1. Map of the Ilam province in Iran

Statistical population and sampling method

The sample size for this research was estimated using Cochran's formula; sample sizes for tractor and combine operators were both 180 people. (Cochran, 1977). The sampling was done using a multi-stage method and three townships of Dehloran, Abdanan and Darrehshahr were selected according to geographical conditions, topography, cultivated area, and the number of tractors and combines. Aforementioned townships include about 50% of the agricultural lands of Ilam province, and then, based on the population size in each township, the sample percentage was calculated.

$$n = \frac{\frac{z^2pq}{d^2}}{1 + \frac{1}{N}\left[\frac{z^2pq}{d^2} - 1\right]} \quad (1)$$

where:

N: statistical sample size

N: the size of the statistical population

z: value of normal variable with a confidence level of 1- α

p: percentage containing the desired attribute

q: the ratio not containing the desired attribute

Validity and reliability of research tools

To assess the reliability of the research tool, Cronbach's alpha coefficients were used (Table 1). Cronbach's alpha is a classic standard for measuring reliability and is a suitable measure for evaluating internal consistency. Internal consistency refers to the degree of correlation between factors and the related questions. A Cronbach's alpha value greater than 0.6 indicates acceptable reliability (Taber, 2018).

Table 1- Validity and reliability of research tools with Cronbach's alpha coefficient

Variable name	Number of questions	Cronbach's alpha
Attitude toward safety in agriculture	20	0.839
Attitude toward health	16	0.755
The level of information accessibility	7	0.700
Risk tolerance	16	0.666
Knowledge about safety	22	0.762
Factors affecting the accident	7	0.943
Impact of various actions increasing accidents	15	0.651

Because Cronbach's alpha values are greater than 0.7, so the questionnaire has adequate reliability.

Accident rate:

Accident frequency rate (AFR) represents the number of different incidents leading to loss of working time that occurred in a specific period (monthly-yearly) per one million working hours as follow (SIGHI, 2006):

$$AFR = \frac{\text{number of accidents} \times 1000000}{\text{total useful hours of workers}} \quad (2)$$

Accident severity rate (ASR) represents the number of lost working days for every 1000 working hours. The entire organization had this amount of production stoppage days (Akanbi, Charles Owaba, & Olley, 2009):

$$ASR = \frac{\text{days lost due to the accidnt} \times 1000}{\text{total number of hours the worker at the same time}} \quad (3)$$

FIR represents the number of accidents per 1000 working hours per the total number of employees:

$$FIR = \frac{\text{number of deaths} \times 1000}{\text{number of workers}} \quad (4)$$

FSI represents frequent severity index, is calculated according to the following formula:

$$FSI = \sqrt{\frac{FIR \times ASR}{1000}} \quad (5)$$

Results and Discussion

Table 2 shows that all respondents were male, with a total of 360 participants

consisting of with a total of 360 participants consisting of 180 combine harvester operators and 180 tractor operators. According to the findings, 69.7 percent of the sample size has primary education, that shows combine and tractor operators do not have higher education.

Table 2- Characteristics of respondents at the working area

Variable	Characteristics	Frequency	Percentage
Gender	**Male**	**360**	**100**
Age	21-30 years	62	17.2
	31-40 years	91	25.3
	41-50 years	104	28.9
	51-60 years	74	20.55
	61-70 years	29	8.05
Education	Primary Education	251	69.72
	Diploma	97	26.9
	Associate degree	8	2.2
	Bachelor	3	0.8
	Other qualification	1	0.3
Working experience	1-6 years	33	9.2
	7-10 years	77	21.4
	10-15 years	135	37.5
	16-20 years	78	21.7
	More than 20	37	10.3
Type of work	Tractor operators	180	50
	Combine operators	180	50

Table 3 shows the number of different accidents involving combine machines over a 5-year period. Although between 2020 and 2023 we have a reduction in accidents and injuries, significant accidents and injuries are still observed and measures should be implemented to prevent accidents involving combine machines. According to the results of (Ceylan, 2012) for the years 2004 to 2010, although there is a serious reduction in the number of accidents in Turkey, there is no significant change in the number of permanent incapacities. Until 2009 for mining, metal and construction sectors, there was no improvement in the number of permanent incapacities as a result of accidents, but in 2009, a remarkable decrease can be seen in these three sectors. However, in 2010, the permanent incapacity number in the metal sector became more than the average value of the last seven years in Turkey. Additionally, Table 3 presents the accident information related to tractor. Results shows that the number of tractor-related accidents during this period is significant, and basic measures are needed to prevent and reduce tractor accidents. According to Volkovski, Chaloska, and Grad (2018), 30.5% of agricultural accidents were due to farm machinery, 34.2% were related to hand tools, and 35.3% were caused by other sources, such as environmental factors, etc. The highest number of accidents was related to tractors (31%), P.T.O (14%) and sprayer (4%). In these agricultural machinery accidents, 5.6 percent of the accidents were fatal, while 94.4%, the remaining percentage, were non-fatal. Also, Park *et al.* (1990) analyzed the causes of fatal tractor accidents, revealing that an average of 9.4 people die each year, with a peak of 27 fatalities (57.45%) attributed to violations of traffic signs and regulations. As a result of poor psycho-physical conditions, pedestrians and second party errors with 12 cases (25.53%), and technical malfunction of the vehicle with 8 cases (17.02%) individuals were killed.

Fig. 2 shows the typical accidents gathered by the authors involving tractors and combines in the study, during 2023 and 2024 years, at the working area.

Table 3- Number of combines and tractors accident types in the study during 2019-2023 period

Machine	Year	Killed	Seriously injured	minor injury	Completely injured/dead
	2019	1	8	8	17
	2020	1	12	5	18
	2021	1	6	4	11
Combine	2022	0	4	3	7
	2023	0	4	4	8
	Total	3	34	24	61
	%	4.91	55.73	39.34	100
	2019	1	5	6	12
	2020	1	4	4	9
	2021	0	4	4	8
Tractor	2022	1	2	5	8
	2023	1	1	4	6
	Total	4	16	23	43
	%	9.30	37.20	53.48	100

Fig. 2. Typical tractors and combines accidents (images provided by authors)

Combines and tractors accident

Result of investigating the number of non-fatal accidents related to agricultural combines and tractors during five years in the current study revealed that the number of accidents involving combines were more frequent than those involving tractors (Fig.3). The accident rate was 6445 per 100,000 for combine harvesters and 4334 per 100,000 for agriculture tractors. This can be due to the difference in the technical and complicated structure of combines compared to agricultural tractors, the type of harvesting operation, and human error. researches related to the Estonian Labor Inspectorate shows that, there were 785 non-fatal accidents (NFA) per 100,000 agricultural workers, while the rate in Eurostat was more than twice as high (1914 per

100,000) (Dimitrovski, 2013). Finland and Sweden, with the same agricultural structures, had different NFA rates: Finland 5,331 and Sweden 554 per 100,000 workers. These examples illustrate the large variation in agricultural accident statistics due to: farm structure, and the type of agricultural machinery that is used by farmers. This study aligns with the findings of Merisalu, Lepala., Jakob, and Rautiainen (2019), indicating that the total number of non-fatal workplace accidents in the EU-27 saw a reduction of 39,818 incidents between 2017 and 2020. Also, according to Mitrev ska, Mitrevski, and Kulevska (2023), accidents in the agricultural sector are critical due to multiple contributing factors, and preventing agricultural accidents can save lives and provide a safer working environment.

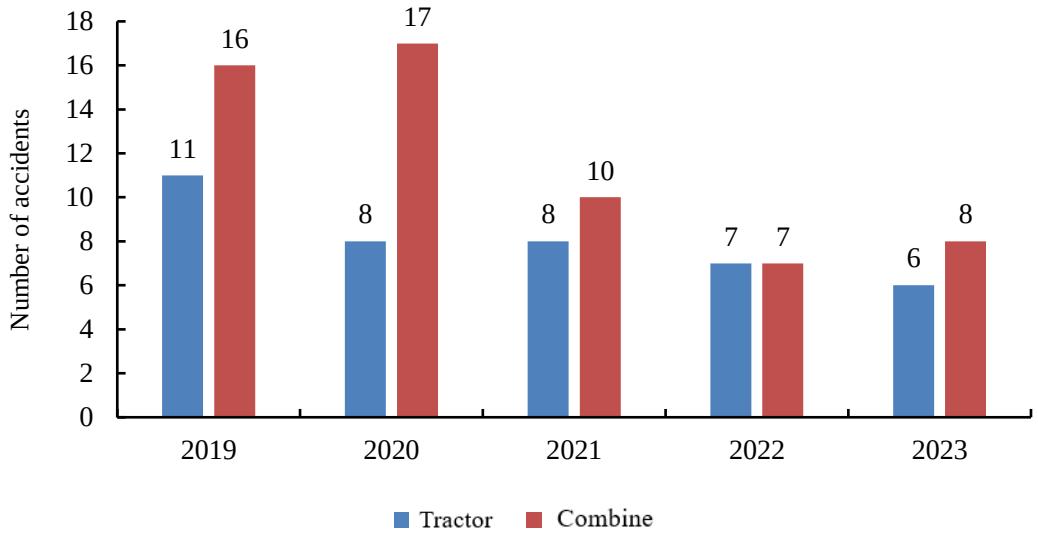

Fig. 3. Number of non-fatal accidents 2019-2023

Figure 4 illustrates the investigation of fatal accidents related to tractor and combine operators. The number of fatal tractor accidents was higher than that of combine accidents (445 per 100,000, for tractors and 333 per 100,000 for combine harvesters in Ilam province). This discrepancy is likely due to the special working conditions, the mechanical structure of tractors, and the excessive fatigue experienced by tractor operators. Also, the continuous use of agricultural tractors during all seasons and the seasonal use of combine harvesters. From 2019 to 2023, the number of fatal accidents related to tractors and combines decreased. According to Health and Safety Authority (2021), between 2017 and 2020, the incidence rates of both non-fatal and fatal accidents at work decreased.in 2019, the EU-27 Member States saw the lowest recorded incidence rates for non-fatal and fatal accidents, standing at 1,447.3 per 100,000 employed individuals for non-fatal incidents and 4.44 per 100,000 employed individuals for fatal accidents.

Figure 5 presents an analysis of data concerning the factors contributing to accidents involving tractors and combines. The result indicates that in the tractor operator group, the most common hazards arise from components such as the power Take-Off (P.T.O) shaft, helices and feeding rollers. In contrast, for the combine operator group, the areas with the highest frequency of incidents are the shear points of the Machin, including cutter bars and gears. According to similar studies (Chio, Kim, & Jung, 2024), most types of accidents in agricultural machines happen due to human errors. Therefore, investigating related causes and preventing operators from driving when tired as well as resting after long work can reduce accidents related to human factors. The main causes of accidents were

insufficient management, inappropriate work conditions, and insufficient training. Factors causing injury in agricultural areas have been influenced by several factors. There are threat factors, capability factors, and vulnerability factors that have been proven capable of causing injury.

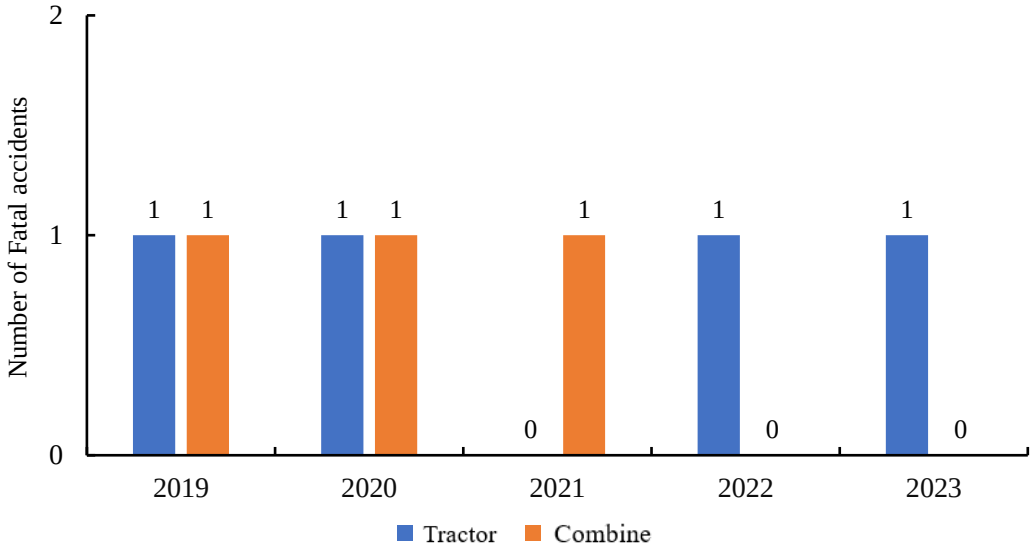

Fig. 4. Number of fatal accidents during 2019-2023

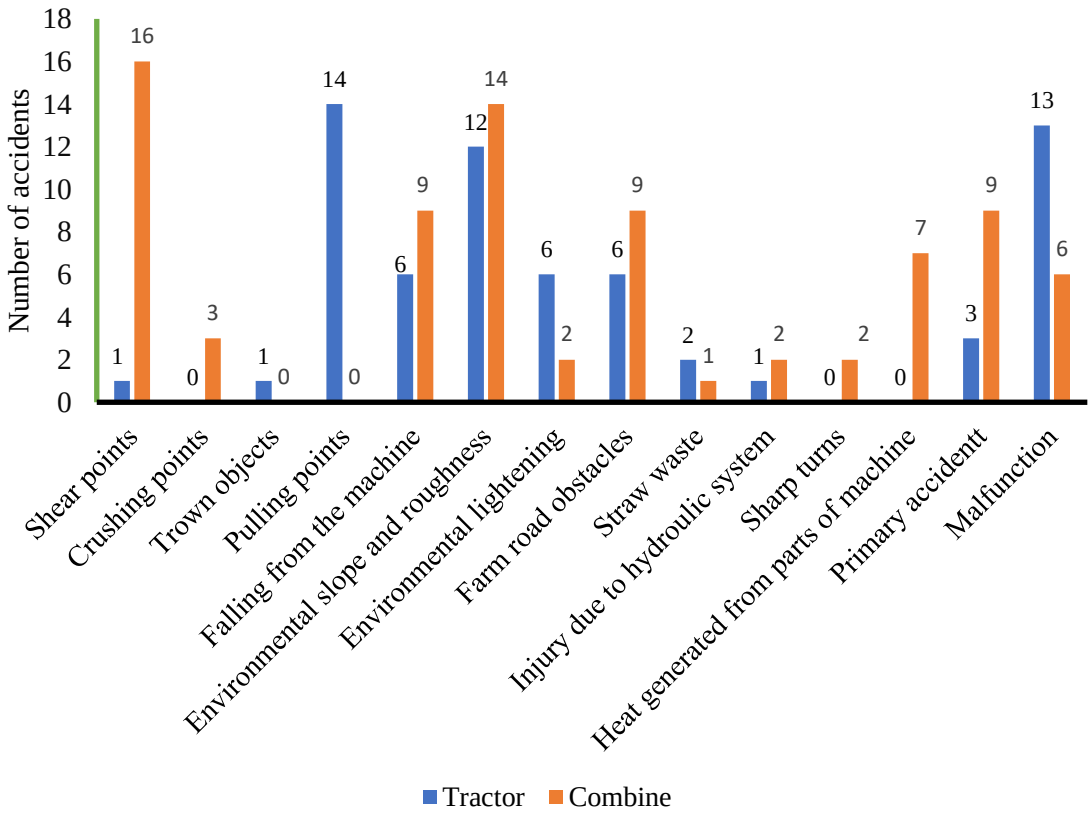

Fig. 5. Factors affecting the occurrence of accidents

According to the findings, tractor drivers ranked fatigue from long working hours (average rating of 4.169), unfavorable environmental conditions such as mountain roads and steep slopes (average rating of 4.167), and driver negligence and distraction (average rating of 4.158) as the top three contributing factors to accidents. Similarly, combine drivers ranked negligence and distraction (average rating of 4.442), adverse environmental conditions (average rating of 4.389), and fatigue from long working hours (average rating of 4.294) as the most significant factors. Tone and Irwin (2021), identified steep slopes, sharp curves, and road conditions (e.g., farm roads and access routes) as primary contributors to accidents. Studies on agricultural work accidents and farmer safety promotion have highlighted uneven or slippery floors, lack of lightening, narrow spaces, and ground obstacles as major causes. Agricultural machinery accidents were found to occur more frequently while moving on farm roads compared to stationary indoor work. These results align with the findings in Table (4). Additionally, a comparison of the average factors affecting accidents for combine and tractor drivers was performed using an independent samples t-test, as shown in Table (5). Since the significance value of the t-test was less than 0.05, this indicates a significant difference in the average values of these factors between the two groups.

Table 4- Ranking of factors affecting accidents related to tractors and combines

Factors	Tractor operator		Combine operator	
Machine worn out	7	3.414	6	3.694
Unfamiliarity with the operation of the machine	6	3.536	7	3.672
Existence of unfavorable environmental conditions (mountainous roads, steep slopes, etc.)	2	4.389	2	4.167
Non-standard equipment and machinery	4	4.172	5	4.061
Insufficient physical ability of the driver	5	3.753	4	4.078
Fatigue from prolonged work	3	4.294	1	4.169
Driver's negligence and distraction	1	4.442	3	4.158
Friedman test results	X^2 = 114.680 Sig = 0.000		X^2 = 46.975 Sig = 0.000	

Table 5- Comparison of the average factors affecting accidents related to combine and tractor drivers

Variable name	Machine type	Number	Average	Standard deviation	Sig	t
Machine worn out	Tractor	180	478.0	977.0	602.0	0.523
	Combine	180	428.0	833.0		
Lack of familiarity with the operation of the machine	Tractor	180	511.0	948.0	0.953	0.059
	Combine	180	506.0	836.0		
Existence of unfavorable environmental conditions (mountainous roads, steep slopes, etc.)	Tractor	180	75.0	176.1	0.114	-1.58
	Combine	180	956.0	285.1		
Non-standard equipment and machinery	Tractor	180	711.0	08.1	0.221	1.226
	Combine	180	856.0	154.1		
Insufficient physical ability of the driver	Tractor	180	706.0	132.1	0.388	0.865
	Combine	180	611.0	93.0		
Fatigue from prolonged work	Tractor	180	0.767	1.158	0.274	-1.09
	Combine	180	0.906	1.245		
Friedman test results	Tractor	180	0.783	1.178	0.086	1.72–
	Combine	180	0.011	1.329		

Table 6 shows the total number of working hours lost due to injuries resulting from accidents involving combine and tractor operators over five years in Ilam province. The injuries are categorized, and the number of hours lost is proportional to the type of injury, providing the total working days lost due to combine and tractor-related incidents during this period. According to Khosravi, Hashemi Nazari, Dehghani Fard, and Jabari (2007), the total number of reported fatal accidents was 9 in 2004 and 6 in 2005, resulting in the loss of 67,500 working days in 2004 and 45,000 working days in 2005.

Table 6- Number of days lost due to disability related to combine and tractor operators

Year	Killed (hour)		Seriously injured (hour)		Minor injury (hour)		Total (hour)
	Combine						
	Number of killed	Hour	Body limb	Hour	Body limb	Hour	
2019	1	48000	Arm amputation	36000	Two fingers	6000	**42000**
					Forearm	36000	
					Finger cut	9600	**141600**
					Disability	48000	
					Toe	2400	**2400**
			Hand amputation	24000	Two fingers	6000	**30000**
					Three fingers	9600	**9600**
2020	1	48000	Foot amputation	24000	Finger cut	9600	**69600**
					Forearm	36000	
			Leg amputation	36000	Toe	2400	**86400**
2021	0	0	Hand amputation	24000	Three fingers	9600	**33600**
			Wrist amputation	24000	Finger cut	7200	**115200**
			Disability	48000	Forearm	36000	
2022	1	48000	Hand amputation	24000	Finger cut	14400	**38400**
			Wrist amputation	24000	Two fingers	6000	**162000**
			Disability	48000	Forearm	36000	
2023	0	0	Arm amputation	36000	Finger cut	14400	**134400**
			Disability	48000	Forearm	36000	
	Tractor						
Year	Killed (hour)		Seriously injured (hour)		Minor injury (hour)		Total (hour)
	Number of killed	Hour	Body limb	Hour	Body limb	Hour	
2019	2	96000	Hand amputation	24000	Toe	2400	**74400**
			Disability	48000			
			Arm amputation	36000	Finger cut	2400	**38400**
			Foot amputation	24000	Two fingers	6000	**126000**
			Disability	48000	Three fingers	9600	**57600**
			Leg amputation	36000	Toe	2400	**38400**
2020	1	48000	Hand amputation	24000	Two fingers	6000	**78000**
			Foot amputation	24000	Finger cut	2400	**2400**
					Three fingers	9600	**33600**
2021	0	0	Arm amputation	36000	Finger cut	2400	**38400**
			Disability	48000	Toe	2400	**50400**
					Finger cut	2400	**2400**
2022	1	48000	Hand amputation	24000	Finger cut	2400	**74400**
			Foot amputation	24000	Toe	2400	**26400**
			Leg amputation	36000	Finger cut	2400	**38400**
2023	1	48000	Foot amputation	24000			**72000**
			Hand amputation	24000			**24000**

With approximately 21,000 workers during these years, this corresponds to 43 deaths per 100,000 workers in 2004 and 26 deaths per 100,000 in 2005. Esmaeili, Vazirineghad, and Shahrokhi (2009), reported that 92.9% of the victims were men, with the most common injuries affecting the legs (35.7%) and hands (25.7%).

Table 7 shows the accident indices, including AFR, ASR, FIR and FSI for various accidents related to working with agricultural combines and tractors during five years. It is for the first time that these indices are used for agricultural machinery accidents in the country of Iran. It was determined that, among the indices, the FSI and ASR index for combine and tractor operators, and AFR for combine operators were higher than the standard (The acceptable level of safety performance for FSI is less than 0.1 and for ASR it is less than 1 and for AFR it is between 0 and 10) By observing the safety principles while working with tractors and agricultural combines, these indices should be brought to the standard. One study result revealed that, during the five years period of 2008 to 2012, in accidents involving tractors, on average 9.4 people die per year, and the largest number of 27 (57.45%) people died tragically due to noncompliance with safety alert symbols and regulations (Lohan, Singh, & Kumar, 2022). The study by Halvani *et al.* (2010) in Yazd province in 2014 found that the frequency of the incident was 5.6. The FIR indices during five years were below the standard level (0-10), which means that per 200,000 working hours, the number of incidents was within the standard.

Table 7- AFR, ASR, FIR and FSI rates for combine and tractor operators in Ilam Province during 2019-2023 years

Machine	Year	AFR	ASR	FIR	FSI
Combine	2019	36.016	59.74	2.77	1.46
	2020	38.13	41.31	2.77	1.25
	2021	23.30	39.40	2.77	0.958
	2022	14.83	53.072	0	0.887
	2023	16.95	35.59	0	0.776
	Mean	25.84	45.82	1.66	1.066
Tractor	2019	7.82	24.15	5.55	0.435
	2020	5.86	12.41	5.55	0.270
	2021	5.21	7.43	5.55	0.196
	2022	5.21	8.21	0	0.206
	2023	3.91	10.95	5.55	0.207
	Mean	5.60	12.63	4.44	0.262

Conclusion

Accidents related to tractors, combines, and agricultural machines are known as one of the serious problems in the agricultural sector. These accidents primarily arise from the unique design and operational methods of these machines. The most important factors affecting accidents are overturns, falling from agriculture machinery, human errors, traffic road accidents and insufficient training related to safety. According to the results of this study, non-fatal accidents related to agricultural combines and tractors from 2019 to 2023 indicated that the number of accidents involving agricultural combines was higher than those involving agricultural tractors. The accident rate for combine harvesters was 6445 per 100,000, while for agricultural tractors, it was 4333 per 100,000. This is due to the complicated structure of combine harvester machines and farm work conditions. However, the number of fatal tractor accidents was higher than that of combines (445 per 100,000 for tractors and 333 per 100,000 for combine harvesters in Ilam province). This is attributed to the special working conditions of tractors, their mechanical structure, excessive fatigue of tractor operators, and the lack of rollover protection structures (ROPS). According to

Ghafari *et al*. (2017), agricultural work in Iran is fraught with risks, leading to numerous fatalities. For instance, a study covering various years noted 39 fatal injuries recorded in agriculture, forestry, hunting, and fishing between 2011 and 2016. According to research in Spain, the total number of fatal accidents between 2010 and 2019 was 644. The rate of fatal accidents per province was between 0 and 223.5 fatal accidents per 100,000 registered tractors. Furthermore, the overall rate for Spain was 6.87 fatal accidents per 100,000 tractors. It was found that the highest number of accidents happened in the areas with high land slope, also the worn-out fleet of tractors and the use of old tractors were the main causes of accidents (Jaren *et al.*, 2022). A comparison between Ilam province in Iran and Spain provinces shows that Ilam province has a higher accident rate. The elevated incidence of accidents tied to tractor and combine operators in this study, particularly when compared to Spain, can be attributed to substandard conditions of agricultural roads in Ilam. Additionally, the prevalence of agricultural vehicles on public and farm roads, especially at night during peak working seasons significantly contributes to the high accident rates observed in I lam. The lack of proper training and awareness among agricultural machine operators, the significant gap between local practices and international standards and the absence of safety culture in the agricultural sector in the studied Ilam province, combined with advancements in agriculture and the standard design of machinery in Spain, could be major factors contributing to the differing accident rates in Ilam province and Spain. The similar results of research in Chaharmahal and Bakhtiari province, Iran, also showed that the human factor with an average ranking of 4.85 and the machine malfunction with an average ranking of 3.91, environment with an average rank of 3.51 and sharp turns of the road with an average rank of 2.78 were the most important accident factors related to agricultural machinery (Omidi Arjanki, Javadiyan & Tabashir, 2022). The results of this research matched our research. Their results also show that other provinces in Iran also suffered from accidents related to agricultural machinery and necessary preventive measures should be taken in this field. Among the types of farm accidents related to combine harvesters and agricultural tractors, incidents involving the power take-off shaft, helices, feeding rollers, and shear points (cutter bars, gears, etc.) were most frequent. Attachments used with tractors and combine harvesters, such as blades, mowers, rotary cutters, scrapers, forks, rakes, and towed parts like grain carts, cutter bars, and trailers, also contributed to accidents. Safety education and maintenance of these devices can prevent accidents related to tractors and combines (Karimi & Fakhri, 2021). Ranking the factors affecting tractor accidents in this study indicated that, fatigue from prolonged work (average rating of 4.169), unfavorable environmental conditions (average rating of 4.167), and driver negligence and distraction (average rating of 4.158) were the top three factors. For combine drivers, negligence and distraction (average rating of 4.442), adverse environmental conditions (average rating of 4.389), and fatigue from long-term work (average rating of 4.294) were ranked highest. Agricultural activities are time-sensitive, requiring farmers to work long hours, especially during planting and harvesting seasons, which can lead to stress, fatigue, and increased accident risk (Edwards & Sherlock, 2021). A t-test comparison of the average factors affecting accidents for combine and tractor drivers showed that unfavorable environmental conditions, non-standard equipment and machinery, and fatigue from long-term work significantly affected accidents related to combine harvesters and tractors. The number of days lost due to disability related to combine and tractor operators was 108,150 and 96,900 days, respectively. This indicates that farm accidents related to combine harvesters are more frequent than those involving agricultural tractors. After calculating the accident indices, the means of AFR, ASR, FIR, and FSI over the last five

years were 25.84%, 45.82%, 1.66%, and 1.066 for combine operators, and 5.602%, 12.63%, 4.44%, and 0.262 for tractor operators, respectively. Among the indices, the FSI and ASR for combine and tractor operators, and AFR for combine operators, were higher than the standard. The acceptable levels of safety performance are: FSI less than 0.1, ASR less than 1, and AFR between 0 and 10. By observing safety principles while working with tractors and agricultural combines, these indices should be brought to standard levels. One study showed that the frequency-severity index (FSI) over six years, except for 2013 and 2016, was less than the standard, indicating appropriate protection in those years (Kors, 2019). In 2013, the FIR index was significantly worse than in 2012. The results of this study show that accident indices in agricultural machinery (combine and tractor) were higher than those in industry activities, despite certain conditions and management in industrial factories in Iran. This finding related to combine harvesters and agricultural tractors shows that, observing safety principles while working with tractors and agricultural combines is crucial. This research analyzed accidents related to agricultural combines and tractors. Among the accident-causing factors, operator distraction, unsafe environmental conditions, unsafe farm roads, personal and operator errors, and machine malfunctions, especially in combine harvesters, were the main causes of agricultural machine accidents in Ilam province. Comparing the accident indices of combines and tractors, combines had a higher mean accident frequency, which is statistically significant due to their more complicated mechanisms and the time-sensitive nature of the harvesting season.

Suggestions

Although in this study, for the first time, the accident indices used in industry and factories were applied in the evaluation of agricultural accidents, it seems that due to the difference in the nature of agriculture and industry, there is a need to adjust the indices for agricultural purposes. It is suggested that, at the level of the province and the country, a database system of statistics of agricultural accidents should be considered in order to provide the possibility of evaluation and planning regarding the improvement of the safety of working with agricultural machines. Investigations showed that tractors and combines do not have an appropriate level of safety appliances and devices, so it is suggested that these affairs be taken into consideration during technical inspections.

It is recommended to improve road infrastructures, steep turns, and steep hills in cooperation with the national Agricultural Jihad Organization to prevent and reduce accidents in farms. Use Roll-Over Protective Structures (ROPS) and cabins for operator protection and install protective shields on PTO systems and rotating parts in order to reduce and prevent accidents related to crush and shear points.

Acknowledgments

We are grateful to the Research Deputy of Agricultural Sciences and Natural Resources University of Khuzestan.

Conflict of Interest: The authors declare no competing interests.

Author Contributions

J. Allahnouri: Data collection, Data analsis, Writing the manuscript

A. Marzban: Conceptualization, Supervision, Management, Methodology, Review and editing

M. Ghasemi Nejad Raeini: Supervision, Review and editing

M. Rahnama: Methodology, Software services

M. Savari: Statistical analysis, Validation

References

1. Abbasi Balochkhaneh, F., Ghotbi Ravandi, M. R., Golkhani, F., Baes mat, S., & Hasan pour Sodre Jani, Z. (2016). Determining the most important hazards in the cement industry. *Health Education and Health Promotion (HEHP)*, *4*(3), 3-11. https://hehp.modares.ac.ir/article-5-9277-en.pdf
2. Abubakar, M. S., Ahmad, D., & Akande, F. B. (2010). A review of farm tractor overturning accidents and safety. *Pertanika Journal of Science and Technology*, *18*(2), 377-385. http://www.pertanika.upm.edu.my/resources/files/PertanikaPAPERS/JSTVol.18(2)Jul.2010/16Pg377-385.pdf
3. Akanbi, O. G., Charles-Owaba, O. E., & Olley, A. (2009). Human factors in traffic accidents in Lagos, Nigeria. *Disaster Prevention and Management: An International Journal*, *18*(4), 397-409. https://doi.org/10.1108/09653560910984456
4. Anonymous. (2023). Ilam Province Agricultural Jihad Organization. *Department of Mechanized Technologies.* (in Persian).
5. Antunes, S. M., Cordeiro, C., & Teixeira, H. M. (2018). Analysis of fatal accidents with tractors in the Centre of Portugal: Ten years analysis. *Forensic Science International*, *287*, 74-80. https://doi.org/10.1016/j.forsciint.2018.03.048
6. Arnal, P., López-Maestre Salas, A., Arazuri, S., Mangado, J. M., & Jaren, C. (2017). A multi-year analysis of traffic accidents involving agricultural tractors. *Chemical Engineering Transactions*, *58*, 88-93. https://doi.org/10.3303/CET1758019
7. Cecchini, M., Bedini, R., Mosetti, D., Marino, S., & Stasi, S. (2018). Safety knowledge and changing behavior in agricultural workers: An assessment model applied in central Italy. *Safety and Health at Work*, *9*(2), 164-171. https://doi.org/10.1016/j.shaw.2017.07.009
8. Ceylan, H. (2012). Analysis of occupational accidents according to the sectors in Turkey. *Gazi University Journal of Science*, *25*(4), 909-918. https://dergipark.org.tr/tr/download/article-file/83575
9. Chio, W., Kim, K., & Jung, W. (2024). A Mini Review (PRISMA) on causes of incidents and injuries occurring in agricultural workplaces. *Journal of Agriculture*, *14*(4), 514. https://doi.org/10.3390/agriculture14040514
10. Cividino, S. R. S., Pergher, G., Zucchi Atti, N., & Gubiani, R. (2018). Agricultural health and safety survey in Friuli Venezia Giulia. *Agriculture*, *8*(1), 9. https://doi.org/10.3390/agriculture8010009
11. Cochran, W. G. (1977). *Sampling techniques*. (3rd ed.). Wiley.
12. Damalas, C. A., Koutroubas, S. D., & Abdollahzadeh, G. (2019). Drivers of personal safety in agriculture: A case study with pesticide operators. *Agriculture*, *9*(2), 34. https://doi.org/10.3390/agriculture9020034
13. Dimitrovski, Z. (2013). Fatal consequences in traffic accidents with tractors in the agriculture of Republic of Macedonia. *Machines, Technologies, Materials*, *6*. Retrieved from https://eprints.ugd.edu.mk/id/eprint/9670
14. Du, Y., Dorneich, M. C., Steward, B. L., & Mackenzie, C. A. (2016). A Bayesian-influence model for error probability analysis of combine operations in harvesting. *Proceedings of the Human Factors and Ergonomics Society Annual Meeting*, *60*(1), 1414-1418. https://doi.org/10.1177/1541931213601325
15. Edwards, J. P., & Sherlock, K. (2021). Opportunities for improving the safety of dairy parlor workers. *Journal of Dairy Science*, *104*, 419-430. https://doi.org/10.3168/jds.2020-18954
16. Ehlers, S. G., & Field, W. E. (2017). Injury/fatality-causing incidents involving the rearward movement of agricultural machinery: Types, causes, and preventive measures. *Safety*, *3*(1), 8. https://doi.org/10.3390/safety3010008
17. Esmaeili, A., Vazirineghad, R., & Shahrokhi, F. (2009). An annual survey of work- induced

accidents in injured farmers referring to health centers in Bam. *Occupational Medicine, 1*(1), 42-46. (in Persian). http://tkj.ssu.ac.ir/article-1-28-en.html
18. Fargnoli, M., Lombardi, M., Haber, N., & Puri, D. (2018). The impact of human error in the use of agricultural tractors: Case study research in vineyard cultivation in Italy. *Agriculture, 8*(6), 82-102. https://doi.org/10.3390/agriculture8060082
19. Ghafari, M., Cheraghi, Z., & Dusti Irani, A. (2017). Occupational risk factors among Iranian farmworkers: A review of the available evidence. *Epidemiology and Health, 39*, e2017027. https://doi.org/10.4178/epih.e2017027
20. Gholami, H., Kalantari, D., & Rajabi Vandechli, M. (2017). Ergonomic evaluation of vibrations of a rototiller with new blade. *Journal of Agricultural Machinery*, *7*(2), 491-502. (In Persian with English abstract). https://doi.org/10.22067/jam.v7i2.56061
21. Gite, L. P., Tiwari, P. S., & Khadatkar, A. (2010). Farm machinery accidents in Indian agriculture. In *Proceedings of the International Ergonomics Conference, HWWE 2009* (Vol. 1, pp. 283-290). University of Calcutta. Retrieved from https://www.researchgate.net/publication/262457121
22. Halvani, G. H., Fallah, H., Barkhordari, A., Khoskdaman, R., Behjat, M., & Koohi, F. (2010). A Survey of causes work related accidents in workplaces covered by Social Security Organization of Yazd in 2005. *Iran Occupational Health, 7*(39). Retrieved from https://www.sid.ir/paper/129161/en
23. Hamalainen, P., Takala, J., & Kiat, T. B. (2017). *Global estimates of occupational accidents and work-related illnesses 2017*. Workplace Safety and Health Institute.
24. Hayati, A., Marzban, A., & Asoodar, M. A. (2022). Workplace and gravity: Two mechanized cow milking systems compared for human physiological strains. *Journal of Agricultural Machinery*, *12*(1), 21-32. https://doi.org/10.22067/jam.2020.58607.0
25. Health and Safety Executive. (2012). *Safe use of combine harvesters* (AIS6 rev2). Retrieved from https://www.hse.gov.uk/pubns/ais6.htm
26. Houshyar, M., & Houshyar, E. (2018). Tractor safety and related injuries in Iranian farms. *Safety Science*, *103*, 88-93. https://doi.org/10.1016/j.ssci.2017.11.018
27. Health and Safety Authority. (2021). *Farm Safety Action Plan* 2021-2024. Retrieved from https://www.hsa.ie/eng/publications_and_forms/publications/agriculture_and_forestry/farm-safety-action-plan-2021-2024.pdf.
28. International Labour Organization. (2011). *Safety and health in agriculture: Code of practice*. International Labour Organization. Retrieved from https://www.ilo.org/publications/safety-and-health-agriculture-code-practice
29. Jaren, I., Ibarrola, A., Mangado, T., Adin, A., Amal, A., López-Maestre Salas, A., Rios, A., & Arazuri, S. (2022). Fatal tractor accidents in the agricultural sector in Spain during the past decade. *Agronomy*, *12*(7), 1694. https://doi.org/10.3390/agronomy12071694
30. Jun, L. J. (2014). The improvement on agricultural machinery safety using wireless sensing system and stability control algorithm. *Sensors & Transducers, 178*(9), 88-93. Retrieved from http://www.sensorsportal.com
31. Karimi, K., & Fakhri, A. (2021). Farm vehicle crashes on U.S. public roads: A review paper. *Journal of Safety Science and Technology*, *1*(2), 34-54. https://doi.org/10.4236/ojsst.2021.112004
32. Karimi, M., Sahragard, A., Rahimi Pordanjani, T., Mohammadi, A., Cousins, R., & Mo Karami, H. (2024). Development and validation of a model for predicting productivity based on psychosocial factors in administrative staff: The mediating role of physical and mental health. *Health Education and Health Promotion*, *12*(2), 291-298. https://doi.org/10.58209/hehp.12.2.291
33. Kasar, O., Comer Pay, E., İlhan, B., Eroğlu, O., & Deniz, T. (2023). An analysis of injuries due

to tractor accidents: A ten-year retrospective study. *The Journal of Kırıkkale University Faculty of Medicine, 25*(3), 472-481. https://doi.org/10.24938/kutfd.1356720
34. Keskin, M., & Şekerli, Y. E. (2018). An evaluation of combine harvester accidents in Turkey. *Journal of Agricultural Faculty of Mustafa Kemal University, 23*(2), 137-147. Retrieved from https://www.researchgate.net/publication/329913129
35. Khosravi, J., Hashemi Nazari, S., Dehghani Fard, S., & Jabari, K. (2007). A survey of work related accidents induced death in Public service and Green space laborers of Tehran Municipality in 2004-2005. *Iranian Journal of Forensic Medicine, 13*(2), 68-77. (in Persian). http://sjfm.ir/article-1-25-en.html
36. Kors, B. (2019). Investigating indicators of safety performance monitoring and analysis of occupational accidents in the Golestan Link Cement Factory. *The Fourth Specialized Conference of Tehran Cement Industrial Group*. (in Persian). Retrieved from https://tehrancement.co.ir/wp-content/uploads/2020/05/4-2.pdf
37. Lohan, S. K., Singh, P., & Kumar, S. (2022). Agricultural work-related fatalities and injuries in Punjab (India). *Injury Prevention, 28*(5), 459-464. https://doi.org/10.1136/injuryprev-2022-044566
38. Maisyaroh, A., Widianto, E. P., & Fibriansari, R. D. (2022). Determinants of injury in agricultural area. Nurse and Health. *Nurse and Health: Jurnal Keperawatan January, 11*(1), 22-33. https://doi.org/10.36720/nhjk.v11i1.321
39. Mayrhofer, H., Quendler, E., & Boxberger, J. (2013). Occupational incidents with self-propelled machinery in Austrian agriculture. *Journal of Agromedicine, 18*(4), 359-367. https://doi.org/10.1080/1059924X.2013.827997
40. Merisalu, E., Lepala, L., Jakob, M., & Rautiainen, R. H. (2019). Variation in Eurostat and national statistics of accidents in agriculture. *Agronomy Research, 17*(5), 1969-1983. https://doi.org/10.15159/AR.19.190
41. Mitrev ska, C., Mitrevski, V., & Kulevska, F. (2023). Statistical indicators for accidents at work in agriculture activity. *Journal on Processing and Energy in Agriculture, 27*(1), 22-24. https://doi.org/10.5937/jpea27-43287
42. Mohammadi, A., Kheiralipour, K., Ghamary, B., Jahan Bakhshi, A., & Shahidi, R. (2023). Predicting whole-body vibration-based on linear regression models and determining permissible exposure time of tractor operator. *Journal of Agricultural Machinery, 13*(2), 227-237. (in Persian with English abstract). https://doi.org/10.22067/jam.2021.73589.1071
43. Moradhaseli, S., Farhadian, H., Abbasi, E., & Ghofranipour, F. (2017). Factors affecting the incidence of occupational accidents among farmers. *Health Education and Health Promotion, 5*(1), 39-56. Retrieved from https://hehp.modares.ac.ir/article-5-866-en.html
44. Murphy, D. J., Myers, J., McKenzie Jr, E. A., Cavaletto, R., May, J., & Sorensen, J. (2010). Tractors and rollover protection in the United States. *Journal of Agromedicine, 15*(3), 249-263. https://doi.org/10.1080/1059924X.2010.484309
45. Omidi Arjanki, M., Javadiyan, R., & Tabashir, A. (2022). Investigating the causes of agricultural vehicle accidents studied in Chaharmahal and Bakhtiari province. *Child and Adolescent Social Injuries Journal*. (in Persian). Retrieved from http://chb.jrl.police.ir/article_102396.html
46. Parak, F., Poursaeed, A., Eshraghi Samani, R., & Chaharsoghi Amin, H. (2021). Analyzing Factors Affecting Reduction of Agricultural Occupational Injuries among Gardeners of Ilam Province. *Iranian Agricultural Extension and Education Journal, 16*(2), 93-107. (in Persian). https://doi.org/10.22034/iaeej.2021.248956.1558
47. Park, N. J., Kang, C. H., Oh, I. S., Lee, Y. B., Jung, H., & Park, W. K. (1990). Survey on farm work accidents of farm machinery: Analysis on the accidents of combine harvester. *Journal of Research Reports of the Rural Development Administration, Farm Management, Agricultural*

Engineering and Sericulture, 32(1), 24-32.
48. Pawlak, H., Nowakowicz-Dębek, B., Wlazło, M., Maksym, P., & Sasakova, N. (2017). Farmers' awareness in the field of occupational safety and health in sustainable management system. In E. Lorencowicz, J. Uziak, & B. Huyghebaert (Eds.), *Proceedings of the IX International Scientific Symposium "Farm Machinery and Processes Management in Sustainable Agriculture"* (pp. 301–305). Lublin, Poland: University of Life Sciences in Lublin. https://doi.org/10.24326/fmpmsa.2017.54
49. Quendler, E. R., Kogler, H., Mayrhofer, S., Ebner, S., Gross, L., TechNet, A., ... & Boxberger, J. (2014). *Identification of new technologies for preventing occupational accidents around vehicles, machines and equipment in agriculture and forestry.* IKA / TechNet / DAFNE.
50. Sadat Haeri, Z., Bagherian, S. Kh., Bahrami, P., Tarjeman, Z., Karmi, Z., Karimi, M., Moradi, Y., Moradbaigi, A., & Mirzai, A. (2019). *Statistical Yearbook of Ilam Province* (pp. 171-172) Ilam Province Management and Planning Organization. (in Persian).
51. Sarkar, S., Vinay, S., Raj, R., Maiti, J., & Mitra, P. (2018). Application of optimized machine learning techniques for prediction of occupational accidents. *Computers and Operations Research, 106*, 210-224. https://doi.org/10.1016/j.cor.2018.02.021
52. Shikha, V., & Chaudhari, S. (2016). Highlights from the literature on risk assessment techniques adopted in the mining industry: A review of past contributions, recent developments and future scope. *International Journal of Mining Science and Technology, 26*(4), 691-702. https://doi.org/10.1016/j.ijmst.2016.05.023
53. *Social Insurance and General Health Insurance (SIGHI) Law* (Law number: 5510), Gazette No. 26200 (2006). Retrieved from https://natlex.ilo.org/dyn/natlex2/r/natlex/fe/details?p3_isn=74711
54. Singh, G., Tewari, V. K., & Hota, S. (2023). Agricultural accidents and ergonomic intervention in agricultural machinery design in India. *Agricultural Engineering International: CIGR Journal, 25*(4), 137-146. Retrieved from https://cigrjournal.org/index.php/Ejounral/article/view/6039
55. Taber, K. S. (2018). The use of Cronbach's alpha when developing and reporting research instruments in science education. *Research in Science Education, 48*, 1273-1296. https://doi.org/10.1007/s11165-016-9602-2
56. Tone, I. R., & Irwin, A. (2021). Safety in the field: Assessing the impact of stress and fatigue on situation awareness in Irish and British farmers. In *Proceedings of the 21st Congress of the International Ergonomics Association (IEA 2021)* (pp. 274-283). Springer. https://doi.org/10.1007/978-3-030-74608-7_35
57. Volkovski, T., Chaloska, J., & Grad, M. P. (2018). *Annual report for fatalities, injuries, and accidents at work*. Macedonian Occupational Safety and Health Association. Retrieved from https://webapps.ilo.org/static/english/protection/safework/cis/about/mtg2009/macedonia.pdf

نشریه ماشین‌های کشاورزی
https://jame.um.ac.ir

مقاله پژوهشی

جلد ۱۶، شماره ۳، پاییز ۱۴۰۵، ص ۴۶۷-۴۴۹

بررسی نرخ و شدت حوادث مربوط به تراکتورهای کشاورزی و کمباین‌های غلات و عوامل مؤثر بر آن در استان ایلام

جلال اله نوری[۱]، افشین مرزبان[۱*]، محمود قاسمی نژاد رائینی[۱]، مجید رهنما[۱]، مسلم سواری[۲]

تاریخ دریافت: ۱۴۰۳/۱۱/۰۶
تاریخ پذیرش: ۱۴۰۳/۱۲/۱۳

چکیده

کشاورزی یک صنعت غالب در کشورهای در حال توسعه است و در رتبه خطرناک‌ترین مشاغل قرار می‌گیرد. تراکتورها و ماشین‌های برداشت غلات از ماشین‌های کشاورزی خودگردان هستند که علی‌رغم نقش بی‌بدیل‌شان در افزایش بهره‌وری، سهم قابل‌توجهی در حوادث دارند. این حوادث هزینه‌های زیادی را به‌همراه دارد و بهره‌وری را کاهش می‌دهد. این مطالعه به‌منظور بررسی میزان و شدت حوادث و تلفات انسانی و عوامل موثر بر حوادث مزرعه‌ای مربوط به تراکتورها و کمباین‌های کشاورزی در استان ایلام با استفاده از داده‌های مربوط به سال‌های ۱۴۰۲-۱۳۹۸ انجام شد. فراوانی حوادث تراکتورها و کمباین‌ها در مطالعه انجام‌شده، به‌ترتیب ۶۱ و ۴۳ بود که نشان‌دهنده‌ی اختلاف آماری معنی‌داری است. در این تحقیق در بین رانندگان تراکتور بیشترین حوادث ناشی از محور (P.T.O.)، هلیس و غلتک‌های تغذیه و در بین رانندگان کمباین، رایج‌ترین حوادث مربوط به نقاط برشی ماشین (شانه برش، چرخ‌دنده‌ها و غیره) بود. نرخ حوادث از جمله AFR (نرخ فرکانس حادثه)، ASR (نرخ شدت حادثه)، FIR (نرخ حادثه مرگبار) و FSI (شاخص شدت تکرار حادثه) محاسبه شد. میزان AFR، ASR، FIR و FSI به‌ترتیب ۲۵/۸۴، ۴۵/۸۲، ۱/۶۶ و ۱/۰۶۶ برای کمباین‌ها و ۵/۶۰، ۱۲/۶۳، ۴/۴۴ و ۰/۲۶۲ درصد برای حوادث تراکتور بوده است. نرخ حوادث غیرمرگبار برای رانندگان کمباین‌ها ۶۴۴۵ در هر ۱۰۰۰۰۰ و برای رانندگان تراکتورها ۴۳۳۴ در هر ۱۰۰۰۰۰ بود، با این حال، تعداد حوادث کشنده تراکتور بیشتر از کمباین‌ها بود (۴۴۵ و ۳۳۰ در هر ۱۰۰۰۰۰ دستگاه).

واژه‌های کلیدی: ایمنی اپراتور، تراکتور، شاخص‌های حوادث، عوامل حادثه، کمباین

۱- گروه مکانیزاسیون و ماشین‌های کشاورزی، دانشکده مهندسی زراعی و عمران توسعه روستایی، دانشگاه علوم کشاورزی و منابع طبیعی خوزستان، ملاثانی اهواز، اهواز، ایران
۲- گروه ترویج و آموزش کشاورزی، دانشکده مهندسی زراعی و عمران توسعه روستایی، دانشگاه علوم کشاورزی و منابع طبیعی خوزستان، ملاثانی اهواز، اهواز، ایران
(*- نویسنده مسئول: Email: afshinmarzban@asnrukh.ac.ir)

https://doi.org/10.22067/jam.2025.91786.1336

Journal of Agricultural Machinery

Homepage: https://jame.um.ac.ir

Research Article
Vol. 16, No. 3, 2026, p. 469-486

Predicting Vitamin C and Color Change of Orange Powder in Four Dryers Using an Electronic Nose

M. Roshan Moghadam[1], R. Amiri Chayjan[1*], N. Aghilinategh[2]

1- Department of Biosystems Engineering, Faculty of Agriculture, Bu-Ali Sina University, Hamedan, Iran
2- Department of Agricultural Machinery Engineering, Sonqor Agriculture Faculty, Razi University, Kermanshah, Iran
(*- Corresponding Author Email: amirireza@basu.ac.ir)

Received: 07 February 2025
Revised: 22 April 2025
Accepted: 29 April 2025
Available Online: 26 August 2025

How to cite this article:
Roshan Moghadam, M., Amiri Chayjan, R., & Aghilinategh, N. (2026). Predicting Vitamin C and Color Change of Orange Powder in Four Dryers Using an Electronic Nose. *Journal of Agricultural Machinery*, *16*(3), 469-486. https://doi.org/10.22067/jam.2025.92037.1340

Abstract

In this research, the amount of vitamin C, aromatic compounds, and color change of orange powder was measured using chemical methods, an olfactory machine, and a scanner in four dryers at 45°C. These dryer apparatuses included normal atmospheric vacuum, atmospheric control vacuum, convective, and convective-infrared. The highest response of sensors to aromatic compounds in convective and lowest response in control vacuum and normal vacuum dryers was observed. The two main components of principal component analysis (PCA) explained 88% of the data variance. The structure of the artificial neural network (ANN) was 8-5-4. Further, based on loading diagrams of partial least squares (PLS) and principal component regression (PCR) models, the MQ3 and MQ6 sensors were the best to predict the amount of vitamin C and the color change of orange powder. MQ135 sensor can also be removed from the set of electronic nose sensors due to their low accuracy and cost reduction. The multiple linear regression (MLR), compared to PCR and PLS models, proved to be more accurate (i.e., R^2= 0.83 and RMSE= 0.144 for vitamin C prediction and R^2= 0.94 and RMSE= 0.68 for predicting color change). The highest and lowest values of measured color change was observed in convective dryer and atmospheric control vacuum dryer, respectively. Also, the highest and lowest measured vitamin C was observed in convective-infrared dryer and atmospheric control vacuum dryer, respectively. The best dryer to maintain the quality of the orange powder is the convective-infrared dryer. The results of this article showed that the data obtained from the olfactory machine is able to predict the color change and vitamin C of orange powder. Also, the olfactory machine can be used to identify and classify the type of dryer used to prepare orange powders with the least time and cost, without distorting the sample, and to determine the best dryer for preparing orange powder.

Keywords: Color change, Dryer, Electronic nose, Orange powder, Vitamin C

Introduction

The orange fruit is widely cultivated and consumed all over the world. This fruit is rich in nutrients and one of the richest sources of vitamin C (53.2 mg per 100 grams of raw fruit) (Finley & Klurfeld, 2013). Vitamin C, is among the essential components of human diets. This compound, also known as ascorbic acid, prevents Scorbut and is a biological antioxidant (Agarwal, Shaharyar, Kumar, Bhat, & Mishra, 2015). Nevertheless, vitamin C is one of the most unstable nutrients in food as it is severely degraded during processing (Spínola, Llorent-Martínez, & Castilho, 2014). Therefore, it is used as an index to examine the quality of nutrients (Drewnowski, 2010). Drying, known as the most important and popular method of post-harvesting food preservation, prevents the activity of many bacteria. This process also minimizes the costs of packaging, storage, and transportation by

Authors retain the copyright. This is an open access article distributed under Creative Commons Attribution 4.0 International License (CC BY 4.0).

https://doi.org/10.22067/jam.2025.92037.1340

removing moisture from the tissue (Shi, Chu, Zhang, Liu, & Yao, 2017). During the drying process, some changes occur in the food's aroma, taste, texture, color, as well as the degradation of its components (Lemus-Mondaca, Ah-Hen, Vega-Gálvez, Honores, & Moraga, 2017). Food color is the most important factor for evaluating quality and consumer satisfaction (Bal, Kar, Satya, & Naik, 2011). The aroma of food is one of its most important characteristics, and its measurement is an advanced and particularly effective method to obtain parameters affecting food quality. In this method, the smell emitted by the food is very sensitive to changes in its ingredients. One common non-destructive method to measure is using an electronic nose, a device consisting of micro-arrayed electronic chemical sensors. Typically, to build a database and create a pattern recognition system, suitable patterns of known smells are used so that subsequent unknown smells can be classified and recognized (Peris & Escuder-Gilabert, 2009; Sanaeifar, ZakiDizaji, & Jafari, 2017). Moreover, drying orange and creating powder from them makes them readily available in the off-season, reduces their size, and enhances storable qualities. Also, this fruit powder can be used as an essential ingredient for food preparation or revitalizing natural fruit juices. However, the process used to obtain the powder must guarantee the maximum product quality and preserve some physical properties of the powder (Otálora, Carriazo, Iturriaga, Nazareno, & Osorio, 2015). Some researchers have analyzed the color changes of food such as tomato varieties (Ashebir, Jezik, Weingartemann, & Gretzmacher, 2009), spinach (Karaaslan & Tunçer, 2008), Japanese medlar (Wang, Lu, Chen, & Zhang, 2016), St. John's wort leaves (Ahmadi Chenarbon *et al.*, 2012), and red beetroot (Fathabadi, Tabatabaekoloor, & Motevali, 2019). In this regard, Karaaslan and Erdem (2014), and Khafajeh, Banakar, Ghobadian, and Motevali (2013) investigated the measurement of the color change of dried orange slices using image processing. Also, several studies have been conducted on the change of aroma of products during different drying methods, e.g., mushroom (Qin *et al.*, 2020), pear (Li *et al.*, 2020), saffron (Chen *et al.*, 2020), and tea (Ni *et al.*, 2020). In this context, much research has been conducted on various drying methods and the preservation of the aromas of products such as pepper (Guclu *et al.*, 2020), cocoa (Sanchez-Reinoso, Osorio, & Herrera, 2017), mint (Kiani, Minaei, & Ghasemi-Varnamkhasti, 2018), and coffee (Kulapichitr, Borompichaichartkul, Suppavorasatit, & Cadwallader, 2019).

In addition, the production of powdered food products is an essential industry due to their high stability and ease of use. On the other hand, the type of dryer used for powder preparation affects the aroma, color, and nutritional quality of the product. Furthermore, after extensive research, no study was found either on the use of different dryers for preparing orange powder or their effects on aroma, color change, and vitamin C, using an e-nose system and a scanner. Hence, the aim of the present paper is to measure and predict the color change and vitamin C content using electronic nose data for orange powder prepared with convective-infrared, convective, normal atmospheric vacuum, and atmospheric control vacuum dryers using Artificial Neural Network (ANN), Principal Component Analysis (PCA), Partial Least Squares (PLS), and Multi-Layer Regression (MLR).

Material and Methods

Sample preparation

In this research, we used orange samples of the Valencia variety (Citrus Sinensis Osbeck) with an initial humidity of 88% on a wet basis. Respiration and moisture loss was reduced by keeping the oranges in the refrigerator at 4 ± 0.5°C until performing the experiments. Before the drying tests, the samples were kept at room temperature for 120 min. After peeling the samples, thin and uniform slices with a thickness of 3 to 4 mm were made from the orange flesh and placed inside the dryers. The drying process and the weight reduction of the samples continued until the moisture of the

samples decreased to 10% (on a dry basis). All experiments were performed at room temperature (27± 3°C) (Fig. 1).

Fig. 1. From left to right; Fresh, dried, and powdered oranges

Drying tests

A convective dryer as a basis and a common dryer were used in this research. The convective drying experiments were performed at 45°C and an outlet air velocity of 1 m s^{-1} (Fig. 2a). Also, the infrared-convective dryer, which includes a dryer chamber, centrifugal blower, heating elements, and control unit, was used for the experiments. Four infrared lamps were used to generate infrared radiation with a total power of 2,000 W inside and above the drying chamber to produce infrared power at an air temperature of 45°C and an exit velocity of 1 m s^{-1} (Fig. 2b) (Amiri Chayjan & Fealekari, 2017). In addition, a vacuum dryer was used, consisting of a chamber with four infrared lamps, a condenser section, and a vacuum pump. These tests were performed under two conditions (i.e., a controlled atmosphere and a normal atmosphere) at 45°C with a pressure of 60 bar (Fig. 2c). Dried orange slices were ground and powdered using a home grinder (Panasonic model, MJ-M176P, made in Malaysia) for 15 s. After the grinding process, to preserve the aroma of the produced powder, the samples were kept in designated plastic bags in the freezer at -19 ± 0.5°C. Before starting the artificial electronic nose tests, the powder samples were placed at ambient temperature for 30 min. Then, 5 g of orange powder was poured into the sample container, and electronic nose tests were performed.

Electronic nose system

The electronic nose used in this study is a multi-sensing system based on metal-oxide-semiconductor (MOS) sensors (Fig. 3). This system includes sensors, sensor housing, sample housing, data acquisition system, display, power supply unit, solenoid valves, pump, and oxygen capsule. This system comprises eight metal oxide semiconductor (MOS) sensors (Table 1). Each sensor reacts to a specific combination of volatile substances emitted. Metal oxide semiconductor (MOS) sensors are among the most common sensors used in electronic noses, which have high sensitivity and chemical stability. The low cost and converting chemical quantities into electrical signals are among the noteworthy advantages of these sensors (Sanaeifar, Mohtesabi, Ghasemi Varnamekhati, & Ahmadi, 2015).

The steps taken in the electronic nose system include 1) baseline correction, 2) sample odor injection, and 3) cleaning the sensors and sample chamber. To mix and saturate the smell of the sample inside the chamber, we poured the sample into the sample chamber and closed the lid. The tests were conducted after 10 min. In the first step, before injecting the air inside the sample chamber toward the sensors, it is necessary to pass the filtered air over the sensors for 60 s (T1). In the second step, the scent of the sample was passed over the sensors (T2) by injecting the smell of the sample into the sensors for 40 s. In the third step, the hoses, connections, and sensors were cleaned with filtered air for 60 s (T3). Thus, the system was prepared for the next sample. The voltage response of the sensors in these 160 s was collected by the data acquisition system.

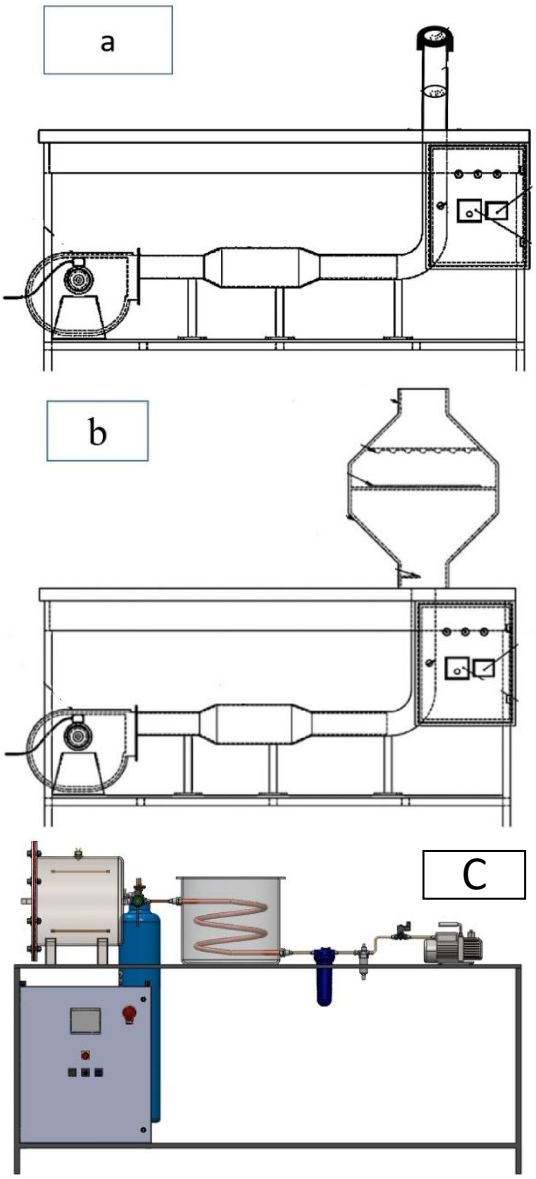

Fig. 2. The schematic view of the dryers: (a) Convective dryer, (b) Convective infrared-dryer, and (c) Vacuum dryer

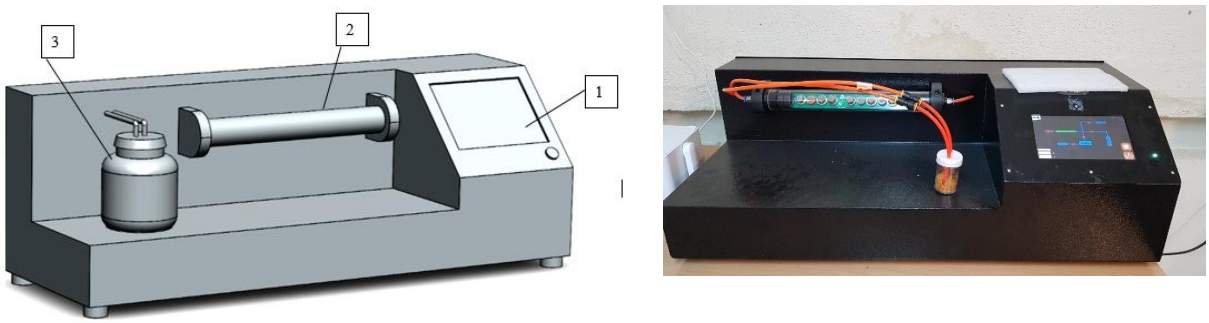

Fig. 3. The schematic and actual photo of the electronic nose system: 1- display, 2- gas sensors, and 3- sample chamber

Table 1- The sensors used in the electronic nose

Sensor number	Sensor name	Diagnostic gases
1	MQ2	Natural gas, butane, propane, methane, alcohol, hydrogen, and smoke
2	MQ3	Alcohol and benzene
3	MQ4	Methane, propane, and butane
4	MQ5	Natural gas, city gas, alcohol, cooking steam, and carbon monoxide
5	MQ6	Natural gas, liquefied petroleum gas, isobutane, propane, alcohol, and smoke
6	MQ7	Carbon monoxide
7	MQ9	Methane, carbon monoxide, and natural gas
8	MQ135	Benzene, ammonia, carbon dioxide, carbon monoxide, and alcohol

The time required for each stage of sensor testing was obtained by trial and error. After pouring 5 g of orange powder into the sample chamber, the temperature of the sample was almost the same as the ambient temperature (about 30℃). A total of 32 samples were utilized for this research. Eight repetitions of tests were performed at 45℃ for each of the four types of dryers. The next step in data analysis is to preprocess the sensor signals. Information preprocessing greatly affects the performance of pattern recognition methods. This process is partly dependent on the type of sensors (Kiani, Minaei, & Ghasemi-Varnamkhasti, 2016). The first stage of preprocessing is to correct the response of the sensors to compensate for deviations and increase the information quality. This preprocessing facilitates the optimization of the output of the sensors before analysis. Differential, relative, and fractional methods are applied to extract features from the signals. This research used the fractional method for this purpose (Eq. 1). The preprocessed response is dimensionless and normalized (Heidarbeigi *et al.*, 2015).

$$y_s(t) = \frac{x_s(t) - x_s(0)}{x_s(0)} \quad (1)$$

where $y_s(t)$ is the preprocessed (dimensionless) response, $x_s(0)$ is the baseline, and $x_s(t)$ is the sensor response.

Measuring the concentration of vitamin C

Vitamin C concentration was measured by a two-step titration method (Ghasemi & Chayjan, 2019). In this method, first, 25 mL of 6% metaphosphoric acid was added to 10 g of orange powder sample (extraction solution). Next, in a 50-mL Erlenmeyer flask, 5 mL of this solution was diluted with 3% metaphosphoric acid and filtered through filter paper. Afterward, 10 mL of the filtered sample was titrated with dichlorophenolindophenol (detector solution). At the endpoint of the experiment, the solution turned pale pink, which lasted for 15 s. The amount of dye used in the titration was recorded, and the amount of ascorbic acid was calculated from Eq. (2) and expressed in terms of mg/100 g of fruit.

$$\text{The amount of ascorbic acid} = \frac{0.5 \times B}{A \times C} \times 100 \quad (2)$$

A= Weight of plant sample (g)

B= The amount of meta-phosphorus used for the prototype (mL)

C= Sample volume used for titration (mL)

The color measurement and calculating its changes

The image processing method was applied to measure the color indices. For this purpose, an HP Scan Jet G4010 scanner was used. The scanner device was first calibrated using standard black and white cards that show the numbers (0.0.0) for black color and (255.255.255) for white color, respectively, according to the RGB color scale. The orange powder with a resolution of 1200 dpi was then scanned. The obtained photos were processed by MATLAB software (version 2017a), and the color values L*, a*, and b* were calculated. In the end, the color changes of orange powder were calculated (Ahmadi & Chayjan, 2017) based on Eq. (3).

$$\Delta E = \sqrt{(L_0^* - L^*)^2 + (a_0^* - a^*)^2 + (b_0^* - b^*)^2} \quad (3)$$

where L* is the value of darkness (0) to lightness (100), a* is the value of red (120+) to green (-120), and b* is the value of yellowness (+120) to blue (-120).

Data analysis

The preprocessed data were analyzed using PCA, ANN, PLS, PCR, and MLR techniques using Unscrambler V.9.7 and MATLAB 2015a software. PCA is a chemical linear unsupervised pattern recognition method used to analyze and reduce the dimensionality of numerical data sets in a multivariate problem. This technique is applied to assess outlier detection, discrimination, and similarity between different samples or groups (Melucci *et al.*, 2016). ANN is a powerful classifier based on machine learning with nonlinear mapping capability. An ANN classifier consists of interconnected layers of artificial neurons and is trained to classify by adjusting the weights and biases of connections between neurons (Rasekh, Karami, Wilson, & Gancarz, 2021). In statistics, PCR is a regression analysis method based on PCA. PCR usually relies on a standard linear regression model derived from results, which are referred to as dependent response variables, in relation to a set of other variables known as predictors, explanatory variables, or independent variables (Heidarbeigi *et al.*, 2015; Sanaeifar, Mohtasebi, Ghasemi-Varnamkhasti, & Ahmadi, 2016). PLS is the gold standard in chemical measurements regarding its ability to handle linear data and reduce the number of calibration samples required (Patel, 2014). This method reduces correlated spectral data with high dimensions to uncorrelated factors called hidden variables (Hansen & Schjoerring, 2003). MLR is a statistical method that examines the relationship between independent and dependent variables. The purpose of MLR is to calculate the values of the regression coefficients of the sensors and to minimize the sum of the squared deviations (downward slope) between the predicted quality indices and the measured quality indices (Patel, 2014).

Results and Discussion

Sensors' response

The observed signals of the electronic nose sensors at 45°C for four types of dryers (Fig. 4) show that the response of sensors to aromatic compounds in control vacuum and normal vacuum dryers are similar. Also, highest response in convective and lowest response in control vacuum and normal vacuum dryers was observed.

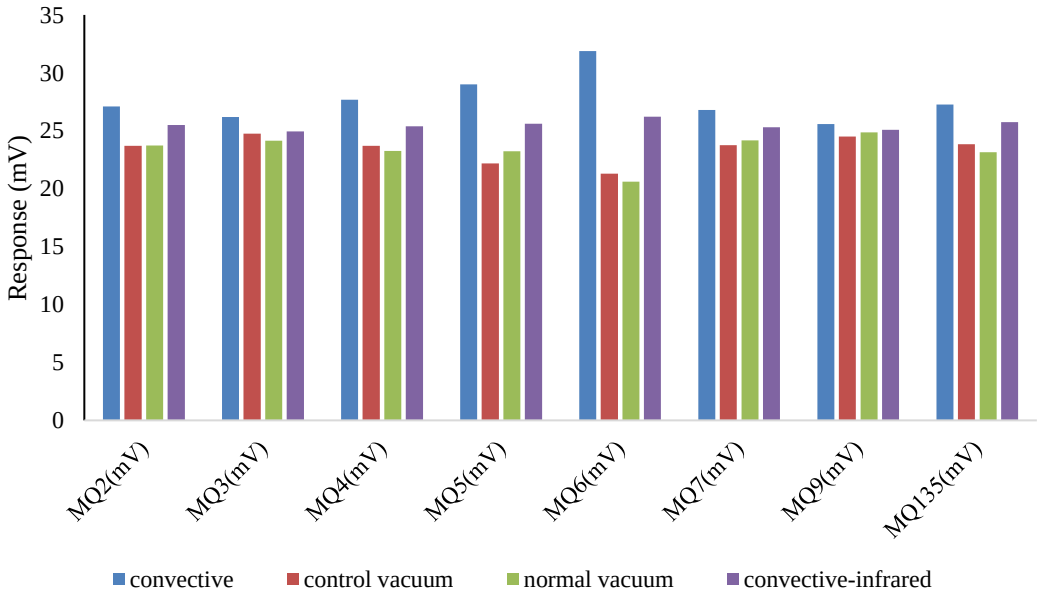

Fig. 4. The sensors response of the electronic nose system in four dryers at 45°C

PCA results

The main components (i.e., those with the most data variance) distributed the data on a new axis for classification. The intended score charts are presented in Fig. 5. The first and second components (PC-1 and PC-2) express the variance between the data obtained from the measurement of the samples. These components are used to determine the existence of separate data clusters for pattern recognition (Heidarbeigi *et al.*, 2015). The data obtained by measuring the diagram of the main components at 45°C are shown in Fig. 5. The two main components of PCA explained 88% of the data variance. In this study, the values of the first (PC-1) and second (PC-2) main components were 73% and 15%, respectively. Fig. 5 illustrates that the powder prepared with a convective dryer is well separated from the others. However, there was an overlap between normal vacuum, control vacuum, and convective-infrared dryers, which can be attributed to the similarity in the aromatic compounds of the dried powder in these three dryers.

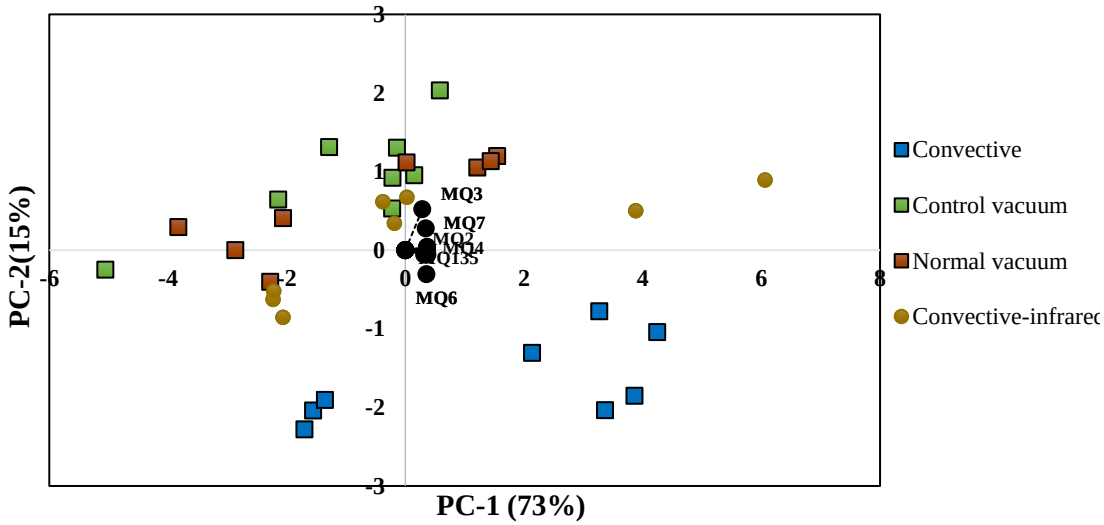

Fig. 5. Score and loading diagrams of the PCA method for four dryers at 45°C

The loading diagram was examined to determine the role of sensors in separating the four groups. It is possible to show the relative role of electronic nose sensors for each main component in the loading diagrams. The higher the sensor loading on the axis of the main components, the closer it is to the outer circle. Therefore, it can be concluded that such a sensor has a greater role in recognizing and differentiating between various samples in the desired application. Also, if certain sensors have a negligible effect on the detection process, they can be removed from the electronic nose system's sensor array, ultimately lowering the overall cost of constructing the electronic nose system (Heidarbeigi *et al.*, 2015). According to the loading diagram (Fig. 4), the classification of orange powder produced using four types of dryers is greatly impacted by the MQ3 and MQ6 sensors, indicating a presence of alcohol in the orange powder. Additionally, the MQ135 sensor has the least impact on the classification, and can be removed to reduce manufacturing costs. Furthermore, ignoring sensors with the lowest loading values can increase the cumulative variance contribution, although it significantly impairs the performance of PCA (Nouri, Mohtasebi, & Rafiee, 2020). Recent studies have shown that PCA is an efficient analysis method for analyzing the aroma of dried products

produced by different drying devices (Dong *et al.*, 2019; Song *et al.*, 2020; Yang *et al.*, 2016). The results of another study, which was conducted on sugarcane, showed that the PCA method had better results than the ANN method (Adibzadeh, Dizaji, & Aghilinategh, 2020).

ANN results

Multilayer Perceptron Backpropagation (ANN-MLP) algorithm was used to classify and detect the type of dryer using the data obtained from the electronic nose as the network's input. The type of dryer was detected using a network that includes three input, hidden, and output layers. The hyperbolic activation function was used in the hidden layer, and the number of neurons in the hidden layer was determined through trial and error. The hidden layer is comprised of several neurons representing the network's nonlinearity. In this research, the mean square error (MSE) is 10^{-8}, the minimum gradient is 10^{-10}, and the maximum number of epochs is 100. Also, a learning rate of 0.02 was used in the designed network. Besides, 75% of the data was used for training the network, and the remaining 25% for the final evaluation. The structure of the neural network built in this study was 8-5-4. The input neurons represent the number of sensors, and the number of output neurons represents the four types of dryers. The neurons of the hidden layer are used to show the nonlinearity of the network and to increase the speed of the system training. The number of these neurons was determined by trial and error. Table 2 shows the confusion matrix resulting from the ANN. The classification accuracy of the dryers at 45°C was 96.9%. Table 2 illustrates that the all eight powders prepared with a convective, vacuum control, and convective-infrared dryers are recognized with 100% accuracy.

Table 2- Confusion matrix resulting from the ANN at 45°C

Dryer	Convective	Control vacuum	Normal vacuum	Convective -infrared	Accuracy	Sensitivity	Property
Convective	8	0	0	0	1.00	1.00	1.00
Control vacuum	0	8	1	0	0.88	1.00	0.95
Normal vacuum	0	0	7	0	1.00	0.87	1.00
Convective-infrared	0	0	0	8	1.00	1.00	1.00

Correct accuracy of classification: 96.9%

In a study focused on assessing the ripeness of blackberries and mulberries, the ANN method provided more accurate classifications than the PCA and LDA methods. ANN was able to classify the blackberry and mulberry samples with 100% and 88.3% accuracy, respectively (Aghilinategh, Dalvand, & Anvar, 2020).

PLS results

The score chart of the PLS model indicates minimal overlap in the predicted vitamin C percentages for control and normal vacuum dryers. However, the color change prediction score chart indicates that there is considerable overlap between normal vacuum, control vacuum, and convective-infrared dryers. Also, the score plot shows that PC-1 covered 91-93% of the data variance for vitamin C and colour change prediction, while PC-2 covered 58-82% of the data variance (Fig. 6).

The PLS model loading diagram was used to analyse the response of each sensor (Fig. 7). In the loading diagram of vitamin C prediction and colour change prediction, the MQ6, MQ3, and MQ5 sensors had the highest response, and the MQ135 sensor provided the lowest response. In this regard, Sanaeifar *et al.* (2016) showed that for banana quality indicators (firmness and TSS index), the R^2 values of MLR and PLS equations in calibration and validation were relatively similar and acceptable.

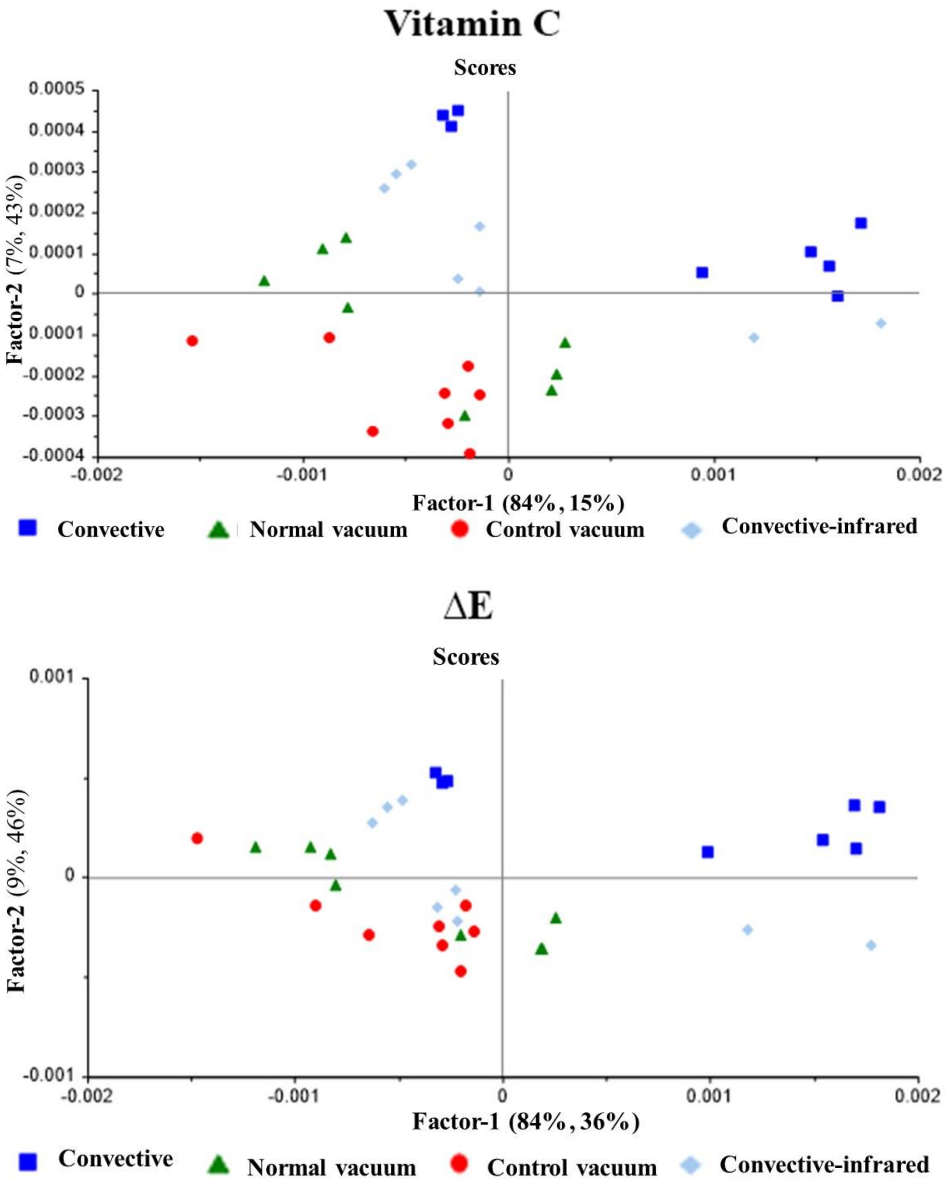

Fig. 6. PLS model diagram for predicting vitamin C and ΔE

PCR results

The score diagram of the PCR model shows the prediction overlap of vitamin C percentage and color change in control vacuum, normal vacuum, and convection-infrared vacuum dryers (Fig. 8). In addition, the score plot reveals that PC-1 accounted for 93% of the variance in predicting vitamin C levels and color change, while PC-2 captured between 18% and 64% of the variance.

PCR model loading diagram was used to analyse the response of each sensor (Fig. 9). In the loading diagram of vitamin C prediction and colour change prediction, the MQ6, MQ3, and MQ5 sensors had the highest response, and the MQ135 sensor provided the lowest response. Zhang, Wang, Ye, and Chang (2012) used electronic nose signals to predict the firmness and PH of peach. The results showed that the PCR model with high correlation coefficients (R= 0.78 for strength, R= 0.82 for sugar content, and R= 0.84 for pH) has a good ability to predict quality indices.

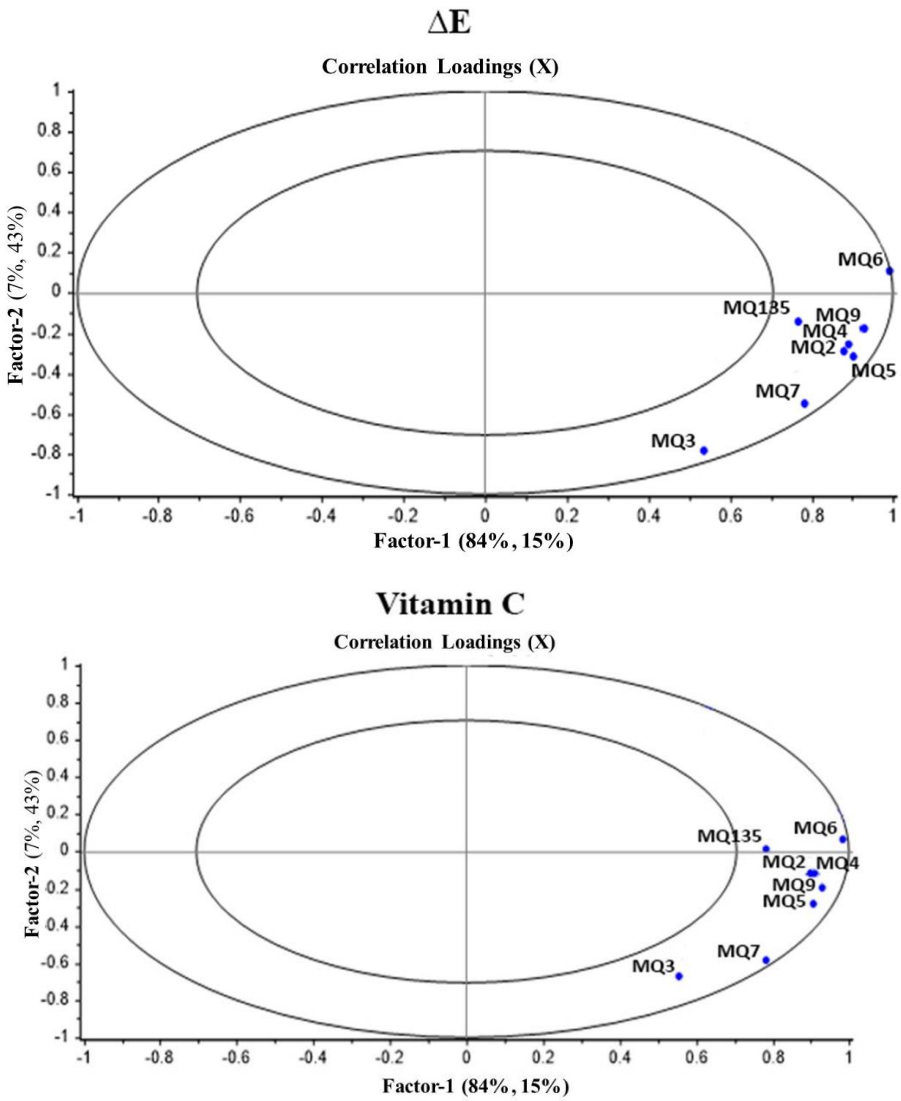

Fig. 7. PLS model loading diagram for vitamin C and ΔE prediction

Comparison between PLS, PCR, and MLR models

The results of the models for predicting vitamin C and colour change using electronic nose data showed that the coefficient of determination (R^2) was in the range of 0.73-0.86, and the standard deviation was in the range of 124-151 for vitamin C. For a colour change, these values were reported as 0.86-0.94 and 0.35-0.7, respectively. The results showed that the prediction performance for color change of dried samples using the smell of the samples was better than vitamin C (Table 3). Also, according to Table 3, the MLR model demonstrates superior predictive capability for vitamin C levels, as observed by its more optimal R^2 and RMSE compared to the other two models. Also, for colour change classification, the most accurate MLR model had an R^2= 0.94 and RMSE= 0.68.

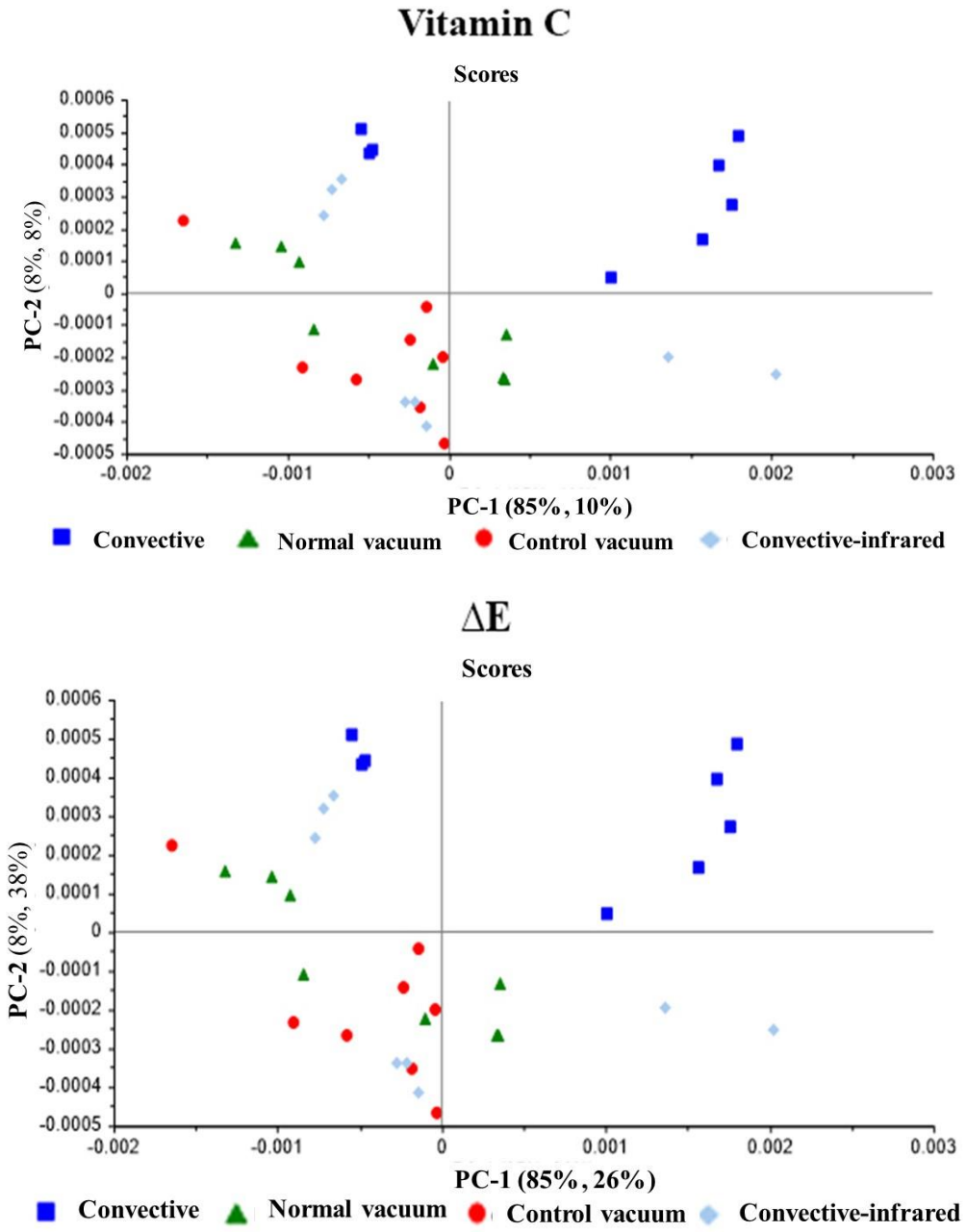

Fig. 8. Score chart of the PCR model for predicting vitamin C and ΔE

Previous studies have shown a good relationship between pear quality indices (i.e., firmness and TSS) and electronic nose signal response. Thus, MLR leads to a more accurate prediction than other multivariate calibration methods with the coefficient of determination values of 0.92 and 0.94 for strength and TSS, respectively. However, in terms of acidity, there is a weak correlation with the electronic nose signal (Zhang, Wang, & Ye, 2008).

Table 4 shows the regression models obtained from PLS, MLR, and PCR for vitamin C and color change. The models are built based on Eq. (4).

$$Y = a_0 + a_1S_1 + a_2S_2 + a_3S_3 + a_4S_4 + a_5S_5 + a_6S_6 + a_7S_7 + a_8S_8 \quad (4)$$

where Y is the quality index, a_0 is the constant coefficient of the equation, S_1 to S_8 are the sensors, and a_1 to a_8 indicate the sensor array.

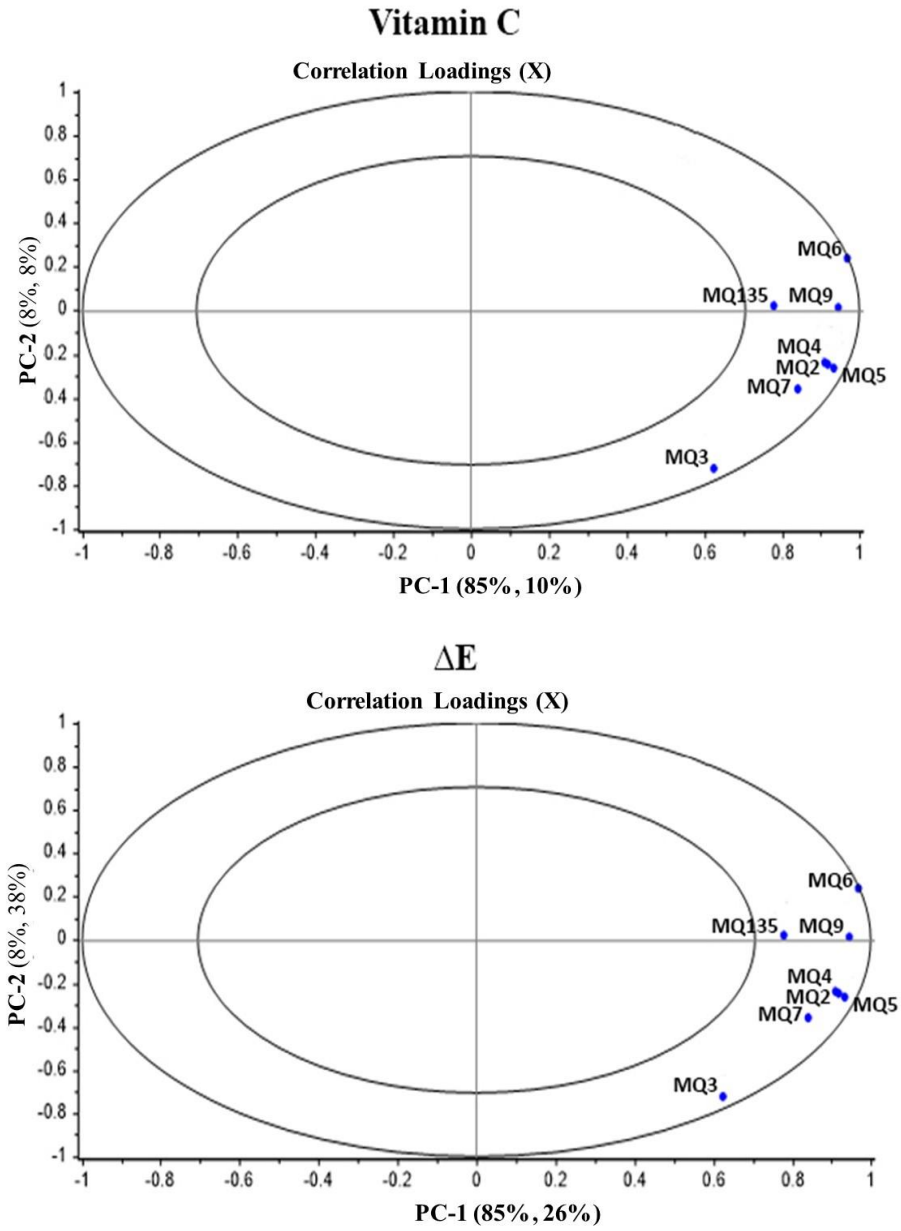

Fig. 9. Loading diagram of PCR model for predicting vitamin C and ΔE

Table 3- Predicting PCR, PLS, and MLR models for quality indicators based on electronic nose data

Quality index	Vitamin C			ΔE		
	PLS	MLR	PCR	PLS	MLR	PCR
R^2	0.81	0.83	0.73	0.91	0.94	0.93
RMSE	124	144	152	0.7	0.68	0.62

* PLS partial least squares, MLR multiple linear regression, and PCR principal component regression

According to Table 5, in vitamin C prediction, the lowest error (216.29) was related to the MLR model, and the highest error (352.65) was related to the PCR model. Furthermore, in the prediction of colour change, the lowest error (0.592) was related to the MLR model, and the highest error (0.86) was related to the PCR model. The highest and

lowest measured color changes were observed in hot air dryer and atmospheric control vacuum dryer, respectively. In Table 5, it is evident that the highest vitamin C levels were found in the convective-infrared dryer, while the atmospheric control vacuum dryer displayed the lowest measurements. In summary, the atmospheric control vacuum dryer results in the most considerable decline in quality, specifically regarding odor and vitamin C concentration, while the hot air dryer causes the highest color change of the prepared orange powder. Therefore, the best dryer to maintain the quality of the orange powder is the convective-infrared dryer.

Table 4- Regression coefficients estimated by PLS, MLR, and PCR models

Quality index	**Vitamin C**			**ΔE**		
Model	**PCR**	**MLR**	**PLS**	**PCR**	**MLR**	**PLS**
a_0	294.31	433.76	-214.26	23.82	23.87	24.03
a_1 (MQ2)	-438548.84	-1868445.38	761930.9	3390.56	2906.89	3194.28
a_2 (MQ3)	-71694.78	-551.41	-716471	-3483.10	-3214.4	-2966.64
a_3 (MQ4)	945351.31	1532044.13	709418.8	2423.40	2784.22	1914.59
a_4 (MQ5)	295335.43	871438.68	4624.4	137.02	213.07	338.86
a_5 (MQ6)	479410.62	237475.81	-53066.9	577.11	1052.71	454.56
a_6 (MQ7)	-1814250	-2279571	-575208	-3447.43	-5826.88	-3110.14
a_7 (MQ9)	-1176795.5	2169078.75	-2194524	-3109.32	11399.49	-5546.62
a_8 (MQ135)	537276.81	560391.37	525199.8	932.08	-93.43	1241.88

* PLS partial least squares, MLR multiple linear regression, and PCR principal component regression

Table 5- Vitamin C and real predicted color change by PLS, MLR, and PCR models

Quality index	**Model**	**Convective dryer**		**Atmospheric control vacuum dryer**		**Normal atmospheric vacuum dryer**		**Convective-infrared dryer**	
		M	**P**	**M**	**P**	**M**	**P**	**M**	**P**
Vitamin C	MLR	1411.2	1440.95	864	942.38	1219.2	1190.48	1660.8	1581.36
	PLS	1411.2	1446.23	864	946.13	1219.2	1191.25	1660.8	1571.57
	PCR	1411.2	1467.3	864	984.22	1219.2	1182.03	1660.8	1521.64
ΔE	MLR	35.71	35.54	29.62	29.70	30.35	30.56	33.13	33
	PLS	35.71	35.57	29.62	29.69	30.35	30.65	33.13	32.9
	PCR	35.71	35.59	29.62	29.73	30.35	30.67	33.13	32.82

* PLS partial least squares, MLR multiple linear regression, and PCR principal component regression; M measurement, and P prediction

Conclusion

This study was conducted to measure and predict the color change and vitamin C content using electronic nose data for orange powder prepared with convective-infrared, convective, normal atmospheric vacuum, and atmospheric control vacuum dryers using ANN, PCA, PLS, PCR, and MLR. The highest and lowest amount of measured color change was observed in convective dryer and atmospheric control vacuum dryer, respectively. Also, the highest and lowest measured vitamin C was observed in convective-infrared dryer and atmospheric control vacuum dryer, respectively. Consequently, the atmospheric control vacuum dryer leads to the greatest decline in quality, specifically in terms of odor and vitamin C, while the convective dryer results in the most significant alteration in color of the processed orange powder. Therefore, the best dryer to maintain the quality of the orange powder is the convective-infrared dryer. The accuracy of the PCA and ANN methods in identifying accuracy of the four types of dryers used in the preparation of orange powder was 88% and 97%, respectively. The MLR model is the best model for predicting the color change and vitamin C of orange powder using the electronic nose data. Therefore, it can be concluded that the electronic nose can predict the amount of vitamin C and the color change

index of dried orange powder utilizing the signals of the electronic nose system.

In this study, in order to reduce the amount of damage in the processing of orange, a non-destructive solution was presented to qualitatively monitor the quality characteristics of orange powder. An electronic nose was used for rapid and early detection of nutritional value of orange powder to evaluate the quality of product and the effect of drying process on the vitamin C content. Therefore, it is suggested that the following should be investigated in future research:

1- Chemical evaluation of powder quality traits during the processing steps.

2- Chemical evaluation of the effect of drying process on dehumidification kinetics.

3- Microscopic evaluation of the development of drying and the destruction of orange tissue during drying.

4- Using other types of sensors and comparing their performance with the performance of MOS types.

Acknowledgment

The authors would like to thank the Bu-Ali Sina University for financial support of this research.

Conflict of Interest: The authors declare no competing interests.

Author Contributions

M. Roshan Moghadam: Methodology, Data acquisition, Data pre and post processing, Statistical analysis, Software services, Numerical/computer simulation, Text mining.

R. Amiri Chayjan: Supervision, Conceptualization, Methodology, Technical advice, Data acquisition, Data pre and post processing, Software services, Validation, Visualization, Text mining, Review and editing services.

N. Aghili Nategh: Methodology, Data pre and post processing, Statistical analysis, Numerical/computer simulation, Text mining, Review and editing services.

References

1. Adibzadeh, A., Dizaji, H. Z., & Aghilinategh, N. (2020). Feasibility of Detecting Sugarcane Varieties by Electronic Nose Technique in Sugarcane Syrup. *Iranian Journal of Biosystem Engineering, 51*(1), 1-10. (in Persian). https://doi.org/10.22059/IJBSE.2019.287027.665209
2. Agarwal, A., Shaharyar, A., Kumar, A., Bhat, M. S., & Mishra, M. (2015). Scurvy in pediatric age group–a disease often forgotten? *Journal of Clinical Orthopedics and Trauma*, *6*(2), 101-107. https://doi.org/10.1016/j.jcot.2014.12.003
3. Aghilinategh, N., Dalvand, M. J., & Anvar, A. (2020). Detection of ripeness grades of berries using an electronic nose. *Food Science and Nutrition, Wiley 8*(9), 4919-4928. https://doi.org/10.1002/fsn3.1788
4. Ahmadi Chenarbon, H., Minaei, S., Bassiri, A., Almassi, M., Arabhosseini, A., & Motevali, M. (2012). Effect of drying on the color of St. John's wort (*Hypericum perforatum* L.) leaves. *International Journal of Food Engineering, 8(4), 1-12*. https://doi.org/10.1515/1556-3758.2545
5. Ahmadi, G. M., & Chayjan, R. A. (2017). Optimization of hazelnut kernel drying in an inferared dryer with microwave pretreatment using response surface metodology. *Iranian Journal of Food Science and Technology*, *14*(64), 165-178. https://fsct.modares.ac.ir/article_25154.html
6. Amiri Chayjan, R., & Fealekari, M. (2017). Optimization of mooseer (A. *hirtifolium Boiss.*) dehydration under infrared conditions. *ACTA Scientiarum Polonorum Technologia Alimentaria 16*(2), 157-170. https://doi.org/10.17306/J.AFS.2017.0471
7. Ashebir, D., Jezik, K., Weingartemann, H., & Gretzmacher, R. (2009). Change in color and other fruit quality characteristics of tomato cultivars after hot-air drying at low final-moisture content. *International Journal of Food Sciences and Nutrition*, *60*(7), 308-315. https://doi.org/10.1080/09637480903114128

8. Bal, L. M., Kar, A., Satya, S., & Naik, S. N. (2011). Kinetics of color change of bamboo shoot slices during microwave drying. *International Journal of Food Science & Technology, 46*(4), 827-833. https://doi.org/10.1111/j.1365-2621.2011.02553.x
9. Chen, D., Xing, B., Yi, H., Li, Y., Zheng, B., Wang, Y., & Shao, Q. (2020). Effects of different drying methods on appearance, microstructure, bioactive compounds and aroma compounds of saffron (*Crocus sativus* L.). *LWT Food Science, 120,* 108913. https://doi.org/10.1016/j.lwt.2019.108913
10. Dong, W., Hu, R., Long, Y., Li, H., Zhang, Y., Zhu, K., & Chu, Z. (2019). Comparative evaluation of the volatile profiles and taste properties of roasted coffee beans as affected by drying method and detected by electronic nose, electronic tongue, and HS-SPME-GC-MS. *Food Chemistry, 272*, 723-731. https://doi.org/10.1016/j.foodchem.2018.08.068
11. Drewnowski, A. (2010) The Nutrient Rich Foods Index helps to identify healthy, affordable foods. *The American journal of Clinical Nutrition, 914*, 1095-1101. https://doi.org/10.3945/ajcn.2010.28450D
12. Fathabadi, M., Tabatabaekoloor, R., & Motevali, A. (2019). Modeling and comparison of color changes and shrinkage of thin layer drying of red beetroot in different dryers. *Journal of Food Science and Technology, 16*(95), 127-142. https://doi.org/10.29252/fsct.16.95.11
13. Finley, J. W., & Klurfeld, D. M. (2013). The USDA-Agricultural Research Service (ARS) program in dietary surveillance and food composition. *Food Science, 2*, 157-164. https://doi.org/10.1016/j.profoo.2013.04.023
14. Ghasemi, A., & Chayjan, R. A. (2019). Numerical simulation of vitamin C degradation during dehydration process of fresh tomatoes. *Journal of Food Process Engineering, 42*(6), 13189. https://doi.org/10.1111/jfpe.13189
15. Guclu, G., Keser, D., Kelebek, H., Keskin, M., Sekerli, Y. E., Soysal, Y., & Selli, S. (2020). Impact of production and drying methods on the volatile and phenolic characteristics of fresh and powdered sweet red peppers. *Food Chemistry, 338*, 128129. https://doi.org/10.1016/j.foodchem.2020.128129
16. Hansen, P. M., & Schjoerring, J. K. (2003). Reflectance measurement of canopy biomass and nitrogen status in wheat crops using normalized difference vegetation indices and partial least squares regression. *Remote Sensing of Environment, 86*(4), 542-553. https://doi.org/10.1016/S0034-4257(03)00131-7
17. Heidarbeigi, K., Mohtasebi, S. S., Foroughirad, A., Ghasemi-Varnamkhasti, M., Rafiee, S., & Rezaei, K. (2015). Detection of adulteration in saffron samples using electronic nose. *International Journal of Food Properties, 18*(7), 1391-1401. https://doi.org/10.1080/10942912.2014.915850
18. Karaaslan, S. N., & Erdem, T. (2014). Mathematical Modelling of Orange Slices during Microwave, Convection, Combined Microwave and Convection Drying. *Turkish Journal of Agricultural and Natural Sciences*, *1*(2), 143-149. https://dergipark.org.tr/en/download/article-file/142069
19. Karaaslan, S. N., & Tunçer I. K. (2008). Development of a drying model for combined microwave- fan-assisted convection drying of spinach. *Biosyst Engineering*, *100*(1), 44-52. https://doi.org/10.1016/j.biosystemseng.2007.12.012
20. Khafajeh, H., Banakar, A., Ghobadian, B., & Motevali, A. (2013). Drying of Orange Slices in CHP Dryer. *Advances in Environmental Biology, 7*(9), 2326-2331. https://www.researchgate.net/publication/287330245_Drying_of_orange_slices_in_CHP_dryer
21. Kiani, S., Minaei, S., & Ghasemi-Varnamkhasti, M. (2016). A portable electronic nose as an expert system for aroma-based classification of saffron. Chemometrics and Intelligent Laboratory *Systems*, *156*, 148-156. https://doi.org/10.1016/j.chemolab.2016.05.013
22. Kiani, S., Minaei, S., & Ghasemi-Varnamkhasti, M. (2018). Real-time aroma monitoring of

mint (*Mentha spicata* L.) leaves during the drying process using electronic nose system. *Measurement, 124*, 447-452. https://doi.org/10.1016/j.measurement.2018.03.033
23. Kulapichitr, F., Borompichaichartkul, C., Suppavorasatit, I., & Cadwallader, K. R. (2019). Impact of drying process on chemical composition and key aroma components of Arabica coffee. *Food Chemistry 291*(1), 49-58. https://doi.org/10.1016/j.foodchem.2019.03.152
24. Lemus-Mondaca, R., Ah-Hen, K., Vega-Gálvez, A., Honores, C., & Moraga, N. O. (2017). Stevia rebaudiana leaves: effect of drying process temperature on bioactive components, antioxidant capacity and natural sweeteners. *Plant Foods for Human Nutrition, 71*(1), 49-56. https://doi.org/10.1007/s11130-015-0524-3
25. Li, J., Li, Z., Li, L., Song, C., Raghavan, G., & He, F. (2020). Microwave drying of balsam pear with online aroma detection and control. *Journal of Food Engineering, 288*, 110139. https://doi.org/10.1016/j.jfoodeng.2020.110139
26. Melucci, D., Bendini, A., Tesini, F., Barbieri, S., Zappi, A., Vichi, S., Conte, L., & Toschi, T. G. (2016). Rapid direct analysis to discriminate geographic origin of extra virgin olive oils by flash gas chromatography electronic nose and chemometrics. *Food Chemistry 204*(1), 263-273. https://doi.org/10.1016/j.foodchem.2016.02.131
27. Nouri, B., Mohtasebi, S. S., & Rafiee, S. (2020). Quality detection of pomegranate fruit infected with fungal disease. *International Journal of Food Properties, 23*(1), 9-21. https://doi.org/10.1080/10942912.2019.1705851
28. Ni, H., Jiang, Q. X., Zhang, T., Huang, G. L., Li, L. J., & Chen, F. (2020). Characterization of the aroma of an instant white tea dried by freeze drying. *Molecules, 25*(16), 3628. https://doi.org/10.3390/molecules25163628
29. Otálora, M. C., Carriazo, J. G., Iturriaga, L., Nazareno, M. A., & Osorio, C. (2015). Microencapsulation of betalains obtained from cactus fruit (*Opuntia ficus-indica*) by spray drying using cactus cladode mucilage and maltodextrin as encapsulating agents. *Food Chemistry 187*(15), 174-181. https://doi.org/10.1016/j.foodchem.2015.04.090
30. Patel, H. K. (2014). *The Electronic Nose: Artificial Olfaction Technology*. Springer. https://link.springer.com/book/10.1007/978-81-322-1548-6
31. Peris, M., & Escuder-Gilabert, L. A. (2009). A 21st century technique for food control: electronic noses. *Analytica Chimica Acta, 638*(1), 1-15. https://doi.org/10.1016/j.aca.2009.02.009
32. Qin, L., Gao, J. X., Xue, J., Chen, D., Lin, S. Y., Dong, X. P., & Zhu, B. W. (2020). Changes in aroma profile of shiitake mushroom (*Lentinus edodes*) during different stages of hot air drying. *Foods, 9*, 444. https://doi.org/10.3390/foods9040444
33. Rasekh, M., Karami, H., Wilson, A. D., & Gancarz, M. (2021). Performance analysis of MAU-9 electronic-nose MOS sensor array components and ANN classification methods for discrimination of herb and fruit essential oils. *Chemosensors, 9*(9), 243. https://doi.org/10.3390/chemosensors9090243
34. Sanaeifar, A., Mohtesabi, S., Ghasemi Varnamekhati, M., & Ahmadi, H. (2015). Design, manufacture, and performance evaluation of an olfactory machine based on metal oxide semiconductor (MOS) sensors for monitoring banana ripening. *Journal of Agricultural Machinery, 5*(1), 111-121. (in Persian). https://doi.org/10.22067/jam.v5i1.27159
35. Sanaeifar, A., Mohtasebi, S., Ghasemi-Varnamkhasti, M., & Ahmadi, H. (2016). Application of MOS based electronic nose for the prediction of banana quality properties. *Measurement, 82*, 105-114. https://doi.org/10.1016/j.measurement.2015.12.041
36. Sanaeifar, A., ZakiDizaji, H., & Jafari, A. (2017). Guardia MDL. Early detection of contamination and defect in foodstuffs by electronic nose. A review. *TrAC Trends in Analytical Chemistry, 97*, 257-271. https://doi.org/10.1016/j.trac.2017.09.014
37. Sanchez-Reinoso, Z., Osorio, C., & Herrera, A. (2017). Effect of microencapsulation by spray

drying on cocoa aroma compounds and physicochemical characterization of microencapsulates. *Powder Technology, 318*, 110-119. https://doi.org/10.1016/j.powtec.2017.05.040

38. Shi, X. F., Chu, J. Z., Zhang, Y. F., Liu, C. Q., & Yao, X. Q. (2017). Nutritional and active in gradients of medicinal chrysanthemum flower heads affected by different drying methods. *Industrial Crops and Products, 104*(1), 45-51. https://doi.org/10.1016/j.indcrop.2017.04.021
39. Song, J., Chen, Q., Bi, J., Meng, X., Wu, X., Qiao, Y., & Lyu, Y. (2020). GC/MS coupled with MOS e-nose and flash GC e-nose for volatile characterization of Chinese jujubes as affected by different drying methods. *Food Chemistry, 331*(30), 127-201. https://doi.org/10.1016/j.foodchem.2020.127201
40. Spínola, V., Llorent-Martínez, E. J., & Castilho, P. C. (2014). Determination of vitamin C in foods: Current state of method validation. *Journal of Chromatography, 1369*, 2-17. https://doi.org/10.1016/j.chroma.2014.09.087
41. Wang, J., Lu, Z., Chen, X., & Zhang, H. (2016). Modeling of Color Changes of Loquat Fruit during Drying. *Food Science, 37*(21), 104-108.
42. Yang, W., Yu, J., Pei, F., Mariga, A. M., Ma, N., Fang, Y., & Hu, Q. (2016). Effect of hot air drying on volatile compounds of Flammulina velutipes detected by HS-SPME–GC–MS and electronic nose. *Food Chemistry, 196*(1), 860-866. https://doi.org/10.1016/j.foodchem.2015.09.097
43. Zhang, H., Wang, J., Ye, S., & Chang, M. (2012). Application of electronic nose and statistical analysis to predict quality indices of peach. *Food Bioprocess Technology, 5*, 65-72. https://doi.org/10.1007/s11947-009-0295-7
44. Zhang, H., Wang, J., & Ye, S. (2008). Predictions of acidity, soluble solids and firmness of pear using electronic nose technique. *Journal of Food Engineering, 86*, 370-378. https://doi.org/10.1016/j.jfoodeng.2007.08.026

نشریه ماشین‌های کشاورزی
https://jame.um.ac.ir

مقاله پژوهشی

جلد ۱۶، شماره ۳، پاییز ۱۴۰۵، ص ۴۸۶-۴۶۹

پیش‌بینی ویتامین C و تغییر رنگ پودر پرتقال در چهار خشک‌کن مختلف با استفاده از بینی الکترونیک

مازیار روشن مقدم[۱]، رضا امیری چایجان[۱*]، ناهید عقیلی ناطق[۲]

تاریخ دریافت: ۱۴۰۳/۱۱/۱۹
تاریخ پذیرش: ۱۴۰۴/۰۲/۰۹

چکیده

در این تحقیق، مقدار ویتامین C، ترکیبات معطر و تغییر رنگ پودر پرتقال با استفاده از روش‌های شیمیایی، دستگاه بویایی و اسکنر در چهار خشک‌کن در دمای $45\ ^{\circ}C$ درجه سانتی‌گراد اندازه‌گیری شد. این دستگاه‌های خشک‌کن شامل خلاء اتمسفر معمولی، خلاء کنترل اتمسفر، همرفتی و همرفتی-مادون قرمز بودند. بیشترین پاسخ حسگرها به ترکیبات معطر در خشک‌کن‌های همرفتی و کمترین پاسخ در خشک‌کن‌های خلاء کنترل و خلاء معمولی مشاهده شد. دو مؤلفه اصلی تحلیل مؤلفه‌های اصلی (PCA) ۸۸٪ از واریانس داده‌ها را توضیح دادند. ساختار شبکه عصبی مصنوعی (ANN) ۴-۵-۸ بود. علاوه بر این، بر اساس نمودارهای بارگذاری مدل‌های حداقل مربعات جزئی (PLS) و رگرسیون مؤلفه‌های اصلی (PCR)، حسگرهای MQ3 و MQ6 بهترین حسگرها برای پیش‌بینی میزان ویتامین C و تغییر رنگ پودر پرتقال بودند. حسگر MQ135 نیز به دلیل دقت پایین و کاهش هزینه، می‌تواند از مجموعه حسگرهای بینی الکترونیکی حذف شود. رگرسیون خطی چندگانه (MLR)، در مقایسه با مدل‌های PCR وPLS، دقیق‌تر عمل کرد، یعنی $R^2=0.83$ و RMSE= 0.144 برای پیش‌بینی ویتامین C و $R^2=0.94$ و RMSE= 0.68 برای پیش‌بینی تغییر رنگ محاسبه شدند. بیشترین و کمترین مقادیر تغییر رنگ اندازه‌گیری‌شده به‌ترتیب در خشک‌کن همرفتی و خشک‌کن خلاء کنترل اتمسفری مشاهده شد. همچنین، بیشترین و کمترین ویتامین C اندازه‌گیری‌شده به‌ترتیب در خشک‌کن همرفتی-مادون قرمز و خشک‌کن خلاء کنترل اتمسفری مشاهده شد. بهترین خشک‌کن برای حفظ کیفیت پودر پرتقال، خشک‌کن همرفتی-مادون قرمز بود. نتایج این مقاله نشان داد که داده‌های به‌دست‌آمده از دستگاه بویایی قادر به پیش‌بینی تغییر رنگ و ویتامین C پودر پرتقال است. همچنین، می‌توان از دستگاه بویایی برای شناسایی و طبقه‌بندی نوع خشک‌کن مورد استفاده برای تهیه پودر پرتقال با کمترین زمان و هزینه، بدون تخریب نمونه، و تعیین بهترین خشک‌کن برای تهیه پودر پرتقال استفاده کرد.

واژه‌های کلیدی: بینی الکترونیک، پودر پرتقال، تغییر رنگ، خشک‌کن، ویتامین C

۱- گروه مهندسی بیوسیستم، دانشکده کشاورزی، دانشگاه بوعلی سینا، همدان، ایران
۲- گروه مهندسی ماشین‌های کشاورزی، دانشکده کشاورزی سنقر، دانشگاه رازی، کرمانشاه، ایران
(*- نویسنده مسئول: Email: amirireza@basu.ac.ir)

https://doi.org/10.22067/jam.2025.92037.1340

Journal of Agricultural Machinery

Homepage: https://jame.um.ac.ir

Research Article
Vol. 16, No. 3, 2026, p. 487-506

A Weighted Group Learning Model for Classification of Grape Leaf Disease Using Image Processing and Machine Learning

M. Najafabadiha[1], D. Mohammad Zamani[1*], M. Gholami Par-Shokohi[2]

1- Department of Mechanization Engineering, Tak.C., Islamic Azad University, Takestan, Iran
2- Department of Mechanical Engineering, ShQ.C., Islamic Azad University, Shahr-e Qods, Iran
(*- Corresponding Author Email: dr.dmzamani@gmail.com)

Received: 28 February 2025
Revised: 23 April 2025
Accepted: 29 April 2025
Available Online: 29 September 2025

How to cite this article:
Najafabadiha, M., Mohammad Zamani, D., & Gholami Par-Shokohi, M. (2026). A Weighted Group Learning Model for Classification of Grape Leaf Disease Using Image Processing and Machine Learning. *Journal of Agricultural Machinery*, *16*(3), 487-506. https://doi.org/10.22067/jam.2025.92388.1347

Abstract

This study proposes a novel method for identifying grape leaf diseases through RGB image analysis combined with weighted group decision-making. The investigation focused on five disease types, *Black Measles*, *Black Rot*, *Leaf Blight*, *Powdery Mildew*, and *Downy Mildew*, along with healthy leaves. Three machine learning classifiers, namely support vector machine (SVM), random forest (RF), and k-nearest neighbor (k-NN), were employed individually and in a weighted ensemble. Each classifier was assigned a weight based on its accuracy, and the final disease classification was determined using a majority voting strategy. To determine the most discriminative features related to texture, color, and shape, the Relief feature selection algorithm was applied, which identified the top five effective features in diagnosing grape leaf diseases. Experimental results indicated that the classification accuracies of SVM, RF, and k-NN were 88.33%, 80.08%, and 75%, respectively. Furthermore, the proposed weighted group decision-making approach improved the overall classification performance, achieving an accuracy of 91.67%.

Keywords: Feature selection, Grape disease, Group decision making, Image processing, Majority voting

Introduction

Accurate and timely diagnosis of plant diseases is essential for sustainable and efficient agriculture, as well as to avoid unnecessary waste of financial resources. Although some plant diseases do not exhibit visible symptoms, advanced analysis methods are crucial for such conditions. However, most plant diseases exhibit visible symptoms, and the current standard technique for diagnosis is for an experienced plant pathologist to visually observe infected plant leaves. Diagnosing plant diseases accurately requires excellent observation skills, which can pose a challenge even for experienced plant pathologists as the effects of climate change and the spread of diseases to new areas create an extremely diverse range of plants (Javidan, Ampatzidis, Banakar, Asefpour Vakilian, & Rahnama, 2024). A smart system that can automatically detect plant diseases accurately is vital for farmers, especially those without crop support and plant pathology infrastructure. Disease diagnosis methods can be divided into direct and indirect methods. Direct methods include serological and molecular methods, while indirect methods include methods based on biological markers and characteristics of plants, such as imaging techniques and spectroscopy-based methods (Abdulridha,

Authors retain the copyright. This is an open access article distributed under Creative Commons Attribution 4.0 International License (CC BY 4.0).

https://doi.org/10.22067/jam.2025.92388.1347

Ampatzidis, Kakarla, & Roberts, 2020). Recent advances in agricultural technology have increased the demand for the development of non-destructive methods of disease detection. Advancements in computer technology have also improved crop growth monitoring using image processing. Automatic disease detection through machine vision technology has many benefits, such as accuracy, non-destructiveness, and improved performance. The application of machine vision technology will increase the productivity of the agricultural industry by reducing labor costs, and advances in artificial intelligence technology are paving the way for the development of automated systems that can provide faster and more accurate results in diagnosing diseases.

Recently, both traditional machine learning approaches and bio-inspired meta-heuristic algorithms have been explored for plant disease detection and classification, with the latter proving particularly effective in handling complex real-world issues (Zhou, Gao, Zhang, & Lou, 2020). As an example, Jaisakthi, Mirunalini, & Thenmozhi (2019) introduced an automated method for diagnosing three grape diseases—Black Rot, Black Measles, and Leaf Blight. Their system first isolated the affected leaf regions and then applied a support vector machine (SVM) to classify diseased and healthy leaves, reaching an accuracy rate of 87%.

Cruz *et al.* (2019) explored the effectiveness of six different neural network models for analyzing digital images of grapevine yellowing disease. Their findings indicated that deep learning significantly enhances disease prediction compared to traditional approaches and even human experts. Specifically, models using deep learning achieved prediction improvements of 97.35% over a baseline system without deep learning and 88.22% over expert assessments.

Hasan *et al.* (2020) focused on applying a convolutional neural network (CNN) to identify and classify common grapevine leaf diseases. The CNN framework incorporated data input, feature extraction, and classification stages. Following training on the dataset, the model reached an accuracy of 91.37%.

Javidan, Banakar, Vakilian, and Ampatzidis (2023a) proposed an image processing approach combined with a multi-class SVM to detect grape leaf diseases such as Black measles, Black rot, and Leaf blight. Disease symptoms were segmented via K-means clustering, and features were extracted using RGB, HSV, and Lab color spaces. Using PCA for feature reduction, the method achieved 98.97% accuracy, outperforming CNN (86.82%) and GoogleNet (94.05%) while also reducing processing time.

Javidan *et al.* (2023b) proposed a weighted majority voting ensemble approach to classify RGB images for detecting various tomato leaf diseases. Color, textural, and shape features were extracted, and the relief method was applied for feature selection. Six machine learning classifiers were used, achieving up to 91.53% accuracy, with ensemble methods further improving classification performance.

Javidan, Banakar, Vakilian, Ampatzidis, and Rahnama (2024) proposed an approach using RGB and hyperspectral imaging to detect four fungal diseases in tomatoes over 11 days post-infection. Machine learning models trained on statistical, texture, and shape features achieved up to 87% accuracy with RGB and 98% with hyperspectral imaging. Spectral analysis differentiated infections as early as day 3, highlighting key wavelength features for disease detection.

Talaat, Shams, Gamel, and ZainEldin. (2025) introduced a plant disease detection framework named DeepLeaf for recognizing four prevalent grapevine diseases. The system combines preprocessing steps, feature extraction, and an optimized CNN-based classification architecture, attaining 99.7% accuracy on the Plant Village dataset. Such performance underscores its promise for scalable and effective monitoring of plant health.

Raghuram & Borah (2025) proposed an advanced plant disease detection system using a hybrid learning model (HLM) with deep

reinforcement learning and transfer learning (DRL-TL). High-resolution plant leaf images are preprocessed using an enhancement algorithm before feature extraction in a three-dimensional manner. The model, utilizing MobileNetV2, demonstrated superior accuracy and robustness in detecting plant diseases across species and environmental conditions.

Shafik, Tufail, Liyanage De Silva, and Awg Haji Mohd Apong (2025) introduced a hybrid Inception-Xception (IX) CNN model that integrates inception and depth-separable convolution layers to enhance feature extraction while reducing complexity and overfitting. The model powers a real-time AI application for disease detection, available on MATLAB, Android, and Servlet. Evaluated on six datasets, it achieved near-perfect accuracy, with Plant Village, Plant Doc, and Turkey Disease datasets reaching 100% accuracy.

Sahabi & Baradaran-Motie (2025) analyzed RGB and NIR images from five randomly selected fields over two years to extract and evaluate spectral vegetation indices for plant disease detection. Two SVM classifiers with RBF kernels were applied separately to NIR and RGB images, achieving test-phase accuracies of 82.3% and 91.4%, respectively. Field evaluation using the confusion matrix method yielded classification accuracies of 75.6% for NIR and 80.3% for RGB images.

Javidan, Ampatzidis, Banakar, Asefpour Vakilian, and Rahnama (2025) evaluated six deep learning models for classifying seven tomato leaf conditions, including six diseases and healthy leaves. MobileNet achieved the highest individual accuracy (96%), while ensemble methods significantly improved performance, with simple majority voting reaching 99.5% and weighted majority voting achieving 100%. These findings highlight the potential of deep ensemble learning for achieving accurate diagnosis of tomato diseases. Developing reliable and precise machine learning models for plant disease detection remains a challenging area, primarily due to the limited availability of large, high-quality datasets needed for training and evaluation. Identifying the optimal number of clusters further complicates the process. Current machine learning approaches often fall short in accuracy and reliability, particularly when they do not isolate the diseased regions from the leaves, leading to delays in diagnosis. Moreover, distinguishing plants affected by multiple diseases or diseases with similar early-stage symptoms poses a significant challenge. Therefore, an effective feature extraction system is essential for precise disease identification and classification, especially when comparing diseases with overlapping or similar symptoms (Barbedo, 2016; 2018).

Selecting the most effective features from plant leaf diseases to diagnose the type of disease greatly increases ML's diagnostic capability. It is crucial to use feature selection methods and compare them to find the best method for selecting features that challenge diseases. Choosing the most efficient ML classification method(s) that can distinguish the performance of ML-based classifiers in terms of processing time and accuracy in disease diagnosis and classification is important. The classifier should be highly accurate in diagnosing the disease in a short time. Group decision making is a promising approach to classifying diseases, particularly for those with a large number of classes. Weighted group decision making, a subgroup of group decision making, assigns higher weights to classifiers with high accuracy, ensuring that the decision-making is based on the most reliable classifier. Weighted group decision making can significantly improve the accuracy and validity of the diagnosis of plant diseases compared to conventional classification methods. Combining multiple classifiers enhances overall classification accuracy, with majority voting providing more reliable plant disease diagnoses. Collaborative decision-making offers an effective approach for handling diseases with numerous classes, simplifying the problem, enabling scalability, and reducing the total time needed for diagnosis.

Recent progress in machine learning (ML) and computer vision has led to the

development of automated models for plant disease classification. Despite these advances, many existing approaches face challenges such as reduced accuracy under varying environmental conditions, difficulty in differentiating visually similar diseases, and dependence on a single classifier that may not perform consistently across diverse datasets. To overcome these issues, this study introduces a weighted majority voting group learning approach for classifying grape leaf diseases using RGB images. The goal is to improve both accuracy and robustness by combining the strengths of multiple ML models. The research focuses on five grapevine diseases, Black Measles, Black Rot, Leaf Blight, Powdery Mildew, and Downy Mildew, along with healthy samples. Rather than relying on a single algorithm, the method employs three well-established classifiers: support vector machine (SVM), random forest (RF), and k-nearest neighbor (k-NN).

A key innovation of this approach is the integration of a weighted majority voting scheme to combine the predictions of individual classifiers. In traditional majority voting, each classifier contributes equally to the final decision, which may lead to suboptimal results if one model significantly outperforms the others. To overcome this limitation, our method assigns higher weights to classifiers that demonstrate superior accuracy, ensuring that more reliable predictions have a greater influence on the final classification outcome. This weighting process is proportional to the classification performance of each model, meaning that the classifiers with the highest accuracy are given more importance when determining the final disease classification.

By implementing this weighted group decision-making approach, the overall classification accuracy is improved, as the weaknesses of one classifier can be compensated by the strengths of another. This method not only enhances the robustness of disease detection under varying environmental conditions but also provides a scalable and efficient solution for real-world vineyard monitoring. The findings of this study contribute to the advancement of automated plant disease detection systems, offering a practical alternative to traditional diagnostic methods while improving decision-making for vineyard management.

Materials and Methods

Proposed algorithm to diagnose and classify grape leaf diseases

The proposed method consists of several steps to detect and classify diseased and healthy grapevine leaves, combining weighted machine learning methods to achieve high classification accuracy. These steps are: (1) database creation, (2) image processing including steps: background removal and image segmentation to detect disease symptoms using k-means clustering, (3) extraction of texture, color features, and shape of images, (4) feature selection using relief algorithm, (5) classification based on support vector machine, random forest, and k-nearest neighbor, (6) combination based on weighting of classifications, and (7) final classification of diseases. The proposed method is described as follow.

Creating a database of images of infected leaves

Creating reliable image classifiers for plant disease detection depends on access to large, validated datasets of both healthy and diseased plants, which were previously scarce. In the past, researchers often had to compile their own datasets, as smaller publicly available datasets were limited. The situation has improved with the availability of larger datasets, enabling the development of more advanced image classifiers for plant disease diagnosis (Hughes, David, & Salathe, 2015).

This study utilized data collected from vineyards in Qazvin province, Iran, consisting of six categories: one representing healthy grape leaves and five representing diseased leaves *Black Measles, Black Rot, Leaf Blight, Powdery Mildew,* and *Downy Mildew*.

Disease name	Disease image	Disease symptoms
Black Measles		Initially, interveinal yellow or reddish-brown streaks appear on the leaves. Over time, dark brown or black necrotic spots develop, often surrounded by a yellow halo. In severe cases, the leaves dry out, and internal wood discoloration may also occur.
Black Rot		Small, circular brown spots with dark edges form on the leaves. As the disease progresses, these spots enlarge, and black fungal fruiting structures (*pycnidia*) appear. Infected leaves may curl and dry out, reducing the plant's ability to photosynthesize.
Leaf Blight		Irregular brown or reddish lesions appear on the leaves, often with a water-soaked appearance. The affected tissue may become brittle and fall out, creating a shot-hole effect. In severe cases, premature leaf drop weakens the vine.
Powdery Mildew		A white or grayish powdery fungal growth appears on the surface of the leaves. Infected leaves may become distorted or curled, and as the infection worsens, the fungal coating thickens, reducing photosynthesis and overall plant health.
Downy Mildew		Yellowish, oily spots develop on the upper leaf surface. Over time, a white, cotton-like fungal growth appears on the underside of the leaves, especially in humid conditions. Severely affected leaves turn brown and fall prematurely, leading to reduced yield and weakened vines.

Fig. 1. Image of symptoms and descriptions of diseased and healthy leaves in this study

A total of 600 images were obtained, with an equal number of samples for each class. The photographs were taken under natural light using a Samsung A32 smartphone equipped with a 64-megapixel camera. For experimental purposes, the dataset was split into training and testing subsets, with 80% (480 images) allocated for training and 20% (120 images) reserved for evaluation. The proposed diagnostic framework was developed and executed on a Windows 10 platform with an Intel® Core™ i3-8130U processor (2.20–2.21 GHz) and 8 GB RAM, while MATLAB 2018 was used to implement the algorithm for grape leaf disease detection and classification. Figure 1 provides visual samples of the disease types considered in this research.

Image preprocessing

In order to remove noise, the images obtained from the previous step were smoothed using conventional methods such as Gaussian smoothing. In this technique, a Gaussian filter was applied to the image, allowing high-frequency noise to be reduced by averaging pixel values with their neighbors in a weighted manner. This ensured that sudden intensity variations were minimized while important edges and structures were preserved. After smoothing, the images were sent to the next step, where processing was performed, and the best feature was selected. Before extracting the disease features, two unsupervised learning techniques were applied to cluster the diseased samples, enabling their separation from healthy plant tissue. While automatic clustering through unsupervised methods has rarely been explored for plant disease diagnosis, this study made an effort to implement such an approach, following the direction of related research. The disease was separated from the leaves manually by assigning a number to the cluster. In Figure 2, the disease area was shown, which was also referred to as the region of interest (ROI) in clustering. Figure 3 illustrated the different stages of pre-processing and the diagnosis of the diseased area.

Feature extraction

To improve the performance of these classifiers, a key step is automatic feature learning through appropriate feature extraction algorithms and techniques. Shape, texture, and color features are commonly used for plant disease diagnosis, and the appropriate algorithm and technique for feature extraction should be selected. It can be challenging to determine the best feature among a set of features and to choose a good extraction technique. Common facts about the feature extraction process are listed below:

The appropriate set of features to use for plant disease diagnosis is dependent on the characteristics of the objects or diseases being detected. Some commonly used features include shape, texture, and color, which can be analyzed using a combination of algorithms, techniques, and descriptors. For texture analysis, the Gray-Level Co-Occurrence Matrix (GLCM) was used as a common technique, while features such as uniformity, entropy, energy, contrast, and correlation were utilized to represent texture patterns (Mohamadzamani, Sajadian, & Javidan, 2020). Color characteristics can be analyzed using color histogram and color co-occurrence matrix, which provide information about the visual characteristics of the object. Shape analysis can be performed by measuring characteristics of the object's contour such as orientation, area, eccentricity, and center. However, there may be limitations in the use of a single attribute type to define the object, and a combination of multiple features can improve the performance of a classification system.

This study employed a combination of three types of features: color, texture, and shape to classify damaged areas on leaves. For the color features, features including mean, maximum, standard deviation, median, and hue were extracted from the RGB, l*a*b, and HSV color space.

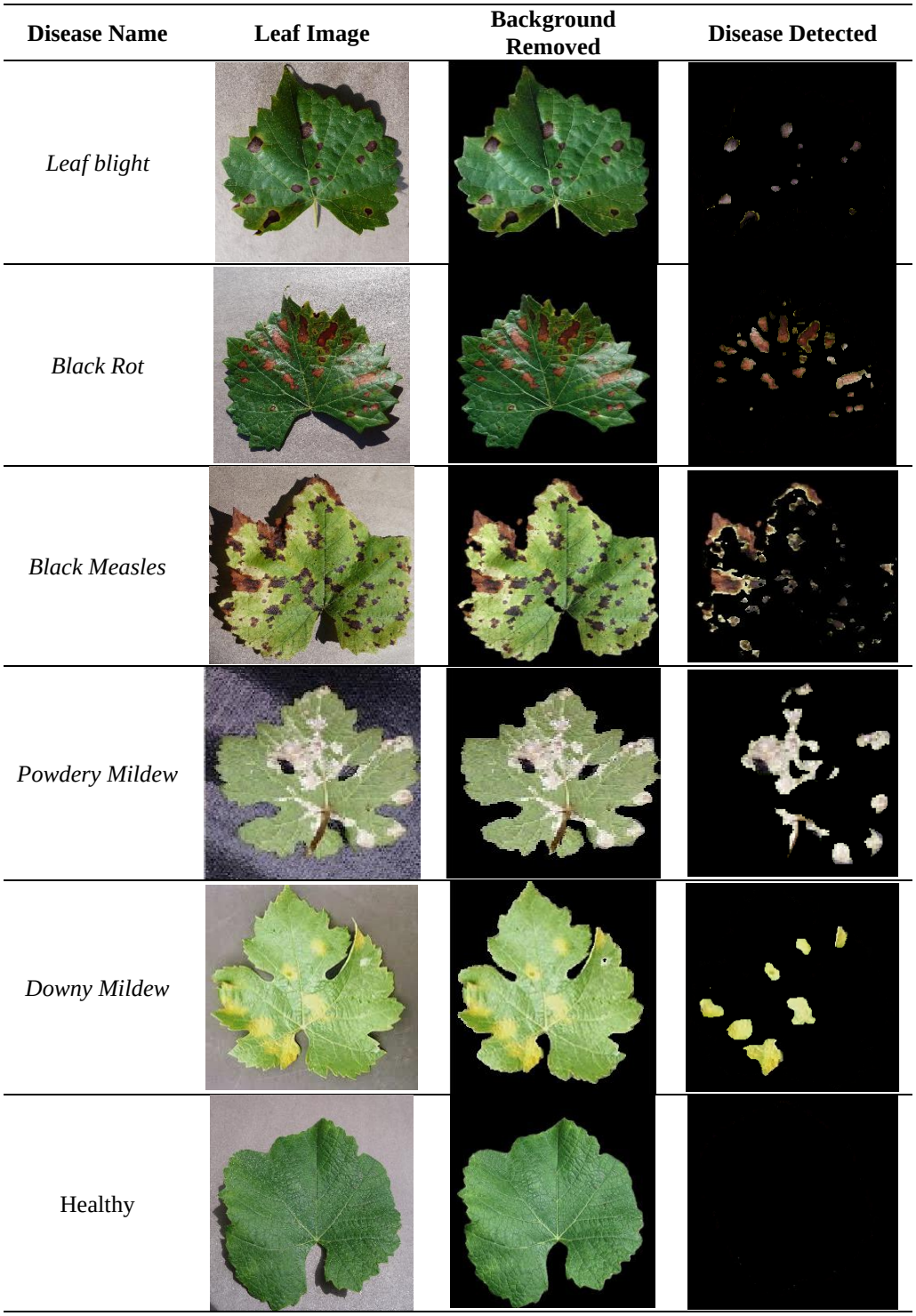

Fig. 2. Isolation of the leaf from the background and detection of the diseased area

Texture features were extracted using the GLCM technique, which extracts features such as contrast, correlation, energy, homogeneity, mean, standard deviation, entropy, variance, smoothness, kurtosis, and skewness. Shape features extracted included area, perimeter, number of objects, length of the major and minor axis of the points, and eccentricity

index. These steps were performed using the feature extraction module in MATLAB version 2018. By combining these features, it was anticipated that the accuracy of the classification system would improve.

Feature selection

At this stage, the Relief algorithm was applied to reduce computational complexity, minimize data dimensionality, and select the most relevant image features. The resulting features were then used as input for the subsequent stage, the intelligent classifier. Consequently, this approach enabled the extraction of the most significant and informative features for plant disease diagnosis in this study. The Relief algorithm was employed to decrease computational complexity, reduce the feature space, and identify the most informative attributes for image-based plant disease classification. The selected features from this stage were then used as input for the subsequent step, which involved an intelligent classifier aimed at improving system performance. In this way, the study was able to extract the most critical and effective features for diagnosing plant diseases (Mohamadzamani *et al.*, 2020).

Classification by machine learning

To classify grapevine leaf diseases, several machine learning algorithms, including k-NN, SVM, and RF, were employed. In a classification problem, the objective is to assign a label to each input sample. For instance, in grape leaf disease detection, the system must identify whether a given leaf image belongs to a healthy or infected class. Among the most common techniques, the k-NN algorithm assigns a label based on the majority class of the k closest neighbors, with its performance being highly dependent on the chosen value of k. Another widely applied method is SVM, which separates classes by constructing an optimal hyperplane in the feature space; its effectiveness is influenced by the type of kernel function selected. Similarly, the RF algorithm is a popular ensemble learning approach that builds multiple decision trees using randomly selected feature subsets, with its accuracy depending on the number of trees and feature selection strategy. For grape leaf disease classification, k-NN, SVM, and RF can all be applied, though their suitability ultimately depends on dataset characteristics, selected features, and evaluation metrics.

Weighted majority voting group learning

In the current study, the task of plant disease diagnosis requires a model that can provide accurate predictions. To achieve this goal, the strategy of group decision learning strategy is used, which integrates multiple learning models to achieve better results. Group decision learning allows for the integration of multiple learning models and the usage of weak models with relatively lower training costs, thereby reducing the need for large training sets. The proposed methodology leverages the combination of classifiers to enhance the performance of the final model, and the final prediction is provided by the category that receives the most votes according to the majority vote. Weighted voting is utilized to determine the impacts of each class on the final prediction, where the weight assigned to each class is typically proportional to its performance in the validation set. If some classifiers demonstrate higher classification accuracy, they will have more votes, leading to higher weights. This process is known as majority voting, and it can be used to achieve consistent results. The importance of the weight assigned to each class for successful classification cannot be overemphasized, and it is essential to link each learned classifier with a different weight based on its performance in the validation set. The proposed method includes three main stages: classification training, weight determination using the validation set, and the combination of individual classifier outputs considering their weights. Figure 3 demonstrates the different stages of diagnosis and classification of grape plant diseases by the weighted combination method incorporating group decision learning techniques.

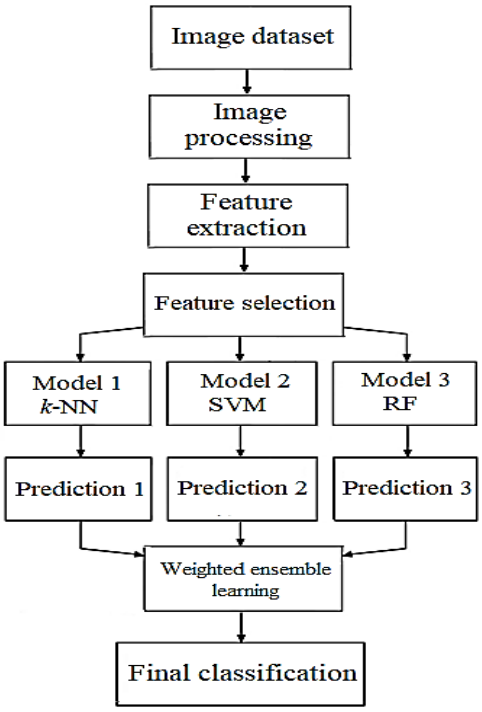

Fig. 3. Different stages of the proposed algorithm in the current research

Performance evaluation of the proposed method

The confusion matrix is an essential tool for evaluating the performance of classification models. In this study, model performance was assessed using classification accuracy along with Precision, Sensitivity, Specificity, and F-Measure, as defined in Equations (1)– (5). The optimized models were trained and validated using 5-fold cross-validation (CV), where the dataset is split into five subsets to ensure robust evaluation. Accuracy from the testing phase was recorded to measure each model's performance. This approach mitigates overfitting by using every data point for both training and validation, while also providing a more reliable estimate of model performance on unseen data. By systematically rotating the validation fold, 5-fold CV ensures consistency and improves the generalizability of the model.

$$Accuracy = \frac{(TP + TN)}{(TP + TN + FP + FN)} \quad (1)$$

$$Precision = \frac{TP}{TP + FP} \quad (2)$$

$$Sensitivity = \frac{TP}{TP + FN} \quad (3)$$

$$Specificity = \frac{TN}{TN + FP} \quad (4)$$

$$F - Measure = \frac{2 \times (Precision \times Sensitivity)}{(Precision + Sensitivity)} \quad (5)$$

Results and Discussion

The results of feature selection extracted in order to diagnose grape plant diseases

To enhance the effectiveness and classification performance of the proposed method, a total of 165 features were extracted from the leaf images, comprising 36 color, 117 textural, and 12 shape features. After selecting the most influential features for classification, the analysis revealed that combining these three feature types yielded the highest accuracy. This demonstrates that the method's performance relies on appropriately selecting and integrating the most discriminative features across different sets. The approach offers a robust and reliable solution for plant disease diagnosis by ensuring accurate

classification based on diverse feature sets. Individually, the classification accuracies were 65.15% for color features, 71.2% for textural features, and 60.31% for shape features, whereas the combined feature set achieved 83.33% accuracy using a random forest (RF) classifier. Table 1 lists the five most effective features for grape leaf disease diagnosis and classification.

Table 1- The results of the best and most important characteristics selected for the diagnosis of grape leaf diseases

Feature rank	1	2	3	4	5	Accuracy (%)
Color	Median (l*a*b) (b)	Max (l*a*b) (b)	Mean (HSV) (V)	Mean (l*a*b) (l)	Median (RGB) (B)	65.15
Texture	Standard Deviation (l*a*b) (b)	Entropy (l*a*b) (l)	Variance (l*a*b) (l)	Entropy (HSV) (H)	Standard Deviation (l*a*b) (l)	71.2
Shape	Area	Perimeter	Number of objects	Major axis length	Minor axis length	60.31
All Features	Skewness (HSV) (S)	Homogeneity (l*a*b) (b)	Correlation (l*a*b) (b)	Energy (RGB) (R)	Entropy (RGB) (R)	83.33

Table 1 presents a detailed overview of the key features used for diagnosing and classifying grape leaf diseases, divided into four categories: Color, Texture, Shape, and All Features combined. Each category represents different aspects of the leaf's visual characteristics that help identify disease symptoms.

Color features are critical for detecting various diseases as changes in leaf color often indicate the presence of infection. The most influential color features include the Median and Maximum values of the blue channel in the l*a*b color space, the Mean value of the V component in the HSV color model, and the Mean and Median values of the l and blue channels in the l*a*b and RGB spaces. These color-based features capture key shifts in the hue and brightness of the leaf, such as yellowing, browning, or discoloration from mildew or fungal infections. The use of multiple color spaces (l*a*b, HSV, and RGB) ensures that a broader range of color variations is captured, helping improve the model's sensitivity to diseases that manifest through color changes.

Texture features describe the surface patterns and spatial distributions of the leaf, providing insight into internal leaf damage that might not be visible through color alone. Features like Standard Deviation, Entropy, and Variance from both l*a*b and HSV color spaces measure the variation in pixel intensity and the randomness of color distribution. These texture features are valuable because many diseases cause changes in the surface texture of the leaf, such as spots, lesions, or mold growth. For example, the Entropy of the HSV hue channel reflects irregularities in color arrangement, and Standard Deviation measures how much the pixel values deviate, both of which are useful for identifying diseased leaves with uneven surface patterns.

Shape features refer to the geometric properties of the leaf, such as Area, Perimeter, Number of objects, and the lengths of the Major and Minor axes. Although shape features alone are not as discriminative as color and texture, they can still provide useful information, especially in cases where the leaf undergoes physical changes due to disease. For instance, a leaf may become deformed, curl, or have holes due to infection. These shape descriptors help capture such alterations and contribute to distinguishing diseased leaves from healthy ones.

The All-Features category combines color, texture, and shape characteristics to provide a comprehensive view of the leaf's health. The top-ranked features in this group, such as Skewness in the HSV color space, Homogeneity and Correlation in the l*a*b space, and energy and entropy metrics in RGB, highlight the effectiveness of using a

wide array of descriptors. By integrating multiple types of features, the model can account for a variety of disease symptoms, including subtle color variations, textural differences, and structural deformations, making it a more robust tool for grape leaf disease detection.

Classification results of grape plant diseases

For training the dataset, a combination of base classifiers was utilized, including k-NN, SVM, RF, and weighted majority group, after which the effective features were selected for all three groups (color, texture, and shape). The classification accuracies for the color features group were respectively 65.15%, 51.42%, 43.78%, and 75.41%, while for texture features, the classification accuracies were 20.71, 50.69, 50.57, and 80.50%, respectively. For shape features, the accuracies were 31.60, 50.70, 20.40, and 44.70%, respectively. The highest overall accuracy was achieved by integrating all three feature types within the weighted combination model. Figure 4 shows the confusion matrices for the three individual ML classifiers as well as the results of the weighted ensemble for grape leaf disease classification. While textural features had the most significant impact on diagnostic and classification accuracy, shape and color features, such as medium and middle attributes (Jaisakthi *et al.,* 2019), also contributed meaningfully. Additionally, the extracted features demonstrated similar performance across all models, highlighting that each feature type plays a distinct role in detection and classification. These results underscore the importance of combining multiple feature sets to achieve effective and reliable disease diagnosis.

Classification results by weighted combination algorithm

As shown in Table 2, the classification accuracies for the individual models were 88.33%, 80.08%, and 75%, respectively. Although these results are moderate, higher performance was achieved using the weighted majority voting approach, which reached an accuracy of 91.67%, outperforming all individual models. Figure 4 presents the confusion matrix for the classification of healthy and diseased grape leaves. In the matrix, each column corresponds to the predicted class, and each row represents the true class label, with the diagonal entries indicating correctly classified samples. The classification task involves six categories: *Black Measles, Black Rot, Leaf Blight, Powdery Mildew, Downy Mildew*, and healthy leaves. The results indicate a higher misclassification rate for *Downy Mildew*, likely due to its similar shape and color to other diseases. Severe discoloration in severe cases may also contribute to this misclassification. Weighted models, which minimize classification errors, can help solve this problem.

In addition to Downy Mildew, other misclassified diseases included *Black Measles* and *Black Rot*. Both are difficult to differentiate from other diseases visually, even for experts. However, unlike *Black Measles*, *Downy Mildew* spots do not have concentric areas and have a

Table 2- Classification results for the diagnosis of grape leaf diseases

No.	Classifier	Accuracy with color features (%)	Accuracy with textural features (%)	Accuracy with shape features (%)	Total accuracy (%)
1	Random Forest	65.15	71.20	60.31	88.33
2	Support Vector Machine (Linear)	51.42	69.50	50.70	80.08
3	k-Nearest Neighbors	43.78	57.50	40.20	75.00
4	Weighted Vote Majority Group	75.41	80.50	70.44	91.67

darker color than *Leaf Blight*. The distribution of these spots on the plant is more uniform, and the initial symptoms of the disease on the leaves are smooth, small, and dark-colored spots. In the case of *Black Rot* disease, the symptoms appear as burnt spots on the leaves, with no clear halo around the affected areas. The leaves become brown, wrinkled, and dry as the disease progresses. On the other hand, *Powdery Mildew* disease exhibits a high classification accuracy. The reason for this is the color difference in disease spots on the leaves of this plant. In *Powdery Mildew* disease, yellow spots (with a diameter of 2 to 10 mm) appear on the upper surface of young leaves, near the margins, and the fungal mass gradually develops on these spots as the disease progresses. The spots eventually form larger, grayish-white masses that cover the entire leaf, causing it to become deformed, dry, and eventually fall.

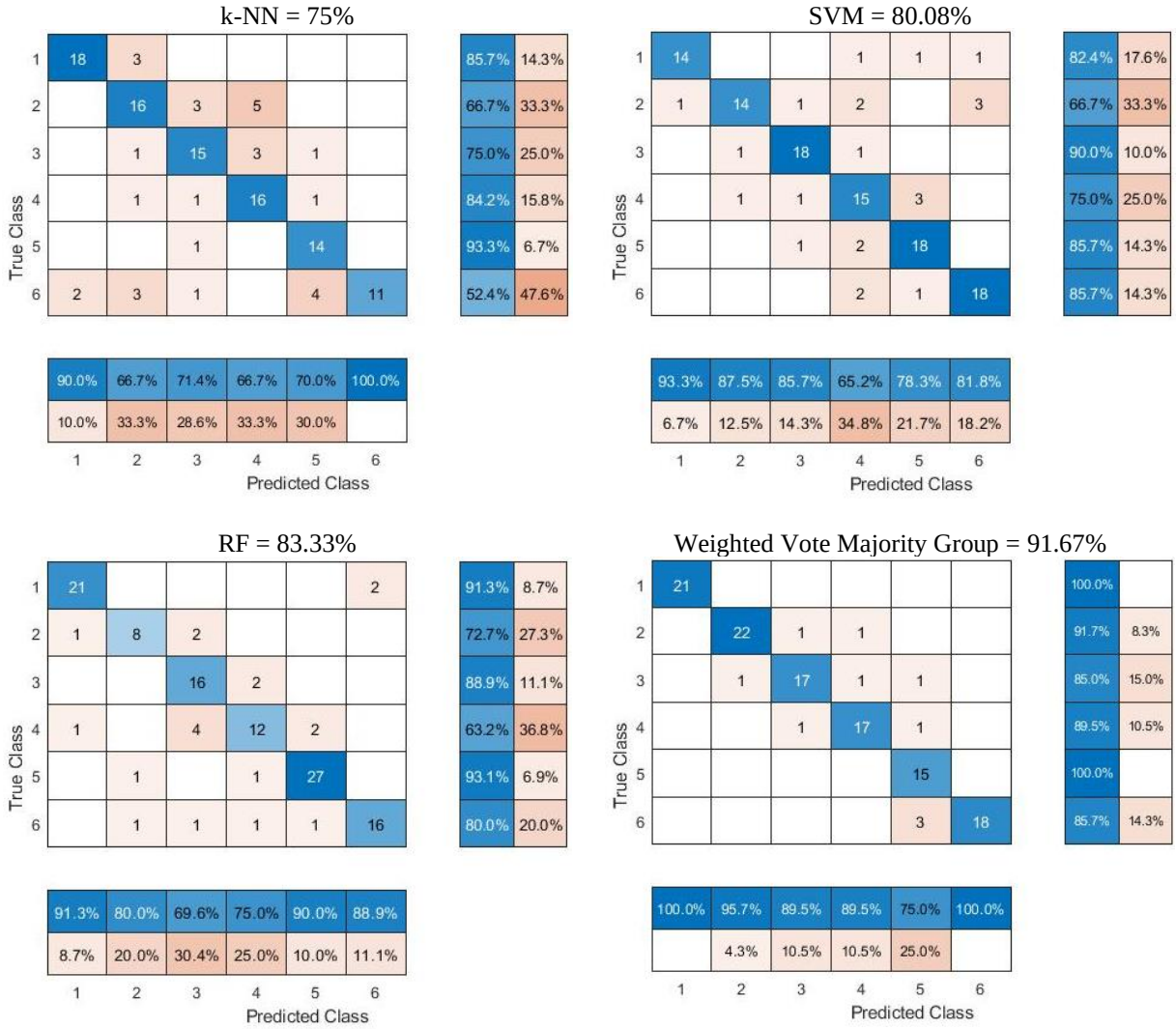

Fig. 4. Confusion matrix results to classify grape leaf diseases

According to the Table 3, the accuracy of the classification improves significantly with the use of the weighted majority voting algorithm, which combines SVM, RF, and k-NN classifiers. As indicated in the evaluation table, the Weighted Majority Voting approach enhances the model's performance across all six grape leaf disease classes. Specifically, the

algorithm achieves perfect Precision and Sensitivity for *Black Measles* (Class 1) and Healthy Leaves (Class 6), demonstrating the model's ability to reliably detect these conditions with minimal false positives and false negatives. For other disease classes such as *Black Rot* (Class 2) and *Powdery Mildew* (Class 4), the model also performs well, showing high precision and sensitivity values, indicating strong disease detection capabilities. However, *Downy Mildew* (Class 5) shows slightly lower precision (75%) and sensitivity (100%), suggesting that the algorithm faces more challenges distinguishing this particular condition. Specificity is consistently high across all classes, with *Black Rot* (Class 2) achieving the highest specificity at 98.96%, indicating that the model effectively identifies negative cases (healthy leaves) for most disease types. The Accuracy remains steady at 91.67% for all classes, emphasizing the robustness of the model in classifying both healthy and diseased leaves correctly. Finally, the F-Measure, which balances precision and sensitivity, is high across most classes, with *Black Measles* (Class 1) achieving a perfect score of 100%. In conclusion, the weighted majority voting algorithm significantly enhances the classification accuracy, providing an effective and reliable method for grape leaf disease detection, although further refinement is needed for *Downy Mildew* detection. Overall, the group decision learning (weighted voting learning) model achieved better classification performance by 10.54% compared to the average accuracy of all baseline classifiers. This observation is further emphasized by the fact that less accurate classification results were obtained in previous studies using different methods, primarily due to the similarity of disease symptoms across grape leaf diseases (Jaisakthi *et al.*, 2019; Liu, Tan, Li, He, & Wang, 2020; Xie *et al.*, 2020).

Table 3- Result of evaluation criteria for disease classification

k-NN = 75%							**SVM = 80.08%**						
Class	**1**	**2**	**3**	**4**	**5**	**6**	**Class**	**1**	**2**	**3**	**4**	**5**	**6**
Precision	90	66.66	71.42	66.66	70	100	Precision	93.33	87.50	8.571	.6522	78.26	8.571
Sensitivity	85.71	66.66	75	84.21	93.33	52.38	Sensitivity	82.35	70	90	75	85.71	8.571
Specificity	97.97	91.66	94	92.07	94.28	100	Specificity	99.02	97.98	96.97	91.92	94.90	96.94
Accuracy	75	75	75	75	75	75	Accuracy	80.08	80.08	80.08	80.08	80.08	80.08
F-Measure	87.80	66.66	73.17	74.41	80	68.75	F-Measure	87.50	77.78	87.80	69.77	81.82	85.71
RF = 83.33							Weighted Vote Majority Group = 91.67%						
Class	1	2	3	4	5	6	Class	1	2	3	4	5	6
Precision	91.30	80	69.57	75	90	88.89	Precision	100	95.65	89.47	89.47	75.00	100
Sensitivity	91.30	72.73	88.89	63.16	93.10	80	Sensitivity	100	91.66	85.00	89.47	100	85.71
Specificity	97.94	98.17	93.14	96.04	96.70	98	Specificity	100	98.96	98	98.02	95.24	100
Accuracy	83.33	83.33	83.33	83.33	83.33	83.33	Accuracy	91.67	91.67	91.67	91.67	91.67	91.67
F-Measure	91.30	76.19	78.05	68.57	91.53	84.21	F-Measure	100	93.62	87.18	89.47	85.71	92.31

Note: Class 1, 2, 3, 4, 5, and 6 correspond respectively to *Black Measles*, *Black Rot*, *Leaf Blight*, *Powdery Mildew*, *Downy Mildew*, and Healthy Leaves.

Table 4 compares the classification results of this study with those of previous research. Earlier studies have shown that Weighted Majority Voting Ensemble (WMVE) methods can improve classification accuracy compared to individual machine learning (ML) models (Javidan *et al.*, 2025). Most prior research focused on classifying a small number of tomato leaf diseases, typically one to three classes (Cruz *et al.*, 2019). As the number of disease categories increases, the accuracy of individual models often declines due to the similarity of disease symptoms, making precise diagnosis more challenging (Liu *et al.*, 2020; Javidan *et al.*, 2023a).

Although deep learning (DL) approaches can achieve higher classification performance, they face practical limitations such as the need for large datasets and high computational resources, which can hinder their use by plant pathologists and agricultural engineers. Data scarcity has been a major challenge in

previous studies, often reducing the effectiveness of DL methods. To address this, data augmentation techniques, including rotation, flipping, cropping, resizing, color jittering, noise addition, image warping, and random erasing, have been applied to expand dataset size and enhance model generalizability (Mumuni & Mumuni, 2022). Despite these strategies, DL models remain heavily dependent on large datasets for optimal performance (Alomar, Aysel, & Cai, 2023).

In contrast, machine learning approaches combined with effective feature extraction such as texture, color, and shape from leaf images can provide a precise and efficient method for disease detection (Vishnoi, Kumar, & Kumar, 2021). Previous findings have shown that the weighted majority voting strategy improves classification performance by leveraging the strengths of multiple classifiers (Azad, Nehal, & Moshkov, 2024; Javidan *et al.*, 2023b; Javidan *et al.*, 2025; Kuncheva & Rodríguez, 2012; Shi, Yuan, Zhang, Zhang, & Wang, 2025). This ensemble approach has proven to deliver more accurate and reliable results compared to individual models, particularly in plant disease identification tasks. As demonstrated in this study, ensemble learning methods show strong potential in recognizing and classifying a greater number of diseases with similar symptoms and offer a more dependable solution for decision-making compared to standalone artificial intelligence techniques.

Table 4- Comparison of the classification results of this study with previous studies

Disease	Detecting Method	Accuracy (%)	Limitation	Reference
Black Rot, Black Measles, and Leaf Blight	SVM Classifier	87	Low accuracy Does not use feature selection method	Jaisakthi *et al.* (2019)
Black rot, Esca measles, Leaf spot	GAN - CNN	90.70	Uses black box method Does not use feature selection method	Liu *et al.* (2020)
Black Rot, Black Measles, Leaf Blight, and Mites	DR-IACNN	81.1	Low accuracy Uses black box method Does not use feature selection method	Xie *et al.* (2020)
Black Rot, Black Measles, Leaf Blight, and Mites	K-means clustering CNN GoogleNet	98.97 86.82 94.05	Uses black box method Does not use feature selection method Just for four diseases Does not use majority voting method	Javidan *et al.* (2023b)
Black Rot, Black Measles, Leaf Blight, and Mites	CNN-based classification module, achieving 99.7% accuracy on the Plant Village dataset	99.7	Uses black box method Does not use feature selection method	Talaat *et al.* (2025)
Black Measles, Black Rot, Leaf Blight, Powdery Mildew, Downy Mildew, and healthy leaves	ROI extraction with Auto K-means clustring, feature extraction (color, texture, and shape), BOA, and SVM	91.67	The proposed algorithm used in this research has several advantages over traditionally used methods. Firstly, it provides accurate diagnosis of the diseased areas by automatically identifying the ROI (Region of Interest) using clustering. Secondly, the algorithm has a short operating time, making it more efficient in diagnosing and classifying the disease. Furthermore, it identifies the best and most important features for the diagnosis of the disease, which can help improve the accuracy of the diagnose. By harnessing the power of AI, this method offers a more reliable and consistent means of disease detection compared to traditional methods. Limitation: dataset size, dependency on manual ROI extraction	Current study

The histopathology of the grape leaves plays a crucial role in the detection of *Downy Mildew*, *Black Measles*, and *Black Rot* diseases as it can affect the classification accuracy. The early stages of these diseases may not be easily observable due to the similarities in symptoms and color, leading to misclasses. The severity of the symptoms can also be influenced by environmental factors, such as temperature and humidity, further contributing to misclassifications. However, this method of detecting disease in grape leaves has been very useful for plant pathologists as it utilizes the latest AI technology, specifically the Weighted Majority Voting Group Learning classifier to accurately identify and classify these diseases. By harnessing the power of AI, this method offers a more reliable and consistent means of disease detection compared to traditional methods.

One of the challenges in detecting grape leaf diseases is the variability in the symptoms and the difficulties in interpreting these symptoms. Additionally, different diseases may have similar symptoms, which can make it challenging to accurately diagnose the diseases. However, the Weighted Majority Voting Group Learning classifier can help to overcome these challenges by utilizing a combination of the color, texture, and shape features of the leaves to accurately identify and classify these diseases. This AI-powered method is not only more reliable in detecting disease, but it is also more efficient and cost-effective compared to traditional methods.

Overall, this method has the potential to revolutionize the field of plant pathology by enabling plant pathologists to quickly and accurately diagnose grape leaf diseases. This can lead to more effective disease management and treatment strategies, which in turn can increase the yield and quality of grapes, thereby benefiting both growers and consumers alike.

AI and IoT integration for real-time grapevine disease detection

The integration of artificial intelligence (AI) into plant disease diagnosis has significantly improved the accuracy and efficiency of disease detection in vineyards. By utilizing advanced machine learning techniques, such as the Weighted Majority Voting Group Learning classifier, plant pathologists can overcome the challenges posed by symptom variability and environmental factors that impact disease severity. This AI-driven approach provides a more consistent and reliable means of identifying grapevine diseases, reducing misclassification risks, and enabling early intervention. One of the key advantages of AI in disease detection is its ability to analyze large datasets and extract meaningful patterns from images. By considering multiple parameters such as color, texture, and shape, AI models can distinguish between visually similar diseases with high precision. This is particularly beneficial for grape diseases like *Downy Mildew*, *Black Measles*, and *Black Rot*, which often exhibit overlapping symptoms in their early stages. Traditional methods, relying on manual inspection, are time-consuming and prone to human error, whereas AI-powered models can process vast amounts of image data rapidly and deliver accurate results consistently. The incorporation of AI into plant disease detection is paving the way for its integration with the Internet of Things (IoT) to enable real-time disease monitoring. By deploying smart sensors and high-resolution cameras in vineyards, it is possible to continuously capture and analyze data related to plant health. IoT-enabled devices can transmit images of grape leaves to cloud-based AI models, which can then process the data and provide instant feedback to farmers. This real-time monitoring system allows for the early detection of diseases, enabling growers to take immediate corrective actions before infections spread and cause significant damage to the crop.

In addition to disease identification, AI combined with IoT can offer predictive analytics for vineyard management. By collecting environmental data such as

temperature, humidity, and soil moisture, AI models can predict the likelihood of disease outbreaks and recommend preventive measures. This predictive capability helps farmers optimize the use of fungicides and other treatments, reducing unnecessary chemical applications and promoting sustainable agricultural practices. By leveraging AI and IoT, vineyards can adopt a proactive approach to disease management, ultimately improving grape yield and quality while minimizing economic losses. Moreover, real-time disease detection using AI and IoT can be integrated into mobile applications, providing farmers with accessible and user-friendly tools for monitoring plant health. These applications can analyze images taken from smartphones or drones and provide instant disease assessments along with suggested treatment options. This level of accessibility empowers farmers with knowledge and actionable insights, even in remote areas where professional pathologists may not be available. The future of AI-driven plant disease diagnosis holds even greater promise with advancements in deep learning and hyperspectral imaging. By incorporating hyperspectral data, AI models can detect disease symptoms that are invisible to the human eye, further enhancing classification accuracy. Additionally, the integration of robotics with AI and IoT could lead to autonomous disease detection systems capable of patrolling vineyards and applying targeted treatments automatically.

In conclusion, the combination of AI and IoT is revolutionizing the detection and management of grapevine diseases. This technology not only enhances diagnostic accuracy but also facilitates real-time monitoring, predictive analytics, and automated interventions. As AI continues to evolve, its application in precision agriculture will contribute to sustainable vineyard management, increased productivity, and improved grape quality, benefiting both growers and consumers in the long run.

Conclusion

Diseases in agricultural and garden plants can have severe consequences, leading to reduced production quantities and quality. Visual plant assessment by human observers is time-consuming, expensive, and prone to errors. Determining plant diseases requires innovative methods and advanced technologies to accurately diagnose and differentiate between different diseases. Advances in agriculture have made it possible to use machine vision systems for non-destructive detection of plant diseases. These advancements have improved the possibility of diagnosing plant diseases in the early stages, differentiating diseases with similar symptoms, and optimizing crop management strategies. In this regard, color imaging sensors have shown great potential in plant pathology interactions and disease diagnosis. This approach has the potential to transform plant disease diagnosis and enhance agricultural productivity and crop quality. The study proposes an efficient and accurate method for detecting and classifying grapevine leaf diseases by analyzing color, texture, and shape features extracted from RGB leaf images. The method integrates multiple machine learning (ML) models with a novel weighted majority voting strategy and employs the Relief feature selection technique to identify the most influential features for disease classification. Initially, the diseased regions were segmented from the leaves, and a total of 165 features were extracted across RGB, HSV, and l*a*b* color spaces. The Relief algorithm was then used to select the most significant features for classification. Individually, the classification accuracies of color, texture, and shape features were 65.15%, 71.20%, and 60.31%, respectively, while combining all features yielded an accuracy of 88.33%. Finally, three classifiers, including RF, SVM, and k-NN, were used for the final diagnosis based on a weighted voting group method. The results demonstrate the potential of this approach to accurately diagnose and classify grapevine leaf diseases, leading to improved crop management strategies. The proposed

weighted voting group learning model in this research provides an advanced approach to diagnose and classify grapevine leaf diseases based on color, texture, and shape features extracted from RGB images of plant leaves. In this method, the performance of each classifier is the basis of its weighting for the calculated vote, and the final decision is made by adding the weighted votes and selecting the class with the most votes. The results obtained for the basic classification models were 88.33%, 80.08%, and 75%, respectively. Meanwhile, in the proposed group learning model, the classification accuracy for the weighted voting group model improved by 10.54% compared to the average accuracy of the basic models in classification.

Conflict of Interest: The authors declare no competing interests.

Author Contributions

M. Njafabadiha: Data acquisition, Text mining, technical advice, Methodology

D. Mohammadzamani: Supervision, Validation, Software cervices

M. Gholami Parashkoohi: Technical advice, Visualization, Review and editing services

References

1. Abdulridha, J., Ampatzidis, Y., Kakarla, S. C., & Roberts, P. (2020). Detection of target spot and bacterial spot diseases in tomato using UAV-based and benchtop-based hyperspectral imaging techniques. *Precision Agriculture, 21*(5), 955-978. https://doi.org/10.1007/s11119-019-09703-4
2. Alomar, K., Aysel, H. I., & Cai, X. (2023). Data Augmentation in Classification and Segmentation: A Survey and New Strategies. *Journal of Imaging, 9*(2), 46. https://doi.org/10.3390/jimaging9020046
3. Azad, M., Nehal, T. H., & Moshkov, M. (2024). A novel ensemble learning method using majority based voting of multiple selective decision trees. *Computing*, *107*(1). https://doi.org/10.1007/s00607-024-01394-8
4. Barbedo, J. G. A. (2016). A review on the main challenges in automatic plant disease identification based on visible range images. *Biosystems Engineering*, *144*, 52-60. https://doi.org/10.1016/j.biosystemseng.2016.01.017
5. Barbedo, J. G. A. (2018). Factors influencing the use of deep learning for plant disease recognition. *Biosystems Engineering*, *172*, 84-91. https://doi.org/10.1016/j.biosystemseng.2018.05.013
6. Cruz, A. C., Ampatzidis, Y., Pierro, R., Materazzi, A., Panattoni, A., De Bellis, L., & Luvisi, A., (2019). Detection of grapevine yellows symptoms in Vitis vinifera L. with artificial intelligence. *Computer and. Electronics in Agriculture*, 63-76. https://doi.org/10.1016/j.compag.2018.12.028
7. Hasan, Moh. A., Riana, D., Swasono, S., Priyatna, A., Pudjiarti, E., & Prahartiwi, L. I. (2020). Identification of Grape Leaf Diseases Using Convolutional Neural Network. *Journal of Physics: Conference Series 1641*(1), 012007. https://doi.org/10.1088/1742-6596/1641/1/012007
8. Hughes, David, P., & Salathe, M. (2015). An open access repository of images on plant health to enable the development of mobile disease diagnostics (Version 2). *arXiv*. https://doi.org/10.48550/ARXIV.1511.08060
9. Jaisakthi, S. M., Mirunalini, P., Thenmozhi, D. (2019). "Grape leaf disease identification using machine learning techniques," *in Proceedings of the 2019 International Conference on Computational Intelligence in Data Science (ICCIDS)*, Chennai, 1-6. https://doi.org/10.1109/ICCIDS.2019.8862084
10. Javidan, S. M., Ampatzidis, Y., Banakar, A., Asefpour Vakilian, K., & Rahnama, K. (2024).

Tomato Fungal Disease Diagnosis Using Few-Shot Learning Based on Deep Feature Extraction and Cosine Similarity. *AgriEngineering 6*(4), 4233-4247. https://doi.org/10.3390/agriengineering6040238

11. Javidan, S. M., Ampatzidis, Y., Banakar, A., Asefpour Vakilian, K., & Rahnama, K. (2025). An Intelligent Group Learning Framework for Detecting Common Tomato Diseases Using Simple and Weighted Majority Voting with Deep Learning Models. *AgriEngineering, 7*(2), 31. https://doi.org/10.3390/agriengineering7020031
12. Javidan, S. M., Banakar, A., Vakilian, K. A., & Ampatzidis, Y. (2023a). Diagnosis of grape leaf diseases using automatic K-means clustering and machine learning. *Smart Agricultural Technology, 3*, 100081. https://doi.org/10.1016/j.atech.2022.100081
13. Javidan, S. M., Banakar, A., Vakilian, K. A., & Ampatzidis, Y. (2023b). Tomato leaf diseases classification using image processing and weighted ensemble learning. *Agronomy Journal.* https://doi.org/10.1002/agj2.21293
14. Javidan, S. M., Banakar, A., Vakilian, K. A., Ampatzidis, Y., & Rahnama, K. (2024). Early detection and spectral signature identification of tomato fungal diseases (Alternaria alternata, Alternaria solani, Botrytis cinerea, and Fusarium oxysporum) by RGB and hyperspectral image analysis and machine learning. *Heliyon 10*(19), e38017. https://doi.org/10.1016/j.heliyon.2024.e38017
15. Kuncheva, L. I., & Rodríguez, J. J. (2012). A weighted voting framework for classifiers ensembles. *Knowledge and Information Systems 38*(2), 259-275. https://doi.org/10.1007/s10115-012-0586-6
16. Liu, B., Tan, C., Li, S., He, J., & Wang, H. (2020). A data augmentation method based on generative adversarial networks for grape leaf disease identification. *IEEE Access, 8*, 102188-102198. https://doi.org/10.1109/access.2020.2998839
17. Mohamadzamani, D., Sajadian, S., & Javidan, S. M. (2020). DDetection of Callosobruchus maculatus F. with image processing and artificial neural network. *Applied Entomology and Phytopathology, 88*(1), 103-112. https://doi.org/10.22092/jaep.2020.341684.1324
18. Mumuni, A., & Mumuni, F. (2022). Data augmentation: A comprehensive survey of modern approaches. *Array, 16*, 100258. https://doi.org/10.1016/j.array.2022.100258
19. Raghuram, K., & Borah, M. D. (2025). A Hybrid Learning Model for Tomato Plant Disease Detection using Deep Reinforcement Learning with Transfer Learning. *Procedia Computer Science, 252*, 341-354. https://doi.org/10.1016/j.procs.2024.12.036
20. Sahabi, H., & Baradaran-Motie, J. (2025). Detection of mite infested saffron plants using aerial imaging and machine learning classifier. *Spanish Journal of Agricultural Research, 22*(4), 20452. https://doi.org/10.5424/sjar/2024224-20452
21. Shafik, W., Tufail, A., Liyanage De Silva, C., & Awg Haji Mohd Apong, R. A. (2025). A novel hybrid inception-xception convolutional neural network for efficient plant disease classification and detection. *Scientific Reports, 15*(1). https://doi.org/10.1038/s41598-024-82857-y
22. Shi, H., Yuan, Z., Zhang, Y., Zhang, H., & Wang, X. (2025). A New Ensemble Strategy Based on Surprisingly Popular Algorithm and Classifier Prediction Confidence. *Applied Sciences, 15*(6), 3003. https://doi.org/10.3390/app15063003
23. Talaat, F. M., Shams, M. Y., Gamel, S. A., & ZainEldin, H. (2025). DeepLeaf: an optimized deep learning approach for automated recognition of grapevine leaf diseases. *Neural Computing and Applications.* https://doi.org/10.1007/s00521-025-11038-3
24. Vishnoi, V. K., Kumar, K., & Kumar, B. (2021). A comprehensive study of feature extraction techniques for plant leaf disease detection. *Multimedia Tools and Applications 81*(1), 367-419. https://doi.org/10.1007/s11042-021-11375-0
25. Xie, X., Ma, Y., Liu, B., He, J., Li, S., & Wang, H. (2020). A deep-learning-based real-time detector for grape leaf diseases using improved convolutional neural networks. *Frontiers in*

Plant Science, 11, 751. https://doi.org/10.3389/fpls.2020.00751
26. Zhou, W., Gao, S., Zhang, L., & Lou, X. (2020). Histogram of Oriented Gradients Feature Extraction from Raw Bayer Pattern Images. *IEEE Transactions on Circuits and Systems II: Express Briefs*, *67*(5), 946-950. https://doi.org/10.1109/tcsii.2020.2980557

نشریه ماشین‌های کشاورزی
https://jame.um.ac.ir

مقاله پژوهشی

جلد ۱۶، شماره ۳، پاییز ۱۴۰۵، ص ۵۰۶-۴۸۷

مدل یادگیری گروهی وزن‌دار برای طبقه‌بندی بیماری برگ انگور با استفاده از پردازش تصویر و یادگیری ماشینی

محسن نجف‌آبادی‌ها[۱]، داود محمدزمانی[۱*]، محمد غلامی پرشکوهی[۲]

تاریخ دریافت: ۱۴۰۳/۱۲/۱۰
تاریخ پذیرش: ۱۴۰۴/۰۲/۰۹

چکیده

در این مطالعه، راهبردی برای تشخیص بیماری‌های برگ انگور با کمک پردازش تصویر RGB و تصمیم‌گیری گروهی وزنی ارائه شد. برای این منظور، پنج گروه بیماری به نام‌های سرخک سیاه، پوسیدگی سیاه، سوختگی برگ، سفیدک پودری و سفیدک کرکی و گروهی از برگ‌های سالم با سه روش یادگیری ماشینی به نام‌های ماشین بردار پشتیبان (SVM)، جنگل تصادفی (RF) و k- نزدیک‌ترین همسایه (k-NN) و ترکیب وزنی طبقه‌بندی شدند. در مرحله بعد، با توجه به دقت هر طبقه‌بندی، وزن هریک از آن‌ها تعیین شد و در نهایت با استفاده از رای اکثریت، طبقه‌بندی نهایی بیماری‌ها انجام شد. همچنین به‌منظور معرفی بهترین ویژگی‌های بافت، رنگ و شکل استخراج‌شده از الگوریتم انتخاب ویژگی برجسته استفاده شد. این الگوریتم برای هر گروه از ویژگی‌های استخراج‌شده، ۵ مورد را به‌عنوان بهترین و موثرترین ویژگی در تشخیص بیماری‌های گیاهی از جمله برگ گیاه انگور به محققان ارائه کرد. نتایج دقت طبقه‌بندی باSVM، RF و k-NN به‌ترتیب ۸۸/۳۳، ۸۰/۰۸ و ۷۵ درصد بود. نتایج نشان داد که الگوریتم تصمیم‌گیری گروه وزنی ارائه‌شده در این تحقیق توانایی بهبود دقت طبقه‌بندی بیماری‌های گیاهی را با دقت ۹۱/۶۷ درصد دارد.

واژه‌های کلیدی: انتخاب ویژگی، بیماری انگور، پردازش تصویر، تصمیم‌گیری گروهی، رای اکثریت

۱- گروه مکانیزاسیون کشاورزی، واحد تاکستان، دانشگاه آزاد اسلامی، تاکستان، ایران
۲- گروه مهندسی مکانیک، واحد شهرقدس، دانشگاه آزاد اسلامی، شهرقدس، ایران
(*- نویسنده مسئول: Email: dr.dmzamani@gmail.com)

https://doi.org/10.22067/jam.2025.92388.1347

Journal of Agricultural Machinery

Homepage: https://jame.um.ac.ir

Research Article
Vol. 16, No. 3, 2026, p. 507-523

Assessing the Influence of Copper Oxide Nanoparticles Combined with Distilled Water on PVT System Performance

M. Ghaderi[1], P. Salami[1*], H. Samimi-Akhijahani[1], S. Zareei[1], M. Safvati[2]

1- Department of Biosystems Engineering, Faculty of Agriculture, University of Kurdistan, Sanandaj, Iran
2- Department of Biosystems Engineering, Faculty of Agriculture, Isfahan University of Technology, Isfahan, Iran
(* Corresponding Author Email: p.salami@uok.ac.ir)

Received: 04 March 2025
Revised: 06 May 2025
Accepted: 02 June 2025
Available Online: 07 July 2025

How to cite this article:
Ghaderi, M., Salami, P., Samimi-Akhijahani, H., Zareei, S., & Safvati, M. (2026). Assessing the Influence of Copper Oxide Nanoparticles Combined with Distilled Water on PVT System Performance. *Journal of Agricultural Machinery*, *16*(3), 507-523. https://doi.org/10.22067/jam.2025.92457.1349

Abstract

The rapid growth of the global population and the increasing demand for energy, coupled with the urgent need for environmental conservation, have prompted researchers to explore renewable energy sources as viable alternatives to non-renewable fossil fuels. This study evaluates the performance enhancement of photovoltaic/thermal (PVT) systems using an immersion cooling method with copper oxide nanofluids. The experimental setup included a glass chamber immersing the panel surface, tested at nanofluid volume ratios of 0.025% and 0.05%, and flow rates of 0.01 and 0.02 L s^{-1}. The immersion height was 5 cm within the glass chamber. The tests were conducted under ambient conditions, which included an ambient temperature of 20.6-31.2 °C and an irradiance of 343-924 W m^{-2}. Results demonstrate that copper oxide nanofluids at a 0.05% volume ratio and a 0.02 L s^{-1} flow rate improved thermal efficiency to 31.87% and reduced panel surface temperature by up to 11.8 °C compared to water cooling. Also, the electrical efficiency of the PVT system exceeded that of the reference panel. The overall efficiency of the PVT system reached 41.89%. These findings highlight the potential of nanofluid-based cooling to optimize PVT system efficiency by enhancing thermal management.

Keywords: Cooling, CuO Nanofluid, Immersion, System temperature, Thermal efficiency

Nomenclature

A_{PV}	Photovoltaic panel area (m^2)	T_r	Reference temperature (°C)
c_p	Specific heat capacity of water (J kg^{-1} °C^{-1})	V_{OC}	Open-circuit voltage (V)
$\dot{E}_{PV}$	Output power of the PV panel (W)		Greek symbols
FF	Fill factor	α_{PV}	Absorptivity coefficient
G	Solar irradiation (W m^{-2})	β_r	Cell temperature coefficient
I_{SC}	Short-circuit current (A)	η_{ele}	Electrical efficiency
$\dot{m}$	Fluid mass flow rate (kg s^{-1})	$\eta_{PV/T}$	Overall efficiency of PVT
$T_{f,in}$	Input fluid temperature (°C)	η_r	Reference (or rated) efficiency of the PV panel under STC
$T_{f,out}$	Output fluid temperature (°C)	η_{th}	Thermal efficiency
T_{PV}	Photovoltaic panel's back surface temperature (°C)	τ_g	Transmittance coefficient

Authors retain the copyright. This is an open access article distributed under Creative Commons Attribution 4.0 International License (CC BY 4.0).

https://doi.org/10.22067/jam.2025.92457.1349

Introduction

The efficiency of power supply systems is critical in the energy sector. In Iran, the emphasis on energy consumption and optimization within energy-intensive systems has traditionally been limited, largely due to the country's abundant fossil fuel resources. However, as these resources become depleted and environmental pollution from their use increases, the Comprehensive National Development Document has established a goal for at least 30% of the country's electricity to be sourced from renewable energy by 2051. Moreover, over half of this renewable energy is expected to come specifically from solar power. Consequently, it is vital to develop and implement systems that can effectively harness renewable energy, either independently or in combination with other energy sources (Mirzaee, Salami, Samimi Akhijahani, & Zareei, 2023, Mohammadi Sarduei, Mortezapour, & Jafari Naeimi, 2017; Salami, Ajabshirchi, Abdollahpoor, & Behfar, 2016).

Solar power holds tremendous potential for alleviating the impacts of climate change associated with fossil fuel reliance in energy production, making it essential to improve the efficiency of solar energy technologies. Recent findings indicate that photovoltaic systems can compete effectively with fossil fuels. However, a significant challenge is the rise in temperature of solar cells, which adversely affects their electrical performance. To address this issue, researchers have developed an innovative solution to dissipate excess heat from these systems, utilizing nanotechnology to reduce temperatures and enhance electrical efficiency (Ahmed, Baig, Sundaram, & Mallick, 2019; Haidar, Orfi, & Kaneesamkandi, 2018; Sathe & Dhoble, 2017).

A photovoltaic cell is a semiconductor device that generates electric current when exposed to light (Elias, AlSadoon, & Abdulgafar, 2014). Among solar energy technologies, the photovoltaic-thermal system is recognized as the most efficient and widely used today, thanks to its stable, environmentally friendly, secure, and aesthetically pleasing attributes. One effective strategy to improve efficiency and reduce thermal degradation in photovoltaic panels is to lower their surface operating temperature. This can be achieved by implementing cooling methods that minimize heat accumulation in the photovoltaic cells during operation (Brahim & Jemni, 2017; Joshi, Andhare, Bhave, & Gudadhe, 2019; Sheeba, Rao, & Jaisankar, 2015; Siah Chehreh Ghadikolaei, 2021). In their study, Tina, Rosa-Clot, Rosa-Clot, and Scandura (2012) introduced a different photovoltaic cooling solution utilizing a photovoltaic system submerged in shallow water. They discovered that minimizing thermal drift and decreasing reflection contributed to an increase in photovoltaic efficiency of about 15% at a water depth of 4 cm. Idoko, Anaya-Lara, and McDonald (2018) explored the effect of water cooling on the performance of two 250-W solar panels. One panel featured a water-cooling system designed to maintain a surface temperature of 20°C, while the other functioned without any cooling mechanism. Utilizing the PV array power output equation with a derating factor of 80%, they assessed the power output of both panels. The results revealed an increase of 20.96 W in output power and a minimum efficiency improvement of 3% for the water-cooled panel. These findings underscore the substantial advantages of water cooling in enhancing the efficiency and performance of solar panels. Findings from a research study showed that employing a water-cooling technique from the upper surface of the panel enhanced the photovoltaic panel's efficiency by around 0.8-1.5%. The cooling process relies on natural water flow through pipes that contain nozzles placed at regular intervals, channeling water from the top to the bottom of the panel. Furthermore, integrating this system with a flat-plate collector allows for the effective use of the water heated by the panel for domestic

purposes (Arefin, 2019).

Nanofluids are innovative fluids that incorporate nanoscale particles suspended in a liquid medium. Their high surface-to-volume ratio provides several benefits, including improved catalytic performance, minimized waste generation in chemical processes, enhanced material strength, and increased thermal conductivity in industrial applications (Amalraj & Michael, 2019; Pordanjani *et al.*, 2021). In photovoltaic (PV) systems, nanofluids are increasingly employed as advanced coolants due to their superior heat transfer properties. For example, circulating nanofluids across PV panels can reduce operating temperatures by 10-20 °C, improving electrical efficiency by 3-15% while simultaneously harvesting thermal energy for secondary applications (Ahmed *et al.*, 2019; Al-Ghezi, Abass, Salam, Jawad, & Kazem, 2021). The photovoltaic-thermal system enhances photovoltaic panel efficiency through nanofluid cooling (Al-Ezzi & Ansari, 2022). In this context, copper oxide (CuO) is a monoclinic semiconducting compound that is the simplest copper compound and possesses various advantageous physical properties, such as high-temperature superconductivity and spin dynamics. CuO nanofluids are particularly effective in PVT systems due to their high thermal conductivity (~40 W (m K)$^{-1}$) and optical absorption, enabling efficient cooling and waste heat recovery (Alktranee, Shehab, Németh, Bencs, & Hernadi, 2023). It is affordable, combines easily with polar liquids and polymers, and stays stable in chemical and physical contexts (Allaker & Yuan, 2019).

In a study, incorporating 2% nano-CuO into water significantly improved thermal conductivity by 100%. Stability tests indicated high zeta potential across all formulations, with better stability at lower nanoparticle concentrations. Use of nanofluids resulted in greater electrical, thermal, and overall efficiencies compared to traditional cooling methods. The optimal system achieved electrical, thermal, and total efficiencies of 29.92%, 61.08%, and 91%, respectively (Al-Ghezi *et al.*, 2021).

Utilizing TRNSYS simulations, researchers analyzed how CuO nanofluid performs at various concentrations (0.10%-0.50%) and flow rates (60-120 kg h^{-1}) in a PVT system. Results showed that increasing nanofluid concentration and flow rate generally improved electrical and thermal efficiencies, but higher flow rates increased pump power consumption, reducing net efficiency. Optimal performance was achieved at 0.10% concentration and 80 kg h^{-1} flow rate, balancing efficiency gains with minimal power consumption (Madas, Narayanan, & Gudimetla, 2023). In a research, a cooling PVT system with TiO_2-CuO hybrid nanofluid, achieving a 39% reduction in PV cell temperature, was investigated. At 0.3 vol%, electrical power improved by 77.5%, overall efficiency by 58.2%, and exergy efficiency by 14.97%, while exergy losses and entropy generation decreased by 37.9% and 69.6%. The economic analysis revealed a payback period of 21 months compared to systems without cooling (Alktranee *et al.*, 2023). The study improved PVT system performance by using CuO-H_2O nanofluid and a rectangular-cut turbulator. The turbulator enhanced TPV uniformity by 20.43% and increased overall efficiency by 4.99% at high irradiation (G = 930 W m^{-2}). Higher inlet velocity boosted PVT efficiency by 3.19% and TPV uniformity by 16.34%, while increased wind speed decreased PVT efficiency by 3.63% (Khalili & Sheikholeslami, 2024).

This study utilized an innovative technique involving immersing the upper surface of the photovoltaic panel within a glass chamber, allowing the copper oxide nanofluid to enter through the inlets located at the top of the chamber and flow out through the outlets integrated in the lower section of the glass chamber. This approach aimed to enhance the cooling of the photovoltaic panel and boost the overall efficiency of the system. In other words, the study presents a novel approach to enhancing photovoltaic-thermal (PVT) system efficiency through the use of an immersion cooling method with copper oxide nanofluids.

Unlike traditional cooling methods using water or air, this innovative technique optimizes thermal management by reducing surface temperatures and increasing thermal efficiency. The research bridges the gap between theoretical studies on nanofluids and practical applications in renewable energy, offering a validated solution to improve PV system performance. By addressing the critical issue of heat dissipation in solar panels, this study provides new insights and actionable strategies for advancing sustainable energy technologies, making it a significant contribution to the field.

Materials and Methods

The photovoltaic-thermal (PVT) system was developed at the Renewable Energy Laboratory at the University of Kurdistan, Iran. Conventional photovoltaic systems employ a variety of silicon materials such as monocrystalline silicon, polycrystalline silicon, and thin-film silicon (amorphous silicon), each demonstrating distinct efficiency ranges. In this study, two monocrystalline silicon panels were employed: one served as the reference panel while the other was the PVT system. Table 1 shows the specifications of the PV modules.

Table 1- PV module specifications

Specification	Value
Maximum Power (P_{max})	100 W
Voltage at P_{max} (V_{mp})	18.50 V
Current at P_{max} (I_{mp})	5.41 A
Open-Circuit Voltage (V_{oc})	22.20 V
Short-Circuit Current (I_{sc})	5.74 A
Nominal Operating Cell Temperature (NOCT)	47±2 °C
Maximum System Voltage	1000 VDC
Dimensions (mm)	1015 × 668 × 30

The tests were conducted under ambient conditions, which included an ambient temperature of 20.6-31.2 ℃ and an irradiance of 343-924 W m^{-2}. To optimize the system for the panel's specific dimensions and the desired height, a custom glass chamber was constructed to facilitate seamless integration. Additionally, two supporting frames were designed and manufactured, one for the PVT system and the other for the reference panel (as shown in Fig. 1). The experimental setup involved testing at two mass flow rates (0.01 and 0.02 L s^{-1}) for both water and nanofluid, as well as at two concentration levels (0.025% and 0.05%) of the nanofluid, with an immersion height of 5 cm within the glass chamber.

Details of the synthesis of nanofluids and the stability of nanofluids

Enhancing the heat transfer coefficient and thermal efficiency can be achieved by adding nanoparticles, such as Fe, Al, and Cu, to pure water. Based on prior research and the advantages of nanofluids, they are considered a suitable choice for use as working fluids in various types of solar collectors. In this study, a 0.025% and 0.05% nanofluid, consisting of CuO nanoparticles mixed with water, was utilized as the working fluid in the PVT, replacing traditional water.

To prepare the nanofluid, CuO nanoparticles were initially added to water, followed by mixing the solution in a beaker with a hand mixer for one minute. The mixture was then placed in a magnetic stirrer for 20 minutes. Subsequently, the nanofluid underwent ultrasonic homogenization at a frequency of 20 kHz and power of 50 watts for approximately five hours to ensure stability (Fig. 2).

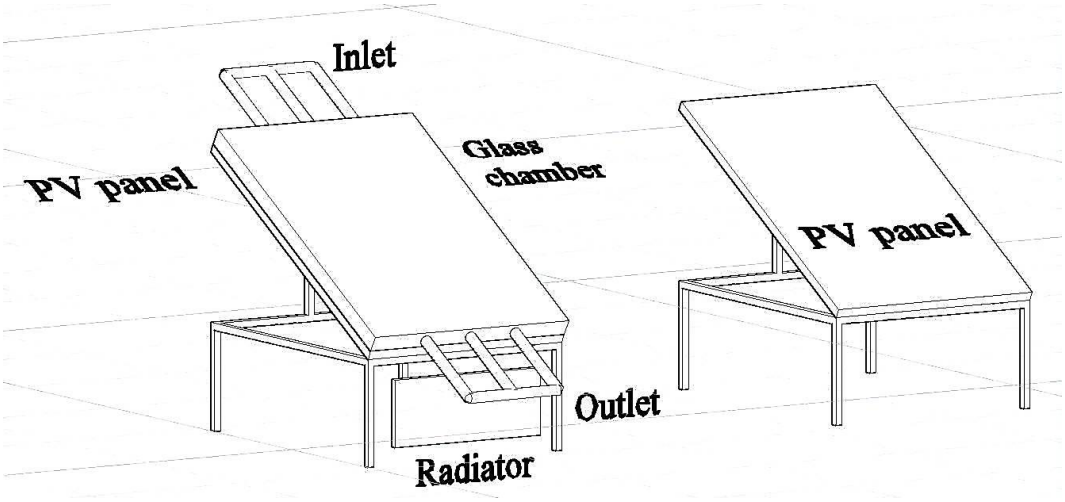

a

b

Fig. 1. The reference panel and PVT system developed in this study: (a) schematic diagram, and (b) the real image

An essential consideration in this process is the prevention of nanofluid deposition within the Photovoltaic Distilled Coolant (PDC) system, as this can reduce thermal efficiency and damage the PVT system. The stability of the nanofluid must therefore be verified. A simple visual observation method was employed by placing the mixture in a container and monitoring it at regular intervals. The results confirmed that the 0.025% and 0.05% water with CuO mixture achieved the desired stability. Over time, no significant differences were observed in the mixture, validating its suitability as a working fluid for the PDC system.

The prevention of nanofluid deposition within the PVT system is crucial, as particle sedimentation can reduce thermal efficiency and potentially damage the system. Thus, in addition to this method, Dynamic Light

Scattering (DLS) was used to monitor nanofluid deposition. Particle size distribution and zeta potential measurements were conducted at regular intervals to quantitatively evaluate the colloidal stability of the CuO nanofluid. The zeta potential values remained above -30 mV throughout the testing period, indicating good electrostatic stability.

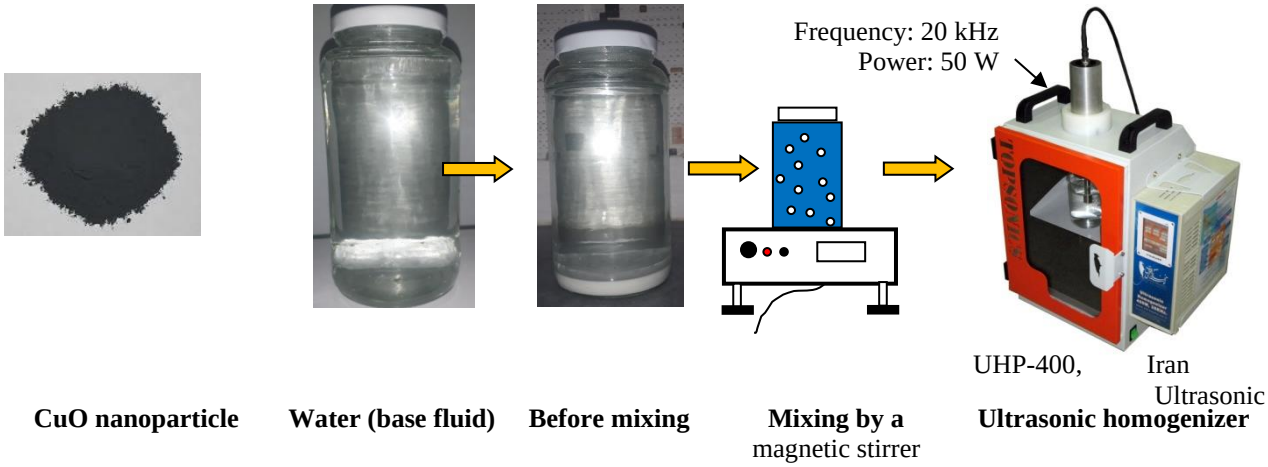

Fig. 2. The steps of preparing the mixture and achieving stability

Ensuring optimal efficiency in solar panels, along with various other factors, is essential for designing an effective photovoltaic system. The performance of a PVT system that utilizes nanofluids can be evaluated using Equations 1 to 3, which take into account thermal, electrical, and overall energy efficiencies (Dubey, Sarvaiya, & Seshadri, 2013; Sardarabadi, Passandideh-Fard, & Zeinali Heris, 2014; Yazdanifard, Ameri, & Ebrahimnia-Bajestan, 2017):

$$\eta_{th} = \frac{\dot{m}c_p(T_{f,out} - T_{f,in})}{G \times A_{PV}} \quad (1)$$

where, η_{th} = Thermal efficiency (dimensionless); $\dot{m}$ = Mass flow rate (kg s^{-1}); c_p = Specific heat capacity of fluid (J (kg K)$^{-1}$); T_{out} = Outlet fluid temperature (K); T_{in} = Inlet fluid temperature (K); G = Solar irradiance (W m^{-2}); A_{PV} = PV panel area (m^2).

$$\eta_{ele} = \frac{V_{OC} \times I_{SC} \times FF}{G \times A_{PV}} \quad (2)$$

where, η_{ele} = Electrical efficiency (dimensionless); I = Current (A); V = Voltage (V)

$$\eta_{PV/T} = \eta_{th} + \eta_{ele} \quad (3)$$

where, η_{PVT} = Overall efficiency (dimensionless).

The output power of the PV panel can be obtained using the following equation:

$$\dot{E}_{PV} = G \times \tau_g \times \alpha_{PV} \times A_{PV} \times \eta_r(1 - \beta_r(T_{PV} - T_r)) \quad (4)$$

where, $\dot{E}_{PV}$ = PV panel output power (W); τ_g = Glass transmittance coefficient (dimensionless); α_{PV} = PV cell absorptivity coefficient (dimensionless); η_r = Reference efficiency at standard test conditions (dimensionless); β_r = Temperature coefficient (K^{-1}); T_{PV} = PV cell temperature (K); T_r = Reference temperature (K); η_r denotes the reference electrical efficiency of the PV panel under Standard Test Conditions (STC), adjusted for temperature effects using the coefficient β_r.

To measure the current intensity and voltage passing through the system, a DC-DC step-down power module was utilized. A thermometer (TM-917, Lutron, Taiwan) was employed to read the temperatures recorded by the temperature sensors. Type K immersion sensors were used to measure the ambient and fluid temperatures, while Type K wired sensors were attached to the back of the panel to monitor its temperature. Data collection was conducted at 15-second intervals to ensure consistent measurements. Solar radiation per unit area was measured using a digital pyranometer (TES1333R, Taiwan) with a precision of 1 W m^{-2}.

In the preparation of the nanofluid, copper oxide nanoparticles with the specific structural properties detailed in Table 2 were used. The nanofluid was prepared at concentrations of 0.05% and 0.025%. The system featured a mechanism for transferring both nanofluid and water from a 20-liter cylindrical plastic tank specifically designed for storing these solutions. A 12 mm diameter hose was employed to facilitate the flow of fluids through the system's inlets and outlets. A comparative analysis of the PVT system was conducted against the reference panel over a period of six consecutive days, with each day consisting of 6 hours of observation in October 2023. This evaluation included two different flow rates, 0.02 and 0.01 L s^{-1}, for the nanofluid at concentrations of 0.05% and 0.025%, as well as for pure water. The experimental procedures were carried out each day, focusing on one concentration level and one distinct flow rate within the Renewable Energy Laboratory at the University of Kurdistan. Each day, the system was initialized at 9:30 AM for experimentation and data collection, which occurred at 15-minute intervals until 3:30 PM.

Table 2- Properties of copper oxide nanoparticles used in the experiment (Amalraj & Michael, 2019)

Property	Description
Size of nanoparticles	20 nanometers
Purity percentage	99.9%
Appearance of nanoparticles	Spherical
Specific surface area	35 m^2 g^{-1}
Bulk density	0.79 g cm^{-3}
Particle density	6.4 g cm^{-3}

Measuring tools and uncertainty analysis considerations

In order to record data including temperature, solar radiation, relative humidity (for volume fraction), wind velocity, and the weight of the nanoparticles, a selection of instruments were used. The details of the instruments, considering the model, measuring range, least measuring unit, and uncertainty, are included in Table 3.

Table 3- Measuring tools used in the experiments and the details

Type of tools	Model	Measuring range	Least measuring unit	Uncertainty
Anemometer	AM-4206, Lutron	0.3–25 m s^{-1}	0.1 m s^{-1}	1%
Thermometer	TM-914C, Lutron	-100–100 °C	0.01 °C	1%
Hygrometer	HT.3006, Lutron	0–100%	0.1%	0.01%
Pyranometer	TES1333R, Lutron	1–2000 W m^{-2}	10 W m^{-2}	5%
Balancer	SJX1502N, Ohaus	1–1500 g	0.01 g	1%

During the period of experimentation, the validity of the measuring technique was validated through the application of uncertainty computations. Given that random error is unavoidable, unforeseeable, and manageable, it is chiefly responsible for the ambiguity in data measurement. Consequently, the measurements were conducted on a minimum of three occasions, with the mean data being factored in. The overall experimental uncertainty is quantifiable through the utilization of Eq. 5 (Ahmadi, Samimi Akhijahani, & Salami, 2024):

$$W_R = \sqrt{(\frac{\partial R}{\partial x_1} w_1)^2 + (\frac{\partial R}{\partial x_2} w_2)^2 + \ ... + \ (\frac{\partial R}{\partial x_n} w_n)^2} \quad (5)$$

where, w and R stand for the dimensional shape factor and the uncertainty function, respectively, and W_R displays the overall degree of uncertainty (%) of the findings. Additionally, w_n represents the unpredictability of the independent variables. The accuracy and measurement range of the data collection devices are given in Table 4.

Table 4- The factors applied to evaluate uncertainty of the test

Parameters	Solar radiation (W m^{-2})	Temperature (K)	Fluid mass flow rate (kg s^{-1})	Test method
Uncertainty (%)	2.1	0.1	0.5	3.21

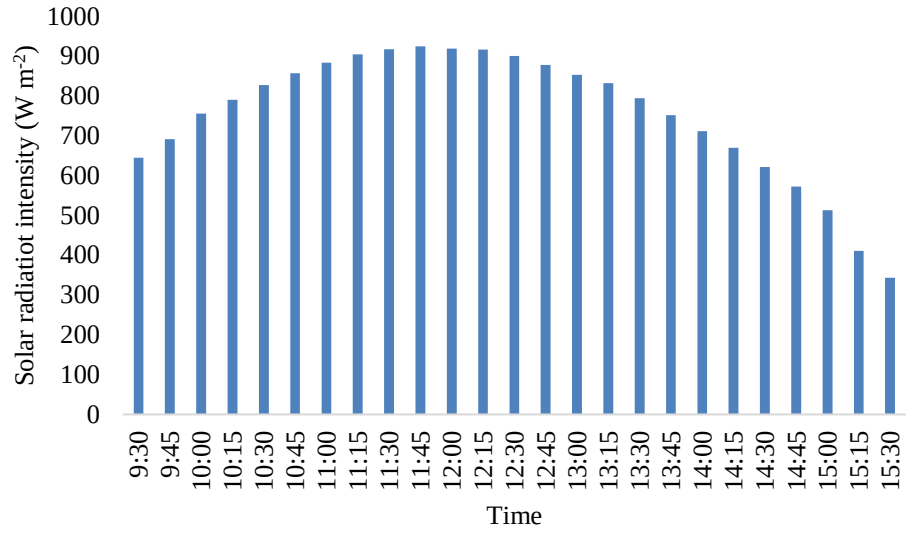

a

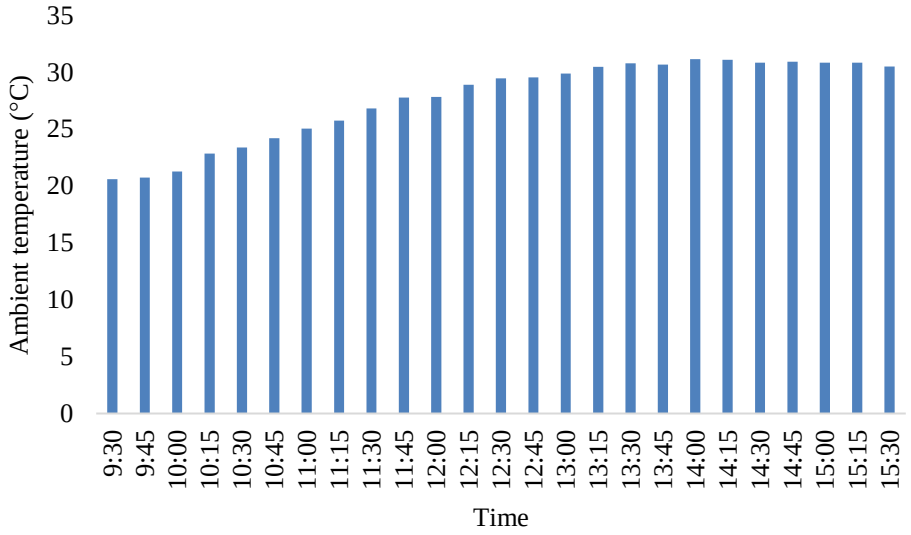

b

Fig. 3. The experimental data of (a) solar radiation intensity, and (b) ambient temperature

Results and Discussions

The experimentation trials were conducted during typical summer days, i.e., 21 to 26 September 2023. As can be seen from Fig. 3, the data during trials were recorded in an unshaded area for the whole trial period. According to data recording procedure, the graphs have been plotted for depicting the trend of changes of solar radiation intensity and ambient temperature over the duration of 09:30 to 15:30. It was observed that the peak value of solar radiation was at a point of

approximately 924±11 W m^{-2} at 11:45 local time. The minimum values were at both the beginning and termination of the experiment. However, ambient temperature followed a different trend compared to that of solar radiation and attained a peak value of around 31.15 °C at 14:00. The variations in airspeed observed on the test days were minimal, fluctuating between 0.2 and 0.9 m s^{-1}. Because of the low convective heat transfer coefficient, the impact on the process is considered negligible.

As illustrated in the graph shown in Fig. 4, both over time and with increasing irradiance intensity, the electrical efficiency of the reference panel exhibits a decline. This decrease can be attributed to the conversion of received light into heat and the resulting rise in the surface temperature of the panel. At peak radiation intensity of 924 W m^{-2}, the electrical efficiency of the reference panel was 12.8%. In contrast, under these conditions, the electrical efficiency of the PVT system was recorded at 9.99%. As the radiation intensity decreased later in the day, the ambient temperature also decreased, and the electrical efficiency of reference panels improved. By 3:30 PM, the reference panel achieved an electrical efficiency of 13.80%, while the PVT system reaches an efficiency of 8.81%. The PVT system also demonstrated its lowest and highest electrical efficiencies at 3:30 AM and 12:30 PM, respectively, with values of 8.81% and 10.21%.

The PVT system's lower electrical efficiency during initial and final periods (e.g., 14:15–15:30) arises from the interplay between cooling benefits and optical losses. At low irradiance, the shading effect of the nanofluid reduces light absorption, outweighing the cooling advantage. Conversely, at peak irradiance, cooling dominates, improving efficiency. The reference panel benefits from natural temperature reduction in the late afternoon, while the PVT system's active cooling becomes less impactful under diminishing solar input.

The reduced electrical efficiency of the PVT system during early and late experimental periods may also stem from optical losses, such as reflection and refraction at the glass-nanofluid interface, particularly under low solar angles. These losses compound the shading effect of the nanofluid, further reducing effective irradiance. Future studies could optimize chamber design (e.g., anti-reflective coatings, tilt adjustments) to minimize these losses.

The efficiency pattern of the reference panel demonstrates physically consistent behavior throughout the day. Starting at 9:30 with a peak efficiency of 14.10%, the panel's performance gradually decreases as the day progresses, reaching 12.80% at 11:45. This initial decline is primarily attributed to the increasing panel temperature as solar radiation intensifies and heat accumulates in the panel. The morning efficiency is highest because the panel starts cool from overnight conditions, allowing optimal photovoltaic conversion. As the day continues into midday (11:45-13:00), the efficiency stabilizes at its lowest range (12.80-12.51%) due to maximum solar radiation and highest panel temperatures, which negatively impact voltage output and overall conversion efficiency. During the early afternoon period (13:00-15:30), as solar radiation decreases and ambient temperatures begin to moderate, the panel's efficiency gradually recovers from 12.51% to 13.80%. This afternoon recovery occurs because the panel begins to cool down, improving its voltage characteristics and conversion efficiency. This pattern aligns with the fundamental physics of photovoltaic panels, which exhibit a negative temperature coefficient, meaning their efficiency decreases as temperature rises.

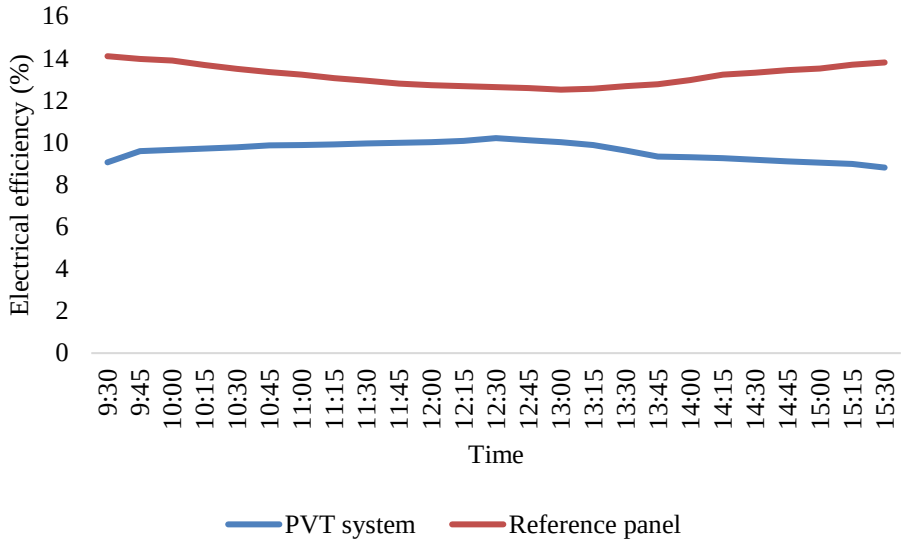

Fig. 4. Average electrical efficiency of the reference and the PVT systems over 6 days

According to Fig. 5, the temperature of the reference panel fluctuated over time in response to changes in irradiation intensity. Specifically, as solar radiation intensity increased, the temperature of the reference panel rose until it reached a maximum value, after which it began to decline. At 11:45 AM, when irradiation intensity peaked at 924 W m^{-2}, the reference panel's temperature reached its highest point of 50.75 °C, followed by a noticeable downward trend. In contrast, the PVT system exhibited an initial upward trend until 2:15 PM, when irradiation intensity was 669 W m^{-2}; it then reached its peak temperature of 39.97 °C before beginning to decrease. The lowest recorded temperatures for the reference and PVT systems in the early hours of the day were 34.30 °C and 22.70 °C, respectively. As anticipated, the presence of the cooling fluid (water or copper oxide nanofluid) resulted in a lower surface temperature for the PVT system, which was reflected in its temperature graph lying below that of the reference panel. The overall efficiency from the beginning to the end of the observation period showed minimum and maximum values of 15.97% and 46.49%, respectively. Notably, when the PVT system temperature peaked at 37.70 °C, the overall efficiency also reached its highest point. Meanwhile, when the temperature of the PVT system peaked at 39.97 °C at 2:15 PM, the overall efficiency for that panel was recorded at 30.16%. Following this peak, as temperatures declined, the efficiency notably increased. This trend also applied to thermal efficiency, which displayed an upward trajectory; when the system temperature was at its peak, the thermal efficiency measured 25.91%. As the temperature decreased, the thermal efficiency continued to rise, ultimately reaching a maximum value of 42.87% in the late afternoon. In contrast, the pattern of electrical efficiency differed significantly. During the early morning hours, when the PVT system temperature was at its lowest at 22.70 °C, electrical efficiency peaked at 9.59%. However, as the system temperature rose and reached a high of 39.97 °C, electrical efficiency reached 10.18%. Then the downward trend continued until 3:30 PM, when efficiency hit its lowest point at 8.81%. The reason for the lesser increase in temperature for the PVT system, compared to the reference panel, can be attributed to the presence of the copper oxide nanofluid, which effectively mitigated temperature rise.

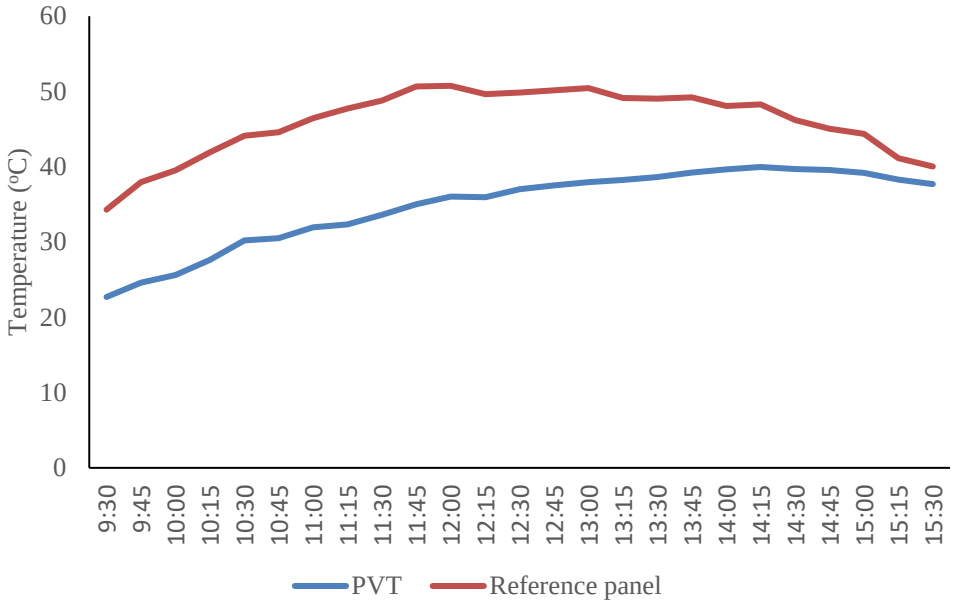

Fig. 5. Average temperature of the reference and the PVT systems over 6 days

Based on the data presented in Fig. 6, it is evident that as the surface temperature of the reference panel increased over time, the intensity of current gradually rose. This increase continued until 2:45 PM, when it peaked at 2.15 A. At this peak moment, the panel's surface temperature was notably high at 45.03 °C, while the voltage measured 20.35 V and the power nearly reached its maximum value of 43.75 W. Following this peak, the intensity of current exhibited a downward trend, reaching a minimum value of 1.69 A by 3:30 PM. In contrast, the voltage decreased until 1:45 PM, when it hit its lowest point of 20.22 V. After this point, the voltage began to increase slightly, but the overall trend remained downward.

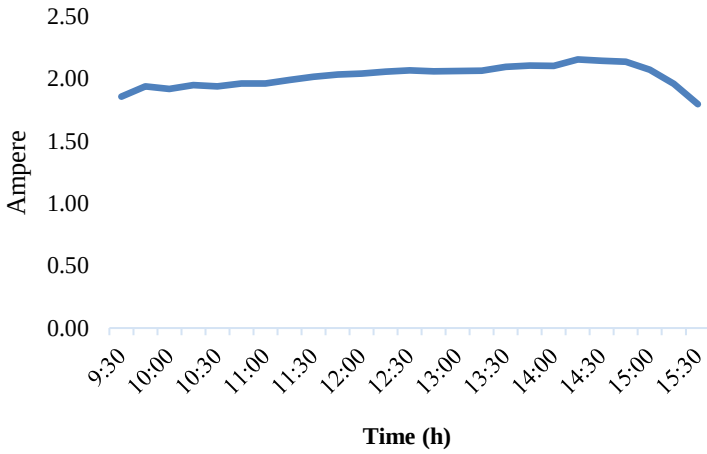

Fig. 6. Average current intensity of the reference panel over 6 days

Furthermore, the maximum values for both voltage and power were recorded at 9:30 AM, reaching 21.8 V and 43.67 W, respectively. At this point, the current intensity was 1.85 A, which was nearly at its peak level. Conversely, the minimum electrical efficiency of 6.56% was observed at 11:45 AM, during which the corresponding values for current, voltage,

power, and temperature were 2.03 A, 20.27 V, 41.14 W, and 50.67 °C, respectively. Thus, it can be concluded that all three factors including current, voltage, and power, have a positive and direct impact on efficiency; as any of these increased or decreased, the electrical efficiency would similarly rise or fall. As shown in Table 5, the output efficiency when using water as a cooling fluid at flow rates of 0.01 and 0.02 L s^{-1} was measured at 22.56% and 26.35%, respectively. In contrast, when copper oxide nanofluid was employed as a coolant at a volume ratio of 0.05%, the output efficiency was 29.66% for a flow rate of 0.01 L s^{-1} and 40.72% for a flow rate of 0.02 L s^{-1}. When the volume ratio was reduced to 0.025%, the recorded output efficiency was 28.73% at a flow rate of 0.01 L s^{-1} and 39.67% at a flow rate of 0.02 L s^{-1}. This data indicated that copper oxide nanofluid had a more significant impact on output efficiency compared to water. Specifically, increasing the flow rate of copper oxide nanofluid enhanced the system's output efficiency. Also, for water, increasing the flow rate led to an increase in output efficiency. Moreover, the reduction of the volume ratio from 0.05% to 0.025% for the nanofluid correlated with an increase in output efficiency, which could be attributed to higher current and voltage intensities within the system.

When maintaining a constant volume ratio of 0.05% and varying flow rates, increasing the flow rate from 0.01 to 0.02 L s^{-1} yielded a thermal efficiency for the system using copper oxide nanofluid that surpassed that of the system utilizing water as a coolant. Specifically, the thermal efficiency values were 31.87% for the nanofluid and 18.53% for water, indicating that the heat transfer rate of copper oxide nanofluid was superior to that of water. However, the electrical efficiency of the system with copper oxide nanofluid (0.05%) was less than that of the system with copper oxide nanofluid (0.025%); at a flow rate of 0.02 L s^{-1}, the values were 8.85% for the 0.05% nanofluid and 10.02% for the 0.025% nanofluid. This discrepancy can be attributed to the lack of shading effects in nanofluid (0.025%), in contrast to the copper oxide nanofluid (0.05%), which has a dark color that reduces the visibility of the panel surface and therefore limits solar energy absorption. Despite this, the overall efficiency of the system employing copper oxide nanofluid was higher than that of the system with water, with overall efficiency values of 40.72% and 26.35%, respectively. Notably, for the water coolant, increasing the flow rate resulted in an improvement in the system's electrical efficiency.

Table 5- Impact of flow rate on system efficiencies

Flow Rate (L s^{-1})	Electrical Efficiency (with copper oxide 0.025%)	Thermal Efficiency (with copper oxide 0.025%)	Overall Efficiency (with copper oxide 0.025%)	Electrical Efficiency (with copper oxide 0.05%)	Thermal Efficiency (with copper oxide 0.05%)	Overall Efficiency (with copper oxide 0.05%)	Electrical Efficiency (with water)	Thermal Efficiency (with water)	Overall Efficiency (with water)
0.01	9.26%	19.47%	28.73%	8.55%	21.11%	29.66%	7.79%	14.77%	22.56%
0.02	10.02%	29.65%	39.67%	8.85%	31.87%	40.72%	7.82%	18.53%	26.35%

At a constant flow rate of 0.01 L s^{-1}, increasing the copper-oxide nanofluid volume ratio to 0.05% enhanced electrical, thermal, and overall efficiencies relative to water. As the volume ratio of the nanofluid decreased from 0.05% to 0.025%, the thermal efficiency of the system declined from 21.11% to 19.47%, while the overall efficiency decreased from 29.66% to 28.73%. Higher volume ratios of nanofluid did not enhance electrical efficiency; in fact, they resulted in a decline in electrical efficiency when the volume ratio exceeded 0.025%. However, reducing the volume ratio of copper oxide nanofluid could improve electrical efficiency, although it still has superiority to the efficiency of pure water.

As the volume ratio neared that of water, the efficiency of the nanofluid system increased correspondingly. Conversely, as the volume ratio decreased, the color of the copper oxide nanofluid became less dark and more transparent, which enhanced its efficiency. Thus, optimizing the volume ratio of the nanofluid was crucial for improving the system's overall performance. At a constant flow rate of 0.02 L s^{-1}, the results were similar. Specifically, reducing the copper oxide concentration from 0.05% to 0.025% led to an increase in electrical efficiency. But thermal efficiency decreased from 31.87% to 29.65%, while electrical efficiency improved from 8.85% to 10.02%. As a result, the overall efficiency of the system demonstrated a similar trend of thermal efficiency, decreasing from 40.72% to 39.67%. Thus, the decrease in the volume ratio of copper oxide nanofluid reduced the overall and thermal efficiencies. When the copper oxide volume ratio was at 0.025%, the thermal and overall efficiencies of the system exceeded those of the water-based system. Also, the electrical efficiency remained higher, indicating that the presence of copper oxide nanofluid enhanced electrical output compared to water, ultimately resulting in higher power production.

At both flow rates of 0.01 and 0.02 L s^{-1}, the electrical efficiency of the system utilizing copper oxide nanofluid as a coolant consistently outperformed that of the system using water. Also, for thermal and overall efficiencies at a flow rate of 0.02 L s^{-1}, the systems with copper oxide coolant demonstrated superior performance compared to those using water, regardless of whether the volume ratio was 0.05% or 0.025%. Similarly, at a lower flow rate of 0.01 L s^{-1}, the thermal and overall efficiencies of the copper oxide-cooled system exceeded those of the water-cooled system. Thus, the copper oxide nanofluid coolant exhibited better electrical, thermal, and overall performance at flow rates of 0.01 and 0.02 L s^{-1}.

According to Table 6, as the flow rate increased, the average temperature difference between the reference panel and the PVT system consistently rose, regardless of the volumetric ratio of the coolant. This trend could be attributed to the increased flow rate of the specific fluid, which allowed for greater heat absorption and subsequently lowered the temperature of the system. As a result, the temperature difference between the reference panel and the PVT system widened. Additionally, the average thermal efficiency showed a clear upward trend in its decrease over the course of the experiment, with values noticeably increasing. Specifically, while thermal efficiency declined on all days of the experiment except for the first day, the overall pattern indicated a significant reduction in average thermal efficiency as the experiment progressed.

Table 6- Average temperature difference between the reference panel and the PVT system at varying flow rates

	Flow rates	
Type of fluid	**0.01 L s^{-1}**	**0.02 L s^{-1}**
Copper oxide nanofluid 0.025%	10.77 ℃	11.29 ℃
Copper oxide nanofluid 0.05%	11.18 ℃	11.80 ℃
Water	8.35 ℃	9.42 ℃

Additionally, the higher thermal efficiency reflects the nanofluid's superior capability to dissipate heat, which benefits thermal energy capture but does not directly enhance electrical output at higher concentration ratios. This trade-off highlights the need to optimize nanofluid composition and optical properties to balance thermal and electrical performance in PVT systems.

Conclusion

This study investigated the impact of copper oxide nanofluid and water on the thermal and electrical efficiency of a photovoltaic thermal system, revealing several key insights. Overall, the electrical efficiency

of the control panel was found to be lower than that of the systems utilizing both coolant types (water and copper oxide nanofluid). Also, the systems using copper oxide nanofluid at both concentrations of 0.025% and 0.05% exhibited higher electrical efficiency compared to water-cooling systems. However, the electrical efficiency of copper oxide nanofluid at a concentration of 0.025% was higher than 0.05%. This observation highlights the influence of the darker color of the copper oxide nanofluid on light absorption. A reduction in the volume percentage of copper oxide from 0.05% to 0.025% resulted in improved electrical efficiencies, attributed to the clearer fluid allowing for greater light penetration to the panel surface. Furthermore, increasing the flow rate from 0.01 to 0.02 L s^{-1} significantly enhanced the thermal and overall performance of the copper oxide nanofluid system, as this change facilitated increased heat absorption from the panel surface and contributed to lower panel temperatures. More study has to be done to examine the optimization of nanofluids' concentrations for even better electrical efficiency, e.g., testing with different nanoparticles with greater transparency or various concentrations of fluids for lowering shading effects such as Al_2O_3. Long-term stability and environmental effect assessments define the commercial viability of nanofluid-based cooling systems. Furthermore, guaranteeing the availability of relevant information for significant acceptance into renewable energy systems calls for scaling of this technology up to large-scale systems and application in hybrid energy solutions.

Conflict of Interest: The authors declare no competing interests.

Author Contributions

M. Ghaderi: Data acquisition, Data pre and post processing, Software services

P. Salami: Supervision, Conceptualization, Methodology, Technical advice, Text mining, Writing the original text

H. Samimi-Akhijahani: Conceptualization, Methodology, Statistical analysis, Software services, Numerical/computer simulation

S. Zareei: Conceptualization, Methodology, Validation

M. Safvati: Visualization, Review and editing services

References

1. Ahmadi, M., Samimi Akhijahani, H., & Salami, P. (2024). Evaluation the performance of drying efficiency and energy efficiency of a solar dryer quipped with phase change materials and air recirculation system. *Iranian Food Science and Technology Research Journal*, *20(2)*, 199-216. https://doi.org/10.22067/ifstrj.2023.79695.1218
2. Ahmed, A., Baig, H., Sundaram, S., & Mallick, T. K. (2019). Use of nanofluids in solar PVThermal systems. *International Journal of Photoenergy*, 2019. https://doi.org/10.1155/2019/8039129
3. Al-Ezzi, A. S., & Ansari, M. N. M. (2022). Photovoltaic solar cells: A review. *Applied System Innovation*, *5*(4), 67. https://doi.org/10.3390/asi5040067
4. Al-Ghezi, M. K., Abass, K. I., Salam, A. Q., Jawad, R. S., & Kazem, H. A. (2021, August). The possibilities of using nano-CuO as coolants for PVT system: An experimental study. *Journal of Physics: Conference Series*, *1973*(1), 012123. IOP Publishing. https://doi.org/10.1088/1742-6596/1973/1/012123
5. Alktranee, M., Shehab, M. A., Németh, Z., Bencs, P., & Hernadi, K. (2023). Experimental study for improving photovoltaic thermal system performance using hybrid titanium oxide-copper oxide nanofluid. *Arabian Journal of Chemistry*, *16*(9), 105102. https://doi.org/10.1016/j.arabjc.2023.105102
6. Allaker, R. P., & Yuan, Z. (2019). *Chapter 10 - Nanoparticles and the control of oral biofilms*. PP 243-275 in K. Subramani and W. Ahmed eds. Micro and Nano Technologies,

Nanobiomaterials in Clinical Dentistry (Second Edition), Elsevier. https://doi.org/10.1016/B978-0-12-815886-9.00010-3
7. Amalraj, S., & Michael, P. A. (2019). Synthesis and characterization of Al_2O_3 and CuO nanoparticles into nanofluids for solar panel applications. *Results in Physics, 15*, 102797. https://doi.org/10.1016/j.rinp.2019.102797
8. Arefin, M. A. (2019). Analysis of an integrated photovoltaic thermal system by top surface natural circulation of water. *Frontiers in Energy Research, 7*, 97. https://doi.org/10.3389/fenrg.2019.00097
9. Brahim, T., & Jemni, A. (2017). Economical assessment and applications of photovoltaic/thermal hybrid solar technology: A review. *Solar Energy, 153*, 540-561. https://doi.org/10.1016/j.solener.2017.05.081
10. Dubey, S., Sarvaiya, J. N., & Seshadri, B. (2013). Temperature dependent photovoltaic (PV) efficiency and its effect on PV production in the world–a review. *Energy Procedia, 33*, 311-321. https://doi.org/10.1016/j.egypro.2013.05.072
11. Elias, B. H., AlSadoon, S. H. M., & Abdulgafar, S. A. (2014). Modeling and Simulation of Photovoltaic Module Considering an Ideal Solar Cell. *International Journal of Advanced Research in Physical Science, 1*(3), 9-18. https://www.arcjournals.org/pdfs/ijarps/v1-i3/2.pdf
12. Haidar, Z. A., Orfi, J., & Kaneesamkandi, Z. (2018). Experimental investigation of evaporative cooling for enhancing photovoltaic panels' efficiency. *Results in Physics, 11*, 690-697. https://doi.org/10.1016/j.rinp.2018.10.016
13. Idoko, L., Anaya-Lara, O., & McDonald, A. (2018). Enhancing PV modules efficiency and power output using multi-concept cooling technique. *Energy Reports, 4*, 357-369. https://doi.org/10.1016/j.egyr.2018.05.004
14. Joshi, S. S., Andhare, A. M., Bhave, N. A., & Gudadhe, N. P. (2019). Thermal management of photovoltaic systems: Case studies. *Journal of Physics: Conference Series, 1240*(1), 012021. IOP Publishing. https://doi.org/10.1088/1742-6596/1240/1/012021
15. Khalili, Z., & Sheikholeslami, M. (2024). Simulation of CuO-water nanofluid flow for cooling of solar photovoltaic module. *Numerical Heat Transfer, Part A: Applications*, 1-12. https://doi.org/10.1080/10407782.2024.2350028
16. Madas, S. R., Narayanan, R., & Gudimetla, P. (2023). Numerical investigation on the optimum performance output of photovoltaic thermal (PVT) systems using nano-copper oxide (CuO) coolant. *Solar Energy*, *255*, 222-235. https://doi.org/10.1016/j.solener.2023.02.035
17. Mirzaee, P., Salami, P., Samimi Akhijahani, H., & Zareei, S. (2023). Life cycle assessment, energy and exergy analysis in an indirect cabinet solar dryer equipped with phase change materials. *Journal of Energy Storage, 61*, 106760. https://doi.org/10.1016/j.est.2023.106760
18. Mohammadi Sarduei, M., Mortezapour, H., & Jafari Naeimi, K. (2017). Numerical analysis of using hybrid photovoltaic-thermal solar water heater in Iran. *Journal of Agricultural Machinery*, *7*(1), 221-233. https://doi.org/10.22067/jam.v7i1.47426
19. Pordanjani, A. H., Aghakhani, S., Afrand, M., Sharifpur, M., Meyer, J. P., Xu, H., …, & Cheraghian, G. (2021). Nanofluids: Physical phenomena, applications in thermal systems and the environmental effects—a critical review. *Journal of Cleaner Production, 320*, 128573. https://doi.org/10.1016/j.jclepro.2021.128573
20. Salami, P., Ajabshirchi, Y., Abdollahpoor, S., & Behfar, H. (2016). A comparison among different parameters for designing a photovoltaic/thermal system using computational fluid dynamics. *Engineering, Technology & Applied Science Research, 6*(5), 1119-1123. https://doi.org/10.48084/etasr.667
21. Sardarabadi, Passandideh-Fard, M., & Zeinali Heris, M. (2014). Experimental investigation of the effects of silica/water nanofluid on PVT (photovoltaic thermal units). *Energy*, *66*, 264-272. https://doi.org/10.1016/j.energy.2014.01.102

22. Sathe, T. M., & Dhoble, A. S. (2017). A review on recent advancements in photovoltaic thermal techniques. *Renewable and Sustainable Energy Reviews*, *76*, 645-672. https://doi.org/10.1016/j.rser.2017.03.075
23. Sheeba, K. N., Rao, R. M. & Jaisankar, S. (2015). A study on the underwater performance of a solar photovoltaic panel. *Energy Sources, Part A: Recovery, Utilization, and Environmental Effects*, *37*(14), 1505-1512. https://doi.org/10.1080/15567036.2011.619632
24. Siah Chehreh Ghadikolaei, S. (2021). Solar photovoltaic cells performance improvement by cooling technology: An overall review. *International Journal of Hydrogen Energy*, *46*(18), 10939-10972. https://doi.org/10.1016/j.ijhydene.2020.12.164
25. Tina, G. M., Rosa-Clot, M., Rosa-Clot, P., & Scandura, P. F. (2012). Optical and thermal behavior of submerged photovoltaic solar panel: SP2. *Energy*, *39*(1), 17-26. https://doi.org/10.1016/j.energy.2011.08.053
26. Yazdanifard, F., Ameri, M., & Ebrahimnia-Bajestan, E. (2017). Performance of nanofluid-based photovoltaic/thermal systems: A review. *Renewable and Sustainable Energy Reviews*, *76*, 323-352. https://doi.org/10.1016/j.rser.2017.03.025

نشریه ماشین‌های کشاورزی
https://jame.um.ac.ir

مقاله پژوهشی

جلد ۱۶، شماره ۳، پاییز ۱۴۰۵، ص ۵۰۷-۵۲۳

بررسی تاثیر ترکیب نانوذرات اکسید مس و آب مقطر بر راندمان یک سامانه فتوولتاییک حرارتی

مهری قادری[۱]، پیمان سلامی[۱*]، هادی صمیمی اخیجهانی[۱]، سمیرا زارعی[۱]، محمد صفوتی[۲]

تاریخ دریافت: ۱۴۰۳/۱۲/۱۴
تاریخ پذیرش: ۱۴۰۴/۰۳/۱۲

چکیده

رشد سریع جمعیت جهان و افزایش تقاضا برای انرژی، همراه با نیاز فوری به حفاظت از محیط‌زیست، محققان را بر آن داشته است تا منابع انرژی تجدیدپذیر را به‌عنوان جایگزینی مناسب برای سوخت‌های فسیلی تجدیدناپذیر بررسی کنند. این مطالعه بهبود عملکرد سیستم‌های فتوولتاییک حرارتی (PVT) را با استفاده از روش خنک‌کننده غوطه‌وری با نانوسیال‌های اکسید مس ارزیابی می‌کند. دستگاه آزمایشی شامل یک محفظه شیشه‌ای بود که سطح پنل خورشیدی در زیر آن غوطه‌ور شده بود. آزمایش‌ها در نسبت حجمی نانوسیال ۰/۰۲۵۰٪ و ۰/۰۵٪ و نرخ جریان ۰/۰۱ و ۰/۰۲ لیتر در ثانیه انجام شد. ارتفاع غوطه‌ور شدن در داخل محفظه شیشه‌ای ۵ سانتی‌متر بود. آزمایش‌ها در شرایط محیطی که شامل دمای محیط ۲۰/۶-۳۱/۲ درجه سلسیوس و تابش ۳۴۳-۹۲۴ وات بر مترمربع انجام شد. نتایج نشان داد که نانوسیال‌های اکسید مس در نسبت حجمی ۰/۰۵ درصد و سرعت جریان ۰/۰۲ لیتر بر ثانیه، راندمان حرارتی را به ۳۱/۸۷ درصد بهبود داده و دمای سطح پانل را تا ۱۱/۸ درجه سلسیوس در مقایسه با خنک‌کننده آب کاهش داده است. همچنین راندمان الکتریکی سامانه PVT از پنل مرجع فراتر رفت. راندمان کلی سیستم PVT به ۴۱/۸۹ درصد رسید. این یافته‌ها پتانسیل خنک‌سازی مبتنی بر نانوسیال را برای بهینه‌سازی راندمان سامانه PVT با افزایش مدیریت حرارتی نشان می‌دهد.

واژه‌های کلیدی: خنک‌کنندگی، دمای سامانه، راندمان حرارتی، غوطه‌وری، نانوسیال اکسید مس

۱- گروه مهندسی بیوسیستم، دانشکده کشاورزی، دانشگاه کردستان، سنندج، ایران
۲- گروه مهندسی بیوسیستم، دانشکده کشاورزی، دانشگاه صنعتی اصفهان، اصفهان، ایران
(*- نویسنده مسئول: Email: p.salami@uok.ac.ir)

https://doi.org/10.22067/jam.2025.92457.1349

Journal of Agricultural Machinery

Homepage: https://jame.um.ac.ir

Research Article
Vol. 16, No. 3, 2026, p. 525-548

Optimization of the Canola Harvester Blade Based on Energy Reduction Approach and Life Cycle Assessment

Gh. Ahmadzade[1], M. R. Maleki[1], P. Salami[1*], K. Mollazade[1]

1- Department of Biosystems Engineering, Faculty of Agriculture, University of Kurdistan, Sanandaj, Iran
(* Corresponding author Email: p.salami@uok.ac.ir)

Received: 09 March 2025
Revised: 13 May 2025
Accepted: 08 June 2025
Available Online: 07 July 2025

How to cite this article:
Ahmadzade, Gh., Maleki, M. R., Salami, P., & Mollazade, K. (2026). Optimization of the Canola Harvester Blade Based on Energy Reduction Approach and Life Cycle Assessment. *Journal of Agricultural Machinery*, *16*(3), 525-548. https://doi.org/10.22067/jam.2025.92546.1353

Abstract

Grain harvesting operations account for approximately 25-30% of total direct energy consumption in crop production systems. Developing appropriate blades for harvesting canola (*Brassica napus* L.) is crucial due to its distinct characteristics compared to other cereal grains. This study investigated the effects of blade angles (placement angles: 30°, 45°, and 60°; sharpness angles: 30°, 45°, and 60°), reciprocating movement speed (800, 1100, and 1400 courses per minute), and moisture levels (19%, 22%, and 24%) on reducing force, shear stress, and energy consumption during canola harvesting. Results showed that a blade sharpness angle of 30° yielded the lowest shear stress (0.175 N mm^{-2}) compared to 60° (0.303 N mm^{-2}). The 45° blade placement angle demonstrated minimum shear stress (0.177 N mm^{-2}) versus 60° (0.320 N mm^{-2}). Increasing moisture content from 19% to 24% reduced shear stress from 0.256 N mm^{-2} to 0.200 N mm^{-2}. The highest reciprocating speed (1400 courses per minute) resulted in the lowest shear stress (0.167 N mm^{-2}) compared to 800 courses per minute (0.286 N mm^{-2}). Life cycle assessment revealed that varying blade placement angles (30° to 60°) could increase marine aquatic ecotoxicity by up to 55,762.55 kg dichlorobenzene equivalent, while changes in blade sharpness angles and reciprocating speed could lead to increases of 377,429.87 kg and 143,185.69 kg dichlorobenzene equivalent, respectively. The optimal configuration—comprising a sharpness angle of 30°, a placement angle of 45°, a moisture content of 24%, and a reciprocating speed of 1400 courses per minute—significantly reduced both shear energy and environmental impact.

Keywords: Blade placement angle, Blade sharpness angle, Life cycle impact assessment, Shear energy, Shear stress

Introduction

In recent years, reducing energy consumption in agricultural machinery has become increasingly important, particularly in EU open-field agriculture where total energy usage reaches 1431 PJ annually, equivalent to 3.7% of total EU energy consumption. Within this sector, on-farm diesel use, which includes harvesting operations, accounts for 31% of total energy inputs. This significant proportion highlights the importance of optimizing agricultural machinery operations, especially in grain harvesting machines, to reduce overall energy consumption and support the transition towards more sustainable farming practices (Paris *et al.*, 2022). The energy required for cutting canola stems varies from 0.76 kJ to 1.1 kJ, depending on moisture content and cutting height, representing a measurable component of harvesting energy consumption.

Authors retain the copyright. This is an open access article distributed under Creative Commons Attribution 4.0 International License (CC BY 4.0).

https://doi.org/10.22067/jam.2025.92546.1353

Understanding these energy requirements is important for optimizing harvester blade design and operational parameters to improve overall harvesting efficiency (Azadbakht, Esmaeilzadeh, & Esmaeili-Shayan, 2015). Numerous studies have already been undertaken to optimize energy consumption related to the cutting process of reciprocating lathes (Kushwaha, Vashnav, & Zoerb, 1983; Mohammadi Baneh, Navid, Alizadeh, & Ghasem Zadeh, 2012; Yin *et al.*, 2021; Yuan *et al.*, 2023).

Canola cultivation is expanding, particularly in tropical regions, as a crucial source of edible oils. Canola harvesting employs two primary methods: (1) using grain combines with specific adjustments, and (2) utilizing a reciprocating cutter bar followed by product collection using a combine with a pick-up nose. While wheat combines are commonly adapted for canola harvesting, the distinct physical and mechanical properties of canola stems necessitate specialized blade design. A study by Azadbakht *et al.* (2015) demonstrated that cutting energy requirements vary significantly ($P < 0.01$) with cutting height and moisture content, ranging from 0.76 kJ at 11.6% moisture content and 30 cm cutting height to 1.1 kJ at 25.5% moisture content and 10 cm cutting height, with an optimal blade velocity of 2.64 m s^{-1}. Baruah & Panesar (2005) reported that crop throughput for canola ranges from 3.87 to 17.85 Mg h^{-1}, compared to 4.61 to 11.49 Mg h^{-1} for wheat, highlighting the need for crop-specific optimization. Several parameters, including blade edge angle, blade angle, blade cutting speed, and product moisture, significantly influence the power and energy requirements in cutter bar harvesters. Therefore, determining optimal values for these parameters is crucial for designing efficient canola harvesting tools. Therefore, by determining the appropriate value for these parameters, they can be used as criteria in the design of canola harvesting tools.

Several studies have been conducted in relation to the energy consumption of cutter bar mowers. According to many studies, the energy required by the stem cutting unit in the cutter bar includes overcoming air friction, cutting products, overcoming the friction of crushed products, and especially the friction in the mechanism of the machine and the cutting stem (Chattopadhyay & Pandey, 2001; Kronbergs, 2000). Studies have shown that several key factors influence the energy required to cut wheat stems. The moisture content, which refers to the water present in the wheat stem, affects its physical properties and cutting resistance. The cultivar type, meaning the specific variety of wheat with its unique stem characteristics such as thickness and fiber density, also impacts cutting energy requirements. The blade angle, defined as the angle at which the cutting blade meets the wheat stem, and cutting speed, which is the rate at which the blade moves through the stem, are crucial mechanical parameters. When moisture content and blade angle were reduced while increasing cutting speed, the energy required for cutting decreased. The diversity factor, which encompasses the variability in physical properties among different wheat varieties and environmental growing conditions, was also found to significantly affect cutting energy requirements (Persson, 1987).

A study was conducted to examine the impact of various factors on the shear strength and energy consumption of wheat stems during the design and construction of a cutting mechanism for clustered wheat. The research focused on three levels of blade sharpness (17, 20, and 24 degrees), four levels of inclination angle (20, 35, 50, and 65 degrees), and three levels of cutting speed (25, 35, and 45 mm min^{-1}). The results indicated that both the inclination angle and blade sharpness had a significant influence on the shear strength and energy consumption of wheat stems, with significance at the 1% level. However, there was no significant interaction effect observed between the angle of sharpness, inclination angle, and cutting speed. Among the two factors, the inclination angle of the blade had a greater impact on the shear strength and energy consumption of the stems. The average

cutting energy consumption per unit area was estimated to be 6.23 mJ mm^{-2}.

A study explored the impact of various cutting unit parameters on energy consumption during the harvesting of Miscanthus plant. The researchers specifically focused on analyzing the effects of cutting speed, diagonal blade angle, and stem diameter on energy consumption. Within their investigation, three different blade cutting angles were taken into consideration. The findings of the study revealed that a diagonal blade angle of 60 degrees and a cutting speed of 12.9 m s^{-1} were identified as the optimal conditions for efficient cutting of the product. Under these conditions, the specific cutting energy was measured to be 741.9 J m^{-1}. However, it was observed that when the cutting speed was increased to 18.7 m s^{-1}, the specific cutting energy experienced a significant rise of 42.6% (Johnson, Clementson, Mathanker, Grift, & Hansen, 2012).

The impact of cutting parameters on the ultimate shear stress and specific cutting energy of Sisal leaves was investigated to design efficient and energy-saving harvesting machinery. In their study, they experimentally examined hybrid (H.) 11648 sisal leaves (at 83% moisture content) using both the single-factor method and response surface methodology under quasi-static cutting conditions. The findings indicated that factors such as cutting speed, blade oblique angle, blade entry angle, and leaf elevation angle significantly affect the ultimate shear stress and specific cutting energy of the leaves. Additionally, the interaction between the blade oblique angle and leaf elevation angle had a notable effect on ultimate shear stress, while the combination of cutting speed and blade oblique angle significantly influenced specific cutting energy. The optimal cutting parameters identified through the multi-objective response equation were a cutting speed of 500 mm min^{-1}, a blade oblique angle of 24.23°, a blade entry angle of -28.8°, and a leaf elevation angle of 20°. With these settings, the ultimate shear stress and specific cutting energy for sisal leaves could be reduced by 43.48% and 10.71%, respectively, compared to conditions typical of practical harvesting. Furthermore, within acceptable limits for ultimate shear stress and specific cutting energy, increasing cutting speed and employing parameter values close to the optimized settings can positively impact peak cutting force reduction, energy efficiency, and the compactness of harvesting machinery (Song *et al.*, 2022).

In a significant study focusing on blade design optimization and energy reduction, Maughan, Mathanker, Grift, Hansen, and Ting (2013) investigated the impact of blade oblique angles on harvesting energy requirements. Their research directly addressed machinery inefficiencies by modifying the disk head of a mower-conditioner and testing different blade angles. Through implementation of blades with 20° and 30° oblique angles, they achieved substantial energy savings. Most notably, the 30° oblique angle blades demonstrated a 27% reduction in energy consumption, requiring only 13.5 MJ Mg^{-1} compared to 18.5 MJ Mg^{-1} for conventional straight (0°) blades. Their study incorporated real-time yield sensing systems to provide point-specific energy consumption data, offering precise measurements of blade performance optimization.

In terms of optimizing harvester blade parameters, Rezahosseini, Jafari Naeimi, and Mortezapour (2019) investigated the effects of forward velocity and blade attack angle on harvesting efficiency. Their findings revealed that both parameters significantly affected harvesting performance at a 5% probability level. The optimal configuration was achieved with a 25-degree attack angle and 2 km h^{-1} forward velocity, resulting in 80% harvesting efficiency. Notably, the highest machine capacity of over 5300 plants per hour was achieved at 3.5 km h^{-1} forward velocity while maintaining the optimal 25-degree attack angle. Their research demonstrates the critical relationship between blade angle optimization and operational parameters.

Recent studies have demonstrated the significant impact of blade design parameters

on harvesting efficiency. Okyere *et al.* (2022) conducted a comprehensive analysis of blade angles and operational parameters, finding that a 45° blade angle produced optimal cutting performance compared to 30° and 60° angles. Their study revealed that machine speed significantly affects cutting efficiency, with 2230 rpm yielding the best results when combined with the optimal 45° blade angle. While their research focused on corn stalks, their findings about blade angle optimization provide valuable insights for harvester blade design across different crops. Their results suggest that blade angle optimization can significantly impact both cutting efficiency and machine performance.

Agricultural harvesting efficiency is highly dependent on crop-specific cutting equipment. Each crop has unique physical properties that demand specialized cutting blades- for instance, wheat stems have different structural characteristics compared to canola stems, making wheat harvester blades unsuitable for canola harvesting. Using inappropriate blades can lead to increased energy consumption, reduced harvesting efficiency, and potential crop damage.

Previous studies on harvester blade optimization have primarily focused on mechanical performance and energy consumption for individual crops. However, these studies lack a comprehensive life cycle assessment approach, which is crucial for understanding the broader environmental implications of harvesting equipment choices. By integrating LCA with energy optimization, this study introduces a novel framework that considers both operational efficiency and environmental impact.

Additionally, this research develops an innovative methodology that combines mechanical testing, energy analysis, and environmental assessment - creating a more holistic approach to agricultural equipment design. This integrated approach not only optimizes harvester blade performance for canola but also establishes a transferable methodology for other crop-specific applications.

Previous studies have indicated that the blade sharpness, blade placement angle, moisture content, and cutting speed play crucial roles in reducing shear energy and energy consumption in cutter bar harvesters. Given that most harvesting combines in Iran are equipped with heads designed for wheat harvesting, it is imperative to explore the impact of these factors on canola harvesting due to the distinct characteristics of wheat and canola. Utilizing optimized reciprocating cutter bars for canola harvesting could be beneficial in this regard. By identifying the optimal values for these parameters, it is possible to minimize energy usage and environmental pollution. Thus, the objective is to assess the potential impact of adjusting the specified parameters on the reduction of energy consumption and the release of pollutants into the environment. This involves determining the extent to which these changes can contribute to minimizing environmental impacts. Therefore, the primary objective of this study was to analyze the influence of blade sharpness, blade positioning angle, moisture, and cutting speed on canola harvesters to ensure sustainable and efficient production. To achieve this aim, the following specific objectives were pursued:

1. To develop an innovative energy-optimization model for canola harvester blades by analyzing the relationship between energy consumption and cutting parameters (moisture content, loading rate, and blade characteristics) using a specially designed laboratory setup.
2. To quantify energy reduction potential through comparative analysis of different blade designs and operational parameters, establishing energy-efficient cutting conditions.
3. To evaluate the environmental impacts through Life Cycle Assessment, creating an integrated framework that optimizes both energy efficiency and environmental performance.

Materials and Methods

Design and development of a cutting mechanism are influenced by many

parameters, such as the type of cutting blade, blade angle, cutting speed, and physical and mechanical properties of the stalks. The latter can be identified by measuring the shear force required for stalk cutting. The canola stalk samples were collected from mature plants at physiological maturity. The stalks had an average height of 120 ± 5 cm and stem diameter of 1.5 ± 0.2 cm at the base. For the cutting tests, the load was applied at 15 cm above ground level, which represents the typical harvesting height in commercial canola production. This location was chosen because it provides optimal stubble height for subsequent field operations. Also, it ensures consistent mechanical properties as the lower portion of the stalk typically has higher structural rigidity. Likewise, it matches common harvester header settings.

A test rig (Figure 1) was developed to determine the shear force of the canola stalk, while adjusting the aforementioned parameters. It consisted of a chassis, a stationary blade holder, a cutter bar, a crank drive and crank drive linkage, a 380 V AC motor (Y-802-4, 0.75 kW), and an inverter. In addition, the system included a measuring unit, an electronic board (Uno R3, Arduino Co., Italy), a 24-bit analog-to-digital converter (HX71, China), and a computer for data collection and monitoring. The aim was to identify the most optimal mode in terms of energy consumption during stalk cutting. This was carried out by a measurement system assembled on the crank drive linkage using a 40 kg ± 0.01 g load cell (Top Sensor, China). The load cell was placed between the crank drive linkage and the beginning of the cutter bar to accurately capture the force exerted during cutting operations.

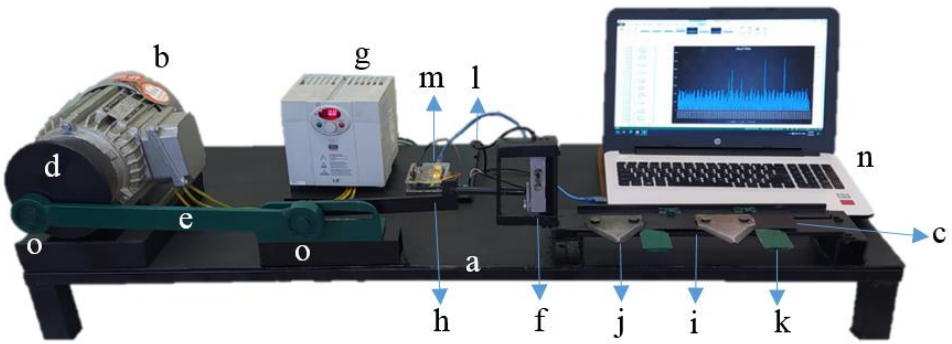

Fig. 1. The fabricated laboratory cutter bar: (a) Chassis, (b) Electric motor, (c) Upper bar, (d) Reluctance center crank drive, (e) Crank drive shaft, (f) Load cell, (g) Inverter, (h) Connecting rod, (i) Lower bar, (j) Cutting blade, (k) Designed blade, (l) HX711 amplifier module, (m) Arduino board, (n) Computer, and (o) Bearing

The experiments were carried out to determine the shearing force of the canola stalks and to analyze the impact of various parameters such as blade edge sharpness angle (30, 45, and 60 degrees), blade angle (30, 45, and 60 degrees), and cutter bar speed at 800, 1100, and 1400 courses per minute. The length of the course was set at 7.6 cm, and the experiments were conducted at three different moisture levels ranging from 18-21%, 21-23%, and 23-25%. The measurements were based on shear force, shear strength, and shear energy, and each condition was tested in triplicate. A sample of the manufactured device is shown in Figure 1. To further investigate the influence of these parameters on the cutting force and shear resistance of canola stalks, a factorial experiment was conducted using a completely random design in SPSS software, with three replications.

Blade angles of 30°, 45°, and 60° were selected based on empirical observations and prior studies (Johnson *et al.*, 2012; Heidari, Chegini, & Kianmehr, 2012). Angles below 30° are avoided in coarse-stemmed crops due to accelerated blade wear (Persson, 1987), while angles exceeding 60° significantly increase shear resistance, as observed in

preliminary trials for this study. Reciprocating speeds (800-1400 cpm) were chosen to align with typical combine harvester operations in Iran, where adjustments are often made to balance cutting efficiency and fuel consumption (Yuan *et al.*, 2023). Moisture levels (18-25%) reflect the range observed during canola harvesting in Kurdistan province, as verified by field measurements.

To develop the energy-optimization model, various blade designs were analyzed for their potential energy efficiency. The blade characteristics were first modeled using SolidWorks (2018) to establish baseline designs. These designs were then evaluated using Ansys 2015 software to understand their mechanical behavior under different loading conditions, which directly influences energy consumption during cutting. The key blade characteristics that influence energy consumption are presented in Table 1. The blades were fabricated using CK75 steel (properties shown in Table 2), selected based on its mechanical properties that affect energy transfer during the cutting process (Roudbari, Refahati, & Mehdipour, 2021).

Table 1- Mechanical and physical properties of the designed blades (Roudbari *et al.*, 2021)

Density (kg m^{-3})	Elastic modulus (GPa)	Poisson's ratio	Shear modulus (GPa)	Ultimate tensile stress (MPa)	Yield stress (MPa)
7850	200	0.3	76.92	460	250

Table 2-Specifications of the material of the blades (Roudbari *et al.*, 2021)

Mechanical properties		
Quantity	**Value**	**Unit**
Young,s modulus	200000	MPa
Tensile strength	650-880	MPa
Elongation	8-25	%
Fatigue	275	MPa
Yield strength	350-550	MPa
Physical properties		
Quantity	Value	Unit
Thermal expansion	10	e-6 K^{-1}
Thermal conductivity	25	W (m K)$^{-1}$
Specific heat	460	J (kg K)$^{-1}$
Melting temperature	1450-1510	°C
Density	7700	kg m^{-3}
Resistivity	0.55	Ohm mm^2 m^{-1}

The blades were designed and underwent meshing in the Ansys environment, as shown in Figure 2. The design of the blades in this study was guided by rigorous adherence to engineering standards and methodologies to ensure mechanical reliability, environmental sustainability, and alignment with industry practices. Material selection prioritized CK75 steel, a high-performance alloy conforming to ASTM A20/A20M-19 and ISO 6935-1:2018 standards, ensuring optimal tensile strength, fatigue resistance, and thermal stability for agricultural applications. The material's mechanical properties, such as Young's modulus and yield strength, were sourced from standardized databases (e.g., Ansys material libraries) to maintain accuracy in computational simulations.

Finite element analysis (FEA) was conducted using ANSYS 2015, an industry-standard software compliant with ISO 10303 (STEP) for geometric modeling. An automatic meshing strategy was employed to optimize computational efficiency, avoiding the labor-intensive process of manual meshing.

Blade geometry was informed by prior research (Nazari Galedar *et al.*, 2008; Song *et al.*, 2022) and designed to balance cutting efficiency, energy consumption, and stress distribution. Angles of 30°, 45°, and 60° were

validated via FEA to ensure compliance with von Mises stress criteria, confirming safe operation within CK75 steel's yield strength limits.

Automatic meshing procedure was employed since a tedious trial and error were required to accomplish appropriate mesh size. Automatic meshing with tetrahedral elements was selected to balance computational efficiency and accuracy, given the geometric complexity of the blade edges and mounting slots. A mesh sensitivity analysis was conducted by iteratively refining element sizes until stress convergence (variation <5%) was achieved at critical regions (blade edge and support interface). For 30°, 45°, and 60° blade angles, a total of 10,361 nodes and 5,380 elements, 11,741 nodes and 5,510 elements, and 11,903 nodes and 6,181 elements were employed, respectively.

The boundary conditions applied in Ansys aimed to replicate real-world operational constraints. The base of each blade (mounting region interfacing with the cutter bar) was assigned a fixed support to simulate rigid attachment to the harvesting mechanism. A tension force of 350 N was applied perpendicular to the blade's sharp edge, distributed uniformly across the blade edge, to reflect the maximum shear stress derived from experimental shear force measurements. The safety factor of 5 was incorporated to account for dynamic loading fluctuations during field operations, such as irregular stem density or foreign object impacts.

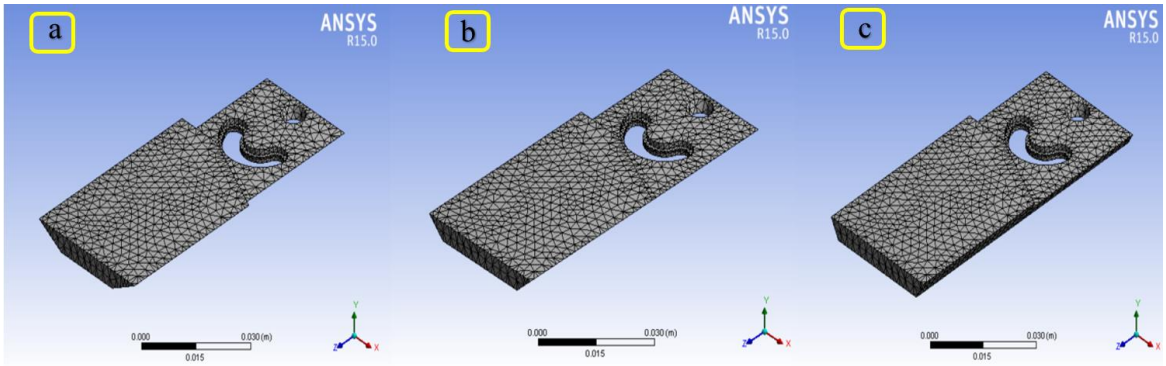

Fig. 2. Meshed models of three different designed blades: (a) the 30-degree blade, (b) the 45-degree blade, and (c) the 60-degree blade

The diagram illustrating the designed blades can be observed in Figure 3. The measurements are expressed in millimeters. The blades were subjected to the maximum force and tension required for cutting canola. To simulate the behavior of the blades during the cutting process, the maximum shear stress needed to cut the stalk was determined. The shear stress was applied to the blades based on the findings of Nazari Galedar *et al.* (2008), with the stress being directed towards the sharp edge of the blades perpendicular to their surface. A tension force of 350 N, with a safety factor of 5, was applied to the edge of the blades and results were expressed as Von Mises stress. Two blades were made for each specification of blade angle degree of 30, 45, and 60 degrees for further reservation.

The FEA simulations were conducted using ANSYS 2015, adhering to ISO 10303 standards for geometric modeling. The analysis incorporated the von Mises criterion to assess yielding, ensuring stresses remained below CK75 steel's yield strength (250 MPa). Elastic deformation was modeled using Hooke's Law, while plastic deformation was accounted for beyond the yield point. A safety factor of 5 was applied to the 350 N tension force, reducing the effective load to 70 N for simulations, aligning with engineering safety protocols.

The theoretical framework for stress analysis included elastic-plastic material behavior, where stresses below the yield point

(250 MPa) ensured reversible deformation. Beyond this threshold, plastic deformation was modeled to identify failure risks. The 30° blade angle demonstrated the lowest shear stress (0.737 N mm^{-2}) but required FEA validation to confirm compliance with safety margins. Stress maps revealed potential plastic deformation at blade edges and supports, prompting design adjustments to redistribute loads and enhance durability.

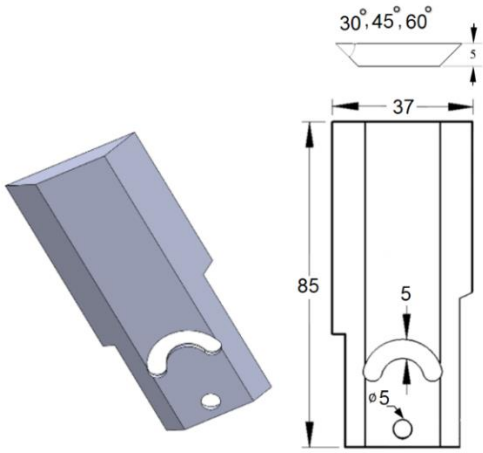

Fig. 3. Schematic of the designed blades (dimensions are in mm)

The Hyola 401 canola cultivar was cultivated in Kurdistan province of Iran during the summer of 2020. This area is situated within the latitudes of 34° to 38°N, and longitudes of 41° to 47°E. Simple random sampling served as the sampling technique for this research.

Once the samples were gathered, they were transported to the laboratory of the Department of Biosystems Engineering, Faculty of Agriculture, University of Kurdistan, Iran to assess the moisture content of canola stalks. The collected stem samples were carefully positioned inside an oven, where they were subjected to a controlled temperature of 103°C for a duration of 24 hours. Subsequently, the moisture content of the samples was measured using Eq. 1, which adheres to established standards and is based on the wet weight of the specimens (Aghbashlo, Kianmehr, & Hassan-Beygi, 2008; Yeganeh & Trystram, 2013):

$$U_w = \frac{G_w}{(G_w + G_{dm})} \quad (1)$$

where, G_w represents the weight of lost moisture, and G_{dm} represents the weight of the dried sample. To measure the dimensions of the canola stem, including length, width, and thickness, a digital caliper (model DC-515, Taiwan) with an accuracy of 0.01 mm was used.

Mechanical attributes refer to a material's mechanical characteristics in various conditions and under diverse external loads. Mechanical qualities vary depending on the substance. Typically, the "tension-compression" examination and the "force-deformation" relationship (stress-strain) are employed to ascertain and elucidate the mechanical properties of materials (Song & Muliana, 2019). When it comes to harvesting agricultural products, these materials are subjected to different mechanical factors such as compressive force, tensile force, and impact. These factors can lead to deformation in the stem of the products, and if the deformation exceeds a certain limit, it can result in breakage and other forms of mechanical damage. To prevent such damage, it is crucial to understand the resistance characteristics of the product's stem under different conditions. This information can be obtained through standardized tests conducted under controlled conditions. The pressure tensile test is one of the key methods used to determine the product's stem tissue properties. Several factors influence the mechanical

properties of agricultural products, including the structure and texture of the product, its moisture content, the speed and type of loading, as well as the duration of loading (Amirian, Shahbazi, & Taheri Garavand, 2018).

The quasi-static tests were performed using a hydraulic Instron stand (STM-1 model, 1000±0.01 N) to determine the shear forces, shear stress, and compressive strength of canola, where the specimen is crushed at a very low speed between two cutting edges. A quasi-static test is described as the energy absorption capability of the composite when they are crushed under axial loads (Figure 4). The tests were conducted by crushing specimens at a controlled speed between two cutting edges. The room temperature was (23±2°C) and the relative humidity was 50±5%. The experiments were performed at three different loading rates of 150, 250, and 350 mm min^{-1}, with 50 mm maximum displacement and 100 Hz data acquisition rate. The specimens were prepared with 11.57 mm length and 10.46 mm stem average diameter. Throughout the experiments, various measurements were recorded, including force-displacement curves, maximum shear force (N), shear stress (MPa), energy absorption (mJ), and compressive strength (MPa). The quasi-static test characterizes the energy absorption capability of the specimens when crushed under axial loads, providing crucial information about their mechanical behavior under controlled loading conditions.

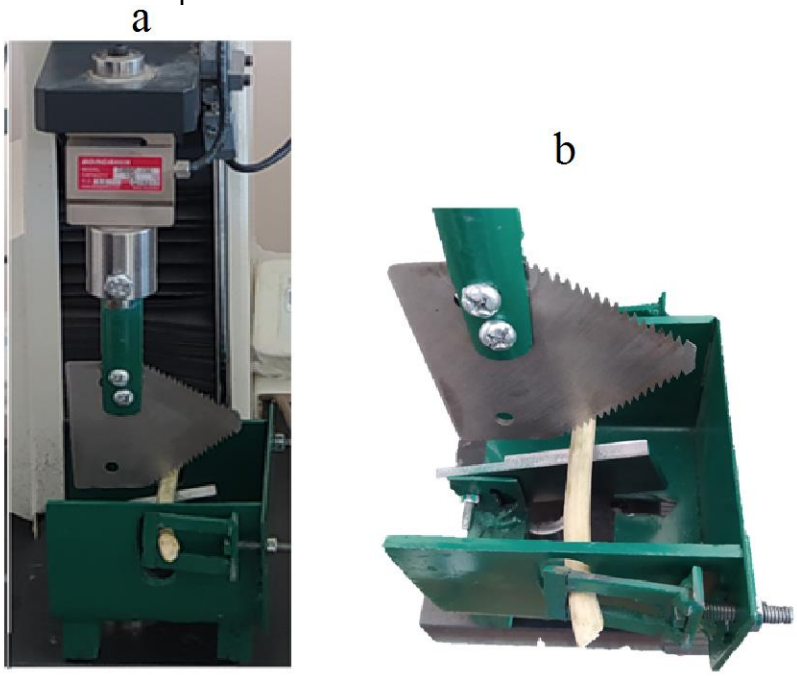

Fig. 4. A mechanism designed for conducting quasi-static tests: (a) an Instron equipped with a blade and counter blade mechanism, and (b) the blade and counter blade mechanism

The Shear Energy Index was determined to evaluate the energy efficiency of the cutting process. This index was calculated as the ratio of the energy absorbed during shearing to the cross-sectional area of the specimen, expressed in mJ mm^{-2}. The energy absorption was obtained by integrating the area under the force-displacement curve up to the maximum shear force using the trapezoidal method. The force-displacement data were recorded through the Instron testing machine's data acquisition system at a sampling rate of 100 Hz.

In order to assess the environmental impact of utilizing different blades and their placement angles in agricultural combines on a national scale, the life cycle assessment approach was employed. The total amount of pollutants released into the environment was

calculated under the assumption that all agricultural combines in the country were outfitted with each of the blade treatments. This analysis aimed to determine the extent to which these treatments could potentially influence the overall level of pollutants emitted nationwide.

Life cycle assessment represents a cutting-edge approach extensively employed for evaluating the energy requirements and possible ecological consequences of a product or manufacturing process from inception to end. The comprehensive "cradle to grave" technique encompasses a thorough examination of all phases, including resource extraction, material production, component manufacturing, and product consumption management in the form of waste, recycling, or final disposal (Mirzaee, Salami, Akhijahani, & Zareei, 2023).

In this research, the SIMAPRO software version 9 utilized the CML 2 baseline 2000 V2.05 life cycle impact assessment method. This particular method, developed by the Swiss Federal Institute of Technology, adopts a comprehensive approach that encompasses various impact groups and injury groups. It incorporates ten midpoint impact groups, providing a holistic perspective on the assessment of life cycle impacts. The midpoint impact categories were: abiotic depletion (elements and fossil fuels), global warming, ozone layer depletion, human toxicity, freshwater aquatic ecotoxicity, marine aquatic ecotoxicity, terrestrial ecotoxicity, photochemical oxidation, acidification, and eutrophication.

Results and Discussion

Finite element analysis of blades

The stress analysis and deformation results of the blades were examined when subjected to a constant force of 350 N, with consideration given to various types of blades that were manufactured.

The stress analysis and blade displacement results obtained through Ansys software for the blades with a sharpness of 30, 45, and 60 degrees are illustrated in Figure 5. Upon closer examination of the stress distribution for the first blade type (I), it was evident that the highest stress concentration occurred at the edge of the blade and in close proximity to the support, reaching a value of 30.618 MPa. This stress concentration is primarily attributed to the blade being constrained within the slot and coming into contact with a steel object (pin) at the support location under actual operating conditions. Analysis of the blade deformation revealed that the maximum displacement of 1.0703×10^{-5} m was observed at the blade tip. Given that the blade can be likened to a beam subjected to a significant lateral load, it is reasonable to expect that the most significant deformation would manifest at the tip of the blade, akin to the tip of a beam. Figure 5 shows the profiles of deformation and maximum stress for the application of a 350 N load.

The stress and deformation analysis outcomes for the second blade type (II) are also illustrated in Figure 5. The findings for the second blade type mirrored those of the first blade type concerning the position of the highest deformation and the peak Von Mises stress. Specifically, the highest deformation was detected at the blade's tip, measuring 7.854×10^{-6} m, while the maximum Von Mises stress was identified at the support's edge, measuring 19.712 MPa.

Figure 5 also presents the stress and deformation analysis results for the third type of blade (III). Similar to the first and second type blades, the third type blade exhibited comparable patterns in terms of the location of the largest deformation and the maximum Von Mises stress. Upon examining the deformation results, it was observed that the tip of the blade experienced a maximum displacement of 6.7606×10^{-6} m, additionally, the highest stress was observed at the edge of the blade and in close proximity to the support, measuring 16.692 MPa.

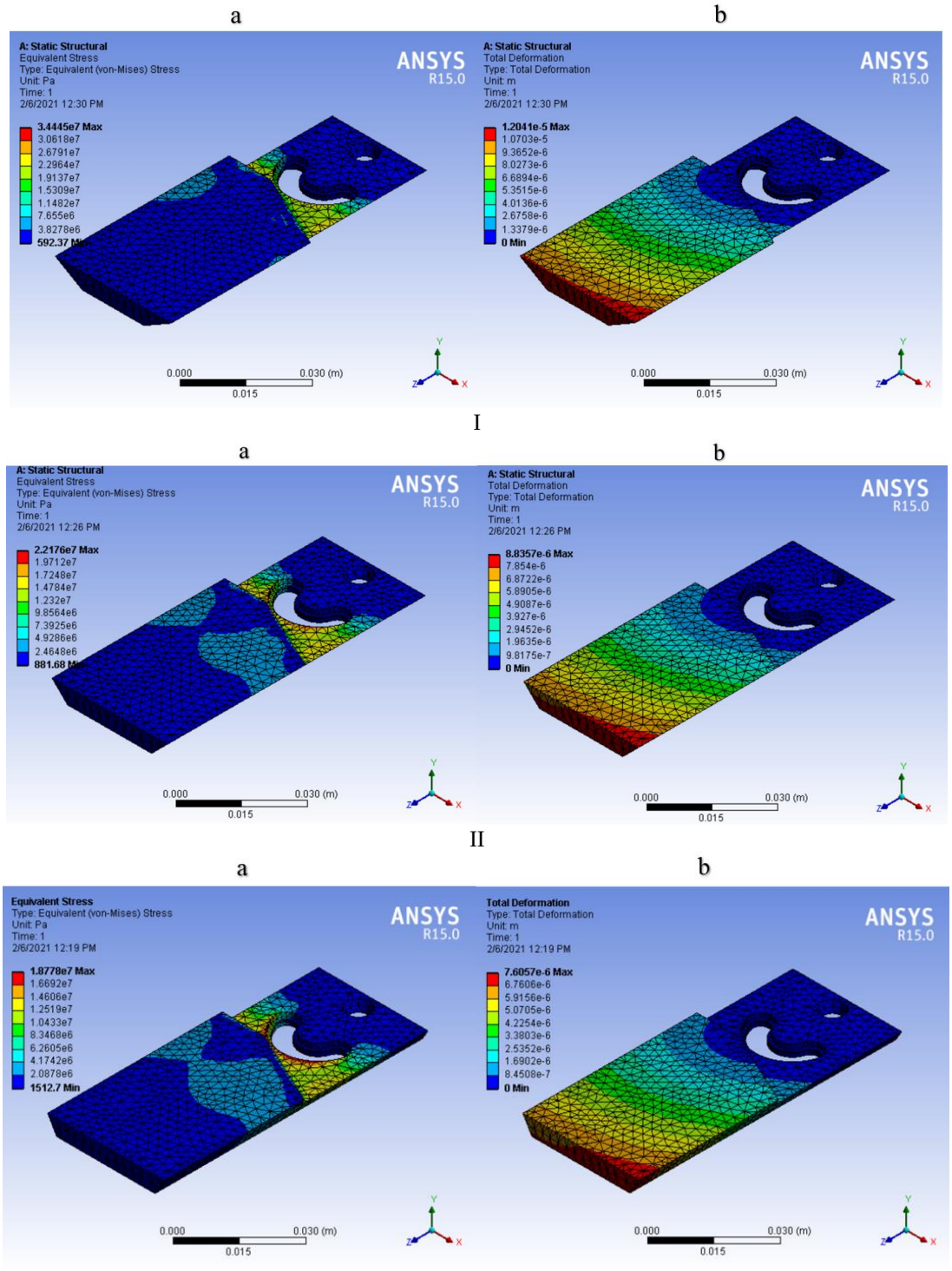

Fig. 5. Finite element analysis of the blades with sharpness angles of 30, 45, and 60 degrees (labeled I to III, respectively) under a 350 N force includes: (a) stress analysis, and (b) deformation analysis

The maximum Von Mises stress was found to decrease as the blade angle increased, with values of 30.618 MPa, 19.712 MPa, and 16.692 MPa recorded for 30°, 45°, and 60° angles, respectively. Similarly, the maximum displacement at the blade tip demonstrated a decreasing trend with increasing angle, measuring values of 1.0703×10^{-5} m, 7.854 ×

10^{-6} m, and 6.7606×10^{-6} m for the respective angles. For all three configurations, the highest stress concentration was consistently observed at the blade edge near the support region, where the blade was constrained within the slot and contacted the steel pin under operating conditions. The maximum displacement invariably occurred at the blade tip, behaving similarly to a beam under lateral loading. These results indicate that increasing the blade angle from 30° to 60° led to a 45.5% reduction in maximum stress and a 36.8% decrease in maximum displacement, suggesting enhanced structural stability at higher angles.

Measuring the mechanical properties of canola stalks

Determination of shear energy

The results of the analysis of variance concerning the primary effect treatments involving blade sharpness angle, blade placement angle, canola moisture, blade movement speed, and their interaction effects on the canola stalk shear energy amount, as measured by the Instron device, have been detailed in Table 3. The statistical analysis revealed that the impact of blade sharpness angle, blade placement angle, blade movement speed, as well as the interactive effects of sharpness angle and blade placement angle, blade sharpness angle and moisture, blade placement angle and moisture, and blade sharpness angle, blade placement angle, and moisture were all statistically significant at a 1% significance level.

The analysis of variance results (Table 3) revealed several significant relationships between cutting parameters and shear energy requirements. The blade sharpness angle demonstrated a significant effect ($P < 0.01$) on shear energy, where increasing the angle from 30° to 60° resulted in a 27.3% increase in energy consumption. This behavior can be attributed to the increased contact area between the blade and stalk material at higher angles, leading to greater resistance during the cutting process. These findings align with Gan *et al.* (2018), who reported a 25.1% reduction in energy consumption when implementing optimized blade angles in Miscanthus harvesting.

The blade placement angle also had a significant influence ($P < 0.01$), indicating that the 45° configuration required 18.9% less energy compared to the 60° placement angle. This optimal angle can be explained by the balance achieved between the normal and tangential forces during cutting, minimizing the total energy requirement. The significant interaction between sharpness and placement angles ($P < 0.01$) indicates that their effects are interdependent, suggesting that optimal blade design requires simultaneous consideration of both parameters.

Moisture content emerged as a critical factor, showing significant interactions with both blade angles ($P < 0.01$). Higher moisture levels (23-25%) resulted in 13.2% lower shear energy compared to drier stalks (18-21%), likely due to reduced material brittleness. This moisture-dependent behavior is almost similar to the findings by Wang *et al.* (2020), who reported a 25% reduction in cutting force for citrus stems, highlighting the unique mechanical properties of canola stalks.

The three-way interaction between sharpness angle, placement angle, and moisture content ($P < 0.01$) suggests that optimal blade configuration should be adjustable based on crop conditions, particularly moisture levels, to maintain energy efficiency throughout the harvesting process.

Determination of shear stress

Table 4 presents the outcomes of the analysis of variance conducted to evaluate the main effects of blade sharpness angle, blade placement angle, canola moisture, blade movement speed, and their interaction effects on canola shear stress, as measured by the Instron device. The data analysis revealed that the influence of blade sharpness angle, blade placement angle, stem moisture, blade movement speed, as well as the interaction effects of sharpness angle and blade placement angle, blade sharpness angle and moisture, blade placement angle and moisture, placement angle and blade movement speed,

blade sharpness angle, blade placement angle and moisture, and blade sharpness angle, and blade placement angle and blade movement speed were all statistically significant at a significance level of 1%.

Table 3- Analysis of variance of the impact of various factors including blade sharpness, blade angle, moisture level, and loading speed on shear energy index measured with the Instron device

Source	df	Sum of Squares	Mean Square	F	p-value
Treatment	81	9516.01	117.48	47.79**	<0.001
Sharpness	2	2212.64	1106.32	449.99**	<0.001
Blade angle	2	50.14	25.07	10.20**	<0.001
Moisture	2	9.89	4.95	2.01ns	0.137
Speed	2	130.70	65.35	26.58**	<0.001
Sharpness × Blade angle	4	130.27	32.57	13.25**	<0.001
Sharpness × Moisture	4	33.62	8.41	3.42**	0.010
Sharpness × Speed	4	25.39	6.35	2.58*	0.039
Blade angle × Moisture	4	54.89	13.72	5.58**	<0.001
Blade angle × Speed	4	0.81	0.20	0.08ns	0.988
Moisture × Speed	4	4.81	1.20	0.49ns	0.743
Sharpness × Blade angle × Moisture	8	93.42	11.68	4.75**	<0.001
Sharpness × Blade angle × Speed	8	12.08	1.51	0.61ns	0.766
Sharpness × Moisture × Speed	8	18.98	2.37	0.97ns	0.464
Blade angle × Moisture × Speed	8	2.30	0.29	0.12ns	0.998
Sharpness × Blade angle × Moisture × Speed	16	16.46	1.03	0.42ns	0.976
Error	162	398.29	2.46		
Total	243	9914.30			

** p-value < 0.01, * p-value < 0.05, ns Not significant (p-value > 0.05)

Table 4- Analysis of variance of the impact of various factors including blade sharpness, blade angle, moisture level, and loading speed on shear stress index measured with the Instron device

Source	df	Sum of Squares	Mean Square	F	p-value
Treatment	81	214.90	2.65	97.80**	<0.001
Sharpness	2	9.53	4.76	175.63**	<0.001
Blade angle	2	1.57	0.79	28.94**	<0.001
Moisture	2	0.26	0.13	4.80**	0.009
Speed	2	3.17	1.58	58.37**	<0.001
Sharpness × Blade angle	4	0.91	0.23	8.35**	<0.001
Sharpness × Moisture	4	1.28	0.32	11.78**	<0.001
Sharpness × Speed	4	0.14	0.03	1.26^ns	0.288
Blade angle × Moisture	4	0.42	0.11	3.89**	0.005
Blade angle × Speed	4	0.77	0.19	7.09**	<0.001
Moisture × Speed	4	0.09	0.02	0.79^ns	0.532
Sharpness × Blade angle × Moisture	8	1.40	0.18	6.45**	<0.001
Sharpness × Blade angle × Speed	8	0.29	0.04	1.31^ns	0.242
Sharpness × Moisture × Speed	8	0.28	0.04	1.29^ns	0.250
Blade angle × Moisture × Speed	8	1.36	0.17	6.26**	<0.001
Sharpness × Blade angle × Moisture × Speed	16	0.32	0.02	0.74^ns	0.753
Error	162	4.40	0.03		
Total	243	219.29			

** p-value < 0.01, * p-value < 0.05, ns Not significant (p-value > 0.05)

The impact of the main factors on stem shear stress was significant. To assess the variations among these factors, Duncan's test comparison method was employed. By comparing the average blade sharpness factor at a 1% probability level, a notable difference in shear stress was observed between sharpness angles of 30 and 45 degrees, when compared to 60 degrees. However, no significant difference was found between the

30 and 45-degree angles. The acute angle of 30 degrees exhibited the lowest shear stress value at 0.737 N mm^{-2}, whereas the acute angle of 60 degrees showed the highest shear energy at 1.171 N mm^{-2}.

Altering the orientation of the blade can be done in order to diminish the shear stress of the stem. Within the three different blade angles tested, namely 30, 45, and 60 degrees, it was observed that the 45-degree angle resulted in the lowest shear stress value of 0.779 N mm^{-2}, while the 60-degree angle exhibited the highest shear stress value of 0.961 N mm^{-2}. Furthermore, the comparison between the average shear stress values of the 30 and 60-degree angles did not yield statistically significant results at the 1% probability level.

Moisture played a significant role in influencing the shear stress of canola stems. The results indicated that the canola stems with 19% moisture exhibited the highest shear stress, while those with 24% moisture had the lowest shear stress. The difference in shear stress between the 19% and 24% moisture levels was statistically significant at the 1% level. However, no significant difference was observed between the 22% moisture level and the other two moisture levels. Specifically, the canola stems with 24% moisture had the lowest shear stress value of 0.885 N mm^{-2}, whereas those with 19% moisture had the highest shear stress value of 0.934 N mm^{-2}. In a study conducted by Wang *et al.* (2020), it was concluded that an increase in stem moisture content leads to a decrease in shear strength. This finding aligns with the results obtained in the present research.

The statistical analysis revealed an interesting phenomenon regarding the influence of moisture content on cutting parameters. While moisture content significantly affected shear stress ($F = 4.802$, $P < 0.01$), it showed no significant effect on shear energy ($F = 2.012$, $P > 0.05$). This apparent discrepancy can be explained by understanding the fundamental differences between these two parameters. Shear stress represents the instantaneous resistance force per unit area that must be overcome to initiate and maintain the cutting process. In contrast, shear energy encompasses the total work done throughout the entire cutting operation, including both the initial penetration and the complete separation of the stem.

The significant effect of moisture on shear stress suggests that water content directly influences the stem's immediate resistance to cutting. This could be attributed to moisture's role in cellular turgidity and tissue elasticity, which affect the stem's instantaneous mechanical response to the blade. Higher moisture levels (24%) resulted in lower shear stress values (0.885 N mm^{-2}) compared to lower moisture levels (19%, 0.934 N mm^{-2}), indicating that increased water content may facilitate easier initial penetration of the blade.

However, the non-significant effect on shear energy implies that the total work required to complete the cutting process remains relatively consistent across different moisture levels. This suggests that while moisture content may alter the instantaneous resistance to cutting, it does not substantially affect the overall energy requirements of the complete cutting operation. This finding has practical implications for harvester design and operation, indicating that while moisture content should be considered for optimizing cutting force requirements, it may be less critical for overall energy consumption calculations.

The statistical analysis revealed a significant difference in the average comparison among three loading speeds of 150, 250, and 350 mm min^{-1} at a 1% probability level. Notably, the speed of 350 mm min^{-1} exhibited the lowest stem shear stress at 0.764 N mm^{-2}, while the speed of 150 mm min^{-1} demonstrated the highest at 1.041 N mm^{-2}. Wang *et al.* (2020) conducted a study where they reported that the blade movement speed had a substantial impact on the shear stress of citrus fruit stems. Their findings indicated that an increase in blade movement speed led to a decrease in stem shear stress. Similarly, Heidari *et al.* (2012) conducted a study focusing on the shear stress and shear energy of Lilium stem. They observed a

significant effect of blade movement speed on these parameters at a 1% level, using speeds of 30, 40, and 50 mm min^{-1}. Their results showed that an increase in blade movement speed resulted in a decrease in shear stress and shear energy of the stem, aligning with the outcomes of the current research.

Measuring the canola stem's shear stress using the designed cutter bar device

The evaluation tests of the cutter bar system involved measuring the mechanical properties of the canola stem, specifically the shear stress, using both the Instron device and a custom-designed device. The effects of various treatments, such as blade sharpness angle, blade placement angle, canola moisture, blade reciprocating movement speed, and their interactions, on the canola shear stress were analyzed using the designed cutter bar device. The results of the analysis of variance, presented in Table 5, indicated that the blade sharpness angle, blade placement angle, blade movement speed, stem moisture, and their interactions had a significant impact on the canola shear stress at a 1% level of significance. These findings suggested that there was a substantial and robust effect among the different levels of each treatment, highlighting the importance of considering these factors in the cutter bar system.

Table 5- Analysis of variance of the impact of various factors including blade sharpness, blade angle, moisture, and reciprocating movement speed on shear stress index measured with the designed cutter bar device

Source	df	Sum of Squares	Mean Square	F	p-value
Model	81	196368.65	2424.30	104.18**	<0.001
Sharpness	2	7764.41	3882.21	166.84**	<0.001
Blade angle	2	11250.51	5625.25	241.75**	<0.001
Moisture	2	1376.71	688.36	29.58**	<0.001
Stroke per minute	2	6061.95	3030.97	130.26**	<0.001
Sharpness × Blade angle	4	23122.02	5780.51	248.42**	<0.001
Sharpness × Moisture	4	3705.82	926.45	39.81**	<0.001
Sharpness × Stroke per minute	4	417.56	104.39	4.49**	0.002
Blade angle × Moisture	4	1391.30	347.83	14.95**	<0.001
Blade angle × Stroke per minute	4	417.46	104.37	4.49**	0.002
Moisture × Stroke per minute	4	478.22	119.56	5.14**	<0.001
Sharpness × Blade angle × Moisture	8	6366.84	795.86	34.20**	<0.001
Sharpness × Blade angle × Stroke per minute	8	671.65	83.96	3.61**	<0.001
Sharpness × Moisture × Stroke per minute	8	892.87	111.61	4.80**	<0.001
Blade angle × Moisture × Stroke per minute	8	972.96	121.62	5.23**	<0.001
Sharpness × Blade angle × Moisture × Stroke per minute	16	2686.51	167.91	7.22**	<0.001
Error	162	3769.64	23.27		
Total	243	200138.28			

** p-value < 0.01, * p-value < 0.05, ns Not significant (p-value > 0.05)

The Duncan's test comparison of blade sharpness factor at the 1% probability level revealed a notable difference among the shear stress values at 30, 45, and 60-degree inclinations. The minimum shear stress value was associated with the acute angle of 30 degrees (0.175 N mm^{-2}), whereas the maximum shear stress value was linked to the acute angle of 60 degrees (0.303 N mm^{-2}).

Within the three blade positioning angles of 30, 45, and 60 degrees, it is observed that the 45-degree angle exhibited the lowest shear stress value of 0.177 N mm^{-2}, while the 60-degree angle demonstrated the highest shear stress value of 0.320 N mm^{-2}. Furthermore, the comparison between the average values of the 30 and 45-degree angles did not yield a significant result at the 1% probability level.

The shear stress of canola stem was also affected by moisture. The difference in shear

stress among these moisture levels was found to be statistically significant at a 1% probability level. Among the moisture levels tested, it was observed that 24% stem moisture exhibited the lowest shear stress at 0.200 N mm^{-2}, while 19% stem moisture showed the highest shear stress at 0.256 N mm^{-2}. In a related study by Wang *et al.* (2020), it was concluded that an increase in stem moisture content led to a decrease in shear strength. This finding aligns with the results obtained in the current research.

The statistical analysis revealed a significant difference in the average comparison among three loading speeds: 800, 1100, and 1400 courses per minute, at a 1% probability level. Notably, the speed of 1400 strokes per minute exhibited the lowest stem shear stress (0.167 N mm^{-2}), while the speed of 800 strokes per minute demonstrated the highest stem shear stress (0.286 N mm^{-2}).

LCA results

The life cycle impact assessment (LCIA) was evaluated using the CML 2 baseline 2000 V2.05 method. Throughout the evaluations, all inputs remained constant except for the specific factor being investigated. This approach allowed for the determination of changes solely related to that factor. The LCIA was analyzed by comparing the blade placement angle, blade sharpness angle, and the reciprocating speed of the cutter bar.

To assess the reliability of the LCA results, an uncertainty analysis was conducted using the Pedigree matrix approach within SimaPro 9 software. This method evaluates the uncertainty of data quality based on five characteristics: reliability, completeness, temporal correlation, geographical correlation, and technological correlation. The analysis focused on the laboratory measurements data used as inputs for the LCA calculations. The uncertainty ranges for key impact categories were calculated using Monte Carlo simulation with 1000 iterations. The results showed coefficient of variation (CV) values of: Marine aquatic ecotoxicity: 15.3%, Global warming potential: 12.7%, and Abiotic depletion: 10.5%.

These CV values indicate moderate uncertainty levels in the results, primarily stemming from variations in laboratory measurements. The relatively controlled laboratory environment helped maintain uncertainty within acceptable ranges. However, it should be noted that these uncertainty estimates are specific to this laboratory setup and may not reflect the full range of variabilities that could be encountered in field conditions.

Figure 6 presents comparative findings regarding the variances in environmental impacts among three different blade placement angles. These findings demonstrated that altering the angle of the blades can significantly affect the influx of pollutants into the environment. The results are particularly noteworthy. For instance, in terms of the global warming index, when the blade placement angle was set at 45 degrees, the quantity of carbon dioxide pollutants amounted to 18,085.78 kg CO_2 eq. Conversely, this index reached 22,295.41 kg CO_2 eq for a blade angle of 60 degrees. This indicated that a mere 15-degree alteration in the blade placement angle of canola combine harvesters in Iran can result in an increase or decrease of approximately 4,209.63 kg CO_2 eq. The marine aquatic ecotoxicity index indicated a substantial difference of 55762.55 kg of dichlorobenzene equivalent between the two mentioned angles. While variations were observed in other indices as well, the most substantial disparity was observed in the marine aquatic ecotoxicity and global warming indices. This can be attributed to the fact that modifying the blade placement angle leads to changes in shear energy, consequently impacting the fuel consumption of combines on a large scale. Considering that the consumption of fossil fuels directly influences the mentioned indices, it becomes evident that this angle adjustment can ultimately generate a significant volume of pollutants. Thus, the significance of the blade placement angle becomes even more pronounced than before.

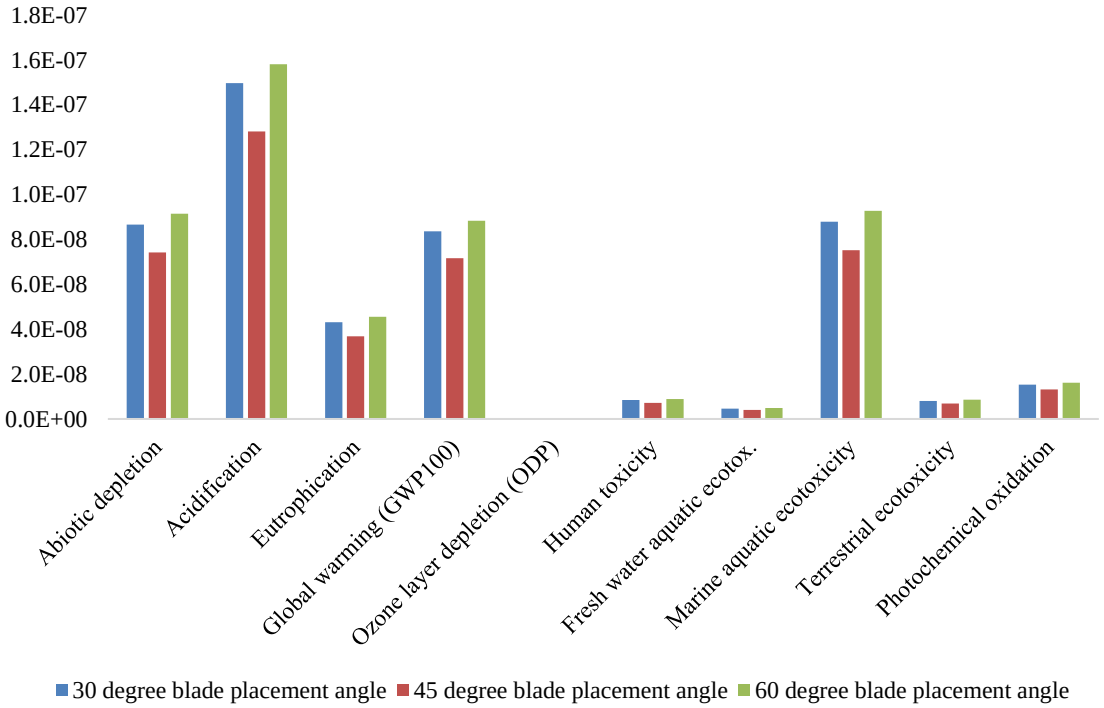

Fig. 6. A diagram of the LCIA normalized dimensionless indices among three distinct blade positioning angles for canola combine harvesters

A comparison was conducted to survey the impact of different blade sharpness angles on the results of the life cycle impact assessment. The findings, presented in Figure 7, revealed interesting insights. Specifically, when analyzing the marine aquatic ecotoxicity index, it was evident that the lowest value of 99133.43 kg of dichlorobenzene equivalent was associated with an acute angle of 30 degrees. On the other hand, the highest value of 476563.30 kg of dichlorobenzene equivalent was observed at an acute angle of 60 degrees. This indicated that a change of 30 degrees in the blade sharpness of canola harvesters in the country can result in a significant alteration of 377429.87 kg dichlorobenzene equivalent in the marine aquatic ecotoxicity index. Similarly, the global warming index also exhibited a notable difference between the 30 and 60 degree blade sharpness angles, with a variance of 28492.91 kg of carbon dioxide equivalent. This outcome is quite astonishing, as it implies that a mere change in blade sharpness at a macro level can introduce approximately 28.5 tons of additional carbon dioxide equivalent and 377.4 tonnes of additional dichlorobenzene equivalent pollution into the environment solely from canola harvesters. The underlying reason for this discrepancy, as previously explained, lies in the variation in fuel consumption.

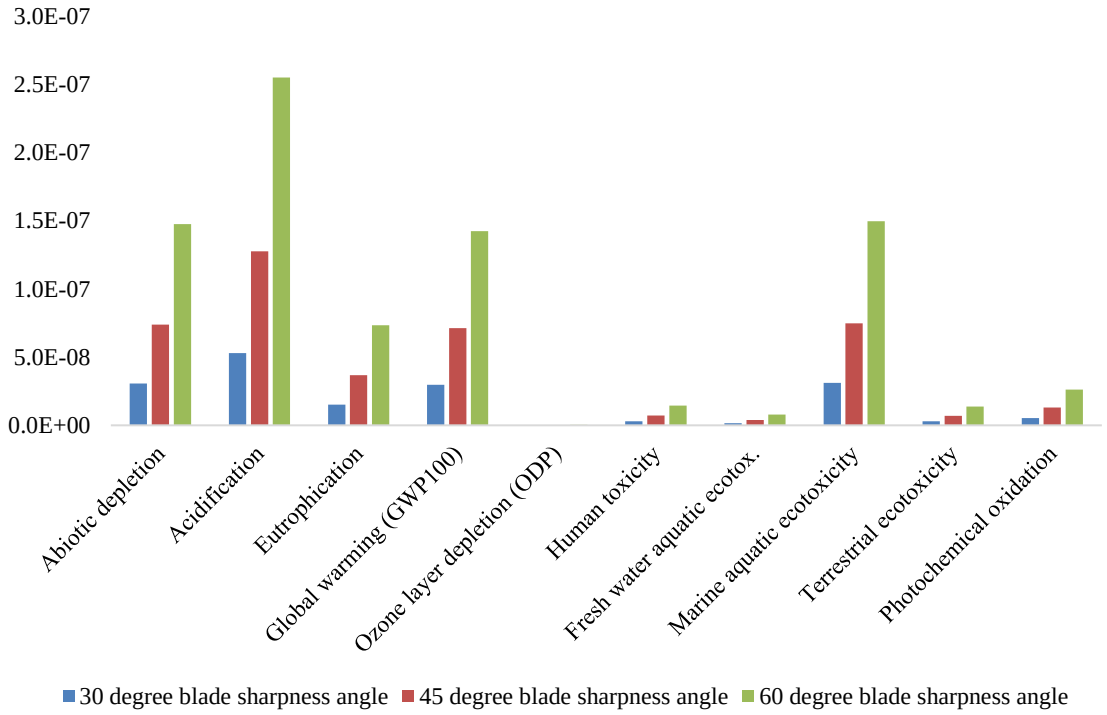

Fig. 7. A diagram of the LCIA normalized dimensionless indices among three distinct blade sharpness angles for canola combine harvesters

Finally, a comparison was carried out to estimate the impact of different blades' reciprocating speed on the outcomes of the LCIA. The results of this comparison can be found in Figure 8. Specifically, when analyzing the marine aquatic ecotoxicity index, it became evident that the lowest value of 200887.39 kg of dichlorobenzene equivalent was associated with 1400 courses per minute. Conversely, the highest value of 344073.07 kg of dichlorobenzene equivalent was observed at 800 courses per minute. This indicated that a change of 600 courses per minute in the blade reciprocating speed of canola harvesters can lead to a significant alteration of 143185.69 kg dichlorobenzene equivalent in the marine aquatic ecotoxicity index in the country. Analogously, the global warming index also showed a noticeable difference between the 800 and 1400 courses per minute in the blade reciprocating speed, with a variance of 25974.74 kg of carbon dioxide equivalent. This finding is quite surprising, as it suggested that a simple adjustment in the blade reciprocating speed at a larger scale can introduce approximately 143 tons of additional dichlorobenzene equivalent and 10.8 tons of additional carbon dioxide equivalent pollution into the environment solely from canola harvesters. The underlying reason for this difference, as explained earlier, lies in the variation in fuel consumption.

The main factors' significance is evident in their impact on the stem's shear energy. Duncan's mean comparison method was utilized to analyze the differences among these factors. The comparison of the average blade sharpness factor at the 1% probability level revealed a notable significance in cutting energy at 30, 45, and 60-degree angles. The data indicated that the lowest shear energy value corresponds to the 30-degree angle (1.92 mJ mm^{-2}), while the highest shear energy value corresponds to the 60-degree angle (9.23 mJ mm^{-2}).

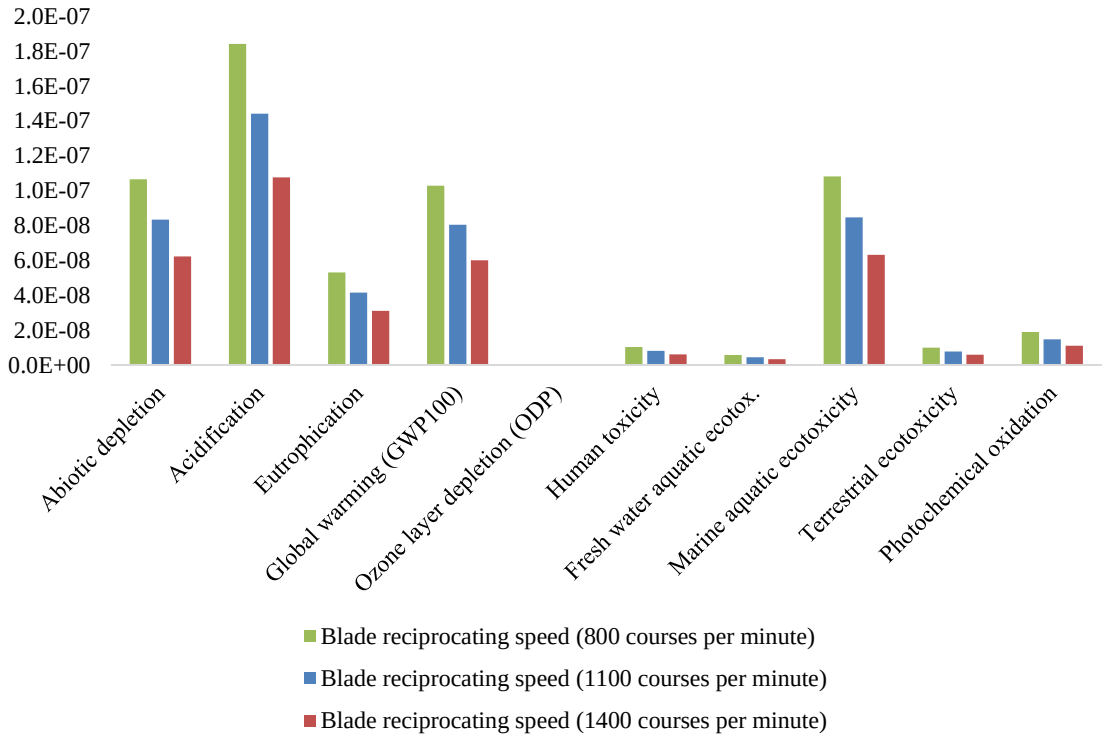

Fig. 8. A diagram of the LCIA normalized dimensionless indices among three distinct blade reciprocating speeds for canola combine harvesters

Heidari *et al.* (2012) conducted a study that yielded similar findings. Their research focused on the impact of loading rate and blade sharpness angle at 30, 45, and 60 degrees on shear stress and specific shear energy in Lilium stems. The results showed that as the blade sharpness angle increased from 30 to 60 degrees, shear stress rose from 0.76 to 1.31 MPa, and specific shear energy increased from 4.02 to 7.34 mJ mm^{-2}.

The modification of blade type and blade angle can be employed to minimize the energy consumption associated with cutting. Among the three blade positioning angles (30, 45, and 60 degrees), the 45-degree angle exhibited the lowest cutting energy (4.64 mJ mm^{-2}), while the 60-degree angle demonstrated the highest cutting energy (5.72 mJ mm^{-2}). Furthermore, the average comparison between the 30-degree and 60-degree angles did not exhibit statistical significance at the 1% probability level.

Mathanker, Grift, & Hansen (2015) concluded that specific cutting energy increases with cutting speed, with the lowest average specific energy recorded at 0.26 mJ mm^{-2} for a 60° oblique cut at an average speed of 7.9 m s^{-1}, and the highest at 1.24 mJ mm^{-2} for a straight cut at 16.4 m s^{-1}. They found a strong correlation between specific cutting energy and both stem diameter and cross-sectional area. For instance, at a 30° oblique angle and an average speed of 11.3 m s^{-1}, cutting energy ranged from 4.5 to 15 J as the sugarcane stem diameter increased from 11 to 17 mm. Additionally, comparisons with sugarcane studies suggested that optimizing cutting speed and blade oblique angle could lead to significant energy savings while enhancing cut quality.

The findings indicated that there were no notable differences in the shear energy levels at different moisture levels, with a 5% probability level. Notably, the cutting energy was found to be the lowest (5.05 mJ mm^{-2}) for 24% stem moisture, while the highest cutting energy (5.53 mJ mm^{-2}) was observed for 19% stem moisture.

The analysis revealed a significant difference in the average comparison across three loading speeds: 150, 250, and 350 mm

min^{-1}, at a 1% probability level. Notably, the speed of 350 mm min^{-1} exhibited the lowest cutting energy (4.31 mJ mm^{-2}), while the speed of 150 mm min^{-1} demonstrated the highest cutting energy (6.10 mJ mm^{-2}).

Soleimani, Kamandar, Khoshnam, and Soleimani (2023) found that the cutting of sesame stalks is a dynamic process primarily characterized by impact cutting. As cutting speed increases, preliminary compaction decreases due to the stalk's inertia and plastic behavior, resulting in lower energy requirements for cutting. They observed that at loading rates of 0.5-2 m s^{-1} and a moisture content of 15%, the cutting force ratios were approximately 58%, 55%, and 40% for the upper, middle, and lower regions of the stalk, respectively. Similarly, the specific shear energy ratios at the same loading rates and moisture content were around 66%, 37%, and 39% for the upper, middle, and lower regions. Given that sesame is typically harvested with low stalk moisture and that cutting occurs in the lower region, a cutting speed of 2 m s^{-1} could lead to reductions in the required cutting force, specific shear energy, and shear strength by about 40%, 39%, and 60%, respectively.

Hence, the appropriate and optimal cutting can be achieved by selecting treatments with the lowest shear stress. The similarity between the treatments can be observed in the analysis of variance and Duncan's test comparison of average shear stress measurements from experimental data obtained from the cutter bar system and the mechanical properties from Instron device data. The comparison of the mechanical properties and evaluation tests of the cutter bar system revealed similar results. While the main treatments had a significant effect in both experiments, the interaction effects were not significant in the mechanical properties test. One possible explanation for this could be the significant difference in blade movement speed between the two experiments. The blade movement speed in the mechanical properties test was 350 mm min^{-1}, whereas in the evaluation tests of the cutter bar system, it was at least 800 strokes per minute, equivalent to 60,800 mm min^{-1}. This speed is approximately 174 times higher than the maximum blade speed in the mechanical properties test. The substantial increase in momentum at high speed, which is obtained by multiplying the object's mass by its speed and represents the force required to stop the object, could account for this difference. Consequently, when the blade speed is 174 times higher, the momentum of the blade will also be proportionally 174 times higher.

In a study conducted by Nazari Galedar *et al*. (2008), an investigation was carried out on the ultimate shear strength of alfalfa stems within the inter-row intervals using a direct cutting method. The findings revealed a range of shear strength values varying from 0.4 to 18 MPa. Additionally, it was noted that an increase in the moisture content percentage along the entire length of the stem led to a decrease in shear resistance. A critical aspect in the development of various grain combines and harvesting machines is the resistance to cutting of agricultural products during the harvesting process.

The findings regarding blade angle effects can be compared with the comprehensive study by Gan *et al.* (2018) on Miscanthus Giganteus harvesting. While a 45-degree blade placement angle resulted in the lowest shear stress (0.779 N mm^{-2}), it was demonstrated that angled blades (30°) consumed less energy (11.31 MJ Mg^{-1}) compared to straight blades (12.31 MJ Mg^{-1}). The consistent enhancement of performance with angled blades across different crops suggests that optimizing blade angles is crucial for energy efficiency in harvesting operations. However, the magnitude of energy reduction differs between studies due to variations in crop properties and testing conditions.

The life cycle impact assessment findings revealed that altering the blade placement angles, blade sharpness angles, and blade reciprocating speed can lead to significant increases in the marine aquatic ecotoxicity index. Specifically, the amount of dichlorobenzene equivalent can rise up to 55762.55 kg, 377429.87 kg, and 143185.69 kg, respectively.

Conclusion

The results from the analysis of variance indicated that various parameters, including blade placement angle, blade sharpness angle, blade reciprocating movement speed, and stem moisture, significantly influenced both shear energy and shear stress at a 1% significance level. The blade sharpness angle of 30 degrees and 60 degrees corresponded to the lowest and highest shear stress values, respectively. Similarly, the blade placement angle at 45 degrees and 60 degrees exhibited the lowest and highest shear stress values, respectively. Furthermore, the moisture content of the canola stalk had a significance impact on shear stress at the 0.01 level, with the lowest and highest values observed at stem moisture levels of 24% and 19%, respectively. Additionally, the blade reciprocating speed of 1400 courses per minute resulted in the lowest stem shear stress, while a speed of 800 courses per minute led to the highest shear stress. Therefore, the combination of a blade sharpness angle of 30 degrees, a blade placement angle of 45 degrees, a stem moisture of 24%, and a blade reciprocating movement speed of 1400 courses per minute was predicted to decrease the shear energy and shear stress of canola stalks. The life cycle assessment results quantified the potential environmental impact of using the designed blades on a national scale. The LCIA findings showed that adjusting the blade placement angles, blade sharpness angles, and blade reciprocating speed can significantly increase the marine aquatic ecotoxicity index. Notably, the amount of dichlorobenzene equivalent can rise up to 55762.55 kg, 377429.87 kg, and 143185.69 kg, respectively.

Conflict of Interest: The authors declare no competing interests.

Author Contributions

Gh. Ahmadzade: Data acquisition, Data pre and post processing, Software services, Statistical analysis

M. R. Maleki: Supervision, Conceptualization, Methodology, Technical advice, Text mining, Writing the original text

P. Salami: Supervision, Conceptualization, Methodology, Technical advice, Statistical analysis, Software services, Numerical/computer simulation, Writing the original text

K. Mollazade: Conceptualization, Methodology, Validation, Visualization, Review and editing services

References

1. Aghbashlo, M., Kianmehr, M. H., & Hassan-Beygi, S. R. (2008). Specific heat and thermal conductivity of Berberis fruit (*Berberis vulgaris*). *American Journal of Agricultural and Biological Sciences, 3*, 330-336. https://doi.org/10.3844/ajabssp.2008.330.336
2. Amirian, F., Shahbazi, F., & Taheri Garavand, A. (2018). Effects of moisture content and stem region on the bending characteristics of chickpea stem. *Agricultural Engineering International, 20*(2), 190-196.
3. Azadbakht, M., Esmaeilzadeh, E., & Esmaeili-Shayan, M. (2015). Energy consumption during impact cutting of canola stalk as a function of moisture content and cutting height. *Journal of the Saudi Society of Agricultural Sciences, 14*(2), 147-152. https://doi.org/10.1016/j.jssas.2013.10.002
4. Baruah, D. C., & Panesar, B. S. (2005). Energy requirement model for combine harvester, Part 2: Integration of component models. *Biosystems Engineering, 90*(2), 161-171. https://doi.org/10.1016/j.biosystemseng.2004.10.003
5. Chattopadhyay, P. S., & Pandey, K. P. (2001). PM—Power and Machinery: Impact Cutting Behaviour of Sorghum Stalk using a Flail-Cutter—a Mathematical Model and its Experimental Verification. *Journal of Agricultural Engineering Research, 78*(4), 369-376. https://doi.org/10.1006/jaer.2000.0623

6. Gan, H., Mathanker, S., Abdul Momin, M., Kuhns, B., Stoffel, N. Hansen, A., & Grift, T. (2018). Effects of three cutting blade designs on energy consumption during mowing-conditioning of Miscanthus Giganteus. *Biomass and Bioenergy, 109*, 166-171. https://doi.org/10.1016/j.biombioe.2017.12.033
7. Heidari, A., Chegini, G., & Kianmehr, M. H. (2012). Influence of knife bevel angle, rate of loading and stalk section on some engineering parameters of lilium stalk. *Iranian Journal of Energy and Environment, 3*(4), 333-340. https://doi.org/10.5829/idosi.ijee.2012.03.04.141
8. Johnson, P. C., Clementson, C. L., Mathanker, S. K., Grift, T. E., & Hansen, A. C. (2012). Cutting energy characteristics of Miscanthus x giganteus stems with varying oblique angle and cutting speed. *Biosystems Engineering, 112*(1), 42-48. https://doi.org/10.1016/j.biosystemseng.2012.02.003
9. Kushwaha, R. L., Vashnav, A. S., & Zoerb, G. C. (1983). Shear strength of wheat straw. *Canadian Agricultural Engineering, 25*(2), 163-166.
10. Kronbergs, E. (2000). Mechanical strength testing of stalk materials and compacting energy evaluation. *Industrial Crops and Products, 11*, 211-216. https://doi.org/10.1016/S0926-6690(99)00052-7
11. Mathanker, S. K., Grift, T. E., & Hansen, A. C. (2015). Effect of blade oblique angle and cutting speed on cutting energy for energycane stems. *Biosystems Engineering, 133*, 64-70. https://doi.org/10.1016/j.biosystemseng.2015.03.003
12. Maughan, J. D., Mathanker, S. K., Grift, T. E., Hansen, A. C., & Ting, K. C. (2013). Impact of blade angle on miscanthus harvesting energy requirement. *Transactions of the ASABE, 57*(4), 999-1006. https://doi.org/10.13031/trans.57.10373
13. Mirzaee, P., Salami, P., Akhijahani, H. S., & Zareei, S. (2023). Life cycle assessment, energy and exergy analysis in an indirect cabinet solar dryer equipped with phase change materials. *Journal of Energy Storage, 61*, 106760. https://doi.org/10.1016/j.est.2023.106760
14. Mohammadi Baneh, N., Navid, H., Alizadeh, M. R., & Ghasem Zadeh, H. R. (2012). Design and development of a cutting head for portable reaper used in rice harvesting operations. *Journal of Applied Biological Sciences, 6*(3), 69-75.
15. Nazari Galedar, M., Jafari, A., Mohtasebi, S. S., Tabatabaeefar, A., Sharifi, A., O'Dogherty, M. J., Rafiee, S., & Richard, G. (2008). Effects of moisture content and level in the crop on the engineering properties of alfalfa stems. *Biosystems Engineering, 101*(2), 199-208. https://doi.org/10.1016/j.biosystemseng.2008.07.006
16. Okyere, F. G., Kim, H. T., Basak, J. K., Khan, F., Bhujel, A., Park, J., & Lee, D. (2022). Influence of operational properties and material's physical characteristics on mechanical cutting properties of corn stalks. *Journal of Biosystems Engineering, 47*, 197-208. https://doi.org/10.1007/s42853-022-00140-2
17. Persson, S. (1987). *Mechanics of cutting plant material*. ASAE Publications, Michigan.
18. Paris, B., Vandorou, F., Balafoutis, A. T., Vaiopoulos, K., Kyriakarakos, G., Manolakos, D., & Papadakis, G. (2022). Energy use in open-field agriculture in the EU: A critical review recommending energy efficiency measures and renewable energy sources adoption. *Renewable and Sustainable Energy Reviews, 158*, 112098. https://doi.org/10.1016/j.rser.2022.112098
19. Rezahosseini, A., Jafari Naeimi, K., & Mortezapour, H. (2019). Development and field evaluation of a cabbage harvester unit. *Journal of Agricultural Machinery, 9*(1), 1-13. https://doi.org/10.22067/jam.v9i1.62703
20. Roudbari, M., Refahati, N., & Mehdipour, A. (2021). Improvement of mechanical properties of aluminum base composite reinforced by steel Ck75 wire through explosive welding. *Revista De Metalurgia, 57*(2), e196. https://doi.org/10.3989/revmetalm.196
21. Soleimani, N., Kamandar, M. R., Khoshnam, F., & Soleimani, A. (2023). Defining and modelling sesame stalk shear behaviour in harvesting by reciprocating cutting blade.

Biosystems Engineering, *229*, 44-56. https://doi.org/10.1016/j.biosystemseng.2023.03.008
22. Song, R., & Muliana, A. (2019). Modeling mechanical behaviors of plant stems undergoing microstructural changes. *Mechanics of Materials*, *139*, 103175. https://doi.org/10.1016/j.mechmat.2019.103175
23. Song, S., Zhou, H., Jia, Z., Xu, L., Zhang, C., Shi, M., & Hu, G. (2022). Effects of cutting parameters on the ultimate shear stress and specific cutting energy of sisal leaves. *Biosystems Engineering*, *218*, 189-199. https://doi.org/10.1016/j.biosystemseng.2022.03.011
24. Wang, Y., Yang, Y., Zhao, H., Liu, B., Ma, J., He, Y., Zhang, Y., & Xu, H. (2020). Effects of cutting parameters on cutting of citrus fruit stems. *Biosystems Engineering*, *193*, 1-11. https://doi.org/10.1016/j.biosystemseng.2020.02.009
25. Yeganeh, R., & Trystram, G. (2013). Intensification of pistachio by deep frying. *Quality Assurance and Safety of Crops & Foods*, *5*(2), 131-139. https://doi.org/10.3920/QAS2012.0144
26. Yin, Y., Qin, W., Zhang, Y., Chen, L., Wen, J., Zhao, C., Meng, Z., & Sun, S. (2021). Compensation control strategy for the cutting frequency of the cutter bar of a combine harvester. *Biosystems Engineering*, *204*, 235-246. https://doi.org/10.1016/j.biosystemseng.2021.01.023
27. Yuan, L., Lan, M., He, X., Wei, W., Wang, W., & Qu, Z. (2023). Design and experiments of a double-cutter bar combine header used in wheat combine harvesters. *Agriculture*, *13*(4), 817. https://doi.org/10.3390/agriculture13040817

نشریه ماشین‌های کشاورزی
https://jame.um.ac.ir

مقاله پژوهشی

جلد ۱۶، شماره ۳، پاییز ۱۴۰۵، ص ۵۴۸-۵۲۵

بهینه‌سازی تیغه برش دروگر برداشت کلزا با رویکرد کاهش مصرف انرژی و ارزیابی چرخه زیست

قانع احمدزاده[۱]، محمدرضا ملکی[۱]، پیمان سلامی[۱*]، کاوه ملازاده[۱]

تاریخ دریافت: ۱۴۰۳/۱۲/۱۹
تاریخ پذیرش: ۱۴۰۴/۰۳/۱۸

چکیده

عملیات برداشت غلات حدود ۳۰-۲۵٪ از کل مصرف مستقیم انرژی در سیستم‌های تولید محصولات کشاورزی را شامل می‌شود. با توجه به ویژگی‌های خاص کلزا در مقایسه با سایر غلات، طراحی تیغه‌های مناسب برداشت آن ضروری است. این پژوهش به بررسی تأثیر زوایای تیغه (زوایای قرارگیری و تیزی: ۳۰، ۴۵ و ۶۰ درجه)، سرعت حرکت رفت و برگشتی (۸۰۰، ۱۱۰۰ و ۱۴۰۰ رفت و برگشت در دقیقه) و سطوح رطوبتی (۱۹، ۲۲ و ۲۴ درصد) بر نیروی برش، تنش برشی و مصرف انرژی در برداشت کلزا پرداخت. نتایج نشان داد زاویه تیزی ۳۰ درجه و زاویه قرارگیری ۴۵ درجه به‌ترتیب کمترین تنش برشی (۰/۱۷۵ و ۰/۱۷۷ نیوتن بر میلی‌متر مربع) را نسبت به زاویه ۶۰ درجه (۰/۳۰۳ و ۰/۳۲۰ نیوتن بر میلی‌متر مربع) ایجاد می‌کنند. افزایش رطوبت از ۱۹ به ۲۴ درصد، تنش برشی را از ۰/۲۵۶ به ۰/۲۰۰ نیوتن بر میلی‌متر مربع کاهش داد. سرعت ۱۴۰۰ رفت و برگشت در دقیقه کمترین تنش برشی (۰/۱۶۷ نیوتن بر میلی‌متر مربع) را در مقایسه با ۸۰۰ رفت و برگشت (۰/۲۸۶ نیوتن بر میلی‌متر مربع) نشان داد. ارزیابی چرخه حیات نشان داد تغییر زوایای قرارگیری، تیزی و سرعت رفت و برگشتی به‌ترتیب می‌تواند سمیت اکولوژیکی آبزیان دریایی را تا ۵۵۷۶۲/۵۵، ۳۷۷۴۲۹/۸۷ و ۱۴۳۱۸۵/۶۹ کیلوگرم معادل دی‌کلروبنزن افزایش دهد. ترکیب بهینه (زاویه تیزی ۳۰ درجه، قرارگیری ۴۵ درجه، رطوبت ۲۴ درصد و ۱۴۰۰ رفت و برگشت در دقیقه) انرژی برشی و اثرات زیست‌محیطی را به‌طور قابل‌توجهی کاهش داد.

واژه‌های کلیدی: ارزیابی اثرات چرخه زیست، انرژی برشی، تنش برشی، زاویه تیزی تیغه، زاویه قرارگیری تیغه

۱- گروه مهندسی بیوسیستم، دانشکده کشاورزی، دانشگاه کردستان، سنندج، ایران
(*- نویسنده مسئول: Email: p.salami@uok.ac.ir)

https://doi.org/10.22067/jam.2025.92546.1353

Journal of Agricultural Machinery

Homepage: https://jame.um.ac.ir

Research Article
Vol. 16, No. 3, 2026, p. 549-561

Physical Property Characterization of Ethiopian Maize Varieties for Adaptive Multi-Crop Planter Design

D. Girma Gadisa[1*], K. Purushottam Kolhe[2], S. Kedir Busse[1], M. Mohammed Issa[3], T. Aseffa Abeye[3], D. Alemu Anawte[3]

1- Department of Mechanical Engineering, College of Mechanical, Chemical, & Materials Engineering, Adama Science and Technology University, Adama, Ethiopia
2- Department of Mechanical Engineering, Sinhgad College of Engineering, Pune University, Vadgaon, India
3- Ethiopian Institute of Agricultural Research, Agricultural Engineering Research, Melkassa Agricultural Research Center, Adama, Ethiopia
(*- Corresponding Author Email: dejene383@gmail.com)

Received: 14 March 2025
Revised: 02 May 2025
Accepted: 08 June 2025
Available Online: 06 September 2025

How to cite this article:
Girma Gadisa, D., Purushottam Kolhe, Kedir Busse, S., Mohammed Issa, M., Aseffa Abeye, T., & Alemu Anawte, D. (2026). Physical Property Characterization of Ethiopian Maize Varieties for Adaptive Multi-Crop Planter Design. *Journal of Agricultural Machinery*, *16*(3), 549-561. https://doi.org/10.22067/jam.2025.92654.1356

Abstract

Smallholder maize production in sub-Saharan Africa, crucial for regional food security, grapples with persistent yield gaps driven by labor-intensive planting practices and a critical lack of mechanization specifically designed to accommodate the traits of native plant varieties. This study characterizes three maize varieties (CML-539, Melkassa 3, and Melkassa 6Q) to develop design parameters for adaptive multi-crop planters. Geometric properties including length, width, and thickness were measured using digital calipers, with 100 seeds per variety. Analysis was performed for elongation, geometric and arithmetic mean diameters, surface area, projected area, transverse cross-sectional area, sphericity, flakiness ratio, aspect ratio, shape index, and roundness. Gravimetric properties including bulk and true densities, porosity, thousand seed mass, and angle of repose were systematically analyzed to optimize seed-handling mechanisms in planter design. Physical property analysis revealed distinct varietal requirements: CML-539's irregular morphology (9.42 mm length, 49.30% porosity) necessitates vibration-assisted metering and aerated delivery systems; Melkassa 6Q's uniform properties (71.11± 6.66% sphericity, 811.62 kg m^{-3} bulk density) permit gravity-fed mechanisms; and Melkassa 3's intermediate characteristics of > 2.3 elongation ratio and 19.31% density variation require adjustable furrow openers of 25-30° rake angles. Geometric variability necessitates the implementation of adaptive solutions, such as curved seed tubes and adjustable furrow openers, to effectively prevent tilt and bridging. The resulting modular planter system, incorporating moisture-responsive metering, adaptive cell sizing, and aerated delivery, aligns with Ethiopia's agroecological standards of 75 cm row spacing and depth range of 4 to 7 centimeters. This framework offers a scalable, sustainable model for precision smallholder mechanization, transferable to global maize systems.

Keywords: Angle of repose, Maize varieties, Multi crop planter, Physical property, Sphericity

Introduction

Maize (*Zea mays* L.), a staple crop critical to global food security, is the most widely cultivated cereal worldwide, achieving a yield of 27,800 kg per hectare surpassing rice, wheat, and millets (FAO, 2023). Its versatility extends to human nutrition, animal feed, and industrial processing, while its grain traits and maturation periods are genetically adapted to thrive across diverse agroecological conditions. In Ethiopia, maize dominates cereal production, accounting for 88.69% of

Authors retain the copyright. This is an open access article distributed under Creative Commons Attribution 4.0 International License (CC BY 4.0).

https://doi.org/10.22067/jam.2025.92654.1356

the total output (Central Statistical Agency, 2021). However, productivity remains constrained by labor-intensive manual planting practices. Traditional methods, plagued by inconsistent seed spacing, uneven depth placement, and significant physical exertion for farmers, compromise germination rates and yield optimization (Sinha *et al.*, 2021; Soyoye, Ademosun, & Agbetoye, 2018).

The design of seed planters' hinges on critical physical of seed properties. Maize kernels, characterized by their angular shapes and varying densities, require carefully designed metering systems to reduce mechanical damage during the singulation process (Pascual, Rafael, Remocal, & Regalado, 2021; Shah *et al.*, 2022). Key parameters include sphericity (governing seed plate cell dimensions), angle of repose (dictating hopper wall slopes for uninterrupted flow), and terminal velocity (influencing seed tube aerodynamics) (Sinha *et al.*, 2021). Density further modulates grain friction coefficients and brittleness, necessitating adaptive components to maintain seed integrity across postharvest handling and planting phases (Dinberu & Megersa, 2023). Neglecting these properties risks planter inefficiencies, including clogging, seed fracture, and placement inaccuracy factors that erode farmer trust and adoption (Omar *et al.*, 2023).

In Ethiopia, agricultural mechanization strategies disproportionately prioritize wheat production, systematically neglecting the mechanization needs of smallholder farmers reliant on maize cultivation. Current multi-crop planters, predominantly retrofitted from temperate-region prototypes, demonstrate limited functional compatibility with indigenous maize varieties and local agroclimatic conditions. These mismatches manifest in critical agronomic inefficiencies, including excessive depth variability and seed spacing (±25% inaccuracy), undermining crop establishment and yield predictability (Liang *et al.*, 2021; Seyoum, Paul, & Sinafikeh, 2013; Theodrose, Kindie, Mezegebu, Nigussie, & Mengistu, 2024). These inefficiencies arise from a systemic failure to integrate agronomic and operational parameters into planter design optimization (Ayele, 2022; Kebede, 2019).

Resolving these inefficiencies requires engineering property optimized planter components tailored to Ethiopia's agroecology. Critical priorities are fluted roller meters that are 10% larger than kernel sizes to lower shear stress (< 2 MPa) (Liang *et al.*,, 2021; Singh, Sahoo, & Bisht, 2017), double-disk furrow openers with optimized rake angles for consistent depth in different soils, and seed tubes calibrated for velocity to achieve at least 85% spatial accuracy. This research thoroughly analyzed essential engineering characteristics to enhance a tractor-drawn multi-crop planter in accordance with Ethiopia's agricultural standards. Key parameters, such as planting depth, intra- and inter-row spacing, and planting density per hectare, are presented in Table 1.

Table 1- Optimal planting depth and inter- and intra-row spacing for maize seeds

Crop	Inter & intra row spacing (cm)	Depth (cm)	Plant per hectare	Location in Ethiopia	Reference
Maize	65 × 15	4-5	102,564	Metu, kombolcha	(Tolossa & Gizawu, 2024)
	65 × 25	5-6	61,538	North Mecha	(Getaneh, Belete, & Tana, 2016)
	75 × 25	5-6	53,334	EIAR, MARC	(Alemayehu *et al.*, 2017) (Bisrat, Laike, & Hae, 2015)
	75 × 20	4-6	66,667	Jimma and Illu-Ababora	(Muhidin, 2019)

Materials and Methods

Study location

The experiments were conducted at the Melkassa Agricultural Research Center of the

Ethiopian Institute of Agricultural Research (EIAR). Located in the East Shewa Zone of the Oromia Region, at an altitude of 1,550 m above sea level, approximately 107 km from Addis Ababa, Ethiopia (Central Statistical Agency, 2021).

Determining maize seed physical properties

A representative sample of 100 seeds per variety was subjected to dimensional analysis using a digital caliper (resolution: ±0.01 mm) to measure axial dimensions (length *l*, width *w*, thickness *t*), as shown in Fig. 1. These measurements were used to calculate derived parameters such as the geometric mean diameter, sphericity, and aspect ratio, which are essential for understanding seed behavior and optimizing planter components.

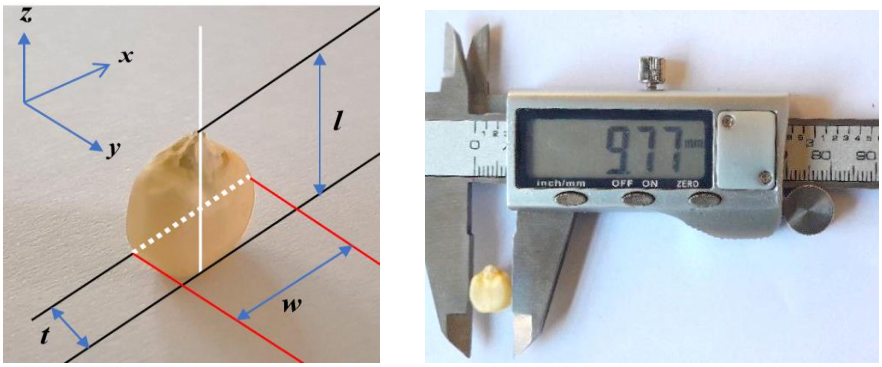

Fig. 1. Maize seed dimensions (length, width, and thickness), and digital caliper

Mathematical modeling of seed properties

The engineering properties of Maize seeds were calculated using established mathematical models. These properties are critical for understanding seed behavior and optimizing the design of a tractor-drawn multi-crop planter.

Mean diameters

Mean diameters are fundamental geometric parameters used to quantify seed size and uniformity, which are critical for designing and optimizing seed metering mechanisms, hoppers, and other planter components. The arithmetic mean diameter (D_a), calculated as the average of the three principal linear dimensions length (l), width (w), and thickness (t) is expressed in Equation (1) (Kawuyo, Aviara, Mari, & Ahmed, 2022; Zewdie, Olaniyan, Wako, Alemu, & Lema, 2024):

$$D_a = \frac{(l+w+t)}{3} \quad (1)$$

This parameter provides a simplified measure of seed size and ensures compatibility with diverse seed dimensions. Geometric mean diameter (D_g) is calculated as the cube root of the product of the three principal linear dimensions: length (l), width (w), and thickness (t) diameters, as stated in Equation (2) (Panwar, Swarnkar, Kumar, & Shukla, 2023; Soyoye *et al.*, 2018):

$$D_g = (l \cdot w \cdot t)^{\frac{1}{3}} \quad (2)$$

It is particularly useful for characterizing irregularly shaped seeds and optimizing seed flow, spacing, and interaction with planter components. Square mean diameter (D_s) which approximates the effective size of irregularly shaped seeds, is calculated using Equation (3) (Zewdie *et al.*, 2024):

$$D_s = \left((l \cdot w)+(l \cdot t)+(w \cdot t)\right)^{\frac{1}{3}} \quad (3)$$

where, l is the longest intercept, w is the longest intercept normal to l, t is the longest intercept normal to l and w. These parameters collectively ensure efficient seed handling and mechanical design for multi-crop planters.

Geometric properties

Geometric properties of seeds, such as projected area, surface area, and cross-sectional areas, are critical for analyzing seed orientation, flow dynamics, and mechanical

interactions within planter components. The projected Area (A_p), which represents the two-dimensional area of a seed as seen from a specific angle, is calculated using Equation (4) (Liang *et al.*, 2021; Zewdie *et al.*, 2024):

$$A_p = \frac{\pi}{4}(l \cdot w) \quad (4)$$

This parameter is essential for understanding seed visibility in 2D planes and optimizing optical sorting systems. The surface area (A_s) representing the total outer surface area of the seed, is approximated using the geometric mean diameter and is expressed in Equation (5) (Liang *et al.*, 2021; Zewdie *et al.*, 2024):

$$A_s = \pi D_g^2 \quad (5)$$

It is crucial for predicting seed friction and drag in airflow systems. The transverse surface area (A_t), which represents the cross-sectional area perpendicular to the seed's major axis, is calculated using Equation (6) (Liang *et al.*, 2021; Zewdie *et al.*, 2024):

$$A_t = \frac{\pi}{4}(w \cdot t) \quad (6)$$

This parameter quantifies the seed's resistance in seed tubes and other mechanical components. Finally, the cross-Sectional area (A_{cs}), which represents the surface exposed when the seed is sliced along a specific plane, is given in Equation (7) (Liang *et al.*, 2021; Zewdie *et al.*, 2024):

$$A_{cs} = \frac{\pi}{4}(l \cdot t) \quad (7)$$

Shape indices

Shape indices are critical parameters for quantifying seed morphology, which directly influence seed flow, orientation, and mechanical interactions in planter components. The sphericity (Φ), which indicates how closely a seed resembles a sphere, is calculated using Equation (8) (Panwar *et al.*, 2023):

$$\Phi = \frac{(l \cdot w \cdot t)^{\frac{1}{3}}}{l} \quad (8)$$

A perfect sphere has a sphericity of 100 %, and this parameter is essential for optimizing seed flow in hoppers and tubes. The flakiness ratio (F_r), which measures seed flatness, is expressed in Equation (9) (Liang *et al.*, 2021; Panwar *et al.*, 2023; Zewdie *et al.*, 2024):

$$F_r = \left(\frac{t}{w}\right) 100\ \% \quad (9)$$

It helps prevent clogging in seed metering mechanisms. The aspect ratio (A_r), which quantifies the relative width-to-thickness proportion, is calculated using Equation (10) (Panwar *et al.*, 2023):

$$A_r = \left(\frac{w}{t}\right) 100\ \% \quad (10)$$

This parameter is crucial for assessing seed stability during orientation. The shape index (S_I), which provides an indication of the relative proportions of the seed's dimensions, is given in Equation (11) (Liang *et al.*, 2021; Zewdie *et al.*, 2024):

$$S_I = \frac{l}{\sqrt{w \cdot t}} \quad (11)$$

It is useful for analyzing shape irregularities and optimizing seed sorting systems. Finally, the roundness (R) which quantifies how closely the two-dimensional profile of a seed approximates a perfect circle and is calculated using Equation (12) (Ghabshyam, Raghunandan, Pankaj, & Kripanarayan, 2023; Zewdie *et al.*, 2024):

$$R = \frac{4 A_p}{\pi l^2} \quad (12)$$

where, A_p is the projected area of the seed and l is the seed length.

Determination of angle of repose

The angle of repose for maize seeds was determined using a funnel setup, where seeds flowed freely onto a closed container to form a conical heap, following methodologies validated in seed flow studies (Huang, 2022; Kawuyo *et al.*, 2022). The apex height (h) and the base radius (r) of the formed cone were measured to calculate the angle of repose (θ), as mentioned in Equation (13) below (Zewdie *et al.*, 2024). Using the trigonometric relationship, the angle of repose is computed as:

$$\theta = \tan^{-1}\left(\frac{h}{r}\right) \quad (13)$$

Determination of the gravimetric parameters

The gravimetric properties of three maize varieties, including porosity, density ratio, and true and bulk density, were analyzed using toluene displacement and weight-volume methods as presented in Equations (14)-(18) below (Soyoye *et al.*, 2018; Zewdie *et al.*, 2024). Each variety's thousand-seed mass was determined using a digital balance with a precision of 0.001 g, complemented by supplementary tools like graduated cylinders, beakers, and stirring rods, as illustrated in Fig. 2 (Panwar *et al.*, 2023).

True density ρ_t (kg m^{-3}):

$$\rho_t = \frac{\text{Weight of the maize sample (g)}}{\text{Volume of toluene displaced (cm}^3\text{)}} \quad (14)$$

Bulk density ρ_b (kg m^{-3}):

$$\rho_b = \frac{\text{Weight of the maize sample (g)}}{\text{Volume of toluene displaced (cm}^3\text{)}} \quad (15)$$

Porosity ε (%):

$$\varepsilon = \left(1 - \frac{\rho_b}{\rho_t}\right) 100\ \% \quad (16)$$

Density ratio R_ρ (%):

$$R_\rho = \left(\frac{\rho_b}{\rho_t}\right) 100\ \% \quad (17)$$

Thousand seed mass T_{sm} (g):

$$T_{sm} = \left(\frac{\sum_i^n \text{weight of Maize samples (g)}}{n}\right) 1000,\ i = 1, 2, 3\ldots, n \quad (18)$$

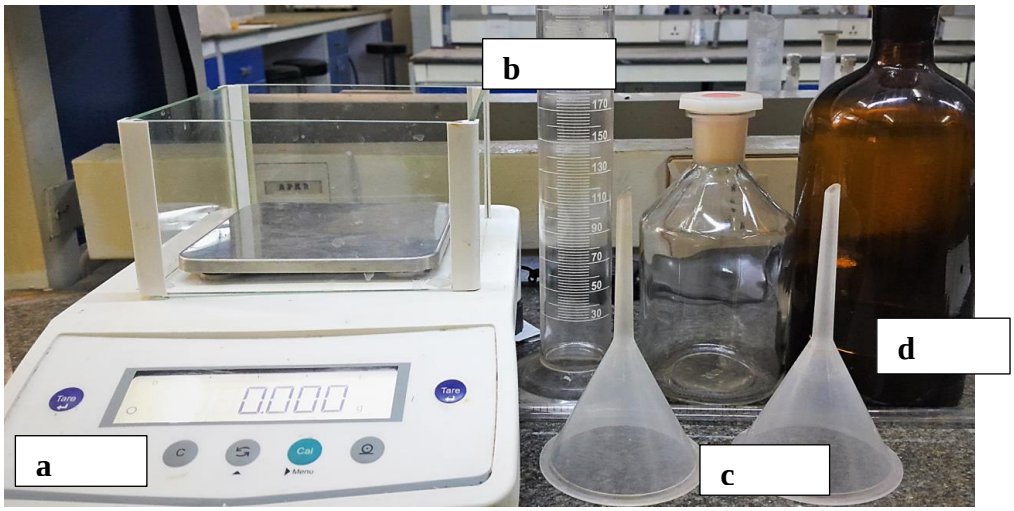

Fig. 2. Instruments for measuring gravimetric properties: (a) Digital balance, (b) 250 ml cylinder, (c) funnels, and (d) toluene; Photo taken during lab experiment by author

Statistical analysis

Statistical analysis was conducted using Minitab Statistical Software to compute key metrics, including means, standard deviations, and variance. These statistical parameters were used to validate the robustness of the data and inform the design and optimization of the multi-crop planter. The results ensured compatibility with the physical properties of maize seeds, enhancing the planter's efficiency and performance (Liang *et al.*, 2021; Zewdie *et al.*, 2024).

Results and Discussion

The physical properties of three maize varieties (CML-539, Melkassa 3, and Melkassa 6Q) were analyzed to optimize multi-crop planter design, as illustrated in the Table 3 and Table 4 below. Kernel dimensions varied significantly across varieties. Melkassa 3 and CML-539 exhibited the longest seed lengths of 10.99 ± 0.94 mm and 9.42 ± 8.06 mm, respectively, as shown in Table 2. This data highlights the need for adjustable seed plates with cell sizes that are 15-20% larger than the maximum seed dimensions to avoid

any clogs, corroborating the findings of Liang *et al.* (2021) and Sinha (2021). The thickness, essential for effective singulation, remained consistent within the range of 4.824-4.984 mm. However, Melkassa 3 exhibited a higher variance of 0.892, which corresponds with Liang *et al.* (2021) findings that attribute this variability to the wear of seed plates.

Elongation ratios revealed critical design differences: Melkassa 3 and Melkassa 6Q exhibited higher thickness elongation (2.337± 0.514 and 2.334± 0.457, respectively) than CML-539 (1.997± 0.383), increasing tilt risks during free fall. This aligns with Panwar (2023b), which associates ratios greater than 2.0 with trajectory errors, highlighting the need for curved seed tubes. Mean diameters further guided hopper design: CML-539's geometric mean diameter (8.019± 2.736 mm, CV 34.12%) highlighted irregular shapes, contrasting with Melkassa 6Q's stability (8.198± 0.382 mm, CV 4.66%), and enabled more uniform flow dynamics, supporting conventional hopper design. Such variability aligns with Dinberu (2023), who noted similar challenges in Ethiopian maize, advocating steeper hopper angles (> 35°) for low-sphericity grains.

A Comparative analysis underscored Ethiopia's unique needs. Melkassa 3's width (8.913 mm) exceeded the 8.5 mm threshold for fluted rollers (Sharma & Dewangan, 2023), while CML-539's arithmetic mean diameter of 7.509 mm (Table 2), fell below the 8.0 mm benchmark, explaining reported spacing deviations (Omar *et al.*, 2023). Melkassa 6Q's sphericity mirrored commercial hybrids, suggesting compatibility with standardized planters. CML-539's irregular seeds (CV of 34.12%) require vibration-assisted metering to prevent mechanical damage, while Melkassa 3's high elongation ratio exceeding 2.3 demands air-assisted tubes to ensure stable seed orientation crucial for smallholder planting.

Table 2- ANOVA of physical properties and elongation indices in maize varieties

Parameter	Variety	Mean	SD	Variance	CV	Minimum	Maximum	Mean ± SD
	CML-539	9.657	0.880	0.775	9.110	7.710	11.720	9.657±0.88
***l* (mm)**	M-3	10.994	0.941	0.886	8.560	7.410	13.160	10.994±0.941
	M-6Q	10.902	0.807	0.651	7.400	8.330	12.740	10.902±0.807
	CML-539	8.616	0.656	0.4296	7.610	6.860	10.50	8.616±0.4296
w (mm)	M-3	8.913	0.901	0.812	10.110	5.930	10.860	8.913±0.901
	M-6Q	8.869	0.861	0.742	9.710	7.130	10.790	8.869±0.861
	CML-539	4.984	0.909	0.827	18.240	3.770	8.360	4.984±0.909
t (mm)	M-3	4.893	0.945	0.892	19.310	3.220	9.150	4.893±0.945
	M-6Q	4.824	0.861	0.741	17.850	3.340	8.260	4.824±0.861
	CML-539	1.118	0.166	0.028	14.870	0.104	1.416	1.118±0.166
E_w	M-3	1.246	0.166	0.028	13.360	0.949	1.891	1.246±0.166
	M-6Q	1.241	0.154	0.024	12.430	0.833	1.582	1.241±0.154
	CML-539	1.997	0.383	0.146	19.160	1.096	2.873	1.997±0.383
E_t	M-3	2.337	0.514	0.264	21.990	0.953	3.460	2.337±0.514
	M-6Q	2.334	0.457	0.209	19.600	1.008	3.503	2.334±0.457
	CML-539	1.908	1.283	1.647	67.240	0.940	14.203	1.908±1.283
E_l	M-3	1.881	0.371	0.138	19.740	0.937	2.754	1.881±0.371
	M-6Q	1.896	0.371	0.138	19.570	0.924	2.723	1.896±0.371
	CML-539	7.509	1.077	1.161	14.350	6.617	17.261	7.509±1.077
D_a (mm)	M-3	7.776	0.514	0.264	6.610	6.366	8.956	7.776±0.514
	M-6Q	7.710	0.436	0.190	5.660	6.743	8.862	7.71±0.436
	CML-539	8.019	2.736	7.485	34.120	7.030	34.803	8.019±2.736
D_g (mm)	M-3	8.266	0.461	0.213	5.580	6.403	9.333	8.266±0.461
	M-6Q	8.198	0.382	0.146	4.660	7.307	9.180	8.198±0.382

l= length, w= width, t= thickness, E_w= Elongation at width, E_t =Elongation at thickness, E_l= Elongation at length, M-3= Melkassa 3, M-6Q= Melkassa 6Q, CML-539= Maize line 539, SD= Standard deviation, and CV= coefficient of variation

Table 3 highlights key geometric properties of maize varieties critical for planter optimization. The square mean diameter demonstrated only slight variation, ranging from 5.631 to 5.791 mm, with CML-539 showing higher variability (CV 10.74%) compared to Melkassa 3 (3.95%) and Melkassa 6Q (3.31%). This observation, shown in Table 3, is consistent with Dinberu (2023), who attributed this stability to the reliable performance of seed plates. Surface area and projected area revealed stark contrasts: CML-539 exhibited extreme variability, with a surface area coefficient of variation (CV) of 43.78% and a projected area CV of 82.22%. This variability underscores the irregular shape of the kernels, which poses a challenge for achieving uniform seed distribution in non-spherical grains. In contrast, Melkassa 6Q's lower surface and projected area variability (CV 11.27-11.96%) suggests suitability of this variety for the standardized metering systems (Kara, 2011; Masa, Tana, & Abdulatif, 2017).

Sphericity further differentiated varieties: CML-539 (78.31±13.09%) surpassed Melkassa 3 and Melkassa 6Q, indicating marginally better flowability (Table 3). However, its high sphericity variability (CV 16.72%) contrasts with Melkassa 6Q's uniformity (CV 9.37%), reinforcing the need for adaptive hopper designs, particularly because low-sphericity grains below 75% necessitate steeper angles to prevent clogging (Girma, Tola, & Olaniyan, 2024; Rabbani, Hossain, Asha, & Khan, 2016). Shape index and roundness underscored design risks: CML-539's higher shape index (1.485 ± 0.224) and roundness variability of 62.98% correlate with Panwar (2023b) findings of increased seed bridging in asymmetric grains, necessitating vibration-assisted hoppers.

CML-539's flakiness ratio of 57.73± 13.63 and cross-sectional area variability of 160.75% far exceed values reported by Sharma (2023) for commercial hybrids of flakiness < 50% and CV < 20%, demanding robust metering mechanisms. Conversely, Melkassa 3 and Melkassa 6Q's moderate aspect ratios align with Omar (2023) guidelines for gravity fed seed tubes but require air assistance to counter tilting caused by elongation. These results validate that Ethiopia's maize diversity, particularly CML-539's irregularity, demands planter components tailored to local varietals, such as adjustable cell sizes and aerated seed tubes, to achieve the precision required for smallholder farming systems.

The gravimetric properties essential for optimizing the design and functionality of maize planter hoppers and storage systems are presented in Table 4. True density showed a near-perfect negative correlation with thousand seed mass (-0.991) and a strong negative correlation with porosity (-0.904), while bulk density positively correlated with flowability metrics. Melkassa 6Q's optimal combination of high bulk density (811.62 kg m^{-3}), low porosity (36.99%), and favorable density ratio (0.630) suggests superior flow characteristics compared to CML-539's high-porosity grains (49.30%), which require greater aeration power (Liang *et al.*, 2021; Panwar *et al.*, 2023; Soyoye *et al.*, 2018).

Thousand-seed mass varied significantly among varieties, with Melkassa 6Q (297.06 g) and Melkassa 3 (290.84 g) exceeding CML-539 (224.11 g) by 32.5% (Table 4). This highlights the impact of varietal mass loading on seed metering mechanisms, as higher thousand seed mass of greater than 280 g increases torque and drive power requirements, consistent with Dinberu (2023) and Panwar (2023b). Melkassa 6Q's steeper angle of repose (31°) aligns with its high bulk density and correlates with increased inter-kernel friction, necessitating steeper hopper angles, while Melkassa 3's smoother grains (26° repose) may require flow restrictors. These findings, consistent with Liang *et al.* (2021) and Panwar (2023b), demonstrate how correlated physical properties directly inform equipment specifications for different maize varieties.

Table 3- ANOVA of geometric properties of areas and shape indices for selected maize varieties

Parameter	Variety	Mean	SD	V	CV	Min	Max	Mean ± SD
	CML-539	5.631	0.605	0.366	10.740	5.237	11.282	5.631±0.605
D_s (mm)	M-3	5.791	0.229	0.052	3.950	4.963	6.277	5.791±0.229
	M-6Q	5.759	0.190	0.036	3.310	5.309	6.259	5.759±0.19
	CML-539	180.760	79.130	6262.06	43.780	137.570	936.010	180.76±79.13
A_s (mm^2)	M-3	190.765	25.157	632.873	13.190	127.299	251.992	190.765±25.157
	M-6Q	187.356	21.107	445.492	11.270	142.822	246.720	187.356±21.107
	CML-539	71.170	58.510	3423.43	82.220	44.010	645.230	71.17±58.51
A_p (mm^2)	M-3	77.025	10.442	109.026	13.560	34.511	102.524	77.025±10.442
	M-6Q	75.924	9.082	82.485	11.960	49.918	95.514	75.924±9.082
	CML-539	37.570	40.820	1665.92	108.63	22.530	437.130	37.57±40.82
A_{ts}	M-3	34.261	7.553	57.055	22.050	19.018	61.587	34.261±7.553
	M-6Q	33.490	6.047	36.566	18.060	22.235	50.847	33.49±6.047
	CML-539	169.00	271.60	73786.9	160.75	116.40	2854.00	169±271.6
A_{cs} (mm^2)	M-3	161.506	17.721	314.032	10.970	96.610	205.251	161.506±17.721
	M-6Q	158.703	14.757	217.778	9.300	125.791	198.562	158.703±14.757
	CML-539	78.310	13.090	171.470	16.720	63.570	186.810	78.31±13.09
Φ (%)	M-3	71.252	7.843	61.513	11.010	58.001	101.031	71.252±7.843
	M-6Q	71.107	6.659	44.348	9.370	59.272	96.844	71.107±6.659
	CML-539	57.730	13.630	185.680	23.600	7.040	106.360	57.73±13.63
F_r (%)	M-3	55.517	12.684	160.887	22.850	36.312	106.768	55.517±12.684
	M-6Q	55.113	12.840	164.876	23.300	36.726	108.257	55.113±12.84
	CML-539	190.800	128.300	16468.4	67.240	94.000	1420.300	190.8±128.3
A_r (%)	M-3	188.138	37.133	1378.87	19.740	93.661	275.389	188.138±37.133
	M-6Q	189.579	37.100	1376.41	19.570	92.373	272.286	189.579±37.1
	CML-539	1.485	0.224	0.050	15.050	0.392	1.973	1.485±0.224
S_i	M-3	1.698	0.261	0.068	15.380	0.985	2.264	1.698±0.261
	M-6Q	1.693	0.223	0.050	13.160	1.049	2.191	1.693±0.223
	CML-539	1.139	0.717	0.515	62.980	0.815	8.168	1.139±0.717
R	M-3	1.050	0.110	0.012	10.470	0.689	1.396	1.05±0.11
	M-6Q	1.054	0.120	0.014	11.370	0.803	1.321	1.054±0.12

M-3= Melkassa 3, M-6Q= Melkassa 6Q, CML-539= Maize line 539, SD= Standard deviation, CV= Coefficient of variation, V=Variance, D_s= Square Mean Diameter, A_s= Surface Area, A_p= Projected Area, A_{ts}= Transverse Surface Area, A_{cs}= Cross-Sectional Area, Φ= Sphericity, F_r= Flakiness Ratio, A_r= Aspect Ratio, S_i= Shape Index, and R= Roundness

Table 4- Statistical description of gravimetric properties of maize varieties

Variable	T_{sm} (kg)	ρ_t (kg m^{-3})	ρ_b (kg m^{-3})	ε (%)	R_ρ	ϑ (^{0})
CML-539	224.110	1482.461*	751.548	49.304*	0.507	28
M-3	290.840*	1275.386	725.715	43.098	0.569	26*
M-6Q	297.060*	1288.146	811.621*	36.993	0.630	31*
Mean	270.670	1348.660	762.962	43.132	0.569	28.333
SD	40.442	116.047	44.076	6.156	0.062	2.517
Variance	1635.550	13466.900	1942.660	37.891	0.004	6.333
CV	14.940	8.600	5.780	14.270	10.820	8.88
Minimum	224.110	1275.390	725.715	36.993	0.507	26
Maximum	297.060	1482.460	811.621	49.304	0.630	31
M± SD	270.67±40.44	1348.6±116.047	762.96±44.076	43.13±6.156	0.57±0.062	28.34±2.517

* Significant at $p < 0.05$, M-3 = Melkassa 3, M-6Q = Melkassa 6Q, CML-539 = Maize line 539, ρ_b= Bulk density, ρ_t = True density, ε = Porosity, T_{sm} = Thousand seed mass, CV = coefficient of variance, M = mean, SD = standard deviation, ϑ = Angle of repose, and R_ρ= Density Ratio.

Table 5 provides a comprehensive overview of the physical characteristics of different maize varieties, focusing on geometric parameters, shape indices, and gravimetric properties. This information is vital for the optimal performance of adaptive multi-crop planters, as it directly impacts mechanical reliability, reduces seed damage and variation, and ensures precise depth control for improved spacing accuracy. This integrated system enhances seed placement precision while simultaneously improving input use efficiency and operational reliability across diverse seed morphologies and field conditions, demonstrating robust improvements in both agronomic outcomes and field productivity.

Table 5- Maize physical properties and their implications on multi-crop planter design optimization

Parameter/seed variety	Design requirement	Engineering implication
Large kernel size and thickness (M-3); Table 2	Seed metering plate: requires a length ≥ 12 mm and depth ≥ 8.5 mm (Liang *et al.*, 2021)	Reduces clogging and increases singulation accuracy (Jyotirmay *et al.*, 2024) and ensures uniform dispersal and minimal seed waste (Kimmelshue, Goggi, & Kenneth, 2022).
High elongation ratio (M-3 and M-6Q); Table 2	Seed tube: helical baffles (30° pitch), diameter ≥ 16 mm (Rabbani *et al.*, 2016)	Ensures vertical drop, optimal planting depth, and reduces germination failure (Omar *et al.*, 2023; Soyoye *et al.*, 2018)
Low sphericity and high shape index (CML-539); Table 2 and Table 3	Hopper: adjustable orifice (15–20 mm) (Kimmelshue *et al.*, 2022)	Reduces clogging (85%) (Panwar *et al.*, 2023) and flow disruptions (CV < 8%) for consistent seed flow and minimal damage (Liang *et al.*, 2021)
High geometric mean diameter (CML-539); Table 3	Hopper wall: slope angle ≥ 45°, optional agitator (Balanian, Karparvarfard, Mousavi Khaneghah, Raoufat, & Nejadian, 2021)	Prevents bridging, improving seed placement and spacing uniformity (Meseret, 2024; Woldesenbet, 2014)
High flakiness and irregular geometry (CML-539); Table 3	Delivery system: seed delivery ranges 15-20 RPM (Pandey & Sawant, 2023)	Prevents bridging, reduces seed damage, and ensures smooth, efficient seed flow (Liang *et al.*, 2021)
Bulk density variability (CML-539, M-3, and M-6Q); Table 4	Hopper: sloped walls ≥ 45°, internal agitator (3-5 RPM) (Soyoye *et al.*, 2018)	Ensures continuous mass flow (CV < 10%) and minimizes refills (≤ 2/ha) (Balanian *et al.*, 2021; Girma *et al.*, 2024)
Medium length kernels (CML-539); Table 2 and Table 3	Singulation mechanism (Liang *et al.*, 2021; Bhiman, Patel, Yaduvanshi, & Gupta, 2019; Van Loon, Krupnik, López-Gómez, Timsina, & Govaerts, 2020)	Maintains singulation accuracy (>90%) for consistent seed spacing and reduced seed waste (Patel, Bhimani, Yduvanshi, & Gupta, 2024)

M-3= Melkassa 3, M-6Q= Melkassa 6Q, CML-539= Maize line 539, RPM= revolution per minute, CV= coefficient of variation

Conclusion

This study analyzes three maize varieties (CML-539, Melkassa 3, and Melkassa 6Q) to establish quantitative relationships between seed physical properties and planter design parameters for adaptive multi-crop systems. The distinct physical properties of each variety dictate specific design requirements: CML-539's irregular dimensions (9.42 mm length, 49.30% porosity) and steep repose angle (31°) necessitate aerated seed tubes, vibration-assisted hoppers, and enlarged seed plates (15-20% oversizing), while Melkassa 6Q's uniform sphericity (71.11 ± 6.66%), high bulk density (811.62 kg m^{-3}), and lower repose angle (26°) enable simpler gravity-fed systems. Melkassa 3's intermediate characteristics, specifically an elongation ratio > 2.3 and density variation of 19.31%, require adjustable furrow openers with 25-30° rake angles to maintain consistent sowing depth. These findings demonstrate that varietal specific modifications, particularly for seed metering, hopper design, and depth

control, are essential for optimizing planting efficiency and seed integrity. The results demonstrate a seed-property-driven framework for modular planters that addresses diverse maize varieties while meeting standard agronomic requirements of 75 cm row spacing, and 4-7 cm planting depth, offering a scalable precision agriculture solution. Future field tests and real-time sensing could enhance this seed-specific planter design for precision agriculture.

Acknowledgments

We express our gratitude to the Department of Agricultural Engineering at Awash Melkassa Agricultural Research Center for providing the improved common maize seed varieties and the Department of Chemistry at Adama Science and Technology University for the laboratory facilities.

Conflict of Interest: The authors declare no competing interests.

Author Contributions

D. Girma Gadisa: Main Researcher, Conceptualization, Methodology, Data Collection, and Writing

K. Purushottam Kolhe: Formal Analysis, Writing Review and Editing

S. Kedir Busse: Supervision, Writing Review and Editing

M. Mohammed Issa: Data Collection, Resources, and Supervision

T. Assefa Abeye: Data Collection, Analysis

D. Alemu Anawte: Review, Editing

References

1. Alemayehu, A., Tamado, T., Nigussie, D., Yigzaw, D., Kinde, T., & Wortmann, C. S. (2017). Maize common bean intercropping to optimize maize-based crop production. *The Journal of Agricultural Science*, *155*(7), 1124-1136. https://doi.org/10.1017/S0021859617000193
2. Ayele, S. (2022). The resurgence of agricultural mechanisation in Ethiopia: rhetoric or real commitment? *Journal of Peasant Studies*, *49*(1), 137-157. https://doi.org/10.1080/03066150.2020.1847091
3. Balanian, H., Karparvarfard, S. H., Mousavi Khanghah, A., Raoufat, M. H., & Azimi-Nejadian, H. (2021). Prediction of Seed Flow Rate of a Multi-Slot Rotor Feeding Device of a Corn Planter. *Journal of Agricultural Machinery*, *11*(1), 17-27. https://doi.org/10.22067/jam.v11i1.79992
4. Bhiman, J., Patel, S., Yaduvanshi, B., & Gupta, P. (2019). Optimization of the operational parameters of a picking-type pneumatic planter using response surface methodology. *Journal of AgriSearch*, *6*(1), 38-43. https://doi.org/10.21921/jas.v6i1.14919
5. Bisrat, G., Laike, K, A., & Hae, K. K. (2015). Evaluation of Conservation Tillage Techniques for Maize Production in Ethiopia. *Ethiopian Journal of Agricultural Sciences*, *25*(2), 47-58.
6. Central Statistical Agency. (2021). Farm Management Practices Agricaltural Sample Survey 2020/21. In *Central Statistical Agency: Vol. III* (Issue 12). Retrieved from https://www.statsethiopia.gov.et
7. Dinberu, A., & Megersa, M. (2023). Effect of Inter and Intra Row Spacing on Growth , Yield and Yield Components of Sorghum (*Sorghum bicolor* (L.) Moench) at Assosa District , Western Ethiopia. *American Journal of Plant Biology*, *8*(1), 20-24. https://doi.org/10.11648/j.ajpb.20230801.14
8. FAO. (2023). *Standard operating procedure for soil bulk density; Cylinder method*. Food and Agriculture Organization of the United Nations. https://doi.org/10.4060/cc7568en
9. Getaneh, L., Belete, K., & Tana, T. (2016). Growth and Productivity of Maize (*Zea mays* L.) as Influenced by Inter- and Intra-Row Spacing in Kombolcha, Eastern Ethiopia. *Journal of Biology, Agriculture and Healthcare*, *6*(13), 90-101. https://doi.org/10.7176/jbah/9-9-05
10. Ghabshyam, P., Raghunandan, S., Pankaj, G., & Kripanarayan, S. (2023). A review of

methodologies and influencing factors in planter performance evaluation for higher maize yield. *The Pharma Innovation Journal*, *12*(12), 1465-1471. Retrieved from www.thepharmajournal.com

11. Girma, O., Tola, S., & Olaniyan, A. (2024). Design and development of a tractor-drawn multi-row garlic planter. *Agricultural Engineering International: CIGR Journal*, *26*(2), 34-56.
12. Huang. (2022). Measurement of physical properties of sorghum seeds and calibration of discrete element modeling parameters. *Agriculture (Switzerland)*, *12*(5), 2-19. https://doi.org/10.3390/agriculture12050681
13. Jyotirmay, M., Prem, S. T., Krishna, P. S., Balaji, M. N., Jagjeet, Singh, A., & Ramesh, K. S. (2024). Flexible orifice seed metering plate to address variability in seed shape, size and orientation enhances field performance of a pneumatic planter. *Discover Applied Sciences*, *6*(11). https://doi.org/10.1007/s42452-024-06275-5
14. Kara, B. (2011). Effect of seed size and shape on grain yield and some ear characteristics of maize. *Research on Crops*, *12*(3), 680-685.
15. Kawuyo, U. A., Aviara, N. A., Mari, H. H., & Ahmed, B. M. (2022). Physical properties of four varieties of sorghum grain at different moisture contents. *Arid Zone Journal of Engineering, Technology & Environment*, *18*(1), 159-168. Retrieved from www.azojete.com.ng
16. Kebede, M. B. (2019). Effect of Inter and Intra Row Spacing on Growth , Yield Components and Yield of Hybrid Maize (*Zea mays* L.) Varieties at Haramaya, Eastern Ethiopia. *American Journal of Plant Sciences*, *10*(7), 1548-1564. https://doi.org/10.4236/ajps.2019.109110
17. Kimmelshue, C. L., Goggi, S., & Moore, K. J. (2022). Seed Size, Planting Depth, and a Perennial Groundcover System Effect on Corn Emergence and Grain Yield. *Agronomy*, *12*(2). https://doi.org/10.3390/agronomy12020437
18. Liang, G., Chi, B., Li, N., Chen, W., Qin, W., Wu, X., & Huang, X. (2021). Evaluating agronomic factors for maize production in a semi-arid Loess Plateau. *Agronomy Journal*, *113*(6), 5157-5169. https://doi.org/10.1002/agj2.20818
19. Masa, M., Tana, T., & Abdulatif, A. (2017). Effect of Plant Spacing on Yield and Yield Related Traits of Common Bean Varieties at Areka ,Southern Ethiopia. *Journal of Plant Biology & Soil Healt*, *4*(2). https://doi.org/10.13188/2331-8996.1000020
20. Meseret, A. (2024). Performance Evaluation of Two Row Animal Drawn Maize Planter with Fertilizer Applicator. *Turkish Journal of Agricultural Engineering Research*, *5*(2), 153-166. https://doi.org/10.46592/turkager.1487496
21. Muhidin, B. (2019). Effect of Inter-and Intra-Row Spacing on Yield and Yield Components of Maize QPM Hybrid, BHQPY545 in Southwestern Ethiopia Muhidin. *International Journal of Research Studies in Agricultural Sciences*, *6*(10), 19-26.
22. Omar, S., Abd Ghani, R., Khalid, N., Jolánkai, M., Tarnawa, Á., Percze, A., Mikó, P. P., & Kende, Z. (2023). Effects of Seed Quality and Hybrid Type on Maize Germination and Yield in Hungary. *Agriculture*, *13*(9), 2-14. https://doi.org/10.3390/agriculture13091836
23. Pandey, H. S., & Sawant, C. P. (2023). Design and Development of a Seed Metering Mechanism for Ginger Planter. *Journal of Scientific and Industrial Research*, *82*(10), 1071-1080. https://doi.org/10.56042/jsir.v82i10.225
24. Panwar, G., Swarnkar, R., Kumar, N., & Shukla, K. (2023). Evaluation of physical properties of maize and pigeonpea seeds for seed metering mechanism. *Journal of Experimental Agriculture International*, *45*(12), 89-97. https://doi.org/10.9734/jeai/2023/v45i122269
25. Pascual, K. S., Rafael, M. L., Remocal, A. T., & Regalado, M. J. C. (2021). Development and evaluation of four-wheel tractor-attached multi-crop planter for mechanized seeding of maize in the Philippines. *CIGR Journal*, *23*(3), 143.
26. Patel, S. K., Bhimani, J. B., Yduvanshi, B. K., & Gupta, P. (2024). Radish (*Raphanus raphanistrum* subsp. sativus) Seed Planter Parameters Optimization using Response Surface

Methodology. *Journal of Scientific and Industrial Research*, *83*(5), 483-489. https://doi.org/10.56042/jsir.v83i5.2823
27. Rabbani, M. A., Hossain, M. M., Asha, J. F., & Khan, N. A. (2016). Design and development of a low cost planter for maize establishment. *Journal of Science Technology and Environment Informatics*, *4*(1), 270-279. https://doi.org/10.18801/jstei.040116.30
28. Seyoum, A., Paul, D., & Sinafikeh, A. (2013). Crop production in Ethiopia: Regional patterns and trends. *Food and Agriculture in Ethiopia: Progress and Policy Challenges*, *9780812208*, 53-83. https://doi.org/10.9783/9780812208610.53
29. Shah, K., Alam, M. S., Nasir, F. E., Qadir, M. O., Haq, I. U., & Tahir Khan, M. (2022). Design and performance evaluation of a novel variable rate multi-crop seed metering unit for precision agriculture. *IEEE Access*, *10*(September), 133152-133163. https://doi.org/10.1109/ACCESS.2022.3231136
30. Sharma, P. T., & Dewangan, K. N. (2023). Design and development of a vertical plate precision seed metering device with positive seed knockout mechanism. *Agricultural Engineering International: CIGR Journal*, *25*(1), 27-42.
31. Singh, S., Sahoo, D. C., & Bisht, J. K. (2017). Development and performance evaluation of manual/bullock operated multicrop planter for hilly region. *Agricultural Engineering International: CIGR Journal*, *19*(1), 81-86.
32. Sinha, A. K., Sinha, A. K., Sharma, S., Khar, S., Gupta, V., Parkash, S., Mishra, S. K., & Gupta, S. (2021). Maize sowing with multi crop planter under rain fed conditions in Rajouri District of J & K proved beneficial. *Journal of Krishi Vigyan*, *9*(2), 120-123. https://doi.org/10.5958/2349-4433.2021.00023.4
33. Soyoye, B. O., Ademosun, O. C., & Agbetoye, L. A. S. (2018). Determination of some physical and mechanical properties of soybean and maize in relation to planter design. *Agricultural Engineering International: CIGR Journal*, *20*(1), 81-89.
34. Theodrose, S., Kindie, T., Mezegebu, G., Nigussie, D., & Mengistu, K. (2024). Calibration and Evaluation of CERES-Maize and CROPGRO-Dry Bean Crop Simulation Models of the DSSAT in the Great Rift Valley Region of Ethiopia. *International Journal of Applied Agricultural Sciences*, *10*(4), 149-156. https://doi.org/10.11648/j.ijaas.20241004.11
35. Tolossa, A., & Gizawu, T. (2024). Effect of Intra and Inter Row Spacing on Yield, Yield Components and Growth Parameter of Hybrid Maize at Mettu, South Western Ethiopia. *Journal of Environment and Earth Science*, *10*(1), 16-19. https://doi.org/10.7176/JEES/10-1-03
36. Van Loon, J., Krupnik, T. J., López-Gómez, J. A., Timsina, J., & Govaerts, B. (2020). A standard methodology for evaluation of mechanical maize seed meters for smallholder farmers comparing devices from Latin America, Sub-Saharan Africa, and Asia. *Agronomy*, *10*(8). https://doi.org/10.3390/agronomy10081091
37. Woldesenbet, M. (2014). Effect of Spacing on the Growth Parameters of Common Bean at Keker, Southwestern Ethiopia. *International Journal of Research in Agricultural Sciences*, *1*(5).
38. Zewdie, B., Olaniyan, A. M., Wako, A., Alemu, D., & Lema, T. (2024). Engineering properties of common bean in perspective of physical and frictional parameters for threshing machine design. *INMATEH Agricultural Engineering*, *73*(2), 771-783. https://doi.org/10.35633/inmateh-73-65

نشریه ماشین‌های کشاورزی
https://jame.um.ac.ir

مقاله پژوهشی

جلد ۱۶، شماره ۳، پاییز ۱۴۰۵، ص ۵۶۱-۵۴۹

ویژگی‌های فیزیکی ارقام ذرت اتیوپی برای طراحی دستگاه کاشت سازگار با چند محصول

دجنه گِرما گادیسا[1*]، کیشور پوروشوتام کوله[2]، سراج کدیر بوسه[1]، مبارک محمد عیسی[3]، تسفایه آسِفا آبَیه[3]، درجه آلمو اناوته[3]

تاریخ دریافت: ۱۴۰۳/۱۲/۲۴
تاریخ پذیرش: ۱۴۰۴/۰۳/۱۸

چکیده

تولید ذرت توسط خرده‌مالکان در کشورهای جنوب صحرای آفریقا، که برای تامین امنیت غذایی منطقه‌ای بسیار مهم است، با معضلات مداوم عملکرد دست و پنجه نرم می‌کند که ناشی از شیوه‌های کاشت پرزحمت و ضعف در مکانیزاسیون است، به‌طوری‌که مطابق با ویژگی‌های ارقام گیاهی بومی طراحی نشده است. این مطالعه سه رقم ذرت (CML-539، Melkassa 3 و Melkassa 6Q) را برای توسعه پارامترهای طراحی برای کاشت‌کننده‌های سازگار با چند محصول توصیف می‌کند. برای ۱۰۰ دانه از هر رقم، خواص هندسی شامل طول، عرض و ضخامت با استفاده از کولیس‌های دیجیتال اندازه‌گیری شد. تجزیه و تحلیل برای کشیدگی، قطرهای میانگین هندسی و حسابی، مساحت سطح، مساحت تصویر شده، سطح مقطع عرضی، کرویت، ضریب فرورفتگی، نسبت ابعاد، شاخص شکل و گردی انجام شد. خواص وزنی شامل چگالی حجمی و واقعی، تخلخل، جرم هزار دانه و زاویه استقرار به‌طور سیستماتیک برای بهینه‌سازی مکانیسم‌های جابه‌جایی بذر در طراحی دستگاه کاشت تجزیه و تحلیل شدند. تجزیه و تحلیل خواص فیزیکی، الزامات متمایزی را برای هر رقم نشان داد: مورفولوژی نامنظم CML-539 (طول ۹/۴۲ میلی‌متر، تخلخل ٪۴۹/۳۰) نیاز به سیستم‌های اندازه‌گیری ارتعاشی و هوادهی را نشان می‌دهد؛ خواص یکنواخت Melkassa 6Q (کرویت ٪۶/۶۶ ± ۷۱/۱۱، چگالی حجمی ۸۱۱/۶۲ کیلوگرم بر متر مکعب) امکان استفاده از مکانیسم‌های تغذیه گرانشی را فراهم می‌کند؛ و ویژگی‌های متوسط Melkassa 3 با نسبت کشیدگی بیش از ۲/۳ و تغییر چگالی ٪۱۹/۳۱ نیاز به شیاربازکن‌های قابل‌تنظیم با زاویه شیب ۲۵ تا ۳۰ درجه را مشخص می‌کند. تغییرپذیری هندسی، پیاده‌سازی راه‌حل‌های تطبیقی، مانند لوله‌های بذر انحنادار و شیاربازکن‌های قابل‌تنظیم را برای جلوگیری موثر از کج شدن و پشته‌سازی ضروری می‌سازد. سیستم کاشت مدولار حاصل، شامل اندازه‌گیری حساس به رطوبت، اندازه‌گیری تطبیقی سلول‌ها و هوادهی، با استانداردهای کشاورزی-اکولوژیکی اتیوپی مبنی بر فاصله ردیف ۷۵ سانتی‌متر و عمق کاشت ۴ تا ۷ سانتی‌متر مطابقت دارد. این چارچوب، یک مدل مقیاس‌پذیر و پایدار برای مکانیزاسیون دقیق خرده‌مالکان را ارائه می‌دهد و قابل‌انتقال به سیستم‌های جهانی تولید ذرت است.

واژه‌های کلیدی: خواص فیزیکی، زاویه استقرار، کاشت چند محصولی، کرویت، واریته ذرت

۱- گروه مهندسی مکانیک، دانشکده مهندسی مکانیک، شیمی و مواد، دانشگاه علوم و فناوری آداما، آداما، اتیوپی
۲- دانشکده مهندسی مکانیک، کالج مهندسی سینگهاد، دانشگاه پونه، وادگان، هند
۳- موسسه تحقیقات کشاورزی اتیوپی، بخش تحقیقات مهندسی کشاورزی، مرکز تحقیقات کشاورزی ملکاسا، آداما، اتیوپی
(*- نویسنده مسئول: Email: dejene383@gmail.com)

https://doi.org/10.22067/jam.2025.92654.1356

Journal of Agricultural Machinery

Homepage: https://jame.um.ac.ir

Research Article
Vol. 16, No. 3, 2026, p. 563-578

Feasibility of Detecting Different Genotypes of *Mentha* plant by E-nose Technique

H. Zaki Dizaji[1*], M. Mahmoodi Surestani[2], N. Aghilinategh[3], A. Boveiri Dehsheikh[2]

1- Department of Biosystems Engineering, Faculty of Agriculture, Shahid Chamran University of Ahvaz, Ahvaz, Iran
2- Department of Horticulture, Faculty of Agriculture, Shahid Chamran University of Ahvaz, Ahvaz, Iran
3- Department of Agricultural Machinery Engineering, Sonqor Agriculture Faculty, Razi University, Kermanshah, Iran
(*- Corresponding Author Email: hzakid@scu.ac.ir)

Received: 16 March 2025
Revised: 30 April 2025
Accepted: 20 May 2025
Available Online: 29 September 2025

How to cite this article:
Zaki Dizaji, H., Mahmoodi Surestani, M., Aghilinategh, N., & Boveiri Dehsheikh, A. (2026). Feasibility of Detecting Different Genotypes of Mentha plant by E-nose Technique. *Journal of Agricultural Machinery*, *16*(3), 563-578. https://doi.org/10.22067/jam.2025.92417.1354

Abstract

In botanical terms, the classification of plants reveals a multitude of species derived from different sources. The first step for quality control of herbal medicines is to identify their different species and genotypes. The present study investigated the classification of ten different mint genotypes using Gas Chromatography-mass Spectrometry (GC-MS) and an electronic nose (e-nose) system utilizing Metal Oxide Semiconductor (MOS) sensors. Leaf samples were harvested from various mint genotypes, and subsequently, the system sensors' responses to each of these samples were recorded. The classification of plants was performed using biplot diagrams based on GC and GC-MS data, with clustering facilitated by the Ward method. The responses of all e-nose sensors were further analysed through various approaches, including Principal Components Analysis (PCA), Linear Discriminant Analysis (LDA), Quadratic Discriminant Analysis (QDA), and Artificial Neural Network (ANN). The results from the qualitative analysis of essential oils via GC-MS demonstrate that more than 99% of the identified compounds belong to four chemical groups: hydrocarbon and oxygenated monoterpenes, as well as hydrocarbon and oxygenated sesquiterpenes. Also, based on biplot analysis, different mint populations could be generally divided into 8 groups. The results of principal component analysis showed that the first two main components can cover a total of 97% of the data variance. The classification accuracy achieved through e-nose data for LDA, QDA, and ANN was 98.9%, 99.9%, and 96%, respectively. Proper classification of mint genotypes by e-nose system could be used as a sensitive, reliable, and low-cost alternative to traditional methods.

Keywords: Artificial Intelligent methods, Classification, E-nose, Essential oil

Table of abbreviations

Definition	Abbreviation
Medicinal and Aromatic Plants	MAPs
Metal Oxide Semiconductor	MOS
Principal Components Analysis	PCA
Linear Discriminant Analysis	LDA
Quadratic Discriminant Analysis	QDA
Artificial Neural Network	ANN
Area Under the Curve	AUC
Retention time of hydrocarbon with smaller alkanes	$t_{r\,(n)}$
Retention time of hydrocarbon with larger alkanes	$t_{r\,(N)}$

Authors retain the copyright. This is an open access article distributed under Creative Commons Attribution 4.0 International License (CC BY 4.0).

https://doi.org/10.22067/jam.2025.92417.1354

Retention time of unknown composition	$t_{r\ (unknown)}$
Carbon number of smaller alkanes	N
Kovats Index	KI
The lowest sensor response before the measurement phase (baseline)	X_s (0)
The sensor response at time t	X_s (t)
The normalized sensor response at time t	Y_s (t)

Introduction

In recent years, there has been an increasing demand for the production of medicinal plants due to the consumers' interest in natural products, as they are thought to be safer and more cost-effective (Tangpao *et al.*, 2022). This has led to the development of pharmaceutical, cosmetic, and food industries based on natural products, which, in turn, has increased the demand for natural raw materials such as medicinal plants (Nguyen, Duong, & Mentreddy, 2019). The global trade in medicinal and aromatic plants, along with their products, has seen remarkable growth both in quantity and quality, indicating a positive outlook (Asl Roosta, Moghaddasi, & Hosseini, 2017). The Lamiaceae family with 200 genera and 3,200 species is one of the largest and most diverse plant families, rich in medicinal plants (Okur *et al.*, 2021a). Different species of mint plant such as *Mentha piperita*, *Mentha spicata*, and *Mentha pulegium* are valuable medicinal and aromatic species of this family, all belonging to the *Mentha* genus. According to the latest published statistics in 2015, the global trade value for mint essential oil exports and imports reached an impressive $185 million, while essential oils from other species of mint totaled $322 million. Ranked just behind citrus, mint essential oil boasts a remarkable annual production of 6,000 to 8,000 tonnes, establishing itself as one of the top essential oils worldwide (Banal, Rañola, Santiago, & Sevilla, 2014; Lubbe & Verpoorte, 2011). The aerial parts of the mint contain a high amount of active ingredients such as essential oils and various phenolic and flavonoid compounds, recognized for their valuable biological properties. The essential oil and extract of this plant are used in the pharmaceutical, food, and cosmetic industries due to its antimicrobial and high antioxidant properties and special taste (Kiani, Minaei, & Ghasemi-Varnamhasti, 2018). In general, botanically, plants have different species from different sources. The first step for quality control of herbal medicines is to identify their different species and genotypes. In the traditional quality evaluation system, odor serves as a vital quality indicator, as most medicinal plants produce scents that can be associated with their species or legitimacy. Smell is one of the most important sensory properties of food. Smell measurement is an advanced method that is especially effective in obtaining parameters affecting food quality because the smell emitted from food is extremely sensitive to the changing constituents. At present, a sensory method or panel test is used for qualitative evaluation and identification of aromatic substances. Although this method is relatively fast, it has many limitations in standard measurement stability and repeatability (Guohua *et al.*, 2015). Accurate laboratory methods are also used, such as gas chromatography (GC), gas chromatography-mass spectrometry (GC-MS), or high-performance liquid chromatography (HPLC) (Kiani *et al.*, 2018; Li, Yu, Xu, & Gao, 2017). Despite having high accuracy, these meticulous methods have a high cost and require knowledgeable people to operate these tools, painstaking sample preparation, and a long time for analysis (Gebicki & Szulczynski, 2018). This led to using non-destructive and less expensive methods, one of which is the e-nose method. This system includes a combination of factors such as understanding of the human olfactory system and rapid advances in sensor technology and pattern recognition systems for smell detection (Zaki Dizaji, Adibzadeh, & Aghili Nategh, 2020). Therefore, olfactory volatile compounds can be identified as a fingerprint. Many studies have been conducted on the application of the

e-nose (olfactory machine) technique in the food industry and quality control of some medicinal and aromatic plants such as berry ripening (Aghili Nategh, Dalvand, & Anvar, 2020), sugar cane syrup sucrose detection (Zaki Dizaji *et al.*, 2020), detection and classification of fungal infection in garlic (Makarichian, Chayjan, Ahmadi, & Zafari, 2022), discrimination of flavoured and unflavoured olive oils (Rodrigues, Silva, Veloso, Pereira, & Peres, 2021), acrylamide detection in olives (Martín-Tornero *et al.*, 2021) and Lamiaceae (Okur *et al.*, 2021a), qualitative classification of 9 genotypes of Rosa essential oils (Gorji-Chakespari, Nikbakht, Sefidkon, Ghasemi-Varnamkhasti, & Valero, 2017), and isolation of different cultivars and species of Chinese Cymbidium (Zhang *et al.*, 2014), mint (Kiani *et al.*, 2018; Okur *et al.*, 2021b), and basil (Tangpao *et al.*, 2022). To date, no preliminary assessments have been performed to ascertain the genotype of the mint. The present study aimed to investigate the performance of an e-nose system in combination with GC-MS and chemometric instruments to identify genotypes and different species of mint.

Materials and Methods

Preparation of Mentha samples

Different populations of *Mentha* plant (10 genotypes) were harvested from the collection of this plant at the farm of the Department of Horticultural Sciences, Faculty of Agriculture, Shahid Chamran University of Ahvaz, Iran (Table 1). Plants were harvested from about 5 cm above the ground level at the early reproductive stage. 100 g of aerial parts of each sample of *Mentha* populations, including leaves and inflorescences, were used for essential oil extraction to perform GC test. Oil extraction of plant was performed by water distillation method and Clevenger apparatus for 3 hours. To remove excess moisture from the extracted essential oils, sodium sulphate was added to them after collecting the essential oils in the dark and sealed vials and the oil samples were kept at 4 °C until the analysis of their chemical compounds.

Table 1- List of mint genotypes with botanical name and origin

Number	Genotype code	Botanical name	Origin
1	E1	*Mentha spicata* L.	Ilam, Iran
2	E4	*Mentha spicata* L.	Ilam, Iran
3	H1S	*Mentha spicata* L.	Budapest, Hungary
4	H1P	*Mentha* × *piperata*	Budapest, Hungary
5	H3	*Mentha spicata* L.	Budapest, Hungary
6	H6	*Mentha spicata* L.	Budapest, Hungary
7	H7	*Mentha* × *piperata*	Budapest, Hungary
8	H10	*Mentha citrata*	Budapest, Hungary
9	H16	*Mentha spicata* L.	Budapest, Hungary
10	T19	*Mentha rotondifolia* L.	Tehran, Iran

Identification of essential oil components (GC and GC-MS)

Quantitative and qualitative analysis of the chemical compounds of the essential oil was performed using gas chromatography (SHIMADZU, Model GC-17A) and gas chromatography-mass spectrometry (Agilent, Model B5977) under the following conditions. The gas chromatography (GC) apparatus utilized was equipped with a BP-5 column, measuring 30 m in length, 0.32 mm in diameter, and featuring a stationary phase layer thickness of 0.25 µm. The oven temperature was kept at 60°C for 1 minute and then increased at a rate of 5 °C per minute to 250 °C. This peak temperature was then maintained for an additional 2 minutes. The injector and flame ionization detector (FID) temperatures were 280 and 300°C, respectively, and helium gas with a flow rate of 1.1 mL min^{-1} was used as the carrier gas.

The gas chromatography-mass spectrometry (GC-MS) system was fitted with

an HP-5 ms column featuring a length of 30 m, a diameter of 0.25 mm, and a stationary phase layer thickness of 0.25 µm. The temperature program of the column included increasing the temperature from 65 to 250°C at a rate of 5°C per minute, which eventually remained at this temperature for 2 minutes. The temperature of the injection chamber and the transmission line to the MS part of the apparatus were 265 and 275°C, respectively, and helium gas was used as the carrier gas at a rate of 1.1 mL min^{-1}. The scan time was 0.6 seconds, and the ionization energy was 70 electron volts. The essential oils were injected into a gas chromatograph-mass spectrometry apparatus, and the mass spectra of the essential oil compounds were obtained. The spectra were identified by utilizing the mass database, assessing inhibition time, and critically analysing the mass spectra of each essential oil component. This process included comparing their failure patterns with standard spectra alongside reference to reputable sources (Adams, 2007). The quantitative percentage of each compound was determined based on the area under its curve in the GC chromatogram and by computer programming (using GC Solution software). The percentage of chemical compounds constituting each essential oil sample and the Kovats index of each compound were calculated, and spectra were identified by calculating the Kovats Index (KI) with injecting normal hydrocarbons (C4- C28) under the same conditions with injecting essential oils. The Kovats index of essential oil compounds was calculated using the Equation (1):

$$KI = 100 \times [n + ((N - n) \times \frac{t_{r(unknown)} - t_{r(n)}}{t_{r(N)} - t_{r(n)}})] \quad (1)$$

where KI = Kovats index, n = carbon number of the smaller alkane, N = carbon number of the larger alkane, $t_{r\ (unknown)}$ = the retention time of unknown composition, $t_{r\ (N)}$ = the retention time of hydrocarbon with the larger alkane, and $t_{r\ (n)}$ = the retention time of hydrocarbon with smaller alkanes.

Preparing samples for e-nose test

20 grams fresh aerial parts of each sample (plant) was poured into the measuring chamber of the e-nose device. Then, this chamber was connected to the e-nose system and the data collection steps were performed from the device. After the sensors started working, data collection of chemical compounds of essential oil from each population of mint was performed by e-nose apparatus.

E-nose device

To conduct the experiments, an e-nose system made at the Shahid Chamran University of Ahvaz was used (Zaki Dizaji *et al.*, 2020). This system includes a sampling chamber, a system equipment box, and a computer (Figure 1). System equipment consists of a sensor chamber, sample housing, two CL10R0 carbon filters, two micro-pumps (model R-385 with a flow rate of 25 $cm^3\ s^{-1}$), three solenoid valves, data collection system, two power supplies 5 and 12 volts, and an inlet air filter. Sensors are tasked with the conversion of chemical changes into electrical signals, highlighting the significance of selecting the correct sensor array (Rafaela, Murilo, Luiza, & Daniel, 2022). The sensor array consists of eight metal oxide semiconductor sensors, including MQ2, MQ3, MQ5, MQ8, MQ9, MQ135, MQ137, and MQ138 (Hanwai Electronics Co., China). Metal oxide semiconductor sensors are used for their high chemical stability, high sensitivity, easy manufacturing, and suitability for a wide range of food and agricultural products. The sensors' responses were captured by a production system linked to a computer running LabVIEW 2015 software. The e-nose system was scheduled for three phases: baseline correction (100 seconds), sample smell injection on the sensors (90 seconds), and cleaning of the sensor chamber and sample with clean air (100 seconds). During these phases, the voltage changes in response from the sensors are meticulously recorded over time. In general, the voltage response of the sensors in these 290 seconds is collected by the produced system. The time required for each step is obtained via trial and error. The

number of e-nose test repetitions for each sample is 15. The sample chamber consists of a closed chamber with a volume of about 500 cc, maintaining the sample's temperature at room conditions, about 30°C, and a humidity of about 25%.

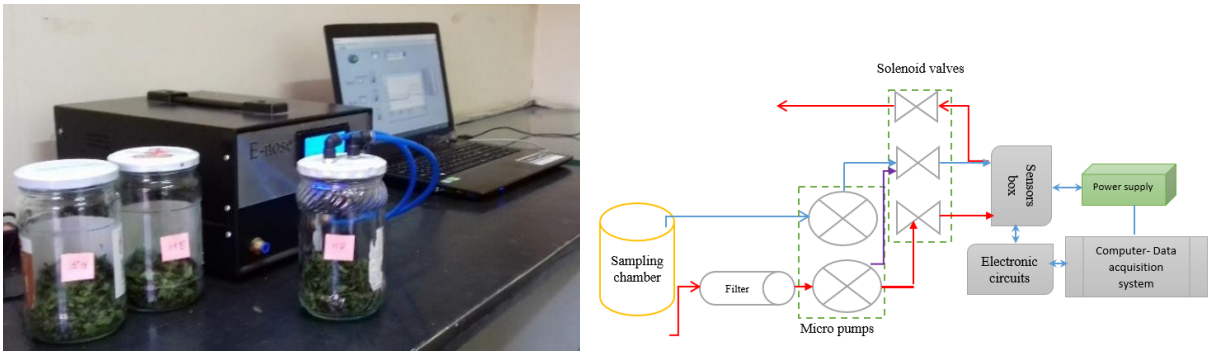

Fig. 1. (Left) The e-nose system, which comprises a sampling chamber, a system equipment box, and a computer, and (right) a schematic block diagram illustrating the components of the e-nose device

Data analysis

To analyse the differences between GC and GC-MS data and to explore the internal relationships among traits using principal component analysis, a two-dimensional biplot diagram was generated through clustering with the Ward method, Euclidean square distance criterion, and SPSS and Genstate software.

Preprocessing is the first step in analysing the response of the array of e-nose sensors. This involves removing irrelevant information to make the information more efficient for the next steps of the analysis. The first preprocessing stage is dedicated to aligning the sensors' responses with a baseline (stable response) to correct for deviations and significantly enhance the contrast of their outputs. In this study, the fractional method was used to correct the baseline (Equation 2). In this method, the baseline is subtracted from the sensor response and then divided by the baseline. The response obtained is not only dimensionless but also normalized and can be used for small or large signals (Zaki Dizaji *et al.*, 2020).

$$Y_s(t) = [X_s(t) - X_s(0)]/X_s(0) \qquad (2)$$

In this regard, $X_s\ (0)$ is the lowest sensor response before the measurement phase (baseline), $X_s\ (t)$ is the sensor response at time t, and $Y_s\ (t)$ is the normalized sensor response. After these steps, the pre-processed data are analysed in different ways, and finally the sample is evaluated. In general, pattern recognition is done by two methods: statistical methods or artificial neural methods. These methods are based on qualitative expression or classification of data. This research involved the analysis of data utilizing various statistical and intelligent techniques, including PCA, LDA, QDA, and ANN. In order to analyse the performance of these methods, the parameters of the classification performance such as accuracy, precision, sensitivity, specificity, and area under the curve (AUC) were used based on the values of the confusion matrix (Kaushal, Nayi, Rahadian, & Chen, 2022; Mahmodi, Mostafaei, & Mirzaee-Ghaleh, 2019).

The main component analysis follows the idea of reducing the data dimension. In fact, a number of interconnected characteristics are expressed in the form of several compact and independent indices that are the main components of the main multiple characteristics. The linear discriminant analysis is one of the most widely used methods for classifying observations in different classes, especially when it has more than two classes. The quadratic discriminant analysis is a statistical method used to find the quadratic composition of properties that best separate two or more groups of objects. A

multi-layer perceptron (MLP) algorithm was also used. The classification involved a network that features an input layer, a hidden layer, and an output layer. The hidden layer contains several neurons that represent a nonlinear network system. Considering that this research utilizes a neural network for real-time classification, it is better to be close to the desired error rate with the same number of epochs or fewer repetitions. Therefore, a hidden layer was considered for the network to increase the speed of training. The hyperbolic tangent activation function was used for the hidden layer. The post-diffusion algorithm was used to train the network, and through a trial-and-error approach, it was concluded that the optimal number of neurons for the hidden layer is 8. Finally, the optimal model was selected. Based on the data from eight sensors at the network input, and with an output layer composed of 10 nodes, the samples are classified using a structure of 8-8-10. Data processing was performed in Microsoft Excel 2019, MATLAB 2015, and Unscrambler 10.3 (CAMO) software.

Results and Discussion

GC and GC-MS results

According to the results of qualitative analysis of essential oil by GC-MS apparatus, 72 different compounds were identified in the essential oils of different populations of *Mentha* plant (Table 2). More than 99% of the identified compounds were in four chemical groups, including hydrocarbon and oxygenated monoterpenes, as well as hydrocarbon and oxygenated sesquiterpenes (Hawrył *et al.*, 2015). Oxygenated monoterpenes made up about 75% of the essential oils from various populations of mint, followed by hydrocarbon monoterpenes, hydrocarbon sesquiterpenes, and oxygenated sesquiterpenes in that order. In other words, aroma of *Mentha* plant covers the subgroups of terpenes, esters, alcohols, and ketones. These results align closely with the majority of results presented in other studies (Kiani *et al.*, 2018; Okur *et al.*, 2021a).

According to the results of biplot and cluster analysis, different populations of mint are generally divided into 8 groups (Table 3). This separate division showed that the desired traits were appropriate criteria for creating diversity in the studied populations (Figure 2). The first group includes H7 and H1P populations of mint with high levels of menthone (60.05%) and Isomenthone (10.93%) compounds. The second group includes the population of H3, rich in Menthol compounds (26.58%) and Menthyl acetate (3.16%). The third group includes E1 and H10 populations with high levels of Linalool compounds (39.93%), α-Cubebene (9.71%), Caryophyllene (E) (5.73%), and Geranyl acetate (2.39%). The fourth group includes E4 populations rich in Limonene (19.27%), α-Terpineol (7.19%), Pulegone (2.81%), *cis*-Sabinene hydrate (1.66%), and α-Humulene (1.23%). The fifth group includes the population of H16 with a high level of Carvone compounds (70.06%). The sixth group has the population of H6 rich in Carvone compounds (62.27%) and 1,8-Cinnamol (14.97%). The seventh group includes the population of T19 containing Pipritenone compounds (5.21%) and α-Pinene (1.12%). Lastly, the eighth group includes the population of H1S with high levels of *cis*-Carvyl acetate compounds (47.41%), Myrcene (6.97), Germacrene D (3.52%), β-Pinene (1.80%), Sabinene (1.32%), and β-Elemene (1.15%).

According to the results of principal components analysis, the biplot diagram, and clustering of different populations of mint based on essential oil components, the biosynthetic pathway of Menthone and isomenthone monoterpenes seems to be active in H7 and H1P populations, and genes responsible for encoding enzymes and the production pathway of Menthol and menthyl acetate were most highly expressed in the H3 population.

Table 2- The essential oil chemical composition of different accessions of mint by GC-MS

Row	Component	RT	KI_c	KI_r	E4	E1	H1S	H1P	H3	H6	H7	H10	H16	T19
1	α-Pinene	5.10	931	932	0.71	0.31	1.02	0.60	0.52	0.41	0.53	0.24	0.55	1.12
2	Camphene	5.38	946	946	0.13	0.06	-	-	-	-	-	-	-	0.14
3	Sabinene	5.81	969	969	0.64	0.81	1.32	0.49	0.52	0.33	0.43	0.60	0.52	1.11
4	β-Pinene	5.94	976	974	1.05	0.67	1.80	0.90	0.79	0.71	0.83	0.57	0.67	1.78
5	Myrcene	6.17	988	988	0.89	11.99	6.97	0.70	0.52	0.49	0.69	2.10	3.17	1.48
6	α-Phellandrene	6.45	1002	1002	-	0.12	0.13	-	0.08	0.39	-	-	0.10	0.09
7	α-Terpinene	6.78	1015	1014	0.07	0.05	0.07	-	0.09	0.15	-	0.06	-	-
8	Limonene	6.98	1023	1024	19.27	0.82	10.71	1.67	5.24	-	2.74	1.02	11.72	12.60
9	1,8-Cineole	7.14	1030	1026	4.62	6.19	8.50	4.23	3.88	14.97	3.66	5.33	1.55	7.50
10	β-Ocimene (Z)	7.19	1032	1032	0.43	0.76	0.42	0.40	0.38	0.56	0.35	0.90	0.11	0.25
11	β-Ocimene (E)	7.50	1045	1044	0.22	1.01	0.09	0.09	0.12	0.25	0.09	0.91	0.06	0.11
12	γ-Terpinene	7.79	1056	1054	0.17	0.30	0.15	-	0.18	-	-	0.22	0.17	-
13	*cis*-Sabinene hydrate	7.95	1063	1065	1.66	0.16	0.51	0.06	1.22	0.30	-	0.25	1.34	0.28
14	Terpineol	8.55	1087	1086	0.08	0.39	0.16	-	0.07	-	-	0.37	0.10	0.07
15	Linalool	8.74	1095	1095	-	39.93	0.60	0.16	0.34	-	0.18	39.76	0.17	0.16
16	*trans*-Sabinene hydrate	8.80	1097	1098	0.23	-	0.06	-	0.08	0.16	-	0.11	0.09	0.17
17	*cis*-Thujene	8.91	1102	1101	0.13	0.63	0.06	0.05	-	0.12	-	0.30	-	0.06
18	*cis*-*p*-menth-2-en-1-ol	9.36	1117	1118	0.11	0.46	0.08	-	0.07	0.17	-	0.38	0.07	-
19	*trans*-*p*-mentha-2,8-dien-1-ol	9.41	1119	1119	0.05	-	0.13	-	-	0.12	-	-	-	-
20	*trans*-Limonene oxide	9.93	1136	1137	0.07	-	0.13	0.11	0.10	0.06	0.13	-	0.07	0.05
21	Comphor	10.02	1139	1141	-	-	-	0.13	0.06	-	0.12	-	0.09	-
22	*cis*-β-Terpineol	10.14	1143	1140	-	-	0.14	-	0.12	-	-	-	-	-
23	Menthone	10.50	1155	1148	-	-	-	53.78	39.29	0.17	60.05	0.07	0.06	-
24	Isomenthone	10.67	1161	1158	0.90	0.49	0.58	10.93	7.17	0.09	10.44	0.16	0.29	0.98
25	Borneol	10.78	1165	1165	-	0.05	-	-	-	0.17	-	-	-	-
26	Menthol	10.86	1167	1167	-	0.05	-	14.44	26.58	0.12	8.52	0.07	-	-
27	*cis*-Linalool oxide (Pyranoid)	10.93	1170	1170	0.85	0.16	0.59	-	-	0.17	0.62	0.31	0.45	0.13
28	Terpinene-8-ol	11.12	1176	1174	-	-	0.21	0.18	0.18	-	0.08	-	-	-
29	Isomenthol	11.28	1181	1179	0.30	-	0.49	0.18	0.19	-	0.16	-	0.32	0.43
30	α-Terpineol	11.38	1185	1186	7.19	6.73	0.28	-	-	0.17	-	6.90	-	1.28
31	Dihydrocarveol	11.54	1190	1192	-	-	0.14	0.08	0.10	2.02	0.06	0.94	0.06	0.09
32	*trans*-Dihydrocarvone	11.84	1200	1200	0.14	0.13	0.20	-	-	0.44	-	-	0.25	0.12
33	*trans*-Carveol	12.29	1217	1215	1.30	1.01	0.06	-	0.07	1.97	-	0.88	0.96	0.62
34	*cis*-Carveol	12.56	1228	1226	0.08	-	0.16	0.09	-	-	0.07	-	-	–
35	Pulegone	12.68	1232	1233	2.81	-	0.11	1.26	0.71	0.61	2.47	0.06	0.13	0.13
36	Carvone	12.78	1236	1239	40.63	16.75	0.48	0.81	2.57	62.27	0.87	13.45	70.06	50.98
37	Pipperiton	13.10	1248	1249	-	-	-	-	-	0.36	-	-	0.12	0.14
38	*cis*-Carvone oxide	13.42	1260	1259	-	-	0.58	-	-	-	-	-	0.06	0.08
39	Geranial	13.55	1265	1264	-	0.07	0.55	-	-	-	-	-	-	-
40	*trans*-Carvone oxide	13.76	1273	1273	0.27	-	-	0.15	0.35	0.13	-	-	0.10	3.50
41	Isobornyl acetate	14.07	1285	1283	0.08	0.15	0.08	0.09	-	-	0.09	-	0.07	-
42	Menthyl acetate	14.25	1291	1294	-	-	0.37	2.94	3.16	0.11	1.54	-	-	-
43	Carvacrol	14.33	1294	1298	0.13	-	0.24	-	-	0.16	-	-	-	-
44	*trans*-Carvyl acetate	15.58	1339	1339	1.22	-	0.31	-	0.05	0.40	-	-	0.13	-
45	Piperitenone	15.63	1341	1340	0.28	-	-	-	-	0.08	-	-	-	5.21
46	α-Cubebene	15.83	1348	1345	-	3.30	-	-	-	-	-	9.71	-	-
47	Neryl acetate	16.07	1357	1359	-	-	0.05	-	-	-	-	-	-	0.13
48	*cis*-Carvyl acetate	16.36	1367	1365	0.18	1.20	47.41	-	-	0.11	-	1.05	0.07	3.73
49	Geranyl acetate	16.75	1381	1379	1.26	2.39	-	-	-	-	-	2.07	-	-
50	β-Borbonene	16.89	1386	1387	-	0.05	0.08	0.13	0.23	1.14	0.15	0.08	0.59	0.13
51	β-Elemene	17.05	1392	1389	0.55	0.35	1.15	0.42	0.17	0.78	0.42	0.85	0.70	0.16
52	*cis*-α-Bergamotene	17.57	1410	1411	0.06	-	0.06	-	0.11	0.06	-	-	-	0.06
53	Caryophyllene (E)	18.82	1420	1417	3.46	5.73	4.99	1.83	0.54	3.76	1.82	2.82	1.11	1.36
54	*trans*-α-Bergamotene	18.20	1434	1432	-	-	0.06	-	-	-	-	-	-	-
55	Aromadendrene	18.51	1445	1439	0.22	-	-	0.09	0.05	0.21	0.08	-	0.11	0.13
56	α-Humulene	18.76	1455	1452	1.23	0.55	0.82	0.29	0.54	0.88	0.31	0.50	0.47	0.67
57	Germacrene-D	19.51	1483	1484	1.67	1.81	3.52	1.89	1.75	1.76	1.76	2.48	0.95	0.51
58	Bicyclogermacrene	19.91	1498	1500	0.34	0.52	1.24	0.33	0.61	0.30	0.33	0.23	0.49	0.05
59	γ-Cadinene	20.35	1515	1513	0.16	0.11	-	-	-	0.14	-	0.15	-	-
60	Δ-Cadinene	20.58	1523	1522	0.49	0.05	0.08	0.05	0.06	0.23	-	0.05	0.08	0.12
61	α-Cadinene	20.95	1538	1537	0.14	-	-	-	-	0.07	-	-	-	-
62	Elemol	21.21	1548	1548	0.08	0.72	-	-	-	-	-	2.14	-	-
63	Germacrene-B	21.45	1557	1559	0.10	0.05	0.15	-	-	0.06	-	0.07	-	0.17
64	Spathulenol	21.95	1576	1577	0.22	0.09	0.29	-	0.15	0.11	-	0.12	0.09	0.05
65	Caryophyllene oxide	22.16	1584	1582	0.39	0.30	0.32	0.11	-	0.23	0.13	0.22	0.06	0.14
66	Viridiflorol	22.35	1592	1592	-	0.82	-	0.11	0.42	-	0.09	0.06	-	-
67	10-epi-γ-Eudesmol	23.07	1621	1622	0.44	0.07	-	-	-	0.22	-	0.14	0.06	0.20
68	γ-Eudesmol	23.39	1634	1630	0.15	0.16	0.07	-	-	-	-	0.37	-	-
69	epi-α-Morolol	23.57	1642	1640	0.36	0.38	0.07	-	0.07	0.08	-	0.18	-	0.05
70	α-Morolol	23.66	1646	1644	-	-	-	-	-	0.44	-	0.15	-	-
71	α-Eudesmol	23.82	1652	1652	-	0.05	-	-	-	-	-	0.16	-	-
72	α-Cadinol	23.92	1656	1652	0.45	0.14	0.15	0.06	0.10	0.22	-	0.31	0.15	0.26
	Monoterpene hydrocarbons	-	-	-	23.66	7.30	22.84	4.85	8.50	3.29	5.66	6.99	17.24	18.76
	Oxygenated monoterpenes	-	-	-	64.52	76.57	63.09	89.66	86.30	85.46	89.05	72.07	76.51	75.90
	Sesquiterpene hydrocarbons	-	-	-	8.41	12.52	12.15	5.03	4.06	9.38	4.88	16.95	4.50	3.37
	Oxygenated sesquiterpenes	-	-	-	2.09	2.74	0.90	0.28	0.73	1.31	0.29	3.85	0.36	0.70
	Total	-	-	-	98.67	99.13	98.98	99.82	99.59	99.43	99.87	99.86	98.61	98.73

RT: Retention time; KI_c: Calculated kovats index; KI_r: Reference kovats index

Table 3- Results of biplot analysis and cluster analysis of different populations of mint by GC-MS

Group	Genotype	Compound	
		High	Zero or low
1	H7 and H1P	Menthone (60.05%), Isomenthone (10.93%)	*cis*-Sabinene hydrate, α-Terpineol, *trans*-Carvone, Piperitenone, α- Cubebene, Carvyl acetate, Geranyl acetate, α-Humulene
2	H3	Menthol (26.58%), Menthyl acetate (3.16%)	Piperitenone, α-Cubebene, Carvyl acetate, Geranyl acetate, β-Pinene
3	E1 and H10	Linalool (39.93%), α- Cubebene (9.71%), Caryophyllene E (5.73%), Geranyl acetate (2.39%)	*cis*-Sabinene hydrate, β-Pinene, Menthone, Pulegone, Menthyl acetate, Piperitenone
4	E4	Limonene (19.27%), α-Terpineol (7.19%), Pulegone (2.81%), *cis*-Sabinene hydrate (1.66%), α-Humulene (1.23%)	Linalool, Menthone, Menthyl acetate, α-Pinene
5	H16	Carvone (70.06%),	Menthone, α-Terpineol, Menthyl acetate, Pipritenone, α-Cubebene, Geranyl acetate Limonene, α- Cubebene, Geranyl acetate β-Elemene, Germacrene D, Menthone, Menthyl, Geranyl acetate
6	H6	Carvone (62.27%), 1,8-cineole (14.97%)	
7	T19	Piperitenone (5.21%), α-Pinene (1.12%)	
8	H1S	*cis*-Carvyl acetate (47.41%), Myrcene (6.97%), Geranyl acetate (3.52%), β-Pinene (1.80%), Sabinene (1.32%), β-Elemene (1.15%)	Menthone, Menthol, Piperitenone, α-Cubebene

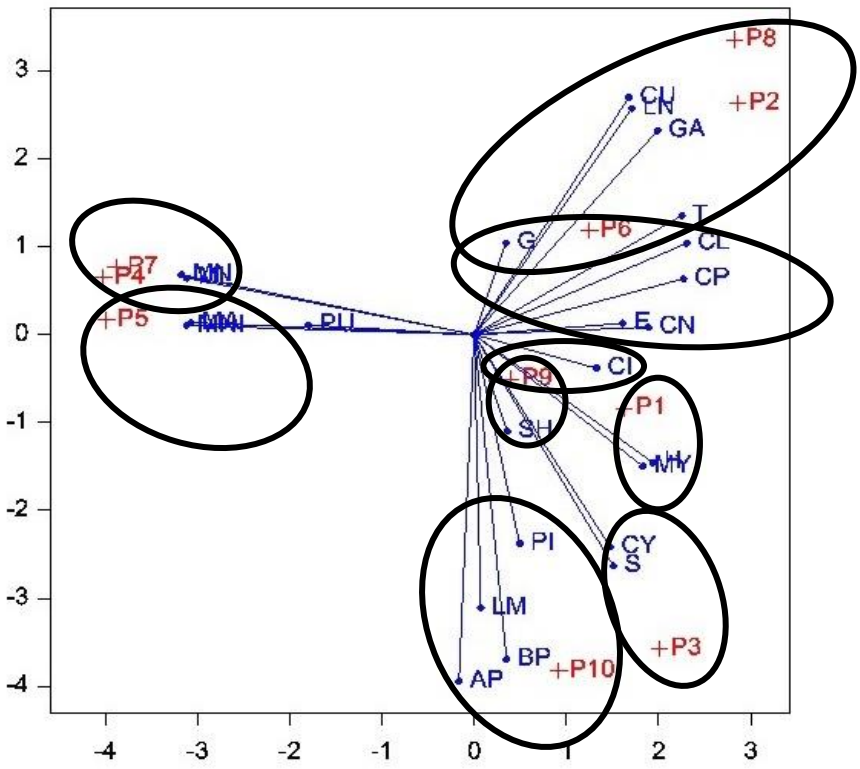

Fig. 2. Graphic display of biplot of different populations of mint using two main components derived from the dominant components of essential oil; P1, P2, P3, P4, P5, P6, P7, P8, P9, and P10 = E4, E1, H1S, H1P, H3, H6, H7, H10, H16, and T19; AP = α-Pinene, S = Sabinene, BP = β-Pinene, MY = Myrcene, LM = Limonene, CI =1,8-cineole, SH = *cis*-Sabinene hydrate, LN = Linalool, MN = Menthone, MNI = Isomenthone, ML = Menthol, T = α-Terpineol, CL = *trans*-Carvone, PU = Pulegone, CN = Carvone, MA = Menthyl acetate, PI = Piperitenone, CU = α- Cubebene, CY = *cis*-Carvyl acetate, GA = Geranyl acetate, E = β-Elemene, CP = caryophyllene E, H = α-Humulene, and G = Germacrene D

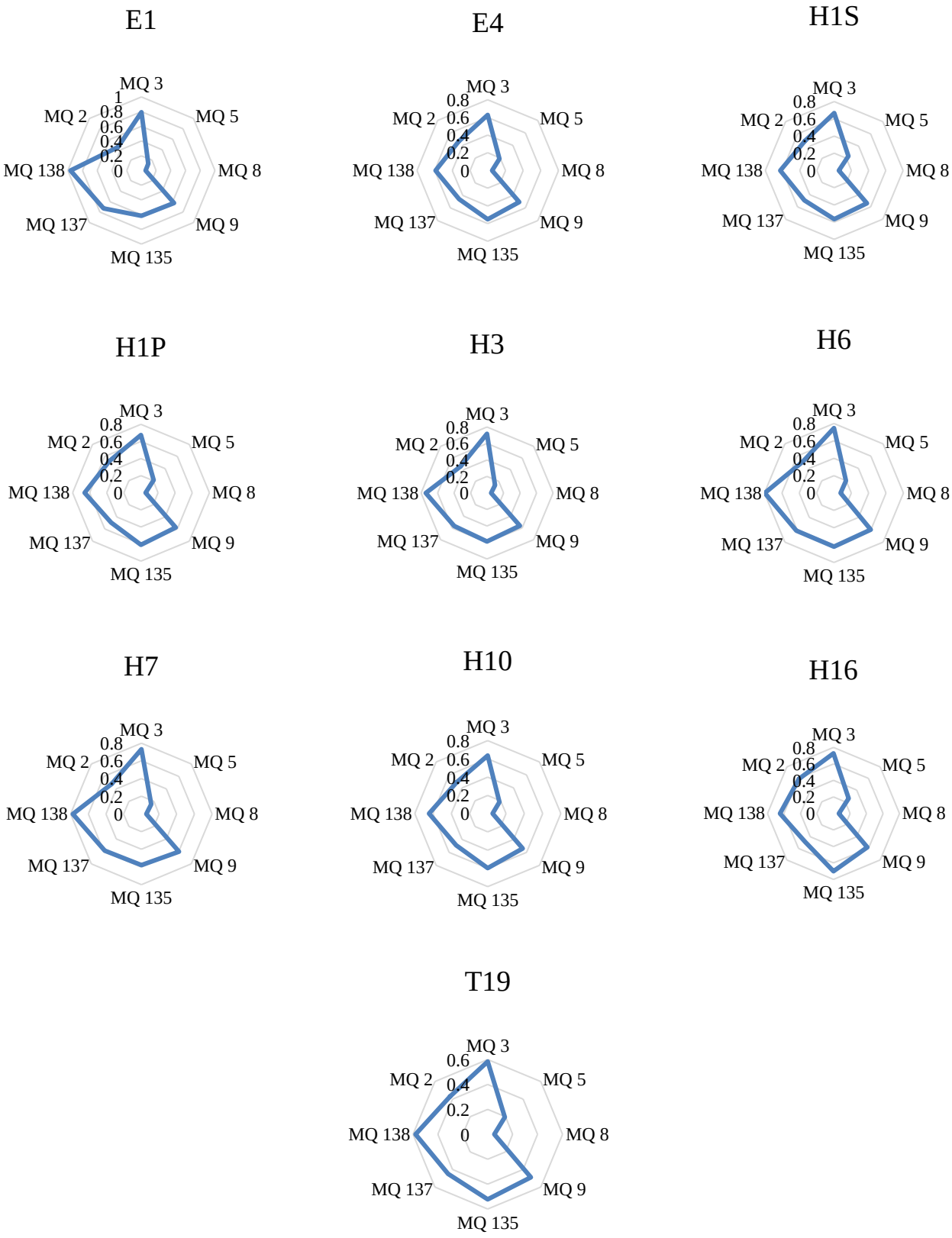

Fig. 3. The mean response of e-nose sensors to ten genotypes

The results demonstrated that the path of synthesis of essential oil compounds in E1 and H10 populations could result in the production of Linalool and Geranyl acetate monoterpenes and α-Cubebene and Caryophyllene (E) sesquiterpenes. Also, the high levels of Limonene, α-Terpinyl, Pulegone, and *cis*-sabinene hydrate monoterpenes in the E4 population indicated that the biosynthetic pathway enzymes of these compounds are more active in the above population. The study of the essential oil components of H16, H6, and T16 populations showed the predominance of the biosynthesis pathway of Carvone and 1,8-cineole compounds in the H16 and H6 populations, and Pipritenone and α-Pinene in the T16 population. Pinene, Sabinene, Germacrene D, and β-Elemene sesquiterpenes have been the most active biosynthetic pathways of essential oil compounds in the H1S population.

E-nose results

The study of the signal form of the sensors of the e-nose system shows that the response set of sensors varies for different types of mint genotypes, indicating that the organic matter of each genotype is distinct. The response pattern of sensors to the essential oil of E1, H3, H6, and H7 genotypes showed that the volatiles from these genotypes had the highest response in the MQ138 sensor, while the highest numerical response for the H16, E4, HIS, and H1P genotypes was in the MQ3 sensor (Figure 3). Both sensors demonstrate impressive accuracy in detecting alcohol compounds, which, as evidenced by GC results, are among the most significant compounds found in mint genotypes.

PCA results

The two main components of PCA covered 97% of the variance in the data. According to Figure 4, the amount of variance in the first and second major components was 85% and 12%, respectively. Genotypes E1, H16, T19, and H6 are clearly identifiable, which is rather consistent with the results of the GC (Table 3). There is a lot of overlap among H1P, E4, H1S, and H10 genotypes. The loading diagram was used to investigate the participation of sensors in the detection of the degree of processing. These sensors are displayed in the loading diagram with the values of specific coefficients. The high coefficient value for a sensor in the loading diagram highlights its important role in detecting different types of mint genotypes. Moreover, by removing the least crucial sensors from the process of identifying mint genotypes and streamlining the data analysis, the overall expenses associated with constructing a sensor array can be significantly lowered (Heidarbeigi *et al.*, 2015). Although all sensors were effective in detecting mint genotypes, the MQ5 sensor showed the least involvement (Figure 4), so it is possible to remove it from the olfactory system when detecting the mint genotypes. In one study, the use of e-nose for identification of the ripeness stage of berries was investigated. The PCA technique was applied for data analysis. Results from the PCA indicated a significant categorization of the volatile profiles of berries at the ripe, nearly ripe, intermediate, nearly unripe, and unripe stages (Aghili Nategh *et al.*, 2020).

LDA results

Figure 5 illustrates the diagram for the LDA linear resolution analysis, showcasing the first two principal components (LD1-LD2) derived from e-nose signals for mint genotype detection. Accordingly, the LDA can determine the genotypes of the mint plant well. In particular, genotypes E1, E4, and T19 are completely differentiated. There was a noticeable overlap not only between H1P and T19 genotypes, but also between H1S and H16, as well as between H6 and H10 genotypes. According to the confusion matrix (Table 4), the analysis accuracy was 95.33%. Table 5 gives the performance parameters of the classifier according to the above-mentioned confusion matrix, including classification accuracy, precision, sensitivity, specificity, and AUC for genotypes of mint.

The average per class accuracy, precision, sensitivity, specificity, and AUC were 98.9%, 95.7%, 95.3%, 99.3%, and 97.6%, respectively. Lin et al. isolated different species of Apiaceae flower via e-nose data in combination with the LDA method (Lin *et al.*, 2013). In a study, researchers used ANN, LDA, and SVM to classify contaminated and healthy mushrooms over a 28-day storage period, with LDA showing the best performance (Makarichian *et al.*, 2022).

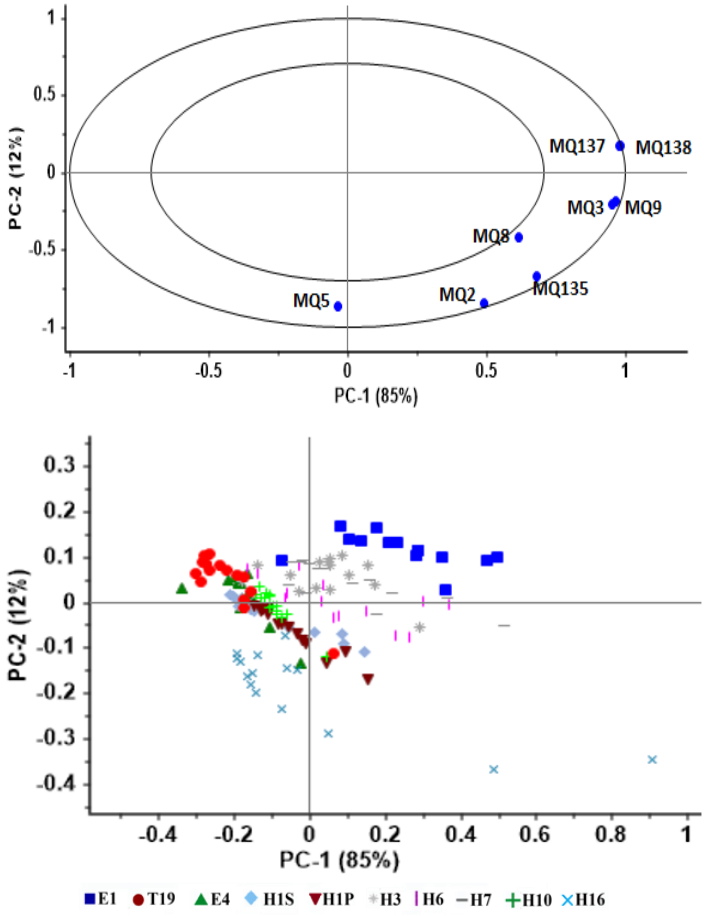

Fig. 4. (top) Loading and (bottom) score plots of PCA to detect the mint genotypes

QDA results

This method is extensively used in statistics, recognition pattern, and machine learning to find a combination of unique traits. Table 4 shows the confusion matrix for the Quadratic Discriminant Analysis (QDA) employed in the nonlinear resolution analysis of e-nose signals for the detection of mint genotypes. According to the confusion matrix, the analysis accuracy was 98.33%. The sample is only misdiagnosed in the H1P genotype 2. The average per class accuracy, precision, sensitivity, specificity, and AUC were 99.9%, 100%, 98.7%, 100%, and 99.3%, respectively (Table 5). In previous research, the quadratic analysis successfully used to classify diesel-biodiesel blends (Mahmodi *et al.*, 2019).

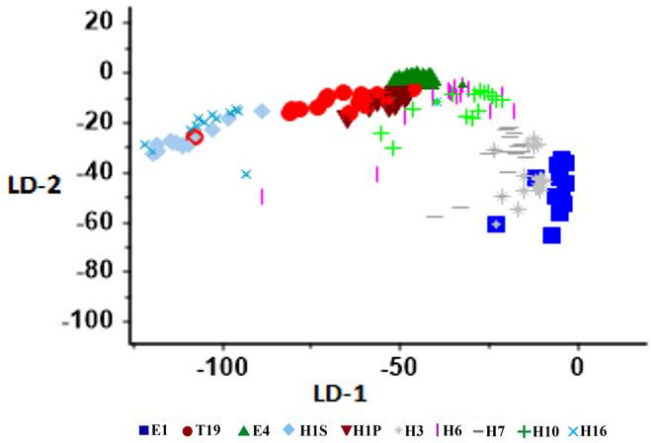

Fig. 5. Score plot of LDA analysis for detecting the mint genotypes

Table 4- Confusion matrices obtained from LDA, QDA, and ANN

		1	**2**	**3**	**4**	**5**	**6**	**7**	**8**	**9**	**10**
	1	13	0	0	0	0	0	0	0	0	0
	2	0	15	0	0	0	1	0	0	0	0
	3	0	0	15	0	0	0	0	0	0	1
	4	0	0	0	15	0	0	0	0	0	0
	5	2	0	0	0	13	0	0	0	0	0
LDA	6	0	0	0	0	0	14	0	0	0	0
	7	0	0	0	0	2	0	15	0	0	0
	8	0	0	0	0	0	0	0	15	1	0
	9	0	0	0	0	0	0	0	0	14	0
	10	0	0	0	0	0	0	0	0	0	14
	Correct classification: 95.33%										
	1	15	0	0	0	0	0	0	0	0	0
	2	0	15	0	0	0	0	0	0	0	0
	3	0	0	15	0	0	0	0	0	0	0
	4	0	0	0	15	0	0	0	0	0	0
	5	0	0	0	0	13	0	0	0	0	0
QDA	6	0	0	0	0	0	15	0	0	0	0
	7	0	0	0	0	2	0	15	0	0	0
	8	0	0	0	0	0	0	0	15	0	0
	9	0	0	0	0	0	0	0	0	15	0
	10	0	0	0	0	0	0	0	0	0	15
	Correct classification: 98.33%										
	1	13	0	0	0	•	0	0	0	0	0
	2	0	15	0	0	0	0	0	0	0	0
	3	0	0	13	0	0	0	0	0	0	0
	4	0	0	0	15	0	0	0	0	0	0
	5	1	0	0	0	14	0	0	0	0	0
ANN	6	0	0	0	0	0	15	0	0	1	0
	7	1	0	0	0	1	0	15	0	0	0
	8	0	0	0	0	0	0	0	15	0	0
	9	0	0	0	0	0	0	0	0	14	0
	10	0	0	2	0	0	0	0	0	0	15
	Correct classification: 96%										

Table 5- Performance measurements of LDA, QDA, and ANN

Classifier Method	LDA					QDA					ANN				
Class	Precision	Sensitivity	Specificity	Accuracy	AUC	Precision	Sensitivity	Specificity	Accuracy	AUC	Precision	Sensitivity	Specificity	Accuracy	AUC
E1	1.00	0.87	1.00	0.99	0.93	1.00	1.00	1.00	1.00	1.00	1.00	0.87	1.00	0.99	0.93
E4	0.94	1.00	0.99	0.99	1.00	1.00	1.00	1.00	1.00	1.00	1	1.00	0.99	0.99	1.00
H1S	0.94	1.00	0.99	0.99	1.00	1.00	1.00	1.00	1.00	1.00	1.00	0.87	1.00	0.99	0.93
H1P	1.00	1.00	1.00	1.00	1.00	1.00	1.00	1.00	1.00	1.00	1.00	1.00	1.00	1.00	1.00
H3	0.87	0.87	0.98	0.97	0.93	1.00	0.87	1.00	0.99	0.93	0.93	0.93	0.99	0.99	0.96
H6	1.00	0.93	1.00	0.99	0.97	1.00	1.00	1.00	1.00	1.00	0.94	1.00	0.99	0.99	1.00
H7	0.88	1.00	0.98	0.99	0.99	1.00	1.00	1.00	1.00	1.00	0.88	1.00	0.98	0.99	0.99
H10	0.94	1.00	0.99	0.99	1.00	1.00	1.00	1.00	1.00	1.00	1.00	1.00	1.00	1.00	1.00
H16	1.00	0.93	1.00	0.99	0.97	1.00	1.00	1.00	1.00	1.00	1.00	0.93	1.00	0.99	0.97
T19	1.00	0.93	1.00	0.99	0.97	1.00	1.00	1.00	1.00	1.00	0.88	1.00	0.98	0.99	0.99
Average	0.957	0.953	0.993	0.989	0.976	1	0.987	1	0.999	0.993	0.963	0.96	0.993	0.992	0.977

ANN results

To minimize neural network training time, only one hidden layer was considered. The best network was found with a topology of 8-11-10, and a network with 11 neurons in the hidden layer. Table 4 shows the confusion matrix. Achieving a 96% classification accuracy across 10 genotypes can likely be explained by the significant variety and abundance of aromatic compounds present in these genotypes. The average class accuracy, precision, sensitivity, specificity, and AUC were 99.2%, 96.3%, 96%, 99.3%, and 97.7%, respectively (Table 5). Aghili Nategh et al. (2020) demonstrated that the optimal architecture (10-11-5) effectively classifies samples into five distinct categories in ANN analysis, achieving an impressive accuracy of 100% for blackberries and 88.3% for white berries.

Conclusion

The e-nose system is essential for the rapid, non-destructive determination of quality indicators without the need for manual measurements in the medicinal and aromatic plants industry. The results of qualitative analysis of essential oil by GC-MS showed that there were 72 unique compounds in the essential oil of different populations of mint. More than 99% of the identified compounds were in four chemical groups, including hydrocarbon and oxygenated monoterpenes and sesquiterpenes. The average values of yield parameters (AUC, Accuracy, Precision, Specificity, and Sensitivity) and classification analysis show that QDA was the best method for the classification of different genotypes of mint, while principal component analysis, linear discriminant analysis, and artificial neural network were less accurate than quadratic discriminant analysis.

Acknowledgments

We acknowledge with gratitude the financial support provided by the Research Council of Shahid Chamran University of Ahvaz (GN: SCU.AA99.585) for the research project number 1306.

Conflict of Interest: The authors declare no competing interests.

Author Contributions

H. Zaki Dizaji: Supervision, Methodology, Conceptualization, Validation, Data acquisition, Text mining, Review and editing services

M. Mahmoodi Surestani: Methodology, Data pre and post processing, Review and editing services

N. Aghili Nategh: Statistical analysis, Technical advice, Review and editing services

A. Boveiri Dehsheikh: Data acquisition, Statistical analysis, Software cervices

References

1. Adams, R. P. (2007). Identification of essential oil components by gaschromatography/quadrupole mass spectrometry. *Journal of the American Society for Mass Spectrometry, 16*, 1902-1903.
2. Aghili Nategh, N., Dalvand, M. J., & Anvar, A. (2020). Detection of ripeness grades of berries using an electronic nose. *Journal of Food Sciene & Nutrition, 8*, 4919-4928. https://doi.org/10.1002/fsn3.1788
3. Asl Roosta, R., Moghaddasi, R., & Hosseini, S. S. (2017). Export target markets of medicinal and aromatic plants, *Journal of Applied Research on Medicinal and Aromatic Plants, 7*, 84-88. https://doi.org/10.1016/j.jarmap.2017.06.003
4. Banal, J. E. P. L., Rañola, R. A. G., Santiago, K. S., & Sevilla, F. B. I. (2014). E-nose Based on Conducting Polymers for the Discrimination of Medicinal Plants. *Applied Mechanics and Materials, 490-491*, 1194-1198. https://doi.org/10.4028/www.scientific.net/amm.490-491.1194
5. Gebicki, J., & Szulczynski, B. (2018). Discrimination of selected fungi species based on their odour profile using prototypes of E-nose instruments. *Measurement, 116*, 3017-313. https://doi.org/10.1016/j.measurement.2017.11.029
6. Gorji-Chakespari, A., Nikbakht, A. M., Sefidkon, F., Ghasemi-Varnamkhasti, M., & Valero, E. L. (2017). Classification of essential oil composition in *Rosa damascena* Mill. genotypes using an E-nose. *Journal of Applied Research on Medicinal and Aromatic Plants, 4*, 27-34. https://doi.org/10.1016/j.jarmap.2016.07.004
7. Guohua, H., Jiaojiao, J., Shanggui, D., Xiao, Y., Mengtian, Z., Minmin, W., & Dandan, Y. (2015). Winter jujube (*Zizyphus jujuba* Mill.) quality forecasting method based on E-nose. *Food Chemistry, 170*, 484-491. https://doi.org/10.1016/j.foodchem.2014.08.009
8. Hawrył, M. A., Skalicka-Woźniak, K., Świeboda, R., Niemiec, M., Stępak, K., Waksmundzka-Hajnos, M., Hawrył, A., & Szymczak, G. (2015). GC-MS fingerprints of mint essential oils. *Open Chemistry, 13*(1), 1326-1332. https://doi.org/10.1515/chem-2015-0148
9. Heidarbeigi, K., Mohtasebi, S. S., Foroughirad, A., Ghasemi-varnamkhasti, M., Rafiee, S., & Rezaei, K. (2015). Detection of adulteration in saffron samples using E-nose. *International Journal of Food Properties, 18*, 1391-1401. https://doi.org/10.1080/10942912.2014.915850
10. Kaushal, S., Nayi, P., Rahadian, D., & Chen, H. H. (2022). Applications of E-nose Coupled with Statistical and Intelligent Pattern Recognition Techniques for Monitoring Tea Quality: A Review. *Agriculture, 12*, 1359. https://doi.org/10.3390/agriculture12091359
11. Kiani, S., Minaei, S., & Ghasemi-Varnamhasti, M. (2018). Real-time aroma monitoring of mint (*Mentha spicata* L.) leaves during the drying process using E-nose system. *Measurement, 124*, 447-452. https://doi.org/10.1016/j.measurement.2018.03.033
12. Li, Q., Yu, X., Xu, L., & Gao, J. (2017). Novel method for the producing area identification of zhongning Goji berries by E-nose. *Food Chemistry, 221*, 1113-1119. https://doi.org/10.1016/j.foodchem.2016.11.049
13. Lin, H., Yonghong, Y., Zhao, T., Peng, L., Zou, H., Li, J., Yang, X., Xiong, Y., Wang, M., & Wu, H. (2013). Rapid discrimination of Apiaceae plants by E-nose coupled with multivariate statical analyses. *Journal of Pharmaceutical and Biomedical Analysis, 84*, 1-4. https://doi.org/10.1016/j.jpba.2013.05.027
14. Lubbe, A., & Verpoorte, R. (2011). Cultivation of medicinal and aromatic plants for specialty

industrial materials. *Industrial Crops and Products, 34*(1), 785-801. https://doi.org/10.1016/j.indcrop.2011.01.019

15. Mahmodi, K., Mostafaei, M., & Mirzaee-Ghaleh, E. (2019). Detection and classification of diesel-biodiesel blends by LDA, QDA and SVM approaches using an E-nose. *Fuel, 258*. https://doi.org/10.1016/j.fuel.2019.116114
16. Makarichian, A., Chayjan, R. A., Ahmadi, E., & Zafari, D. (2022). Early detection and classification of fungal infection in garlic (A. sativum) using electronic nose. Computers and Electronics in Agriculture, Available online 22 November 2021, 106575. https://doi.org/10.1016/j.compag.2021.106575
17. Martín-Tornero, E., Sánchez, R., Lozano, J., Martínez, M., Arroyo, P., & Martín-Vertedor, D. (2021). Characterization of Polyphenol and Volatile Fractions of Californian-Style Black Olives and Innovative Application of E-nose for Acrylamide Determination. *Foods, 10*, 2973. https://doi.org/10.3390/foods10122973
18. Nguyen, L., Duong, L. T., & Mentreddy, R. S. (2019). The U.S. import demand for spices and herbs by differentiated sources. *Journal of Applied Research on Medicinal and Aromatic Plants, 12*, 13-20. https://doi.org/10.1016/j.jarmap.2018.12.001
19. Okur, S., Li, C., Zhang, Z., Vaidurya Pratap, S., Sarheed, M., Kanbar, A., Franke, L., Geislhöringer, F., Heinke, L., Lemmer, U., Nick, P., & Wöll, C. (2021a). Sniff Species: SURMOF-Based Sensor Array Discriminates Aromatic Plants beyond the Genus Level. *Chemosensors, 9*(7), 171. https://doi.org/10.3390/chemosensors9070171
20. Okur, S., Sarheed, M., Huber, R., Zhang, Z., Heinke, L., Kanbar, A., Wöll, C., Nick, P., & Lemmer, U. (2021b). Identification of Mint Scents Using a QCM Based E-Nose. *Chemosensors, 9*(2), 31 https://doi.org/10.3390/chemosensors9020031
21. Rafaela, S. A., Murilo, H. M. F., Luiza, A. M., & Daniel, S. C. (2022). Electronic nose based on hybrid free-standing nanofibrous mats for meat spoilage monitoring. *Sensors and Actuators B: Chemical, 353*, 131114. https://doi.org/10.1016/j.snb.2021.131114
22. Rodrigues, N., Silva, K., Veloso, A. C. A., Pereira, J. A., & Peres, A. M. (2021). The Use of E-nose as Alternative Non-Destructive Technique to Discriminate Flavored and Unflavored Olive Oils. *Foods, 10*, 2886. https://doi.org/10.3390/foods10112886
23. Tangpao, T., Charoimek, N., Teerakitchotikan, P., Leksawasdi, N., Jantanasakulwong, K., Rachtanapun, P., Seesuriyachan, P., Phimolsiripol, Y., Chaiyaso, T., Ruksiriwanich, W., Jantrawut, P., Van Doan, H., Cheewangkoon, R., & Sommano, S. R. (2022). Volatile Organic Compounds from Basil Essential Oils: Plant Taxonomy, Biological Activities, and Their Applications in Tropical Fruit Productions. *Horticulturae, 8*(2), 144. https://doi.org/10.3390/horticulturae8020144
24. Zaki Dizaji, H., Adibzadeh, A., & Aghili Nategh, N. (2020). Application of E-nose technique to predict sugarcane syrup quality based on purity and refined sugar percentage. *Journal of Food Science and Technology*. https://doi.org/10.1007/s13197-020-04879-4
25. Zhang, B, Huang, Y., Zhang, Q., Liu, X., Li, F., Chen, K. 2014. Fragrance discrimination of Chinese Cymbidium species and cultivars using an electronic nose. *Scientia Horticuturae, 172*, 271-277. https://doi.org/10.1016/j.scienta.2014.04.019

نشریه ماشین‌های کشاورزی
https://jame.um.ac.ir

مقاله پژوهشی

جلد ۱۶، شماره ۳، پاییز ۱۴۰۵، ص ۵۷۸-۵۶۳

امکان‌سنجی تشخیص ژنوتیپ‌های مختلف گیاه نعنا با تکنیک E-Nose

حسن ذکی دیزجی[1*]، محمد محمودی سورستانی[2]، ناهید عقیلی ناطق[3]، آناهیتا بویری ده شیخ[2]

تاریخ دریافت: ۱۴۰۳/۱۲/۲۶
تاریخ پذیرش: ۱۴۰۴/۰۲/۳۰

چکیده

مطالعه حاضر به بررسی طبقه‌بندی ده ژنوتیپ نعناع توسط یک سیستم بینی الکترونیکی مبتنی بر حسگرهای نیمه‌هادی اکسید فلزی (MOS) می‌پردازد. نمونه‌های برگ از ژنوتیپ‌های مختلف نعناع برداشت شد، سپس پاسخ سنسورهای سیستم به هر نمونه ثبت شد. برای طبقه‌بندی گیاهان، پاسخ تمام حسگرهای بینی الکترونیکی با روش‌های تجزیه و تحلیل اجزای اصلی (PCA)، تجزیه و تحلیل تشخیص خطی (LDA)، تجزیه و تحلیل متمایز درجه دوم (QDA) و شبکه عصبی مصنوعی (ANN) مورد بررسی قرار گرفت. بر اساس نتایج تجزیه و تحلیل کیفی اسانس‌ها توسط دستگاه GC-MS، بیش از ۹۹ درصد ترکیبات شناسایی‌شده در چهار گروه شیمیایی شامل هیدروکربن‌ها و مونوترپن‌ها و سسکوئی‌ترپن‌های اکسیژن‌دار قرار داشتند. همچنین بر اساس تجزیه و تحلیل بای پلات، جمعیت‌های مختلف نعناع را می‌توان به‌طور کلی به ۸ گروه تقسیم کرد. نتایج تحلیل مؤلفه‌های اصلی با استفاده از داده‌های به‌دست‌آمده از سیستم نشان داد که دو مؤلفه اصلی اول می‌توانند در مجموع ۹۷ درصد از واریانس داده‌ها را پوشش دهند. دقت طبقه‌بندی با استفاده از داده‌های بینی الکترونیکی برای تجزیه و تحلیل وضوح خطی، تجزیه و تحلیل وضوح درجه دوم و شبکه عصبی مصنوعی به‌ترتیب ۹۸/۹، ۹۹/۹ و ۹۶٪ به‌دست آمد. طبقه‌بندی مناسب ژنوتیپ‌های نعناع توسط سیستم بینی الکترونیکی می‌تواند به‌عنوان جایگزینی حساس، قابل‌اعتماد و کم‌هزینه برای روش‌های سنتی مورد استفاده قرار گیرد.

واژه‌های کلیدی: اسانس، بویایی ماشینی، روش‌های هوشمند، طبقه‌بندی

۱- گروه مهندسی بیوسیستم، دانشگاه شهید چمران اهواز، اهواز، ایران
۲- گروه باغبانی، دانشگاه شهید چمران اهواز، اهواز، ایران
۳- گروه مهندسی ماشینهای کشاورزی، دانشکده کشاورزی سنقر، دانشگاه رازی، کرمانشاه، ایران
(*- نویسنده مسئول: Email: hzakid@scu.ac.ir)

https://doi.org/10.22067/jam.2025.92417.1354

Journal of Agricultural Machinery

Homepage: https://jame.um.ac.ir

Research Article
Vol. 16, No. 3, 2026, p. 579-597

Comparative Modeling of Drying Kinetics for Potato Slices: AI-Based vs. Empirical and Semi-Empirical Approaches

R. Raeesi[1], M. Moradi[1*], A. Dehghani[1]

1- Department of Biosystems Engineering, Faculty of Agriculture, Shiraz University, Shiraz, Iran
(*- Corresponding Author Email: moradih@shirazu.ac.ir)

Received: 20 March 2025
Revised: 15 June 2025
Accepted: 21 June 2025
Available Online: 08 October 2025

How to cite this article:
Raeesi, R., Moradi, M., & Dehghani, A. (2026). Comparative Modeling of Drying Kinetics for Potato Slices: AI-Based vs. Empirical and Semi-Empirical Approaches. *Journal of Agricultural Machinery*, *16*(3), 579-597. https://doi.org/10.22067/jam.2025.92739.1358

Abstract

Drying is a vital preservation method in the food industry, reducing moisture content while maintaining product quality and extending shelf life. This process involves complex heat and mass transfer mechanisms, necessitating accurate predictive models. This study compares various modeling approaches, including regression models, semi-empirical, and artificial intelligence (AI)-based methods, to simulate the drying process of potato slices. Experimental drying trials were run at 40°C, 50°C, and 60°C, both with and without phase change materials (PCM) and infrared radiation (IR). AI models (ANN, SVM, and RF) were trained and validated using experimental data. Their performance was evaluated against conventional and semi-empirical models using R^2, RMSE, MAE, and MBE. Results indicate that ANN achieved the highest predictive accuracy (R^2= 0.998, RMSE= 0.0656 g water g^{-1} dry matter), outperforming other models. SVM also demonstrated strong predictive capability, while RF performed slightly lower. Among semi-empirical models, the Midilli model provided the best fit but was less accurate than AI-based models. These findings highlight the superiority of AI-driven approaches, particularly ANN, in optimizing drying processes for the food industry.

Keywords: AI Modeling, Drying rate, Random forest, Semi-Empirical, SVM

Introduction

Drying is a widely used preservation technique used in the food and agricultural industries, aiming to reduce moisture content while preserving product quality and extending shelf life. The drying process is inherently complex, involving simultaneous heat and mass transfer, which makes mathematical modeling essential for optimizing drying conditions and improving energy efficiency. Over the years, researchers have developed various empirical, semi-empirical, and theoretical models to explain the drying kinetics of different products. Empirical models, such as the Page, Henderson-Pabis, and Newton models, are popular because of their simplicity and ability to fit experimental data (Lopes, Santos, Rodrigues, Pinho, & Viegas, 2023; Simpson, Ramírez, Nuñez, Jaques, & Almonacid, 2017). In a study on thin-layer drying models for rapeseed, the Page model demonstrated the best performance, with an R^2 value ranging from 0.9924 to 0.9966 and an RMSE between 0.0169 and 0.0296 (Lee, Lee, Kim, Kim, & Han, 2016). However, these models lack a strong physical foundation and are limited to specific experimental conditions. Semi-empirical models, including the Logarithmic and Wang-Singh models, attempt to bridge the gap between empirical and theoretical approaches by incorporating some physical principles while maintaining a simple mathematical form (Kutlu, İşcİ, & Demİrkol,

Authors retain the copyright. This is an open access article distributed under Creative Commons Attribution 4.0 International License (CC BY 4.0).

https://doi.org/10.22067/jam.2025.92739.1358

2015). Semi-empirical modeling of thin-layer drying has been extensively studied. Ertekin and Firat (2017) provided a comprehensive review of these approaches, while Chukwunonye, Nnaemeka, Chijioke, and Obiora (2016); Mahesh, Rengaraju, and Selvakumarasamy (2024); Kumar, Kumar, Hota, and Pandey (2025); and Benseddik, Azzi, and Allaf (2018) explored specific applications across diverse agricultural products. For example, in one study, a semi-empirical model based on Fick's second law was developed, achieving a coefficient of determination (R^2) between 0.991 and 0.999, with a mean absolute error (MAE) ranging from 0.008 to 0.032 (Kumar *et al.*, 2025). Similarly, in another study on the thin-layer drying of pumpkin slices, various semi-empirical models were tested, with the Midilli model showing the highest accuracy for predicting the moisture content of apple slices (Benseddik *et al.*, 2018). However, semi-empirical models are not universally applicable and require fitting to specific experimental conditions. Mathematical models derived from Fick's second law of diffusion provide a more fundamental understanding of the drying process, assuming moisture movement occurs through internal diffusion. These models are commonly applied to food materials with homogeneous structures. For more complex structures, researchers have extended these models using numerical techniques and computational fluid dynamics (CFD) simulations to enhance accuracy (Arpaci, Atayılmaz, & Gemici, 2025). In recent years, Machine Learning (ML) and artificial intelligence (AI) models, such as Support Vector Machines (SVM), Artificial Neural Networks (ANN), and Random Forest (RF), have gained attention for predicting drying kinetics with high accuracy (Przybył & Koszela, 2023; Sağlam & Çetin, 2022). These models can capture complex nonlinear relationships between drying parameters without relying on explicit physical assumptions. Despite their advantages, the application of AI models presents several challenges. These models generally require large, diverse datasets to minimize the risk of overfitting and to promote generalizability. Furthermore, models such as artificial neural networks (ANNs) are often considered "black boxes," as they provide limited transparency regarding their internal decision-making processes. Effective hyperparameter tuning and rigorous validation procedures are also critical to enhance model robustness and ensure reliable performance in real-world scenarios. In another study, the drying kinetics of solid wastes were modeled using both artificial neural networks (ANN) and semi-empirical models, with ANN demonstrating the most accurate simulation results (Perazzini, Freire, & Freire, 2013). Similarly, another study examined the thin-layer drying of tea leaves using various semi-empirical and AI-based models. The results showed that multilayer perceptron networks achieved the highest accuracy (Fathi, Roshanak, Rahimmalek, & Goli, 2016). This study aims to compare different mathematical models, including semi-empirical, regression, and AI-based methods, for simulating the drying kinetics of potato slices. The novelty of this research lies in the comparative analysis of AI-based methods (ANN, SVM, RF) and traditional models under varying drying conditions, demonstrating the superior predictive capability of AI in optimizing drying processes. By highlighting the strengths and limitations of each modeling approach, this study contributes to the growing body of knowledge on drying process optimization, with potential applications in food preservation, quality control, and energy-efficient drying technologies.

Materials and Methods

Sample preparation

Fresh potatoes (*Solanum tuberosum* L.) were procured daily from local markets to ensure consistent freshness and quality. The tubers were washed under running tap water, manually peeled, and sliced to a uniform thickness of 1.00± 0.05 mm using a precision slicer. Each experiment utilized approximately 60 g of fresh potato sample, with the initial

mass measured using a high-precision balance (A&D GR-202, readability: 0.001 g). Initial moisture content (wet basis) was determined via oven-drying method by placing about 10 g of each sample in a forced convection oven (BMS55, Fan Azma Gostar, Iran) at 105 °C for 24 hours, following AOAC method 934.06 (AOAC International, 2000).

Solar dryer

The solar dryer used in this study was a custom-built hybrid system designed to provide controlled drying conditions for agricultural samples. It consisted of a compound parabolic collector (CPC), a temperature regulation unit, an equalizing chamber, a forced convection fan, a heating channel, a diffuser, and a drying chamber, as illustrated in Figure 1.

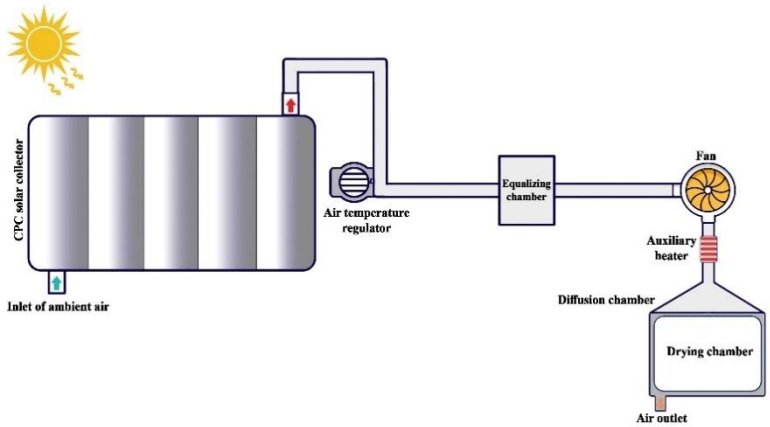

Fig.1. Schematic of the drying system

The CPC collector had an effective aperture area of 2.4 m^2 and a concentration ratio of 2.5. It was equipped with matte black-coated aluminum absorber tubes to enhance solar heat absorption. Polished stainless-steel reflectors, each 0.4 cm thick, were used to concentrate incident solar radiation onto the absorber tubes. The entire collector was installed at a 45-degree angle, matching the latitude (30° N) of the experimental site located at Shiraz University, to maximize solar gain throughout the day (Duffie, Beckman, & Blair, 2020). Solar energy served as the primary heat source, while a 1.5 kW auxiliary electric heater provided supplemental heating during periods of reduced solar radiation. The heater was activated when solar energy alone was insufficient to maintain the set drying temperature and was installed downstream of the air flow path to avoid interfering with solar collection.

Airflow was managed by a motorized damper controlled via a stepper motor (Ts310n247, torque: 6.5 kg·cm), which adjusted airflow based on target temperature input. Air circulated through the system using a centrifugal fan (Techtop, 0.4 kW, Italy), which delivered a consistent airflow of 2 meters per second, measured at the fan inlet using a Testo 435 anemometer with an accuracy of ±0.03 m s^{-1}.

An equalizing chamber, constructed from particle board and measuring 30 × 50 × 70 cm, was installed after the heating section to stabilize and distribute air evenly before entering the drying chamber. Inside the drying chamber, a mesh drying tray (25 × 25 cm, galvanized sheet metal) held the potato slices, and an IR lamp (250 W, Philips) was positioned 30 cm above the tray surface to provide additional thermal radiation during selected treatments.

Real-time mass loss during drying was tracked using a load cell (model L6D, Class C3, 3 kg capacity), installed beneath the drying tray. The load cell was connected to a data acquisition system that logged mass data at 30-second intervals, enabling accurate monitoring of drying progress. Drying continued until the samples reached a final

moisture content of approximately 10% on a dry basis.

Phase change materials were used in select experiments to investigate their thermal storage effect. A total of 1500 g of paraffin wax (melting point approximately 56°C and latent heat of about 190 kJ kg^{-1}) was melted and divided into ten aluminum containers, each holding 150 g. These containers were placed uniformly at the base of the drying chamber beneath the drying tray to absorb and release thermal energy, helping to stabilize temperature fluctuations during the drying cycle.

Temperature control system

A temperature controller (XMT-803, China) automatically regulated the drying chamber's temperature. The system included an SSR relay (25DA, CRYDOM) and a PT100 sensor (±0.1°C accuracy). Ten temperature sensors were installed throughout the setup, while an SHT15 sensor (±0.05% RH, ±0.1°C accuracy) measured humidity changes before and after the drying chamber. Air velocity was set at 2 m s^{-1} at the fan inlet (182 cm^2 cross-sectional area) and monitored using a Testo 435 anemometer (±0.03 m s^{-1} accuracy).

Experimental design

The experiments were conducted to assess the combined effects of air temperature, infrared (IR), and phase change materials (PCM) integration on the drying behavior of potato slices. A factorial design with three variables was used, including three levels of air temperature (40°C, 50°C, and 60°C), two levels of IR radiation (with and without a 250-watt IR lamp), and two levels of PCM use (with and without PCM). This resulted in 12 distinct treatment combinations. Each treatment was replicated three times following a completely randomized design, resulting in 36 experimental runs in total. Drying continued until the samples reached a final moisture content of approximately 10% on a dry basis, as determined by the stabilization of mass readings. The resulting data were analyzed using analysis of variance (ANOVA) with a significance level of 0.05. When significant differences were detected, means were separated using Tukey's honest significant difference (HSD) test. All statistical analyses were performed using SPSS version 25.

Mathematical modeling

In this study, three categories of models were developed to simulate the drying kinetics of potato slices: (1) machine learning (ML) models, (2) regression models (linear and non-linear), and (3) empirical and semi-empirical models.

Machine learning (ML) methods

To model and predict the drying kinetics of potato slices, three supervised machine learning algorithms were employed: Support Vector Machine (SVM)**,** Artificial Neural Network (ANN), and Random Forest (RF). These models were selected for their proven ability to capture complex, nonlinear relationships between input variables and target outputs, especially in regression tasks related to food processing and drying kinetics.

In this study, the following input features were used for all ML models: drying temperature (°C), drying time (s), presence of infrared (IR) radiation (binary: 0= absent, 1= present), and presence of PCM (binary: 0= absent, 1= present). The target output variable for prediction was the moisture content of the potato slices, expressed on a dry basis.

Model assumptions

- The drying process was conceptualized as a functional mapping from a set of input features, namely drying temperature, time, presence of IR radiation, and presence of PCM, to the corresponding moisture content. Although moisture content naturally evolves in a continuous, time-dependent manner, each observation in the dataset was treated as an independent instance for the purposes of supervised learning. This approach enables the models to estimate moisture content at any given time point based solely on current experimental conditions,

without incorporating sequential dependencies.

- Temporal dynamics were not explicitly modeled; instead, the machine learning models operated under the assumption that the moisture content at each time step could be predicted independently of previous values. This simplification facilitates the use of standard regression models and reduces computational complexity, while still achieving high predictive accuracy within the controlled experimental setup.
- External environmental factors, such as variations in ambient humidity or solar radiation, were considered negligible or effectively controlled. This assumption is supported by the presence of an automated temperature control system and an auxiliary electric heater, which together maintained stable thermal conditions across all experiments.

ANN was chosen for its ability to model complex patterns through multiple hidden layers. The network architecture comprised three hidden layers with 64, 32, and 16 neurons, respectively. The hidden layers utilized the Rectified Linear Unit (ReLU) activation function, while the output layer employed a linear activation function. The model was trained with the Adam optimizer, employing a learning rate of 0.001 and a batch size of 32. The selected network architecture was determined based on practical constraints related to dataset size and model performance. Given the limited number of experimental samples, deeper architectures with more layers or neurons were avoided to reduce the risk of overfitting. Consequently, a relatively shallow configuration was adopted. The final architecture (64–32–16) was established through an iterative trial-and-error process, during which various configurations were evaluated and validated. This particular setup achieved an effective balance between model complexity and generalization capability, as evidenced by cross-validation performance.

SVM was selected for its robustness in high-dimensional spaces. It effectively captures nonlinear relationships through kernel functions. A radial basis function (RBF) kernel was employed, with hyperparameters including a regularization parameter (C) of 100, an epsilon value of 0.01 to define the regression margin, and a gamma value of 0.1.

RF was included as an ensemble learning method to enhance generalization and reduce variance. The model was trained using 100 decision trees, with a minimum of two samples per split to prevent overfitting.

Prior to model training, all input features, including temperature, drying time, infrared radiation, and the presence of PCM, were standardized to ensure optimal model performance. Standardization was performed using the transformation Equation (1) to center the data around zero with unit variance (Kelleher, 2019):

$$X_{scaled} = \frac{X-\mu}{\sigma} \quad (1)$$

where X represents the original feature value, μ denotes the mean, and σ represents the standard deviation of the feature.

To ensure robust model performance and generalization, the dataset was split into a training set (80%) and a test set (20%). Furthermore, ten-fold cross-validation was performed on the training set, where it was randomly partitioned into ten subsets. Each model was trained on nine subsets and verified on the remaining one, with this process repeated ten times. The final performance was averaged across all iterations, and the best hyperparameters were selected during this process. Model performance was subsequently tested on the test set to evaluate its generalization capability, reducing the risk of overfitting and providing a reliable accuracy estimate.

Model performance was assessed using multiple statistical metrics: the coefficient of determination (R^2) indicates how well the predicted values align with actual values; RMSE (g water g^{-1} dry matter) quantifies the average value of prediction errors; mean absolute error (MAE, g water g^{-1} dry matter) measures the total discrepancies between predicted and observed values; and mean bias error (MBE, g water g^{-1} dry matter) evaluates

any systematic over- or underestimation. Lower RMSE and MAE values signify higher accuracy, while an R^2 value closer to one indicates a stronger model fit. The complete workflow of the ML models is summarized in Figure 2, which demonstrates the steps involved from gathering and preparing data to choosing a model and assessing its performance. By integrating these ML techniques, this study aimed to develop accurate and reliable predictive models for drying kinetics.

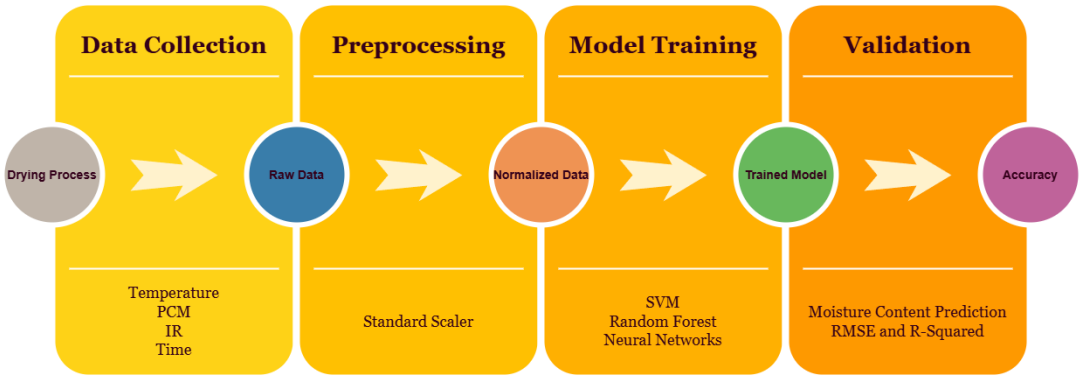

Fig. 2. The workflow of ML models for drying kinetics

Linear and non-Linear regression

Linear regression assumes a direct linear relationship between the dependent variable (moisture content) and the independent variables (time, temperature, PCM, and IR). In contrast, non-linear regression uses an exponential equation to model the relationship between moisture content and the independent variables, capturing more complex patterns in the data.

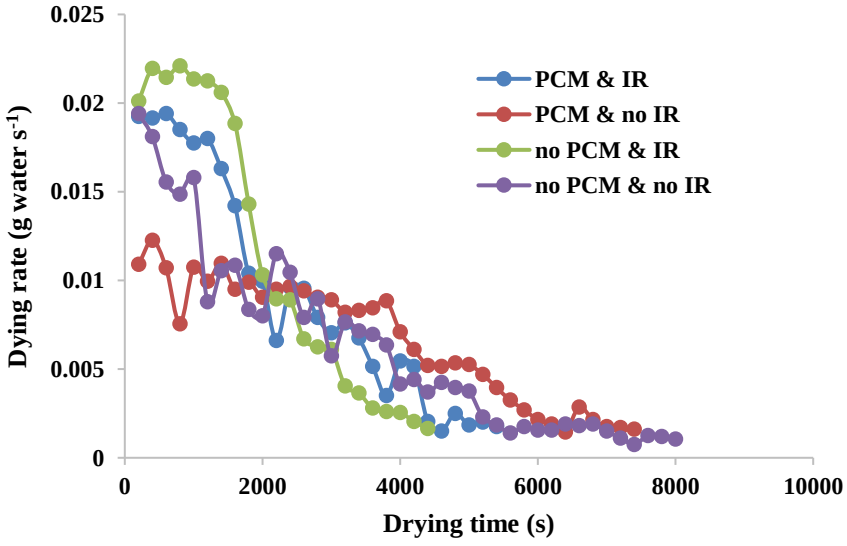

Fig. 3. Drying rate vs. time under different conditions at 40°C

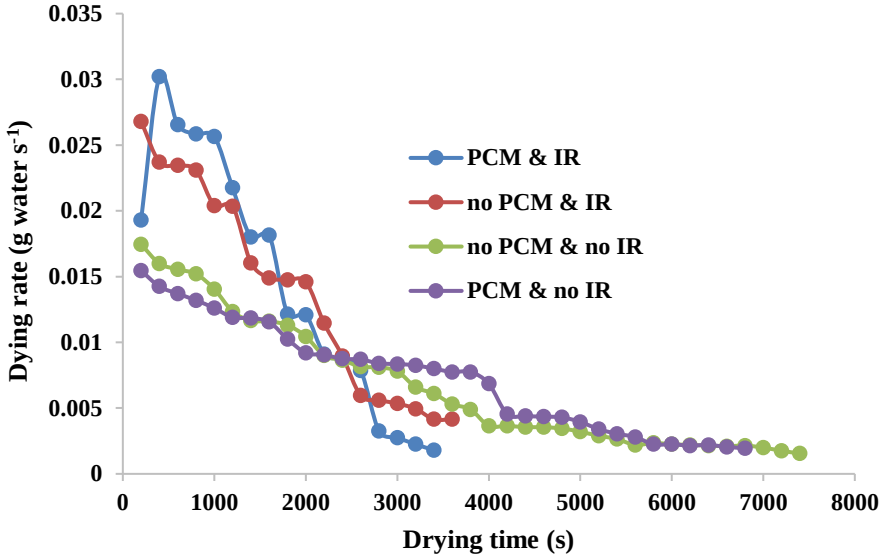

Fig. 4. Drying rate vs. time under different conditions at 50°C

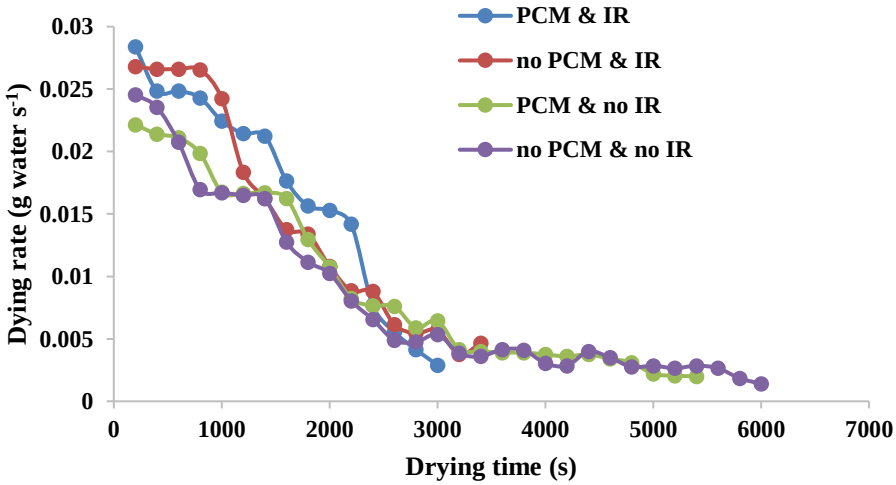

Fig. 5. Drying rate vs. time under different conditions at 60°C

Empirical and semi-empirical models

Empirical models are based solely on experimental data fitting without requiring a strong physical foundation. These models are developed by analyzing experimental drying data and identifying the mathematical equations that best describe moisture loss. In this study, commonly used models, such as Newton, Page, Modified Page, Two-Term, Exponential Two-Term, Logarithmic, Midilli, and Approximation of Diffusion, were applied to represent the moisture ratio as a function of drying duration.

Results and Discussion

Drying rate

The drying rate of potato slices was calculated under different operating conditions (Figures 3 to 5).

The average slope of each drying curve is presented in Table (1), from which the following insights were derived:

1. **Effect of Temperature on Drying rate:** As temperature increases from 40°C to 60°C, the slope of the drying curves rises, indicating a higher drying rate. This trend is expected, as higher temperatures

enhance moisture evaporation from the sample surface. Specifically, under no PCM & no IR conditions, the slope increases from 0.006249 at 40°C to 0.00817 at 60°C. Similarly, under PCM & IR conditions, the slope rises from 0.009217 at 40°C to 0.01671 at 60°C. These results confirm that increasing temperature significantly accelerates the drying process.

2. **Effect of PCM:** PCM serves as a thermal stabilizer, reducing temperature fluctuations and influencing the drying rate. In most cases: with PCM but without IR, the drying rate is slightly higher than without PCM. For example, at 60°C, the slope is 0.009267 with PCM compared to 0.00817 without PCM. Previous studies confirm the effectiveness of PCM in improving drying performance. Rakshamuthu *et al.* (2021) reported that PCM increased the drying rate of gooseberries in a solar dryer. Similarly, other researchers illustrated that PCM enhances dryer efficiency (Atia, Teggar, & Laouer, 2024; Poonia, Singh, & Jain, 2022; Madhankumar, Viswanathan, Wu, & Taipabu, 2023). With both PCM and IR combined, the drying rate is higher than when PCM is absent. At 60°C, the slope is 0.01671 with PCM & IR, compared to 0.014512 without PCM & IR. These findings suggest that PCM is more effective when combined with IR, leading to a more efficient drying process.
3. **Effect of IR radiation:** At all temperature settings, the addition of IR significantly increases the drying rate. For example, at 40°C without PCM, the slope increases from 0.006249 (without IR) to 0.011295 (with IR). Similarly, at 60°C without PCM, the slope rises from 0.00817 (without IR) to 0.014512 (with IR). This increase is attributed to the deeper penetration of infrared energy into the samples, accelerating moisture evaporation. However, a significant difference observed at 50°C can be attributed to the pronounced effect of infrared (IR) radiation at this temperature. At 40°C, although IR has a positive impact, the lower thermal potential of the drying air limits its effectiveness, and therefore, no sharp increase is observed in the IR curves. At 60°C, despite the high thermal potential of the air, the influence of IR appears to be limited, likely due to increased internal moisture diffusion resistance within the potato slices, which restricts further enhancement of the drying rate.
4. **Comparison of PCM and IR effects:** IR has a stronger impact on the drying rate compared to PCM, as seen in the larger differences in slope between IR and non-IR conditions. The combination of PCM and IR yields the highest drying rate. For example, at 60°C, the highest slope (0.01671) is observed under PCM & IR conditions.

For optimal drying performance, a combination of IR and PCM is recommended, as it maximizes the drying rate while maintaining thermal stability.

Table 1- Slopes of drying rate curves under different conditions

Experiment	Slope of curves
40C PCM & IR	0.009217
40C PCM & No IR	0.006651
40C No PCM & No IR	0.006249
40C No PCM & IR	0.011295
50C PCM & IR	0.014438
50C PCM & No IR	0.007337
50C No PCM & No IR	0.006689
50C No PCM & IR	0.013814
60C PCM & IR	0.01671
60C PCM & No IR	0.009267
60C No PCM & No IR	0.00817
60C No PCM & IR	0.014512

Mathematical modeling

After developing the ML, empirical, and semi-empirical models, validation was conducted, yielding the following results.

One-way analysis of variance for model performance

To statistically validate the differences in predictive performance among the developed models, an ANOVA was conducted using the RMSE values obtained under different drying conditions (temperature, presence of PCM, and IR application). The models compared included the ANN, SVM, RF, Non-linear Regression, and the best-performing Semi-Empirical model (Midilli). The tested null hypothesis was that there are no significant differences in mean RMSE across the different modeling approaches. The results of the ANOVA are presented in Table 2.

Table 2- One-way ANOVA results comparing model RMSE across drying conditions

Source of Variation	SS	Df	MS	F	p-value
Between groups	0.379	4	0.0948	12.51	0.0004
Within groups	0.076	10	0.0076		
Total	0.455	14			

The ANOVA results reveal a statistically significant difference in RMSE among the different modeling approaches ($F = 12.51$, $p < 0.001$). Post-hoc comparisons using Tukey's HSD test further indicated that the ANN model's performance (lowest RMSE) was significantly better than that of the semi-empirical and regression-based models. Although SVM and RF also performed well, only ANN showed statistically significant superiority in prediction accuracy across all tested conditions. These findings validate that the enhanced prediction accuracy of the ANN model is not merely a product of chance; instead, it signifies a statistically significant improvement in model performance.

Artificial neural network (ANN) model

The comparison between actual and predicted moisture content using the ANN model is shown in Figure 6. The performance metrics for the ANN model were evaluated for both training and test sets. For the training set, the R^2, RMSE, MAE, and SMBE were calculated as 0.999, 0.0583 g water g^{-1} dry matter, 0.0251 g water g^{-1} dry matter, and 0.005 g water g^{-1} dry matter, respectively. For the test set, the corresponding values were 0.998, 0.0656 g water g^{-1} dry matter, 0.03409 g water g^{-1} dry matter, and 0.0091 g water g^{-1} dry matter. These results demonstrate the ANN model's strong predictive accuracy and generalization capability. Since $|SMBE| \leq 0.1$, the model demonstrates excellent predictive accuracy. Additionally, Figure 7 presents the residuals versus fitted values, confirming the model's reliability. Several studies have reported similar high accuracy in moisture content prediction using ANN models. For instance, another research simulated the thin-layer drying of apple slices using convective and microwave drying methods, achieving R^2 values of 0.993 and 0.9991, respectively, underscoring the strong predictive capability of ANN models (Rasooli Sharabiani, Kaveh, Abdi, Szymanek, & Tanaś, 2021). Similarly, Sabzevari, Behroozi-Khazaei, and Darvishi (2021) employed an ANN architecture of 3-5-5-1 to model the drying of banana slices in a thin layer, successfully predicting moisture content. In another study, the impact of a novel vortex/swirling flow generator on fluidization streams in a fluidized bed dryer was investigated. ANN modeling was used to optimize the drying process for paddy, achieving an R^2 of 0.999 and an RMSE of 0.111, demonstrating the model's effectiveness (Chokphoemphun, Hongkong, & Chokphoemphun, 2024). Another study investigated the drying rate of *Citrus medica* under freeze-drying conditions, considering different slice thicknesses (3 mm, 5 mm, and 7 mm) and cabin pressures (0.008 mbar, 0.010

mbar, and 0.012 mbar). A feedforward multilayer perceptron ANN was employed to estimate the moisture content, mass loss ratio (MR), and rate of drying. The ANN model achieved an R^2 of 0.998 and an RMSE of 0.010574, demonstrating its high precision and reliability in characterizing the freeze-drying process (Topal, Şahin, & Vela, 2024). Additionally, another research analyzed the drying kinetics of potato cubes in a fluidized bed dryer using ANN modeling. Their findings provided important understanding into the effectiveness of ANN techniques for predicting the drying characteristics of potato products, further supporting the applicability of ANN in food drying processes (Azadbakht, Torshizi, Aghili, & Ziaratban, 2018).

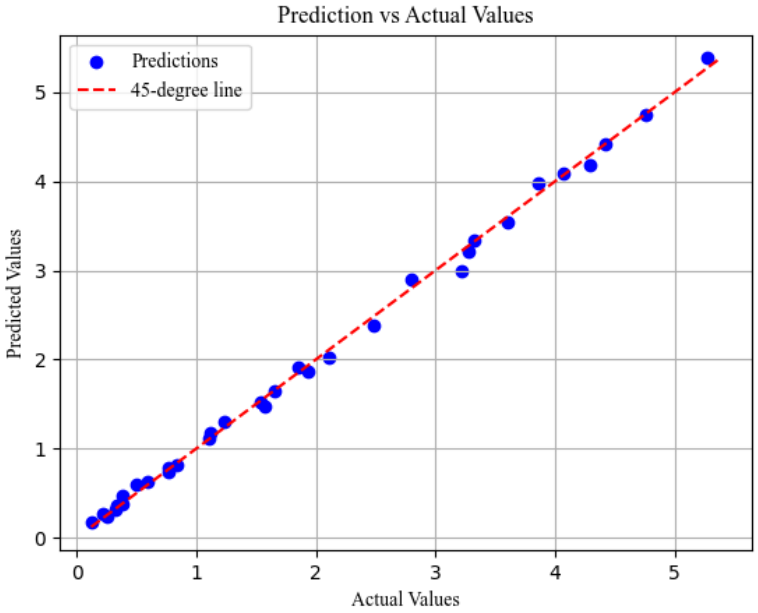

Fig. 6. Comparison of actual and predicted moisture content using the ANN model

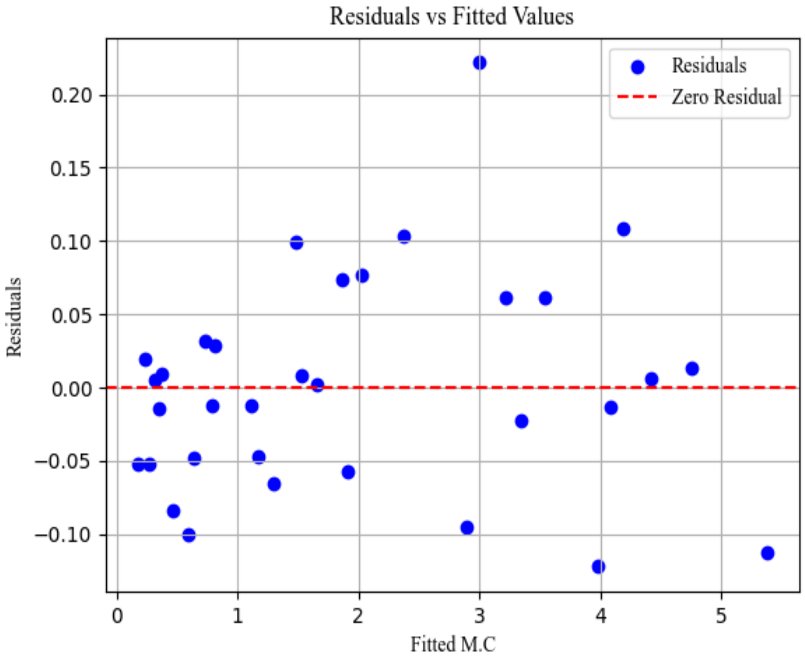

Fig. 7. Residuals of the ANN model versus fitted moisture content

Support vector machine (SVM) model

The relationship between actual and predicted moisture content is presented in Figure 8. The statistical evaluation of the SVM model on the training dataset yielded an R^2 of 0.998, RMSE of 0.0702 g water g^{-1} dry matter, MAE of 0.0512 g water g^{-1} dry matter, and SMBE of 0.008 g water g^{-1} dry matter. For the evaluation dataset, the corresponding values were 0.996, 0.0882 g water g^{-1} dry matter, 0.0603 g water g^{-1} dry matter, and SMBE of 0.010 g water g^{-1} dry matter, respectively. These results indicate strong predictive performance of the SVM model. Additionally, the residuals plotted against the predicted moisture contents, as shown in Figure (9), further confirm the model's reliability. To evaluate whether the difference in predictive performance between the ANN and SVM models was statistically significant, an independent two-sample t-test was conducted using RMSE values obtained under different drying conditions. The results showed that the ANN model (mean RMSE = 0.0656 0702 g water g^{-1} dry matter) performed significantly better than the SVM model (mean RMSE = 0.0882 0702 g water g^{-1} dry matter), with a t-value of –3.45 and a p-value of 0.0061 ($p < 0.01$). This confirms that the superior performance of the ANN model is not due to random variation, but is statistically significant. This trend has been observed in previous studies, where SVM performs well but generally does not surpass ANN in predictive capability. For instance, another research, investigated the prediction of moisture content in mushrooms during drying using ANN and SVM models. Their results showed that ANN achieved an R^2 of 0.998 and a relative RMSE (rRMSE) of 3.958%, in contrast the corresponding values for SVM were 0.973% and 15.749%, respectively (Karaağaç, Ergün, Ağbulut, Gürel, & Ceylan, 2021). These findings further support the superior accuracy of ANN over SVM in moisture content prediction. A similar study developed predictive models for the pyrolytic conversion of *Sargassum* sp. (Red Sea seaweed) using ANN and SVM. Their study demonstrated that ANN outperformed SVM, yielding higher accuracy and lower error rates, further validating the effectiveness of ML techniques in forecasting pyrolytic conversion processes (Saleem & Ali, 2017). Another research investigated ML modeling for the drying of mushroom slices, where ANN outperformed the SVM method, confirming its higher predictive accuracy in drying applications (Fartash Naeimi, Khoshtaghaza, Selvi, Ungureanu, & Abbasi, 2024).

Random forest (RF) model

The comparison of actual and predicted moisture content using the RF model is depicted in Figure 10, while Figure 11 presents the residuals of the RF model plotted against the predicted moisture content. Following the development of the RF model, the statistical metrics R^2, RMSE, MAE, and SMBE for the training dataset were calculated as 0.991, 0.153 g water g^{-1} dry matter, 0.1120 g water g^{-1} dry matter, and 0.0020 g water g^{-1} dry matter, respectively. For the evaluation dataset, the corresponding values were 0.9853, 0.1859 g water g^{-1} dry matter, 0.1397 g water g^{-1} dry matter, and 0.0030 g water g^{-1} dry matter, respectively. Thus, the RF algorithm can be considered a reliable model for predicting moisture content in potato slices during drying; however, its predictive accuracy is generally lower than that of ANNs and SVMs. Despite this, RF remains a valuable benchmark for assessing the performance of various machine learning models under consistent conditions. For applications where predictive accuracy is paramount, ANNs are particularly recommended due to their superior performance. Their architecture, characterized by hidden layers, enables them to capture complex, non-linear relationships in the data, making them especially well-suited for modeling drying processes. The thin-layer drying process of potato slices involves heat and mass transfer, which is strongly influenced by environmental conditions, temperature, and moisture. Compared to other methods, ANNs are better able to capture these dependencies.

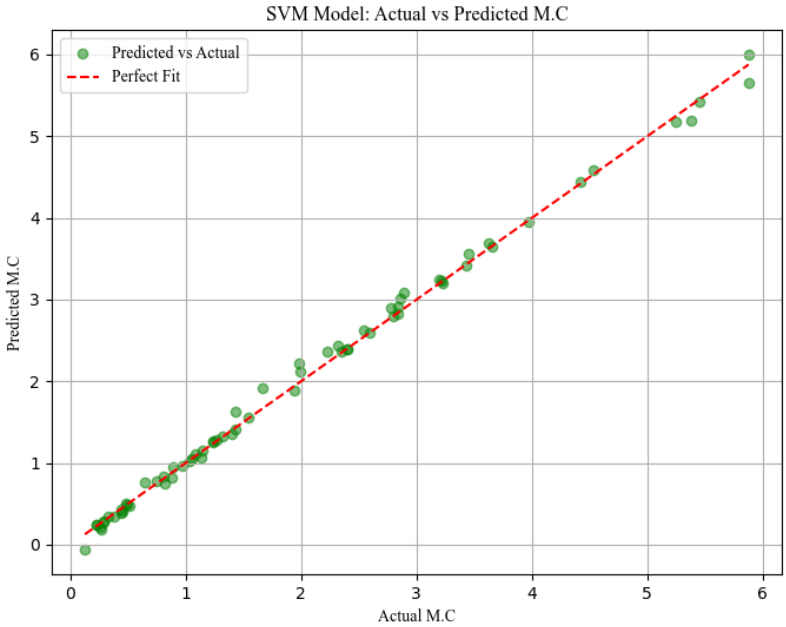

Fig. 8. Comparison of actual and predicted moisture content using the SVM model

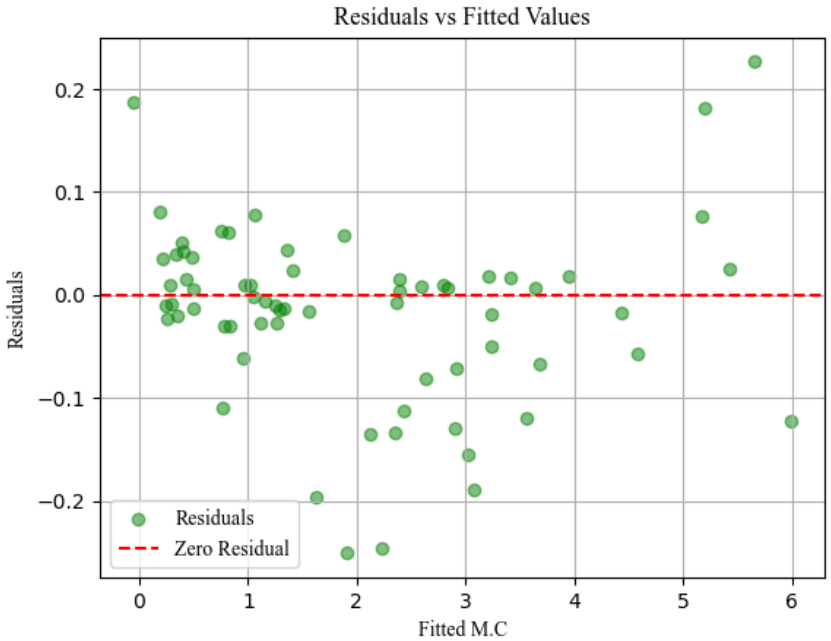

Fig. 9. Residuals of the SVM model versus predicted moisture content

SVMs generally perform well in regression and classification tasks, especially with smaller datasets and optimized feature sets. Unlike RF, which relies on an ensemble of decision trees, SVM excels at finding optimal decision boundaries. As a result, when dealing with highly nonlinear data and minimal noise, SVM's performance can be comparable to that of ANN. However, RF tends to have lower accuracy in time-dependent predictions and

continuous datasets, such as moisture variation over time. This is because RF is inherently more suited for classification tasks rather than regression problems. Additionally, RF may struggle to capture subtle moisture variations, leading to less accurate predictions with higher fluctuations. In summary, ANNs perform best when trained on large and diverse datasets, as they can optimize their weights and architecture to extract complex features. SVMs are more effective for small to medium-sized datasets, while RF may underperform when dealing with a high number of input variables or time-dependent data.

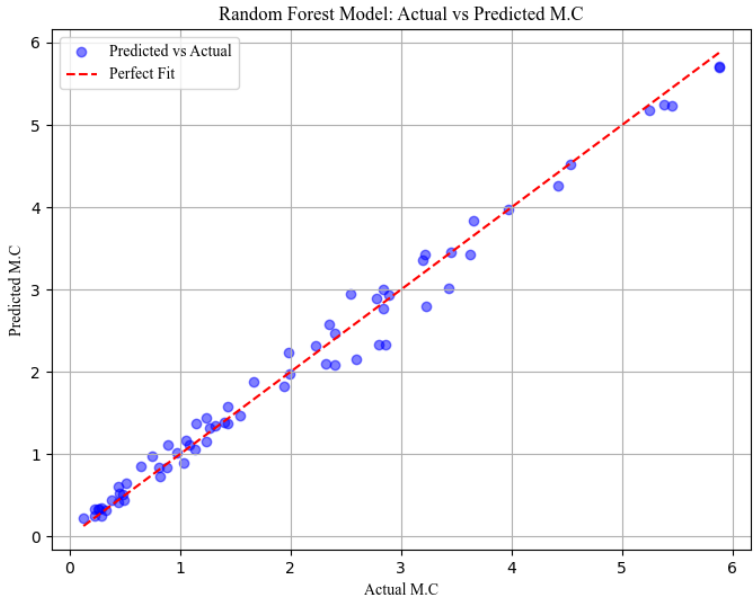

Fig. 10. Comparison of actual and predicted moisture content using the RF model

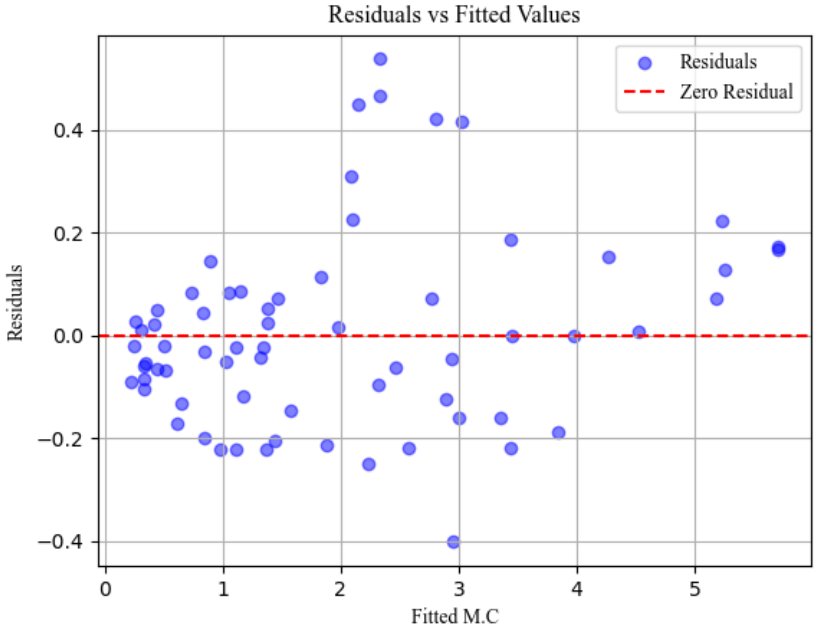

Fig. 11. Residuals of the RF model versus predicted moisture content

Regression models

Linear regression

We developed superposition mathematical models for different drying conditions: with PCM & with IR, with PCM & without IR, without PCM & with IR, and without PCM & without IR (Equations (2) to (5) in Table 3). These models predict the moisture content of potato slices as a linear function of temperature and time. As expected, the moisture content decreases as time and temperature increase, which is a typical result of the drying process. However, the models exhibit lower R^2 values and higher RMSE, MAE, and SMBE, indicating that they are less accurate compared to the AI models. Additionally, the predicted moisture content by the linear regression model versus the actual moisture content is shown in Figure 12.

Table 3- Performance of linear regression models for different drying conditions

Model	Equation	Eq. no	R^2	RMSE	MAE	MBE
PCM & IR	$M.C = -0.4929\,T - 1.5599\,Time + 1.8464$	(2)	0.7736	0.8877	0.6935	-0.3764
PCM & No IR	$M.C = -0.4212\,T - 1.5346\,Time + 1.9308$	(3)	0.94684	0.4019	0.3413	-0.1053
No PCM & IR	$M.C = -0.1588\,T - 1.6363\,Time + 1.9496$	(4)	0.9009	0.5021	0.4292	0.1419
No PCM & No IR	$M.C = -0.2810\,T - 1.2822\,Time + 1.6125$	(5)	0.7913	0.8964	0.6565	-0.4214

Note: RMSE, MAE, and MBE values are in g water g^{-1} dry matter

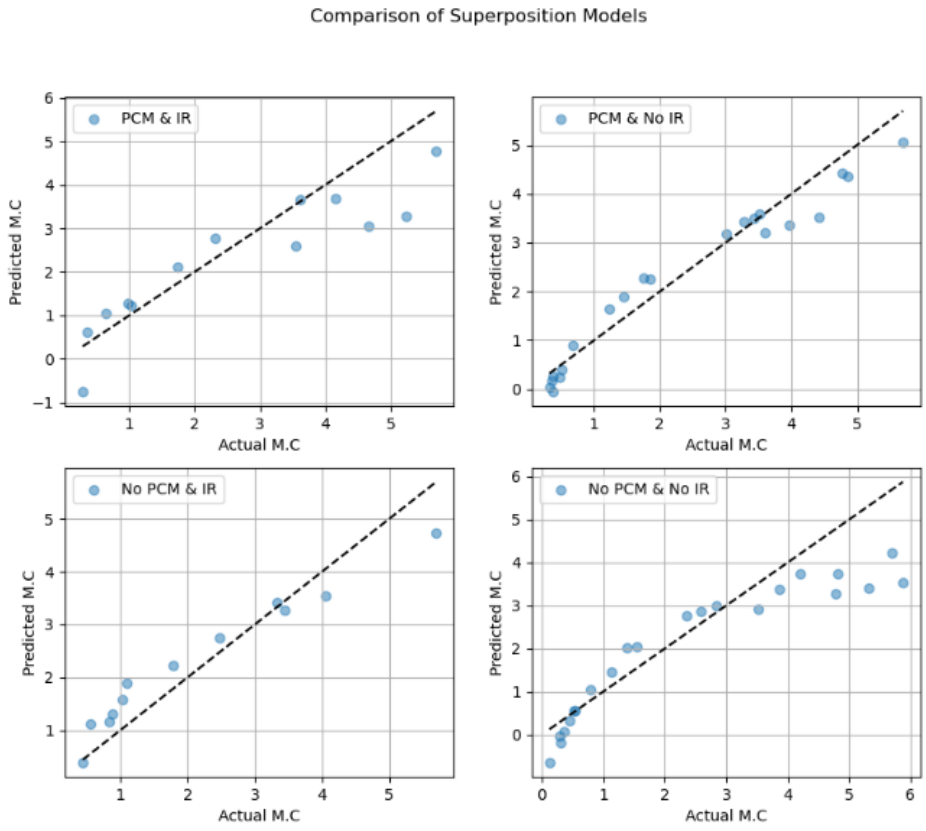

Fig. 12. Comparison of actual and predicted moisture content using the linear regression model

Non-linear regression

Among the different equations tested, the exponential model provides the best prediction of the moisture content during the drying process. Equation (6) is defined as:

$$M.C = 5.9893\exp(-0.0005\,Time) - 0.0111\log(T+1) + 0.1219\,PCM - 0.8198\,IR \quad (6)$$

where, Time is the drying time (in seconds), T is the drying temperature (°C), PCM and IR can either be 0 or 1, where 0 represents experiments without PCM or IR, and 1 represents experiments with PCM or IR.

The evaluation of the model shows that it has R^2, RMSE, MBE, and SMBE values of 0.93, 0.4058 g water g^{-1} dry matter, 0.3173 g water g^{-1} dry matter, and 0.0056 g water g^{-1} dry matter, respectively. These results display better proficiency than the linear regression models, but still fall short of the accuracy achieved by the AI models (ANN, SVM, and RF). This nonlinear model combines the empirical Henderson model with linear regression, leading to a better prediction than either model alone. However, since it does not utilize AI techniques for modeling, its accuracy is lower than that of the AI models. Given that the absolute value of SMBE is below 0.1, the model's accuracy is considered acceptable. The comparison between actual moisture content and the moisture content predicted by the non-linear regression model is presented in Figure 13.

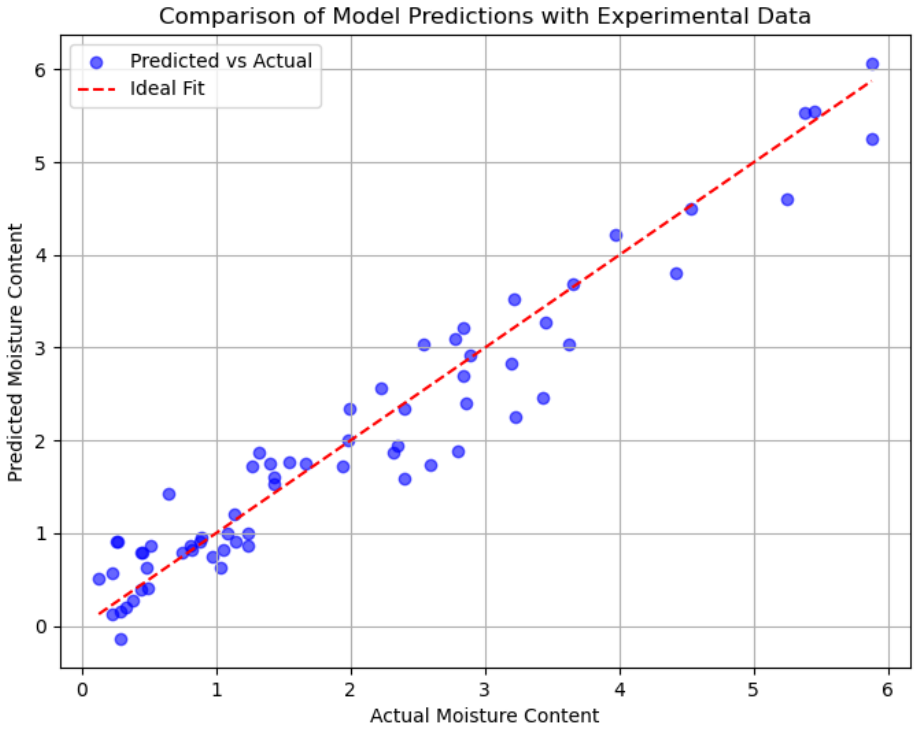

Fig. 13. Comparison of actual and predicted moisture content using the non-linear regression model

Semi-empirical models

The coefficients and statistical parameters of each model are provided in Table 4. Among them, the Midilli and the Approximation of Diffusion models exhibit the lowest errors. However, the evaluation of the results from the empirical and semi-empirical models shows that their accuracy is lower compared to the AI and nonlinear regression models. Another study was conducted to examine the modeling of drying kinetics using two different methods: semi-empirical and ANN models. The results showed that when total experimental data were involved, ANN outperformed the Midilli model (Karakaplan, Goz, Tosun, & Yuceer, 2019). ML models, particularly ANN, provide

the most accurate predictions, significantly outperforming other models in terms of precision and error reduction. Nonlinear regression also proves superior to linear regression, as moisture content changes inherently exhibit nonlinearity. Among empirical models, the Midilli. model performs best, though with lower accuracy compared to ML models. While empirical models are useful for quick estimations, they lack the precision of ML approaches. For optimal predictions, ANN is recommended, but if computational efficiency is a concern, SVM serves as a viable alternative. Nonlinear regression offers better interpretability, and the Midilli model is suitable for fast empirical estimations.

Table 4- Coefficients of different semi-empirical models

Model	Coefficients	R^2	RMSE	MAE	MBE
Newton	k = 0.0005	0.8851	0.5283	0.4000	-0.0090
Page	k = 0.0009, n = 0.939	0.8863	0.5255	0.3972	-0.0045
Henderson and Pabis	a = 0.964, k = 0.0005	0.8868	0.5243	0.3994	-0.0198
Logarithmic	a = 0.945, k = 0.0006, c = 0.0325	0.8884	0.5209	0.3904	0.0000
Two-term	a = 0.9625, k_1 = 0.0006, b = 0.0133, k_2 = -0.0001	0.8885	0.5204	0.3904	0.0000
Midilli et al. (2002)	a = 0.955, k = 0.0003, n = 1.09, b = 0.0000	0.8892	0.5186	0.3915	-0.0017
Modified page	k = 0.0008, n = 0.7159	0.8851	0.5283	0.4000	-0.0090
Exponential	a = 0.4923, k = 0.0008	0.8871	0.5238	0.3932	0.0022
Approximation of diffusion	A = 0.9675, k = 0.0006, b = -0.0435	0.8879	0.5220	0.3898	0.0107

Conclusion

This study systematically compared different modeling approaches to predict the drying kinetics of potato slices under various drying conditions. The results demonstrated that AI models, particularly ANN, exhibited the highest accuracy in predicting moisture content over time, outperforming both empirical and semi-empirical models. While conventional models such as the Midilli and Approximation of Diffusion models provided reasonable fits, they lacked the precision and adaptability of AI-based approaches. Among AI techniques, ANN achieved the best performance, followed by SVM and RF, confirming the capability of ML in capturing complex, non-linear drying dynamics. Additionally, the study revealed that the drying rate increases significantly with temperature, IR radiation, and the presence of PCM. IR had a stronger effect on enhancing drying efficiency compared to PCM alone. The combination of PCM and IR yielded the highest drying rate, making it the most effective drying condition. Overall, the findings emphasize the superiority of AI models for drying process optimization. For industrial applications, ANN is the recommended model due to its ability to generalize drying kinetics accurately. Future research could focus on integrating hybrid AI models with computational fluid dynamics (CFD) for further optimization and exploring the impact of different drying conditions on food quality attributes.

Conflict of Interest: The authors declare no competing interests.

Author Contributions

M. Moradi: Methodology, Project administration, Software, Supervision, Text Mining, Data pre and post processing, Validation, Writing, Review and editing services

R. Raeesi: Methodology, Software, Conceptualization, Data acquisition

A. Dehghani: Writing, Data pre and post processing, Statistical analysis, Visualization, Validation

References

1. AOAC International. (2000). AOAC Official Method 934.06: Moisture in dried fruits. In Official Methods of Analysis (17th ed.). Gaithersburg, MD: AOAC International.
2. Arpaci, E., Atayılmaz, Ş. Ö. & Gemici, Z. (2025). Exploring Mathematical Modeling and CFD in Convective Drying of Fruits and Vegetables: A Review. *Food and Bioprocess Technology*, 18, 3195-3222. https://doi.org/10.1007/s11947-024-03627-2
3. Atia, A., Teggar, M., & Laouer, A. (2024). Performance of various solar dryer types integrating latent heat storage for drying agricultural products: An up-to-date review. *Journal of Energy Storage*, *102*, 114048. https://doi.org/10.1016/j.est.2024.114048
4. Azadbakht, M., Torshizi, M. V., Aghili, H., & Ziaratban, A. (2018). Application of artificial neural network (ANN) in drying kinetics analysis for potato cubes. *Carpathian Journal of Food Science & Technology*, *10*(2), 96-106.
5. Benseddik, A., Azzi, A., & Allaf, K. (2018). Mathematical empirical models of thin-layer airflow drying kinetics of pumpkin slice. *Engineering in Agriculture, Environment and Food*, *11*(4), 220-231. https://doi.org/10.1016/j.eaef.2018.07.003
6. Chokphoemphun, S., Hongkong, S., & Chokphoemphun, S. (2024). Artificial neural network for drying behavior prediction of paddy in developed chamber fluidized–bed dryer. *Computers and Electronics in Agriculture*, *220*, 108888. https://doi.org/10.1016/j.compag.2024.108888
7. Chukwunonye, C. D., Nnaemeka, N. R., Chijioke, O. V., & Obiora, N. C. (2016). Thin layer drying modelling for some selected Nigerian produce: a review. *American Journal of Food Science and Nutrition Research*, *3*(1), 1-15.
8. Duffie, J. A., Beckman, W. A., & Blair, N. (2020). *Solar engineering of thermal processes, photovoltaics and wind*. John Wiley & Sons. https://doi.org/10.1002/9781119540328
9. Ertekin, C., & Firat, M. Z. (2017). A comprehensive review of thin-layer drying models used in agricultural products. *Critical Reviews in Food Science and Nutrition*, *57*(4), 701-717. https://doi.org/10.1080/10408398.2014.910493
10. Fartash Naeimi, E., Khoshtaghaza, M. H., Selvi, K. Ç., Ungureanu, N., & Abbasi, S. (2024). Optimization of the Drying Process for Gamma-Irradiated Mushroom Slices Using Mathematical Models and Machine Learning Algorithms. *Agriculture*, *14*(12), 2351. https://doi.org/10.3390/agriculture14122351
11. Fathi, M., Roshanak, S., Rahimmalek, M., & Goli, S. A. H. (2016). Thin-layer drying of tea leaves: Mass transfer modeling using semi-empirical and intelligent models. *International Food Research Journal*, *23*(1), 40.
12. Karaağaç, M. O., Ergün, A., Ağbulut, Ü., Gürel, A. E., & Ceylan, I. (2021). Experimental analysis of CPV/T solar dryer with nano-enhanced PCM and prediction of drying parameters using ANN and SVM algorithms. *Solar Energy*, *218*, 57-67. https://doi.org/10.1016/j.solener.2021.02.028
13. Karakaplan, N., Goz, E., Tosun, E., & Yuceer, M. (2019). Kinetic and artificial neural network modeling techniques to predict the drying kinetics of *Mentha spicata* L. *Journal of Food Processing and Preservation*, *43*(10), e14142. https://doi.org/10.1111/jfpp.14142
14. Kelleher, J. D. (2019). *Deep learning*. MIT press.
15. Kumar, R., Kumar, P., Hota, N. K., & Pandey, O. P. (2025). Semi-empirical thin-layer drying model for the agricultural products. *Chemical Engineering Communications*, *212*(5), 728-738. https://doi.org/10.1080/00986445.2024.2432672
16. Kutlu, N., İşcİ, A., & DemİrkoI, Ö. Ş. (2015). Thin layer drying models in food systems.
17. Lee, H. J., Lee, S. K., Kim, H., Kim, W., & Han, J. W. (2016). Thin-layer Drying Characteristics of Rapeseed. *Journal of Biosystems Engineering*, *41*(3), 232-239. https://doi.org/10.5307/jbe.2016.41.3.232
18. Lopes, S., Santos, S., Rodrigues, N., Pinho, P., & Viegas, D. X. (2023). Modelling sorption processes of 10-h dead Pinus pinaster branches. *International Journal of Wildland Fire*, *32*(6),

903-912. https://doi.org/10.1071/WF22127
19. Madhankumar, S., Viswanathan, K., Wu, W., & Taipabu, M. I. (2023). Analysis of indirect solar dryer with PCM energy storage material: Energy, economic, drying and optimization. *Solar Energy*, *249*, 667-683. https://doi.org/10.1016/j.solener.2022.12.009
20. Mahesh, J. S., Rengaraju, B., & Selvakumarasamy, S. (2024). Effect of ANN and semi-empirical models on dried Annona muricata leaves. *Biomass Conversion and Biorefinery*, 1-13. https://doi.org/10.1007/s13399-024-05546-w
21. Perazzini, H., Freire, F. B., & Freire, J. T. (2013). Drying kinetics prediction of solid waste using semi-empirical and artificial neural network models. *Chemical Engineering & Technology*, *36*(7), 1193-1201. https://doi.org/10.1002/ceat.201200593
22. Poonia, S., Singh, A. K., & Jain, D. (2022). Performance evaluation of phase change material (PCM) based hybrid photovoltaic/thermal solar dryer for drying arid fruits. *Materials Today: Proceedings*, *52*, 1302-1308. https://doi.org/10.1016/j.matpr.2021.11.058
23. Przybył, K., & Koszela, K. (2023). Applications MLP and Other Methods in Artificial Intelligence of Fruit and Vegetable in Convective and Spray Drying. *Applied Sciences*, *13*(5), 2965. https://doi.org/10.3390/app13052965
24. Rakshamuthu, S., Jegan, S., Benyameen, J. J., Selvakumar, V., Anandeeswaran, K., & Iyahraja, S. (2021). Experimental analysis of small size solar dryer with phase change materials for food preservation. *Journal of Energy Storage*, *33*, 102095. https://doi.org/10.1016/j.est.2020.102095
25. Rasooli Sharabiani, V., Kaveh, M., Abdi, R., Szymanek, M., & Tanaś, W. (2021). Estimation of moisture ratio for apple drying by convective and microwave methods using artificial neural network modeling. *Scientific Reports*, *11*(1), 9155. https://doi.org/10.1038/s41598-021-88270-z
26. Sabzevari, M., Behroozi-Khazaei, N., & Darvishi, H. (2021). Real-time evaluation of artificial neural network-developed model of banana slice kinetics in microwave-hot air dryer. *Journal of Food Process Engineering*, *44*(9), e13796. https://doi.org/10.1111/jfpe.13796
27. Sağlam, C., & Çetin, N. (2022). Machine learning algorithms to estimate drying characteristics of apples slices dried with different methods. *Journal of Food Processing and Preservation*, *46*(10), e16496. https://doi.org/10.1111/jfpp.16496
28. Saleem, M., & Ali, I. (2017, September). Machine learning based prediction of pyrolytic conversion for red sea seaweed. In *Proceedings of the 7th International Conference on Biological, Chemical & Environmental Sciences (BCES-2017), Budapest, Hungary* (pp. 6-7). https://doi.org/10.17758/EAP.C0917043
29. Simpson, R., Ramírez, C., Nuñez, H., Jaques, A., & Almonacid, S. (2017). Understanding the success of Page's model and related empirical equations in fitting experimental data of diffusion phenomena in food matrices. *Trends in Food Science & Technology*, *62*, 194-201. https://doi.org/10.1016/j.tifs.2017.01.003
30. Topal, M. E., Şahin, B., & Vela, S. (2024). Artificial Neural Network Modeling Techniques for Drying Kinetics of Citrus medica Fruit during the Freeze-Drying Process. *Processes*, *12*(7), 1362. https://doi.org/10.3390/pr12071362

نشریه ماشین‌های کشاورزی
https://jame.um.ac.ir

مقاله پژوهشی

جلد ۱۶، شماره ۳، پاییز ۱۴۰۵، ص ۵۹۷-۵۷۹

مدل‌سازی مقایسه‌ای سینتیک خشک‌کردن برش‌های سیب‌زمینی: روش‌های مبتنی بر هوش مصنوعی در مقایسه با روش‌های تجربی و نیمه‌تجربی

رضا رئیسی[۱]، مهدی مرادی[۱*]، علیرضا دهقانی[۱]

تاریخ دریافت: ۱۴۰۳/۱۲/۳۰
تاریخ پذیرش: ۱۴۰۴/۰۳/۳۱

چکیده

خشک‌کردن یکی از روش‌های حیاتی نگهداری در صنعت غذا است که با کاهش رطوبت، کیفیت محصول را حفظ کرده و ماندگاری آن را افزایش می‌دهد. این فرآیند شامل مکانیزم‌های پیچیده انتقال حرارت و جرم بوده و به مدل‌های پیش‌بینی دقیقی نیاز دارد. در این مطالعه، روش‌های مختلف مدل‌سازی شامل مدل‌های رگرسیون، مدل‌های نیمه‌تجربی، و روش‌های مبتنی بر هوش مصنوعی (AI) برای شبیه‌سازی فرآیند خشک‌کردن برش‌های سیب‌زمینی مورد مقایسه قرار گرفتند. آزمایش‌های خشک‌کردن در دماهای ۴۰، ۵۰ و ۶۰ درجه سانتی‌گراد، با و بدون استفاده از مواد تغییر فازدهنده (PCM) و تابش مادون قرمز (IR) انجام شد. مدل‌های هوش مصنوعی شامل شبکه عصبی مصنوعی (ANN)، ماشین بردار پشتیبان (SVM) و جنگل تصادفی (RF) با استفاده از داده‌های تجربی آموزش دیده و اعتبارسنجی شدند. عملکرد این مدل‌ها با مدل‌های سنتی و نیمه‌تجربی از نظر ضریب تعیین (R^2)، ریشه میانگین مربع خطا (RMSE)، میانگین قدرمطلق خطا (MAE) و خطای میانگین بایاس (MBE) مقایسه شد. نتایج نشان داد که شبکه عصبی مصنوعی (ANN) با دقت پیش‌بینی بسیار بالا (R^2= 0.998, RMSE= 0.0656) بهترین عملکرد را داشته و از سایر مدل‌ها دارای دقت بیشتری است. روش SVM نیز قابلیت پیش‌بینی مناسبی نشان داد، در حالی‌که RF عملکردی اندکی ضعیف‌تر داشت. در میان مدل‌های نیمه‌تجربی، مدل میدیلی (Midilli) بهترین برازش را داشت، اما نسبت به مدل‌های مبتنی بر هوش مصنوعی دقت کمتری نشان داد. این یافته‌ها برتری روش‌های مبتنی بر هوش مصنوعی، به‌ویژه ANN، را در بهینه‌سازی فرآیند خشک‌کردن در صنعت غذا برجسته می‌سازد.

واژه‌های کلیدی: جنگل تصادفی، مدل‌های نیمه‌تجربی، مدل‌سازی هوش مصنوعی، نرخ خشک‌کردن، SVM

۱- بخش مهندسی بیوسیستم، دانشکده کشاورزی، دانشگاه شیراز، شیراز، ایران
(*- نویسنده مسئول: Email: moradih@shirazu.ac.ir)

https://doi.org/10.22067/jam.2025.92739.1358

Journal of Agricultural Machinery

Homepage: https://jame.um.ac.ir

Review Article
Vol. 16, No. 3, 2026, p. 599-624

A Review on the Physicomechanical Properties of Polysaccharide-Based Edible Films Incorporating Essential Oil-Loaded Pickering Emulsions

H. Mirzaee Moghaddam[1*], A. Nahalkar[1], A. Rajaei[1]

1- School of Agricultural Engineering, Shahrood University of Technology, Shahrood, Iran
(*- Corresponding Author Email: H_mirzaee@shahroodut.ac.ir)

Received: 13 February 2025
Revised: 19 April 2025
Accepted: 14 May 2025
Available Online: 06 September 2025

How to cite this article:
Mirzaee Moghaddam, H., Nahalkar, A., & Rajaei, A. (2026). A Review on the Physicomechanical Properties of Polysaccharide-Based Edible Films Incorporating Essential Oil-Loaded Pickering Emulsions. *Journal of Agricultural Machinery, 16*(3), 599-624. https://doi.org/10.22067/jam.2025.92162.1343

Abstract

Pickering emulsion-based edible biodegradable films have emerged as a promising sustainable alternative to conventional food packaging materials. These films exhibit enhanced mechanical properties, including tensile strength, flexibility, and water vapor barrier performance, which are critical for maintaining food integrity throughout storage and transportation. A key advancement in this field is the incorporation of essential oils into the emulsion matrix, which, despite their hydrophobic nature, significantly improve the functional and mechanical properties of polysaccharide-based films. This review examines the physicomechanical properties of polysaccharide-based edible biodegradable films incorporating Pickering emulsions, with a focus on flexibility, tensile strength, water vapor permeability, and moisture retention capacity. Furthermore, it explores the role of these films in extending food shelf life and analyzes how interactions between essential oils and polysaccharides influence their structural and barrier properties. Findings demonstrate that Pickering emulsions containing essential oils substantially enhance the mechanical and moisture barrier performance of edible biodegradable films. Solid stabilizing particles contribute to increased tensile strength, while essential oils improve flexibility—though excessive concentrations may compromise structural integrity. Additionally, these emulsions reduce water absorption and solubility, thereby improving film stability in humid conditions. Finally, this review examines the current challenges and identifies key research opportunities in the development of essential oil-loaded Pickering emulsion systems for polysaccharide-based biodegradable films, while outlining their potential for scalable industrial applications.

Keywords: Edible film, Essential oil, Packaging, Pickering emulsion

Introduction

The environmental impact of packaging materials, particularly plastics, poses a significant challenge to ecosystems. Conventional packaging contributes to pollution, often ending up in landfills or oceans, where it can take centuries to decompose. A sustainable alternative that is gaining attention is the use of edible biodegradable films (EBFs) as active packaging to replace traditional packaging methods (Eshagh, Abbaspour-Fard, Tabasizadeh, & Hosseini, 2019). EBFs are made from biodegradable materials such as starches, proteins, or other plant-based compounds, and serve as protective barriers for food products (Olawade, Wada, & Ige, 2024). This innovative approach not only reduces the environmental footprint associated with packaging waste but also offers additional benefits. EBFs can extend the shelf life of food, prevent spoilage, and enhance food safety (Rajesh & Subhashini, 2021).

Aromatic compounds are generally

Authors retain the copyright. This is an open access article distributed under Creative Commons Attribution 4.0 International License (CC BY 4.0).

https://doi.org/10.22067/jam.2025.92162.1343

classified into two main categories: simple aromatic hydrocarbons, such as benzene, toluene, and xylene, which are composed solely of carbon and hydrogen; and oxygen- or nitrogen-containing aromatic derivatives, such as phenols, flavonoids, alkaloids, and compounds found in essential oils (Mirzaee Moghaddam & Rajaei, 2021). Essential oils, extracted from the plants, not only have appealing fragrances but also exhibit significant physical and chemical properties. These oils are used as effective agents in improving the physicomechanical properties of Pickering emulsion-based edible biodegradable films (EBFs) (De Farias *et al.*, 2025). The incorporation of essential oils into these films can enhance properties such as tensile strength, flexibility, and resistance to water vapor permeability. Additionally, these compounds may positively influence the moisture content and solubility of the films (Ponnampalam *et al.*, 2022). In the context of food packaging, the use of essential oils in the form of Pickering emulsions represents an innovative approach to enhancing the mechanical properties of the films and improving their performance in food preservation (Pandita *et al.*, 2024). These films can serve as biodegradable alternatives to conventional packaging materials in the food industry, helping to maintain food quality while offering suitable physical and functional properties (Tajari, Sadrnia, & Hosseini, 2024).

Emulsions, which are colloidal dispersions of two immiscible liquids, play a significant role across various industries, with different types used in a wide range of products (Tan & McClements, 2021). One specific category is Pickering emulsions, which are stabilized by solid particles at the liquid–liquid interface. In the field of essential oils, Pickering emulsions have gained prominence due to their unique advantages. Essential oils, which are typically hydrophobic, can be difficult to incorporate uniformly into aqueous-based systems. Pickering emulsions overcome this limitation by providing a stable and efficient method for dispersing essential oils in water-based formulations. The solid particles at the interface prevent coalescence and contribute to the enhanced stability of the emulsion (Shahbazi, Rajaei, Tabatabaei, Mohsenifar, & Bodaghi, 2021).

In recent years, the development of EBFs has emerged as a groundbreaking solution to mitigate the environmental burden of conventional plastic packaging. However, a critical challenge remains: enhancing the physicomechanical and functional properties of EBFs to match or surpass those of synthetic polymers while maintaining biodegradability and food safety. Unlike conventional emulsion-based films, Pickering emulsions ensure superior stability, controlled release of bioactive compounds, and enhanced mechanical strength (Cheng *et al.*, 2024). Furthermore, the synergistic integration of essential oils not only improves tensile strength, flexibility, and barrier properties but also introduces antimicrobial and antioxidant functionalities, extending food shelf life more effectively than passive biodegradable films (Zhang, Jiang, Rhim, Cao, & Jiang, 2022). This review article explores the innovative approach of Pickering emulsions containing essential oils in polysaccharide-based biodegradable films to address key limitations in current biodegradable packaging. By optimizing the structural integrity and performance of EBFs through this novel emulsion system, this research provides a sustainable and versatile alternative to traditional packaging. Finally, a discussion is presented on current challenges and future opportunities in this field. These findings pave the way for next-generation smart packaging, where biodegradability, enhanced food preservation, and advanced material properties coexist, representing a significant leap forward in eco-friendly food packaging innovation.

Polysaccharides

Edible biodegradable films and coatings are composed of polymeric matrices made from edible biodegradable polymers, such as polysaccharides and proteins. These thin matrices are used in food packaging applications. Their primary functions include

preventing gas exchange, microbial spoilage, and the loss of moisture and solutes from food products, while preserving the physicochemical and sensory properties of the food Notably, these polymer matrices are designed to be consumed along with the packaged food, offering a unique interactive experience (Ogwu & Ogunsola, 2024).

The preparation of these matrices involves the use of edible biopolymers, many of which are derived from renewable resources or agro-industrial byproducts (Iñiguez-Moreno *et al.*, 2024). Due to their natural origin, these biopolymers are inherently biodegradable, contributing to their environmentally friendly profile. The adoption of such biopolymers presents a promising approach to reducing reliance on non-biodegradable plastic packaging materials. Additionally, the use of naturally sourced polymers provides a significant economic benefit to the food industry (Dutta & Sit, 2024).

In recent years, there has been a notable increase in the interest in polysaccharide-based EBFs and coatings. This growing interest can be attributed to the ease of chemically modifying polysaccharides, which offers researchers the flexibility to effectively tailor the properties of these matrices (Mirzaee Moghaddam, Tavakkoli, Minaee, & Rajaee, 2007). Polysaccharides are broadly classified into starch and non-starch categories, with non-starch polysaccharides exhibiting greater hydrophilicity (Li *et al.*, 2023). The incorporation of these hydrophilic polysaccharides into aqueous solutions increases viscosity, enabling tailored adjustments to the hardness, crispness, and adhesiveness of biopolymer matrices. Non-starch polysaccharides include cellulose and its derivatives, seaweed extracts, microbial fermentation gums, exudate gums, and seed gums (Sahraeian, Rashidinejad, & Niakousari, 2023). This section briefly discusses some of the polysaccharides that have been recently investigated by food scientists for the development of innovative EBFs and coatings (Anis, Pal, & Al-Zahrani, 2021). Some of the commonly used polysaccharides in edible films include the following.

Carrageenan

Carrageenan, a water-soluble polysaccharide extracted from red seaweeds, is a partially sulfated galactan that forms stable films due to its strong film-forming abilities, particularly in the kappa and iota types (Abdallah, Ghazouani, & Fattouch, 2024). These polysaccharides create a three-dimensional network through physical interactions, leading to gelation and stable film formation. Carrageenan-based EBFs are widely used in food packaging to prevent gas exchange, microbial spoilage, and moisture loss (Kokkuvayil Ramadas, Rhim, & Roy, 2024). While refined kappa-carrageenan can be costly, semi-refined versions provide a more cost-effective alternative, demonstrating both the versatility and economic potential of carrageenan-based films (Ciancia, Matulewicz, & Tuvikene, 2020).

Chitosan

Chitosan, derived from chitin found in the exoskeletons of crustaceans, is a biopolymer with significant potential for use in EBFs for food packaging (Malm *et al.*, 2021; Heydarian, Ahmadi, Dashti, & Normohammadi, 2022). It possesses antimicrobial properties, is biodegradable, and exhibits excellent film-forming ability. The cationic nature of chitosan enables it to interact with negatively charged components such as proteins and nucleic acids, enhancing its antimicrobial effectiveness (Nasaj *et al.*, 2024). This makes chitosan particularly effective in extending the shelf life of food by inhibiting microbial growth. Additionally, its biodegradability contributes to sustainable packaging solutions, positioning chitosan as a promising material for both food preservation and environmentally friendly packaging (Priyadarshi & Rhim, 2020).

Alginate

Alginate, a polysaccharide derived from brown seaweeds, is widely used in EBFs due to its biocompatibility, gel-forming ability, and

excellent film-forming properties (Bukhari, Rawi, Hassan, Saharudin, & Kassim, 2023). Alginate-based EBFs are flexible, transparent, and offer strong oxygen barrier capabilities, contributing to food preservation. The ability of alginate to form gels in the presence of calcium ions enhances the mechanical strength of the films (Eslami, Elkoun, Robert, & Adjallé, 2023). These films are effective in controlling moisture migration, preventing dehydration, and maintaining food quality. Due to its biodegradability, alginate is considered a sustainable material, making it a promising choice for food packaging applications (Jayakody, Vanniarachchy, & Wijesekara, 2022).

Cellulose derivatives

Cellulosic derivatives, such as carboxymethyl cellulose, hydroxypropyl cellulose, methylcellulose, hydroxypropyl methylcellulose, and microcrystalline cellulose, are key materials in EBFs for food packaging (Yildirim-Yalcin, Tornuk, & Toker, 2022). These derivatives enhance viscosity, improve stability, and modify film properties such as thickness and mechanical strength. Hydroxypropyl methylcellulose, in particular, is well known for its excellent film-forming ability. The use of these materials in EBFs supports sustainable packaging while enabling the customization of film properties to meet the specific requirements of different food products (Y. Liu *et al.*, 2021).

Agar

Agar, derived from seaweed, is widely used in EBFs due to its unique gelling properties. It forms stable films and coatings that serve as effective barriers against gas exchange, microbial spoilage, and moisture loss, thereby helping to preserve food and extend shelf life (Fadiji, Rashvand, Daramola, & Iwarere, 2023). Agar solidifies at low temperatures, making it ideal for film formation without compromising food quality. Its natural origin and biodegradability align with the growing demand for sustainable packaging, and food scientists are increasingly exploring its potential to enhance food preservation and packaging practices (Mostafavi & Zaeim, 2020).

Starch

Starch, a polysaccharide derived from plants, is widely used in the production of EBFs for food packaging. It is known for its film-forming ability, biodegradability, and versatility in modifying film properties (Pei *et al.*, 2024). Starch-based EBFs are flexible, transparent, and offer moisture barrier properties, which help maintain food quality. The film-forming capability of starch can be enhanced through crosslinking or blending with other materials, such as plasticizers or natural polymers (Jayarathna, Andersson, & Andersson, 2022). Starch films are particularly effective in controlling moisture migration and preventing dehydration, making them suitable for packaging a variety of food products. Given its renewable origin and biodegradability, starch is considered a promising candidate for sustainable food packaging solutions (Chen *et al.*, 2023).

Konjac glucomannan

Konjac glucomannan, derived from the konjac plant, is widely used in EBFs due to its thickening and gelling properties. It forms stable films that serve as effective barriers against moisture loss, microbial spoilage, and gas exchange, thereby enhancing food preservation (Moeini, Pedram, Fattahi, Cerruti, & Santagata, 2022). These films are flexible, transparent, and biodegradable, making them a sustainable packaging option. The unique properties of konjac glucomannan offer significant potential for enhancing food preservation and packaging practices in the food industry (Ni *et al.*, 2021).

Essential oils

Essential oils play a crucial role in the food industry due to their ability to enhance flavors, aromas, and overall sensory experiences. These compounds are widely used in various food and beverage products, offering unique and natural profiles that cannot be achieved

through other means. In the food industry, essential oils are categorized based on their intended use (Yu, 2025).

Table 1- Origin of the plant or herb, the plant part utilized, and the primary constituents of essential oils

Essential oil	Source plant/herb	Part of the plant	Major components	Reference
Lavender	*Lavandula angustifolia*	Flowers	Linalool, linalyl acetate	(Rusanov, Vassileva, Rusanova, & Atanassov, 2023)
Peppermint	*Mentha piperita*	Leaves	Menthol, menthone	(Beigi, Torki-Harchegani, & Ghasemi Pirbalouti, 2018)
Lemon	*Citrus limon*	Peel	Limonene, β-pinene	(Akarca & Sevik, 2021)
Tea Tree	*Melaleuca alternifolia*	Leaves	Terpinen-4-ol, γ-terpinene	(Brun, Bernabè, Filippini, & Piovan, 2019)
Eucalyptus	*Eucalyptus globulus*	Leaves	Eucalyptol, α-pinene	(Almas, Innocent, Machumi, & Kisinza, 2021)
Rosemary	*Rosmarinus officinalis*	Leaves	A-Pinene, camphor	(Katar *et al.*, 2019)
Cinnamon	*Cinnamomum verum*	Bark tree	Cinnamaldehyde, eugenol, benzaldehyde, linalool, various terpenes	(Gotmare & Tambe, 2019)
Oregano	*Origanum vulgare*	Leaves	Carvacrol, thymol, p-cymene, γ-terpinene, β-caryophyllene	(Kosakowska *et al.*, 2021)
Clove	*Syzygium aromaticum*	Flowers	Eugenol, eugenyl acetate, caryophyllene, various other sesquiterpenes and aldehydes	(Yadav, Gupta, Bharti, & Yogi, 2020)
Lemon Myrtle	*Backhousia citriodora*	Leaves	Citral (a compound that gives it a lemony scent), linalool, myrcene, citronellal	(Southwell, 2021)
Perilla	*Perilla frutescens*	Leaves	Perillaldehyde, limonene, caryophyllene, myrcene	(Ahmed & Al-Zubaidy, 2020)
Basil	*Ocimum basilicum*	Leaves	Linalool, methyl chavicol (also known as estragole), eugenol, cineole, various other monoterpenes and sesquiterpenes	(Dhama *et al.*, 2023)
Ginger	*Zingiber officinale*	Rhizomes of the ginger plant	Gingerol, zingiberene, β-sesquiphellandrene, various other sesquiterpenes and monoterpenes	(Akshitha, Umesha, Leela, Shivakumar, & Prasath, 2020)
Lemongrass	*Cymbopogon citratus*	Leaves	Citronellal, geranial (also known as citral), limonene, myrcene	(Kumoro, Wardhani, Retnowati, & Haryani, 2021)
Thyme	*Thymus vulgaris*	Leaves and Flowers	Thymol, carvacrol, p-cymene, linalool, various terpenes	(Wesolowska & Jadczak, 2019)
Grapefruit	*Rutaceae*	Peel	Limonene, myrcene, α-pinene, other terpenes	(Molnar, Gašo-Sokač, Komar, Kovač, & Bušić, 2024)
Tangerine	*Rutaceae*	Peel	Limonene, myrcene, γ-terpinene, α-pinene, other terpenes	(Ngo, Tran, Nguyen, & Mai, 2020)
Cumin	*Cuminum cyminum*	Seeds	Cuminaldehyde, γ-terpinene, β-pinene, cymene, various other terpenes	(Tavakoli-Rouzbehani *et al.*, 2021)
Cardamom	*Elettaria cardamomum*	Seeds	A-terpinyl acetate, 1,8-cineole (eucalyptol), limonene, sabinene, various other terpenes	(Alam, Hussain, Ahmad, Ali, & Khan, 2023)
Ho Wood	*Cinnamomum camphora*	Wood	Camphor, limonene, cineole	(Kanyal *et al.*, 2023)
Marjoram	*Origanum majorana*	Leaves and Flowers	Terpinen-4-ol, γ-terpinene, cis-sabinene hydrate, linalool, other terpenes	(Prerna & Vasudeva, 2016)

They may function as natural flavorings, enhancing or mimicking specific flavors in food products. Additionally, essential oils can serve as food additives, providing antimicrobial properties or acting as antioxidants to extend the shelf life of food (Upadhye, Mujawar, & Kashte, 2025). Some essential oils are also incorporated into food

and beverage packaging materials to impart desirable aromas and prevent the transfer of unwanted flavors (Mirzaee Moghaddam & Rajaei, 2021). The extraction of essential oils for the food industry follows similar methods as those used in other industries (Bolouri *et al.*, 2022). Steam distillation is commonly employed, ensuring that the essential oils retain their natural flavors and aromas while removing any unwanted components. Cold-press extraction is also utilized for citrus fruits, where the oils are obtained by mechanically pressing the rinds. Solvent extraction is less common in the food industry but may be used for specific applications (Giacometti *et al.*, 2018). Table 1 presents the essential oils and their properties.

Pickering emulsion

Emulsions play a crucial role in various industries and are primarily classified based on the type of emulsifying agent used, resulting in two main categories: conventional emulsions containing emulsifiers and Pickering emulsions (de Carvalho-Guimarães *et al.*, 2022). Emulsions are colloidal systems consisting of two immiscible liquids, typically oil and water, stabilized either by emulsifying agents or solid particles. In conventional emulsions, emulsifiers reduce the interfacial tension between the immiscible phases, thereby promoting stability (Nazari, Rajaei, & Mirzaee Moghaddam, 2025). In contrast, Pickering emulsions are stabilized by solid particles, such as colloidal particles or nanoparticles. Several factors influence the stability of Pickering emulsions, including particle concentration, size, and surface properties (Chevalier & Bolzinger, 2013). Higher particle concentrations generally enhance stability, while smaller particle sizes improve stabilization due to increased surface area. Moreover, the wettability of the particles and their interaction with the liquid phases also affect stability (Yang *et al.*, 2023). More hydrophilic particles tend to stabilize oil-in-water emulsions more effectively, while more hydrophobic particles are preferable for water-in-oil emulsions (Tabatabaei *et al.*, 2022).

The use of nanoparticles in enhancing the stability of Pickering emulsions

The use of nanoparticles in the stability of Pickering emulsions has emerged as a key strategy for enhancing their performance in various applications. Nanoparticles, typically made from inorganic materials, organic polymers, or biopolymers, act as highly effective stabilizers by adsorbing at the oil-water interface, where they reduce interfacial tension and prevent coalescence of droplets (Lashari *et al.*, 2022). Their small size and high surface area provide better interaction with the emulsion phases, ensuring more stable and long-lasting emulsions. By controlling the size, surface charge, and composition of these nanoparticles, it is possible to fine-tune the stability of Pickering emulsions under different environmental conditions, such as variations in pH, temperature, and ionic strength (Kour *et al.*, 2024). Furthermore, the incorporation of nanoparticles can enhance the emulsions' mechanical strength, making them more resistant to destabilization and improving their performance in food, pharmaceutical, and cosmetic formulations (Shahbazi *et al.*, 2021). Ultimately, the ability of nanoparticles to provide both physical and chemical stabilization makes them invaluable in the development of robust Pickering emulsions with improved shelf-life and functional properties (Mirzaee Moghaddam, Khoshtaghaza, Salimi, & Barzegar, 2014).

Fundamentals of Pickering emulsion-based EBF

Pickering emulsions represent a class of emulsions stabilized by solid particles rather than traditional surfactants. In the context of EBF, these emulsions utilize the ability of solid particles to adsorb at the oil–water interface, thereby preventing droplet coalescence and enhancing overall emulsion stability (Tabatabaei *et al.*, 2022). The solid stabilizers, which may include natural or synthetic materials such as cellulose, starch, silica, and clays, play a pivotal role not only in stabilizing the emulsion but also in reinforcing the mechanical properties of the resultant EBF

(Cheng *et al.*, 2024). These solid stabilizers are advantageous due to their biocompatibility and their ability to impart desired structural integrity to the films, which is particularly important for applications in food packaging. The incorporation of Pickering emulsions into EBF has been shown to enhance several critical physicomechanical properties, including tensile strength, flexibility, and water vapor permeability (Niro, Medeiros, Freitas, & Azeredo, 2021).

The solid particles contribute to the formation of a more cohesive and mechanically robust film structure, improving its resistance to mechanical stress while maintaining the flexibility required for practical use. Additionally, these emulsions can significantly improve the barrier properties of the films, such as moisture retention, which is essential for controlling moisture release and extending the shelf life of packaged food products. The ability to control moisture migration within the film is particularly important for preventing spoilage and maintaining the quality of food items. The integration of Pickering emulsions into EBF not only addresses the challenges associated with incorporating essential oils but also facilitates the development of films with tailored properties for specific food packaging needs. These films are not only biodegradable and environmentally friendly but also offer a promising alternative to conventional synthetic packaging materials, aligning with the growing demand for sustainable and natural food packaging solutions (Hussain, Akhter, & Maktedar, 2024).

Synthesis methods

EBF are thin, flexible films usually composed of biopolymers such as proteins, polysaccharides, or lipids, which can be derived from plant and animal sources. Film ingredients are carefully selected to meet specific performance and barrier requirements for various food applications. Common methods for film preparation include solution casting, extrusion, and compression molding. In solution casting, the film-forming materials are dissolved in a solvent, and then the solution is cast in a thin layer and dried to form the film (Borbolla-Jiménez *et al.*, 2023). Extrusion involves processing a paste-like mixture through a die to create a continuous sheet, while compression molding compresses the material into a film using heat and pressure (Seoane-Viaño, Januskaite, Alvarez-Lorenzo, Basit, & Goyanes, 2021).

The preparation of Pickering emulsions containing encapsulated essential oils for application onto edible films involves a sophisticated process that merges the principles of emulsion science and colloid chemistry (Sharkawy, Barreiro, & Rodrigues, 2020). In this innovative approach, solid particles, often in the form of colloidal materials or nanoparticles, play a pivotal role as stabilizers, forming a protective interfacial layer around oil droplets (Jiang, Sheng, & Ngai, 2020). To initiate the emulsification process, essential oils, renowned for their aromatic and functional properties, are carefully chosen and incorporated into the oil phase. These oil droplets are then dispersed in an aqueous phase containing the selected stabilizing particles. The emulsification process can be facilitated through mechanical methods such as homogenization or ultrasonication (Figure 1). Once the Pickering emulsion is formed, it can be applied to food films, with the stabilized droplets acting as carriers for the encapsulated essential oils. The choice of solid particles, their concentration, and their surface properties are critical factors influencing the stability and functionality of the resulting emulsion and, consequently, the performance of the food film. This innovative methodology not only addresses the challenges associated with essential oil stability but also opens up avenues for creating functional and sustainable food packaging materials, contributing to the broader efforts in enhancing the quality and shelf life of food products.

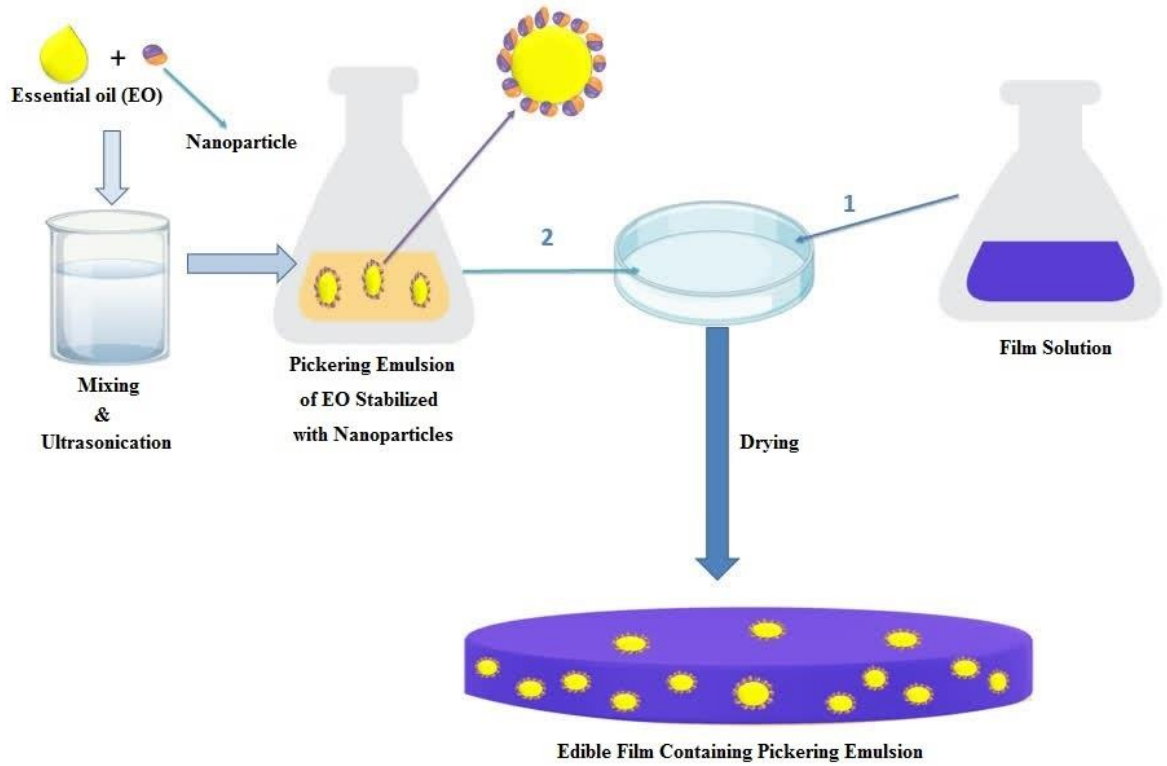

Fig. 1. Schematic of the process of producing EBF containing essential oil Pickering emulsions

Incorporation of essential oils in Pickering emulsion-based EBF

The incorporation of essential oils into Pickering emulsion-based EBF represents a promising strategy for enhancing the physicomechanical properties of these films. Pickering emulsions, which are stabilized by solid particles at the oil-water interface, offer significant advantages in terms of reinforcing the structural integrity and stability of EBF Unlike conventional emulsions that rely on surfactants, Pickering emulsions create a more robust network, providing greater resistance to droplet coalescence and preserving the structural and mechanical properties of the film matrix (Zhang *et al.*, 2024). This unique stabilization mechanism is crucial in preventing the loss of essential oils, which are prone to volatilization, thereby improving the overall functional performance of EBF. The addition of essential oils to Pickering emulsions can significantly influence the physicomechanical properties of the resulting EBF (Amrani, Pourshamohammad, Tabibiazar, Hamishehkar, & Mahmoudzadeh, 2023).

In particular, the tensile strength and flexibility of the films are affected by the type and concentration of essential oils. The solid particles used to stabilize the emulsion also play a critical role in enhancing the mechanical strength of the films, as they help create a more cohesive and uniform structure (Cai *et al.*, 2023). This improvement is especially important in the context of EBF, which must maintain their integrity under mechanical stress, such as stretching or bending. Additionally, the films must remain flexible enough to allow for practical applications in food packaging (Low, Siva, Ho, Chan, & Tey, 2020).

Water vapor permeability is another key property influenced by the incorporation of essential oils into Pickering emulsion-based EBF. Essential oils, when incorporated into the film matrix, can reduce the permeability of the films to water vapor, which is crucial for extending the shelf life of moisture-sensitive food products. This improved barrier property helps preserve the quality of the food by

limiting moisture loss (Almasi, Azizi, & Amjadi, 2020). Furthermore, the hydrophobic nature of many essential oils contributes to the water-resistant characteristics of the films, providing an additional layer of protection for food items that require moisture control (Low *et al.*, 2020). Solubility is another critical aspect that is affected by the incorporation of essential oils into the films. The solubility properties of the films influence their performance in various environmental conditions.

By controlling the solubility and dissolution rates, the films can be tailored to release essential oils in a controlled manner, which is beneficial for active food packaging applications (Amrani *et al.*, 2023). The controlled release of bioactive components, such as the antimicrobial and antioxidant properties of the essential oils, can be optimized by adjusting the concentration of solid stabilizers and the oil phase composition (Jafarzadeh & Jafari, 2021). Overall, the incorporation of essential oils into Pickering emulsion-based EBF offers a versatile approach to enhancing the physicomechanical properties of these films. By improving mechanical strength, flexibility, and water vapor permeability, these films not only provide functional benefits for food preservation but also contribute to the development of more sustainable and bioactive packaging solutions. The potential for controlled release of bioactive components further aligns with the growing demand for natural, biodegradable, and functional food packaging materials that are capable of preserving food quality while reducing environmental impact (Nilsen-Nygaard *et al.*, 2021).

Impact of Pickering emulsions containing essential oils on physicomechanical properties of EBF

The incorporation of essential oils into EBF, particularly those based on Pickering emulsions, significantly influences their physicomechanical properties, which are critical for performance in food packaging applications. Essential oils, rich in bioactive compounds such as terpenes, aldehydes, and phenolic compounds, interact with the polymeric matrices of EBF, thereby altering their mechanical, structural, and barrier properties (Versino *et al.*, 2023). These changes depend on various factors, including the type and concentration of the essential oils, the composition of the matrix, and the method of incorporation.

Physical properties affecting the effectiveness of EBFs

Moisture of EBF

Moisture absorption and retention are fundamental properties for EBF, as they directly affect the shelf life and stability of food products. The addition of essential oils can influence the hygroscopic nature of the films. Generally, essential oils, especially those with hydrophobic properties, reduce the moisture absorption capacity of the films. This reduction in moisture uptake is beneficial for food packaging, as it prevents the film from absorbing excess moisture from the surrounding environment, which could lead to the deterioration of food quality (Mirzaee Moghaddam, Khoshtaghaza, Salimi, & Barzegar, 2014).

Moisture in EBF refers to the amount of water present within the film's structure. It is a critical parameter influencing the mechanical, sensory, and functional properties of the film. Moisture content is typically expressed as a percentage of the film's total weight or in terms of thermal properties. The process of moisture release or absorption can have significant effects on the behavioral and functional characteristics of EBF (Zoghi, Khosravi-Darani, & Mohammadi, 2020). The moisture content (MC) of a film is commonly calculated using the equation (1):

$$W\% = \frac{W_0 - W_1}{W_0} \times 100 \quad (1)$$

where, W_0: The initial weight of biodegradable film, and W_1: The weight of the film after drying.

The incorporation of Pickering emulsion containing essential oils into EBF can influence its moisture content. Essential oils

(EOs), known for their hydrophobic nature, tend to reduce the overall hydrophilicity of the film. This reduction in hydrophilicity affects the interaction of water molecules with the polymer chains, leading to a decrease in moisture content (Cui *et al.*, 2023).

Solubility of EBF

Solubility is a critical property of EBF that determines its ability to dissolve or disperse when exposed to environmental conditions, particularly in the presence of water. The solubility of EBF is influenced by its composition and the interactions within the polymer matrix. Essential oils, when incorporated into the film, can alter solubility behavior by interacting with the polymer chains. These interactions can reduce the film's solubility, making it more resistant to dissolution when exposed to moisture or aqueous environments. This reduction in solubility can be beneficial in food packaging applications, where films are designed to maintain their structural integrity and functionality under varying humidity or moisture conditions. By adjusting the concentration of essential oils, the solubility of EBF can be precisely controlled, ensuring the desired performance in food preservation and packaging (Nahalkar, Rajaei, & Mirzaee Moghaddam, 2025a). Dissolution in the context of EBF refers to the process of breaking down and dispersing the film's components in a solvent or liquid medium. It is a critical aspect influencing the release of bioactive compounds, flavor agents, or other additives incorporated into the film matrix. The rate and extent of dissolution are key factors in determining the functionality and performance of EBF in various applications (Díaz-Montes & Castro-Muñoz, 2021). The dissolution rate (DR) of a biodegradable film can be expressed using equation (2):

$$\text{Ws}\% = \frac{W_1 - W_2}{w_1} \times 100 \quad (2)$$

where, W_1: Initial weight of dried EBF, and W_2: Weight of dried film after immersion.

The inclusion of Pickering emulsion containing essential oils in EBF can significantly influence its dissolution characteristics. Essential oils, being inherently hydrophobic, may slow down the dissolution process due to their limited affinity for water (Barradas & de Holanda e Silva, 2021).

Water vapor permeability of EBF

Water vapor permeability (WVP) is a critical property for EBF, as it determines the rate at which moisture can pass through the film. The incorporation of essential oils into Pickering emulsion-based EBF can influence WVP, depending on the type and concentration of oils used. Essential oils, due to their hydrophobic nature, generally reduce the water vapor permeability of films. This is especially important for food packaging applications, where preventing excessive moisture exchange between the film and the product is essential for extending shelf life and preserving the quality of the food. The reduction in WVP is achieved through the hydrophobic interactions between the essential oils and the polymer matrix, which create a more compact and less permeable film structure (Nahalkar, Rajaei, & Mirzaee Moghaddam, 2025b). The measurement of WVP provides insights into the barrier properties of the film, affecting its suitability for various applications, especially in food packaging (Hammam, 2019). The WVP of a biodegradable film can be calculated using the equation (3):

$$\text{WVP} = \frac{\Delta W \times FT}{S \times \Delta p} \quad (3)$$

where, ΔW is the weight reduction of the vial (g), FT is the thickness (mm), S is the area (m^2), and Δp is the pressure difference (kPa). The incorporation of Pickering emulsion containing essential oils in EBF can alter its water vapor permeability. Essential oils, known for their hydrophobic nature, can enhance the hydrophobicity of the film matrix, potentially reducing water vapor transmission (Zhang *et al.*, 2022).

Table 2 presents research findings on the changes in solubility, moisture, and water vapor permeability of EBF in response to Pickering emulsions containing essential oils.

Table 2- Some recent studies on the effect of Pickering emulsion containing essential oils on moisture, solubility, and water vapor permeability of EBF

Biodegradable film	Essential oil	Pickering particle	Application	Analyzed food product	Reference
Chitosan/gelatin	Cinnamon	Zein nanoparticles	Reducing water vapor permeability	-	(Fan *et al.*, 2023)
Chitosan	Cinnamon	Cellulose nanocrystal	Improving film resistance to water	Pork meat	(J. Liu *et al.*, 2022)
Konjac glucomannan	Oregano	Zein–pectin nanoparticle	Reducing water vapor permeability	_	(Zhang *et al.*, 2022)
Carrageenan/agar	Tea tree	Nanocellulose fibers	Slightly improving the water vapor barrier, water resistance	_	(Roy & Rhim, 2021)
Chayote tuber starch	Cinnamon	Zein-pectin nanoparticle	Reducing the moisture content of EBF, reducing water vapor permeability of EBF	Ground beef	(Wu *et al.*, 2023)
Chitosan	Lemon myrtle	Alkali lignin	Resistance to moisture	_	(Liu, Swift, Tollemache, Perera, & Kilmartin, 2022)
Pearl millet starch	Clove bud	Kudzu cellulose nanocrystals	Water barrier	_	(Bangar, Whiteside, Dunno, Cavender, & Dawson, 2023)
Anthocyanidin/chitosan	Cinnamon-perilla	Collagen	Reducing water vapor permeability, increased hydrophobicity	Chilled fish fillet	(Zhao, Guan, Zhou, Lao, & Cai, 2022)
Konjac glucomannan and Pullulan	Tea tree	Cellulose nanofibrils	Improving water resistance	_	(Bu, Huang, *et al.*, 2022)
Konjac glucomannan	Corn germ oil-oregano essential oil	Zein-pectin nanoparticle	Water resistance	_	(Du *et al.*, 2023)
Sodium alginate	Lemongrass	Cellulose nanofibers	Improving water repellency	_	(Wardana, Wigati, Van, Tanaka, & Tanaka, 2023)
Chitosan	Clove	Zein and sodium caseinate	Reducing water vapor permeability	_	(Hua *et al.*, 2021)
Konjac glucomannan	Oregano	Chitin nanocrystal	Water vapor permeability firstly decreased and then increased	_	(Xu *et al.*, 2023)
Chitosan	Grapefruit	Amphiphilic octenyl succinic anhydride konjac glucomannan	Improved water resistance and water vapor permeability	_	(Bu, Sun, *et al.*, 2022)
Tapioca starch/polyvinyl alcohol	Thymus vulgaris	Cellulose nanocrystals	Lower water vapor transmission coefficient	Fish fillets	(Guo *et al.*, 2024)
Starch	Ginger	Tempo-oxidized cellulose nanocrystals	Reducing water vapor permeability	Tomato	(Chen *et al.*, 2023)
Hydroxypropyl methyl cellulose	Cinnamon	Zein/carboxymethyl tamarind gum	Reducing water vapor permeability	Cherry tomatoes	(Yao *et al.*, 2023)
Persian gum-Gelatin	Thyme	Persian gum-Gelatin	The reduction of films' permeability to water vapor and moisture enhances their functionality	Fish fillets	(Sayadi, Abedi, & Oliyaei, 2025)
Chitosan/silk fibroin (CS/SF)	Cinnamon essential oil	Cellulose nanocrystals	Reduced the water vapor transmission rate	-	(Wang *et al.*, 2024)
Pectin (PEC) and konjac glucomannan (KGM)	Clove essential oil	Cellulose nanocrystals	Reduced permeability to water vapor	Grape	(Wang *et al.*, 2024)

The moisture, solubility, and WVP properties of EBF incorporating Pickering emulsions containing essential oils play a crucial role in determining their effectiveness

for active food packaging. The presence of Pickering emulsions generally reduces moisture absorption, as the solid stabilizing particles, along with the hydrophobic nature of essential oils, create a protective barrier that limits water penetration and prevents excessive swelling of the film. Furthermore, the solubility of the film in water decreases due to the nanoemulsion structure and the water-repellent characteristics of essential oils, which hinder direct interaction between water molecules and the film matrix, thereby enhancing its mechanical stability in humid environments. Additionally, WVP, a key factor in controlling moisture transfer in packaged foods, is significantly reduced in films containing Pickering emulsions, as the stabilizing particles act as a physical barrier that complicates the diffusion path of water vapor molecules, while the presence of essential oils decreases surface polarity, further restricting moisture transmission. The extent of these effects depends on various factors such as the type and concentration of essential oils, the size and distribution of stabilizing particles, and the composition of the biopolymeric matrix, all of which can be optimized to enhance the barrier properties and functional performance of the film in food packaging applications (Bangar *et al.*, 2023; Du *et al.*, 2023; Fan *et al.*, 2023; Hua *et al.*, 2021; Roy & Rhim, 2021).

Effects on mechanical properties of EBF

Mechanical properties of EBF, including tensile strength, elongation, and Young's modulus, play a crucial role in their functionality and performance as food packaging materials. The incorporation of emulsion-based Pickering emulsion containing essential oils can have significant effects on the mechanical properties of these films. Tensile strength is a measure of a film's resistance to breaking under tension, while elongation represents the ability of the film to stretch without breaking (Javadi Farsani, Mirzaee Moghaddam, & Rajaei Najafabadi, 2023). Young's modulus, also known as the elastic modulus, is an indicator of a film's stiffness and its ability to return to its original shape after deformation (Mirzaee Moghaddam, 2019). These mechanical properties are important for ensuring the integrity and durability of the EBF during storage, handling, and transportation.

Table 3 presents research findings on the mechanical changes in EBF in response to Pickering emulsions containing essential oils. When essential oils are incorporated into EBF through emulsion-based Pickering, they can influence the film's mechanical properties in several ways. Firstly, the presence of the emulsion droplets within the film matrix can affect the film's microstructure and morphology, leading to changes in its mechanical behavior. The dispersed droplets act as physical barriers, altering the overall film structure and potentially influencing the interaction between polymer chains (Farajpour, Djomeh, Moeini, Tavakolipour, & Safayan, 2020). Secondly, the essential oils themselves can interact with the film matrix, affecting its mechanical properties. Essential oils are known to have plasticizing effects on polymers, reducing their rigidity and increasing their flexibility (Abedi, Sayadi, & Oliyaei, 2024). This plasticizing effect can lead to an increase in elongation and a decrease in tensile strength. However, the specific impact of essential oils on the mechanical properties of the films can vary depending on several factors such as the type of oil used, its concentration, and the compatibility between the oil and the film matrix (Mirzaee Moghaddam & Rajaei, 2021).

Incorporating emulsion-based Pickering particles into EBF can also offer advantages in terms of mechanical properties. The emulsion droplets act as reinforcing agents, enhancing the film's mechanical strength and stiffness. The droplets can improve the interfacial adhesion between polymer chains, resulting in a stronger film structure. This reinforcement effect can lead to increased tensile strength and Young's modulus (Mirzaee Moghaddam *et al.*, 2007).

Table 3- Some recent studies on the effect of Pickering emulsions containing essential oils on the mechanical properties of EBF

Biodegradable film	Essential oil	Pickering particle	Application	Analyzed food product	Reference
Chitosan	Cinnamon	Zein nanoparticles	Improvement of mechanical properties	–	(Fan *et al.*, 2023)
Chitosan	Cinnamon	Cellulose nanocrystal	Reduces its mechanical strength	Pork meat	(Liu *et al.*, 2022)
Konjac glucomannan	Oregano	Zein–pectin nanoparticle	Increased the elongation at break	–	(Zhang *et al.*, 2022)
Carrageenan/agar	Tea tree	Nanocellulose fibers	Maintained mechanical strength with slightly improved flexibility	–	(Roy & Rhim, 2021)
Chayote tuber starch	Cinnamon	Zein-pectin nanoparticle	Increased elongation at break and reduced tensile strength	Ground beef	(Wu *et al.*, 2023)
Chitosan	Lemon myrtle	Alkali lignin	Resisted mechanical stress	–	(Liu *et al.*, 2022)
Potato starch and polyvinyl alcohol	Clove	Clove essential oil	Reduced tensile strength and elongation percentage	Pork meat	(Zhao *et al.*, 2023)
Pearl millet starch	Clove bud	Kudzu cellulose nanocrystals	Improved the mechanical resistance of the film	Chilled fish fillet	(Bangar *et al.*, 2023)
Konjac glucomannan and Pullulan	Tea tree	Cellulose nanofibrils	Improving the mechanical properties of films	–	(Bu, Huang, *et al.*, 2022)
Gelatin/agar	Clove	Copper-modified zinc oxide nanoparticles	Improving the mechanical properties of films	Pork meat	(Roy, Priyadarshi, & Rhim, 2022)
Carboxymethyl cellulose/polyvinyl alcohol	Ginger	Ginger essential oil	Increased elongation at break and reduced tensile strength	Bread	(Fasihi, Noshirvani, & Hashemi, 2023)
Konjac glucomannan	Corn germ oil-oregano essential oil	Zein-pectin nanoparticle	Highest tensile strength	–	(Du *et al.*, 2023)
Chitosan	Clove	Zein and sodium caseinate	Increased tensile strength and break elongation	–	(Hua *et al.*, 2021)
Konjac glucomannan	Oregano	Chitin nanocrystal	Reduced the mechanical properties of the films	–	(Xu *et al.*, 2023)
Chitosan	Grapefruit	Amphiphilic octenyl succinic anhydride konjac glucomannan	Improved mechanical strength	–	(Bu, Sun, *et al.*, 2022)
Tapioca starch /polyvinyl alcohol	Thymus vulgaris	Cellulose nanocrystals	Enhanced the film's elongation at break	Fish fillets	(Guo *et al.*, 2024)
Starch	Ginger	Tempo-oxidized cellulose nanocrystals	Improved tensile strength	Tomato	(Chen *et al.*, 2023)
Persian gum- Gelatin	Thyme	Persian gum- Gelatin	Reduced the tensile strength, and elongation of the films	Fish fillets	(Sayadi *et al.*, 2025)
Carrageenan	Oregano essential oil	Nanocellulose	The tensile strength of the films significantly decreased, whereas the elongation at break increased	-	(Amanda, Ismadi, Ningrum, Nabila, & Prasetyo, 2024)
Chitosan/silk fibroin (CS/SF)	Cinnamon essential oil	Cellulose nanocrystals	Increasing the mechanical stability of films	-	(Wang *et al.*, 2024)
Pectin (PEC) and konjac glucomannan (KGM)	Clove essential oil	Cellulose nanocrystals	Highest tensile strength	Grape	(Wang *et al.*, 2025)

It should be noted that achieving the desired mechanical properties in EBF with emulsion-based Pickering emulsions requires careful formulation and optimization. The choice of

emulsion stabilizers, the concentration of essential oils, and the processing conditions play vital roles in determining the mechanical performance of the films (Moghaddam & Rajaei, 2021).

In general, the incorporation of Pickering emulsions can significantly influence the film's tensile strength, elongation at break, and flexibility, depending on the nature and concentration of stabilizing particles and essential oils. The presence of solid stabilizing particles enhances the mechanical strength of the film by reinforcing the polymer matrix and creating a more cohesive structure, while the encapsulated essential oils may act as plasticizers, potentially increasing flexibility but reducing tensile strength if present in high concentrations. Additionally, the distribution and size of emulsion droplets within the film matrix can impact its homogeneity and resistance to mechanical stress. The interactions between the biopolymer network, stabilizing particles, and essential oils determine the overall mechanical behavior, which can be fine-tuned to achieve the desired balance between strength, flexibility, and durability. By optimizing these parameters, Pickering emulsion-based films can be engineered to provide superior mechanical performance, ensuring their suitability for various food packaging applications while maintaining their functional and protective properties (Bangar *et al.*, 2023; Du *et al.*, 2023; Fan *et al.*, 2023; Guo *et al.*, 2024; Hua *et al.*, 2021; Roy & Rhim, 2021; Xu *et al.*, 2023).

Possible uses in food packaging

The incorporation of Pickering emulsion-based EBF containing essential oils into food packaging presents significant advancements in extending shelf life and maintaining product quality. These films offer a biodegradable and functional alternative to conventional synthetic packaging by providing enhanced barrier properties against moisture transfer and mechanical degradation (Yue *et al.*, 2024). The incorporation of essential oils into the emulsion system enhances the physicomechanical characteristics of the films while also boosting their capacity to manage water vapor permeability and solubility, thus guaranteeing optimal functionality across diverse storage environments. One of the primary applications of these films is in the packaging of perishable food products, where moisture retention and controlled gas exchange are critical for preventing spoilage (Deng *et al.*, 2024). The reduced water vapor permeability of these films, due to the incorporation of hydrophobic essential oils, minimizes excessive moisture transfer, thereby preventing undesirable textural changes in food products such as bakery items, dairy, and fresh produce. Additionally, their improved mechanical strength enhances the integrity of the packaging, making it more resistant to physical stress during transportation and storage (Zomorodian, Javanshir, Shariatifar, & Rostamnia, 2023).

Beyond primary food packaging, these films can be utilized as protective coatings for fresh-cut fruits, vegetables, and processed meat products (Gupta, Lall, Kumar, Patil, & Gaikwad, 2024). By forming a uniform and stable edible barrier, they regulate moisture loss, reduce dehydration rates, and maintain product freshness for extended periods. Moreover, their controlled solubility ensures that the film structure remains intact until consumption, preventing premature degradation in humid environments. Another critical application of Pickering emulsion-based EBF is in active packaging systems, where selective permeability plays a role in preserving food quality. The ability to fine-tune the physicomechanical properties of these films by adjusting the concentration and type of essential oil allows for the development of tailored packaging solutions suitable for different food matrices. By optimizing film composition and emulsion characteristics, these packaging systems can be designed to offer improved flexibility, adhesion, and resistance to environmental stressors, further enhancing their potential for commercial implementation in the food industry. The integration of Pickering emulsion technology

into EBF aligns with the growing demand for sustainable and eco-friendly packaging alternatives. These films not only reduce reliance on petroleum-based plastics but also provide functional advantages that contribute to the overall quality and longevity of packaged food products (Yin & Woo, 2024).

Challenges and future perspectives

The development and application of Pickering emulsion-based edible EBF containing natural essential oils in food packaging face several challenges that need to be addressed to ensure their commercial viability. One of the primary challenges is achieving a balance between the physicomechanical properties and functional performance of the films. While essential oils enhance hydrophobicity and moisture barrier properties, their inclusion may also impact the mechanical integrity of the films, potentially reducing tensile strength and increasing brittleness.

Optimizing emulsion stabilization, film composition, and processing conditions is essential to maintain desirable mechanical properties while ensuring barrier performance is not compromised. Another significant challenge is the uniform dispersion and controlled release of essential oils within the polymer matrix. Due to the volatile nature of essential oils, their retention in the film structure is often limited, resulting in inconsistent physicomechanical performance over time. Strategies like encapsulation in biopolymeric carriers, nanoemulsification, or using interfacial stabilizers can improve essential oil retention and controlled release, thus enhancing the long-term effectiveness of these films in food packaging applications.

Scalability and industrial feasibility also remain crucial considerations. Transitioning from laboratory-scale formulations to large-scale production requires careful evaluation of material costs, processing efficiency, and compatibility with existing food packaging technologies. Developing cost-effective, high-throughput manufacturing processes that preserve the physicomechanical integrity of the films is key for widespread industry adoption. Additionally, regulatory approval and compliance with food safety standards must be addressed to ensure the films are suitable for direct food contact.

Future research should focus on integrating advanced characterization techniques to gain a better understanding of the interactions between Pickering emulsions, essential oils, and biopolymeric matrices. Investigating the molecular mechanisms behind film formation, mechanical reinforcement, and moisture resistance will offer deeper insights into optimizing formulation strategies. Moreover, incorporating multifunctional biopolymers or hybrid emulsifier systems could enhance the film's stability, mechanical strength, and environmental adaptability, making them more suitable for diverse packaging applications. Sustainability considerations will also be central to the future of Pickering emulsion-based edible films. Using biodegradable and renewable biopolymers as film-forming agents, alongside green processing techniques, can align these packaging materials with global sustainability goals. Furthermore, exploring bio-based emulsifiers and natural stabilizers will contribute to the development of more eco-friendly formulations, reducing reliance on synthetic additives.

Conclusion

The integration of Pickering emulsion-based edible biodegradable films with essential oils represents promising advancement in the field of food packaging, offering enhanced physicomechanical properties while maintaining natural and biodegradable characteristics. These films demonstrate improved mechanical strength, reduced water vapor permeability, and enhanced resistance to moisture-induced degradation, making them viable alternatives to conventional synthetic packaging materials. The stabilization of essential oils within Pickering emulsions ensures a more uniform distribution of hydrophobic compounds, leading to consistent physicomechanical performance and extended functional efficacy.

Despite these advantages, several challenges must be addressed to fully exploit the potential of these films in commercial applications. The optimization of formulation parameters, including the type and concentration of stabilizing particles, essential oils, and biopolymeric matrices, is critical for achieving desirable mechanical flexibility and moisture resistance. Additionally, controlling the interactions between film components and environmental factors remains a key aspect of improving long-term stability and performance. Future research should focus on the development of advanced stabilization strategies, such as the incorporation of multifunctional biopolymers, nanoemulsions, or hybrid emulsifier systems, to enhance the physicomechanical robustness of these films. Moreover, investigating the molecular mechanisms governing film formation and structural integrity will provide valuable insights into optimizing their physicomechanical characteristics. The integration of biodegradable and renewable materials, coupled with eco-friendly processing techniques, will further contribute to the sustainability of these packaging systems. Overall, Pickering emulsion-based edible EBF enriched with essential oils offer a sustainable, high-performance solution for food packaging applications. However, continued advancements in material science, processing technologies, and regulatory considerations are essential to facilitate their widespread industrial adoption. By addressing existing limitations and leveraging innovative approaches, these films have the potential to revolutionize the future of sustainable food packaging, aligning with consumer demand for safer and more environmentally friendly alternatives.

Conflict of Interest: The authors declare no competing interests.

Author Contributions

H. Mirzaee Moghaddam: Supervision, Conceptualization, Methodology, Technical advice

A. Nahalkar: Data acquisition, Software services

A. Rajaei: Validation, Visualization, Text mining, Review and editing services

References

1. Abdallah, R. B., Ghazouani, T., & Fattouch, S. (2024). Carrageenan Based Films *Polysaccharide Based Films for Food Packaging: Fundamentals, Properties and Applications* (pp. 175-195): Springer. https://doi.org/10.1007/978-981-99-4898-7_7
2. Abedi, E., Sayadi, M., & Oliyaei, N. (2024). Fabrication and characterization of emulsion-based edible film containing cinnamon essential oil using chia seed mucilage. *International Journal of Biological Macromolecules, 266*, 131173. https://doi.org/10.1016/j.ijbiomac.2024.131173
3. Ahmed, H. M., & Al-Zubaidy, A. M. A. (2020). Exploring natural essential oil components and antibacterial activity of solvent extracts from twelve *Perilla frutescens* L. Genotypes. *Arabian Journal of Chemistry, 13*(10), 7390-7402. https://doi.org/10.1016/j.arabjc.2020.08.017
4. Akarca, G., & Sevik, R. (2021). Biological Activities of *Citrus limon* L. and *Citrus sinensis* L. Peel essential oils. *Journal of Essential Oil Bearing Plants, 24*(6), 1415-1427. https://doi.org/10.1080/0972060x.2021.2022000
5. Akshitha, H., Umesha, K., Leela, N., Shivakumar, M., & Prasath, D. (2020). Quality attributes and essential oil profiling of ginger (*Zingiber officinale* Rosc.) genotypes from India. *Journal of Essential Oil Research, 32*(5), 456-463. https://doi.org/10.1080/10412905.2020.1789000
6. Alam, W., Hussain, Y., Ahmad, S., Ali, A., & Khan, H. (2023). Neuroprotective effect of essential oils *Phytonutrients and Neurological Disorders* (pp. 305-333): Elsevier. https://doi.org/10.1016/b978-0-12-824467-8.00011-5
7. Almas, I., Innocent, E., Machumi, F., & Kisinza, W. (2021). Chemical composition of essential

oils from Eucalyptus globulus and Eucalyptus maculata grown in Tanzania. *Scientific African, 12*, e00758. https://doi.org/10.1016/j.sciaf.2021.e00758

8. Almasi, H., Azizi, S., & Amjadi, S. (2020). Development and characterization of pectin films activated by nanoemulsion and Pickering emulsion stabilized marjoram (*Origanum majorana* L.) essential oil. *Food Hydrocolloids, 99*, 105338. https://doi.org/10.1016/j.foodhyd.2019.105338
9. Amanda, P., Ismadi, I., Ningrum, R. S., Nabila, S., & Prasetyo, K. W. (2024). Carrageenan functional film integrated with Pickering emulsion of oregano oil stabilized by cationic nanocellulose for active packaging. *Food Science and Technology International, 30*(1), 61-72. https://doi.org/10.1177/10820132221132912
10. Amrani, M., Pourshamohammad, S., Tabibiazar, M., Hamishehkar, H., & Mahmoudzadeh, M. (2023). Antimicrobial activity and stability of satureja khuzestanica essential oil pickering emulsions stabilized by starch nanocrystals and bacterial cellulose nanofibers. *Food Bioscience, 55*, 103016. https://doi.org/10.1016/j.fbio.2023.103016
11. Anis, A., Pal, K., & Al-Zahrani, S. M. (2021). Essential oil-containing polysaccharide-based edible films and coatings for food security applications. *Polymers, 13*(4), 575. https://doi.org/10.3390/polym13040575
12. Bangar, S. P., Whiteside, W. S., Dunno, K. D., Cavender, G. A., & Dawson, P. (2023). Fabrication and characterization of active nanocomposite films loaded with cellulose nanocrystals stabilized Pickering emulsion of clove bud oil. *International Journal of Biological Macromolecules, 224*, 1576-1587. https://doi.org/10.1016/j.ijbiomac.2022.10.218
13. Barradas, T. N., & de Holanda e Silva, K. G. (2021). Nanoemulsions of essential oils to improve solubility, stability and permeability: a review. *Environmental Chemistry Letters, 19*(2), 1153-1171. https://doi.org/10.1007/s10311-020-01135-1
14. Beigi, M., Torki-Harchegani, M., & Ghasemi Pirbalouti, A. (2018). Quantity and chemical composition of essential oil of peppermint (*Mentha× piperita* L.) leaves under different drying methods. *International Journal of Food Properties, 21*(1), 267-276. https://doi.org/10.1080/10942912.2018.1440238
15. Bolouri, P., Salami, R., Kouhi, S., Kordi, M., Asgari Lajayer, B., Hadian, J., & Astatkie, T. (2022). Applications of essential oils and plant extracts in different industries. *Molecules, 27*(24), 8999. https://doi.org/10.3390/molecules27248999
16. Borbolla-Jiménez, F. V., Peña-Corona, S. I., Farah, S. J., Jiménez-Valdés, M. T., Pineda-Pérez, E., Romero-Montero, A., ..., & Leyva-Gómez, G. (2023). Films for wound healing fabricated using a solvent casting technique. *Pharmaceutics, 15*(7), 1914. https://doi.org/10.3390/pharmaceutics15071914
17. Brun, P., Bernabè, G., Filippini, R., & Piovan, A. (2019). In vitro antimicrobial activities of commercially available tea tree (*Melaleuca alternifolia*) essential oils. *Current Microbiology, 76*, 108-116. https://doi.org/10.1007/s00284-018-1594-x
18. Bu, N., Huang, L., Cao, G., Lin, H., Pang, J., Wang, L., & Mu, R. (2022). Konjac glucomannan/Pullulan films incorporated with cellulose nanofibrils-stabilized tea tree essential oil Pickering emulsions. *Colloids and Surfaces A: Physicochemical and Engineering Aspects, 650*, 129553. https://doi.org/10.1016/j.colsurfa.2022.129553
19. Bu, N., Sun, R., Huang, L., Lin, H., Pang, J., Wang, L., & Mu, R. (2022). Chitosan films with tunable droplet size of Pickering emulsions stabilized by amphiphilic konjac glucomannan network. *International Journal of Biological Macromolecules, 220*, 1072-1083. https://doi.org/10.1016/j.ijbiomac.2022.08.127
20. Bukhari, N. T. M., Rawi, N. F. M., Hassan, N. A. A., Saharudin, N. I., & Kassim, M. H. M. (2023). Seaweed polysaccharide nanocomposite films: A review. *International Journal of Biological Macromolecules, 245*, 125486. https://doi.org/10.1016/j.ijbiomac.2023.125486

21. Cai, Z., Wei, Y., Shi, A., Zhong, J., Rao, P., Wang, Q., & Zhang, H. (2023). Correlation between interfacial layer properties and physical stability of food emulsions: Current trends, challenges, strategies, and further perspectives. *Advances in Colloid and Interface Science, 313*, 102863. https://doi.org/10.1016/j.cis.2023.102863
22. Chen, Q., You, N., Liang, C., Xu, Y., Wang, F., Zhang, B., & Zhang, P. (2023). Effect of cellulose nanocrystals-loaded ginger essential oil emulsions on the physicochemical properties of mung bean starch composite film. *Industrial Crops and Products, 191*, 116003. https://doi.org/10.1016/j.indcrop.2022.116003
23. Cheng, Y., Cai, X., Zhang, X., Zhao, Y., Song, R., Xu, Y., & Gao, H. (2024). Applications in Pickering emulsions of enhancing preservation properties: current trends and future prospects in active food packaging coatings and films. *Trends in Food Science & Technology*, 104643. https://doi.org/10.1016/j.tifs.2024.104643
24. Chevalier, Y., & Bolzinger, M.-A. (2013). Emulsions stabilized with solid nanoparticles: Pickering emulsions. *Colloids and Surfaces A: Physicochemical and Engineering Aspects, 439*, 23-34. https://doi.org/10.1016/j.colsurfa.2013.02.057
25. Ciancia, M., Matulewicz, M. C., & Tuvikene, R. (2020). Structural diversity in galactans from red seaweeds and its influence on rheological properties. *Frontiers in Plant Science, 11*, 559986. https://doi.org/10.3389/fpls.2020.559986
26. Cui, C., Gao, L., Dai, L., Ji, N., Qin, Y., Shi, R., & Sun, Q. (2023). Hydrophobic biopolymer-based films: Strategies, properties, and food applications. *Food Engineering Reviews, 15*(2), 360-379. https://doi.org/10.1007/s12393-023-09344-4
27. de Carvalho-Guimarães, F. B., Correa, K. L., de Souza, T. P., Rodriguez Amado, J. R., Ribeiro-Costa, R. M., & Silva-Júnior, J. O. C. (2022). A review of Pickering emulsions: perspectives and applications. *Pharmaceuticals, 15*(11), 1413. https://doi.org/10.3390/ph15111413
28. De Farias, P. M., De Sousa, R. V., Maniglia, B. C., Pascall, M., Matthes, J., Sadzik, A., & Fai, A. E. C. (2025). Biobased Food Packaging Systems Functionalized with Essential Oil via Pickering Emulsion: Advantages, Challenges, and Current Applications. *ACS omega, 10*(5), 4173-4186. https://doi.org/10.1021/acsomega.4c09320
29. Deng, H., Su, J., Zhang, W., Khan, A., Sani, M. A., Goksen, G., & Rhim, J.-W. (2024). A review of starch/polyvinyl alcohol (PVA) blend film: A potential replacement for traditional plastic-based food packaging film. *International Journal of Biological Macromolecules*, 132926. https://doi.org/10.1016/j.ijbiomac.2024.132926
30. Dhama, K., Sharun, K., Gugjoo, M. B., Tiwari, R., Alagawany, M., Iqbal Yatoo, M., & Michalak, I. (2023). A comprehensive review on chemical profile and pharmacological activities of Ocimum basilicum. *Food Reviews International, 39*(1), 119-147. https://doi.org/10.1080/87559129.2021.1900230
31. Díaz-Montes, E., & Castro-Muñoz, R. (2021). Edible films and coatings as food-quality preservers: An overview. *Foods, 10*(2), 249. https://doi.org/10.3390/foods10020249
32. Du, Y., Zhang, S., Sheng, L., Ma, H., Xu, F., Waterhouse, G. I., & Wu, P. (2023). Food packaging films based on ionically crosslinked konjac glucomannan incorporating zein-pectin nanoparticle-stabilized corn germ oil-oregano oil Pickering emulsion. *Food Chemistry, 429*, 136874. https://doi.org/10.1016/j.foodchem.2023.136874
33. Dutta, D., & Sit, N. (2024). A comprehensive review on types and properties of biopolymers as sustainable bio-based alternatives for packaging. *Food Biomacromolecules, 1*(2), 58-87. https://doi.org/10.1002/fob2.12019
34. Eshagh, S., Abbaspour-Fard, M. H., Tabasizadeh, M., & Hosseini, F. (2019). Effect of Zinc Oxide Nanoparticles on Mechanical, Thermal and Biodegradability of Gelatin-Based Biocomposite Properties Films. *Iranian Journal of Polymer Science and Technology, 32*(5), 411-426. https://doi.org/10.22063/jipst.2020.1693

35. Eslami, Z., Elkoun, S., Robert, M., & Adjallé, K. (2023). A review of the effect of plasticizers on the physical and mechanical properties of alginate-based films. *Molecules, 28*(18), 6637. https://doi.org/10.3390/molecules28186637
36. Fadiji, T., Rashvand, M., Daramola, M. O., & Iwarere, S. A. (2023). A review on antimicrobial packaging for extending the shelf life of food. *Processes, 11*(2), 590. https://doi.org/10.3390/pr11020590
37. Fan, S., Wang, D., Wen, X., Li, X., Fang, F., Richel, A., & Zhang, D. (2023). Incorporation of cinnamon essential oil-loaded Pickering emulsion for improving antimicrobial properties and control release of chitosan/gelatin films. *Food Hydrocolloids, 138*, 108438. https://doi.org/10.1016/j.foodhyd.2022.108438
38. Farajpour, R., Djomeh, Z. E., Moeini, S., Tavakolipour, H., & Safayan, S. (2020). Structural and physico-mechanical properties of potato starch-olive oil edible films reinforced with zein nanoparticles. *International Journal of Biological Macromolecules, 149*, 941-950. https://doi.org/10.1016/j.ijbiomac.2020.01.175
39. Fasihi, H., Noshirvani, N., & Hashemi, M. (2023). Novel bioactive films integrated with Pickering emulsion of ginger essential oil for food packaging application. *Food Bioscience, 51*, 102269. https://doi.org/10.1016/j.fbio.2022.102269
40. Giacometti, J., Kovačević, D. B., Putnik, P., Gabrić, D., Bilušić, T., Krešić, G., & Barbosa-Cánovas, G. (2018). Extraction of bioactive compounds and essential oils from mediterranean herbs by conventional and green innovative techniques: A review. *Food Research International, 113*, 245-262. https://doi.org/10.1016/j.foodres.2018.06.036
41. Gotmare, S., & Tambe, E. (2019). Identification of chemical constituents of cinnamon bark oil by GCMS and comparative study garnered from five different countries. *Global Journal of Science Frontier Research: C Biological Science, 19*(1), 34-42.
42. Guo, X., Wang, X., Wei, Y., Liu, P., Deng, X., Lei, Y., & Zhang, J. (2024). Preparation and properties of films loaded with cellulose nanocrystals stabilized Thymus vulgaris essential oil Pickering emulsion based on modified tapioca starch/polyvinyl alcohol. *Food Chemistry, 435*, 137597. https://doi.org/10.1016/j.foodchem.2023.137597
43. Gupta, D., Lall, A., Kumar, S., Patil, T. D., & Gaikwad, K. K. (2024). Plant based edible films and coatings for food packaging applications: Recent advances, applications, and trends. *Sustainable Food Technology*. https://doi.org/10.1039/d4fb00110a
44. Hammam, A. R. (2019). Technological, applications, and characteristics of edible films and coatings: A review. *SN Applied Sciences, 1*, 1-11. https://doi.org/10.1007/s42452-019-0931-4
45. Heydarian, A., Ahmadi, E., Dashti., & Normohammadi, A. (2022). Evaluation of Mechanical and Chemical Parameters of Okra with Chitosan Coating in Nano Packaging Films and Atmospheric Modified Conditions. *Journal of Agricultural Machinery, 12*(4), 600-612. https://doi.org/10.22067/jam.2021.69257.1027
46. Hua, L., Deng, J., Wang, Z., Wang, Y., Chen, B., Ma, Y., & Xu, B. (2021). Improving the functionality of chitosan-based packaging films by crosslinking with nanoencapsulated clove essential oil. *International Journal of Biological Macromolecules, 192*, 627-634. https://doi.org/10.1016/j.ijbiomac.2021.10.047
47. Hussain, S., Akhter, R., & Maktedar, S. S. (2024). Advancements in sustainable food packaging: from eco-friendly materials to innovative technologies. *Sustainable Food Technology, 2*(5), 1297-1364. https://doi.org/10.1039/d4fb00084f
48. Iñiguez-Moreno, M., Calderón-Santoyo, M., Ascanio, G., Ragazzo-Calderón, F. Z., Parra-Saldívar, R., & Ragazzo-Sánchez, J. A. (2024). Harnessing emerging technologies to obtain biopolymer from agro-waste: application into the food industry. *Biomass Conversion and Biorefinery, 14*(23), 29265-29282. https://doi.org/10.1007/s13399-024-05622-1
49. Jafarzadeh, S., & Jafari, S. M. (2021). Impact of metal nanoparticles on the mechanical, barrier,

optical and thermal properties of biodegradable food packaging materials. *Critical Reviews in Food Science and Nutrition, 61*(16), 2640-2658. https://doi.org/10.1080/10408398.2020.1783200

50. Javadi Farsani, M., Mirzaee Moghaddam, H., & Rajaei Najafabadi, A. (2023). Study of some qualitative and organoleptic properties of enriched apple leather. *Journal of Food Science and Technology (Iran), 19*(133), 175-186. https://doi.org/10.22034/FSCT.19.133.175
51. Jayakody, M. M., Vanniarachchy, M. P. G., & Wijesekara, I. (2022). Seaweed derived alginate, agar, and carrageenan based edible coatings and films for the food industry: A review. *Journal of Food Measurement and Characterization, 16*(2), 1195-1227. https://doi.org/10.1007/s11694-021-01251-8
52. Jayarathna, S., Andersson, M., & Andersson, R. (2022). Recent advances in starch-based blends and composites for bioplastics applications. *Polymers, 14*(21), 4557. https://doi.org/10.3390/polym14214557
53. Jiang, H., Sheng, Y., & Ngai, T. (2020). Pickering emulsions: Versatility of colloidal particles and recent applications. *Current Opinion in Colloid & Interface Science, 49*, 1-15. https://doi.org/10.1016/j.cocis.2020.04.010
54. Kanyal, B., Pande, C., Tewari, G., Aabha, Rana, L., Padalia, R. C., ..., & Singh, S. (2023). Influence of Post-Harvest Drying Processes on the Composition and Biological Activities of Essential Oils from Leaves of Camphor Tree from Uttarakhand Himalaya, India. *Journal of Essential Oil Bearing Plants, 26*(1), 161-175. https://doi.org/10.1080/0972060x.2023.2179426
55. Katar, N., Katar, D., Temel, R., Karakurt, S., Bolatkiran, İ., Yildiz, E., & Soltanbeigi, A. (2019). The effect of different harvest dates on the yield and quality properties of rosemary (*Rosmarinus officinalis* L.) plant. *Biological Diversity and Conservation, 12*(3), 7-13. https://doi.org/10.5505/biodicon.2019.29292
56. Kokkuvayil Ramadas, B., Rhim, J.-W., & Roy, S. (2024). Recent progress of carrageenan-based composite films in active and intelligent food packaging applications. *Polymers, 16*(7), 1001. https://doi.org/10.3390/polym16071001
57. Kosakowska, O., Węglarz, Z., Pióro-Jabrucka, E., Przybył, J. L., Kraśniewska, K., Gniewosz, M., & Bączek, K. (2021). Antioxidant and antibacterial activity of essential oils and hydroethanolic extracts of Greek oregano (O. *vulgare* L. subsp. hirtum (Link) Ietswaart) and common oregano (O. *vulgare* L. subsp. vulgare). *Molecules, 26*(4), 988. https://doi.org/10.3390/molecules26040988
58. Kour, P., Shaheen, A., Tak, U. N., Gani, A., Qadri, H. K., & Dar, A. A. (2024). Pickering emulsions of zein nanoparticles co-stabilized by Tween 20: An effective strategy to stabilize citral in low pH environment. *Colloids and Surfaces A: Physicochemical and Engineering Aspects, 701*, 134876. https://doi.org/10.1016/j.colsurfa.2024.134876
59. Kumoro, A., Wardhani, D., Retnowati, D., & Haryani, K. (2021). *A brief review on the characteristics, extraction and potential industrial applications of citronella grass (Cymbopogon nardus) and lemongrass (Cymbopogon citratus) essential oils.* Paper presented at the IOP Conference Series: Materials Science and Engineering. https://doi.org/10.1088/1757-899x/1053/1/012118
60. Lashari, N., Ganat, T., Elraies, K. A., Ayoub, M. A., Kalam, S., Chandio, T. A., & Sharma, T. (2022). Impact of nanoparticles stability on rheology, interfacial tension, and wettability in chemical enhanced oil recovery: A critical parametric review. *Journal of Petroleum Science and Engineering, 212*, 110199. https://doi.org/10.1016/j.petrol.2022.110199
61. Li, S., Chen, W., Zongo, A. W.-S., Chen, Y., Liang, H., Li, J., & Li, B. (2023). Effects of non-starch polysaccharide on starch gelatinization and digestibility: A review. *Food Innovation and Advances, 2*(4), 302-312. https://doi.org/10.48130/FIA-2023-0023
62. Liu, J., Song, F., Chen, R., Deng, G., Chao, Y., Yang, Z., & Hu, Y. (2022). Effect of cellulose

nanocrystal-stabilized cinnamon essential oil Pickering emulsions on structure and properties of chitosan composite films. *Carbohydrate Polymers*, *275*, 118704. https://doi.org/10.1016/j.carbpol.2021.118704

63. Liu, L., Swift, S., Tollemache, C., Perera, J., & Kilmartin, P. A. (2022). Antimicrobial and antioxidant AIE chitosan-based films incorporating a Pickering emulsion of lemon myrtle (*Backhousia citriodora*) essential oil. *Food Hydrocolloids*, *133*, 107971. https://doi.org/10.1016/j.foodhyd.2022.107971
64. Liu, Y., Ahmed, S., Sameen, D. E., Wang, Y., Lu, R., Dai, J., & Qin, W. (2021). A review of cellulose and its derivatives in biopolymer-based for food packaging application. *Trends in Food Science & Technology*, *112*, 532-546. https://doi.org/10.1016/j.tifs.2021.04.016
65. Low, L. E., Siva, S. P., Ho, Y. K., Chan, E. S., & Tey, B. T. (2020). Recent advances of characterization techniques for the formation, physical properties and stability of Pickering emulsion. *Advances in Colloid and Interface Science*, *277*, 102117. https://doi.org/10.1016/j.cis.2020.102117
66. Malm, M., Liceaga, A. M., San Martin-Gonzalez, F., Jones, O. G., Garcia-Bravo, J. M., & Kaplan, I. (2021). Development of chitosan films from edible crickets and their performance as a bio-based food packaging material. *Polysaccharides*, *2*(4), 744-758. https://doi.org/10.3390/polysaccharides2040045
67. Mirzaee Moghaddam, H., Tavakkoli, T., Minaee, S., & Rajaee, A. (2007). *Some physical properties kiwifruit (cv. Hayward)*. Paper presented at the Proceedings of the 3th National Congress on Agricultural Machinery, Shiraz, Iran.
68. Mirzaee Moghaddam, H., Khoshtaghaza, M. H., Salimi, A., & Barzegar, M. (2014). The TiO_2–Clay-LDPE nanocomposite packaging films: investigation on the structure and physicomechanical properties. *Polymer-Plastics Technology and Engineering*, *53*(17), 1759-1767. https://doi.org/10.1080/03602559.2014.919652
69. Mirzaee Moghaddam, H., & Rajaei, A. (2021). Effect of pomegranate seed oil encapsulated in Chitosan-capric acid nanogels incorporating thyme essential oil on physicomechanical and structural properties of Jelly Candy. *Journal of Agricultural Machinery*, *11*(1), 55-70. https://doi.org/10.22067/jam.v11i1.84882
70. Mirzaee Moghaddam, H., (2019). Investigation of PhysicoMechanical Properties of Functional Gummy Candy Fortified with Encapsulated Fish Oil in Chitosan-Stearic Acid Nanogel by Pickering Emulsion Method. *Journal of Food Science and Technology (Iran)*, 16(90), 53-64. http://fsct.modares.ac.ir/article-7-34530-fa.html
71. Moeini, A., Pedram, P., Fattahi, E., Cerruti, P., & Santagata, G. (2022). Edible polymers and secondary bioactive compounds for food packaging applications: Antimicrobial, mechanical, and gas barrier properties. *Polymers*, *14*(12), 2395. https://doi.org/10.3390/polym14122395
72. Molnar, M., Gašo-Sokač, D., Komar, M., Kovač, M. J., & Bušić, V. (2024). Potential of Deep Eutectic Solvents in the Extraction of Organic Compounds From Food Industry By-Products and Agro-Industrial Waste. *Separations*, *11*(1), 35. https://doi.org/10.3390/separations11010035
73. Mostafavi, F. S., & Zaeim, D. (2020). Agar-based edible films for food packaging applications-A review. *International Journal of Biological Macromolecules*, *159*, 1165-1176. https://doi.org/10.1016/j.ijbiomac.2020.05.153
74. Nahalkar, A. Rajaei, A., & Mirzaee Moghaddam, H. (2025a). Investigation of some structural and physicomechanical properties of bilayer and composite edible films based on sodium carboxymethyl cellulose. *Journal of Agricultural Machinery*, *16*(1), 137-152. https://doi.org/10.22067/jam.2025.90690.1312
75. Nahalkar, A. Rajaei, A., & Mirzaee Moghaddam, H. (2025b). Investigation of the possibility of producing a stabilized walnut oil emulsion with chia seed mucilage and its application in edible

films. *Journal of Food Science and Technology* (FSCT). *22*(161), 260-274. https://doi.org/10.22034/FSCT.22.161.260
76. Nasaj, M., Chehelgerdi, M., Asghari, B., Ahmadieh-Yazdi, A., Asgari, M., Kabiri-Samani, S., & Arabestani, M. (2024). Factors influencing the antimicrobial mechanism of chitosan action and its derivatives: A review. *International Journal of Biological Macromolecules*, 134321. https://doi.org/10.1016/j.ijbiomac.2024.134321
77. Nazari, N., Rajaei, A., & Mirzaee Moghaddam, H. (2025). Comparative Effects of Basil Seed and Cress Seed Gums on Stability of Flaxseed Oil Pickering Emulsion and Functional Kiwifruit Bar Characteristics. *Food Biophysics, 20*(2), 1-15. https://doi.org/10.1007/s11483-025-09947-w
78. Ngo, T., Tran, T., Nguyen, V., & Mai, H. (2020). Optimization of green mandarin (Citrus reticulata) essential oil extraction using microwave-assisted hydrodistillation and chemical composition analysis. Paper presented at the *IOP Conference Series: Materials Science and Engineering*. https://doi.org/10.1088/1757-899x/991/1/012122
79. Ni, Y., Liu, Y., Zhang, W., Shi, S., Zhu, W., Wang, R., & Pang, J. (2021). Advanced konjac glucomannan-based films in food packaging: Classification, preparation, formation mechanism and function. *LWT, 152*, 112338. https://doi.org/10.1016/j.lwt.2021.112338
80. Nilsen-Nygaard, J., Fernández, E. N., Radusin, T., Rotabakk, B. T., Sarfraz, J., Sharmin, N., & Pettersen, M. K. (2021). Current status of biobased and biodegradable food packaging materials: Impact on food quality and effect of innovative processing technologies. *Comprehensive Reviews in Food Science and Food Safety, 20*(2), 1333-1380. https://doi.org/10.1111/1541-4337.12715
81. Niro, C. M., Medeiros, J. A., Freitas, J. A., & Azeredo, H. M. (2021). Advantages and challenges of Pickering emulsions applied to bio-based films: a mini-review. *Journal of the Science of Food and Agriculture, 101*(9), 3535-3540. https://doi.org/10.1002/jsfa.11020
82. Ogwu, M. C., & Ogunsola, O. A. (2024). Physicochemical Methods of Food Preservation to Ensure Food Safety and Quality *Food Safety and Quality in the Global South* (pp. 263-298): Springer. https://doi.org/10.1007/978-981-97-2428-4_9
83. Olawade, D. B., Wada, O. Z., & Ige, A. O. (2024). Advances and recent trends in plant-based materials and edible films: a mini-review. *Frontiers in Chemistry, 12*, 1441650. https://doi.org/10.3389/fchem.2024.1441650
84. Pandita, G., de Souza, C. K., Gonçalves, M. J., Jasińska, J. M., Jamróz, E., & Roy, S. (2024). Recent progress on Pickering emulsion stabilized essential oil added biopolymer-based film for food packaging applications: A review. *International Journal of Biological Macromolecules*, 132067. https://doi.org/10.1016/j.ijbiomac.2024.132067
85. Pei, J., Palanisamy, C. P., Srinivasan, G. P., Panagal, M., Kumar, S. S. D., & Mironescu, M. (2024). A comprehensive review on starch-based sustainable edible films loaded with bioactive components for food packaging. *International Journal of Biological Macromolecules*, 133332. https://doi.org/10.1016/j.ijbiomac.2024.133332
86. Ponnampalam, E. N., Kiani, A., Santhiravel, S., Holman, B. W., Lauridsen, C., & Dunshea, F. R. (2022). The importance of dietary antioxidants on oxidative stress, meat and milk production, and their preservative aspects in farm animals: Antioxidant action, animal health, and product quality—Invited review. *Animals, 12*(23), 3279. https://doi.org/10.3390/ani12233279
87. Prerna, & Vasudeva, N. (2016). Comparative Study of Volatile Oil of Stem and Aerial Parts of Origanum majorana Linn. *Journal of Essential Oil Bearing Plants, 19*(8), 2091-2099. https://doi.org/10.1080/0972060X.2016.1224689
88. Priyadarshi, R., & Rhim, J.-W. (2020). Chitosan-based biodegradable functional films for food packaging applications. *Innovative Food Science & Emerging Technologies, 62*, 102346.

https://doi.org/10.1016/j.ifset.2020.102346
89. Rajesh, P., & Subhashini, V. (2021). Sustainable packaging from waste material: A review on innovative solutions for cleaner environment. *Bioremediation and Green Technologies: Sustainable Approaches to Mitigate Environmental Impacts*, 259-270. https://doi.org/10.1007/978-3-030-64122-1_18
90. Roy, S., Priyadarshi, R., & Rhim, J.-W. (2022). Gelatin/agar-based multifunctional film integrated with copper-doped zinc oxide nanoparticles and clove essential oil Pickering emulsion for enhancing the shelf life of pork meat. *Food Research International, 160*, 111690. https://doi.org/10.1016/j.foodres.2022.111690
91. Roy, S., & Rhim, J.-W. (2021). Carrageenan/agar-based functional film integrated with zinc sulfide nanoparticles and Pickering emulsion of tea tree essential oil for active packaging applications. *International Journal of Biological Macromolecules, 193*, 2038-2046. https://doi.org/10.1016/j.ijbiomac.2021.11.035
92. Rusanov, K., Vassileva, P., Rusanova, M., & Atanassov, I. (2023). Identification of QTL controlling the ratio of linalool to linalyl acetate in the flowers of Lavandula angustifolia Mill var. Hemus. *Biotechnology & Biotechnological Equipment, 37*(1), 2288929. https://doi.org/10.1080/13102818.2023.2288929
93. Sahraeian, S., Rashidinejad, A., & Niakousari, M. (2023). Enhanced properties of non-starch polysaccharide and protein hydrocolloids through plasma treatment: A review. *International Journal of Biological Macromolecules, 249*, 126098. https://doi.org/10.1016/j.ijbiomac.2023.126098
94. Sayadi, M., Abedi, E., & Oliyaei, N. (2025). Effect of Persian gum-gelatin based-pickering emulsion film loaded with Thyme essential oil on the storage quality of Barred mackerel (*Scomberomorus commerrson*) fillet. *LWT, 215*, 117241. https://doi.org/10.1016/j.lwt.2024.117241
95. Seoane-Viaño, I., Januskaite, P., Alvarez-Lorenzo, C., Basit, A. W., & Goyanes, A. (2021). Semi-solid extrusion 3D printing in drug delivery and biomedicine: Personalised solutions for healthcare challenges. *Journal of Controlled Release, 332*, 367-389. https://doi.org/10.1016/j.jconrel.2021.02.027
96. Shahbazi, N., Rajaei, A., Tabatabaei, M., Mohsenifar, A., & Bodaghi, H. (2021). Impact of Chitosan-Capric Acid Nanogels Incorporating Thyme Essential Oil on Stability of Pomegranate Seed Oil-in-Water Pickering Emulsion. *Iranian Journal of Chemistry and Chemical Engineering, 40*(6), 1737-1748. https://doi.org/10.30492/ijcce.2020.43345
97. Sharkawy, A., Barreiro, M. F., & Rodrigues, A. E. (2020). Chitosan-based Pickering emulsions and their applications: A review. *Carbohydrate Polymers, 250*, 116885. https://doi.org/10.1016/j.carbpol.2020.116885
98. Southwell, I. (2021). Backhousia citriodora F. Muell. (Lemon Myrtle), an unrivalled source of citral. *Foods, 10*(7), 1596. https://doi.org/10.3390/foods10071596
99. Tabatabaei, M., Ebrahimi, B., Rajaei, A., Movahednejad, M. H., Rastegari, H., Taghavi, E., & Lam, S. S. (2022). Producing submicron chitosan-stabilized oil Pickering emulsion powder by an electrostatic collector-equipped spray dryer. *Carbohydrate Polymers, 294*, 119791. https://doi.org/10.1016/j.carbpol.2022.119791
100. Tajari, N., Sadrnia, H., & Hosseini, F.(2024) Investigating the Effect of Storage Time on the Mechanical Properties of Biodegradable Polylactic Acid Film Containing Zinc Oxide Nanoparticles. *Journal of Agricultural Machinery, 14*(3), 283-299. https://doi.org/10.22067/jam.2023.81863.1160
101. Tan, C., & McClements, D. J. (2021). Application of advanced emulsion technology in the food industry: A review and critical evaluation. *Foods, 10*(4), 812. https://doi.org/10.3390/foods10040812

102. Tavakoli-Rouzbehani, O. M., Faghfouri, A. H., Anbari, M., Papi, S., Shojaei, F. S., Ghaffari, M., & Alizadeh, M. (2021). The effects of Cuminum cyminum on glycemic parameters: A systematic review and meta-analysis of controlled clinical trials. *Journal of Ethnopharmacology, 281*, 114510. https://doi.org/10.1016/j.jep.2021.114510
103. Upadhye, S., Mujawar, S. S., & Kashte, S. B. (2025). Eco-friendly, antibacterial, antioxidant, ultraviolet blocking sodium alginate-gelatin films loaded with clove essential oil for food packaging. *Journal of Food Measurement and Characterization, 19*(4), 2803-2817. https://doi.org/10.1007/s11694-025-03148-2
104. Versino, F., Ortega, F., Monroy, Y., Rivero, S., López, O. V., & García, M. A. (2023). Sustainable and bio-based food packaging: A review on past and current design innovations. *Foods, 12*(5), 1057. https://doi.org/10.3390/foods12051057
105. Wang, J.-D., Yang, S.-L., Liu, G.-S., Zhou, Q., Fu, L.-N., Gu, Q., & Fu, Y.-J. (2024). A degradable multi-functional packaging based on chitosan/silk fibroin via incorporating cellulose nanocrystals-stabilized cinnamon essential oil pickering emulsion. *Food Hydrocolloids, 153*, 109978. https://doi.org/10.1016/j.foodhyd.2024.109978
106. Wang, X., Li, S., Zeng, M., Gong, H., Zhang, Z., Yuan, X., & Wu, H. (2025). Preparation, Characterization and Application of Antimicrobial Pectin-Konjac Glucomannan Composite Films Incorporating Cellulose Nanocrystals Stabilized Clove Essential Oil Pickering Emulsion. *Available at SSRN 5102163*. https://doi.org/10.2139/ssrn.5102163
107. Wardana, A. A., Wigati, L. P., Van, T. T., Tanaka, F., & Tanaka, F. (2023). Antifungal features and properties of Pickering emulsion coating from alginate/lemongrass oil/cellulose nanofibers. *International Journal of Food Science & Technology, 58*(2), 966-978. https://doi.org/10.1111/ijfs.16192
108. Wesolowska, A., & Jadczak, D. (2019). Comparison of the chemical composition of essential oils isolated from two thyme (*Thymus vulgaris* L.) cultivars. *Notulae Botanicae Horti Agrobotanici Cluj-Napoca, 47*(3), 829-835. https://doi.org/10.15835/nbha47311490
109. Wu, H., Wang, J., Li, T., Lei, Y., Peng, L., Chang, J., & Zhang, Z. (2023). Effects of cinnamon essential oil-loaded Pickering emulsion on the structure, properties and application of chayote tuber starch-based composite films. *International Journal of Biological Macromolecules, 240*, 124444. https://doi.org/10.1016/j.ijbiomac.2023.124444
110. Xu, J., He, M., Wei, C., Duan, M., Yu, S., Li, D., & Wu, C. (2023). Konjac glucomannan films with Pickering emulsion stabilized by TEMPO-oxidized chitin nanocrystal for active food packaging. *Food Hydrocolloids, 139*, 108539. https://doi.org/10.1016/j.foodhyd.2023.108539
111. Yadav, S., Gupta, S. K., Bharti, D., & Yogi, B. (2020). Syzygium aromaticum (clove): a review on various phytochemicals and pharmacological activities in medicinal plant. *World Journal of Pharmacy and Research, 9*(11), 349-363.
112. Yang, Y., Aghbashlo, M., Gupta, V. K., Amiri, H., Pan, J., Tabatabaei, M., & Rajaei, A. (2023). Chitosan nanocarriers containing essential oils as a green strategy to improve the functional properties of chitosan: A review. *International Journal of Biological Macromolecules, 236*, 123954. https://doi.org/10.1016/j.ijbiomac.2023.123954
113. Yao, L., Man, T., Xiong, X., Wang, Y., Duan, X., & Xiong, X. (2023). HPMC films functionalized by zein/carboxymethyl tamarind gum stabilized Pickering emulsions: Influence of carboxymethylation degree. *International Journal of Biological Macromolecules, 238*, 124053. https://doi.org/10.1016/j.ijbiomac.2023.124053
114. Yildirim-Yalcin, M., Tornuk, F., & Toker, O. S. (2022). Recent advances in the improvement of carboxymethyl cellulose-based edible films. *Trends in Food Science & Technology, 129*, 179-193. https://doi.org/10.1016/j.tifs.2022.09.015
115. Yin, Y., & Woo, M. W. (2024). Transitioning of petroleum-based plastic food packaging to sustainable bio-based alternatives. *Sustainable Food Technology, 2*(3), 548-566.

https://doi.org/10.1039/d4fb00028e
116. Yu, J. (2025). Chemical Composition of Essential Oils and Their Potential Applications in Postharvest Storage of Cereal Grains. *Molecules, 30*(3), 683. https://doi.org/10.3390/molecules30030683
117. Yue, S., Zhang, T., Wang, S., Han, D., Huang, S., Xiao, M., & Meng, Y. (2024). Recent progress of biodegradable polymer package materials: nanotechnology improving both oxygen and water vapor barrier performance. *Nanomaterials, 14*(4), 338. https://doi.org/10.3390/nano14040338
118. Zhang, Q., Kong, B., Liu, H., Du, X., Sun, F., & Xia, X. (2024). Nanoscale Pickering emulsion food preservative films/coatings: Compositions, preparations, influencing factors, and applications. *Comprehensive Reviews in Food Science and Food Safety, 23*(1), e13279. https://doi.org/10.1111/1541-4337.13279
119. Zhang, S., He, Z., Xu, F., Cheng, Y., Waterhouse, G. I., Sun-Waterhouse, D., & Wu, P. (2022). Enhancing the performance of konjac glucomannan films through incorporating zein–pectin nanoparticle-stabilized oregano essential oil Pickering emulsions. *Food Hydrocolloids, 124*, 107222. https://doi.org/10.1016/j.foodhyd.2021.107222
120. Zhang, W., Jiang, H., Rhim, J.-W., Cao, J., & Jiang, W. (2022). Effective strategies of sustained release and retention enhancement of essential oils in active food packaging films/coatings. *Food Chemistry, 367*, 130671. https://doi.org/10.1016/j.foodchem.2021.130671
121. Zhao, R., Guan, W., Zhou, X., Lao, M., & Cai, L. (2022). The physiochemical and preservation properties of anthocyanidin/chitosan nanocomposite-based edible films containing cinnamon-perilla essential oil pickering nanoemulsions. *LWT, 153*, 112506. https://doi.org/10.1016/j.lwt.2021.112506
122. Zhao, Z., Liu, H., Tang, J., He, B., Yu, H., Xu, X., & Su, Y. (2023). Pork preservation by antimicrobial films based on potato starch (PS) and polyvinyl alcohol (PVA) and incorporated with clove essential oil (CLO) Pickering emulsion. *Food Control, 154*, 109988. https://doi.org/10.1016/j.foodcont.2023.109988
123. Zoghi, A., Khosravi-Darani, K., & Mohammadi, R. (2020). Application of edible films containing probiotics in food products. *Journal of Consumer Protection and Food Safety, 15*(4), 307-320. https://doi.org/10.1007/s00003-020-01286-x
124. Zomorodian, N., Javanshir, S., Shariatifar, N., & Rostamnia, S. (2023). The effect of essential oil of Zataria multiflora incorporated chitosan (free form and Pickering emulsion) on microbial, chemical and sensory characteristics in salmon (*Salmo trutta*). *Food chemistry: X, 20*, 100999. https://doi.org/10.1016/j.fochx.2023.100999

نشریه ماشین‌های کشاورزی
https://jame.um.ac.ir

مقاله مروری

جلد ۱۶، شماره ۳، پاییز ۱۴۰۵، ص ۶۲۴-۵۹۹

مروری بر خواص فیزیکومکانیکی فیلم‌های خوراکی بر پایه پلی‌ساکارید شامل امولسیون‌های پیکرینگ حاوی اسانس

حسین میرزایی مقدم[1*]، آرین نهالکار[1]، احمد رجایی[1]

تاریخ دریافت: ۱۴۰۳/۱۱/۲۵
تاریخ پذیرش: ۱۴۰۴/۰۲/۲۴

چکیده

فیلم‌های خوراکی زیست‌تخریب‌پذیر حاوی امولسیون پیکرینگ به‌عنوان جایگزینی پایدار و نویدبخش برای مواد بسته‌بندی غذایی مرسوم مطرح شده‌اند. این فیلم‌ها دارای خواص مکانیکی بهبودیافته‌ای از جمله استحکام کششی، انعطاف‌پذیری و قابلیت ممانعت بخار آب هستند که برای حفظ یکپارچگی مواد غذایی در طول نگهداری و حمل‌ونقل اهمیت دارند. یکی از پیشرفت‌های کلیدی در این حوزه، استفاده از اسانس‌ها در ماتریس امولسیون است که با وجود ماهیت آب‌گریز خود، خواص عملکردی و مکانیکی فیلم‌های بر پایه پلی‌ساکارید را به‌طور قابل‌توجهی ارتقا می‌دهند. این مقاله به بررسی خواص فیزیکومکانیکی فیلم‌های خوراکی زیست‌تخریب‌پذیر بر پایه پلی‌ساکارید که شامل امولسیون‌های پیکرینگ حاوی اسانس هستند می‌پردازد، با تمرکز ویژه بر انعطاف‌پذیری، استحکام کششی، نفوذپذیری بخار آب و ظرفیت نگهداری رطوبت. همچنین نقش این فیلم‌ها در افزایش ماندگاری مواد غذایی مورد بررسی قرار گرفته و نحوه تعامل میان اسانس‌ها و پلی‌ساکاریدها در تأثیرگذاری بر ساختار و ویژگی‌های ممانعتی فیلم‌ها تحلیل می‌شود. یافته‌ها نشان می‌دهند که امولسیون‌های پیکرینگ حاوی اسانس‌ها به‌طور قابل‌توجهی عملکرد مکانیکی و ممانعتی نسبت به رطوبت را در فیلم‌های خوراکی زیست‌تخریب‌پذیر ارتقا می‌دهند. ذرات پایدارکننده جامد موجب افزایش استحکام کششی می‌شوند، در حالی‌که اسانس‌ها، انعطاف‌پذیری را بهبود می‌بخشند. علاوه بر این، امولسیون‌ها جذب آب و حلالیت را کاهش داده و در نتیجه پایداری فیلم در شرایط مرطوب را افزایش می‌دهند. در نهایت، این مرور، به بررسی چالش‌های موجود و شناسایی فرصت‌های پژوهشی کلیدی در توسعه سیستم‌های امولسیون پیکرینگ حاوی اسانس، برای فیلم‌های مذکور پرداخته و همچنین ظرفیت بالقوه آن‌ها برای کاربردهای صنعتی در مقیاس وسیع را تبیین می‌کند.

واژه‌های کلیدی: اسانس، امولسیون پیکرینگ، بسته‌بندی، فیلم خوراکی

۱- گروه مکانیک بیوسیستم، دانشکده کشاورزی، دانشگاه صنعتی شاهرود، شاهرود، ایران
(*- نویسنده مسئول: Email: H_mirzaee@shahroodut.ac.ir)

https://doi.org/10.22067/jam.2025.92162.1343

مندرجات

مقالات پژوهشی

ارزیابی پتانسیل تصاویر ماهواره‌ای چندطیفی سنتینل-۲ برای شناسایی هجوم آفت زنجرک در مناطق کشت نخل خرما ۳۸۱
هادی کریمی، محمدجواد عصاری، هادی زهدی، فروغ رنجبر ورندی

بهینه‌سازی مصرف انرژی در سامانه‌های کاشت لوبیا چیتی: با رویکرد الگوریتم ژنتیک چندهدفه ۳۹۷
رضا رئیسی، محمد غلامی پرشکوهی، حامد افشاری، احمد محمدی

بهبود و تحلیل اجزای دستگاه یکپارچه فرآوری محصول Enset با نام علمی *Ensete ventricosum* ۴۲۵
بِکا آدوگنا، کیشور پوروشوتام کوله، موئرا گوتو

ارزیابی ویسکوزیته و سطوح آلاینده در روان‌کننده دیزل از طریق طیف‌سنجی دی‌الکتریک با استفاده از روش‌های محاسباتی نرم ۴۴۷
محمدرضا پوررمضان، عباس روحانی، محمدحسین عباسپورفرد

بررسی نرخ و شدت حوادث مربوط به تراکتورهای کشاورزی و کمباین‌های غلات و عوامل مؤثر بر آن در استان ایلام ۴۶۷
جلال اله نوری، افشین مرزبان، محمود قاسمی نژاد رائینی، مجید رهنما[1]، مسلم سواری

پیش‌بینی ویتامین C و تغییر رنگ پودر پرتقال در چهار خشک‌کن مختلف با استفاده از بینی الکترونیک ۴۸۶
مازیار روشن مقدم، رضا امیری چایجان، ناهید عقیلی ناطق

مدل یادگیری گروهی وزن‌دار برای طبقه‌بندی بیماری برگ انگور با استفاده از پردازش تصویر و یادگیری ماشینی ۵۰۶
محسن نجف‌آبادی‌ها، داود محمدزمانی، محمد غلامی پرشکوهی

بررسی تاثیر ترکیب نانوذرات اکسید مس و آب مقطر بر راندمان یک سامانه فتوولتاییک حرارتی ۵۲۳
مهری قادری، پیمان سلامی، هادی صمیمی اخیجهانی، سمیرا زارعی، محمد صفوتی

بهینه‌سازی تیغه برش دروگر برداشت کلزا با رویکرد کاهش مصرف انرژی و ارزیابی چرخه زیست ۵۴۸
قانع احمدزاده، محمدرضا ملکی، پیمان سلامی، کاوه ملازاده

ویژگی‌های فیزیکی ارقام ذرت اتیوپی برای طراحی دستگاه کاشت سازگار با چند محصول ۵۶۱
دجنه گِرما گادیسا، کیشور پوروشوتام کوله، سراج کدیر بوسه، مبارک محمد عیسی، تسفایه آسِفا آبَیه، درجه آلمو اناوته

امکان‌سنجی تشخیص ژنوتیپ‌های مختلف گیاه نعنا با تکنیک E-Nose ۵۷۸
حسن ذکی دیزجی، محمد محمودی سورستانی، ناهید عقیلی ناطق، آناهیتا بویری ده شیخ

مدل‌سازی مقایسه‌ای سینتیک خشک‌کردن برش‌های سیب‌زمینی: روش‌های مبتنی بر هوش مصنوعی در مقایسه با روش‌های تجربی و نیمه‌تجربی ۵۹۷
رضا رئیسی، مهدی مرادی، علیرضا دهقانی

مقالات مروری

مروری بر خواص فیزیکومکانیکی فیلم‌های خوراکی بر پایه پلی‌ساکارید شامل امولسیون‌های پیکرینگ حاوی اسانس ۶۲۴
حسین میرزایی مقدم، آرین نهالکار، احمد رجایی

نشریه ماشین های کشاورزی

با شماره پروانه ۸۹/۱۲۶۳۹ **و درجه علمی – پژوهشی شماره** ۳/۱۱/۳۷۸۱ **از وزارت علوم، تحقیقات و فناوری**

۸۹/۶/۱۳ **۸۹/۳/۱۷**

"بر اساس مصوبه وزارت عتف از سال ۱۳۹۸، کلیه نشریات دارای درجه "علمی-پژوهشی" به نشریه "علمی" تغییر نام یافتند."

جلد ۱۶ شماره ۳ پاییز ۱۴۰۵

صاحب امتیاز: دانشگاه فردوسی مشهد

مدیر مسئول: سید محمدرضا مدرس رضوی — استاد- گروه مکانیک دانشکده مهندسی (دانشگاه فردوسی مشهد)

سردبیر: محمدحسین عباسپور فرد — استاد- گروه مهندسی مکانیک بیوسیستم (دانشگاه فردوسی مشهد)

اعضای هیئت تحریریه:

آق خانی، محمدحسین	گروه مهندسی بیوسیستم، دانشکده کشاورزی، دانشگاه فردوسی مشهد، مشهد، ایران
آغباشلو، مرتضی	گروه مهندسی ماشین‌های کشاورزی، دانشگاه تهران، پردیس کرج، ایران
ابونجمی، محمد	گروه فنی کشاورزی، پردیس ابوریحان دانشگاه تهران، ایران
خوش تقاضا، محمدهادی	گروه مهندسی مکانیک بیوسیستم، دانشگاه تربیت مدرس، تهران، ایران
راجی، عبدالغنی	گروه مهندسی کشاورزی و محیط زیست، دانشکده فنی، دانشگاه ایبادان، نیجریه
روحانی، عباس	گروه مهندسی بیوسیستم، دانشکده کشاورزی، دانشگاه فردوسی مشهد، مشهد، ایران
سعیدی راد، محمدحسین	مرکز تحقیقات کشاورزی و منابع طبیعی خراسان رضوی، بخش تحقیقات فنی و منهدسی، مشهد، ایران
سوپاکیت، سایاسونترن	دانشکده کشاورزی، دانشگاه کاستسارت، تایلند
عباسپور فرد، محمدحسین	گروه مهندسی بیوسیستم، دانشکده کشاورزی، دانشگاه فردوسی مشهد، مشهد، ایران
علیمردانی، رضا	گروه مهندسی ماشین‌های کشاورزی، دانشگاه تهران، پردیس کرج، ایران
عمادی، باقر	گروه مهندسی شیمی و بیولوژیک، دانشگاه ساسکاچوان، ساسکاتون، کانادا
غضنفری مقدم، احمد	گروه مهندسی مکانیک بیوسیستم، دانشگاه شهید باهنر کرمان، کرمان، ایران
کدخدایان، مهران	گروه مهندسی مکانیک، دانشکده مهندسی، دانشگاه فردوسی مشهد، مشهد، ایران
لغوی، محمد	گروه مهندسی بیوسیستم، دانشگاه شیراز، ایران
محتسبی، سید سعید	گروه مهندسی ماشین‌های کشاورزی، دانشگاه تهران، پردیس کرج، ایران
مدرس رضوی، محمدرضا	گروه مهندسی مکانیک، دانشکده مهندسی، دانشگاه فردوسی مشهد، مشهد، ایران
نصیراحمدی، ابوذر	گروه مهندسی کشاورزی، دانشگاه کاسل، آلمان

ناشر: دانشگاه فردوسی مشهد

مقالات این نشریه در پایگاه‌های معتبر زیر نمایه می‌شود:

AGRIS، Scopus، Web of Science: Emerging Sources Citation Index™ (ESCI)، CABI، DOAJ، EBSCO، Google scholar، Internet Archive، پایگاه استنادی جهان اسلام (ISC)**، سامانه نشریات علمی ایران و پایگاه اطلاعات علمی جهاد دانشگاهی** (SID)

پست الکترونیک: jame@um.ac.ir

مقالات این شماره در سایت http://jame.um.ac.ir **به‌صورت مقاله کامل نمایه شده است.**

این نشریه به تعداد ۴ شماره در سال و به‌صورت آنلاین منتشر می‌شود.

انجمن مهندسان مکانیک ایران

نشریه علمی
ماشین های کشاورزی

دانشگاه فردوسی مشهد

جلد۱۶ شماره ۳
سال ۱۴۰۵
(شماره پیاپی: ۴۱)

شاپا: ۶۸۲۹-۲۲۲۸

عنوان مقالات

مقالات پژوهشی

ارزیابی پتانسیل تصاویر ماهواره‌ای چندطیفی سنتینل-۲ برای شناسایی هجوم آفت زنجرک در مناطق کشت نخل خرما..... ۳۸۱
هادی کریمی، محمدجواد عصاری، هادی زهدی، فروغ رنجبر ورندی

بهینه‌سازی مصرف انرژی در سامانه‌های کاشت لوبیا چیتی: با رویکرد الگوریتم ژنتیک چندهدفه..... ۳۹۷
رضا رئیسی، محمد غلامی پرشکوهی، حامد افشاری، احمد محمدی

بهبود و تحلیل اجزای دستگاه یکپارچه فرآوری محصول Enset با نام علمی *Ensete ventricosum*..... ۴۲۵
بکا آدوگنا، کیشور پوروشوتام کوله، موئرا گوتو

ارزیابی ویسکوزیته و سطوح آلاینده در روان‌کننده دیزل از طریق طیف‌سنجی دی‌الکتریک با استفاده از روش‌های محاسباتی نرم..... ۴۴۷
محمدرضا پوررمضان، عباس روحانی، محمدحسین عباسپورفرد

بررسی نرخ و شدت حوادث مربوط به تراکتورهای کشاورزی و کمباین‌های غلات و عوامل مؤثر بر آن در استان ایلام..... ۴۶۷
جلال اله نوری، افشین مرزبان، محمود قاسمی نژاد رائینی، مجید رهنما[1]، مسلم سواری

پیش‌بینی ویتامین C و تغییر رنگ پودر پرتقال در چهار خشک‌کن مختلف با استفاده از بینی الکترونیک..... ۴۸۶
مازیار روشن مقدم، رضا امیری چایجان، ناهید عقیلی ناطق

مدل یادگیری گروهی وزن‌دار برای طبقه‌بندی بیماری برگ انگور با استفاده از پردازش تصویر و یادگیری ماشینی..... ۵۰۶
محسن نجف‌آبادی‌ها، داود محمدزمانی، محمد غلامی پرشکوهی

بررسی تاثیر ترکیب نانوذرات اکسید مس و آب مقطر بر راندمان یک سامانه فتوولتاییک حرارتی..... ۵۲۳
مهری قادری، پیمان سلامی، هادی صمیمی اخیجهانی، سمیرا زارعی، محمد صفوتی

بهینه‌سازی تیغه برش دروگر برداشت کلزا با رویکرد کاهش مصرف انرژی و ارزیابی چرخه زیست..... ۵۴۸
قانع احمدزاده، محمدرضا ملکی، پیمان سلامی، کاوه ملازاده

ویژگی‌های فیزیکی ارقام ذرت اتیوپی برای طراحی دستگاه کاشت سازگار با چند محصول ۵۶۱
دجنه گِرما گادیسا، کیشور پوروشوتام کوله، سراج کدیر بوسه، مبارک محمد عیسی، تسفایه آسِفا آبیه، درجه آلمو اناوته

امکان‌سنجی تشخیص ژنوتیپ‌های مختلف گیاه نعنا با تکنیک E-Nose..... ۵۷۸
حسن ذکی دیزجی، محمد محمودی سورستانی، ناهید عقیلی ناطق، آناهیتا بویری ده شیخ

مدل‌سازی مقایسه‌ای سینتیک خشک‌کردن برش‌های سیب‌زمینی: روش‌های مبتنی بر هوش مصنوعی در مقایسه با روش‌های تجربی و نیمه‌تجربی..... ۵۹۷
رضا رئیسی، مهدی مرادی، علیرضا دهقانی

مقاله مروری

مروری بر خواص فیزیکومکانیکی فیلم‌های خوراکی بر پایه پلی‌ساکارید شامل امولسیون‌های پیکرینگ حاوی اسانس..... ۶۲۴
حسین میرزایی مقدم، آرین نهالکار، احمد رجایی